Constraint Effects in Fracture

Hackett/Schwalbe/Dodds, editors

STP 1171

ASTM

STP 1171

Constraint Effects in Fracture

E. M. Hackett, K.-H. Schwalbe, and R. H. Dodds, Jr., editors

ASTM Publication Code Number (PCN)
04-011710-30

ASTM
1916 Race Street
Philadelphia, PA 19103

Library of Congress Cataloging in Publication Data

Constraint effects in fracture/E.M. Hackett, K.-H. Schwalbe, R.H.
Dodds, editors.
p. cm.—(STP;1171)
"ASTM publication code number (PCN)
Contains papers presented at the symposium held in Indianapolis on
8–9 May 1991.
Includes bibliographical references and index.
ISBN 0-8031-1481-8
1. Fracture mechanics. 2. Micromechanics. 3. Continuum
mechanics. I. Hackett, E. M. II. Schwalbe, K.-H. (Karl-Heinz)
III. Dodds, R. H. (Robert H.), 1955- . IV. Series: ASTM special
technical publication : 1171.
TA409.C66 1993
620.1′126—dc20 92-42112
CIP

Peer Review Policy

Each paper published in this volume was evaluated by three peer reviewers. The authors addressed all of the reviewers' comments to the satisfaction of both the technical editor(s) and the ASTM Committee on Publications.

The quality of the papers in this publication reflects not only the obvious efforts of the authors and the technical editor(s), but also the work of these peer reviewers. The ASTM Committee on Publications acknowledges with appreciation their dedication and contribution to time and effort on behalf of ASTM.

Printed in Baltimore, MD
March 1993

Foreword

This publication, *Constraint Effects in Fracture,* contains papers presented at the symposium of the same name held in Indianapolis, Indiana on 8–9 May 1991. The symposium was sponsored by ASTM Committee E-24 on Fracture Testing in cooperation with the European Structural Integrity Society (ESIS), a multinational group that oversees the development of new fracture standards for the European community. Edwin M. Hackett, U.S. Nuclear Regulatory Commission, was chairman of the symposium. Karl-Heinz Schwalbe, GKSS Research Center, Federal Republic of Germany, and Robert H. Dodds, Jr., University of Illinois, acted as co-chairmen.

Contents

Overview

The science of fracture mechanics has experienced rapid advancement during the past decade with significant contributions in the areas of experimental mechanics, numerical modeling, applications, and micro-mechanical effects. This rapid advancement comes at a time when economic considerations in government and industry have necessitated extension of the "service lives" of engineering structures. A consequence of service life extension has been an increased use of fracture mechanics to defer repairs or retirement of structures or components. Application of fracture mechanics in such instances is hindered by the inability of small specimen testing, coupled with structural analysis, to accurately describe the fracture behavior of large-scale structures containing flaws. In fracture mechanics terms, this is generally regarded as a consequence of improperly accounting for crack tip and/or structural "constraint."

The purpose of the symposium was to provide a forum for an exchange of ideas on constraint effects in fracture, and to provide a focus for future work in this area. This volume includes a collection of papers that serve as a state-of-the-art review of the technical area. The volume will be useful to researchers in fracture mechanics and to engineers applying fracture mechanics in design, failure analysis, and life extension. Work presented in this volume provides a framework for quantifying constraint effects in terms of both continuum mechanics and micro-mechanical modeling approaches. Such a framework is useful in establishing accurate predictions of the fracture behavior of large structures (e.g., pressure vessels, pipelines, offshore platforms) subjected to complex loading.

The chairmen would like to acknowledge the assistance of Dorothy Savini of ASTM in the planning and smooth execution of the symposium, and Monica Siperko and Rita Hippensteel of ASTM for their guidance and assistance during the review process. We are grateful to M. T. Kirk of DTRC, Annapolis, Maryland and J. A. Joyce of the U.S. Naval Academy, Annapolis, Maryland for assistance in organizing the symposium and for technical review of the program.

The chairmen also thank the authors for their presentations and for submitting the papers which comprise this publication. The outstanding presentations and lively discussions by the authors and attendees created a very stimulating atmosphere during the symposium. We would especially like to thank the reviewers for their critiques of the papers submitted for this volume. Their careful reviews helped ensure the quality and professionalism of this special technical publication.

E. M. Hackett

U.S. Nuclear Regulatory Commission, Washington, DC; symposium chairman and co-editor

K.-H. Schwalbe

GKSS Research Center, Federal Republic of Germany; symposium co-chairman and co-editor

R. H. Dodds, Jr.

University of Illinois, Urbana, IL; symposium co-chairman and co-editor

C. Fong Shih,[1] Noel P. O'Dowd,[1] and Mark T. Kirk[2]

A Framework for Quantifying Crack Tip Constraint

REFERENCE: Shih, C. F., O'Dowd, N. P., and Kirk, M. T. "**A Framework for Quantifying Crack Tip Constraint,**" *Constraint Effects in Fracture, ASTM STP 1171,* E. M. Hackett, K.-H. Schwalbe, and R. H. Dodds, Eds., American Society for Testing and Materials, Philadelphia, 1993, pp. 2–20.

ABSTRACT: The terms high and low constraint have been loosely used to distinguish different levels of near tip stress triaxiality in different crack geometries. In this paper, a precise measure of crack tip constraint is provided through a stress triaxiality parameter Q. It is shown that the J-integral and Q are sufficient to characterize the full range of near-tip fracture states. Within this framework J and Q have distinct roles: J sets the size scale over which large stresses and strains develop, while Q scales the near-tip stress distribution relative to a reference high triaxiality state. Specifically, negative (positive) Q values mean that the hydrostatic stress ahead of the crack is reduced (increased) by $Q\sigma_0$ from the plane strain reference distribution.

The evolution of near-tip constraint as plastic flow progresses from small-scale yielding to fully yielded conditions is examined. It is shown that the Q parameter adequately characterizes the full range of near-tip constraint states in several crack geometries. Through-thickness deformation and stress conditions affect near-tip triaxiality. Stress triaxiality near a three-dimensional crack front is measured by pointwise values of Q.

The J-Q theory provides a framework that allows the toughness locus to be measured and utilized in engineering applications. A method for evaluating Q in fully yielded crack geometries and a scheme to interpolate for Q over the entire range of yielding are presented. Extension of the J-Q theory to creep crack growth is discussed in the concluding section.

KEY WORDS: fracture, elastic-plastic fracture, fracture toughness, crack tip fields, constraint, stress triaxiality, small-scale yielding, large-scale yielding, finite element method

The idea underlying a one-parameter fracture mechanics approach is that a crack tip singularity dominates over microstructurally significant size scales and that the amplitude of this singularity serves to correlate crack initiation and growth. In elastic-plastic fracture mechanics this is the notion of J-dominance, whereby J alone sets the stress level as well as the size scale of the zone of high stresses and strains that encompasses the process zone. There is now general agreement that the applicability of the J-approach is limited to so-called high constraint crack geometries. A framework to address fracture covering a broad range of loading and crack geometries is discussed in this article. Within this framework J scales the zone of large stresses and strains (or process zone) while a second parameter Q scales the near-tip stress distribution relative to a reference high triaxiality stress state.

The existence of a Q-family of self-similar fields can be shown by dimensional analysis. This family of fields has been constructed by using a modified boundary layer analysis. More importantly, the full range of near-tip states associated with different fully yielded crack geometries

[1] Professor of engineering and graduate student, respectively, Division of Engineering, Brown University, Providence, RI 02912.

[2] Mechanical engineer, Fatigue and Fracture Branch, David Taylor Research Center, Annapolis, MD 21402.

has been identified with members of the Q-family of solutions [1,2]. The J-Q theory is discussed in this paper. Contact is made with related approaches as well as procedures involving the T-stress [3–9].

The plan of this paper is as follows. In the next section, the Q-family of fields is introduced. Near-tip constraint or stress triaxiality is defined in terms of the Q parameter. Under small-scale yielding there is a one-to-one relationship between Q and T-stress in the Williams' eigenfunction expansion. This is discussed in the section on small-scale yielding results. Then, the evolution of near-tip constraint in finite width crack geometries loaded to fully yielded conditions is examined, followed by a section concerned with methods for evaluating Q over a wide range of loading conditions. Cleavage toughness data for A515 steels from differently sized specimens are ordered into a J-Q toughness locus. An outline of constraint notions for three-dimensional crack geometries and creep crack growth concludes this paper.

J-Q Theory

Fracture mechanics provides a framework to correlate fracture data from small specimens and to use such data to predict failure of typically larger-sized flawed structural components. To accomplish this, elastic-plastic solutions are used to interpret the test data, which in turn are used in conjunction with elastic-plastic solutions or elasticity solutions (when small-scale yielding conditions are appropriate) to predict failure of the structure. Because of this, fracture mechanics necessarily involves quantifying near-tip fracture states over conditions ranging from small- to large-scale yielding. Thus, a small-scale yielding analysis is a natural starting point for our discussion.

Q-Family of Fields

The Q-family of fields can be constructed from a modified boundary layer formulation in which the remote tractions are given by the first two terms of the small-displacement-gradient linear elastic solution (Williams [9])

$$\sigma_{ij} = \frac{K_I}{\sqrt{2\pi r}} \tilde{f}_{ij}(\theta) + T\delta_{1i}\delta_{1j} \tag{2.1}$$

Here σ_{ij} is the Kronecker delta and r and θ are polar coordinates centered at the crack tip with $\theta = 0$ corresponding to a line ahead of the crack. Cartesian coordinates, x and y with the x-axis running directly ahead of the crack, are used when it is convenient.

Let σ_0 be the yield stress of the material. Different near-tip fields are obtained by applying different combinations of the loading parameters, K_I and T. Now observe that T has the dimension of stress. Therefore K_I/σ_0 or equivalently J/σ_0, where J is Rice's J-integral [12], is the only length scale in the modified boundary layer formulation. Consequently, displacements and quantities with dimensions of length must scale with J/σ_0. Furthermore, the fields can depend on distance only through $r/(J/\sigma_0)$, that is, the fields are of the form

$$\sigma_{ij} = \sigma_0 \tilde{f}_{ij}\left(\frac{r}{J/\sigma_0}, \theta; T/\sigma_0\right) \tag{2.2}$$

T-stress effects on the near-tip field have been investigated by Betegón and Hancock [5], Bilby et al. [6], and Harlin and Willis [7]. However, the representation in Eq 2.2 is not suited for applications to full-yielded crack geometries because T-stress has no relevance under fully yielded conditions.

Looking ahead to applications to fully yielded crack geometries, it is helpful to identify members of the above family by a parameter Q that arises naturally in the plasticity analysis. O'Dowd and Shih [1,2], hereafter referred to as OS, write

$$\sigma_{ij} = \sigma_0 f_{ij}\left(\frac{r}{J/\sigma_0}, \theta; Q\right), \qquad \epsilon_{ij} = \epsilon_0 g_{ij}\left(\frac{r}{J/\sigma_0}, \theta; Q\right), \qquad u_i = \frac{J}{\sigma_0} h_i\left(\frac{r}{J/\sigma_0}, \theta; Q\right) \tag{2.3}$$

where the additional dependence of f_{ij}, g_{ij} and h_i on dimensionless combinations of material parameters is understood. The form in Eq 2.3 constitutes a one-parameter family of self-similar solutions or, in short, a Q-family of solutions. Indeed, one member of the Q-family has received much attention. This is the self-similar solution of McMeeking [8].

It can be argued that near-tip fields of finite width crack bodies must also obey the form of Eq 2.3 provided that the characteristic crack dimension L is much larger than J/σ_0. This argument relies on the material possessing sufficient strain-hardening capacity so that the governing equations remain elliptic as the plastic deformation spreads across the body.

The form in Eq 2.3 is also applicable to generalized plane strain and three-dimensional tensile mode crack tip states. This assertion can be rationalized by considering a neighborhood of the crack front, which is sufficiently far away from its intersection with the external surface of the body. As $r \rightarrow 0$, the three-dimensional fields approach the two-dimensional fields given by Eq 2.3 so that the Q-family of solutions still applies. We should add that the Q-fields exist within small strain as well as finite strain treatment of near-tip behavior.

Asymptotic Expansion Under Small-Strain Assumption

Consider the following asymptotic expansion for power law hardening materials within a small-displacement gradient formulation

$$\frac{\sigma_{ij}}{\sigma_0} = \left(\frac{J}{\alpha\epsilon_0\sigma_0 I_n r}\right)^{1/(n+1)} \tilde{\sigma}_{ij}(\theta; n) + Q\left(\frac{r}{J/\sigma_0}\right)^q \hat{\sigma}_{ij}(\theta; n) + \text{higher order terms} \tag{2.4}$$

The material constants in Eq 2.4 pertain to the Ramberg-Osgood stress-strain relation where σ_0 is the yield stress, ϵ_0 the reference strain ($\epsilon_0 = \sigma_0/E$, E is the Young's modulus), n the strain-hardening exponent, and α a material constant. The first term in the above expansion is the Hutchinson-Rice-Rosengren (HRR) singularity (Hutchinson [10], Rice and Rosengren [11], which is scaled by J (Rice [12]). J-dominance implies that the first term in Eq 2.4 sets the stress level and the size scale of the high stress and strain zone (McMeeking and Parks [13], Shih and German [14], and Hutchinson [15]).

The second order term in Eq 2.4 was obtained by Li and Wang [3] and Sharma and Aravas [4] as a solution to a linear eigenvalue problem arising from a perturbation analysis in which the HRR field served as the leading order solution. Q, an arbitrary dimensionless parameter scaling the second order term, can be determined by matching Eq 2.4 with small-scale yielding solutions to the modified boundary layer problem (Eq 2.1) or full-field solutions for finite-width crack geometries. These investigators have established that the second order stress term in Eq 2.4 is nonsingular and weakly dependent on the radial distance r, that is, $0 < q \ll 1$ for $n > 4$. Li and Wang have proposed to characterize the full range of near-tip states by using the two-term expansion in Eq 2.4. Careful numerical studies by Sharma and Aravas indicate that in general the region of dominance of the two-term expansion is larger than that of the leading term. However, their results also suggest that more than two terms in the expansion (Eq 2.4) are required to represent accurately the stresses in the angular sector $|\theta| < 60°$ ahead of the crack. Thus the advantage that is gained by using the two-term expansion in Eq 2.4 is unclear.

Difference Field and Near-Tip Constraint

OS took a different approach for characterizing the full range of near-tip environment. They obtained small-scale yielding solutions to the modified boundary layer problem (Eq 2.1) and considered these as exact solutions. The solutions were obtained by finite element analysis, the details of which are outlined in Refs *1* and *2*. They then systematically investigated the difference between these exact solutions and the HRR field in an annular region $J/\sigma_0 < r < 5J/\sigma_0$. These fields are referred to as difference fields in the ensuing discussion.

The approach advocated by OS differs from that proposed by Li and Wang [*3*] in one important respect. This can be understood in the context of the modified boundary layer formulation described earlier. The sum of the second order solution and the HRR field in Eq 2.4 only provides a two-term approximation to the modified boundary layer problem. In contrast, the sum of the difference field and the HRR field provides the exact solution to the modified boundary layer problem. Stated another way, the difference field can be regarded as equivalent to the sum of second and higher order terms in Eq 2.4.

Remarkably, the difference field determined in the manner described above is effectively independent of distance r. Taking note of this behavior, OS writes

$$\sigma_{ij} = (\sigma_{ij})_{\mathrm{HRR}} + Q\sigma_0\hat{\sigma}_{ij}(\theta) \tag{2.5}$$

where the first term is the HRR field. The difference field is parameterized by Q. The definition of Q in Eq 2.5 is the one used in Ref *1* and *2* and is different from the one given in Eq. 2.4. It is convenient to normalize the angular functions $\hat{\sigma}_{ij}$ by requiring $\hat{\sigma}_{\theta\theta}(\theta = 0)$ to equal unity. Additionally, OS noticed that within the forward section $|\theta| < \pi/2$, the angular functions exhibit these features: $\hat{\sigma}_{rr} \approx \hat{\sigma}_{\theta\theta} \approx$ constant and $|\hat{\sigma}_{r\theta}| \ll |\hat{\sigma}_{\theta\theta}|$ (see Figs. 3, 4, and 5 in Ref *1*). We note that the form in Eq 2.5 is consistent with a four-term asymptotic expansion recently obtained by Xia et al. [*33*].

In summary, the difference field within the forward sector $|\theta| < \pi/2$ possesses a surprisingly simple structure. It effectively corresponds to a uniform hydrostatic stress in that sector. Therefore, Q defined by

$$Q \equiv \frac{\sigma_{\theta\theta} - (\sigma_{\theta\theta})_{\mathrm{HRR}}}{\sigma_0} \quad \text{at} \quad \theta = 0,\ r = 2J/\sigma_0 \tag{2.6}$$

is a natural measure of near-tip triaxiality relative to a reference stress state. For definiteness, Q is evaluated at $r|(J/\sigma_0) = 2$; however, we point out that Q is effectively independent of distance. Stated in words, Q represents the difference between the actual hoop stress evaluated outside the finite strain zone and the corresponding HRR stress component evaluated at the same location normalized by σ_0.

To fix ideas, hydrostatic stress distributions identified by different Q-values are shown in Fig. 1. The $Q = 0$ distribution is indicated by the solid line in Figs. 1*a* and 1*b*. These distributions support the interpretation of Q as a hydrostatic stress parameter.

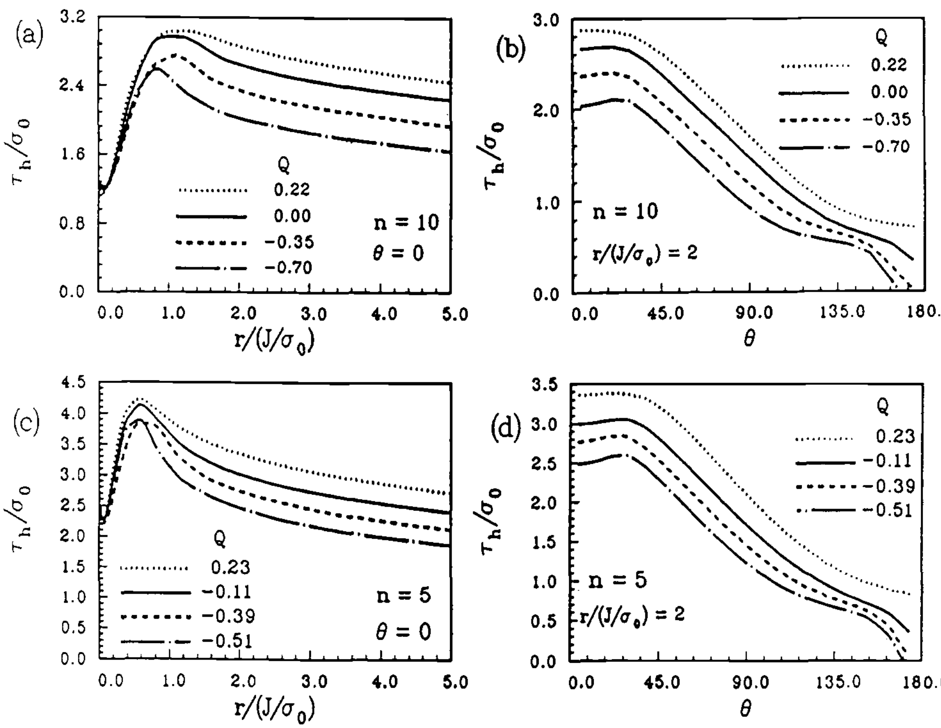

FIG. 1—*Hydrostatic stress distributions for a range of* Q: (a) *and* (b) n = *10*, (c) *and* (d) n = *5. These results were generated by a finite deformation analysis where the Kirchhoff stress is the convenient stress measure. For metals the Kirchhoff stress,* τ, *and Cauchy stress,* σ, *are approximately equal.*

Simplified Forms of the Q*-Family of Fields*

Two simplified forms for the Q-family of fields have been proposed by OS. The first form uses the plane strain HRR field as the reference distribution

$$\sigma_{ij} = (\sigma_{ij})_{\text{HRR}} + Q\sigma_0\delta_{ij} \quad \text{for} \quad |\theta| < \pi/2 \tag{2.7}$$

The second form uses the standard small-scale yielding distribution as the reference solution

$$\sigma_{ij} = (\sigma_{ij})_{\text{SSY}} + Q\sigma_0\delta_{ij} \quad \text{for} \quad |\theta| < \pi/2 \tag{2.8}$$

where the $(\sigma_{ij})_{\text{SSY}}$ distribution is the small-scale yielding solution driven by K alone (with T = 0). The physical interpretation of the form in Eqs 2.7 and 2.8 is this: *negative (positive) Q values mean that the hydrostatic stress is reduced (increased) by $Q\sigma_0$ from the J-dominant state, or Q = 0 state.*

By virtue of its definition in Eq 2.6, member fields of Eqs 2.7 and 2.8 with the same Q value have the same stress triaxiality at $r/(J/\sigma_0) = 2$. At other distances, however, the stresses given by Eq 2.7 can differ slightly from those of Eq 2.8. Our numerical studies indicate that Eq 2.8 provides a more accurate representation of the Q-family of fields.

The approximate representations Eqs 2.7 and 2.8 were introduced to simplify the calculation of Q in finite width crack geometries and its interpretation as a hydrostatic stress param-

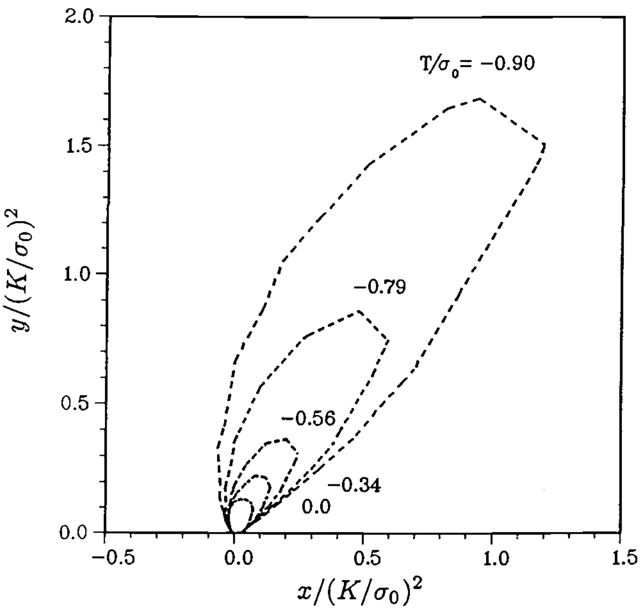

FIG. 2—*Plastic zones from modified boundary layer analysis for negative* T*-stresses.*

eter. The approximate nature of these explicit forms does not deny the existence of the Q-fields, which can be deduced from dimensional grounds.

Reference Field: Small Strain Versus Finite Strain

A reference distribution determined from a small-displacement-gradient formulation is adequate for most applications. However, some applications require accurate quantification of the field near and within the zone of finite strains, for example, quantitative studies on the micromechanisms of ductile failure and cleavage fracture. For such applications the reference distribution could be established by a finite deformation analysis. By using the finite strain distribution as the reference solution, the region of dominance of Eq 2.8 is extended for some distance inside the finite strain zone (this can be seen from the distributions given in Refs *1,2*). In any case we should point out that the difference between finite strain and small strain reference distributions is negligible at radial distances greater than about $2J/\sigma_0$ (see Fig. 2 in Ref *1*). The annular zone over which Eqs 2.7 or 2.8 accurately quantify the actual field is called the J-Q annulus.

Small-Scale Yielding Results

Plastic Zone Size

The plastic zones for positive T values are shown in Fig. 2, while those for negative T values are shown in Fig. 3. The distances are normalized by $(K_I/\sigma_0)^2$. It can be seen that at large negative T values, the plastic zones can be as much as ten times larger than that for $T = 0$. These features have also been reported by Larsson and Carlsson [*16*] and Rice [*17*]. The effect of positive T-stresses is less dramatic. We note that solutions for $|T/\sigma_0| > 1$ cannot be generated

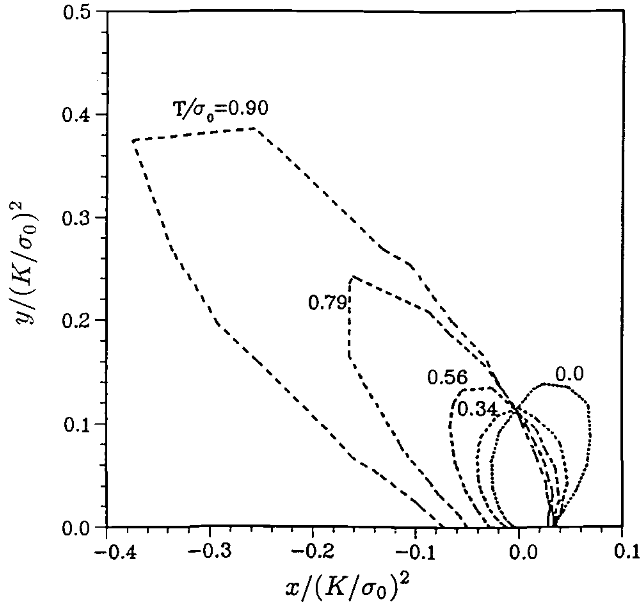

FIG. 3—*Plastic zones from modified boundary layer analysis for positive* T-*stresses.*

by the present boundary layer formulation since in this case the plastic zone extends to the remote boundary. The spatial extent of the plastic zone can be written in the form

$$r_p = \Lambda(T/\sigma_0)\left(\frac{K_I}{\sigma_0}\right)^2 \tag{3.1}$$

A plot of Λ versus T/σ_0 is shown in Fig. 4 for an $n = 10$ material. Note that Λ increases rapidly for large negative T/σ_0. ASTM standards for a valid K_{IC} test require the plastic zone size at fracture to be less than a fraction of the relevant crack dimension. r_p is estimated by Eq 3.1 with $\Lambda = 0.16$. This Λ value is nonconservative for large negative Ts since $\Lambda > 0.3$ for $T/\sigma_0 < -0.5$.

Q-T *Relation*

Within the modified boundary layer formulation (2.1), J and K are related by

$$J = \frac{1 - \nu^2}{E} K_I^2 \tag{3.2}$$

Using a dimensional argument Q can be shown to depend only on T [*1,2*], that is

$$Q = F(T/\sigma_0;\, n) \tag{3.3}$$

Solutions to the modified boundary layer formulation (Eq. 2.1) for an admissible range of T-values show that F is a monotonically increasing function of T/σ_0. Strain hardening n and other dimensionless combinations of material parameters affect F weakly.

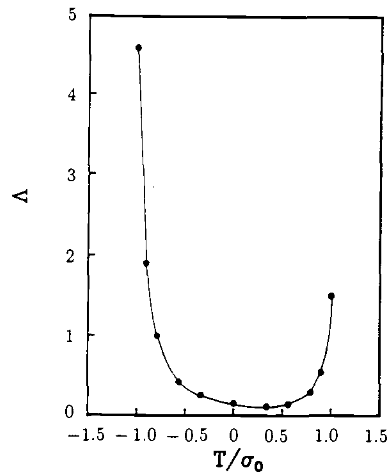

FIG. 4—$\Lambda (\equiv r_p/(K_I/\sigma_0)^2)$ *versus* T/σ_0 *from the modified boundary layer analysis.*

Figure 5 shows the range of Q values for $n = 5$ and 10 materials ($E/\sigma_0 = 300$ and Poisson's ratio $\nu = 0.3$) for $|T/\sigma_0| \leq 1$ [2]. It can be seen that the stress triaxiality can be significantly lower than the HRR value, or the $Q = 0$ distribution, but cannot be much above it. The weak dependence of Q on the hardening exponent is also noted. Using a least square fit, the curves in Fig. 5 can be approximated closely by

$$Q = a_1\left(\frac{T}{\sigma_0}\right) + a_2\left(\frac{T}{\sigma_0}\right)^2 + a_3\left(\frac{T}{\sigma_0}\right)^3 \tag{3.4}$$

For $n = 10$, $a_1 = 0.76$, $a_2 = -0.52$, and $a_3 = 0$, and for $n = 5$, $a_0 = -0.1$, $a_1 = 0.76$, $a_2 = -0.32$, and $a_3 = -0.01$. Betegón and Hancock [5] have provided a relation between the near-tip hoop stress and T which is consistent with Eq 3.4. We must emphasize that both relationships are based on small-scale yielding.

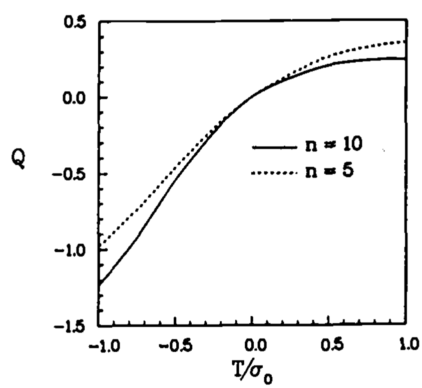

FIG. 5—Q-T *relation from the modified boundary layer analysis for* n = *5 and 10.*

Finite Width Crack Geometries

The geometries are shown in Fig. 6. The center-cracked panel is loaded in biaxial tension. Stress biaxiality is given by the ratio $\sigma_{xx}^{\infty}/\sigma_{yy}^{\infty}$. The edge-cracked bend bar geometry is loaded by remote moment. Shallow and deep crack geometries are investigated. A crack is considered shallow if the crack length is the relevant dimension. It is considered as deeply cracked if the ligament is the relevant dimension.

The evolution of near-tip constraint with increasing plastic flow in the two crack geometries is shown in Fig. 7. These solutions were obtained by finite element analysis as described in Ref *1* and *2*; J is evaluated using the domain integral method described in Ref *32*. For shallow cracks the extent of plastic yielding is measured by $J/(a\sigma_0)$ while $J/(b\sigma_0)$ is used for deep cracks. Results for center-cracked panels with $a/W = 0.1$ and 0.7 and several biaxiality ratios are plotted in Figs. 7*a* and 7*b*. The rapid loss of constraint with increasing plastic flow under zero biaxiality contrasts sharply with the slight elevation of constraint for the highest biaxiality ratios.

Figures 7*c* and 7*d* show the Q values for the bend bar for $a/W = 0.1$, 0.3, and 0.5; Q is evaluated at $r/(J/\sigma_0) = 1$ and 2. In the case of $a/W = 0.5$, it can be seen that Q values at fully yielded conditions are somewhat sensitive to the choice of distance. Though not shown, a similar trend was observed for $a/W = 0.7$. The sensitivity of Q to the choice of distance can be explained by the high gradient of the hoop stress across the ligament. The hoop stress is compressive at the free surface and increases rapidly to a tensile state as the crack tip is approached. Thus the Q term, which represents a state of uniform hydrostatic stress in the forward sector, has a small region of dominance. Loss of constraint becomes rapid when the global bending stress distribution impinges on the near-tip region $r \approx 2J/\sigma_0$. This occurs in deeply cracked geometries for $J/(b\sigma_0) > 0.04$.

The reduction of the hydrostatic stresses as plastic flow spreads across the ligaments of the center-cracked panels loaded under zero stress biaxiality is shown in Figs. 8*a* and 8*b*. These angular distributions for the short and deep crack geometries at $r/(J/\sigma_0) = 2$ correspond to the

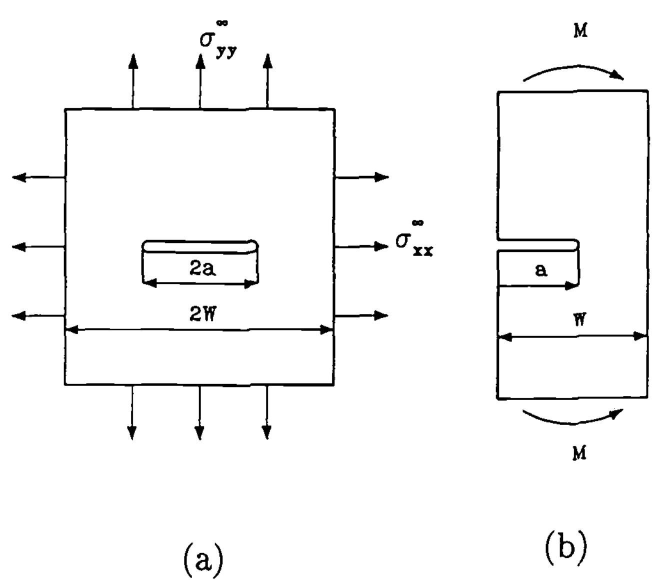

FIG. 6—*Geometries investigated:* (a) *biaxially loaded center-cracked panel and* (b) *edge-cracked bend bar.*

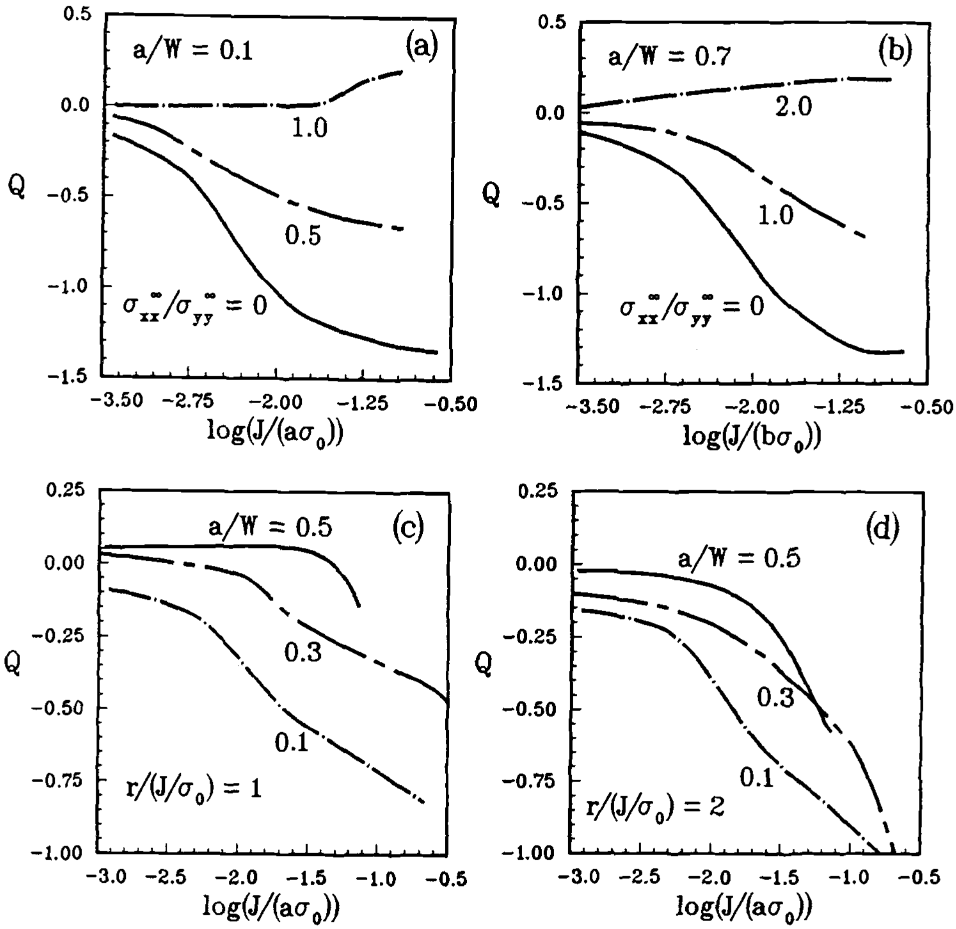

FIG. 7—*Evolution of* Q *with deformation as measured by* J: (a) *and* (b) *center-cracked panel for three biaxiality ratios,* (c) *and* (d) *edge-cracked bend bar.*

range of Q values in Figs. 7*a* and 7*b* and are representative of low triaxiality fields. Hydrostatic stress distributions for shallow and deep crack bend bars are displayed in Figs. 8*c* and 8*d*. The stress distributions in Fig. 8 strongly resemble the angular distributions in Figs. 1*b* and 1*d*, thus providing support for the existence of the Q-fields in these two crack geometries.

Methods for Evaluating Q

Q Estimates Under Contained Yielding

The one-to-one correspondence between Q and T was discussed earlier. Here we make advantageous use of this result and the known connection between T and the applied load to provide estimates of Q. For example, Leevers and Radon [*18*] and Sham [*19*] have calibrated the T-stress for a number of crack geometries in the following way

$$T = \frac{K}{\sqrt{\pi a}}\,\Sigma(\text{geometry}) \tag{5.1}$$

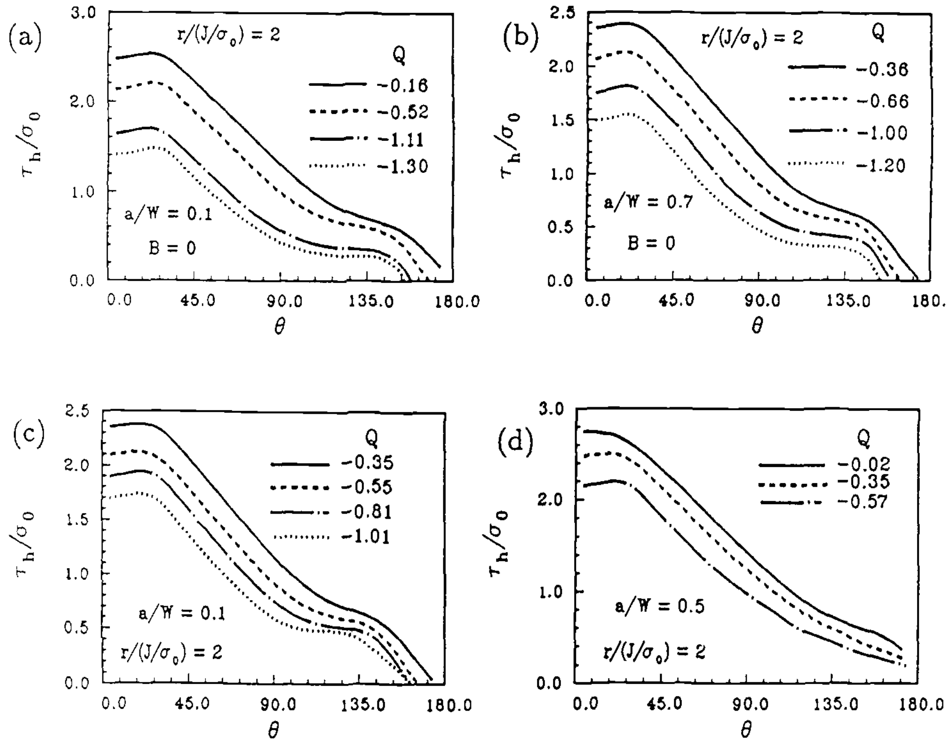

FIG. 8—*Angular distribution of hydrostatic stress for several* Q *values:* (a) *and* (b) *center-cracked panel,* (c) *and* (d) *edge-cracked bend bar.*

The dimensionless shape factor Σ depends only on dimensionless groups of geometric parameters. A more convenient representation is

$$T = \sigma^{\infty} h_T(\text{geometry}) \tag{5.2}$$

where σ^{∞} is a representative stress magnitude and the dimensionless function h_T depends only on dimensionless groups of geometric parameters. We combine Eqs 5.2 with 3.3 to get

$$Q_{SSY} = F_{\sigma}(\sigma^{\infty}/\sigma_0;\ \text{geometry},\ n) \tag{5.3}$$

F_{σ} depends on the normalized load, geometry, n, and combinations of material parameters, though the dependence on the latter is expected to be weak.

It must be emphasized that the Q-T relation (Eq 3.3) and the Q-σ^{∞} relation (Eq 5.3) are exact under small-scale yielding conditions. This has also been noted by Betegón and Hancock [5]. Both they and OS have demonstrated that Eq 3.3, or Eq 5.3, accurately predicts the evolution of constraint in edge-cracked bend bars and center-cracked panels under contained yielding conditions. These aspects are discussed in greater detail in Ref *2*. In addition, Betegón and Hancock have proposed to quantify crack tip constraint in fully yielded crack geometries in terms of T, though T is not defined under such conditions. Reliable methods which can provide accurate estimates of near-tip triaxiality over a broad range of loading and crack geometries is taken up in the next section.

Q Estimates Under Fully Yielded Conditions

Under fully plastic conditions Q can be determined from fully plastic crack solutions used in simplified engineering fracture analysis (Kumar, German, and Shih [*20*]). Consider a crack geometry of characteristic dimension L. The crack is loaded by σ^{∞}, a representative stress magnitude. The material obeys a pure power-law stress-strain relation. It then follows that the hoop stress ahead of the crack has the form [*20*]

$$\frac{\sigma_{\theta\theta}}{\sigma_0} = \frac{\sigma^{\infty}}{\sigma_0}\,\overline{\sigma}_{\theta\theta}\left(\frac{x}{L}\,;\ \text{geometry},\ n\right) \tag{5.4}$$

where $\overline{\sigma}_{\theta\theta}$ is a dimensionless function of normalized spatial position and depends only on geometry and strain-hardening exponent n.

The stress at the point $x = 2J/\sigma_0$ is given by

$$\frac{\sigma_{\theta\theta}}{\sigma_0} = \frac{\sigma^{\infty}}{\sigma_0}\,\overline{\sigma}_{\theta\theta}\left(\frac{2J}{\sigma_0 L}\,;\ \text{geometry},\ n\right) \tag{5.5}$$

Since $J/(\sigma_0 L) \propto (\sigma^{\infty}/\sigma_0)^{n+1}$ for a pure power-law material, we can combine σ^{∞}/σ_0 with the first argument in $\overline{\sigma}_{\theta\theta}$ in Eq 5.5 and use this form in Eq 2.6 to get the "fully plastic" Q

$$Q_{FP} = H_Q\left(\frac{J}{\sigma_0 L}\,;\ \text{geometry},\ n\right) \tag{5.6}$$

The dimensionless function H_Q depends on the load $J/\sigma_0 L$, dimensionless groups of geometric parameters, and n. If the fully plastic fields within the zone $r \leq 2J/\sigma_0$ converge onto a single distribution, then Q is given by its steady-state value, that is

$$Q_{SS} = h_Q(\text{geometry},\ n) \tag{5.7}$$

The steady-state constraint does not depend on the load level, that is, it is a property of the crack geometry.

Appropriately normalized J results have been catalogued in a fracture handbook [*20*]. These J results were extracted from full-field solutions for pure power-law crack problems. In a similar way Q_{FP} also can be extracted from these full-field solutions and catalogued in a handbook. An efficient numerical method for generating fully plastic crack solutions is described by Shih and Needleman [*21*]. Slip-line field solutions can be used to provide estimates of Q_{FP} and Q_{SS} for materials exhibiting little strain hardening ($n > 10$). This is discussed in Ref *2*.

Interpolating Between Q_{SSY} *and* Q_{FP}

Let $\mathcal{L}$ denote the generalized load and $\mathcal{L}_0$ the load at fully yielded conditions. Small-scale yielding will prevail as long as $\mathcal{L}$ is sufficiently small compared to $\mathcal{L}_0$, that is, the result in Eq 5.3 will be valid. At the other extreme, when $\mathcal{L}$ is equal to or greater than $\mathcal{L}_0$, the fully plastic solution (Eq 5.6) can be expected to be a good approximation. A scheme to interpolate over the entire range of yielding is outlined.

The dependence of Q_{SSY} on $\mathcal{L}$ is known from Eq 5.3, and so the slope $dQ_{SSY}/d\mathcal{L}$ can be determined. Moreover, the relationship between J and $\mathcal{L}$ is also known for small-scale yielding: $J \propto K_I^2 \propto \mathcal{L}^2$ (see Eq 3.2). Therefore, $dQ_{SSY}/d(J/\sigma_0 L)$ is available as well.

Under fully plastic conditions, Q is in general given by Eq 5.6 and the slope $dQ_{FP}/d(J/\sigma_0 L)$

can be evaluated from dependence of H_Q on the first argument. Since $J/(\sigma_0 L) \propto (\mathcal{L}/\mathcal{L}_0)^{(n+1)}$, we can also determine $dQ_{FP}/d\mathcal{L}$. If the crack geometry is one with a steady-state constraint, Q is given by Eq 5.7 and $dQ_{SS}/d(J/\sigma_0 L)$ is zero.

Using the above procedures we can determine Q_{SSY}, $dQ_{SSY}/d\mathcal{L}$ and Q_{FP}, $dQ_{FP}/d\mathcal{L}$, that is, the Q values and slopes at both ends of load states are known. The Q values for intermediate load states can be obtained by interpolation. Alternatively we regard Q as a function of J and interpolate for Q using Q_{SSY}, $dQ_{SSY}/d(J/\sigma_0 L)$ and Q_{FP}, $dQ_{FP}/d(J/\sigma_0 L)$. Both approaches are under investigation.

Fracture Toughness Data

Kirk *et al.* [23] have obtained cleavage toughness data for A515 steels at room temperature. They tested edge-cracked bend bars with thicknesses B = 10, 25.4, and 50.8 mm and various

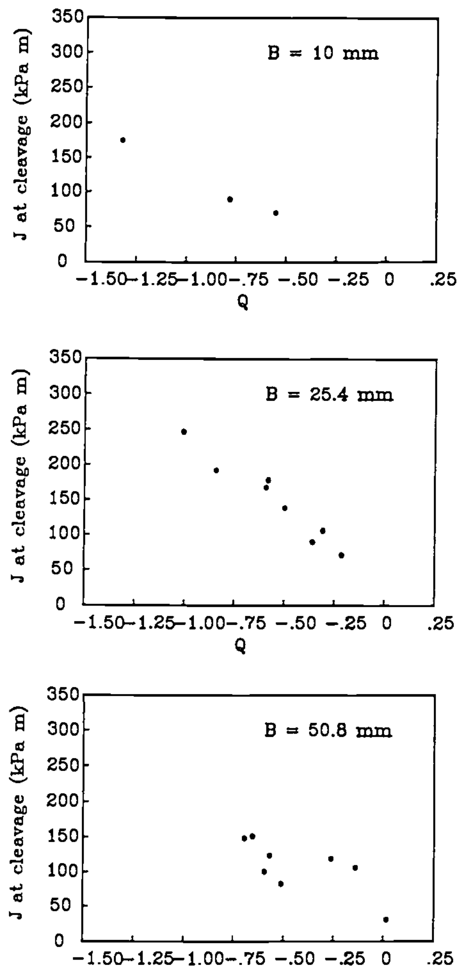

FIG. 9—*Fracture toughness versus Q for ASTM A515 Grade 70 steels at 20°C from edge-cracked bend bar for three thicknesses (Kirk et al.* [23]*).*

crack length-to-width ratios. They have shown plots of J at cleavage versus Q and T/σ_0. Their data are displayed in a more revealing form in Figs. 9 and 10. Figure 9 shows that for the B = 10 and 25.5-mm geometries, J at cleavage decreases monotonically as near-tip constraint increases. A similar trend is also observed for the thickest geometry, B = 50.8 mm, though the scatter is greater. The same data are plotted against T/σ_0 in Fig. 10. The trends are similar to those observed in Fig. 9 though the scatter appears somewhat larger.

One may be led to conclude on the basis of the data in Figs. 9 and 10 that J-Q and J-T toughness loci depend on specimen thickness. We should point out that the experimental data for both the thick and thin specimens were interpreted using J and Q solutions obtained from plane strain analysis. It is uncertain to what extent plane strain conditions apply to the near tip region in the thinner specimens. Plane strain solutions for J and Q are very different from plane stress solutions especially when large-scale yielding conditions prevail. Moreover, deLorenzi and Shih [*24*] have shown that J (Fig. 12 in Ref *24*) and Q (estimated from the hoop

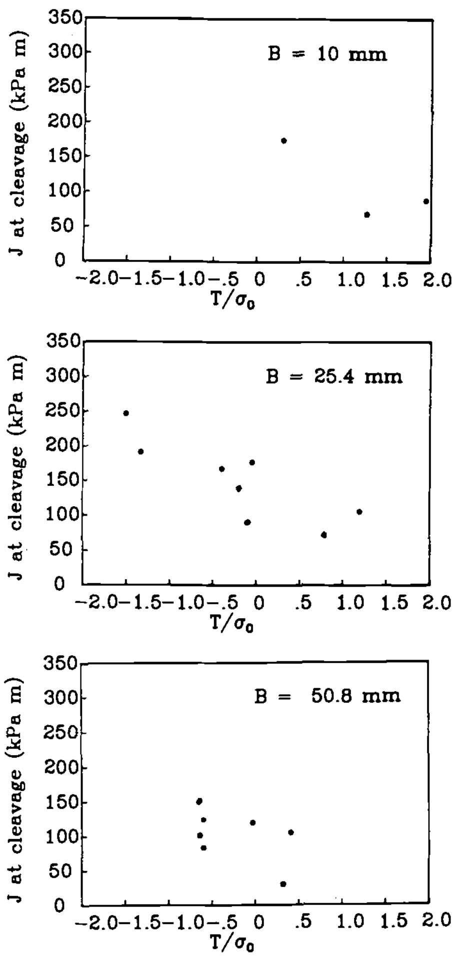

FIG. 10—*Fracture toughness versus T for ASTM A515 Grade 70 steels at 20°C from edge-cracked bend bar for three thicknesses (Kirk et al.* [23]*).*

stress in Fig. 15 in Ref *24*) can vary considerably along a crack front in fully yielded compact specimens. A proper accounting of thickness effects could yield J and Q values at the midplane of the specimen (presumably the critical location for cleavage fracture), which are different from values provided by plane strain analysis. This can in part explain the measured fracture toughness dependence on thickness shown in Fig. 9.

For the purpose of demonstrating constraint effect on fracture toughness we adopt a fracture criterion based on the attainment of a critical normal stress, $\sigma_{22} = \sigma_c$, at a critical distance, $r = r_c$ (Ritchie *et al.* [*25*]). Within the J-Q annulus, the normal stress ahead of the crack is given by Eq 2.7 or more accurately by Eq 2.8. For simplicity we work with the closed form representation in Eq 2.7. Assume that r_c is within the J-Q annulus. Applying the Ritchie-Knott-Rice (RKR) [*25*] fracture criterion to Eq 2.7 we get

$$\frac{\sigma_c}{\sigma_0} = \left(\frac{J_C}{\alpha\epsilon_0\sigma_0 I_n r_c}\right)^{1/(n+1)} \tilde{\sigma}_{22}(\theta = 0) + Q \tag{6.1}$$

Therefore we can solve for J_C as a function of Q for specified values of σ_c and r_c. Taking the toughness value for $Q = 0$ as J_O, we rearrange Eq 6.1 and arrive at

$$J_C = J_O\left(1 - \frac{Q\sigma_0}{\sigma_c}\right)^{n+1} \tag{6.2}$$

The variation of J_C with Q for $\sigma_c = 3.5\sigma_0$, $J_O = 40$ kPa·m, and $n = 5$ is shown in Fig. 11 (strain hardening of A515 steel is about 5). The trend of the toughness data is captured.

Extension of *J-Q* Approach

Three-Dimensional Tensile Mode States

We provide heuristic arguments that the J-Q field (Eq 2.3) exists near a three-dimensional crack front. Consider a planar crack front with a continuously turning tangent and focus on a

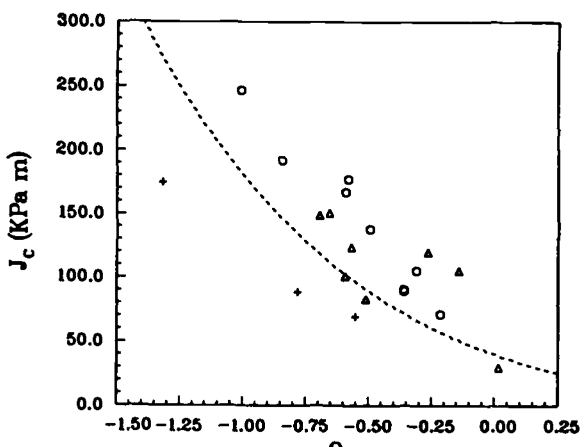

FIG. 11—*Comparison of predicted* J-Q *locus with fracture data for ASTM A515 Grade 70 steels at 20°C from edge-cracked bend bar for three thicknesses; + for* B = *10 mm, O for* B = *25.4 mm, △ for* B = *50.8 mm (Kirk et al.* [23]*).*

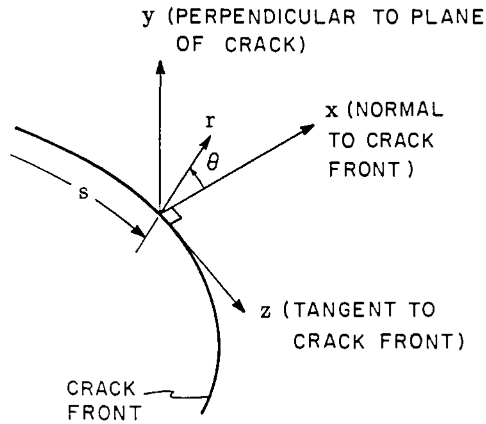

FIG. 12—*Plane strain* J-Q *field is defined with respect to local orthogonal Cartesian coordinates at the point* s *on a planar crack front. The crack plane is the* x-z *plane.*

neighborhood of the crack front which is sufficiently far away from its intersection with the external surface of the body. Let r and θ be the polar coordinates in the x-y plane as indicated in Fig. 12. As $r \rightarrow 0$, plane strain conditions prevail so that the three-dimensional fields approach the plane strain J-Q field given by Eq 2.3. Therefore, the $Q = 0$ distribution can be used as the reference constraint state for three-dimensional crack geometries. In this case, the Q value at each point on the crack front, designated by $Q(s)$, measures the departure from the plane strain reference distribution. Thus the tensile mode crack tip state at s is completely described by the pair $J(s)$ and $Q(s)$.

Following the definition for an average J, we introduce a measure of average constraint for a segment of the crack front $s_a \leq s \leq s_b$

$$Q_{\text{ave}} = \frac{1}{s_b - s_a} \int_{s_a}^{s_b} Q(s) ds, \qquad J_{\text{ave}} = \frac{1}{s_b - s_a} \int_{s_a}^{s_b} J(s) ds \tag{7.1}$$

The overall constraint for thick test geometries, Q_{ave}, will be nearly identical to Q evaluated by plane strain analysis; Q_{ave} for thin specimens will be smaller than Q for plane strain.

The elastic T-terms that can arise in three-dimensional crack problems are (Rice [*17*]); Parks [*26*])

$$\begin{pmatrix} \sigma_{xx} & \sigma_{xy} & \sigma_{xz} \\ \sigma_{yx} & \sigma_{yy} & \sigma_{yz} \\ \sigma_{zx} & \sigma_{zy} & \sigma_{zz} \end{pmatrix} = \frac{K_{\text{I}}}{\sqrt{2\pi r}} \begin{pmatrix} f_{xx} & f_{xy} & f_{xz} \\ f_{yx} & f_{yy} & f_{yz} \\ f_{zx} & f_{zy} & f_{zz} \end{pmatrix} + \begin{pmatrix} T_{xx} & 0 & T_{xz} \\ 0 & 0 & 0 \\ T_{zx} & 0 & T_{zz} \end{pmatrix} \tag{7.2}$$

Under small-scale yielding

$$Q(s) = F(T_{xx}(s)/\sigma_0,\ T_{xz}(s)/\sigma_0,\ T_{zz}(s)/\sigma_0;\ n) \tag{7.3}$$

The above generalizes the plane strain result in Eq 3.3 based on $T_{xz} = 0$ and $T_{zz} = \nu T_{xx}$.

The relation in Eq 7.3 can be determined by generalized plane strain analysis using remote boundary conditions given by Eq 7.2 and by full-field three-dimensional analysis of finite-thickness crack geometries. We expect Q to depend strongly on T_{xx} and less strongly on T_{xz}

and T_{zz}. Wang [27] has shown through a generalized plane strain analysis that near-tip constraint is only weakly affected by ϵ_{zz}/ϵ_0. Similar conclusions were reached by Schwartz [28] for axisymmetric crack geometries. Thus, Q will not vary much along the crack front of a typical specimen when small-scale yielding conditions prevail. In contrast, we expect Q to vary considerably along the crack front of a fully yielded fracture specimen (as evident from the through thickness variation of the hoop stress shown in Fig. 15 in Ref 24). Under such conditions, full-field three-dimensional solutions are required to discriminate thickness effects on fracture toughness data.

Creep Crack Growth

The J-Q approach can be extended to creep crack growth. Various aspects of $C(t)$ and C^* approach to creep crack growth are reviewed in a volume by Riedel [29] and articles by Saxena [30] and Bassani and Hawk [31]. Consider an elastic-nonlinear viscous solid for which the total uniaxial strain rate is given by

$$\dot{\epsilon} = \frac{\dot{\sigma}}{E} + \dot{\epsilon}_0 \left(\frac{\sigma}{\sigma_0}\right)^n \tag{7.4}$$

Here n is the creep exponent and $\dot{\epsilon}_0$ the reference creep strain rate at the reference stress σ_0. The J-Q field that governs the near-tip deformation has the form

$$\frac{\sigma_{ij}}{\sigma_0} = \left(\frac{C(t)}{\dot{\epsilon}_0\sigma_0 I_n r}\right)^{1/(n+1)} \tilde{\sigma}_{ij}(\theta; n) + Q(t)\left(\frac{r}{C(t)/\dot{\epsilon}_0\sigma_0}\right)^q \hat{\sigma}_{ij}(\theta; n) \tag{7.5}$$

where t is the time elapsed since load application. Within the modified boundary layer formulation (Eq 2.1), Q depends on the T-stress and t

$$Q(t) = F(T/\sigma_0, t/\dot{\epsilon}_0; n) \tag{7.6}$$

Let $C^* = \lim_{t\to\infty} C(t)$ be the steady state value of $C(t)$. At steady state creep, the near tip field has the form

$$\begin{aligned} \frac{\sigma_{ij}}{\sigma_0} &= \left(\frac{C^*}{\dot{\epsilon}_0\sigma_0 I_n r}\right)^{1/(n+1)} \tilde{\sigma}_{ij}(\theta; n) + Q^*\left(\frac{r}{C^*/\dot{\epsilon}_0\sigma_0}\right)^q \hat{\sigma}_{ij}(\theta; n) \\ \frac{\dot{\epsilon}_{ij}}{\dot{\epsilon}_0} &= \left(\frac{C^*}{\dot{\epsilon}_0\sigma_0 I_n r}\right)^{n/(n+1)} \tilde{\epsilon}_{ij}(\theta; n) + Q^*\left(\frac{r}{C^*/\dot{\epsilon}_0\sigma_0}\right)^q \left(\frac{C^*}{\dot{\epsilon}_0\sigma_0 I_n r}\right)^{(n-1)/(n+1)} \hat{\epsilon}_{ij}(\theta; n) \end{aligned} \tag{7.7}$$

where $Q^* = \lim_{t\to\infty} Q(t)$.

The steady-state relation in Eq 7.7 corresponds to the pure power-law relation in Eq 2.4 so that Q^* corresponds to Q_{FP}. In addition, features that pertain to the field in Eq 2.4 also apply to the field in Eq 7.7. Therefore the stress field at steady state can be written in the form (see Eq 2.7)

$$\sigma_{ij} = (\sigma_{ij})_{C^*} + Q^*\sigma_0\delta_{ij} \quad \text{for} \quad |\theta| < \pi/2 \tag{7.8}$$

Q^* can be determined by fully plastic analysis since $Q^* = \lim_{t\to\infty} Q(t) = Q_{FP}$ [20,21]. The above discussion suggests that the crack growth rates under steady state conditions can be correlated by C^* and Q^*. The latter quantifies crack tip constraint under extensive creep. Further investigations are required.

Concluding Remarks

Our investigations suggest that J and Q will suffice to characterize the full range of near-tip fracture states. Specifically, the zone of large stresses and strains (or process zone) is scaled by J while the near-tip stress triaxiality is scaled by Q. Stress triaxiality near a three-dimensional crack front can be quantified by pointwise values of Q. The J-Q methodology has a sound, theoretical basis. A correlation between cleavage fracture toughness and constraint for A515 steels can be seen in Fig. 11. The trend of the experimental toughness data is also captured by the toughness locus predicted by the J-Q theory.

In this paper results have been presented for the center-cracked panel and three point bend bar for selected a/W ratios and two hardening exponents. Solutions for a broad range of n values ($n = 3, 5, 10, 20$) and the full range of a/W ratios ($0.05 < a/W < 0.9$) for the center-cracked panel, three point bend bar, and double-edge-cracked panel are presented in a more recent study [*22*].

Methods for evaluating Q for fully yielded crack geometries are under investigation. Fully plastic Q solutions can be catalogued in a handbook much like the fully plastic J solutions that are catalogued in the Electric Power Research Institute (EPRI) fracture handbook [*20*]. Simple procedures for estimating Q over the entire range of yielding are being investigated as well. In this way, detailed numerical calculations are not required to determine Q.

Acknowledgments

This investigation is supported by the Office of Naval Research (ONR) through ONR Grant N00014-86-K-0616. The computations were performed at the Computational Mechanics Facility of Brown University supported in part by grants from the U.S. National Science Foundation (Grant DMR-8714665), the Office of Naval Research (Grant N00014-88-K-0119) and matching funds from Brown University.

References

[*1*] O'Dowd, N. P. and Shih, C. F., *Journal of Mechanics and Physics of Solids,* Vol. 39, 1991, pp. 989–1015.
[*2*] O'Dowd, N. P. and Shih, C. F., *Journal of Mechanics and Physics of Solids,* 1991, Vol. 40, 1992, pp. 939–963.
[*3*] Li, Y. C. and Wang, T. C., *Scientia Sinica (Series A),* Vol. 29, 1986, pp. 941–955.
[*4*] Sharma, S. M. and Aravas, N., *Journal of Mechanics and Physics of Solids,* Vol. 39, 1991, pp. 1043–1072.
[*5*] Betegón, C. and Hancock, J. W., *Journal of Applied Mechanics,* Vol. 58, 1991, pp. 104–110.
[*6*] Bilby, B. A., Cardew, G. E., Goldthorpe, M. R., and Howard, I. C., *Size Effects in Fracture,* Institution of Mechanical Engineers, London, United Kingdom, 1986, pp. 37–46.
[*7*] Harlin, G. and Willis, J. R., *Proceedings of the Royal Society,* Vol. A 415, 1988, pp. 197–226.
[*8*] McMeeking, R. M., *Journal of Mechanics and Physics of Solids,* Vol. 25, 1977, pp. 357–381.
[*9*] Williams, M. L., *Journal of Applied Mechanics,* Vol. 24, 1957, pp. 109–114.
[*10*] Hutchinson, J. W., *Journal of Mechanics and Physics of Solids,* Vol. 16, 1968, pp. 13–31.
[*11*] Rice, J. R. and Rosengren, G. F., *Journal of Mechanics and Physics of Solids,* Vol. 16, 1968, pp. 1–12.
[*12*] Rice, J. R., *Journal of Applied Mechanics,* Vol. 35, 1968, pp. 379–386.
[*13*] McMeeking, R. M. and Parks, D. M., *Elastic-Plastic Fracture Mechanics, ASTM STP 668,* American Society for Testing and Materials, Philadelphia, 1979, pp. 175–194.
[*14*] Shih, C. F. and German, M. D., *International Journal of Fracture Mechanics,* Vol. 17, 1981, pp. 27–43.
[*15*] Hutchinson, J. W., *Journal of Applied Mechanics,* Vol. 50, 1983, pp. 1042–1051.

[16] Larsson, S. G. and Carlsson, A. J., *Journal of Mechanics and Physics of Solids,* Vol. 21, 1973, pp. 263–277.
[17] Rice, J. R., *Journal of Mechanics and Physics of Solids,* Vol. 22, 1974, pp. 17–26.
[18] Leevers, P. S. and Radon, J. C., *International Journal of Fracture,* Vol. 19, 1982, pp. 311–325.
[19] Sham, T. L., *International Journal of Fracture,* Vol. 48, 1991, pp. 81–102.
[20] Kumar, V., German, M. D., and Shih, C. F., "An Engineering Approach for Elastic-Plastic Fracture Analysis," EPRI Topical Report NP-1931, Electric Power Research Institute, Palo Alto, CA., July 1981.
[21] Shih, C. F. and Needleman, A., *Journal of Applied Mechanics,* Vol. 51, 1984, pp. 48–64.
[22] O'Dowd, N. P. and Shih, C. F., "Two Parameter Fracture Mechanics: Theory and Applications," presented at the 24th National Symposium on Fracture Mechanics, 1992. To appear in an ASTM STP.
[23] Kirk, M. T., Koppenhoefer, K. C., and Shih, C. F., "Effect of Constraint on Specimen Dimensions Needed to Obtain Structurally Relevant Toughness Measures," this publication.
[24] deLorenzi, H. G. and Shih, C. F., *International Journal of Fracture,* Vol. 21, 1983, pp. 195–220.
[25] Ritchie, R. O., Knott, J. F., and Rice, J. R., *Journal of Mechanics and Physics of Solids,* Vol. 21, 1973, pp. 395–410.
[26] Parks, D. M. in *Defect Assessment in Components—Fundamentals and Applications,* Mechanical Engineering Publications, London, United Kingdom, 1991, pp. 205–231.
[27] Wang, Y.-Y., "On the Two-Parameter Characterization of Elastic-Plastic Crack-Front Fields in Surface-Cracked Plates," this publication.
[28] Schwartz, C. W., "Influence of Out-of-Plane Loading on Crack Tip Constraint," this publication.
[29] Riedel, H., *Fracture at High Temperatures,* Springer-Verlag Berlin, Heidelberg, 1987.
[30] Saxena, A. in *Fracture Mechanics: Microstructure and Micromechanics,* American Society for Metals, Metas Park, OH, 1989, pp. 283–334.
[31] Bassani, J. L. and Hawk, D. E., *International Journal of Fracture,* Vol. 42, 1990, pp. 157–172.
[32] Moran, B. and Shih, C. F., *Engineering Fracture Mechanics,* Vol. 27, 1987, pp. 615–642.
[33] Xia, L., Wang, T. C., and Shih, C. F., "Higher-Order Analysis of Crack-Tip Fields in Elastic Power-Law Hardening Materials," 1992, to appear in *Journal of Mechanics and Physics of Solids.*

DISCUSSION

R. E. Johnson[1] *(written discussion)*—What physical significance do you ascribe to the ratio T/σ_0 greater than unity? I note that on one of your graphs data were plotted for T/σ_0 greater than unity.

C. F. Shih, N. P. O'Dowd, and M. T. Kirk (author's closure)—The T-stress is only defined under small-scale yielding conditions. When these conditions apply, T is linearly related to the applied load as given by Eq 5.2 in the Methods for Evaluating Q section of the paper. This relationship is used by Hancock and coworkers as an operational definition of T for the purpose of evaluating crack tip constraint in fully yielded crack geometries. Since T is undefined under fully yielded conditions, we attach no significance to the ratio T/σ_0 greater than unity.

[1] U.S. Nuclear Regulatory Commission, Washington, DC.

John W. Hancock,[1] *Walter G. Reuter,*[2] *and David M. Parks*[3]

Constraint and Toughness Parameterized by *T*

REFERENCE: Hancock, J. W., Reuter, W. G., and Parks, D. M., "**Constraint and Toughness Parameterized by *T*,**" *Constraint Effects in Fracture, ASTM STP 1171,* E. M. Hackett, K.-H. Schwalbe, and R. H. Dodds, Eds., American Society for Testing and Materials, Philadelphia, 1993, pp. 21–40.

ABSTRACT: A series of cracked specimen configurations have been tested to correlate the geometry dependence of crack tip constraint and fracture toughness in full plasticity. Specimens with through cracks included a range of edge-cracked bend bars, compact tension specimens, and center-cracked panels. Surface-cracked panels were tested in tension to produce resistance curves.

The geometry dependence of ductile crack extension in plane strain has been correlated with crack tip constraint as parameterized by the *T* stress, which indicates the nature of the development of higher order terms in the nonlinear asymptotic crack tip expansion.

KEY WORDS: *T* stress, toughness, constraint

Fracture mechanics attempts to ensure structural integrity by applying toughness measurements obtained from laboratory specimens to real defects. Current design and inspection methods are based on the application of geometry-independent data. Nevertheless, crack tip deformation and fracture toughness are only geometry independent within a limited range of loading and geometric conditions, which ensures similar crack tip constraint. The restrictive nature of these size and geometry requirements is a major limitation on the application of plane strain elastic-plastic fracture mechanics. The present work describes developments intended to relax these limitations by characterizing fracture toughness as a function of constraint and thus allow the application of fracture mechanics to a wider and less restrictive range of configurations.

The approach has its foundation in the nature of Mode I elastic crack tip fields, where the local stress field can be expressed as an asymptotic series [*1*] in cylindrical coordinates (r,θ) centered at the crack tip

$$\sigma_{ij} = A_{ij}r^{-1/2} + B_{ij}r^{0} + C_{ij}r^{+1/2} + \ldots \tag{1}$$

Within small-scale yielding, the assumption that fracture processes occurring close to the crack tip are dominated by the leading term to the neglect of the higher order terms has enabled the use of the stress intensity factor K as the single fracture characterizing parameter

$$\sigma_{ij} = \frac{K}{\sqrt{(2\pi r)}} f_{ij}(\theta) \tag{2}$$

[1] Department of Mechanical Engineering, University of Glasgow, Glasgow, Scotland G12 8QQ.
[2] EG & G, Idaho National Engineering Laboratory, Idaho Falls, Idaho.
[3] Massachusetts Institute of Technology, Cambridge, MA.

The application of linear elastic fracture mechanics is subject to severe size limitations [2] intended to ensure that plasticity is restricted to a local perturbation of the elastic field. These restrictions are relaxed by nonlinear elastic-plastic fracture mechanics. As in the case of linear elastic deformation, the crack tip field can be expressed as an asymptotic series. Interest has, until recently, been restricted to the first term, which was identified by Hutchinson [3] and Rice and Rosengren [4] (henceforth HRR) as

$$\sigma_{ij} = \sigma_0 \left[\frac{J}{\alpha \varepsilon_0 \sigma_0 I_n r} \right]^{\frac{1}{n+1}} \tilde{\sigma}_{ij}(\theta, n) \tag{3}$$

$$\varepsilon_{ij} = \alpha \varepsilon_0 \left[\frac{J}{\alpha \varepsilon_0 \sigma_0 I_n r} \right]^{\frac{n}{n+1}} \tilde{\varepsilon}_{ij}(\theta, n) \tag{4}$$

In these equations, I_n and $\tilde{\sigma}_{ij}(\theta, n)$, and $\tilde{\varepsilon}_{ij}(0, n)$ are tabulated functions of the strain-hardening exponent n and (where appropriate) the angular coordinate θ. The strength of the singular field is characterized by the J integral, introduced by Rice [5], which provides the most general single parameter characterization of crack tip deformation.

However, McClintock [6] has noted that in the absence of strain hardening, single parameter characterization is limited by the lack of uniqueness of the fully plastic flow fields. Both the kinematics of flow in plane strain and the associated crack tip constraint depend on loading and geometry. As an illustration, the plane strain slip line field of a center-cracked panel subject to uniaxial tension is shown in Fig. 1*a*. In contrast, the deeply cracked bend bar shown by the solid lines in Fig. 1*b* exhibits a fully constrained flow field in which plasticity is confined to the ligament.

A dimensional argument demonstrates that the constraint of deeply cracked flow fields and associated single parameter characterization by J can be maintained under conditions which depend on the size of a critical dimension, c, such as the ligament or crack length, and the yield stress σ_0.

$$c \geq \frac{\mu J}{\sigma_0} \tag{5}$$

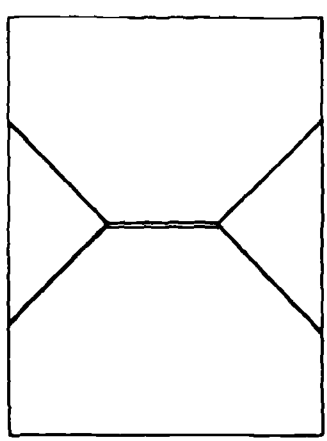

FIG. 1*a*—*The plane strain slip line field for a center-cracked panel in tension.*

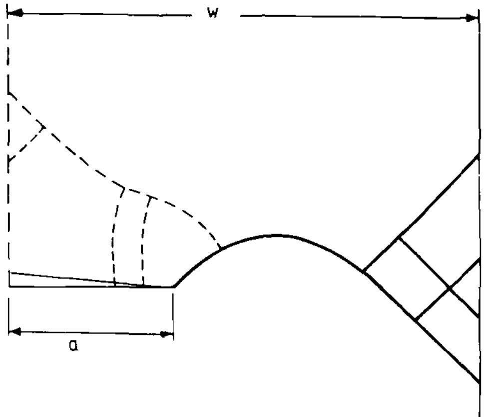

FIG. 1*b*—*The plane strain slip line field for a deeply cracked bend bar is indicated by the solid lines, while the broken lines indicate the extension to the slip line field for short cracks proposed by Ewing* [10].

When plasticity is restricted to the ligament (and it becomes the controlling dimension), McMeeking and Parks [7] and Shih and German [8] suggested that single-parameter characterization was maintained within the requirements

$$\begin{aligned} c = (W - a) &\geq \frac{25J}{\sigma_0} \text{ in bending} \\ c = (W - a) &\geq \frac{200J}{\sigma_0} \text{ in tension} \end{aligned} \tag{6}$$

However, when a/W is less than 0.3 in bending or 0.55 in tension, Al-Ani and Hancock [9] have demonstrated that plasticity develops initially to the cracked face in accord with Ewing's [10] extension to the deeply cracked bending field indicated by the broken lines in Fig. 1*b*. In this case the crack length becomes the controlling dimension, and single parameter characterization is lost before

$$c = a \geq \frac{200J}{\sigma_0} \tag{7}$$

Here the underlying concept is that lack of uniqueness arises from the the nonunique form of the fully plastic flow field discussed by McClintock [6]. Although the fully plastic flow fields are clearly not unique, Hancock and co-workers [9,11,12] have argued that the lack of uniqueness is not associated with the sudden development of the fully plastic flow field but rather evolves initially from small-scale yielding and the geometry dependent nonsingular stresses associated with the elastic field. Loss of constraint originating from the contained yielding field is now accepted to lead to markedly more severe single parameter characterization criteria for ligaments in tension and crack lengths in both tension and bending [11] than given by Eqs 6 and 7.

The first evidence that the loss of constraint has its origin in the small-scale yielding field can be inferred from the work of Larsson and Carlsson [13], which showed systematic changes in the shape and size of the plastic zone within the ASTM [2] limits for linear elastic fracture mechanics (LEFM). These results were rationalized following a suggestion of Rice [14] that the differences could be attributed to the second term in the Williams expansion which Rice denoted the T stress. This term corresponds to a uniform stress parallel to the crack flanks.

$$\sigma_{ij} = \frac{K}{\sqrt{2\pi r}} f_{ij}(\theta) + T_{ij}\delta_{i1}\delta_{1j} \tag{8}$$

In addition to modifying the shape of the plastic zone, T affects crack tip deformation. Crack tip plasticity can be modelled by boundary layer formulations which model small-scale yielding by applying the asymptotic elastic field as remote loadings to a local region containing a crack tip, thus avoiding the need to represent a complete cracked body. Within such formulations, deformation may be represented by numerical frameworks which take account of the finite geometry changes associated with crack blunting, or by small strain solutions, as exemplified by the HRR field.

Such solutions are illustrated in Figs. 2 and 3 for a Ramberg-Osgood material with a power-hardening exponent of 13. Comparison between the fields has been made in terms of the ratio of the mean stress, $\sigma_m = \sigma_{kk}/3$ to the Mises stress $\bar{\sigma}$. This parameter has been chosen both as a widely used measure of constraint and on the basis of its physical relevance to ductile fracture processes in the steel used in the associated experimental work, where $(\sigma_m/\bar{\sigma})$ controls the rate of void growth as discussed by Rice and Tracey [15] and Hancock and Mackenzie [16].

The triaxiality parameter, $\sigma_m/\bar{\sigma}$, is also of interest because in the HRR field it is independent of r and can therefore be used as one measure of the size of the HRR annulus. Numerical solutions for low-hardening materials, such as those shown in Fig. 2, clearly indicate that it is

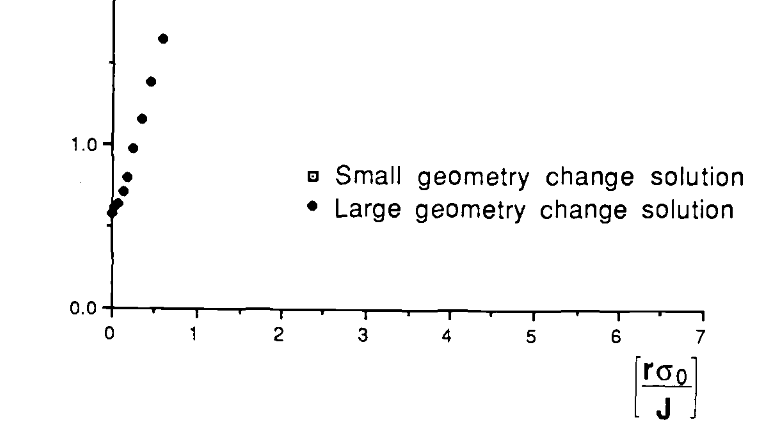

FIG. 2—*A comparison of the triaxiality ahead of a crack as given by small and large geometry change boundary layer formulations. The triaxiality of the HRR field is independent of* r *and is indicated by the horizontal straight line.*

a function of r at all finite distances from the tip. The HRR field, as an asymptotic small geometry change solution, is recovered at the crack tip, but at low-hardening rates the triaxiality associated with the HRR field is lost within the large geometry change blunting zone. This is consistent with the anti-plane shear solutions of Rice [17], which indicate that the size of the region dominated by the leading singularity decreases with declining strain-hardening rate and finally becomes vanishingly small for perfect plasticity.

Close to the crack tip, large geometry change solutions have been used to elucidate the local crack tip blunting process. In this context the large geometry change solutions of Bilby et al. [18] have shown that compressive T stresses substantially reduce triaxial stress levels. The present large geometry change modified boundary layer formulations are given in Fig. 3. These can be used to index the constraint as measured by the maximum value of $\left[\frac{\sigma_m}{\bar{\sigma}}\right]$ as a function of the T stress, as given in Fig. 4.

The large strain region close to the blunting tip is contained in an outer field which can be examined within the framework of small deformation theory. In this region Betegón and Hancock [11] found that tensile T stresses produced only modest elevations of the stress level independent of the nondimensional distance $(r\sigma_0/J)$. However, compressive T stresses were demonstrated to produce a marked decrease in the stress level and associated crack tip constraint independent of $(r\sigma_0/J)$. This was interpreted as corresponding to the introduction of a second term in the asymptotic crack tip expansions. Single parameter characterization then simply corresponds to situations when T is positive and the higher order terms of the series are insignificant, leaving the HRR field as the dominant term. Higher order terms in nonlinear fields

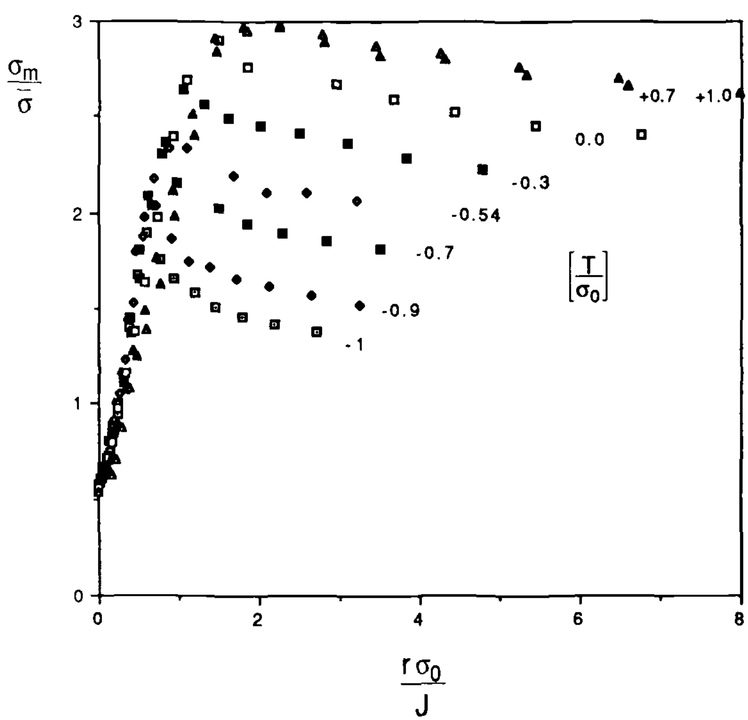

FIG. 3—*The triaxiality, $\sigma_m/\bar{\sigma}$, ahead of plane strain blunting cracks obtained from modified boundary layer formulations,* n = *13.*

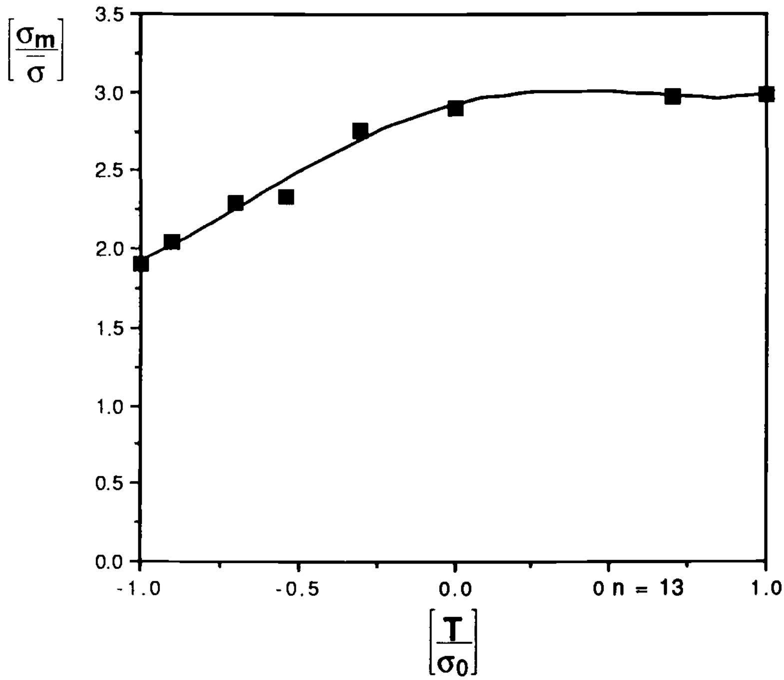

FIG. 4—*The peak triaxiality ahead of a plane strain blunting crack as a function of the nondimensionalized* T *stress.*

have been examined initially by Li and Wang [*19*] and systematically by Sharma and Aravas [*20*]. In the nonhardening limit the nature of the second term is capable of a particularly simple interpretation, as discussed by Du and Hancock [*12*], who showed that within the plastic zone, the T stress simply changes the hydrostatic stress or the constraint at the crack tip by a term that is a function of T. O'Dowd and Shih [*21*] also identified the second order term as having a largely hydrostatic component, which they identify by subtracting the HRR field from full field solutions.

The ability of modified boundary layer formulations to describe contained yielding fields is not surprising; however, remarkably, Betegón and Hancock [*12*] and Al-Ani and Hancock [*9*] were able to correlate modified boundary layer formulations with full field solutions of a wide range of geometries into full plasticity. Although the T stress is an elastic parameter, the correlation was made by identifying T with the applied load or the elastic component of J. On this basis it was possible to correlate crack tip deformation for edge-cracked bars in tension and bending from (a/W) 0.03 to 0.9, as well as center-cracked panels and double edge cracked bars.

The ability of an elastic parameter to correlate fully plastic flow fields of such a diverse range of geometries can be explained qualitatively. At infinitesimally small loads, plasticity is only a minor local perturbation of the leading term of the elastic field, allowing crack tip deformation to be represented by single parameter characterization in a boundary layer formulation with the K field displacements imposed on the boundaries. As the load increases within contained yielding, the outer elastic field can be characterized by K and T, both of which are rigorously defined. Within the plastic zone the crack tip field now evolves in a way that is correctly represented by a modified boundary layer formulation with both K and T as boundary conditions.

The initial evolution of the crack tip field is thus rigorously determined by T. Geometries with negative T stresses start to lose crack tip constraint, while those which have positive T stresses maintain the character of the small-scale yielding field. For simplicity it is appropriate to restrict discussion to small geometry change perfect plasticity when the appropriately nondimensionalized crack tip field reaches a steady state, independent of deformation. At limit load, the value of T calculated from the applied load, or equivalently the elastic component of J, also remains constant. When T, as calculated from the limit load, is used to make contact with the modified boundary layer formulations, the predicted stress field also reaches a steady state.

The justification for using T to correlate modified boundary layer formulations with full elastic-plastic full fields solutions is that within small-scale yielding it gives rigorously correct solutions which start to evolve in the correct manner towards full plasticity. In full plasticity the method produces fields which reach steady state and moreover have been shown to match full field solutions for a very wide range of geometries. The method provides a good practical method of *predicting* the nature of the higher order term in full field solutions, whereas other work has concentrated on *deducing* the second term by subtracting the HRR field from full field solutions and has no predictive power as a practical engineering method.

Plane strain analyses have been extended into three-dimensional deformation by Wang [*22*] and Al-Ani [*23*]. For modest departure from plane strain conditions, the crack tip deformation was successfully correlated by J and T without the need to introduce the out-of-plane effects. The analysis of wide plates containing semi-elliptical defects has been addressed by Parks and Wang [*24*] and Wang [*22*]. Within the framework of small deformation theory the stress fields at various positions around semi-elliptical cracks were compared with modified plane strain boundary layer formulations based on J and T. Wang [*22*] has shown that the major features of the modified boundary layer formulation based on J and T captures the essential features of the deviations from one parameter characterization along the crack fronts of semi-elliptical cracks in both tension and bending.

As the crack fields for both through and semi-elliptical cracks can now be characterized by J and T over a wide range of constraint, it is natural to introduce an associated failure criterion. This takes the form of failure locus in which J_c is given as a function of constraint as parameterized by T. Interpretations of experimental data in this form have been presented by Betegón [*25*], Betegón and Hancock [*26*], and Sumpter and Hancock [*27*].

Materials and Experimental Methods

Specimens were fabricated from an as-rolled grade ASTM 710 Grade A steel of yield stress 470 MN/m^2 and ultimate tensile strength of 636 MN/m^2. The chemical composition of the steel is given in Table 1. Tension test data on this steel has been given by Reuter and Lloyd [*28*] and can be described by a Ramberg-Osgood relationship with a strain-hardening exponent close to 10.

A range of precracked geometries, without side grooves, were tested at 20°C. These included edge-cracked bars oriented in the *T-L* direction with a/W ratios 0.1, 0.2, 0.3, 0.5, and 0.64 which were tested in three-point bending. The specimens were 12.7 mm thick, and the bend bars had a ligament width, $W - a$, of 12.7 mm. Additional data for bend bars with an a/W

TABLE 1—*Chemical composition of A710 steel, in weight %.*

C	Mn	P	S	Si	Cr	Ni	Mo	Cu	Ti	Fe
0.05	0.47	0.01	0.04	0.25	0.74	0.85	0.21	1.2	0.038	bal

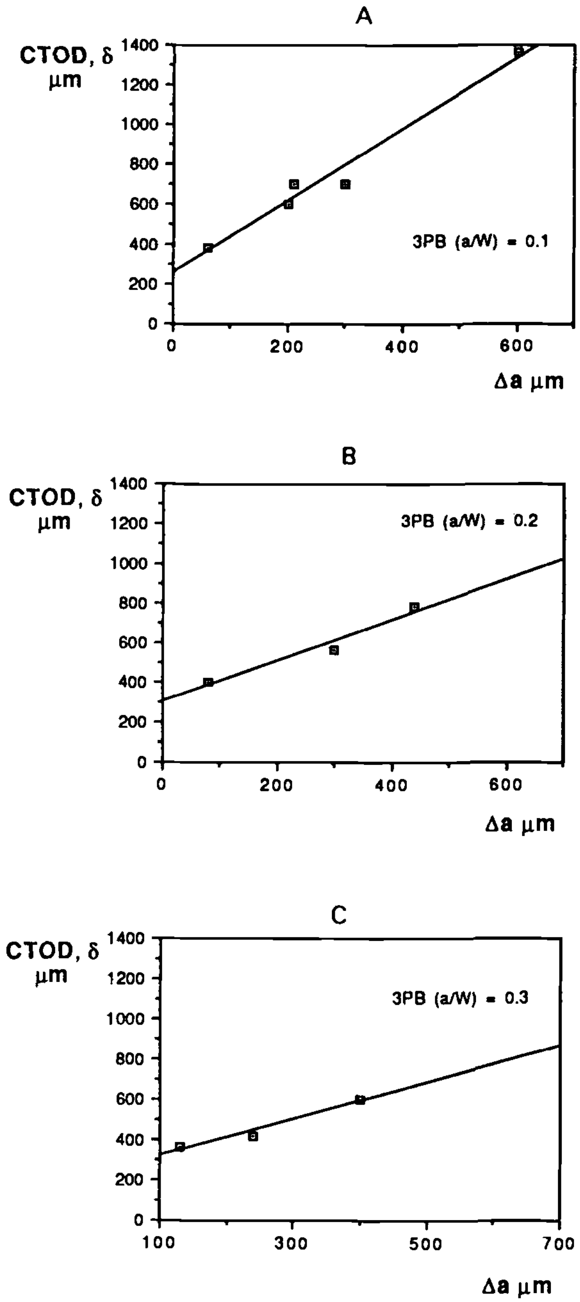

FIG. 5—*The crack tip opening δ as a function of crack extension for a range of bend bars with different* (a/W) *ratios:* (a) *three-point bend bar* (a/W) = *0.1;* (b) *three-point bend bar* (a/W) = *0.2;* (c) *three-point bend bar* (a/W) = *0.3;* (d) *three-point bend bars,* (a/W) = *0.5 and 0.64;* (e) *compact tension specimens,* B = *12.7 and 15.9 mm.*

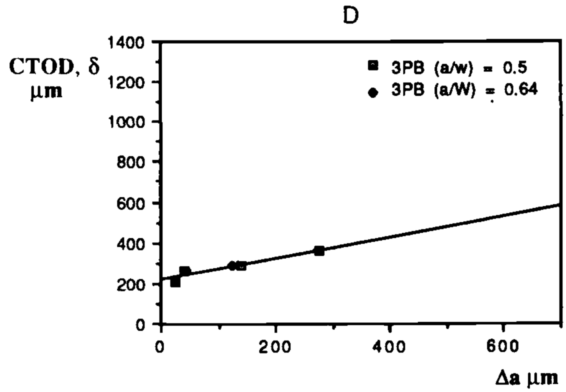

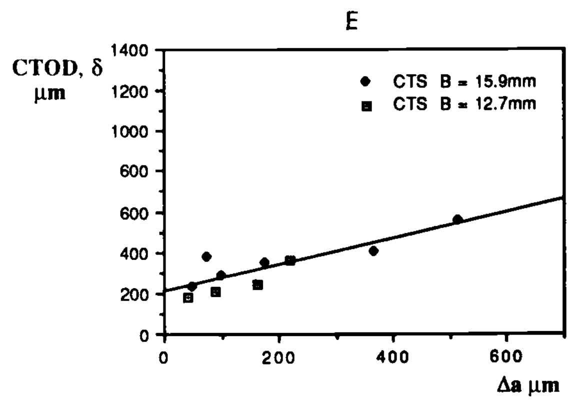

FIG. 5—*continued.*

ratio of 0.5 and a thickness of 15.9 mm were also incorporated. J was calculated from the applied load and the mouth opening clip gauge displacement, following the method proposed by Sumpter and Turner [*29*] and Sumpter [*30*]. As usual, J is decomposed into elastic and plastic components J_e and J_p. In all the tests the plastic component was the important term and was determined from relations of the form

$$J_p = \frac{\eta U_p}{B(W - a)} \tag{9}$$

Here U_p is a plastic work term, B is the specimen thickness, and η is a factor given by Sumpter [*30*] as a function of the a/W ratio. The plastic work term, U_p, was calculated from the mouth-opening displacement on the basis that deformation can be described by a rotation about a plastic hinge whose location is a function of the a/W ratio, as discussed in detail by Sumpter [*30*]. The results are shown in Figs. 5*a* to 5*e* and Figs. 10*a* to 10*f*.

The T stress was calculated from the applied load using the tabulated data of Sham [*31*], who gives the ratio of T to a nominal applied stress as a simple stress concentration factor.

Compact tension specimens with the same orientation with respect to the rolled plate, shown in Fig. 5*e* and Fig. 10*f*, was obtained, and thicknesses of 12.7 mm and 15.9 mm and a ligament ($W - a$) of 14.3 mm were tested. J was obtained from load point displacement records obtained from a clip gauge mounted on the specimen directly below the loading pins. T was calculated from the applied load using the data given by Leevers and Radon [*32*].

Center-cracked panels with crack lengths $2a$ of 6.7, 12.5, and 25 mm in a plate of thickness 6.4 mm and width 101 mm were tested in tension, as described in detail by Reuter, Graham, Lloyd, and Williamson [*33*]. T was calculated from the applied load using the data of Kfouri [*34*].

Surface-cracked panels were also tested in tension, as described in detail by Reuter and Lloyd [*28*]. These specimens had a crack depth to plate thickness ratio (a/t) of 0.59 and crack depth to surface length ratios $(a/2c)$ of 0.1 and 0.5. The T stress at the deepest point of these cracks was calculated by an extension of the line spring analysis of Rice and Levy [*35*] as extended and implemented by Parks [*36*] in ABAQUS [*37*].

In line spring analysis, a plate is idealized as a two-dimensional continuum in which the part-through surface crack is represented by a one-dimensional discontinuity. The force and the bending moment transmitted by each section of the crack are related to discontinuities in normal displacement of the plate's mid-surface and relative rotation by a local compliance which can be regarded as the response of a generalized spring whose compliance is matched with that of a plane strain edge-cracked bar. Line spring analysis is usually motivated towards determining the stress intensity factors by adding the stress intensity of edge-cracked bars subject to the appropriate levels of bending and tension. In the present context the T stress can be similarly calculated by superimposing the T stresses for the tension and bending components of edge-cracked bars as discussed by Parks and Wang [*24*] and Al-Ani [*23*]. On this basis the T stress at the deepest point of the surface-cracked panel with $(a/2c = 0.12)$ was estimated as $-0.6\sigma_{\text{nominal}}$, and $T = -0.65\sigma_{\text{nominal}}$, for $(a/2c) = 0.5$.

In all cases multiple specimens were tested and sectioned metallographically to measure the extent of ductile tearing, Δa, from the blunt crack tip and the crack tip opening displacement (CTOD). This enabled the construction of CTOD-Δa plots for all the geometries, as given in Figs. 5 through 9. For each geometry the data were described by a straight line fitted on a least squares basis. The CTOD-Δa data for the bend and CTS geometries are unified in Fig. 6.

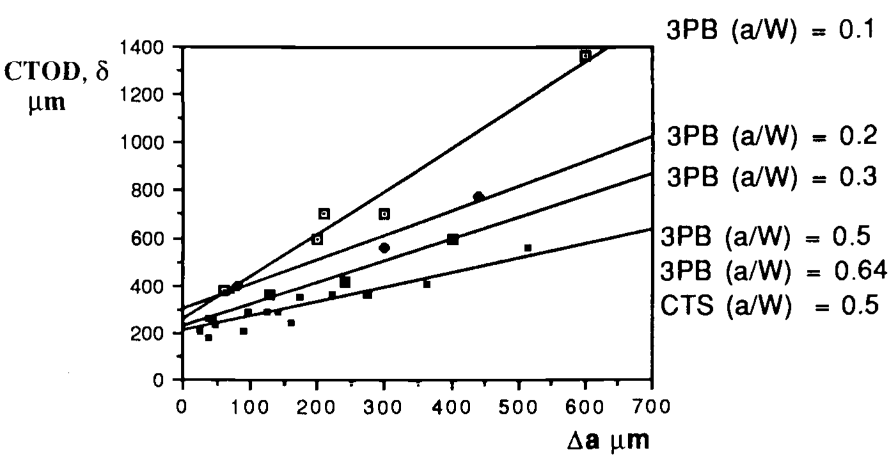

FIG. 6—*The combined crack tip opening data for the bend and CTS geometries.*

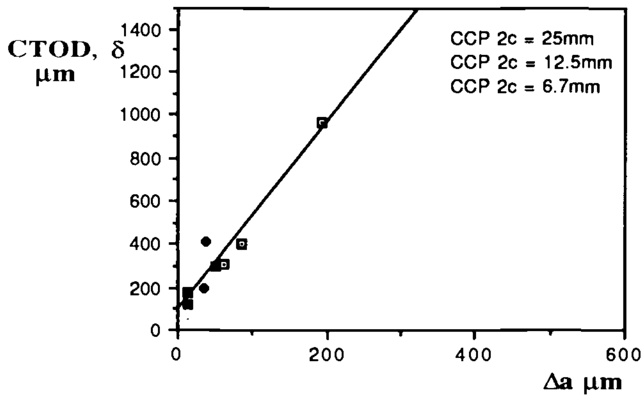

FIG. 7—*The crack tip opening, δ, as a function of crack extension* Δa, *for the center-cracked panels,* a/W = *0.066, 0.124, and 0.248.*

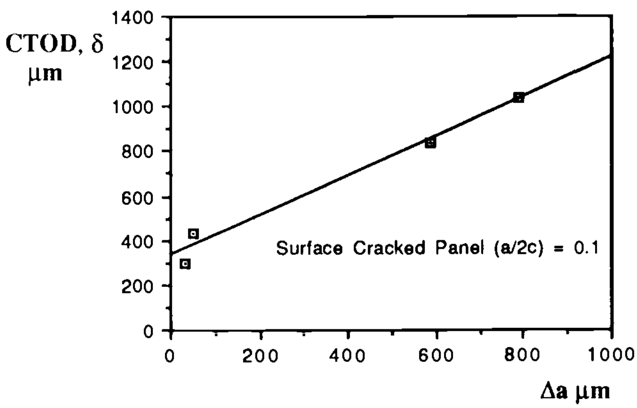

FIG. 8—*The crack tip opening, δ, as a function of crack extension,* Δa, *for a surface-cracked panel,* a/2c = *0.1 and* a/t = *0.59.*

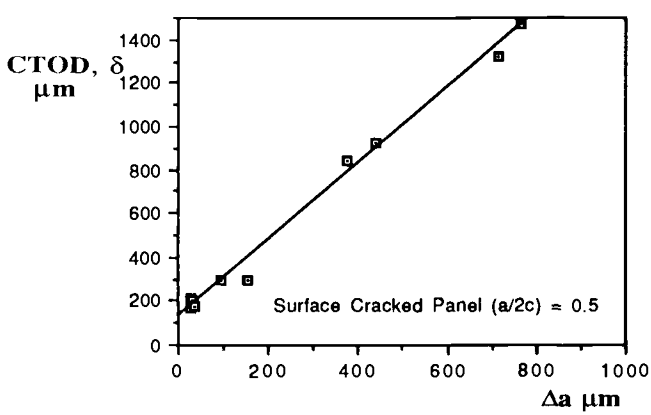

FIG. 9—*Crack tip opening, δ, as a function of crack extension* Δa, *for a surface-cracked panel,* a/2c = *0.5 and* a/t = *0.59.*

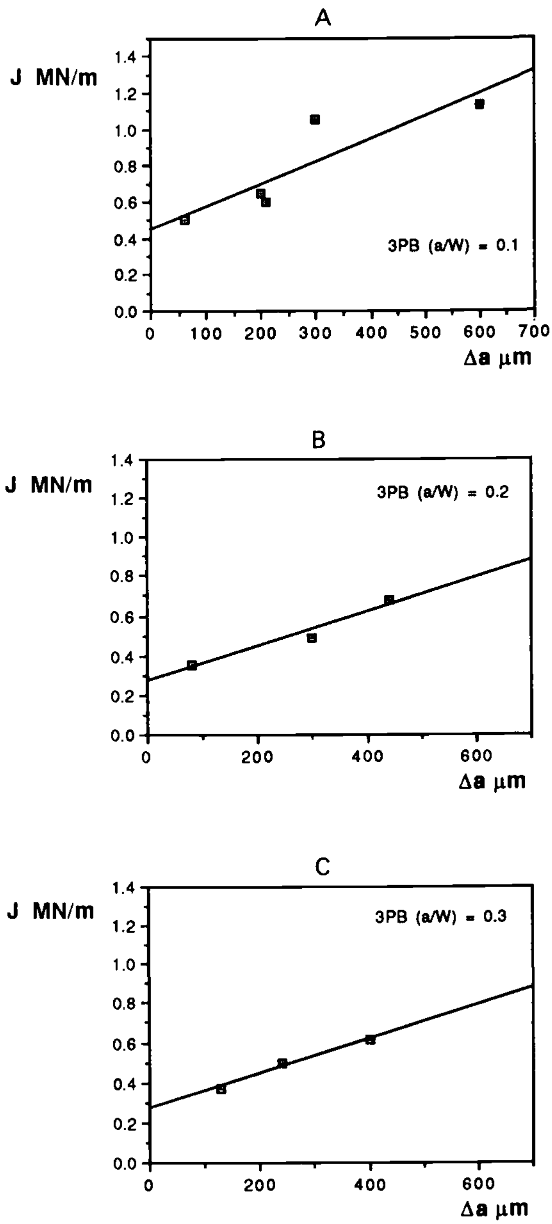

FIG. 10—J *as a function of crack extension,* Δa, *for a range of bend bars with different* (a/W) *ratios:* (a) *three-point bend bar* (a/W) = *0.1;* (b) *three-point bend bar* (a/W) = *0.2;* (c) *three-point bend bar* (a/W) = *0.3;* (d) *three-point bend bars with* a/W = *0.5;* (e) *three-point bend bars with* a/W = *0.64;* (f) *compact tension specimens,* B = *12.7 and 15.9 mm.*

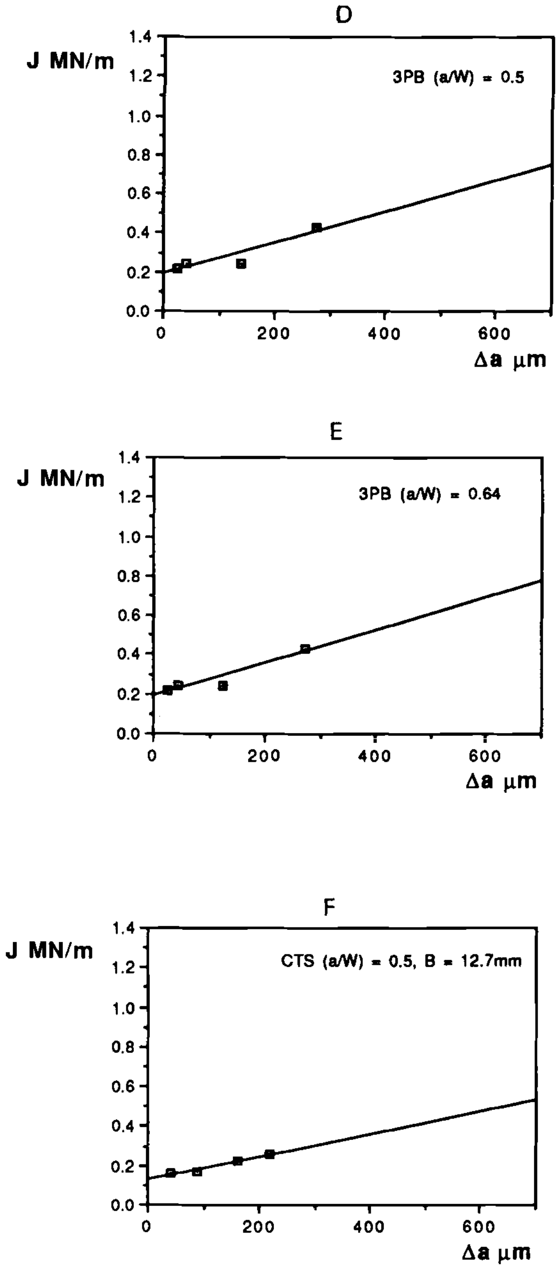

FIG. 10—*continued*

Data for the center-cracked panels are given in Fig. 7, while the CTOD at the deepest point of the semi-elliptical cracks is shown in Figs. 8 and 9.

Established procedures, such as those discussed by Sumpter [*30*] and Sumper and Turner [*29*], allow J to be calculated directly from the load displacement records of the bend bars and compact tension specimens as given in Fig. 10 and Fig. 11. In contrast, there is no standard method for calculating J for semi-elliptical cracks, although such specimens have been analyzed by White, Ritchie, and Parks [*38*] and Parks and Wang [*39*]. In the present work J has been determined from the crack tip opening displacement, δ, through the relation

$$J = \delta\sigma_0/d_n \tag{10}$$

Here d_n was taken as ½, which is consistent with the geometries for which experimental comparisons of J and δ allowed d_n to be estimated. For example for the shallow edge-cracked bar [3PB $(a/W) = 0.1$] $d_n = 0.48 \pm 0.13$, while for the deeply edge-cracked bar [3PB $(a/W) = 0.63$)] $d_n = 0.48 \pm 0.07$. These values are consistent with those given by Shih [*40*] for power hardening exponents $n \approx 10$. The crack tip opening displacement was measured on all the specimens by sectioning to the center line and examining polished unloaded metallographic sections. The CTOD comprises a plastic and an elastic component in which the elastic component is recovered on unloading. The effect of unloading was estimated by calculating the elastic component of the CTOD using the elastic component of J. On this basis the elastic component of the CTOD was shown to be very small in comparison to the plastic component and was thus neglected. The CTOD was measured on the original blunted crack tip, using the construction suggested by Shih [*40*]. Crack extension was similarly measured on unloaded metallographic specimens. In a macroscopic sense, crack extension occurred in a direction broadly coplanar with the original fatigue crack, allowing the extension Δa to be measured from the original blunted tip.

For all the specimen geometries, crack extension initiated in full plasticity. The deeply cracked bend and CTS specimens just satisfied the $25J/\sigma_0$ criterion for the ligament and were thus capable of single parameter characterization. In contrast, measurements on the center and surface-cracked panels tested in tension severely violated the requirement that the ligament should exceed $200J/\sigma_0$. Single parameter characterization for such specimens would require that the ligament should exceed approximately 100 mm, which is impracticable for both specimens and, more importantly, for engineering structures. However, this difficulty is overcome by the ability of two-parameter fracture mechanics to characterize such specimens.

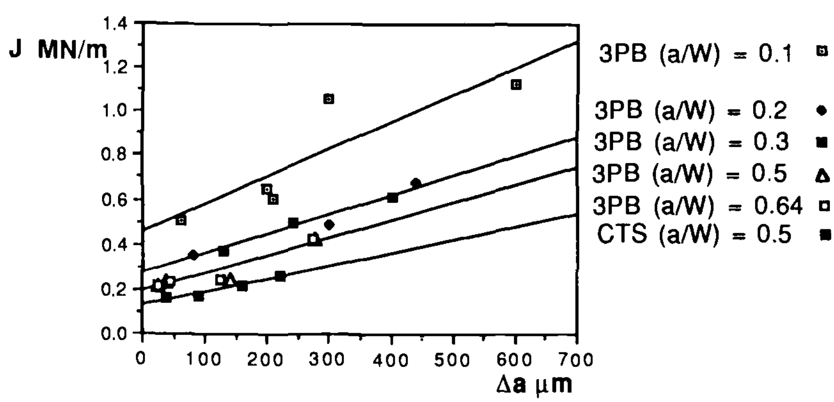

FIG. 11—J-Δa *resistance curves for the three-point bend and compact tension specimens.*

In the same way, the short-cracked bend specimens violated the crack length criterion for single parameter characterization, which would also require crack lengths in excess of 100 mm. The proposed two-parameter methodology is capable of overcoming the crack length limitation, but the authors would have preferred the ligaments of the bend specimens to have been larger, as this has led to a modest overestimate of crack tip constraint.

Discussion

The geometries tested demonstrate fracture behaviour across a broad range of crack tip constraint. The discussion of the results is couched in terms of the initiation of crack extension and the subsequent resistance to tearing.

In tough materials the start of crack tip extension is capable of a number of rather arbitrary definitions. Firstly, it is possible to extrapolate resistance curves back to the point of zero crack extension. Alternatively, it is possible to define a critical value of *J* or CTOD at a small amount of extension. For example, the current ASTM standard for J_{Ic} testing [*41*] gives *J* at the intersection of a resistance curve with a blunting line with an offset of 200 μm. Finally the standard for the determination of *J-R* curves allows crack extension measurements without offsets for crack blunting [*42*]. The draft British standards, currently under development, allow a range of measurements.

From a physical point of view, crack extension is usually regarded as a discrete process in which voids formed at second phase particles grow and coalesce with the crack tip. From this viewpoint it is problematic to think of crack extension over arbitrarily small microstructural

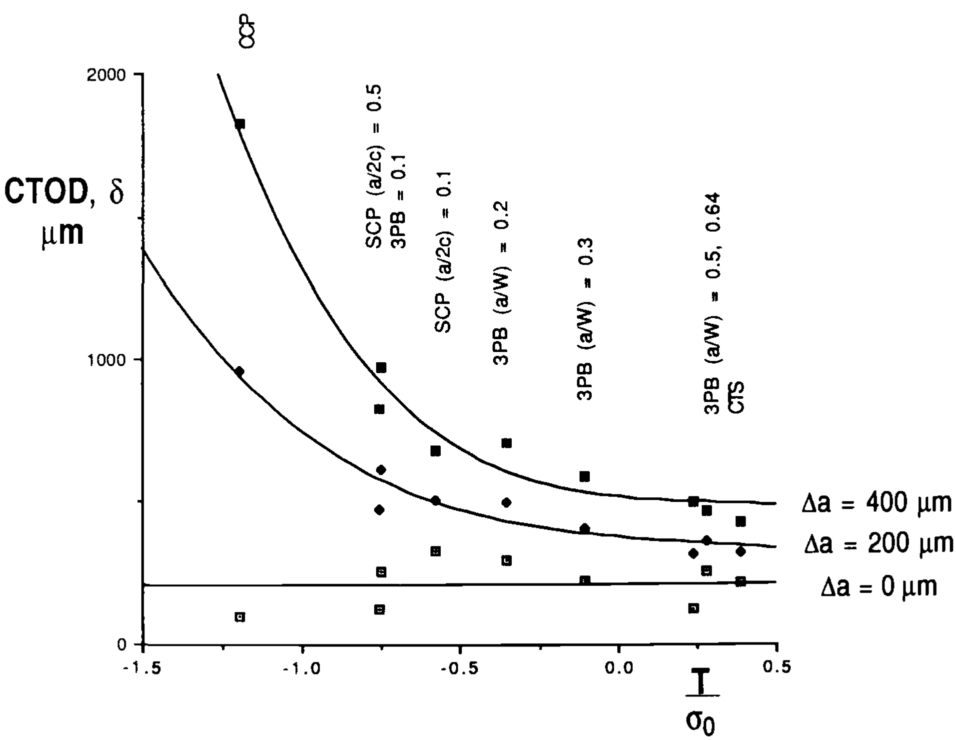

FIG. 12—*The CTOD as a function of the* T *stress at crack extensions of 0, 200, and 400 μm.*

distances, and indeed such measurements are rather subjective. There is, of course, a sense in which the random distribution of particles along the crack front allows crack extension at sections in which the nearest void happens to be statistically closer to the tip than average; however, crack extension is rarely measured in the corresponding statistical manner. In the present context it seems less than practical to pursue a statistical definition of initiation as a toughness at $\Delta a = 0$. These arguments tend to detract from the interpretation of resistance curves at points of zero extension. Nevertheless, it is clearly a practical procedural definition of initiation and as such has been shown in Figs. 12 and 13. The salient point is that on this definition of initiation A710 shows little effect of crack tip constraint on toughness. Indeed, paradoxically the toughness of the unconstrained center-cracked panel and SCP $(a/2c) = 0.5$ is significantly lower than that of the fully constrained deeply cracked bend bars and CTS specimens. This may arise from the rather subjective nature of crack extension measurements over small distances in geometries with very low constraint and from the choice of a linear curve fitting procedure. However, it is to be noted as the crack extension distance approaches zero, or some small fraction of δ, the triaxiality approaches 0.577 independent of geometry and indicates a geometry-independent failure criterion.

A simpler and preferable procedure is to define toughness at a small but significant amount of crack extension, such as 200 μm, as given in Figs. 12 and 13. In this case the results show a significant effect of constraint on toughness for crack extension. Thus the J and CTOD values for center-cracked panels are approximately four times greater than that of the highly constrained deeply cracked bend bars and CTS specimens. The effect is even more marked if

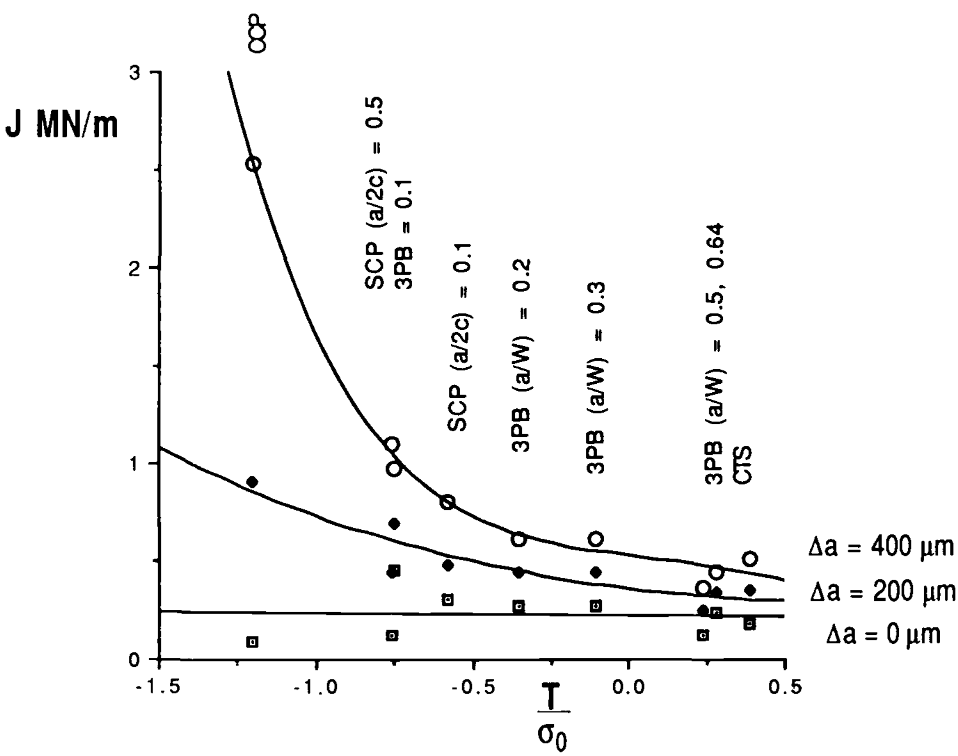

FIG. 13—*J as a function of the* T *stress at crack extensions of 0, 200, and 400 μm.*

extension is compared at Δa = 400 μm as shown in Figs. 12 and 13; however, caution must be exercised as tearing now starts to alter the geometry and associated constraint, particularly for short cracks. The reason for the strong effect of the amount of crack extension on the constraint sensitivity of toughness is due to the effect of constraint on the slope of the resistance curves, as illustrated in Figs. 14 and 15. For example, the slope of the δ-Δa plot of the center-cracked panels is so high that it exceeds that of the usual blunting line construction and prevents its use as a practical definition of initiation, in contrast to the behaviour of the deeply cracked bend bars and CTS specimens. Once more the T stress correctly orders the resistance to crack tip tearing. Geometries with negative T stresses show an enhanced resistance to tearing which is correctly parameterized by T. As a simple specific illustration, it is appropriate to compare the behaviour of a surface-cracked panel ($a/2c$ = 0.5) tested in tension and the edge-cracked bar (a/W = 0.1) tested in three-point bending, as shown in Fig. 12. Both configurations have similar T stresses and exhibit closely similar behaviour in terms of initiation and toughness. It would be difficult to have made such a connection without the use of the current methodology. Indeed, the size limitations for ligaments in tension would have completely prohibited the analysis and characterization of center and surface-cracked tension panels. The

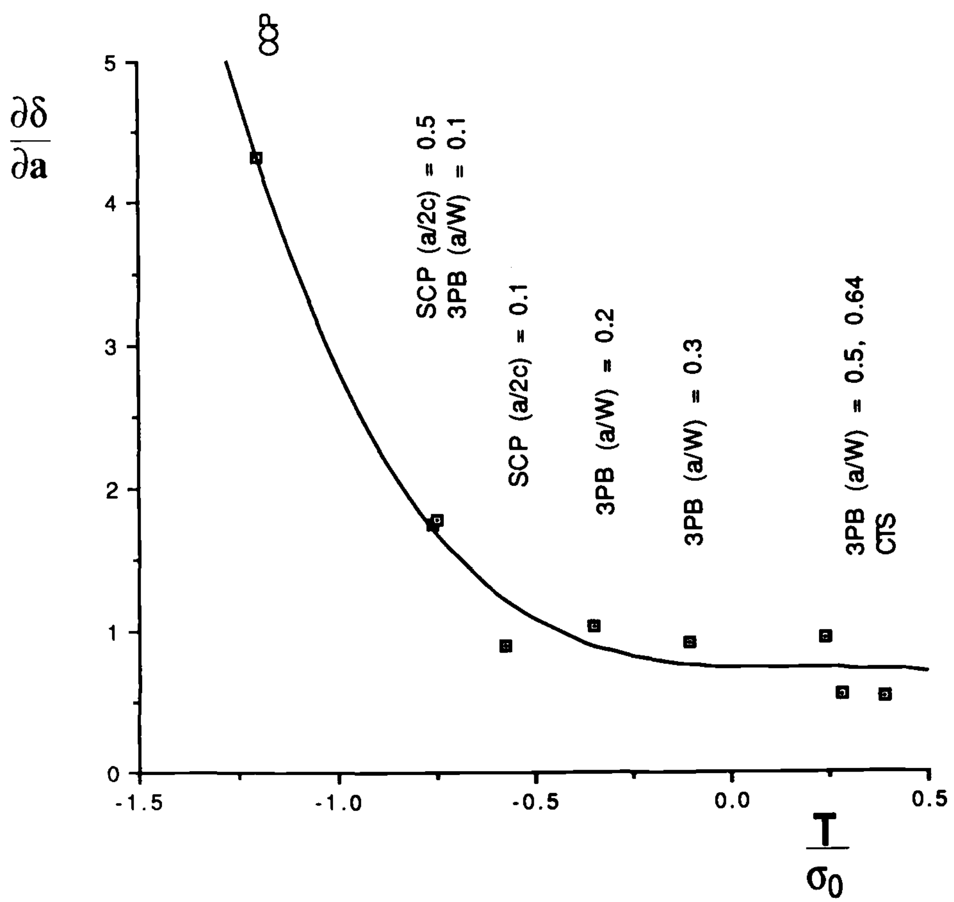

FIG. 14—*The initial slope of the CTOD-*Δa *resistance curve as a function of* T.

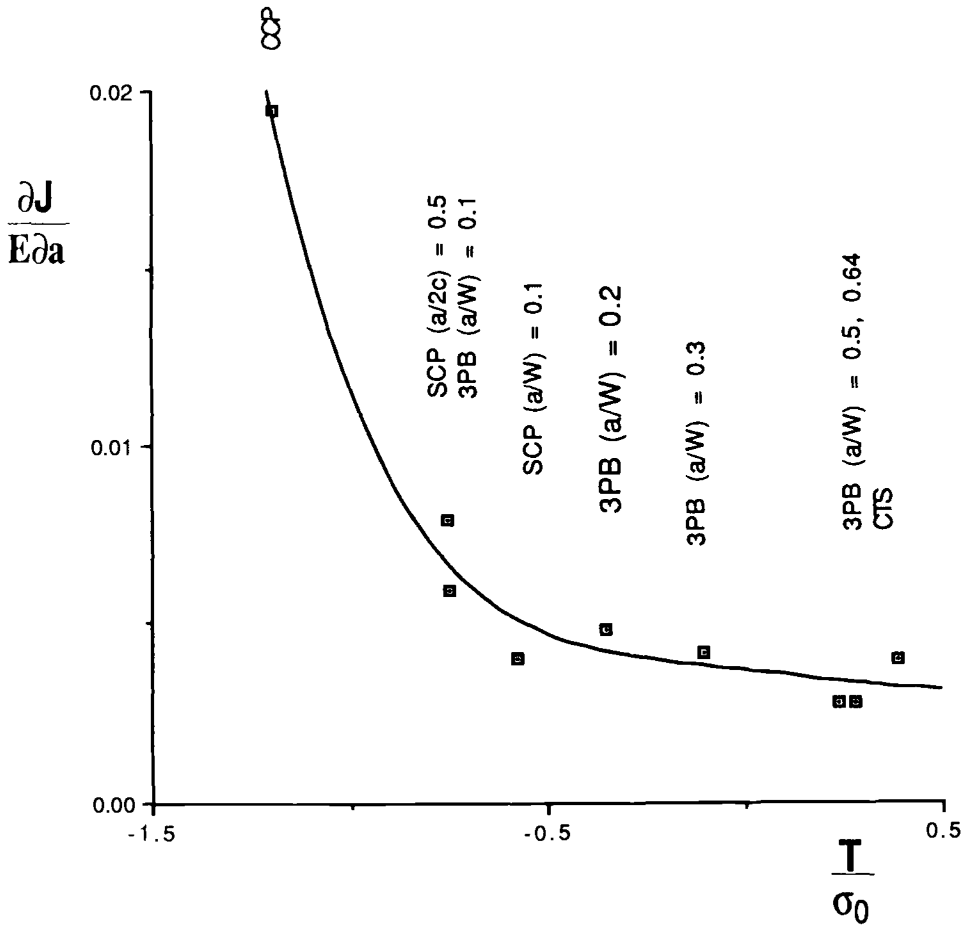

FIG. 15—*The initial slope of the* J-Δa *resistance curve as a function of* T.

work has thus relaxed the limitations of single parameter fracture mechanics by using T to characterize fracture toughness as a function of constraint and enabled the application of fracture mechanics to a wider and less restrictive range of configurations.

Conclusion

T has been validated as an appropriate parameter to characterize crack tip constraint in a wide range of fully plastic configurations. Geometries which show positive T stresses exhibit geometry-independent toughness. An enhanced geometry-dependent toughness and resistance to tearing geometry is associated with negative T stresses. The T stress correctly orders the toughness and resistance to tearing of a wide range of through and surface-cracked configurations in bending and tension. This allows the use of a practical two-parameter failure criterion in the form of a J-T locus. The appropriate toughness for real structural defects can now be matched against that of specimens with similar constraint through the use of a J-T fracture locus, allowing the conservatism associated with the use of deeply cracked geometries to predict the behaviour of unconstrained geometries to be removed.

Acknowledgments

The work was supported by the U.S. Department of Energy, Office of Energy Research under DoE contract number DE-ACO7-761DO1570. One of the authors (J.W.H.) acknowledges the support of the Associated Western Universities for the award of a visiting Fellowship to EG&G, Inc., Idaho National Engineering Laboratories, where much of the work was performed. JWH would also like to acknowledge the support and encouragement of J. Sumpter through MoD grant D/ERI/9/4/2048/59/ARE(D). Thanks are due to Hibbitt Karlsson and Sorensen, Inc., for access to ABAQUS.

References

[1] Williams, M. L., "On the Stress Distribution at the Base of a Stationary Crack," *Journal of Applied Mechanics*, Vol. 24, 1957, pp. 111–114.

[2] ASTM E 399-83: Standard Method for Plane Strain Fracture Toughness Testing of Metallic Materials, *ASTM Annual Book of Standards*, Section 3, Vol. 03 01, ASTM, Philadelphia, pp. 487–511.

[3] Hutchinson, J. W., "Singular Behavior at the End of a Tensile Crack in a Hardening Material," *Journal of the Mechanics and Physics of Solids*, Vol. 16, 1968, pp. 13–31.

[4] Rice, J. R. and Rosengren, G. F., "Plane Strain Deformation Near a Crack Tip in a Power Law Hardening Material," *Journal of the Mechanics and Physics of Solids*, Vol. 16, 1968, pp. 1–12.

[5] Rice, J. R., "A Path Independent Integral and the Approximate Analysis of Strain Concentration by Notches and Cracks," *Journal of Applied Mechanics*, Vol. 35, 1968, pp. 379–386.

[6] McClintock, F. A., *Plasticity Aspects of Fracture*, Vol. 3, *Fracture*, H. Liebowitz, Ed., Academic Press, London, 1971, pp. 47–225.

[7] McMeeking, R. M. and Parks, D. M., "On Criteria for J-Dominance of Crack-Tip Fields in Large-Scale Yielding," *Elastic-Plastic Fracture Mechanics, ASTM STP 668*, American Society for Testing and Materials, Philadelphia, 1979, pp. 175–194.

[8] Shih, C. F. and German, M. D. "Requirements for a One Parameter Characterization of Crack Tip Fields by the HRR Singularity," *International Journal of Fracture*, Vol. 17, 1981, pp. 27–43.

[9] Al-Ani, A. A. and Hancock, J. W., "J-Dominance of Short Cracks in Tension and Bending," *Journal of the Mechanics and Physics of Solids*, Vol. 39, 1991, pp. 23–34.

[10] Ewing, D., "The Plastic Yielding of V Notched Tension Bars with Circular Roots," *Journal of the Mechanics and Physics of Solids*, Vol. 16, 1968, pp. 205–213.

[11] Betegón, C. and Hancock, J. W., "Two Parameter Characterisation of Elastic-Plastic Crack Tip Fields," *Journal of Applied Mechanics*, Vol. 58, 1991, pp. 104–110.

[12] Du, Z. Z. and Hancock, J. W., "The Effect of Non-singular Stresses on Crack Tip Constraint," *Journal of the Mechanics and Physics of Solids*, Vol. 39, 1990, pp. 555–567.

[13] Larsson, S. G. and Carlsson, A. J., "Influence of Non-Singular Stress Terms and Specimen Geometry on Small-Scale Yielding at Crack Tips in an Elastic-Plastic Material," *Journal of the Mechanics and Physics of Solids*, Vol. 21, 1973, pp. 263–278.

[14] Rice, J. R., "Limitations to the Small Scale Yielding Approximation for Crack Tip Plasticity," *Journal of the Mechanics and Physics of Solids*, Vol. 22, 1974, pp. 17-26.

[15] Rice, J. R. and Tracey, D. M., "On the Enlargement of Voids in Triaxial Stress Fields," *Journal of the Mechanics and Physics of Solids*, Vol. 17, 1969, pp. 201–217.

[16] Hancock, J. W. and Mackenzie, A. C., "On the Mechanics of Ductile Failure in High Strength Steels Subjected to Multiaxial States of Stress," *Journal of the Mechanics and Physics of Solids*, Vol. 14, 1977, pp. 147–169.

[17] Rice, J. R., "Stresses Due to a Sharp Notch in a Work Hardening Material Loaded by Longitudinal Shear," *Journal of Applied Mechanics*, Vol. 43, 1967, pp. 287–298.

[18] Bilby, B. A., Cardew, G. E., Goldthorpe, M. R., and Howard, I. C., "A Finite Element Investigation of the Effect of Specimen Geometry on the Fields of Stress and Strain at the Tip of Stationary Cracks," in *Size Effects in Fracture, Institution of Mechanical Engineers*, London, pp. 37–46.

[19] Li, Y. and Wang, Z., "High-Order Asymptotic Field of Tensile Plane-Strain Nonlinear Crack Problems," *Scientia Sinica (Series A)*, Vol. 29, 1986, pp. 942–955.

[20] Sharma, S. M. and Aravas, N. J., "Determination of Higher Order Terms in Elastoplastic Crack Tip Solutions," *Journal of the Mechanics and Physics of Solids*, Vol. 39, 1991, p. 1043.

[21] O'Dowd, N. P. and Shih, C. F., "A Family of Crack Tip Fields Characterised by a Triaxiality Parameter," *Journal of the Mechanics and Physics of Solids*, Vol. 39, 1991, pp. 989–1015.

[22] Wang, Y. Y., Ph.D. thesis, Department of Mechanical Engineering, M.I.T., Cambridge, MA, 1991.

[23] Al-Ani, A., Ph.D. thesis, Department of Mechanical Engineering, University of Glasgow, Scotland, 1991.
[24] Parks, D. M. and Wang, Y. Y. in *Analytical, Numerical, and Experimental Aspects of Three Dimensional Fracture Processes,* Rosakis et al., Eds., ASME, AMD-91, ASME New York, 1988, pp. 19–32.
[25] Betegón, C., Ph.D. thesis, Department of Construction, University of Oviedo, Spain, 1990.
[26] Betegón, C. and Hancock, J. W., "Two Parameter Characterisation of Elastic-Plastic Crack Tip Fields and an Associated Failure Criterion," *Fracture Behaviour and Design of Materials and Structures,"* ECF8 Turin, D. Firrao, Ed., EMAS, Warley, U.K, pp. 999–1002.
[27] Sumpter, J. D. G. and Hancock, J. W., "Shallow Crack Toughness of HY80 Welds: An Analysis Based on T Stress," *International Journal of Pressure Vessels and Piping,* Vol. 45, 1991, pp. 207–221.
[28] Reuter, W. G. and Lloyd, W. R., "Measurements of CTOD and CTOA Around Surface Crack Perimeters and Relationships between Elastic and Elastic Plastic CTOD Values," *Surface Crack Growth: Models, Experiments, and Structures, ASTM STP 1060,* W. G. Reuter, J. H. Underwood, and J. C. Newman, Jr., Eds., ASTM, Philadelphia, 1990, pp. 152–176.
[29] Sumpter, J. D. G. and Turner, C. E., "Method for the Laboratory Determination of J_c," *Cracks and Fracture, ASTM STP 601,* ASTM, Philadelphia, 1976, pp. 3–18.
[30] Sumpter, J. D. G., "J Determination for Shallow Notch Welded Bend Specimens," *International Journal of Fracture,* Vol. 19, 1982, pp. 311–325.
[31] Sham, T. L., "The Determination of the Elastic T Term Using Higher Order Weight Functions," *International Journal of Fracture,* Vol. 48, 1991, pp. 81–102.
[32] Leevers, P. S. and Radon, J. C., "Inherent Stress Biaxiality in Various Fracture Specimen Geometries," *International Journal of Fracture,* Vol. 19, 1983, pp. 311–325.
[33] Reuter, W. G., Graham, S. M., Lloyd, R. W., and Williamson, R., "Ability of Measurements of δ to Predict Crack Initiation for Structural Components," in *Defect Assessment in Components: Fundamentals and Applications,* European Symposium on Fracture Mechanics, Freiburg FRG October 9–11, J. G. Blauel and K.-H. Schwalbe, Eds., Mechanical Engineering Press, London, U.K., pp. 175–180.
[34] Kfouri, A. P., "Some Evaluations of the Elastic T Term Using Eshelby's Method," *International Journal of Fracture,* Vol. 30, 1986, pp. 301–315.
[35] Rice, J. R. and Levy, N., "The Part Through Surface Crack," *Journal of Applied Mechanics,* Vol. 39, 1972, pp. 185–195.
[36] Parks, D. M., "Inelastic Line-Spring: Estimates of Elastic-Plastic Fracture Mechanics Parameters for Surface Cracked Plates and Shells," *Journal of Pressure Vessel Technology,* Vol. 103, 1981, pp. 246–254.
[37] *ABAQUS Users Manual,* Hibbitt Karlsson and Sorensen Inc., Providence, Rhode Island, 1987.
[38] White, C. S., Ritchie, R. O., and Parks, D. M., "Ductile Growth of Par Through Surface Cracks: Experiments and Analysis," *Elastic-Plastic Fracture, ASTM STP 803,* C. F. Shih and J. Gudas, Eds., 1984, pp. 384–409.
[39] Wong, Y. Y. and Park, D. M., "Calculation of the Elastic T Stress in Surface Cracked Plates Using the Line Spring Method," *International Journal of Fracture,* in press.
[40] Shih, C. F., "Relationships between the J-Integral and the Crack Tip Opening Displacement for Stationary and Extending Cracks," *Journal of the Mechanics and Physics of Solids,* Vol. 29, 1981, pp. 305–326.
[41] ASTM E 813-87: Standard Method for J_{Ic}, a Measure of Fracture Toughness," *ASTM Annual Book of Standards,* Section 3, Vol. 03, ASTM, Philadelphia, pp. 686–700.
[42] ASTM E 1152-87: Standard Method for J-R Curves, *ASTM Annual Book of Standards,* Section 3, Vol. 03, ASTM, Philadelphia, pp. 800–810.

Eberhard Roos,[1] Ulrich Eisele,[2] and Horst Silcher[2]

Effect of Stress State on the Ductile Fracture Behavior of Large-Scale Specimens

REFERENCE: Roos, E., Eisele, U., and Silcher, H., "**Effect of Stress State on the Ductile Fracture Behavior of Large-Scale Specimens,**" *Constraint Effects in Fracture, ASTM STP 1171*, E. M. Hackett, K.-H. Schwalbe, and R. H. Dodds, Eds., American Society for Testing and Materials, Philadelphia, 1993, pp. 41–63.

ABSTRACT: It is well-known from experimental investigations that at specific test conditions and specimen dimensions a sudden fracture, that is, a fracture without or after very confined plastic deformation, can occur even for materials that are characterized by small-specimen results as "tough materials." This effect usually is defined as a constraint effect without further explanation as to how to describe constraint.

Different constraint definitions were considered originating from theoretical investigations of well-known stress and deformation states of idealized nondamaged structures. As a result of these considerations, the quotient of multiaxiality q is used to analyze the constraint effects on large-scale specimens made of steels of different toughness.

It is possible to define a critical q-value as a local fracture criterion. From the location of this q_c-value in the ligament of the specimen and from the variation of the q-values in the ligament, it is also possible to assess whether stable crack growth will occur or not.

KEY WORDS: constraint, quotient of multiaxiality, q-factor, cleavage fracture strength, Sandel fracture theory, stress redistribution, stable crack extension

Specimens and components that are made of ductile materials with rather pronounced plastic deformation and that contain cracks should be assessed in accordance with the methods of ductile fracture mechanics. In the elastic-plastic stress range, the crack tip or notch tip is very strongly plastically deformed because of the stress concentration in this region. On reaching a material-dependent deformation limit, the crack begins to extend further. This crack growth phase is designated *stable crack extension* since, in order to drive the crack forward, a monotonic increase of loading is necessary. This process is dealt with on the basis of the two ductile fracture mechanics parameters, the J-integral [*1*] and the crack opening displacement (COD) [*2*] in the form of crack resistance curves. The crack resistance curves are determined on compact tension [CT, C(T)] or three-point bending specimens [TPB, SE(B)] in accordance with prescribed test methods [*3–5*]. The J-integral can be interpreted as the change in strain energy relative to the crack growth and is therefore relatively easily determined from integral deformation magnitudes. By contrast, the crack opening displacement is only independent of specimen geometry and size at the crack tip. The determination of the crack tip opening displacement (CTOD) thus occasions great demands on measurement technology [*6,7*].

There is, however, no difference in outcome whether the crack resistance curve is determined from the J-integral or the CTOD. Therefore the following statements are derived from crack resistance curves based on the J-integral, the so-called J_R curves.

[1] Energie-Versorgung Schwaben (EVS), Stuttgart, FRG.
[2] Staatliche Materialpruefungsanstalt, 7000 Stuttgart 80, FRG.

Experimental Findings

In a large research program [*8*] conducted at Staatliche Materialprüfungsanstalt (MPA) Stuttgart, the behavior of small- and large-scale specimens of different geometries, Fig. 1, made from steels of different properties was investigated. The most important material properties are given in Fig. 2 [*9*].

Experimentally determined J_R-curves, which were determined on proportionally enlarged CT specimens of thickness B = 10 to 100 mm made of a material based on the fine-grained

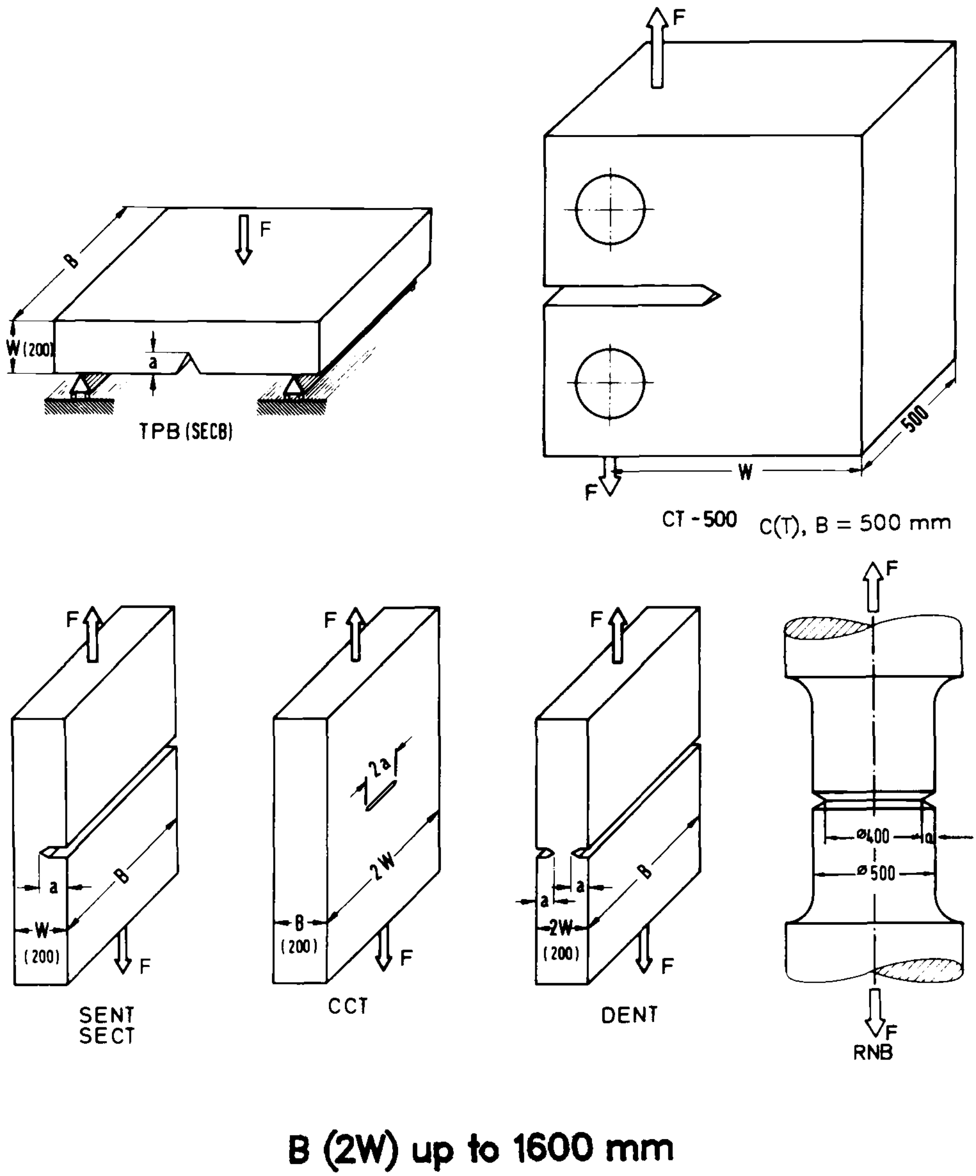

FIG. 1—*Investigated large-scale specimens.*

	C	Si	Mn	P	S	Cr	Mo	Ni	Al	Cu	V	Sn	Co	As	Sb	Ta
material A (KS17) (20 MnMoNi 55)	0,19	0,25	1,38	0,008	0,006	0,09	0,50	0,76	0,026	0,05	<0,01		0,011			<0,005
material B (KS07) (22 NiMoCr 37, modified test melt)	0,30	0,29	0,63	0,021	0,021	0,46	0,99	0,74	<0,004	0,26	0,05	0,011	0,017	0,027	<0,004	
material C (KS01) (22 NiMoCr 37)	0,23	0,20	0,73	0,015	0,014	0,42	0,74	0,95	0,032	0,12	0,01	0,01	0,016			<0,01
material D (KS14) (20 MnMoNi 55)	0,21	0,30	1,27	0,006	0,007	0,13	0,52	0,74	0,026	0,08	0,01	0,006	0,013			0,01

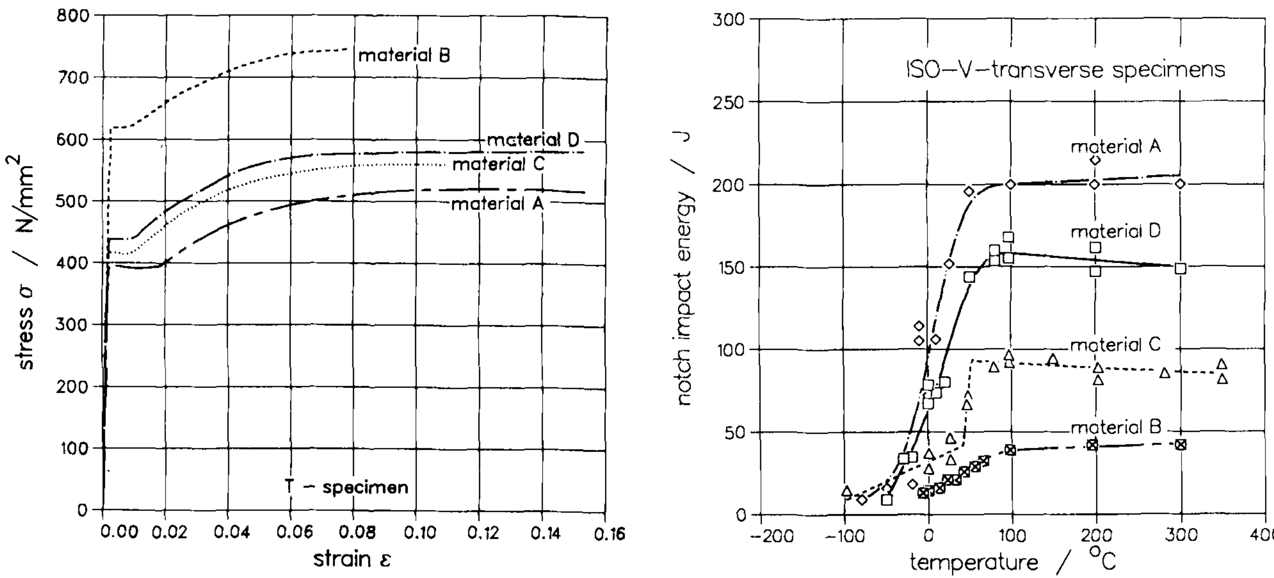

FIG. 2—*Chemical analyses and material characterization tests of investigated materials.*

steel 22 NiMoCr 3 7 (similar to A533 Class 2) with an upper shelf notch toughness of 90 J (ISO-V-transverse specimens) at 65°C (Material C, Fig. 2) are reproduced in Fig. 3. The J-values for these CT specimens are determined by the J_m method introduced by Ernst [*10*]. The specimens, which are 20% side-grooved, show a distinct size effect on the path of the crack resistance curves up to a value of $B = 50$ mm. On the contrary, the effective crack initiation value J_i is independent of size [*11,12*]. J_i can be determined from the stretched zone as measured in a scanning electron microscope. It signifies the beginning of the actual crack extension over the whole crack front.

This statement may be further generalized if the independence of the J_i-value on the specimen or component geometry is also proven. To this end relationships were derived at MPA Stuttgart [*13*] based on a proposal of Sumpter and Turner [*14*]. This method yields J values, which for CT and TPB specimens are very close to those obtained by the J_m formula from Ref *10*. It is incorporated into a program system [*15*] with which through easily measured integral openings (for example, loading line extension) the J-integral can be calculated online.

By way of example, the J_R-curves determined on a number of large specimens of thickness B of 300 mm and width W or $2W$ of 200 mm are given in Figs. 4 to 6. From these results a strong effect of the geometry on the crack resistance behavior becomes evident. In this it is especially striking that the J_R-curves of the CT specimens do not form the lower boundary of the crack resistance curves, that is, it cannot be assumed that the tearing resistance from CT specimens will cover all components conservatively, that is, safely [*16*].

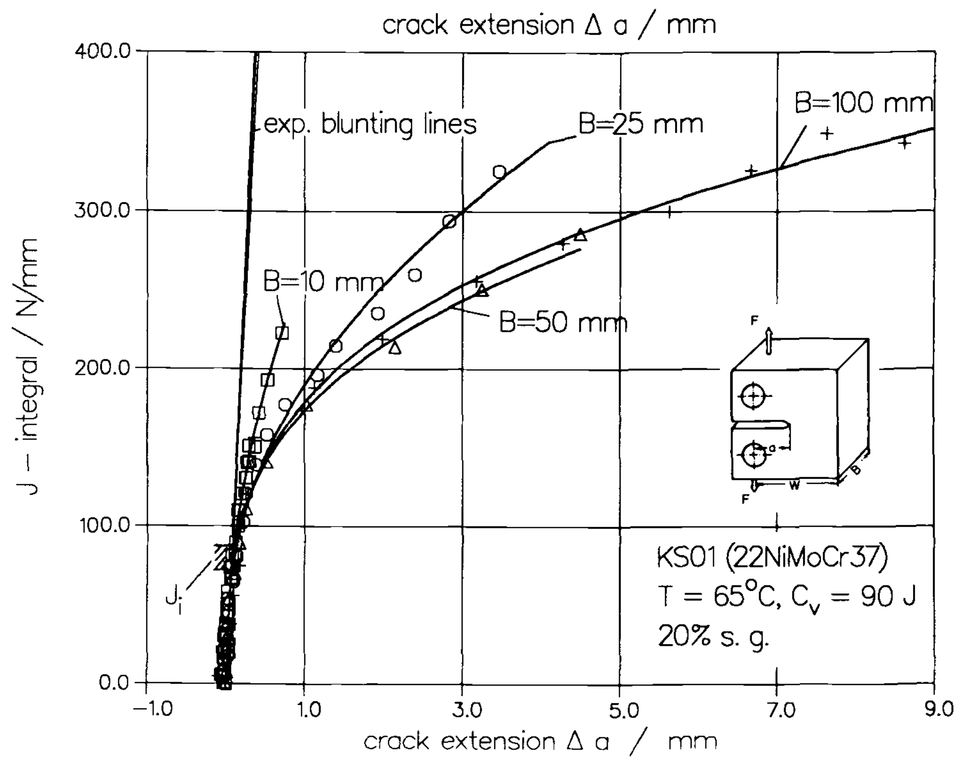

FIG. 3—*Crack resistance curves based on the* J*-integral determined on CT specimens of thicknesses from* B = *10 mm to* B = *100 mm (all specimens 20% side grooved, Material C).*

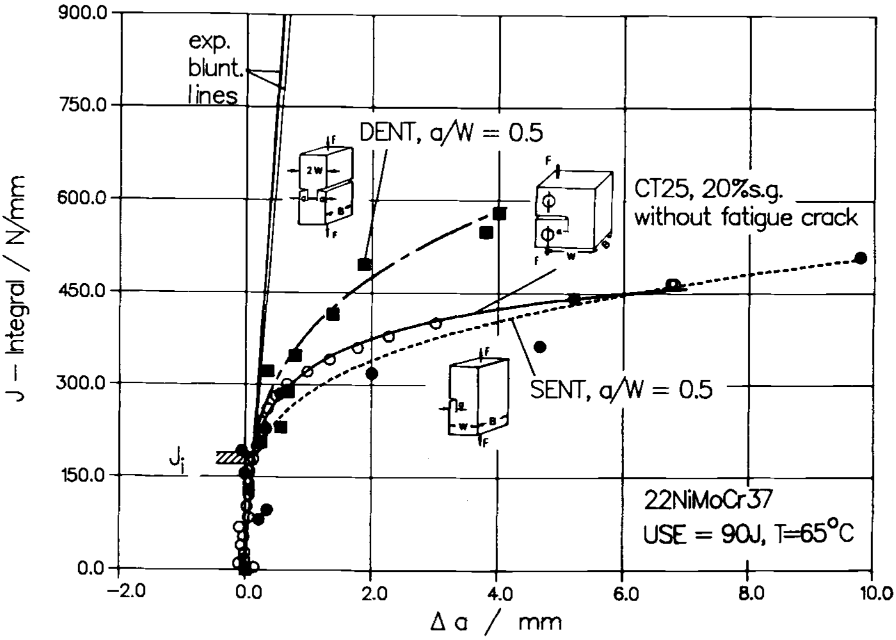

FIG. 4—*Crack resistance curves based on the* J*-integral of large SENT and DENT specimens compared with a crack resistance curve from a CT 25 specimen (20% side grooved, Material C), notch root radius* $\rho \sim 0.1$ *mm.*

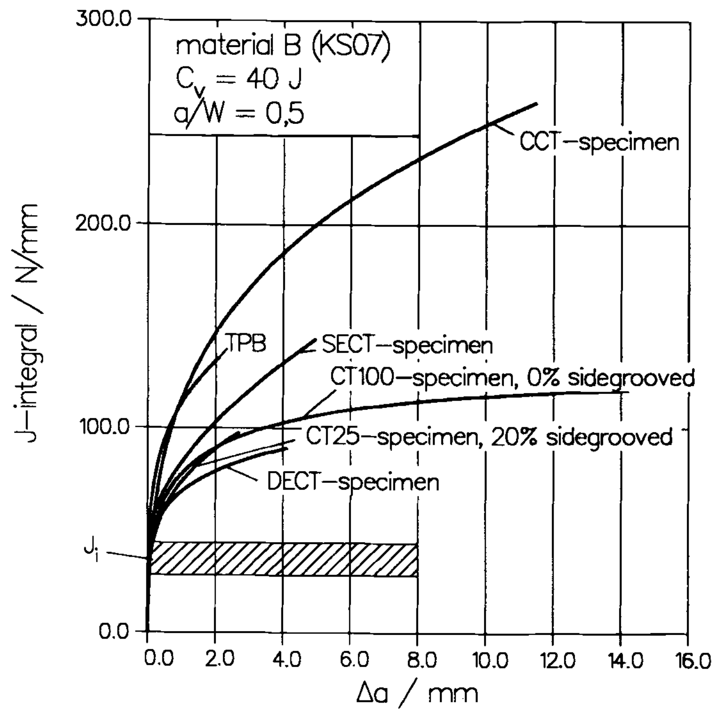

FIG. 5—J_R*-curves determined on large-scale specimens of various geometries compared with a crack resistance curve from a CT25 specimen (20% side grooved).*

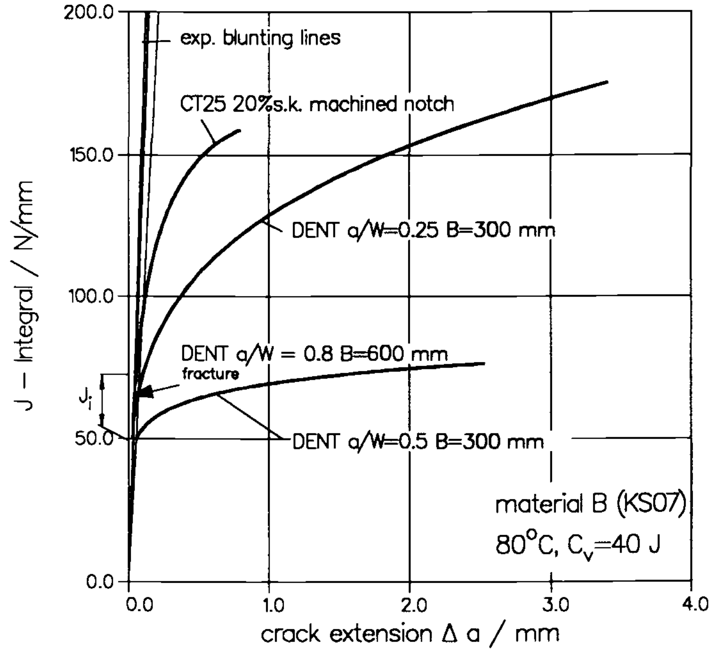

FIG. 6—J_R *curves of large DENT-specimens with different notch depths (a/W ratio), notch root radius* $\rho \sim 0.1$ *mm.*

In considering the same type of specimen, for example, double edge notch tension (DENT) specimens in Fig. 6, it becomes obvious that by enlargement of the initial crack depth, the contribution of stable crack extension becomes smaller (determined up to maximum load). In the limiting case, spontaneous failure of the specimen occurs through fracture perpendicular to the external loading direction when the imposed J-integral value reaches the effective initiation value J_i, as in the case of the DENT specimen with $a/W = 0.8$ (Fig. 6). The investigation of the fracture surface by means of a scanning electron microscope showed greater areas of cleavage, Fig. 7; shear lips did not exist.

In all the investigations it could be shown that within the compass of material scatter, the effective crack initiation value J_i is independent of the specimen size and geometry, as is stated in Fig. 8 for Material C as an example (see also Refs *11,12,15*).

Comparing specimens of identical geometry, size, and loading type, one finds increasing slopes of the J_R-curves with increasing material toughness, Fig. 9.

These experimental results show, in addition to other studies, an influence of the constraint situation on the fracture behavior that depends on specimen shape and dimensions as well as on material toughness. Under certain circumstances this can lead to sudden fracture after reaching the initiation value, as in the case of the deeply notched tension specimen in Figs. 6 and 7. Since in components such situations have to be avoided, it is necessary to have another parameter describing the constraint situation, especially in cases where a transition from ductile-to-brittle fracture has to be expected.

Strength Hypotheses

For ductile materials the maximum shear stress $(\sigma_3 - \sigma_1)/2$ and the quadratic invariant J_2' of the deviator of the stress tensor have proved themselves above all others as equivalence cri-

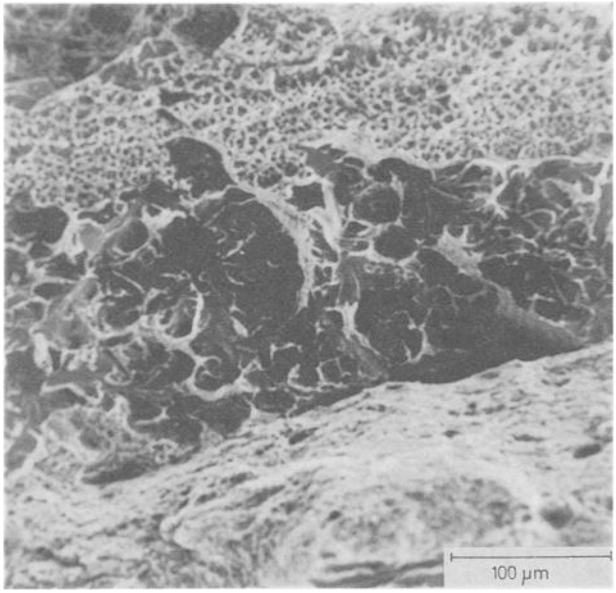

FIG. 7—*Fracture surface of the DENT specimen (*a/W *= 0.8, made of Material B).*

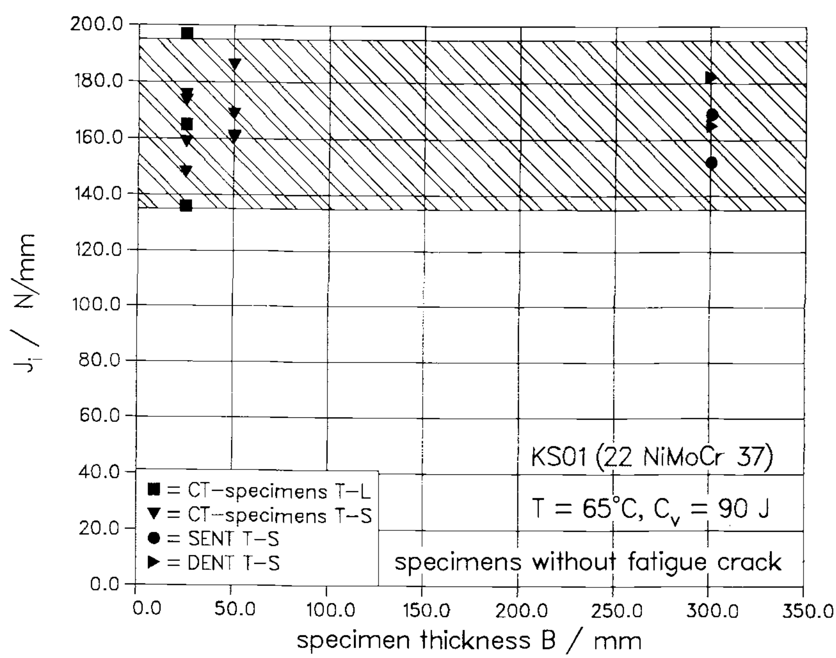

FIG. 8—*Dependence of the effective* J_i*-value on specimen thickness and geometry, Material C.*

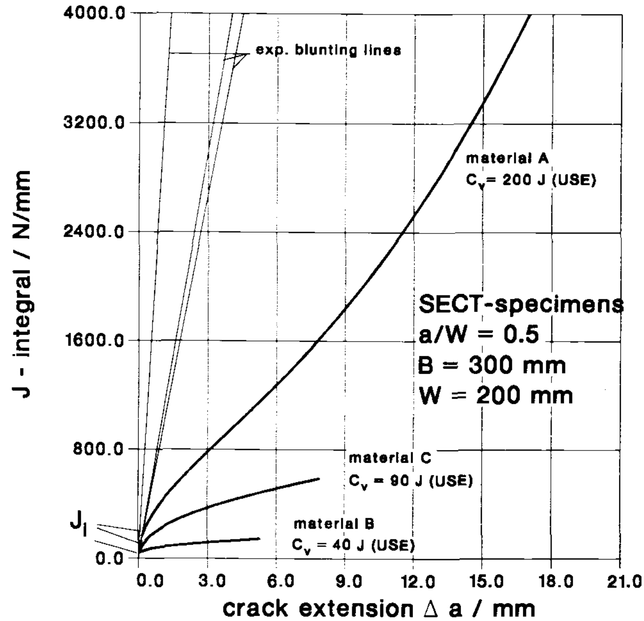

FIG. 9—J_R *curves of large SECT specimens with* a/W *ratio of 0.5 made of materials of different toughness.*

teria in the generation of σ_v. Plastic flow commences when the equivalent stress reaches the yield stress R_e of the material as measured from the uniaxial tension test.

Assuming for three-dimensional stress states

$$\sigma_1 \geq \sigma_2 \geq \sigma_3$$

the first named criterion leads to the yield condition

$$\sigma_v = \sigma_1 - \sigma_3 = R_e \tag{1}$$

This is known as the Tresca or Mohr-Guest theory [17]. The second named J_2'-criterion originates from von Mises [18] and leads to a yield condition in the form

$$\sigma_v = \sqrt{\tfrac{1}{2}\,[(\sigma_1 - \sigma_2)^2 + (\sigma_2 - \sigma_3)^2 + (\sigma_3 - \sigma_1)^2]} = R_e \tag{2}$$

Both the Mohr and the von Mises theories contain the principal shear stresses as the characterizing quantities: Eq 1 the largest and Eq 2 all three. One is therefore justified in speaking of the principal shear stress theories, of which the von Mises represents the generalized form.

Equation 2 is also referred to as the distortion energy or shear strain energy theory because, with the aid of the distortion energy associated with the deviator, it may be derived as an equivalence criterion. This derivation assumes the validity of Hooke's law, a limitation that is not necessary as the use of the J_2' criterion by von Mises shows.

If one transforms the tensor $\{\sigma_{ij}\}$ into its principal axis system, and in this system the stress state on the faces of an octahedron whose face normals form equal angles with the principal axes is considered, then one obtains as the octahedral normal stress

$$\sigma_{oct} = \tfrac{1}{3}(\sigma_1 + \sigma_2 + \sigma_3) = \sigma_0 \tag{3}$$

and as the octahedral shear stress

$$\tau_{oct} = \tfrac{1}{3}\sqrt{(\sigma_1 - \sigma_2)^2 + (\sigma_2 - \sigma_3)^2 + (\sigma_3 - \sigma_1)^2} \tag{4}$$

In Ref *19* Nadai has treated the relationship between τ_{oct} and σ_v from von Mises in the following manner

$$\tau_{oct} = \sigma_v\sqrt{2}/3 \tag{5}$$

Yield commences when

$$\sigma_v = R_e \text{ (see Eq 1 and Eq 2)} \tag{6}$$

or

$$\tau_{oct} = \sqrt{2}/3\, R_e = 0.47\, R_e \tag{7}$$

Using the invariants

$$J_1 = \sigma_1 + \sigma_2 + \sigma_3 \tag{8}$$

$$J_2 = \sigma_1\sigma_2 + \sigma_2\sigma_3 + \sigma_3\sigma_1 \tag{9}$$

of the stress tensor, after some algebraic operation, one finds the reduced shear stress τ_r

$$\tau_r^2 = (J_1^2 - 3J_2)/3 \tag{10}$$

as von Mises actually proposed. As the equivalent stress one now obtains not a uniaxial tensile stress but the biaxial shear stress condition. Slip processes depend on shear and hence on the action of shear stresses. Accordingly, the onset of yield is also described in a characteristic manner by $\tau_r = \tau_F$. A simple relationship

$$R_e = \tau_F\sqrt{3} \tag{11}$$

exists between the yield stress in the tension test R_e and the torsional yield stress τ_F in the torsion test.

All shear stress-free stress states can make no contribution to yield because slip processes are excluded. Accordingly, under the effect of σ_0 cleavage fracture must be considered as the failure mode.

The combination of the failure threshold onset of yield with that of the cleavage fracture in a component obviously comes down to a relationship $(\tau_r, \sigma_0) = f(\sigma_1, \sigma_2, \sigma_3)$ for the characterization of multiaxial stress states. Such a relationship was dealt with by Hencky by use of a representation τ_r (σ_0) [*20*]. Each stress state can be characterized by σ_0 and τ_r; this forms a radius vector on the (σ_0, τ_r) diagram, which in the case of yield is limited by the value $\tau_r = \tau_F$, Fig. 10. Since τ_F is independent of σ_0, τ_F lies parallel to the abscissa σ_0. When failure occurs by

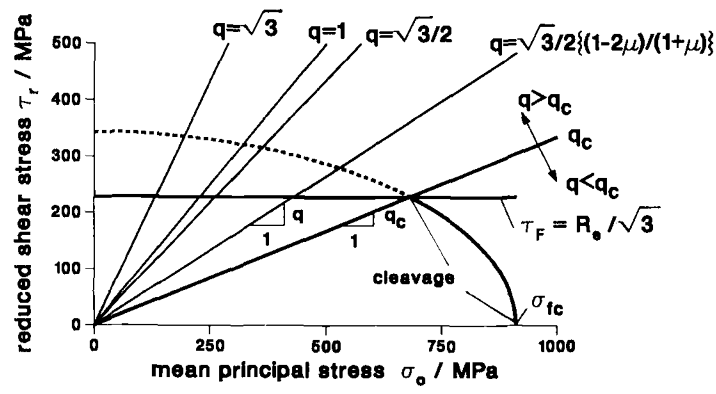

$$q_c = \begin{cases} \tau_F/\sigma_{fc}\sqrt{\dfrac{3(1-n)}{3(1-n)-(2+n)(\tau_F/\sigma_{fc})^2}} & , \ n = \dfrac{2\mu(2-\mu)}{1+2\mu^2} \\ \dfrac{1-2\mu}{2(1+\mu)}\sqrt{3} & , \ \mu < 0.5 \end{cases}$$

FIG. 10—*Sandel's fracture criterion in Hencky's representation. The lines* q = *constant represent special stress states.*

fracture, the cleavage fracture limit reaches the position of the yield point. The cleavage fracture limit is dependent on σ_0. This dependence should be treated as a closed function and should be confirmed experimentally.

On the basis of a fracture condition formulated by Sandel [*21*], the cleavage fracture dependence may be represented in the form

$$F(\sigma_v, \sigma_0, \tau_r) = 0 \tag{12}$$

The resulting strain of a multiaxial strain state serves as a criterion that is related to that of the uniaxial equivalent stress state, thus

$$\sqrt{\varepsilon_1^2 + \varepsilon_2^2 + \varepsilon_3^2} = \varepsilon_v\sqrt{1 + 2\mu^2} \tag{13}$$

Using Hooke's law and the abbreviation

$$n = 2\mu(2 - \mu)/(1 + 2\mu^2),\ \mu = \text{Poisson's ratio} \tag{14}$$

together with the invariants (J_1, J_2) from Eqs 8 and 9, one obtains from Eq 13

$$\sigma_v = E\varepsilon_v = \sqrt{J_1^2 - (2 + n)J_2}, \qquad \text{with } n < 1 \tag{15}$$

For $n = 1$

$$\sigma_v = \sqrt{J_1^2 - 3J_2} \tag{16}$$

The Sandel theory therefore includes the von Mises theory as a special case for $n = 1$. Thus, a powerful tool for the uniform description of fracture and yield processes is obtained.

Equation 15 may also be expressed in the following form

$$\sigma_v(\sigma_0, \tau_r) = \sqrt{3(1 - n)\sigma_0^2 + (2 + n)\tau_r^2} \tag{17}$$

This elliptical equation is normalized by means of

$$\sigma_v = \sigma_{fc}\sqrt{3(1 - n)} \tag{18}$$

and thus expressed

$$\left(\frac{\sigma_0}{\sigma_{fc}}\right)^2 + \frac{2 + n}{3(1 - n)}\left(\frac{\tau_r}{\sigma_{fc}}\right)^2 = 1 \tag{19}$$

where σ_{fc} represents the microscopic cleavage strength for the case that $\sigma_1 = \sigma_2 = \sigma_3$ and consequently $\tau_r = 0$, Fig. 10.

Although up to now σ_{fc} has not been successfully determined by experiment, the physical reality of the quantity is indisputable. It characterizes the resistance of the material to unstable crack extension without being influenced in any way by assumed plastic deformation processes. Yielding is suppressed by the equal universal tension stress state. In Fig. 10, in addition to the yield condition $\tau_r = \tau_F$, the cleavage fracture curve $\tau_r(\sigma_0)$ in accordance with Eq 19 is plotted. The attainment of the cleavage fracture strength is in general very localized, and the component tears in this region. The surrounding areas can, however, exhibit completely plastic deformation. This condition, observed from fracture-element (FE) analysis, does not conflict with Eq 19 as unstable fracture is only postulated for the region as σ_{fc} is attained. Unstable fracture of the component occurs, however, if, because of the stress state, regions of large cross-section draw near to the sections of the curve, which indicate fracture as represented in Fig. 10.

Characteristic Quantities of Multiaxiality

By multiaxiality or three dimensionality of a stress state is meant a triplet of values (σ_1, σ_2, σ_3) as compared with (σ_1, 0, 0), in which it is customarily assumed that $\sigma_1 > 0$. If one wishes to determine the influence of multiaxiality on material properties and hence draw conclusions as to the differences between uniaxially loaded specimens and multiaxially loaded components, then a description by means of

$$F(\sigma_1, \sigma_2, \sigma_3) = 0 \tag{20}$$

will not suffice. One must undertake a reduction to a quantity $R(\sigma_1, \sigma_2, \sigma_3)$ that experiences characteristic changes according to how a stress state of a varying degree of multiaxiality affects the impediment or facilitation of slip or cleavage processes in the material. The reduction with the aid of (σ_0, τ_r) presents itself immediately in accordance with the exposition in the previous section and a connection in the form of a multiaxiality quotient [*22,23*]

$$q = \tau_r/\sigma_0 \tag{21}$$

that takes into account the mutual relationship of both the pure shear and the universal tension, which in the ideal case triggers slip deformation or cleavage fracture mechanisms in the material. Clearly q describes the slope of straight lines through the origin in the (σ_0, τ_r) coordinate system, Fig. 10. Since in the (σ_0, τ_r) coordinate system the shear yield and cleavage fracture strength limits can be indicated in a simple manner—Eqs 11 and 19—the following distinctions may be arrived at: radial lines of stress states whose q is so large that they intersect the shear yield limit before reaching the Sandel limit curve indicate degrees of multiaxiality that make yield possible. If the radial line having a low q hits the limit curve for fracture directly, then a degree of multiaxiality is present that excludes yield. The critical degree of multiaxiality q_c is characterized by the point of intersection of the shear yield limit τ_F and the Sandel limit curve for fracture. For this the following relationship holds [*24*]

$$q_c = \tau_F/\sigma_0 = (\tau_F/\sigma_{fc}) \sqrt{\frac{3(1-n)}{3(1-n) - (2+n)(\tau_F/\sigma_{fc})^2}} \tag{22}$$

Equation 22 signifies that multiaxial stress states for which

$$q(\sigma_0, \tau_r) \leq q_c(\mu, \tau_F, \sigma_{fc}) \tag{23}$$

must lead to cleavage fracture without prior yielding. Hence a material-dependent minimum condition for q is established.

A further minimum condition for q results from the stress states produced by form closure. From the condition $F(\sigma_1, \sigma_2, \sigma_3) = 0$ these stress states may be expressed by

$$\varepsilon_2 = 0: \frac{\sigma_2}{\sigma_1} - \mu\left(1 + \frac{\sigma_3}{\sigma_1}\right) = 0 \tag{24}$$

and

$$\varepsilon_3 = 0: \frac{\sigma_3}{\sigma_1} - \mu\left(1 + \frac{\sigma_2}{\sigma_1}\right) = 0 \tag{25}$$

For

$$\varepsilon_2 = 0 \text{ and } \varepsilon_3 = 0: \frac{\sigma_2}{\sigma_1} = \frac{\sigma_3}{\sigma_1} = \mu/(1-\mu) \tag{26}$$

From this dependence of the stress state produced by form closure, this minimum condition, which depends on μ but not on τ_f/σ_{fc} [*25*], follows

$$q = \frac{\sqrt{3}}{2} \cdot \frac{(1-2\mu)}{2(1+\mu)}, \ \mu < 0.5 \tag{27}$$

This condition is valid if plastic flow, that is, $\mu = 0.5$, is ruled out by constraint. For $\varepsilon_3 = 0$ and $\mu = 0.3$, this is for the case of plain strain for linear elastic fracture mechanics (LEFM), $q = 0.266$ [*25*].

Other means of expressing q result from the relationships between (σ_0, τ_r) and the fracture and yield conditions based on (J_1, J_2). The following identities may be quoted

$$q = \frac{\tau_r}{\sigma_0} = \frac{\sigma_v}{\sigma_0} \cdot \frac{\sqrt{3}}{3} = \frac{\tau_{oct}}{\sigma_{oct}} \frac{\sqrt{3}}{\sqrt{2}} = \sqrt{3(1 - 3J_2/J_1^2)} \tag{28}$$

where $\sigma_0 \equiv \sigma_{oct}$.

Instead of q, various other characteristic quantities for the characterization of the degree of multiaxiality exist. They may be summarized as follows

from Refs *26–28* $$\pi = \sigma_v/\sigma_1 = 1 - \kappa \tag{29}$$

from Refs *29,30* $$h = \sigma_0/\sigma_v \tag{30}$$

from Ref *31* $$R = \sqrt{3} - q \tag{31}$$

from Ref *32* $$c = \sigma_0/\sigma_1 \tag{32}$$

Obviously q represents a combination of π and c. The expressions for h and R differ from q only in their formal constitution without going beyond q in the statement; π and c at any given time do not take into account the effect of σ_0 or τ_r. Most crucially, the equivalence of the triplet of values (σ_1, σ_2, σ_3) is estimated differently with respect to its degree of accommodation from the quantities q, π, and c [*22,23*]. Moreover, h displays a singularity ($h = \infty$) in the case of the hydrostatic stress state: for this important limit, case h therefore becomes unusable as a characteristic quantity. The singularity $q = \infty$ for the case where $\sigma_3 = -\sigma_1$ with $\sigma_2 = 0$ is of no importance because, in connection with critical multiaxiality and danger of cleavage fracture, only tensile stress states are of interest.

Whether one decides upon q or R as the characteristic quantity is a question of the preferred numerical order and interval spread in specified ranges of values.

All things considered, a comparison of the alternative characteristic quantities gives an indication that the use of the quotient q for the description of the degree of multiaxiality of the stress states offers advantages over the others owing to the rigor of its underlying assumptions and is to be preferred, as has been done for the subsequent studies on constraint behavior.

Quantification of Constraint in Fracture Mechanics Specimens

To quantify the constraint in specimens and components it is necessary, as stated above, to have knowledge of the stress distribution in the ligament. For these reasons, the behavior of all the experimentally investigated specimens described in the experimental findings section was calculated using elastic plastic finite element methods. Results and details on the methods used are reported in Refs *8* and *25*; the most important results are given in the following.

Determination of Cleavage Fracture Strength

In Fig. 11 results of a finite element computation of a large DENT specimen (B = 300 mm, $2W$ = 200 mm, a/W = 0,5) are plotted. The calculation was performed for Material B (Fig. 2) and a temperature of 80°C, that is, the beginning of the upper shelf level of the notch impact energy curve. Experimental results for this specimen expressed in terms of J versus Δa are given in Fig. 6.

In Fig. 11 the plastic zone sizes for different net section stresses σ_n up to the experimentally determined maximum load ($\simeq\sigma_n$ = 520 MPa) are given as well as the stress σ_{zz} and the resulting q-values.

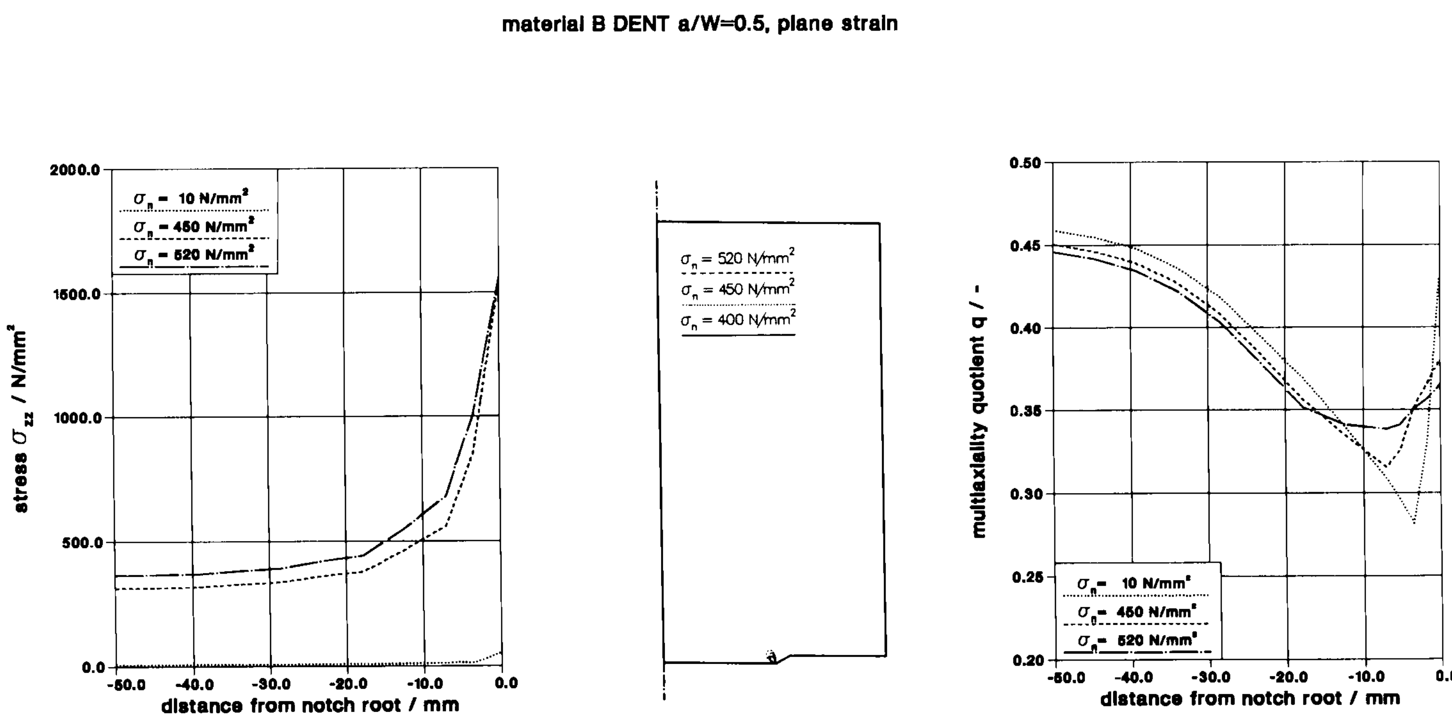

FIG. 11—*Distribution of the normal stress σ_{zz} and multiaxiality quotient q in the ligament of a DENT specimen and the extension of the plastic zone up to maximum load.*

As can be seen, the stress distribution was rearranged with increasing nominal stress, though only in the crack tip region; here q changed from 0.28 to 0.34 over the range of loading investigated. Some noteworthy conclusions may be established from these results.

If no stress redistribution occurs as a result of local plastic deformation, then a minimum q of 0.28 near the notch tip must be reckoned with.

In general, FE-calculations are not successful in determining the stress patterns and quantitative stress values reliably, if very large gradients exist, as is the case in the specimens considered. Because of the very fine mesh employed in the region of the crack tip and the fact that the minimum q_{min} value occurs in a region in front of the notch tip in which the high gradients are already diminished together with the nature of the multiaxiality quotient q as a stress relationship, it may be taken that the q_{min}-values so determined do justice to the actual relationship.

If one applies Eq 22 just to the determination of σ_{fc}, τ_F is known from Eq 11, and q_c is taken as 0.28 as the minimum q-value from Fig. 11, one obtains

$$\sigma_{fc} = R_e \sqrt{\frac{1}{3}\left(\frac{1}{q_c^2} + \frac{2+n}{3(1-n)}\right)} \sim 2.57 \cdot R_e \tag{33}$$

with n from Eq 14.

This result is not incompatible with those of earlier investigations [*33,34*]. By way of example, the micrograph of a large DENT specimen of a high toughness fine-grained steel 20 MnMoNi 5 5 (Material D, Fig. 2) confirms that local material severances occur in the specimen interior in the region where $q \sim q_c = 0.31$, Fig. 12, which leads to a σ_{fc}-value of $\sim 2{,}4 \cdot R_e$. Also a q_c-value of 0.31 could be confirmed by analytical considerations [*25*].

On the Necessity of Fracture Mechanics Assessments

The highest degree of multiaxiality of the stress state is attained immediately in front of the crack or notch tip, see Figs. 11 and 12. In this region, which generally coincides with the highest stressing and multiaxiality, the first material separation begins to occur, Fig. 12.

This, however, only applies to cracks and sharp notches. With decreasing notch acuity, that is, increasing notch root radius ρ, this region of maximum stressing is displaced from the areas close to the surface of the specimen or component center. In this case, failure begins by local separation processes in the interior of the component; this means that evaluation by fracture mechanics methods is no longer reliable. To show this effect, specimens with various notch root radii from a material similar to Material C, Fig. 2, were investigated [*35*].

From these results, conclusions can be drawn which indicate that with the aid of the multiaxiality quotient q the limits of applicability of fracture mechanics methods can be estimated, Fig. 13. If the location of the q_{min} values is close to the notch tip in relation to the ligament length, the application of fracture mechanics methods is necessary in contrast to cases where the q_{min}-location is remote from the notch tip (cited from Fig. 13) and the failure process starts in the center of the specimen.

Even if quantitative data concerning the value of y_B are presently lacking, one may roughly estimate the maximum permissible distance y_B of the point of q_{min} from the notch tip for fracture mechanics analysis still to be able to be applied.

Estimation of Stable Crack Growth Subsequent to Initiation

In Fig. 14, the calculated q_{min}-value from the individual loading steps are plotted against the related J-integral for the single edge cracked tension specimens shown in Fig. 9. From this it

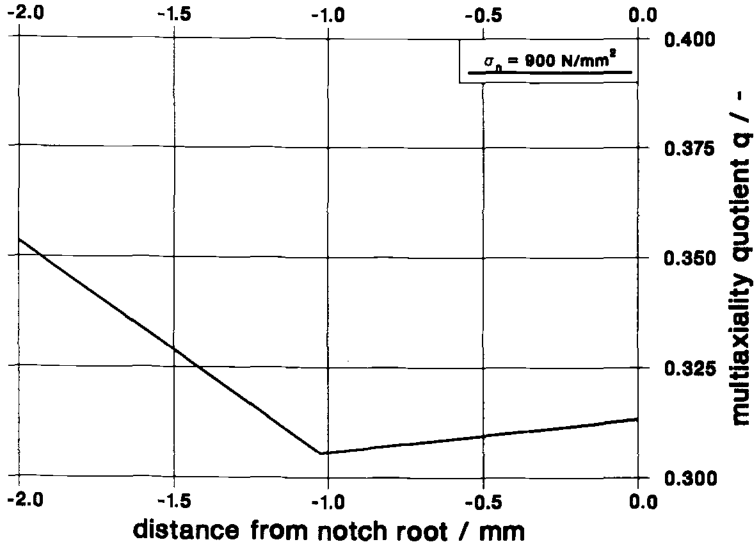

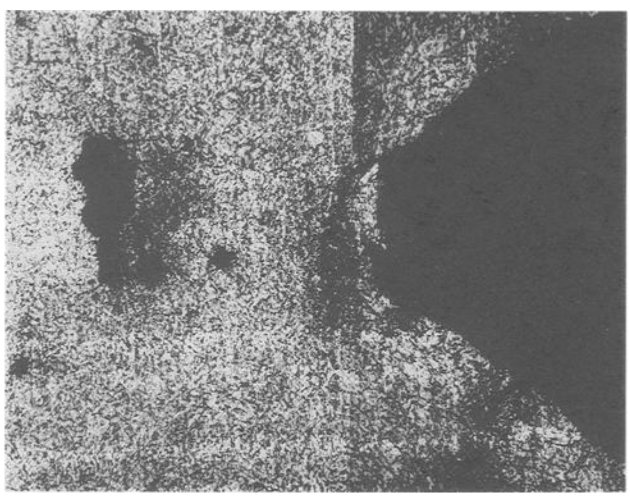

FIG. 12—*Distribution of* q *in the ligament of a large DENT specimen at maximum load and micrographic section through plane of the specimen after test.*

is clear that the diverse crack growth behavior cannot be classified by means of q_{min} as one might expect; the q_{min}-values in the region immediately in front of the crack tip are practically the same and independent of the specimen form [*36*]. The same also applies for the other specimens from Figs. 3 to 6.

An evaluation of the stable crack extension capacity can be made if the pattern of the q-value in the ligament is taken into consideration. In principle the different crack resistance behavior of the single edge cracked tension (SECT) specimens in Fig. 9 can be explained in this way. As expected, in the linear-elastic stressing range the pattern of q in the ligament is the same for all specimens independent of the toughness level. With increasing loading and

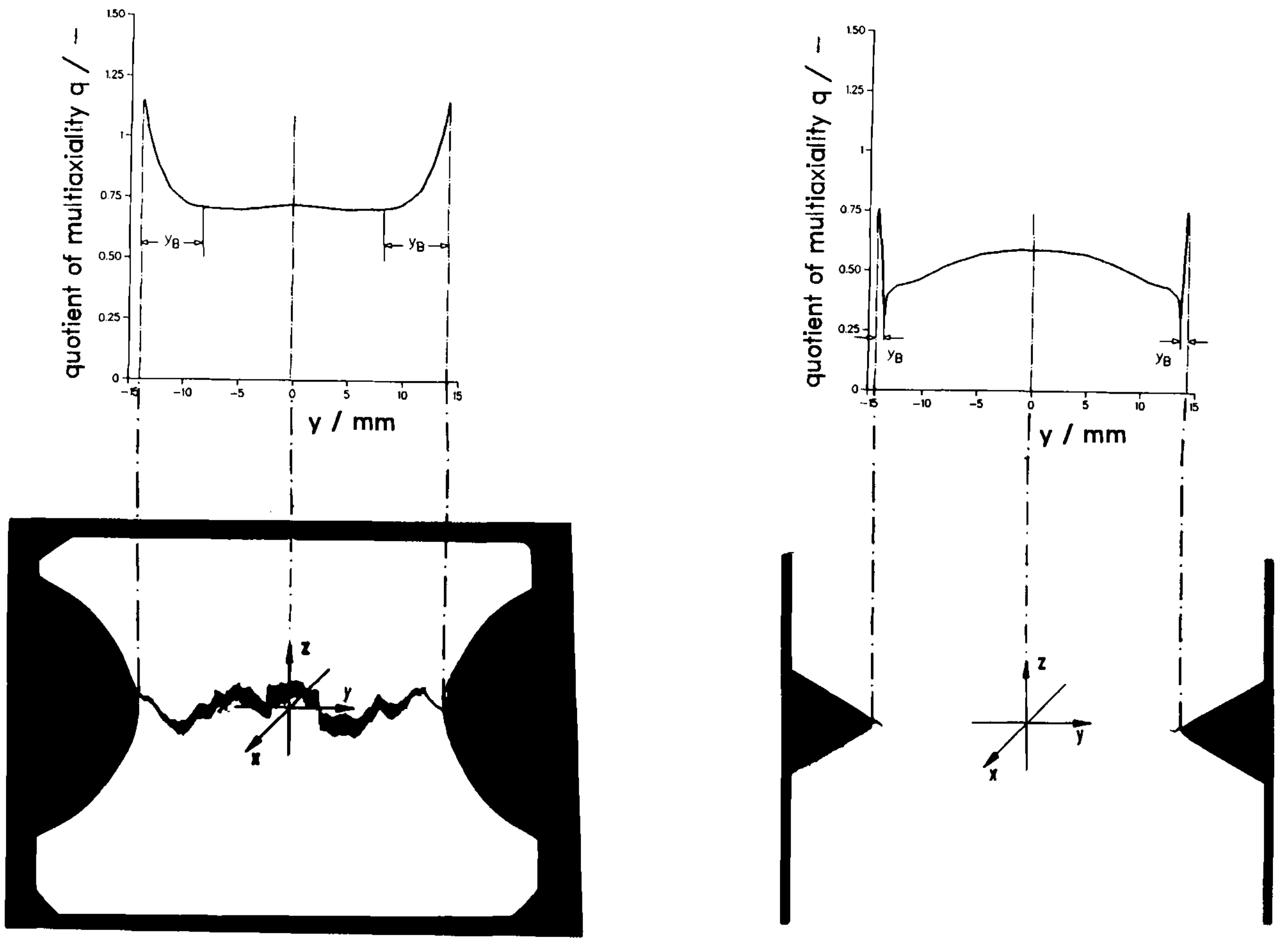

FIG. 13—*Distributions of the multiaxiality quotient* q *across the cross section of sharply* (α_k = 8.5) *and bluntly* (α_k = 1.5) *notched round tension specimens.*

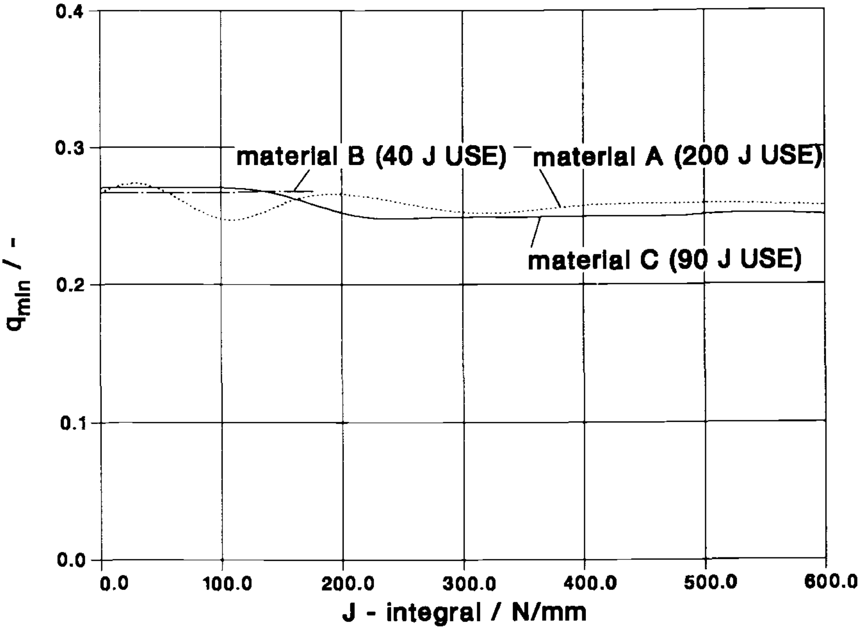

FIG. 14—*Minimum value* q_{min} *ahead of the crack tip as a function of the* J*-integral of the SECT specimens from Fig. 9.*

because of the higher toughness of Material A, the stresses are redistributed as a result of widespread plastic flow, the degree of multiaxiality of the stress state being thereby reduced, which manifests itself in the displacement of the path of the multiaxiality quotient q to higher q values, Fig. 15.

In the specimen of the low toughness Material B, only narrowly limited plastic flow in the crack tip region occurs so that the q pattern only deviates from that of the linear elastic condition in this region, Fig. 15. Correspondingly, the derivative of q across the ligament in the latter specimen is practically independent of the loading and lies in the region of zero, while in the specimen of Material A the slope of dq/dy is a function of the loading and with increasing plastification diverges more sharply from zero.

Looking at the specimen geometry and size as the varying parameters, the variations of q are determined, Fig. 16, for both of the specimens that form the upper (CCT) and lower (DECT) bounds of the band of J_R-curves in Fig. 5. For the CCT specimen a rapid rise of q results in values greater than 0.6 at a distance of 50 mm from the crack tip and more than $q = 1.0$ for greater distances. In the DECT specimen the q value remains low in the whole ligament, that is, a high multiaxial stress state acts. Accordingly, both the stable crack growth and the tearing resistance are significantly less in the DECT specimen than in the CCT specimen. This also shows itself in the derivative of the q-factor dq/dy across the ligament. For the DECT specimen the value of dq/dy across the ligament is closer to zero compared to the CCT specimen.

From these first exemplary analyses it may be deduced that for small multiaxiality quotients in the ligament ($q \sim 0.3$) and the derivative $dq/dy \sim 0$, only very little or no stable crack extension can be expected, that is, if $q(y)$ and dq/dy are not functions of the loading. This can be explained by another example of the DENT specimen with $a/W = 0.8$ from Fig. 6, which

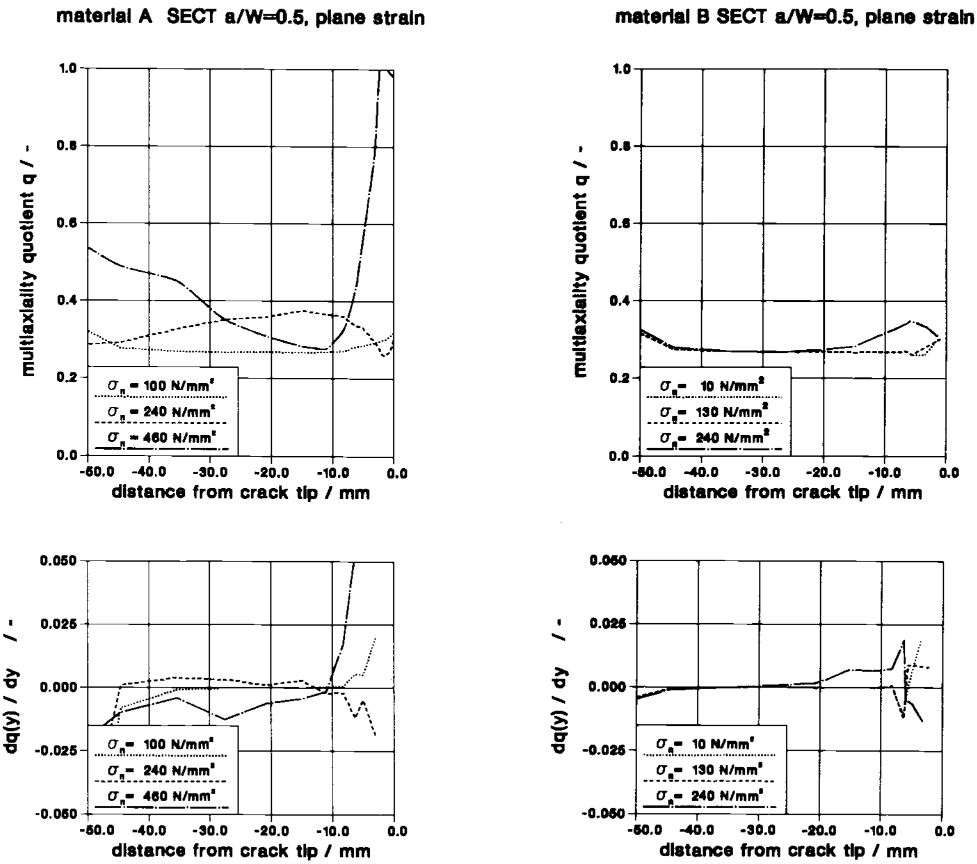

FIG. 15—*Distribution of* q *and* dq/dy *across the ligament of the SECT specimens from Fig. 9.*

failed without stable crack growth. The q-values of this specimen remain constant at $q_{\min} \simeq 0.29$ and $dq/dy \simeq 0$ over large parts of the ligament, especially close to the specimen center, Fig. 17.

Increasing stable crack growth appears if the above-mentioned conditions are not observed, that is, if a marked load dependence of the quantities $q(y)$ and dq/dy are evident. In this case the multiaxiality of the stress state is reduced by stress redistribution as a consequence of plastic flow.

If in the linear-elastic condition $dq/dy \neq 0$, that is, the value of q increases across the ligament, pronounced stable crack growth is to be expected, even if $q \neq f$(loading).

Conclusions

From the test results of large-scale specimens, it is a well-known fact that fracture may occur after smaller plastification than expected from small-scale specimen test results.

Occasionally, very high states of multiaxiality may arise in components in the case of sufficiently sharp transitions in geometry or in the presence of cracks because, despite excellent deformation capability of the material, deformationless fracture is practically inevitable.

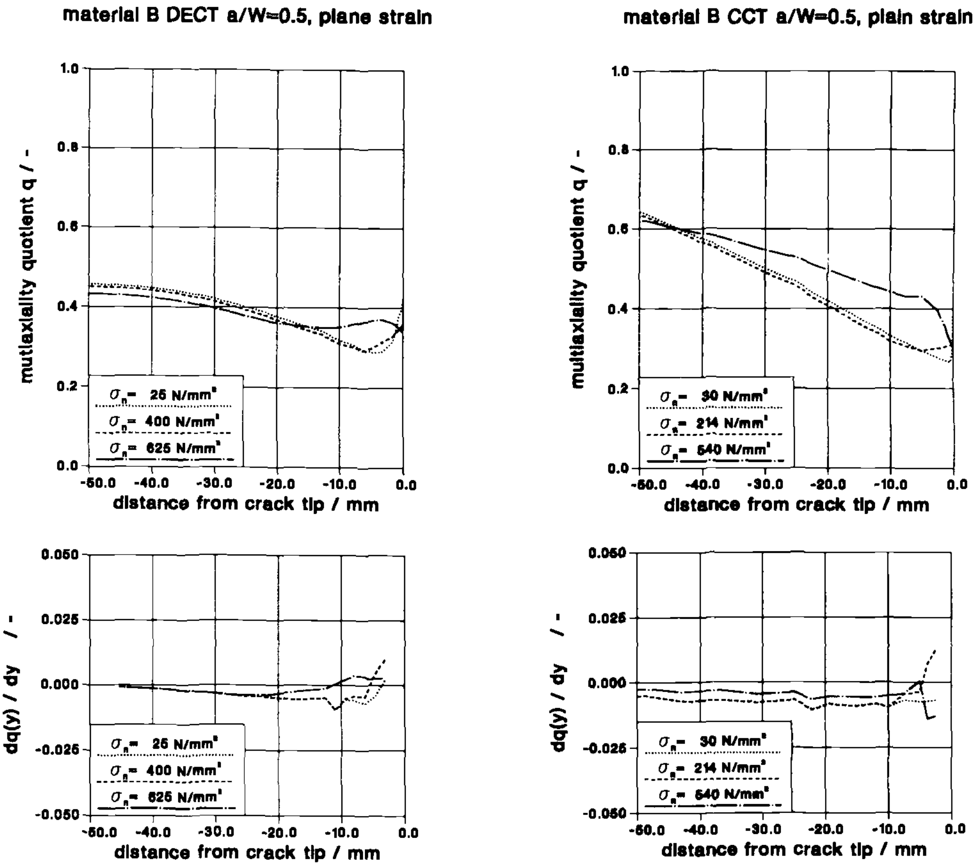

FIG. 16—*Distribution of* q *across the ligament of the DECT and CCT specimens from Fig. 5. The derivative of* q, dq/dy, *across to the ligament for both specimens is also shown.*

If one generates from the principal normal stresses (σ_1, σ_2, σ_3), the multiaxiality quotient q, which represents a characteristic quantity for the degree of multiaxiality of the stress state, the effect of the stress states on the strength and deformation behaviour of a component can be estimated. In so doing, stress redistributions as a consequence of plastic flow processes are also determined.

With the aid of the Sandel fracture theory, which includes the von Mises yield theory as a special case, the critical q-value q_c that characterizes the stress conditions leading to low deformation fractures, if $q < q_c$, can be calculated. Where $q > q_c$, ductile fractures are to be expected accordingly. This value was confirmed by finite element calculations on sharply notched large specimens. Using the q_c-value it was possible to estimate the microscopically observed cleavage fracture strength. Furthermore, by the determination of the variation of q over the notch cross section, it is possible to pronounce whether fracture mechanics methods may be applied for calculation of the failure loading.

The investigations have shown that the multiaxiality quotient q that characterizes the degree of multiaxiality of the stress state represents a characteristic quantity with which, in combination with fracture mechanics methods, the failure behavior of components, even with respect to stable crack extension, may be estimated more accurately.

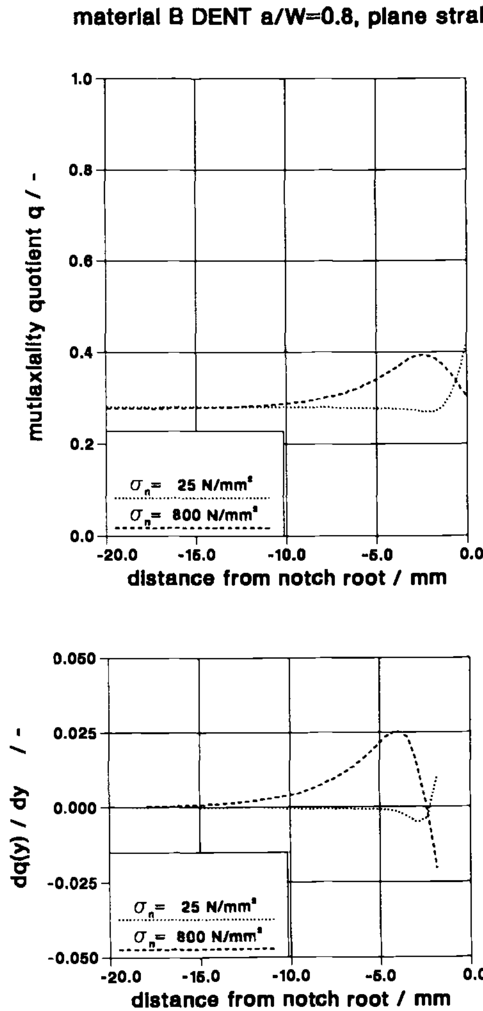

FIG. 17—*Distribution of* q *and* dq/dy *across the ligament of the DENT specimen with* a/W = *0.8 from Figs. 6 and 7.*

References

[1] Rice, J. R., "A Path Independent Integral and the Approximate Analysis of Strain Concentration by Notches and Cracks," *Journal of Applied Mechanics*, Vol. 35, 1968, pp. 379–386.

[2] Wells, A. A., "Unstable Crack Propagation in Metals—Cleavage and Fast Fracture," *Crack Propagation Symposium Proceedings*, Vol. 1, Cranfield College of Aeronautics, 1961.

[3] ASTM E 813-88, Standard Test Method for J_{Ic}, a Measure of Fracture Toughness," *Annual Book of ASTM Standards*, American Society for Testing and Materials, Philadelphia, 1989.

[4] DVM-Merkblatt 002: "Ermittlung von Rissinitiierungswerten und Risswiderstands-kurven bei Anwendung des J-Integrals," *Deutscher Verband für Materialprüfung*, June 1987.

[5] Methods for Crack Opening Displacement (COD) Testing, BS 5762, British Standards Institution, London, 1979.

[6] Roos, E. and Kockelmann, H., "A Survey of Different Experimental Methods for the Determination of Crack Initiation Parameters of Small and Large Scale Specimens," *Proceedings*, CSNI Principal Working Group 3: Primary Circuit Integrity, 2–3 Dec. 1982, Paris, France.

[7] Roos, E., "Erweiterte experimentelle und theoretische Untersuchungen zur Quantifizierung des Zähbruchverhaltens am Beispiel des Werkstoffs 20 MnMoNi 5 5," Dissertation, Universität Stuttgart, 1982.
[8] Roos, E. et al., Abschlussberichte zum "Forschungsvorhaben Komponentensicherheit," *Werkstoffmechanische Untersuchungen,* Teil A und Teil B, MPA, Stuttgart, 1990.
[9] Eisele, U., Roos, E., Seidenfuss, M., and Silcher, H., "Determination of *J*-Integral Based Crack Resistance Curves and Initiation Values for the Assessment of Cracked Large Scale Specimens," 22nd ASTM Symposium on Fracture, Atlanta, 1990, in press.
[10] Ernst, H. A., "Material Resistance and Instability Beyond *J*-Controlled Crack Growth," *Elastic-Plastic Fracture: Second Symposium; Vol. I: Inelastic Crack Analysis, ASTM STP 803,* C. F. Shih and J. P. Gudas, Eds., American Society for Testing and Materials, Philadelphia, 1983, pp. 191–213.
[11] Roos, E. and Eisele, U., "Determination of Material Characteristic Values in Elastic-Plastic Fracture Mechanics by Means of *J*-Integral Crack Resistance Curves," *Journal of Testing and Evaluation,* Vol. 16, No. 1, 1988.
[12] Roos, E., Eisele, U., Beyer, H., and Gillot, R., "Classification and Characterization of Materials by Means of Fracture Mechanics Parameters," *Nuclear Eng. and Design,* Vol. 102, 1987.
[13] Roos, E., Eisele, U., and Silcher, H., "A Procedure for the Experimental Assessment of the J-Integral by Means of Specimens of Different Geometries," *International Journal of Pressure Vessel Piping,* Vol. 23, 1986, pp. 81–93.
[14] Sumpter, J. D. G. and Turner, C. E., "Method for Laboratory Determination of J_{Ic}," *Cracks and Fracture: 9th Conference, ASTM STP 601,* American Society for Testing and Materials, Philadelphia, 1976, pp. 3–18.
[15] Roos, E., Eisele, U., Silcher, H., and Kie*ß*ling, D., "Ermittlung von Risswiderstandskurven auf der Basis des J-Integrals an Grossproben," *13th MPA Seminar,* 8–9 Oktober 1987, Stuttgart, FGR.
[16] Aurich, D. and Sommer, E., "The Effect of Constraint on Elastic-Plastic Fracture," *Steel Research,* Vol. 59, No. 8, 1988, pp. 358–367.
[17] Tresca, H., "Memoire sur l'écoulement des corps solides," *Mem. presents par div. savant,* Vol. 18, 1868, pp. 733–799 et Vol. 20, 1872.
[18] Mises, R. v., "Die Mechanik der festen Körper im plastisch deformablen Zustand," *Göttinger Nachrichten,* 1913, pp. 582–592.
[19] Nadai, A., "Plastic Behaviour of Metals in the Strain-Hardening Range," *Journal of Applied Physics,* Vol. 8, 1937, pp. 205–213.
[20] Hencky, H., "Ermüdung, Bruch, Plastizität," *Stahlbau,* Vol. 16, 1943, pp. 95–97.
[21] Sandel, G. D., "Die Anstrengungsfrage," *Schweizerische Bauzeitung,* Vol. 95, 1930, pp. 335–338.
[22] Clausmeyer, H., "Über die Versprödung von Stahl unter mehrachsiger Beanspruchung," *Habilitationsschrift,* Technische Hochschule Darmstadt D17, 1967.
[23] Clausmeyer, H., "Über die Beanspruchung von Stahl bei mehrachsigen Spannungszuständen," *Konstruktion,* Vol. 20, Heft 10, 1968, pp. 395–401.
[24] Clausmeyer, H., "Kritischer Spannungszustand und Trennbruch unter mehrachsiger Beanspruchung," *Konstruktion,* Vol. 21, H. 2, 1969, pp. 52–59.
[25] Clausmeyer, H., Kussmaul, K., and Roos, E., "Influence of Stress State on the Failure Behavior of Cracked Components Made of Steel," *Applied Mechanics Review,* Vol. 44, No. 2, February 1991, pp. 77–92.
[26] Schnadt, H., "Neue Prüfmethoden von Stählen und Schwei*ß*werkstoffen für grosse Schweisskonstruktionen," *Eisenberger Schweißnachrichten,* No. 4, 1957.
[27] Kochendörfer, A. and Rohrbach, C., "Kennzeichnung der Sprödbruchneigung von Stählen durch Messung der Fliesspannung, Rei*ß*spannung und Brucheinschnürung an dreiachsig beanspruchten Proben," *Archiv Eisenhüttenwesen,* Vol. 26, 1955, pp. 213–229.
[28] Kochendörfer, A. and Scholl, H., "Die Sprödbruchneigung von Stählen in Abhängigkeit von Spannungszustand und Temperatur," *Stahl und Eisen,* Vol. 77, 1957, pp. 1006–1018.
[29] Kordisch, H., Sommer, E., and Schmitt, W., "The Influence of Triaxiality on Stable Crack Growth," *Nuclear Engineering and Design,* Vol. 112, 1989.
[30] Hancock, J. W. and Brown, D. K., "On the Role of Strain and Stress State in Ductile Fracture," *Journal of Mechanics and Physics of Solids,* Vol. 31, No. 1, 1983.
[31] Wittwer, H.-J., "Zur Theorie der Trennfestigkeit metallischer Werkstoffe," *Archiv Eisenhüttenwesen,* Vol. 46, 1976, Nr. 1, pp. 41–49.
[32] Rühl, K. H., *Die Sprödbruchsicherheit von Stahlkonstruktionen,* Werner-Verlag, Düsseldorf, 1959, p. 31.
[33] Clausmeyer, H., "Einfluss von Kerbspannungszuständen auf die Versprödung von Stahl, Zähigkeit und Trennbruchsicherheit," *Konstruktion,* Vol. 21, H. 6, 1969, pp. 225–235.
[34] Wellinger, K. and Wittwer, H.-J., "Untersuchungen über die Trennfestigkeit von Stahl," *Archiv Eisenhüttenwesen,* Vol. 47, 1971, No. 4, pp. 213–221.

[35] Eisele, U., "Entwicklung und Überprüfung von Methoden zur experimentellen Bestimmung zähbruchmechanischer Kennwerte an bauteilähnlichen Proben," Dissertation, University of Stuttgart, Germany, 1988.
[36] Roos, E. and Schwantes, S., "Problems of Transferring Fracture Mechanics Parameters to Components," *Transactions of the 8th International Conference on Structural Mechanics in Reactor Technology*, Brüssel, 19 to 23 August 1985, North-Holland Publishing Co., Amsterdam.

Wolfgang Brocks[1] *and Winfried Schmitt*[2]

Quantitative Assessment of the Role of Crack Tip Constraint on Ductile Tearing

REFERENCE: Brocks, W. and Schmitt, W., **"Quantitative Assessment of the Role of Crack Tip Constraint on Ductile Tearing,"** *Constraint Effects in Fracture, ASTM STP 1171*, E. M. Hackett, K.-H. Schwalbe, and R. H. Dodds, Eds., American Society for Testing and Materials, Philadelphia 1993, pp. 64–78.

ABSTRACT: The quantities describing constraint and triaxiality and their relation with each other are discussed for various loading conditions and specimen geometries by comparing numerical simulations of crack growth based on the J-integral concept and on micromechanical damage models with the corresponding experiments.

It is shown that the "geometry dependence" of J_R-curves is a natural feature due to different patterns of plastic flow and micromechanical processes depending on the local stress state. Hence, this dependence cannot and should not be overcome by manipulating the definition of J. A pragmatic definition of a local triaxiality parameter is given that gives reliable and reproducible results. A linear relationship is found between the triaxiality and the tearing modulus of various specimens of the same material.

KEY WORDS: constraint, triaxiality, ductile fracture, tearing resistance, micromechanical models, J-integral, J-resistance curve, geometry effects

The influence of crack tip constraint and stress triaxiality on ductile fracture has been emphasized recently in explaining the geometry-dependent resistance of specimens and structures to ductile tearing. As this is of major importance for the assessment of structural integrity by means of fracture mechanics concepts, it seems worthwhile to discuss the underlying idea and physical significance of constraint.

Constraint is a structural feature that inhibits plastic flow and causes a higher triaxiality of stresses. It therefore may promote fracture because the input of external work, for example, measured by J, will to a lesser part be dissipated by plastic deformation but be available to enhance material degradation and damage. However, an engineering application of this concept requires a unique description of the quantities constraint, triaxiality, damage, and so on, allowing the quantitative evaluation of the involved parameters, for example, by finite element analyses. Although there is no doubt that the resistance against ductile tearing depends on the constraint or triaxiality of stresses, the problem still to be solved is how to define and quantify this parameter in a significant, reliable, and reproducible manner. Different definitions and measures are in use and impede a comparison of various approaches to account for constraint.

On the micromechanical level, stress triaxiality influences void growth and thus the development of damage in the process zone. Constitutive equations that account for damage as e.g. Gurson's model, are hence able to describe the physical effect of constraint on the tearing resistance as well. Both approaches will be used to describe the "geometry" effect on J_R-curves.

[1] Bundesanstalt für Materialforschung und -prüfung (BAM); D1000 Berlin 45, Germany. At Fraunhofer-Institut since Jan. 1, 1992.

[2] Fraunhofer-Institut für Werkstoffmechanik (FhIWM), D-7800 Freiburg, Germany.

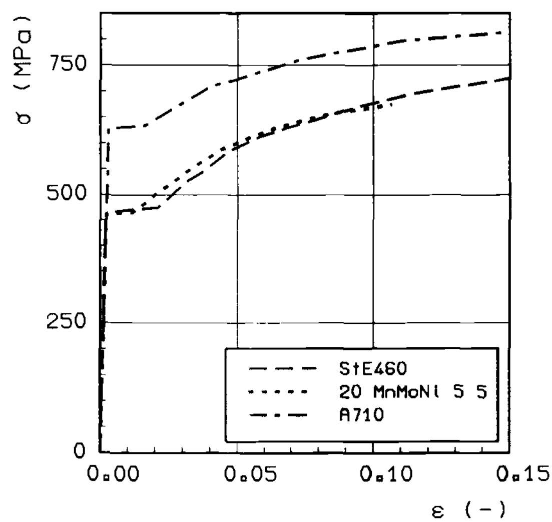

FIG. 1—*True stress strain curves of investigated steels from tension tests.*

Three different steels, i.e. the German standard steels StE 460 and 20 Mn Mo Ni 5 5 and the American A710, two having significantly different mechanical properties (Fig. 1) and fracture toughnesses, are investigated. Various specimen geometries under bending and tension have been tested and analyzed by finite element (FE) calculations. The results, which have been obtained independently at two different research institutes, BAM Berlin and FhIWM Freiburg, show that the correlations between the tearing modulus and the stress triaxiality are reliable and reproducible. As the tested specimens were side grooved and plane strain conditions were assumed for all calculations, only the effects of in-plane constraint are covered by the present investigations.

The Ductile Failure Process

An extensive survey of microstructural aspects of crack initiation and crack propagation may be found [*1*]. Introducing substantial simplifications, the fracture process for most of the structural steels may take place by either:

1. By the formation of microcracks and their coalescence, usually in an unstable manner.
2. By the formation, growth, and coalescence of (micro)voids, usually in a stable manner.

In the first case of brittle or cleavage fracture, only little plastic deformation is involved. The energy dissipation is low, and the appearance of the fracture surfaces is bright. The fast-propagating unstable crack may pass through or around grains. The introduction of a critical cleavage stress made the quantitative description of these processes possible.

In the second case of ductile fracture, significant amounts of plastic deformation are involved. Void formation takes place by decohesion of the particle-matrix interface, usually at nonmetallic inclusions. With increasing stresses and strains, the voids grow larger until they reach a critical size when they coalesce, mainly by localized shear failure of the matrix between voids. The fracture surfaces show dimples and appear like honeycomb. In view of the plastic deformations involved, a critical failure strain was used by many authors (for example, Ref *2*) to describe the onset of failure.

The growth of voids was investigated by McClintock [*3*], Rice and Tracey [*4*], and by Budiansky et al. [*5*], all of whom found an exponential dependence of the growth rate on the stress triaxiality that is well in agreement with experimental observations. The size and shape of voids calculated at the experimental failure load came out much smaller than expected. The coalescence process can, therefore, not be explained by the failure of the matrix in a homogeneous strain field. Instead, localized (for example, shear) deformation modes between voids must be considered in the final phase.

In terms of continuum mechanics, cracks represent singularities of the strain and/or stress fields. A measure of the singularities in the case of a nonlinear elastic material is the J integral. In combination with suitable material parameters, it may be used to describe the criticality of a crack.

The consideration of conservation laws within the theory of elasticity lead to the observation by Eshelby [*6*] that the generalized (material) force on a defect in an elastic solid could be expressed as a surface integral of the energy momentum tensor. Cherepanov [*7*] and, independently, Rice [*8*] introduced path-independent integrals for the evaluation of two-dimensional crack problems. Rice's work especially gave a significant impulse towards the application of the J integral in cases beyond the limits of linear elastic fracture mechanics (LEFM) based on the K concept.

The starting point of Rice's considerations was the assumption of elastic (linear or nonlinear) material behavior. This implies that the stresses can be derived from a potential, the strain energy density, which is a unique function of stresses or strains. On that basis it was not only shown that J is path independent but also that J is equivalent to the energy release rate. This latter interpretation established the correlation with the K concept of LEFM via the energy release rate G and, therefore, the potential of J as a fracture parameter became evident.

Begley and Landes [*9,10*] used J as a fracture criterion parameter and proposed a multispecimen procedure to measure the material fracture toughness J_{Ic}. To avoid principal difficulties arising from a multispecimen technique, Rice et al. [*11*] proposed estimation techniques for J from a single load-displacement record. The acceptance of the J-integral concept was promoted by the fact that J is easily determined by both experimental and numerical analyses.

By plotting J from their original results versus crack length change, Δa, Begley and Landes [*12*] derived the J integral resistance curve as a characterization of the material resistance against ductile tearing after initiation. The application of J-resistance curves to the evaluation of crack stability under ductile conditions was established by Paris et al. [*13*] and Hutchinson and Paris [*14*], who introduced a tearing instability theory.

A major concern regarding the application of J to materials described by an incremental or flow theory of plasticity (as is the case for most of the structural materials like e.g. steels or aluminium alloys) came from the fact that the theoretical basis of J was within a deformation theory of plasticity. The J integral evaluated on the basis of deformation theory was considered a valid fracture parameter, provided that J uniquely defines the stress and strain field in the vicinity of the crack. For plane situations and for certain approximations to the stress-strain curve, asymptotic solutions for the stress and strain field in the vicinity of a crack, the so-called HRR field, have been derived by Hutchinson [*15*] and Rice and Rosengren [*16*]. Much attention has, therefore, been paid to investigate under which conditions and to what extent the real stresses approach the HRR plane strain solution [*17–19*], which is supposed to be the most severe stress state.

In the case of crack extension, the assumption of proportional loading is not valid, but the possible error was considered tolerable if the relative amount of crack extension stayed within certain limits and if it was ensured that the nonproportional loading zones (elastic unloading and nonproportional plastic loading) at the crack tip was surrounded by a much larger zone of nearly proportional loading controlled by the HRR field [*14*].

J represents the force on a defect and is in the linear elastic case equivalent to the crack-driving force or energy release rate G in the Griffith sense. Griffith [*20*] proposed a fracture criterion in which the reduction in strain energy of a material containing a crack, when the crack extends, could be equated to the increase in surface energy due to the increase in surface area. The term "energy" means elastic energy that is recoverable by the system and may be used to drive the crack. The only dissipative term is the surface energy of the newly formed crack surfaces during crack extension.

The fact that for many materials a significant part of the work performed on the specimen or component is used to build up a plastic zone and is therefore no longer available to drive the crack has been the reason for additional concern. Especially the fact that significantly different J resistance curves were measured from different specimen geometries has led to the introduction of modifications to the original J integral (for example, Miyamoto et al. [*21*] and Ernst [*22*]).

Crack Tip Constraint and Triaxiality of Stresses

The effects of crack tip constraint are well known, qualitatively, but still no reliable definitions exist to quantify these effects. After the discussion of different definitions of constraint and triaxiality, a few results will be presented in the following which have been obtained by two-dimensional elastic-plastic finite element (FE) analyses. Plane strain condition was assumed as an appropriate model for side-grooved specimens. The elastic-plastic analyses use an incremental theory of plasticity by von Mises, Prandtl, and Reuss in an updated Lagrangian formulation. Some of the analyses simulated crack growth by a combined node shift/node release technique [*23*]. The utilization of a local damage model for the numerical analysis of ductile rupture [*24*] will be explained in the next section.

A global measure of constraint is the plastic constraint factor

$$L = \frac{F_{pl}}{F_0} \geq 1 \tag{1}$$

defined by the ratio of the actual collapse load, F_{pl}, of a flawed structure over the ideal plastic limit load, F_0, of an unflawed body of the same net section, thus quantifying the restraint of plastic flow due to the presence of a flaw. This factor allows the setting up of a rank correlation between different specimen geometries (see Table 1 and Ref *25*) but is not suited to characterize the local variation of crack tip constraint in a structure.

TABLE 1—*Constraint and triaxiality parameters of various specimens: results from finite element calculations (plane strain), material 20 Mn Mo Ni 5 5.*

Specimen	W, mm	a/W	L	d_n^{-1}	$K_{\sigma p}$	h_0
CT	50	0.5	1.69	2.35	4.1	2.8
DECT	125	0.8	1.70	2.01	3.8	2.5
CCT	125	0.8	1.18	1.68	3.3	1.7
CCT	125	0.1	1.16	1.70	3.4	1.8

For $J \simeq 150$ N/mm, $\Delta a = 0$.

The local constraint at the crack tip may be measured by the ratio of the load parameter, J, over the resulting characteristic deformation, crack tip opening displacement (CTOD), normalized by the yield stress, σ_0, since less CTOD at a given J means more crack tip constraint [26]. The linear relationship between J and δ_t

$$d_n^{-1}(z) = \frac{J(z)}{\sigma_0 \delta_t(z)} \tag{2}$$

can be derived from the two-dimensional HRR theory. In a three-dimensional structure the ratio d_n^{-1} may vary along the crack front.

The tensile stress criterion relies on the maximum principal stress. Thus, the plastic stress concentration factor, defined for Mode I loading by

$$K_{op}(z) = \max_r \left(\frac{\sigma_{yy}(r,\theta,z)}{\sigma_0} \right)_{\theta=0} \tag{3}$$

is relevant for cleavage fracture phenomena. It establishes the same hierarchy of specimen geometries as L and d_n^{-1} (see Table 1). However, as normal stresses in FE calculations are subject to numerical oscillations near the crack front, its reliability is limited.

A physically significant definition of the triaxiality of the stress state resulting from crack tip constraint is given by the ratio, h, of the hydrostatic stress, σ_h, or first invariant of the stress tensor, which does not cause any plastic deformation, over the von Mises effective stress, σ_e, (which is the square root of the second invariant of the deviatoric stresses) being responsible for plastic flow.

$$h(r,\theta,z) = \frac{\sigma_h(r,\theta,z)}{\sigma_e(r,\theta,z)} = \frac{\sqrt{2}\,\sigma_{kk}}{3\sqrt{3}\,\sqrt{\sigma'_{ij}\sigma'_{ij}}} \tag{4}$$

This idea dates back to Hencky's diagram [27] of effective shear stress, $\tau_e = \sigma_e/\sqrt{3}$, versus hydrostatic stress. The physical meaning of this ratio was substantiated by the investigations of McClintock [3] and Rice and Tracey [4], who found that the growth rate of cavities in perfectly plastic materials is proportional to exp $(3\sigma^\infty/2\sigma_0)$, where σ^∞ and σ_0 are the remote mean or hydrostatic stress and the yield stress, respectively. For a hardening material the yield stress equals the actual von Mises effective stress, σ_e, under fully plastic conditions. Apart from the multiplying coefficient, the exponential is equal to h. Figures 2*a* and *b* show the variation of σ_h/σ_e in the ligament ahead of the crack tip for a compact specimen (CT) and a center-cracked panel (CCT) of two different materials, the German standard steel St E 460 and the American A710. The FE calculations performed at BAM and FhIWM, respectively, used two different constitutive models, the incremental theory of plasticity by von Mises and a damage model described in the next section. Despite these basic differences in material properties and constitutive modeling, the results for the respective specimen geometries agree quite well and show significantly different triaxiality between the two geometries, CT and CCT.

At this point it is not possible to decide which of the parameters defined above is to be preferred. Different specimen geometries can be put in an order of constraint by any of these quantities (see [25] and Table 1). Generally, bend specimens like CT and single edge cracked bending (SECB) have a higher constraint than tension specimens like CCT and single edge cracked tension (SECT); thickness and/or side grooving raise the constraint. Advantages and drawbacks exist for each of the parameters.

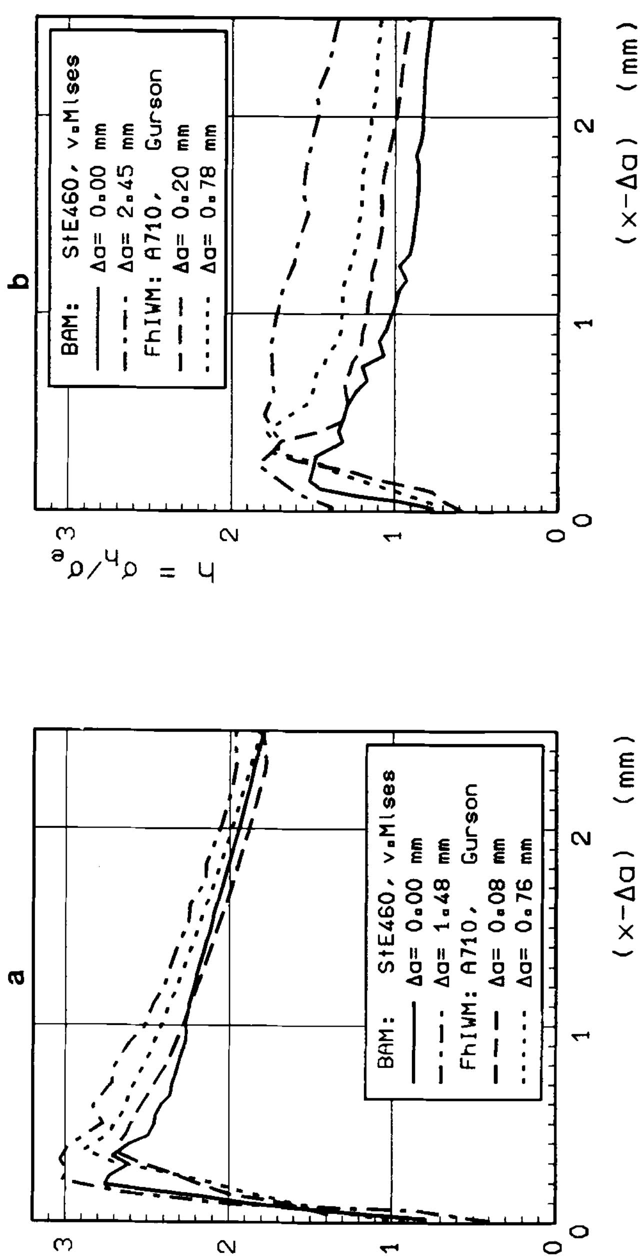

FIG. 2—*Triaxiality of the stress state in the ligament, results from plane-strain FE calculations:* (a) *CT specimen, and* (b) *center-cracked panel.*

1. The global plastic constraint factor can be determined rather easily and reliably, even in experiments, but it is not suited to characterize the local variation of crack tip constraint in a structure.
2. The local ratio d_n^{-1} is strongly dependent on the hardening exponent, n, for high hardening, which may even outweigh the discrimination between plane strain and plane stress. The definition of CTOD, δ_t, is normally restricted to a stationary crack and would have to be extended for a growing crack.
3. The range of values the ratio h may take between the limiting cases of plane strain and plane stress is much wider than that of d_n^{-1}, giving it a much better quantitative significance. But as the evaluation of h requires nonlinear FE calculations in any case, it will depend on the FE mesh and the solution strategy more than CTOD and J do. In addition, the underlying stresses are usually subject to numerical oscillations along the crack front in three-dimensional problems.

Despite the fact that various authors [*25,28–31*] use the ratio $h = \sigma_h/\sigma_e$ or its reciprocal as an appropriate measure of stress triaxiality, there are still some unsolved problems. Unlike δ_t, the ratio h is a local field quantity that varies not only with the crack front coordinate, z, but also with the distance to the crack front, r, and the ligament angle, θ. Hence, an additional assumption has to be made in order to decide which value is to be taken. This assumption is not only necessary to obtain reproducible numbers but will also be a question of physical importance. It may require the introduction of another material parameter, for example, some critical length, L_c, over which h is measured.

A few proposals how to determine the stress triaxiality exist. HRR theory and finite element (FE) analyses show that for Mode I problems σ_h/σ_e has its maximum in the ligament, $\theta = 0$. Kordisch et al. [*28*] extrapolated $h(r)$ to the crack tip, $r \rightarrow 0$, from a small strain analysis whereas Brocks et al. [*25,30*] used the maximum value ahead of the crack tip obtained from a geometrically nonlinear updated Lagrangian formulation. In a recent paper, Clausmeyer, Kussmaul, and Roos [*31*] took the slope $d(h^{-1})/dx$ to account for the shape of the curve in the ligament. Further studies are necessary before a widely accepted definition of constraint or stress triaxiality seems possible.

If incremental theory of plasticity is employed and if crack tip blunting is modelled, the ratio of triaxiality, h, has its maximum a small distance away from the crack tip followed by a rather linear decrease of the curve up to several millimeters. However, whether this maximum is picked up accurately enough depends on details of the finite element mesh. It is, therefore, not suited to define a characterizing and reproducible measure of the triaxiality. Therefore, in the present paper the ratio of triaxiality, h_0, has been calculated by a linear extrapolation to the crack tip, $(x\text{-}\Delta a) \rightarrow 0$, from the approximately linear branch of the $h(x\text{-}\Delta a)$-curve (see Fig. 3).

The Physical Effect of Constraint on Ductile Crack Growth

Figure 4*a* shows the fundamental dependence of J_R-curves on the specimen geometry for the steel StE 460 [*32*]: The tensile-loaded center-cracked panel (CCT) apparently has a higher tearing resistance than the bending-loaded compact specimen (CT), that is, more external work is needed for the CCT specimen to drive the crack by a given amount Δa as more energy is consumed by plastic dissipation. Besides the type of loading, bending, or tension, the specimen size, thickness, width, and side grooving of the specimen influences this balance of mechanical work and, hence the J_R-curves obtained. Figure 4*b* gives a few examples. This "geometry effect" is unquestionable with respect to the slopes of the J_R-curves, dJ/da. Whether or not the initiation value, J_i, is affected by the specimen geometry, too, is not yet clear. As the

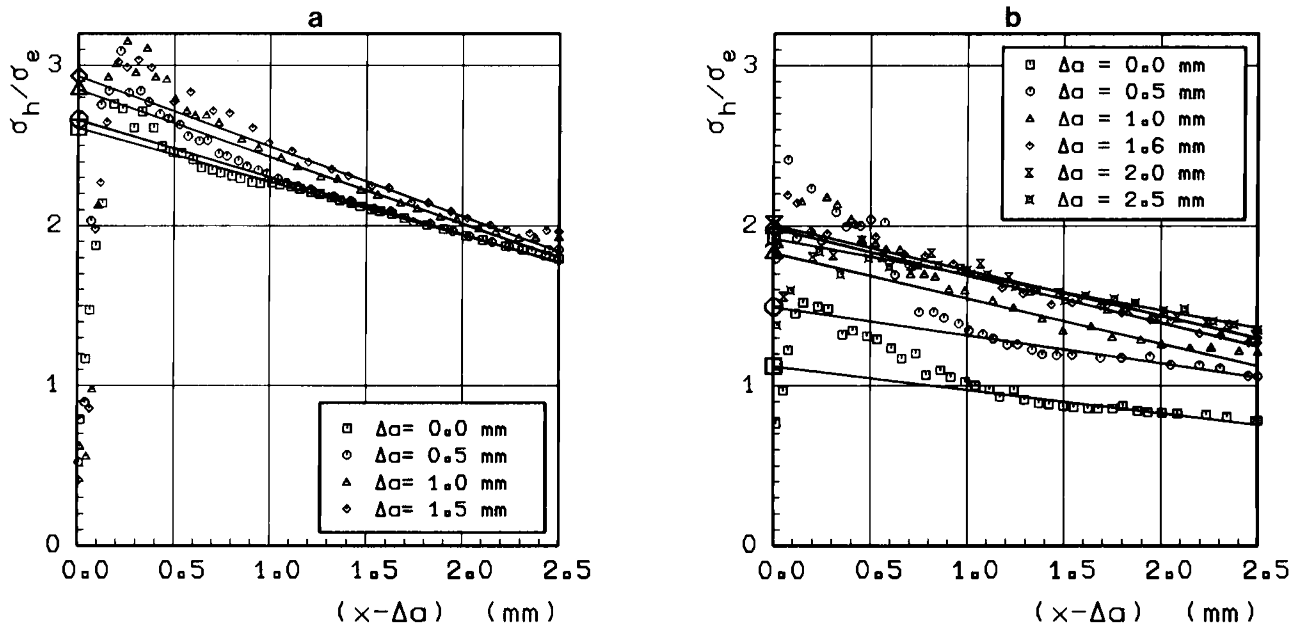

FIG. 3—*Determination of the triaxiality parameter* h_0 *by linear extrapolation, results from plane-strain FE calculation by simulating crack growth:* (a) *CT specimen, and* (b) *center-cracked panel.*

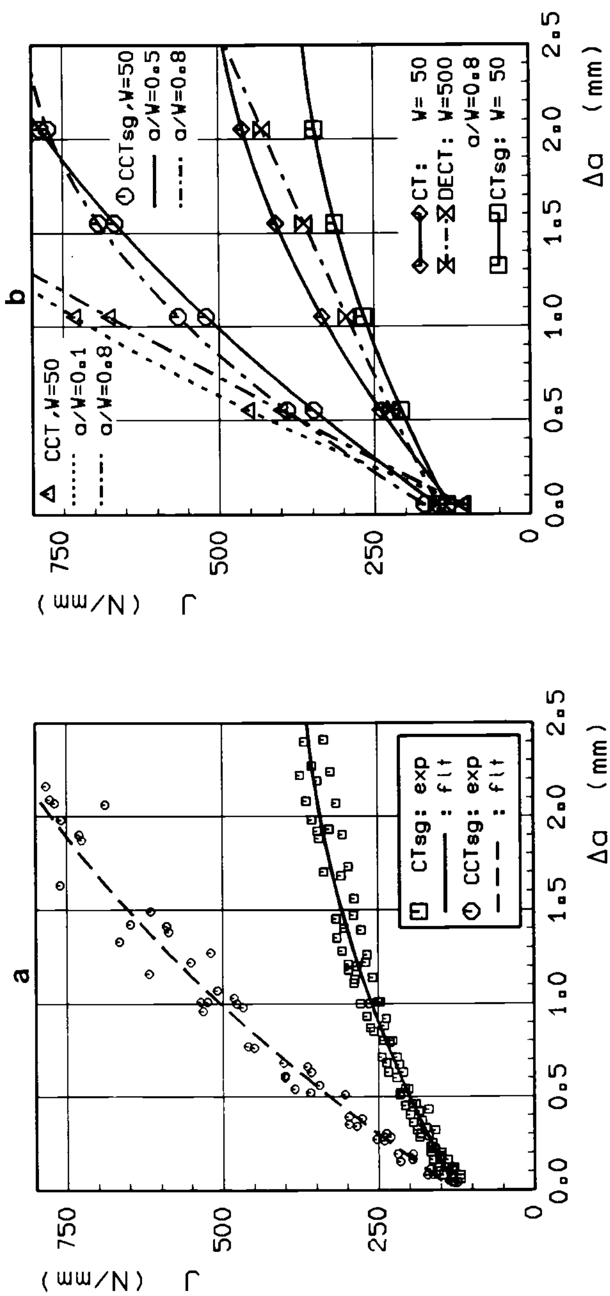

FIG. 4—*Geometry dependence of* J-R *curves for S+E 460:* (a) *CT and CCT single specimen technique tests, curve fit by quadratic polynomials, and* (b) *tests of various specimens, curve fit by quadratic polynomials.*

point of physical initiation is difficult to identify experimentally, little evidence exists. Commonly, J_i is supposed to be a material constant, but there is some indication contrary to this assumption (see Ref *33*). The present paper is restricted to the correlation of the slopes of the R-curves or tearing moduli

$$T = \frac{E}{\sigma_0^2}\frac{dJ}{da} \tag{5}$$

with the triaxiality of the stress state as defined by Eq 4 and Fig. 3. Table 2 gives the results for the two tested and analyzed specimens, CT and CCT, at initiation. The tearing modulus was determined from a quadratic curve fit of all the experimental data obtained in single specimen technique tests (see Fig. 4*a*).

The dependence of J resistance curves on the stress state is not only due to the fact that J as a loading parameter measures plastic work performed on the cracked specimen and that the amount of plastic work depends on the slip line pattern that develops out of the crack front and reaches the opposite free surface of the specimens when tested into the plastic collapse regime. Even the micromechanical process of ductile tearing, namely void nucleation, growth, and coalescence, depends strongly on the state of stress in the process zone.

Recently, a series of micromechanical models based on the concepts of continuum damage mechanics have been established to find alternatives. One of the new methods for ductile fracture analysis based on a yield condition by Gurson [*34*] has been developed and modified by Needleman, Tvergaard, and others [*35–39*]. In this material model the plastic flow is influenced by microscopic voids which are represented by a single parameter, the void volume fraction. This model had been used to predict J resistance curves from the behavior of notched and smooth tension bars [*24,40*]. Here this model will be applied to different specimen and loading situations in order to investigate the correlation of crack tip constraint with the slopes of the resistance curves.

The basis for the modified Gurson model is a plastic potential ϕ applicable to porous solids given by

$$\phi = \frac{3\sigma'_{ij}\sigma'_{ij}}{2\sigma_m^2} + 2qf\cos h\left(\frac{\sigma_{kk}}{2\sigma_m}\right) - [1 + (qf)^2] = 0 \tag{6}$$

Here, σ_{ij} and σ'_{ij} are the stress tensor and its deviator, respectively, σ_m is the flow stress of the material, f is a function of the volume fraction of voids representing the accumulated damage,

TABLE 2—*Tearing modulus and triaxiality at initiation, plane strain analysis for side-grooved specimens of various materials.*

Specimen	W, mm	a/W	Material	Constitutive Model	T_i	h_0
CT	50	0.5	StE 460	von Mises	160	2.61
CCT	50	0.5	σ_0 = 460 MPa		425	1.12
CT	50	0.5	20MnMoNi55	von Mises	141	2.80
			σ_0 = 460 MPa			
CT	50	0.6	A 710	Gurson	277	2.76
SENB	50	0.6	σ_0 = 619 MPa		398	2.45
CCT	100	0.6			781	1.40
SENT-C	50	0.6			687	1.69
SENT-P	50	0.6			296	2.60
SENT-S	50	0.1			715	1.59

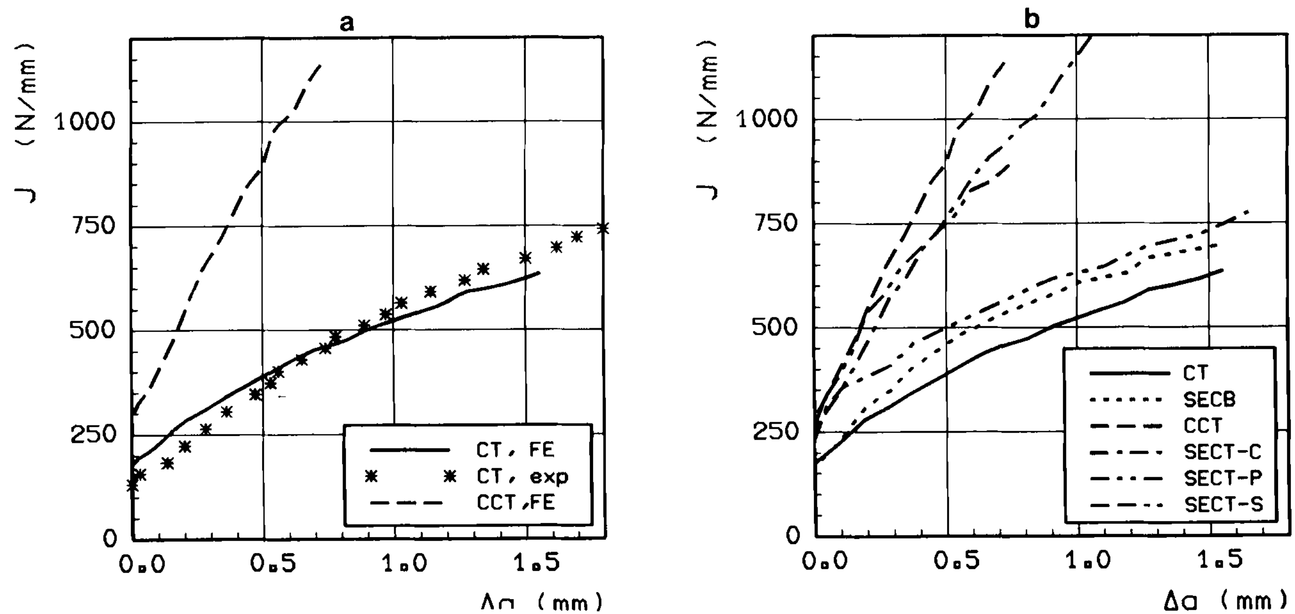

FIG. 5—*Geometry dependence of* J-R *curves for A710, plane-strain FE calculations with Gurson model:* (a) *comparison with test data of CT, and* (b) *various specimens.*

and the parameter q was introduced by Tvergaard [38] to improve the prediction of the Gurson model at small f values. If f reaches the limit $1/q$, the material loses its load-carrying capacity because all stress components have to vanish in order to satisfy Eq 6. A detailed description of the evaluation of f is given in [24,40]. Because for small f the von Mises equivalent stress σ_e is equal to the flow stress σ_m, it is evident that ϕ is strongly dependent on the ratio of the hydrostatic stress over the von Mises equivalent stress, $\sigma_{kk}/3\sigma_e$.

The constitutive equations of damage allow simulation of the ductile tearing behavior of cracked specimens and structures without the use of any kind of resistance curve. Instead of this, the damage parameters of a specific material have to be determined, which can be done by tension tests and quantitative optical microscopy. In addition, for cracked specimens, a characteristic material length, l_c, has to be introduced. This l_c is, most likely, correlated with microstructural features, for example, the inclusion spacing. It can be determined from cracked specimens [24,40]. J_R-curves of different specimen geometries can thus be generated by finite element calculations. After implementing the modified Gurson model into the finite element program ADINA, these analyses have been executed for the steel ASTM A710. Figure 5*a* shows a remarkable agreement between the calculated J versus Δa curve of a compact specimen and the measured R-curve of a side-grooved specimen. It also shows that the analysis of a CCT specimen yields a J_R-curve that is much steeper than that of the CT specimen as was found in experiments (see Fig. 4*a*). Although the toughness of the steel A710 is significantly higher than that of StE 460, the calculated variations of the stress triaxiality, h, in the ligament are quite similar as was shown in Figs. 2*a,b*. This confirms that h primarily characterizes loading and structural features.

Additionally, single-edge cracked specimens under bending (B) and tension (T) have been investigated by the same model. Their J_R-curves in Fig. 5*b* reproduce the well-known geometry effects though corresponding test data are not yet available. The tearing modulus, Eq 5, and the triaxiality h_0 according to Fig. 3 are evaluated at initiation for all these specimens and listed in Table 2 together with the results for the steel StE 460.

All data from Table 2 that refer to crack initiation only in different specimen geometries and for different materials are plotted together in one diagram in Fig. 6. In addition, the results of

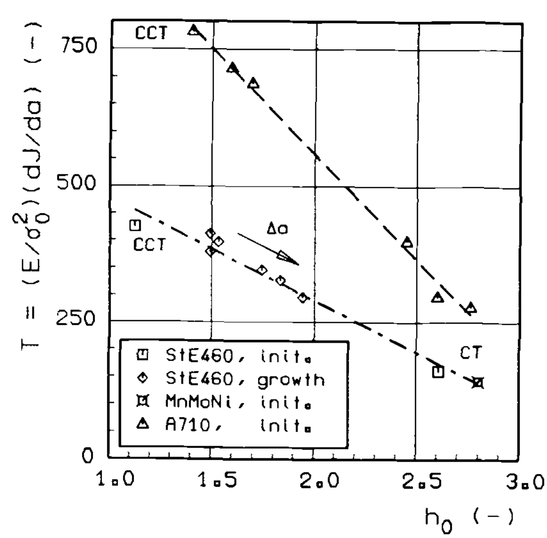

FIG. 6—*Triaxiality and tearing modulus, various materials and specimens.*

a J-controlled elastic-plastic crack growth analysis of a CCT specimen made of StE 460 [*30*] are included up to a crack growth of Δa = 1.5 mm. In Fig. 4 the experimental $J(\Delta a)$ data and the polynomial curve fit used for calculating $T(\Delta a)$ are shown. The corresponding h_0- values are taken from Fig. 5*b*. The T versus h_0 diagram shows a linear dependence between the tearing modulus and the triaxiality. This holds not at initiation (Table 2) but, at least for the CCT-specimen, also for a small amount of stable crack growth, that is, $T(\Delta a)$ decreases when $h_0(\Delta a)$ increases. This correlation does not work for steady state crack growth as h_0 approaches a saturation value (see Fig. 5*b*).

Conclusions

The influence of the state of stress in the process zone ahead of a crack front on initiation and ductile crack extension has been demonstrated for two different steels utilizing different experimental and numerical techniques including micromechanical damage models.

The appropriate quantitative assessment of constraint is possible by nonlinear finite element analyses but depends on details of the numerical models. In order to make findings from different studies comparable, a pragmatical extrapolation scheme has been proposed to define a constraint parameter h_0.

With increasing stress triaxiality h_0, the slopes of the resistance curves decrease within each material obviously in a self-similar way.

The dependence of the slope of the resistance curve on constraint and therefore on geometry and size of the specimen or structure is an inherent feature of the ductile failure process. It is in particular supported by all available micromechanical failure models. This fact should, therefore, not be overruled by modifications of the J-integral.

The trends and correlations found in several studies will facilitate the transferability of toughness values and resistance curves from laboratory specimens to real structures by taking into account the constraint in the specimen and in the structure.

It would be important to verify the results reported here by experiments with other materials, specimens, and structures. Especially the problem of ductile crack initiation in different specimen types needs further experimental investigations.

References

[*1*] Knott, J. F., *Fundamentals of Fracture Mechanics*, Butterworths, London, United Kingdom, 1973.
[*2*] Hancock, J. W. and Mackenzie, A. C., "On the Mechanisms of Ductile Failure in High-Strength Steels Subjected to Multi-Axial Stress-States," *Journal of Mechanics and Physics of Solids*, Vol. 24, 1976, pp. 147–169.
[*3*] McClintock, F. A., "A Criterion for Ductile Fracture by the Growth of Holes," *Transactions of ASME, Journal of Applied Mechanics*, Vol. 35, 1968, pp. 363–371.
[*4*] Rice, J. R. and Tracey, D. M., "On the Ductile Enlargement of Voids in Triaxial Stress Fields," *Journal of Mechanics and Physics of Solids*, Vol. 17, 1969, pp. 201–217.
[*5*] Budiansky, B., Hutchinson, J. W., and Slutsky, S., "Void Growth and Collapse in Viscous Solids," *Mechanics of Solids*, The Rodney Hill 60th Anniversary Volume, H. G. Hopkins and M. J. Sewell, Eds., Pergamon Press, Oxford, United Kingdom, 1981, pp. 13–45.
[*6*] Eshelby, J. D., "The Force on an Elastic Singularity," *Philosophical Transactions of the Royal Society of London*, Vol. 244, 1951, pp. 87–112.
[*7*] Cherepanov, G. P., "Crack Propagation in Continuous Media," *Journal of Applied Mathematics and Mechanics*, Vol. 31, 1967, pp. 503–512.
[*8*] Rice, J. R., "A Path-Independent Integral and the Approximate Analysis of Strain Concentrations by Notches and Cracks," *Journal of Applied Mechanics*, Vol. 35, 1968, pp. 379–386.
[*9*] Begley, J. A. and Landes, J. D., "The J-Integral as a Fracture Criterion," *Fracture Toughness, ASTM STP 514*, American Society for Testing and Materials, Philadelphia, 1972, pp. 1–23.
[*10*] Begley, J. A. and Landes, J. D., "The Effect of Specimen Geometry on J_{Ic}," *Fracture Toughness, ASTM STP 514*, American Society for Testing and Materials, Philadelphia, 1972, pp. 24–39.

[11] Rice, J. R., Paris, P. C., and Merkle, J. G., "Some Further Results of *J*-Integral Analysis and Estimates," *Progress in Flaw Growth and Fracture Toughness Testing, ASTM STP 536,* American Society for Testing and Materials, Philadelphia, 1973, pp. 231–245.
[12] Begley, J. A. and Landes, J. D., "Test Results from *J*-Integral Studies: an Attempt to Establish a J_{Ic} Testing Procedure," *Fracture Analysis, ASTM STP 560,* American Society for Testing and Materials, Philadelphia, 1974, pp. 170–186.
[13] Paris, P. C., Tada, H., Zahoor, H., and Ernst, H., "The Theory of Instability of the Tearing Mode of Elastic-Plastic Crack Growth," *Elastic-Plastic Fracture, ASTM STP 668,* American Society for Testing and Materials, Philadelphia, 1979, pp. 5–36.
[14] Hutchinson, J. W. and Paris, P. C., "Stability Analysis of *J*-Controlled Crack Growth," *Elastic-Plastic Fracture, ASTM STP 668,* American Society for Testing and Materials, Philadelphia, 1979, pp. 37–64.
[15] Hutchinson, J. W., "Singular Behaviour at the End of a Tensile Crack in a Hardening Material," *Journal of Mechanics and Physics of Solids,* Vol. 16, 1968, pp. 13–31.
[16] Rice, J. R. and Rosengren, G. F., "Plane Strain Deformation Near a Crack Tip in a Hardening Material," *Journal of Mechanics and Physics of Solids,* Vol. 16, 1968, pp. 1–12.
[17] McMeeking, R. M. and Parks, D. M., "On Criteria for *J*-Dominance of Crack-Tip Fields in Large Scale Yielding," *Elastic-Plastic Fracture, ASTM STP 668,* American Society for Testing and Materials, Philadelphia, 1979, pp. 175–194.
[18] Shih, C. F. and German, M., "Requirements for a One Parameter Characterization of Crack Tip Fields by the HRR-Singularity," *International Journal of Fracture,* Vol. 29, 1985, pp. 73–84.
[19] Shih, C. F., "*J*-Dominance under Plane Strain Fully Plastic Conditions: The Edge Panel Subject to Combined Tension and Bending," Report DOE/ER/10556/102, Brown University, Providence, RI, 1985.
[20] Griffith, A. A., "The Phenomena of Rupture and Flow in Solids," *Philosophical Transactions of the Society of London,* Vol. 221A, 1920, pp. 163–198.
[21] Miyamoto, H., Kageyama, K., Kikuchi, M., and Machida, K., "The J_{ext}-Integral Based on the Concept of Effective Energy Release Rate," *Elastic-Plastic Fracture, ASTM STP 803,* American Society for Testing and Materials, Philadelphia, 1983, pp. 116–129.
[22] Ernst, H. A., "Material Resistance and Instability beyond *J*-Controlled Crack Growth," *Elastic-Plastic Fracture, ASTM STP 803,* American Society for Testing and Materials, Philadelphia, 1983, pp. 191–213.
[23] Siegele, D. and Schmitt, W., "Determination and Simulation of Stable Crack Growth in ADINA," *Computers and Structures,* Vol. 17, 1983, pp. 697–703.
[24] Sun, D.-Z., Siegele, D., Voss, B., and Schmitt, W., "Application of Local Damage Models to the Numerical Analysis of Ductile Rupture," *Fatigue and Fracture of Engineering Materials and Structures,* Vol. 12, 1989, pp. 201–212.
[25] Brocks, W., Künecke, G., Noack, H.-D., and Veith, H., "On the Transferability of Fracture Mechanics Parameters to Structures using FEM," *Nuclear Engineering and Design,* Vol. 112, 1989, pp. 1–14.
[26] Steenkamp, P. A. J. M., "Investigation into the Validity of *J*-Based Methods for the Prediction of Ductile Tearing and Fracture," PhD thesis, Technical University of Delft, Delft, The Netherlands, 1986.
[27] Hencky, H., "Ermüdung, Bruch, Plastizität," ("Fatigue, Fracture, Plasticity"), *Stahlbau,* Vol. 16, 1943, pp. 95–97.
[28] Kordisch, H., Sommer, E., and Schmitt, W., "The Influence of Triaxiality on Stable Crack Growth," *Nuclear Engineering and Design,* Vol. 112, 1989, pp. 27–35.
[29] Aurich, D. and Sommer, E., "The Effect of Constraint on Elastic-Plastic Fracture," *Steel Research,* Vol. 59, 1988, pp. 358–367.
[30] Brocks, W. and Künecke, G., "On the Influence of Triaxiality of the Stress State on Ductile Tearing Resistance," *Proceedings of the Symposium on Elastic-Plastic Fracture Mechanics: Elements of Defect Assessment,* ESIS/EGF Publication 9, Mechanical Engineering Publishers, London, United Kingdom, 1991, pp. 189–201.
[31] Clausmeyer, H., Kussmaul, K., und Roos, E., "Der Einfluβ des Spannungszustandes auf den Versagensablauf angerissener Bauteile aus Stahl," ("The Influence of the Stress State on the Failure Event of Cracked Stee Components,") *Material-wissenschaft und Werkstofftechn,* Vol. 20, 1989, pp. 101–117.
[32] Aurich, D., Wobst, K., and Krafka, H., "J_R-Curves of Wide Plates and CT25 Specimens—Comparison of the Results of a Pressure Vessel," *Nuclear Engineering and Design,* Vol. 112, 1989, pp. 319–328.
[33] Brocks, W. and Schmitt, W., "The Role of Crack Tip Constraint for Ductile Tearing," *Fracture Behaviour and Design of Materials and Structures, Preprints of the 8th European Conference on*

Fracture, Vol. II, Engineering Materials Advisory Services, Warley, United Kingdom, 1990, pp. 1023–1032.

[34] Gurson, A. L., "Continuum Theory of Ductile Rupture by Void Nucleation and Growth: Part I—Yield Criteria and Flow Rules for Porous Ductile Media," *Journal of Engineering Materials Technology,* Vol. 99, 1977, pp. 2–15.

[35] Needleman, A. and Tvergaard, V., "An Analysis of Ductile Rupture in Notched Bars," *Journal of Mechanics and Physics of Solids,* Vol. 32, 1984, pp. 461–490.

[36] Needleman, A. and Tvergaard, V., "An Analysis of Ductile Rupture Modes at a Crack Tip," *Journal of Mechanics and Physics of Solids,* Vol. 35, 1987, pp. 151–183.

[37] Becker, R., Needleman, A., Suresh, S., Tvergaard, V., and Vasudevan, A. K., "An Analysis of Ductile Failure by Grain Boundary Void Growth," *Acta Metallurgica,* Vol. 37, 1989, pp. 99–120.

[38] Tvergaard, V., "On Localization in Ductile Materials Containing Spherical Voids," *International Journal of Fracture,* Vol. 18, 1982, pp. 237–252.

[39] Chu, C. C. and Needleman, A., "Void Nucleation Effects in Biaxially Stretched Sheets," *Journal of Engineering Materials Technology,* Vol. 102, 1980, pp. 249–256.

[40] Sun, D.-Z., Voss, B., and Schmitt, W., "Numerical Prediction of Ductile Fracture Resistance Behaviour Based on Micromechanical Models," *Proceedings of the Symposium on Elastic-Plastic Fracture Mechanics: Elements of Defect Assessment,* ESIS/EGF Publication 9, Mechanical Engineering Publishers, London, United Kingdom, 1991, pp. 447–458.

Mark T. Kirk,[1] *Kyle C. Koppenhoefer,*[1] *and C. Fong Shih*[2]

Effect of Constraint on Specimen Dimensions Needed to Obtain Structurally Relevant Toughness Measures

REFERENCE: Kirk, M. T., Koppenhoefer, K. C., and Shih, C. F., "**Effect of Constraint on Specimen Dimensions Needed to Obtain Structurally Relevant Toughness Measures,**" *Constraint Effects in Fracture, ASTM STP 1171,* E. M. Hackett, K.-H. Schwalbe, and R. H. Dodds, Eds., American Society for Testing and Materials, Philadelphia, 1993, pp. 79–103.

ABSTRACT: This study examines the feasibility of predicting the fracture toughness for structurally relevant situations (shallow cracks in thick plates) based on toughness values measured with experimentally convenient specimen geometries (deep cracks in small specimens). The cleavage fracture toughness, J_c, of ASTM A515 Grade 70 steel plate was measured using single edge notch bend specimens. Specimen size and initial crack depth were varied to obtain J_c values over a range of constraint conditions. The results of these experiments indicate that crack depth and thickness cannot be traded off against each other to achieve the same constraint and thereby the same fracture toughness. The absence of this simple trade-off is due to the greater effect of crack depth than of specimen size on J_c and to the scatter in fracture toughness data characteristic of temperatures in the transition range. Alternative techniques for determining structurally relevant toughness measures from specimens based on recently proposed constraint parameters were therefore examined. These various parameters divide into two categories: those which index constraint and those which correct for constraint. Application of these constraint parameters to the A515 data indicate that all of the currently proposed techniques can account for the constraint-induced changes in cleavage fracture toughness. However, the feasibility of applying these techniques during a structural fracture safety assessment depends upon the experimental complexity and cost associated with fracture toughness determination and the ease with which the constraint parameter can be calculated for a structure.

KEY WORDS: constraint, fracture toughness, cleavage, size effects, *T*-stress, *Q*-stress, micromechanics

Standardized fracture toughness testing procedures require both sufficient specimen thickness to ensure predominantly plane strain conditions at the crack tip and a crack depth of at least half the specimen width. Within certain limits on load level and crack growth, these restrictions ensure the existence of very severe conditions for fracture as described by the Hutchinson-Rice-Rosengren (HRR) field equations [*1,2*]. These conditions generally make the applied driving force needed to initiate fracture in a laboratory specimen lower than that needed to initiate fracture in common civil and marine structures where such geometric restrictions are usually not met. This difference between specimens and structures indicates

[1] Mechanical engineer, Fatigue and Fracture Branch, Code 2814, David Taylor Research Center, Annapolis, MD 21402. (Kirk is currently employed as a senior research engineer by The Edison Welding Institute, 1100 Kinner Rd., Columbus, OH 43212; Koppenhoefer is currently employed as a graduate research assistant by the Department of Civil Engineering, University of Illinois, Urbane, IL 61801.)
[2] Professor, Division of Engineering, Brown University, Providence, RI 02912.

that structures can often carry greater loads without failure than predicted using fracture toughness values measured using standardized procedures.

Work by Sumpter [3] and by Kirk and Dodds [4] indicates that matching both the thickness and the crack depth of the specimen to the structure produces good agreement between J_c values for single edge notched bend [SE(B)] specimens and structures containing part-through semi-elliptical surface cracks. Finite element studies of simple specimen geometries with sufficient mesh refinement to fully resolve the near tip fields show that variations of specimen crack depth, geometry, and loading mode significantly alter the magnitude of opening mode stresses in front of the crack tip over microstructurally relevant distances for cleavage fracture [5–7]. These results suggest that matching thickness and crack depth between specimen and structure may force approximate agreement of opening stress magnitudes. This rationale for the observed similarity of J_c values between different specimen and crack geometries implies that the micromechanistic requirement for cleavage fracture, achievement of a critical stress over a sufficient distance in front of the crack tip [8], can be reached in different geometries at the same applied J.

These results suggest that fracture toughness values determined using shallow cracked SE(B) specimens of structural thickness provide useful data for structural integrity assessments. However, complexities associated with preparation [9] and testing [10] of these specimens, the high load capacity required, and the large volume of material needed for each specimen make such experiments difficult to perform. The testing of smaller, easier to prepare specimens that give J_c values similar to that of a structure would be highly desirable. Considerable experimental and theoretical evidence indicates that increasing the crack depth from that which matches the structure increases constraint and thus reduces J_c [7,11]. However, reducing specimen thickness from that of the structure has the opposite effect [12]. Thus, it may be possible to achieve constraint similar to a structure, and thus a relevant fracture toughness, by testing a specimen that is thinner and more deeply cracked than the structure. The aim of this study is to experimentally investigate this possibility. Further, recently proposed constraint parameters are evaluated for their ability to predict the fracture toughness of structurally relevant situations based on toughness values measured with experimentally convenient specimen geometries.

Approach

To determine if crack depth constraint can be traded off against thickness constraint to achieve the same fracture toughness, SE(B) specimens removed from a 127-mm (5-in.)-thick plate of ASTM A515 Grade 70 steel (hereafter A515) and notched in the *T-S* orientation were tested. Table 1 details the measured strength properties for this alloy. The notched surface of

TABLE 1—*Tensile properties of ASTM A515 Grade 70 steel at 20°C.*

0.2% Offset Yield Strength, MPa	Ultimate Tensile Strength, MPa	Reduction in Area, %	Elongation over 25.4-mm Gage Length, %
287	543	52	34
314	547	51	36
297	536	51	32

NOTE: Properties were measured using round bar specimens having an initial diameter of 7.95 mm and an initial gage length of 25.4 mm. Each line above gives the results for a single specimen.

all specimens was between 3 and 6 mm from the original plate surface. Various crack depths (a/W from 0.1 to 0.5) and thicknesses were used. Specimen thicknesses included those typical of structures (50.8 and 25.4 mm) as well as a smaller specimen (10 mm) whose overall dimensions match those of a standard Charpy V-notch specimen. All specimens were tested at +20°C where A515 fails predominantly by cleavage.

Constraint Corrections and Indexing Parameters

The notion of correcting fracture toughness data for constraint loss or of indexing laboratory specimens and structures using a constraint parameter is not new. In 1960 Irwin [*13*] proposed the empirical β_{Ic} correction to estimate K_{Ic} results from experiments in which fracture does not occur under fully plane strain conditions. More recently, Dodds and Anderson [*5,14*] developed micromechanics-based scaling rules that quantify the magnitude of deformation-induced geometry effects on the cleavage fracture toughness (J_c) of SE(B) specimens. Alternatively, researchers at the Welding Institute have long advocated the use of the ratio of crack depth to plate thickness to index the constraint of specimens relative to structures [*15*]. Other proposed indexing parameters include the J/crack tip opening displacement (CTOD) ratio [*16*], the amplitude of the constant stress parallel to the crack (T-stress) in the linear elastic crack tip solution [*17*], and the amplitude of the second term (Q) of an asymptotic solution for the deformation fields around a crack tip in a power law hardening material [*6,18*]. In this study, the recently proposed constraint correction due to Dodds and Anderson, the T-stress, and the Q-stress are considered. These parameters and the relations needed to estimate them from experimental data are detailed in this section.

Dodds/Anderson Correction

Dodds and Anderson reported plane strain finite element analyses of SE(B) specimens for a wide range of a/W ratios and strain-hardening coefficients [*5*]. These analyses had sufficient mesh refinement to resolve accurately the deformation fields over microstructurally significant distances from the crack tip (two to ten times the CTOD for cleavage fracture [*19*]). Their results show that both high loads and shallow cracks reduce the opening mode stress in an SE(B) specimen below that of an infinite body loaded to the same J (or CTOD). As attainment of a critical stress over a microstructurally significant volume is an appropriate condition for transgranular cleavage fracture [*8*], these findings indicate that equivalence of applied J (or CTOD) does not imply equal risk of cleavage fracture for different geometries because the magnitude of the opening mode stress does not scale with J alone. This explains the specimen-size dependence found in experimental data [*11*]. These authors also found that the near tip stress distributions in an SE(B) specimen is a simple scalar multiple of the full infinite body, or small-scale yield (SSY) solution, between 2 and 10 CTODs from the crack tip. This indicates that the ratio of J in the infinite body to J in the finite size SE(B) specimen (J_{SSY}/J_{BB}) needed to achieve the same crack tip stress field could serve as the second parameter needed to fully describe the near tip stresses. Further, because the infinite and finite body stress distributions are self-similar, the J_{SSY}/J_{BB} ratio can be determined unambiguously without needing to know the critical microstructural conditions (that is, the critical maximum stress and the size of the critically stressed volume) required for cleavage fracture. Thus, Dodds and Anderson presented constraint correction curves relating J_{SSY} to J_{BB} for SE(B) specimens, as illustrated in Fig. 1. These curves are useful for predicting the variation of apparent (or structural) cleavage fracture toughness with crack depth based on toughness data from one specimen geometry or for determining the true specimen size-independent fracture toughness, J_{SSY}, from any speci-

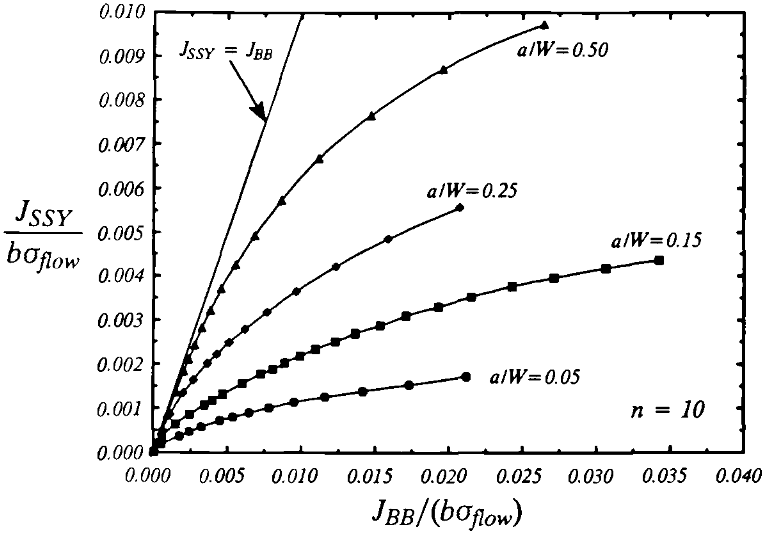

FIG. 1—*Curves for scaling cleavage fracture toughness* (J_c) *measured with SE(B) specimens for* n = *10* [5].

men that fails by cleavage. Dodds and Anderson demonstrated the accuracy of these techniques using data for A36 steel. Curves of this type for A515 steel are presented in a later section.

T-*Stress Indexing Parameter*

Hancock and coworkers [*7,17*] suggest that the amplitude of the constant stress (or T-stress) in the linear elastic crack tip solution may be an effective constraint indexing parameter. In the linear elastic crack tip stress distribution, the T-stress only alters the stress parallel to the crack. However, Larsson and Carlsson [*20*] found that the sign of T significantly alters the shape of the crack tip plastic zone from that corresponding to $T = 0$. Thus, the effect of a remote elastic T-stress on the elastic-plastic crack tip stress field might not be a simple intensification or reduction of σ_{xx}. Detailed finite element analyses by Hancock and coworkers confirm that a negative T-stress reduces the opening mode stress relative to that of an infinite body. Further, they report that a negative T-stress is associated with low constraint geometries, while a zero or positive T-stress corresponds to high constraint geometries. To successfully parameterize constraint effects, a correspondence between the near tip stress fields and the T-stress is needed, even after the T-stress cannot be calculated due to unconfined yielding around the crack tip. Parks showed that predicted reductions in near tip opening mode stress based on T-stress are within 10% of those determined by elastic-plastic finite element analyses for all T/σ_0 values above -0.9 for shallow edge cracks loaded in either tension or bending [*21*].

To assess the data developed in this study in terms of T-stress, the results of Al-Ani and Hancock [*7*] were used. These investigators report a biaxiality parameter, β

$$\beta = \frac{T\sqrt{\pi a}}{K} \tag{1}$$

for SE(B) specimens as a function of a/W. A fit to their data (Fig. 2) gives the relation

$$\beta(a/W) = -0.462 + 0.461\left(\frac{a}{W}\right) + 2.47\left(\frac{a}{W}\right)^2 \text{ for } 0.025 \leq \frac{a}{W} \leq 0.90 \tag{2}$$

Combining Eqs 1 and 2 and the K solution for an SE(B) specimen with a span-to-width ratio of 4:1 [*22*] gives the following relation between T-stress and applied load

$$T = 1.5\frac{PS}{BW^2}\beta(a/W)\left[\frac{1.99 - \frac{a}{W}\left(1 - \frac{a}{W}\right)\left[2.15 - 3.93\frac{a}{W} + 2.7\left(\frac{a}{W}\right)^2\right]}{\sqrt{\pi}\left(1 + 2\frac{a}{W}\right)\left(1 - \frac{a}{W}\right)^{1.5}}\right] \tag{3}$$

The value of T-stress reported for an experiment corresponds to the value of Eq 3 evaluated using the load at cleavage failure.

Q *Indexing Parameter*

O'Dowd and Shih propose that the amplitude of the second term of the asymptotic expansion for the deformation fields around a crack tip in a power law hardening material may serve as an effective constraint indexing parameter [*6,18*]. Beyond the finite strain region, this expansion is

$$\frac{\sigma_{ij}}{\sigma_0} = \left(\frac{J}{\alpha\epsilon_0\sigma_0 I_n r}\right)^{1/(n+1)}\tilde{\sigma}_{ij}(\theta; n) + Q\left(\frac{r}{J/\sigma_0}\right)^q \hat{\sigma}_{ij}(\theta; n) \tag{4}$$

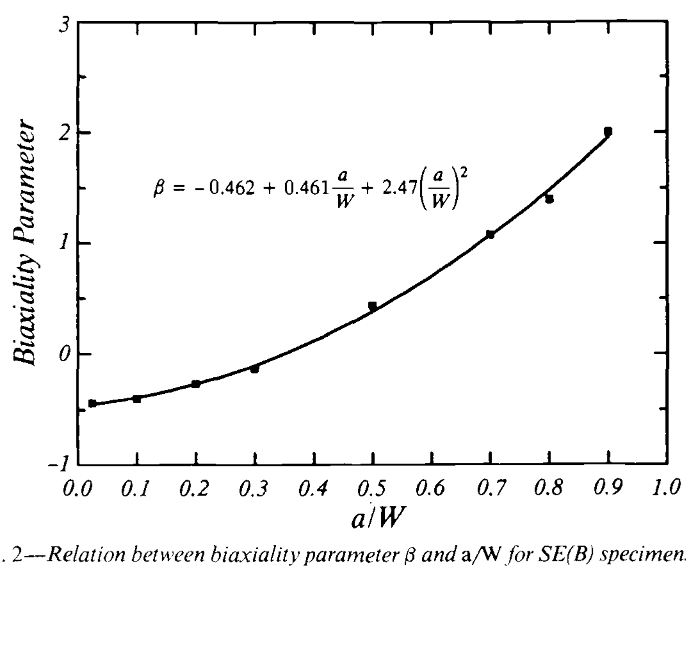

FIG. 2—*Relation between biaxiality parameter* β *and* a/W *for SE(B) specimens* [7].

The first term is the HRR singularity [*1,2*], which has an amplitude characterized by the J-integral [*23*]. O'Dowd and Shih found that: (1) the power on the radial coefficient in the second term (q) is approximately zero; (2) for $|\theta| \leq 90°$ the second order normal stresses ($\hat{\sigma}_r$ and $\hat{\sigma}_{\theta\theta}$) are approximately equal; and (3) the second order shear stress ($\hat{\sigma}_{r\theta}$) is approximately zero. Thus, Q is the amplitude of a hydrostatic, or triaxiality, term. Based on these observations, Eq 4 simplifies in Cartesian coordinates to

$$\sigma_{xx} = \sigma_{xx}|_{HRR} + Q\sigma_0 \tag{5a}$$

$$\sigma_{yy} = \sigma_{yy}|_{HRR} + Q\sigma_0 \tag{5b}$$

$$\sigma_{xy} = \sigma_{xy}|_{HRR} \tag{5c}$$

This definition is only appropriate for $|\theta| \leq 90°$ and outside of the finite strain region, for which $r = J/\sigma_0$ serves as the outer boundary. An alternative definition of Q replaces the reference solution (the HRR solution in Eq 5) with a full field solution determined by finite element analysis. In this case, Eq 5 becomes

$$\sigma_{xx} = \sigma_{xx}|_{Q=0} + Q\sigma_0 \tag{6a}$$

$$\sigma_{yy} = \sigma_{yy}|_{Q=0} + Q\sigma_0 \tag{6b}$$

$$\sigma_{xy} = \sigma_{xy}|_{Q=0} \tag{6c}$$

again for $|\theta| \leq 90°$. O'Dowd and Shih indicate that either finite strain or small strain finite element formulations can be used to determine the reference ($Q = 0$) solution for Eq 6. On this basis, these authors developed relations between Q and applied loading for SE(B) specimens with a strain hardening coefficient of 10, as shown in Fig. 3. The value of Q at cleavage failure can be determined for experimental fracture toughness data using these curves by entering the x-axis with an experimentally measured toughness value and reading Q off of the y-axis. Curves of this type for A515 steel are presented in the section on results.

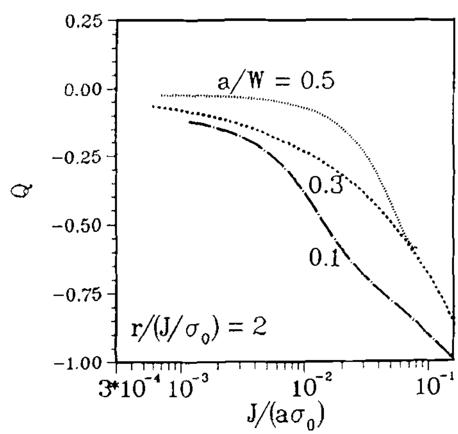

FIG. 3—*Variation of* Q *for SE(B) specimens (*n = *10) with applied* J *and* a/W [18].

Summary

In the preceding sections, both constraint corrections and constraint indexing parameters were summarized. As implied by the labels, corrections versus indexing parameters, these represent two fundamentally different approaches to accounting for toughness differences between different specimen geometries, or by extension, between specimens and structures.

The correction approach attempts to predict the toughness of some configuration different from that for which toughness data are available using the micromechanistic requirements for crack initiation to establish the conditions for fracture. Numerical estimates of the stress and strain fields near the crack tip serve as input to a micromechanics model, allowing the effects of finite structural size on critical fracture toughness to be quantified. The only correction currently available is that developed by Dodds et al. for cleavage fracture. The self-similarity of the stress fields in the crack tip region between infinite and finite bodies, combined with the unique dependence of cleavage fracture initiation on stressed volume, makes this correction equally applicable to all materials that fail by transgranular cleavage.

Constraint indexing parameters offer a systematic means to order the interrelated effects of geometry, loading mode, and thickness on critical fracture toughness. However, as no micromechanical failure criteria is introduced, the functional relationship between constraint indexing parameters and critical fracture toughness is unknown. Consequently, fracture toughness values measured using both high and low constraint specimens are needed to establish this relationship [*24*]. An indexing parameter cannot be used to predict toughness differences between different specimens or between specimens and structures without having first performed these experiments.

Procedures

Experimental

Equation 7 indicates that the measurement of load and load line displacement for an SE(B) specimen allows estimation of applied J [*25*]

$$J_1 = \frac{K^2(1 - \nu^2)}{E} + \frac{\eta_{pl}}{Bb} \int P \, d\Delta_{pl} \tag{7}$$

where K is the linear elastic stress intensity factor, η_{pl} is the plastic eta factor, b is the initial remaining ligament, P is the load, and Δ_{pl} is the plastic component of load line displacement. Sumpter suggested the following equation for η_{pl}

$$\begin{aligned} \eta_{pl} &= 0.32 + 12\frac{a}{W} - 49.5\left(\frac{a}{W}\right)^2 + 99.8\left(\frac{a}{W}\right)^3 \quad \text{for } a/W < 0.282 \\ \eta_{pl} &= 2.0 \quad \text{for } a/W \geq 0.282 \end{aligned} \tag{8}$$

Thus, every test was instrumented for load and load line displacement. The load was measured using a calibrated 267-kN load cell. The load line displacement was measured using a flex bar transducer instrumented with a full bridge array of strain gages [*26*]. This transducer, calibrated under the same deflection experienced during testing, was mounted on the specimen so that it deflected with the specimen but did not offer significant resistance to bending. Three different specimen sizes were tested, each size having a range of different initial crack depths. Several variations of the test procedure were required to accommodate this variety of specimens. Prior to testing, each specimen was cyclically reverse bent to improve fatigue precrack front straightness [9]. After cyclic reverse bending for 5400 cycles, the specimens were precracked as per the requirements of ASTM Test Method for J_{Ic}, a Measure of Fracture Toughness (E 813-89) at $\Delta K = 22$ MPa$\sqrt{m}$ to the prescribed a/W ratio. All tests were conducted in a screw-driven test machine under a constant, quasistatic displacement rate of approximately 25.4×10^{-6} m/s.

As A515 steel is in lower transition at +20°C, the fracture parameter of interest was the applied J at cleavage, J_c. As explained previously, only load and load line displacement are required to obtain J_c. For the 10-mm specimens, use of a flex bar for load line displacement was difficult due to the small specimen size. Therefore, one specimen of each crack depth was tested while the displacements were monitored with a flex bar and a crosshead transducer. An eddy current gage was used to measure crosshead displacement by mounting it on the loading tup. By keeping this transducer near the specimen, the overall effect of machine compliance on the correlation between load line and crosshead displacement was minimized. A least squares fit of the displacements measured by the eddy current transducer and the flex bar was used to relate these two displacement measurements. As this correlation varied slightly with crack depth, a crack depth dependent correlation was necessary to properly relate load line and cross head displacement. Due to the larger size of the 25.4- and 50.8-mm specimens, a flex bar was easily mounted, so load line displacement was measured directly.

All data was taken digitally on a personal computer over an IEEE-488 interface. A digital multimeter/scanner was used for analog-to-digital conversion with a resolution of 0.0002 V/count. This corresponds to a minimum resolvable load change of 0.053 kN over a 267-kN range and a minimum resolvable displacement change of 25.4×10^{-6} mm over a 1.27-mm range.

Finite Element

Two-dimensional plane strain finite element analyses of SE(B) specimens were performed using conventional small strain theory and a material model appropriate to A515 steel. These analyses allowed estimation of both Q and J_{SSY}/J_{BB} for A515 steel. Four different models were constructed with crack depth to specimen width ratios of 0.05, 0.15, 0.25, and 0.50. These analyses were conducted using the POLO-FINITE finite element analysis software [27] on an engineering workstation.

Uniaxial stress strain behavior was described using the Ramberg-Osgood model

$$\frac{\epsilon}{\epsilon_0} = \frac{\sigma}{\sigma_0} + \alpha \left(\frac{\sigma}{\sigma_0}\right)^n \tag{9}$$

where σ_0 is the reference (yield) stress, $\epsilon_0 = \sigma_0/E$ is the reference (yield) strain, α is a dimensionless parameter, and n is the strain hardening coefficient. A value of $n = 4$ was used to match closely the uniaxial constitutive behavior of the A515 steel tested in the experimental investigation. A value of $\sigma_0 = 414$ MPa was used; correspondence of this value to that of A515 steel is not important as the solution scales with σ_0. The multi-axial material model is described by J2 deformation plasticity theory, which in reality is nonlinear elasticity. Total strains and total stresses were related by

$$\epsilon_{ij} = \left[\frac{1+\nu}{E} + \frac{3\alpha\epsilon_0}{2\sigma_0}\left(\frac{\sigma_e}{\sigma_0}\right)^{n-1}\right] s_{ij} + \frac{1-2\nu}{3E}\sigma_{kk}\delta_{ij} \qquad \sigma_e = \sqrt{\frac{3}{2}s_{ij}s_{ij}} \tag{10}$$

where s_{ij} is the stress deviator, σ_e is the Mises equivalent tensile stress, σ_{kk} is the trace of the stress tensor, and δ_{ij} is the Kronecker delta.

Different finite element models were constructed for each of the four a/W ratios investigated. Standard proportions for SE(B) specimens recommended by ASTM E 813 were modelled, so the span between support points was four times the specimen width. Symmetry of geometry and loading permitted use of a half-symmetric model. These models each contained approximately 350 elements and 1200 nodes. Figure 4 illustrates the model for $a/W = 0.25$; the mesh has been reflected about the symmetry axis for clarity. Eight-noded plane strain isoparametric quadrilateral elements were used throughout. Reduced (2 by 2) Gaussian integration was used to eliminate locking of arbitrarily shaped elements. A half-circular core of elements surrounding the crack tip was common to all models. This core consisted of eight equally sized wedges, 22.5° each, of elements in the θ direction. Each wedge contained 30 quadrilateral elements whose radial dimension decreased geometrically with decreasing element distance to the crack tip. The eight elements at the crack tip were collapsed into wedges with the initially coincident nodes left unconstrained to permit development of crack tip blunting deformations. The side nodes of these elements were retained at the midpoint position. This modelling produces a $1/r$ strain singularity appropriate in the limit of perfect plasticity. Crack tip element size ranged from 0.2 to 0.02% of the crack depth for the different crack depths modelled.

Load was uniformly distributed over two small elements and applied at the center of the compression face of the specimen to eliminate the local singularity effects caused by a concentrated nodal load. Between 30 and 50 variably sized load steps were taken to deform the specimen well into the elastic-plastic regime. Strict convergence criteria at each step ensured convergence of calculated stresses and strains to the third significant figure. Two to three full Newton iterations at each load step were generally required to satisfy this criteria. As deformation plasticity is strain path independent, converged solutions are load step size invariant.

The J-integral was estimated at each load step using a domain integral method [*28,29*]. J values calculated over domains adjacent to and remote from the crack tip were within 1% of each other, as expected for deformation plasticity. CTOD was estimated from the blunted shape of the crack flanks using the Rice 45° intercept procedure. Load line displacement was taken as the displacement in the loading direction of a node on the symmetry plane located at approximately $0.4b$ in front of the crack tip to avoid the spuriously high displacements in the vicinity of the load point.

Stresses calculated at the Gauss points were extrapolated to the nodes and arithmetically averaged. Values of these average nodal stresses acting perpendicular to the crack plane were extracted from the finite element results along the remaining ligament over a distance of 2 to

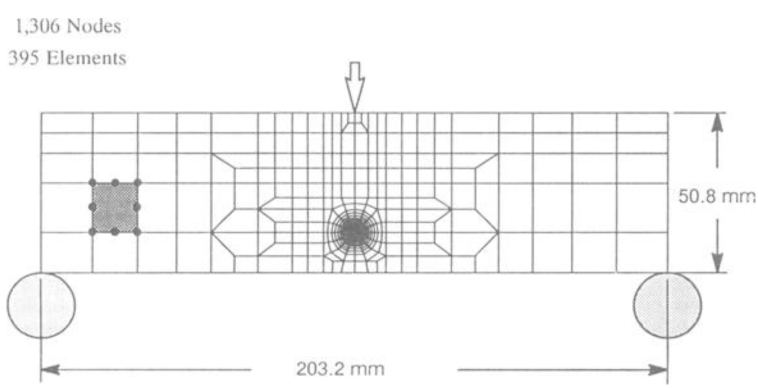

FIG. 4—*Plane strain finite element model for* a/W = *0.25 SE(B) specimen. Model is reflected about symmetry line for clarity.*

10 CTODs to facilitate calculation of both J_{SSY}/J_{BB} and Q. J_{SSY}/J_{BB} was calculated by comparing these stresses to those determined for an $n = 4$ material from a small strain boundary layer analysis. Dodds et al. [5] defined J_{SSY}/J_{BB} at a given applied J in the SE(B) as that ratio needed to bring the stresses between 2 and 10 CTODs on the SE(B) ligament into agreement with the stresses over this same length scale in the boundary layer analysis.[3] The same procedure was used here. Q was defined using Eq 6 as

$$Q = \frac{\sigma_{yy}|_{SE(B)} - \sigma_{yy}|_{SSY}}{\sigma_0} \tag{11}$$

where $\sigma_{yy}|_{SE(B)}$ is the opening mode stresses along the unbroken ligament of an SE(B) specimen determined from small strain finite element analyses, and $\sigma_{yy}|_{SSY}$ is the opening mode stresses ahead of the crack from a small strain theory boundary layer analysis. This equation indicates that Q is the difference between the opening mode stresses acting on the net ligament calculated from the finite element SE(B) solutions and the stresses from a small strain theory boundary layer solution. This difference was calculated at $r/(J/\sigma_0) = 2$ as suggested by O'Dowd and Shih [18]. It should be noted that small strain theory, used for both the boundary layer and the SE(B) solutions, is not accurate within the zone of finite strains, $r/(J/\sigma_0) < 2$. However, it is not expected that this inaccuracy will result in Q values inapplicable to the A515 fracture toughness data because the events that lead to cleavage fracture occur beyond this zone.

Results and Discussion

Fracture Toughness Variation with Thickness and Crack Depth

Figure 5 shows the effect of specimen size and initial crack depth on the cleavage fracture toughness of the A515 steel tested at +20°C. The scatter in these J_c data, characteristic of steels tested in transition, can make identification of trends difficult. For this reason, attention is initially focused on the 25.4-mm specimens (Fig. 5*b*) for which the largest number of specimens were tested at each a/W ratio. The trend of increasing J_c with decreasing initial crack length is apparent, with five to six specimens tested at each crack length. It is difficult to draw any conclusions about the variation of J_c with crack depth for either the 10- or the 50.8-mm specimens because a limited number of these specimens were tested. However, the work of both Sorem [30] and Sumpter [3] on SE(B) specimens of different sizes showed a variation of J_c with crack depth similar to that of the 25.4-mm specimens reported herein. Thus, a similar variation of J_c should be seen for the 10.0- and 50.8-mm specimens once a larger number of specimens are tested at each crack depth.

In contrast to the effect of initial crack depth on cleavage fracture toughness, the data of Fig. 5 indicate that specimen size has a much more modest influence, if any at all. While firm conclusions cannot be drawn from these data, the trends noted qualitatively agree with expectations based on the effect of crack depth and specimen size on the opening mode stresses which initiate cleavage. Dodds et al. showed that changing a/W from 0.5 to 0.15 at the same applied J (or CTOD) causes a 30% drop of the opening mode stress [5]. Conversely, Sorem showed by three-dimensional finite element analyses of square cross-section SE(B) specimens that reducing specimen width and thickness from 31.8 to 12.7 mm at the same applied J (or CTOD) only causes a 5% drop of the opening mode stress [30]. Sorem reported similar findings for both $a/$

[3] Exact agreement was forced at $r/CTOD = 4$; however, calculated J_{SSY}/J_{BB} ratios depend only slightly on the exact location at which agreement is forced due to the self-similarity of crack tip region stresses between finite and infinite bodies.

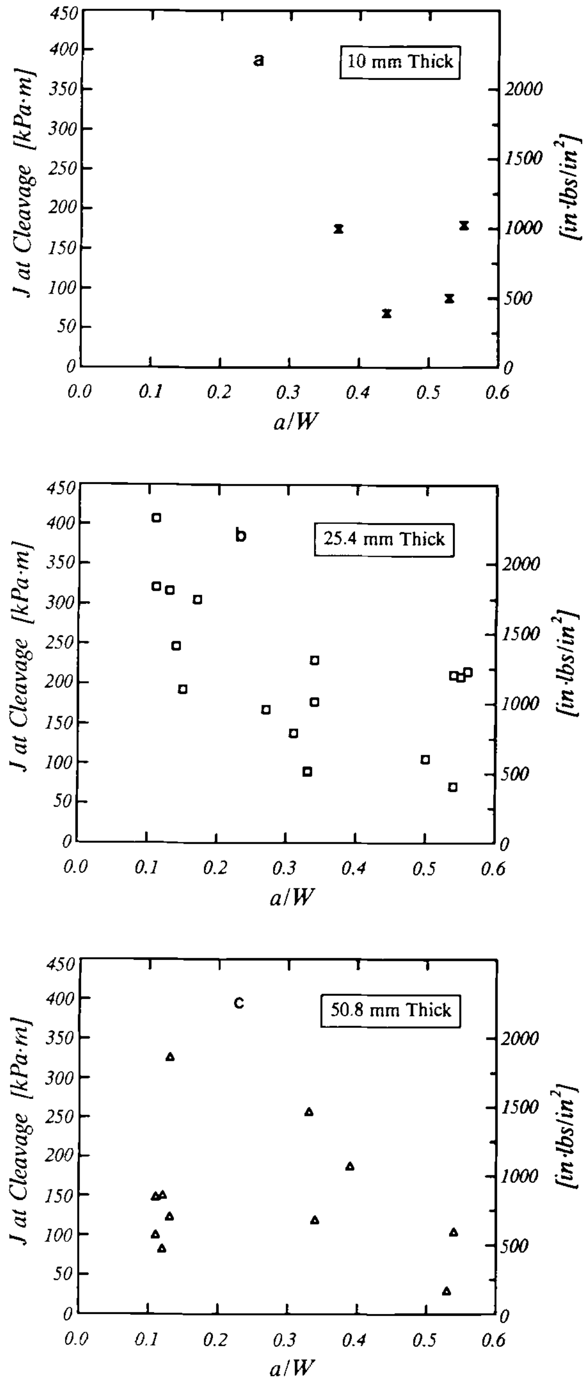

FIG. 5—*Variation of cleavage fracture toughness* (J_c) *with* a/W *and specimen size for ASTM A515 Grade 70 steel at +20°C* (a) *for 10-mm SE(B) specimens,* (b) *for 25.4-mm SE(B) specimens,* (c) *for 50.8-mm SE(B) specimens.*

$W = 0.5$ and $a/W = 0.15$ specimens. As cleavage fracture is stress controlled, these finite element results indicate that crack depth should have a stronger effect on cleavage fracture toughness than does specimen size. The slight trend of reducing toughness with increasing specimen size that can be expected for stress-controlled fracture is obscured in Fig. 5 by both scatter and by the limited number of specimens tested.

In summary, these data for A515 steel indicate that crack depth and thickness cannot be reliably traded off against each other to achieve the same constraint and thereby the same fracture toughness with two specimens of greatly different geometry. The absence of this simple trade-off can be attributed to both the modest effect of specimen size relative to crack depth on cleavage fracture toughness and to the scatter in fracture toughness data characteristic of temperatures in the transition range.

Finite Element Results Needed to Calculate Constraint Corrections and Parameters for ASTM A515 Grade 70 Steel

Information reported in the literature to date are inadequate to permit calculation of either the Dodds/Anderson correction or the Q parameter for a material with a strain-hardening coefficient of 4, such as the A515 steel investigated. Thus, plane strain small geometry change finite element analyses were conducted, as detailed earlier, to determine the required relationships. Figure 6 shows the variation of J_{SSY}/J_{BB} and of Q with applied loading for a range of a/W ratios determined by these analyses.

The curves in Fig. 6 should only be used to correct (or index) toughness data for which no slow stable crack growth precedes cleavage failure because the finite element analyses did not model crack growth. This restriction limits the range of temperatures over which these corrections and parameters can be applied to those very near the lower shelf. However, it may be possible to permit some small amount of crack extension and still use the constraint corrections and parameters presented in Fig. 6. To determine what errors are thereby incurred, crack growth can be viewed as consisting of two separable processes not considered by a stationary crack analysis: (1) a geometry change, and (2) a history effect on the deformation fields around the crack tip. Taken alone, the geometry change (increased crack length) increases constraint above that associated with the original crack length, which increases both J_{SSY}/J_{BB} and Q above their stationary crack values. Conversely, the stress singularity for a growing crack, $ln(1/r)$, is weaker than that of a stationary crack, $1/r$ [*31*]. This should reduce both J_{SSY}/J_{BB} and Q relative to their stationary crack values. Thus, the two errors introduced by not considering crack growth may be self-compensating. Of the two, the effect of geometry change alone can be assessed directly from the available stationary crack results. However, an analyses which explicitly models crack growth is needed to quantify errors associated with history effects. This in itself is an arduous task, and the topic of considerable current computational research. In this investigation, geometry change will be accounted for to establish a positive error bound. History effects needed to establish a negative error bound will be ignored. As these errors are of a different sense, it is not unreasonable to expect that they may approximately counteract each other, at least for small amounts of crack growth.

The effect of increased crack length on J_{SSY}/J_{BB} and Q can be determined directly from Fig. 6 by determining the variation of J_{SSY}/J_{BB} and Q with a/W at various fixed deformation levels (vertical lines on these graphs). Figure 7 shows this variation at four different deformation levels. The construction lines on this graph indicate that, if some small error can be tolerated in the value of J_{SSY}/J_{BB} or Q calculated for a particular experiment, then some small amount of crack growth prior to cleavage failure can be allowed. Figure 8 shows the variation of allowable crack growth with initial a/W and deformation level at fracture permitted by accepting 5%

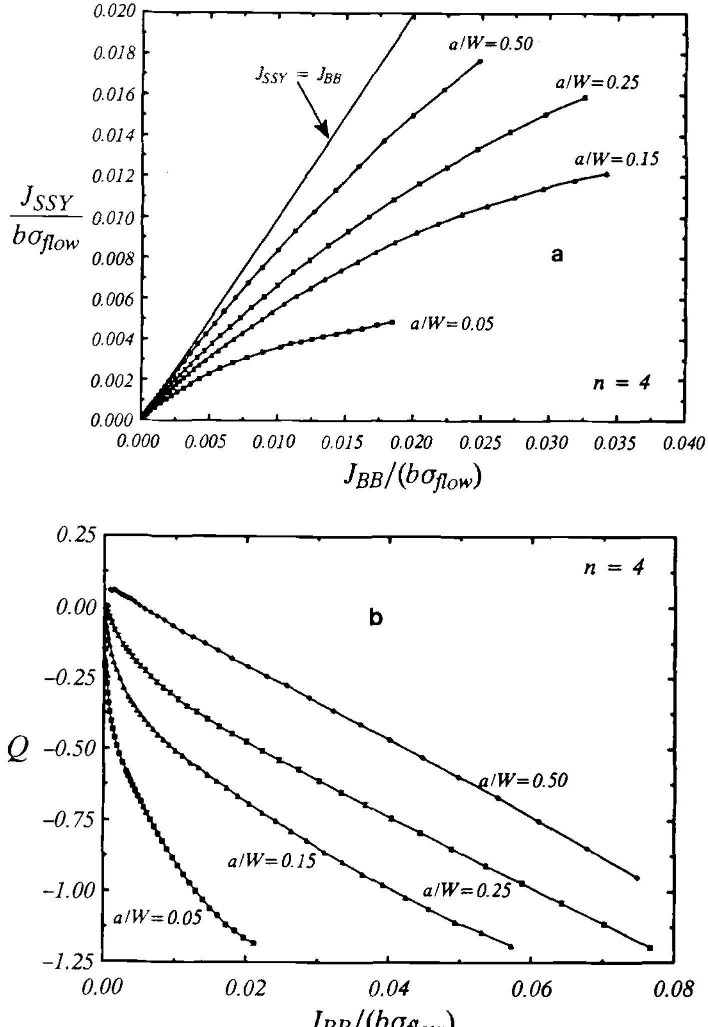

FIG. 6—*Variation of* (a) J_{SSY}/J_{BB} *and of* (b) Q *with applied* J *for a range of* a/W *ratios determined by conventional small strain finite element analyses for* n = *4.* J_{SSY}/J_{BB} *is the instantaneous slope of the curves in* 6a.

errors in J_{SSY}/J_{BB} or Q. These curves, combined with those of Fig. 6, provide the necessary information to estimate both J_{SSY}/J_{BB} and Q for a material with a strain-hardening coefficient of 4 that fails by cleavage following some small amount of ductile crack growth. Figure 9 summarizes the A515 fracture toughness data from Fig. 5 having less than this allowable amount of crack growth.[4]

[4] While the allowable crack growth for Q, Fig. 8*b*, is somewhat less than for J_{SSY}/J_{BB}, Fig. 8*a*, the same fracture toughness data set (Fig. 9) is used in all subsequent analyses to permit comparison of the various constraint parameters on an equivalent basis.

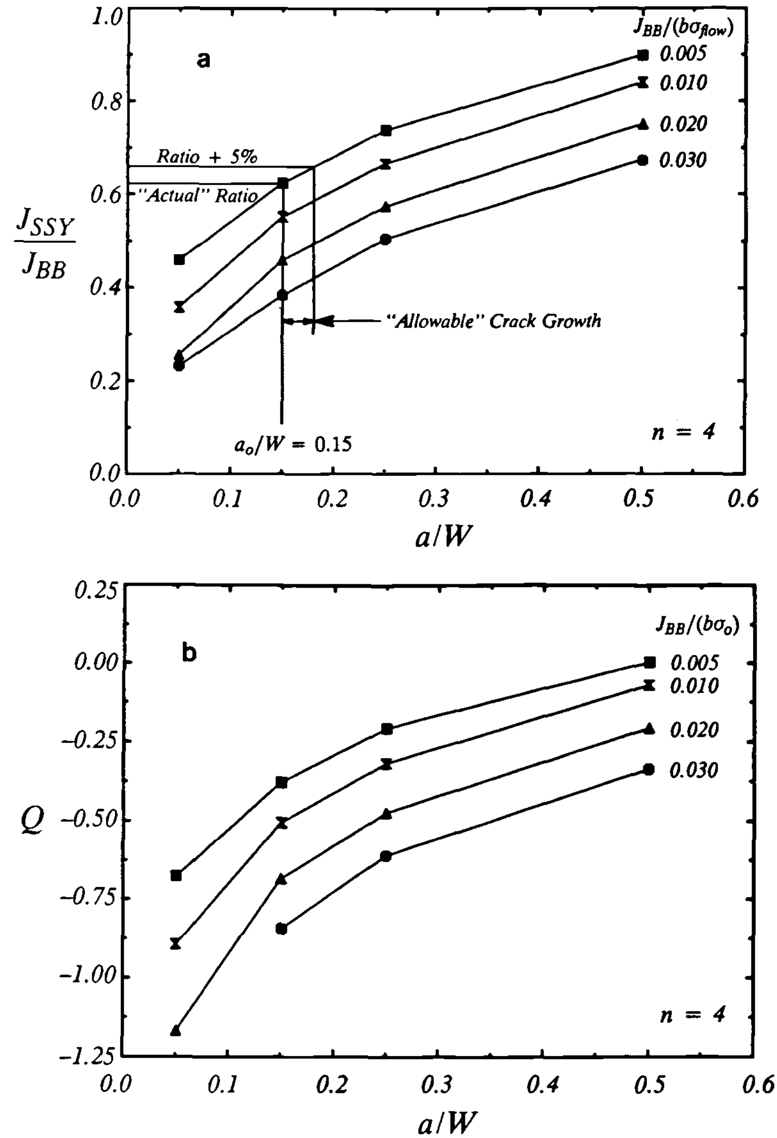

FIG. 7—*Variation of* (a) J_{SSY}/J_{BB} *and of* (b) Q *with* a/W *at several discrete applied* J *levels for* n = 4.

Use of Constraint Parameters with ASTM A515 Grade 70 Fracture Toughness Data

The fracture toughness data for A515 steel presented above indicate that specimen size cannot reliably be traded off against crack depth to achieve two specimens of different geometry that fail by cleavage at the same applied *J*. Alternative approaches to developing a relationship between the toughness of different-sized specimens and structures involve the use of various constraint corrections and indexing parameters. These possibilities are now considered.

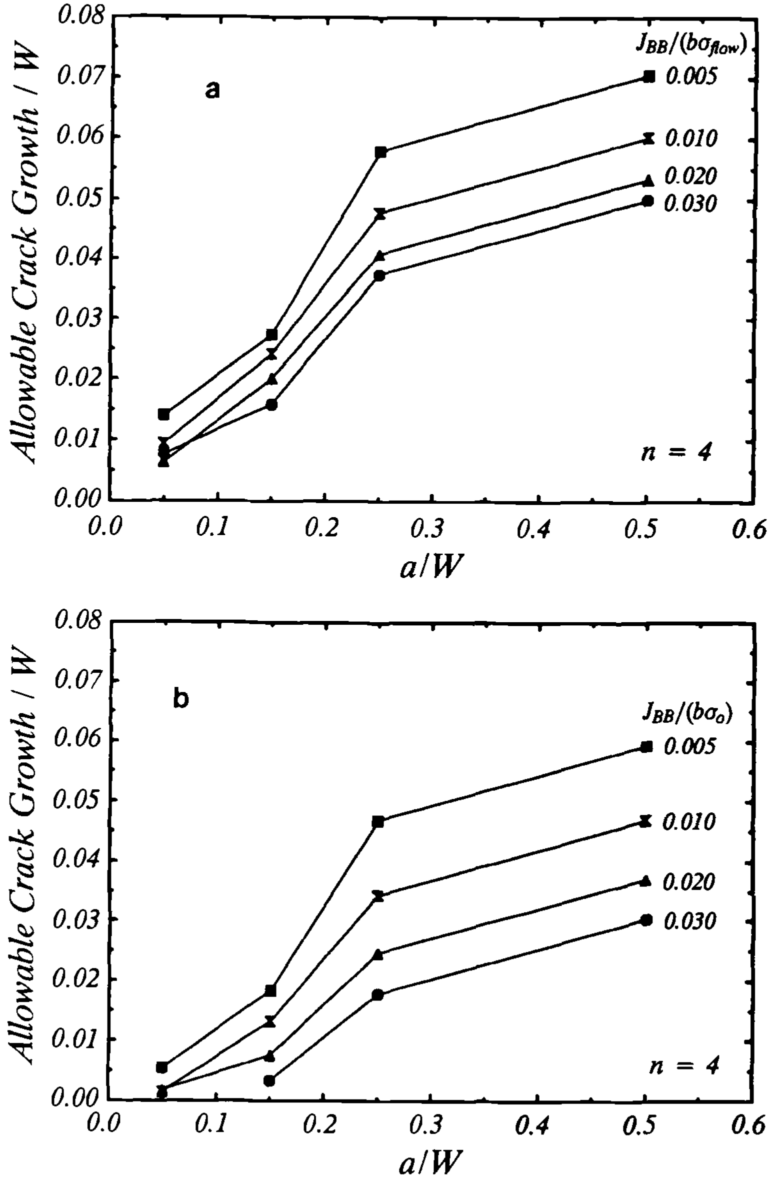

FIG. 8—*Variation of allowable crack growth with* a/W *and applied* J *if 5% error in calculated value of* (a) J_{SSY}/J_{BB} *or of* (b) Q *is permissible. For* n = *4.*

Figure 10 shows the variation of J_{SSY} with a/W and specimen size for the A515 steel. This graph was constructed using the fracture toughness data of Fig. 9 and the scaling relationship shown in Fig. 6*a*. The preponderance of these data indicate that the micromechanics-based constraint correction proposed by Dodds and Anderson accounts for the effect of a/W on the measured fracture toughness, with J_{SSY} representing the true driving force for cleavage fracture

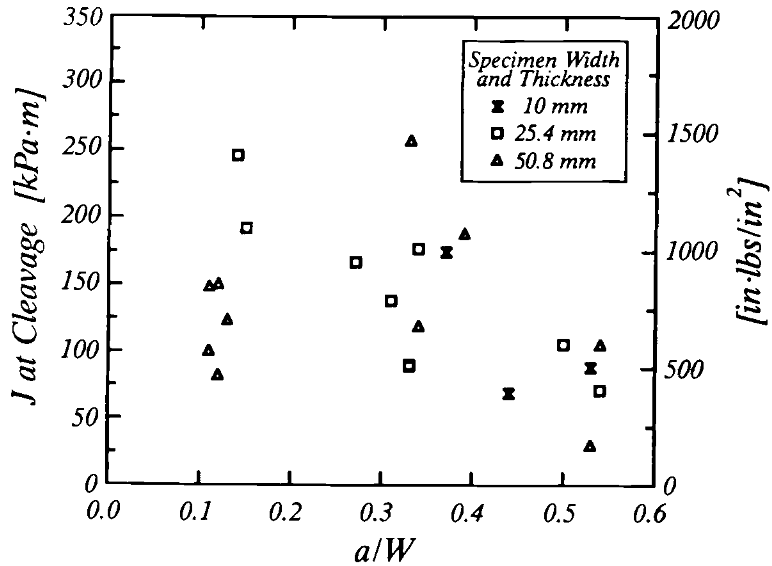

FIG. 9—*Variation of cleavage fracture toughness* (J_c) *with* a/W *and specimen size for ASTM A515 Grade 70 steel at +20°C. Only specimens having less than the allowable crack growth shown in Fig. 8*(a) *are plotted.*

independent of finite geometry effects. However, these data do not test the ability of this constraint correction to properly account for specimen size variations because the effect of specimen size on toughness in the original data set (Fig. 9) cannot be distinguished from scatter.

Figure 11 shows the variation of cleavage fracture toughness, J_c, with the constraint indexing parameters T and Q. The T-stress effectively indexes constraint, ordering the data into a sys-

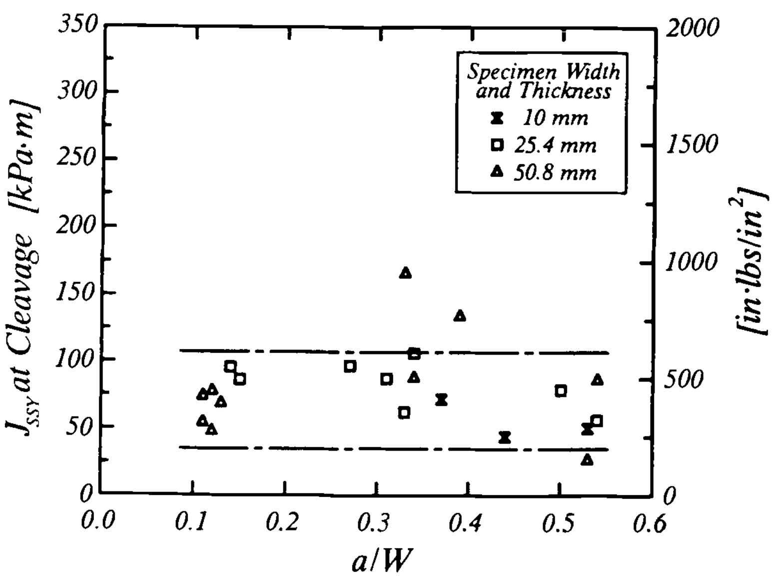

FIG. 10—*Variation of* J_{SSY} *with* a/W *and specimen size for ASTM A515 Grade 70 steel at +20°C.*

tematic trend of decreasing fracture toughness with increasing T, albeit with some scatter. Q does not exhibit such a clear trend; however, this may be because Q expands the low constraint region while T compresses it. Although Fig. 11*b* suggests that Q may be a thickness-dependent constraint index, the A515 fracture toughness data do not provide clear evidence of this. However, Fig. 12 shows that the variation of $(1 - Q)$ with a/W and specimen size exhibits similar characteristics to the variation of the microstructurally based constraint correction J_{BB}/J_{SSY} with a/W and specimen size. In specific, Fig. 12 shows that J_{BB}/J_{SSY} and $(1 - Q)$ both:

1. Approach unity for large, deeply cracked specimens.
2. Increase with reducing a/W and, to a lesser extent, with reductions in thickness.

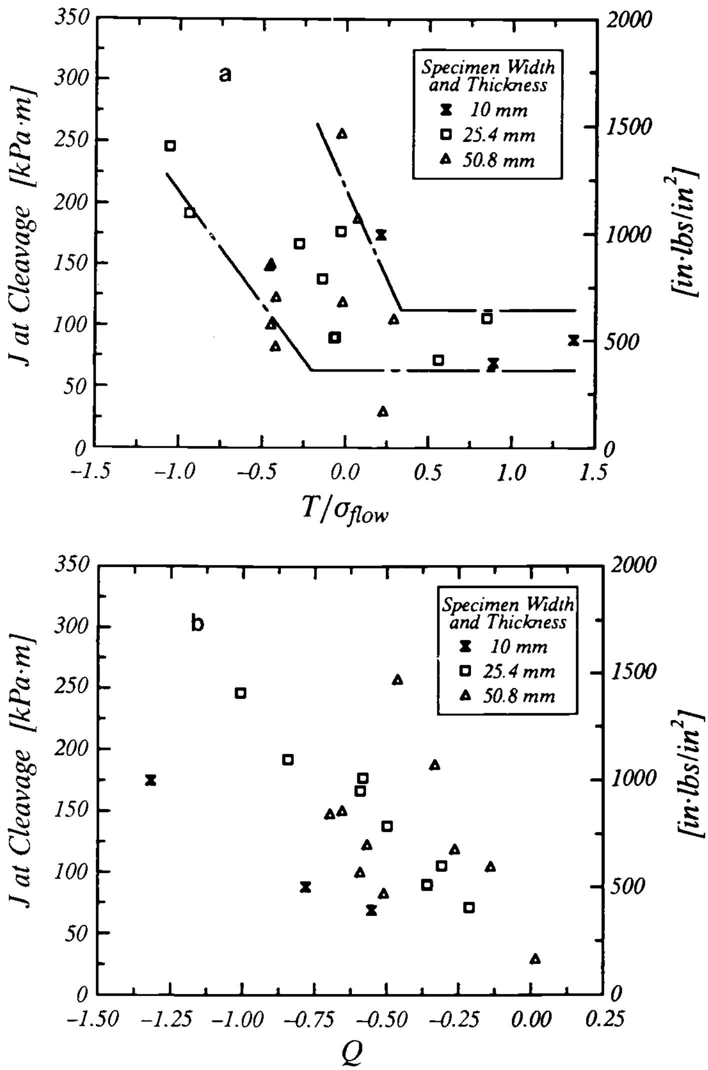

FIG. 11—*Variation of cleavage fracture toughness* (J_c) *data for ASTM A515 Grade 70 steel at +20°C with constraint indexing parameters* (a) T, *and* (b) Q. *Dashed lines drawn by hand to indicate data trend.*

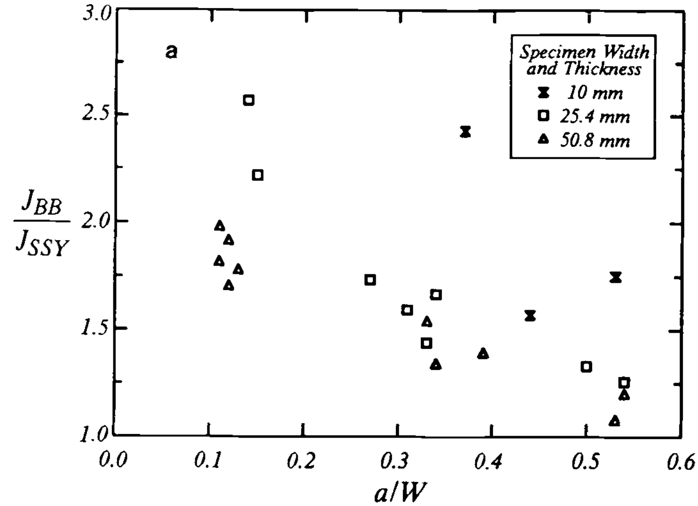

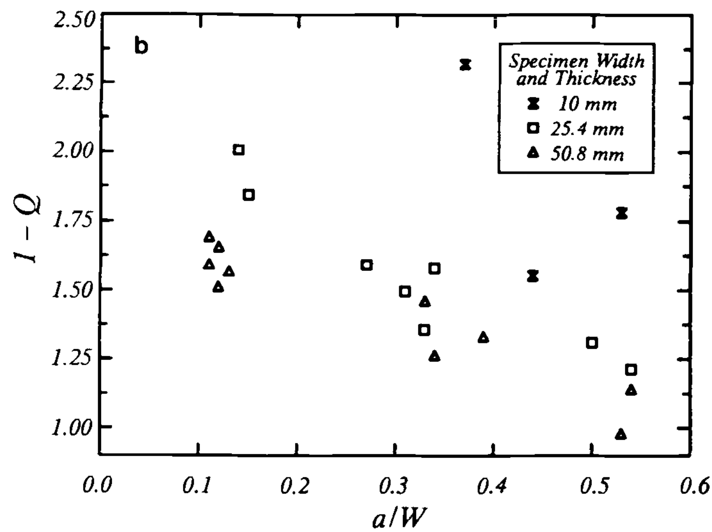

FIG. 12—*Variation of* (a) J_{BB}/J_{SSY} *and* (b) $(1 - Q)$ *with* a/W *and specimen size for ASTM A515 Grade 70 steel at +20°C.*

3. Exhibit "scatter" in much the same way as a plot of J_c versus a/W and specimen size does (Fig. 9).

Noting that the geometry-independent fracture toughness J_{SSY} is formed as the ratio of the measured fracture toughness (J_c) to the constraint correction (J_{BB}/J_{SSY})

$$J_{SSY} = \frac{J_c}{J_{BB}/J_{SSY}} \tag{12}$$

it is apparent that the ratio J_{BB}/J_{SSY} must have the characteristics listed above for J_{SSY} to be geometry independent. Figure 12*b* shows that $(1 - Q)$ has these characteristics, suggesting a candidate geometry independent toughness parameter

$$J_Q = \frac{J_c}{1 - Q} \tag{13}$$

Figure 13 shows that J_Q does in fact provide some form of geometry independent toughness measure for these data. The value "1" is used in the denominator of J_Q to enforce a correction of unity, that is, no correction, when fracture occurs under small-scale yielding conditions.

Application of Constraint Corrections and Indices to Assessment of Structural Fracture Integrity against Cleavage

Ultimately, none of these constraint corrections and indices have any engineering utility unless they improve the accuracy with which structural fracture integrity can be assessed. To be most helpful, a constraint correction or index would alleviate the need to conduct experiments with multiple specimen configurations (for example, shallow crack, deep crack, bending loading, tension loading) by providing a reliable means to scale toughness between different geometries. Further, calculation of the correction or indexing parameter cannot be so arduous as to preclude application to a reasonably complex structure. None of the corrections/indices examined in this study fully satisfy both of these criteria.

As the functional relationship between J_c with T is unknown, specimens of different geometries, and thereby different β values, must be tested to define this relationship. Thus, the constraint index T is unsuccessful at simplifying experimental determination of the "appropriate" fracture toughness for use in a structural fracture integrity assessment. However, definition of

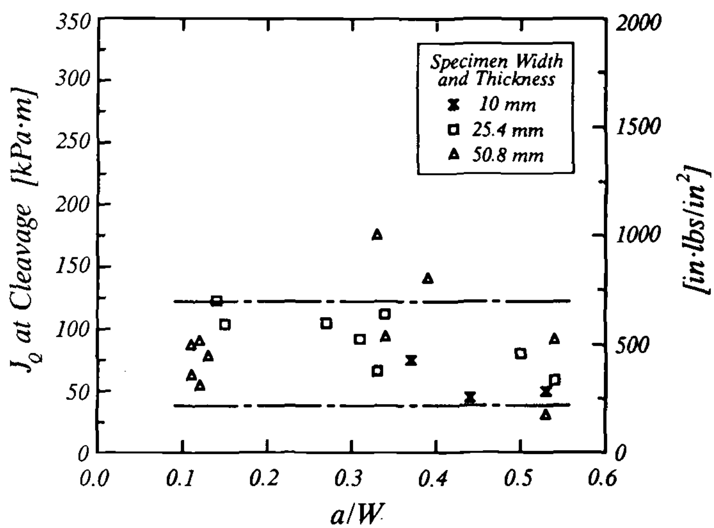

FIG. 13—*Variation of* J_Q *and with* a/W *and specimen size for ASTM A515 Grade 70 steel at +20°C.*

T only requires a linear elastic analysis of the cracked structure. This makes calculation of T less costly than calculation of any of the proposed constraint correction parameters, all of which require an elastic-plastic analysis.

One advantage that correction approaches hold over indexing is that, since all employ a geometry independent toughness value, only one specimen geometry need be tested to determine J_c. Thus, the reliability of these approaches rests on whether or not the proposed toughness measures are truly geometry independent. Of the proposed corrections, J_{SSY} offers the best assurance of geometry independence as it was derived from the micromechanistic requirements for cleavage fracture. The geometry independence of J_Q seems likely because the definition of Q (Eq 11) is based on near tip stresses, which are known to control cleavage fracture. The A515 data for J_{SSY} and for J_Q indicate that both toughness values are geometry independent over the range of conditions considered.

A disadvantage of the correction approaches relative to the T-stress indexing approach is the difficulty of computing the correction parameters. The considerable computational and post-processing effort needed to determine these parameters for even simple geometries [for example, SE(B) specimens] makes these approaches inappropriate for routine application to structures at the current time. Thus, the (relative) ease with which T can be calculated makes it more attractive from an applications perspective than either of the constraint corrections. However, application of T in an actual structural fracture safety analysis depends upon the feasibility of conducting a sufficient quantity and variety of fracture experiments to define the variation of the critical fracture toughness, J_c, with T.

Summary and Conclusions

This study examined the feasibility of predicting the fracture toughness in structurally relevant situations (shallow cracks in thick plates) based on toughness values measured with experimentally convenient specimen geometries (deep cracks in small specimens). The cleavage fracture toughness, J_c, of ASTM A515 Grade 70 steel plate was measured using SE(B) specimens. Specimen size and initial crack depth were varied to obtain J_c values over a range of constraint conditions. As fracture occurred by cleavage, the following conclusions apply only to this fracture mode.

1. Crack depth and thickness cannot be traded off against each other to achieve the same constraint and thereby the same fracture toughness. The absence of this simple trade-off is due to the greater effect of crack depth than of specimen size on J_c and to the scatter in fracture toughness data characteristic of temperatures in the transition range.
2. The various techniques proposed to account for constraint effects on fracture toughness fall into two categories: indexing parameters and correction parameters. Indexing parameters offer a systematic means to order the interrelated effects of geometry, loading mode, and thickness on critical fracture toughness. Conversely, the correction approach attempts to predict the toughness of some configuration different from that for which toughness data are available.
3. The T-stress constraint index was successful at indexing the different J_c values obtained by varying the thickness and crack depth in SE(B) specimens of the A515 steel. Q does not exhibit such a clear trend; however, available data suggest that Q may be a thickness-dependent constraint index. Additionally, Q was found to have the characteristics of a constraint correction.
4. The geometry independence of the toughness parameters J_{SSY} and J_Q, determined using constraint corrections J_{SSY}/J_{BB} and Q, respectively, was demonstrated using the A515 steel fracture toughness data.

Acknowledgments

The authors are pleased to recognize the able technical support of J. W. Hein and J. P. Waskey in assisting with the experimental investigation. Additionally, the many helpful discussions with R. Dodds, T. Anderson, M. Natishan, and J. Merkle are gratefully acknowledged. The experimental work was performed at the David Taylor Research Center (DTRC) as part of the Office of Naval Technology Materials Block, administered at DTRC by I. Caplan. The analytical work was conducted at the University of Illinois as part of a training program administered by DTRC. Numerical computations were performed on the Apollo workstation network operated by the Department of Civil Engineering made possible, in part, by grants from Hewlett-Packard, Inc.

References

[*1*] Hutchinson, J. W., "Singular Behavior at the End of a Tensile Crack in a Hardening Material," *Journal of Mechanics and Physics of Solids,* Vol. 16, 1986, pp. 13–31.

[*2*] Rice, J. R. and Rosengren, G. F., "Plane Strain Deformation Near a Crack Tip in a Power-Law Hardening Material," *Journal of Mechanics and Physics of Solids,* Vol. 16, 1968, pp. 1–12.

[*3*] Sumpter, J. D. G., Prediction of Critical Crack Size in Plastically Strained Welded Panels," *Nonlinear Fracture Mechanics, Volume II: Elastic-Plastic Fracture, ASTM STP 995,* J. D. Landes, A. Saxena, and J. G. Merkle, Eds., American Society for Testing and Materials, Philadelphia, 1989, pp. 415–432.

[*4*] Kirk, M. T. and Dodds, R. H., "An Analytical and Experimental Comparison of J_i Values for Shallow Through and Part Through Surface Cracks," *Engineering Fracture Mechanics,* Vol. 39, No. 3, 1991, pp. 535–551.

[*5*] Dodds, R. H., Anderson, T. L., and Kirk, M. T., "A Framework to Correlate a/W Ratio Effects on Elastic-Plastic Fracture Toughness (J_c)," *International Journal of Fracture,* Vol. 48, 1991, pp. 1–22.

[*6*] O'Dowd, N. P. and Shih, C. F., "Family of Crack-Tip Fields Characterized by a Triaxiality Parameter: Part I—Structure of Fields," *Journal of Mechanics and Physics of Solids,* Vol. 39, No. 8, 1991, pp. 989–1015.

[*7*] Al-Ani, A. M. and Hancock, J. W., "*J*-Dominance of Short Cracks in Tension and Bending," *Journal of Mechanics and Physics of Solids,* Vol. 39, 1991, pp. 23–43.

[*8*] Richie, R. O., Knott, J. F., and Rice, J. R., "On the Relationship Between Critical Tensile Stress and Fracture Toughness in Mild Steel," *Journal of Mechanics and Physics of Solids,* Vol. 21, 1973, pp. 395–410.

[*9*] Kirk, M. T., "A Cyclic Reverse Bending Technique for Fatigue Precracking from Shallow Notches in SE(B) Specimens," *22nd Fracture, ASTM STP 1131,* American Society for Testing and Materials, Philadelphia, 1992, pp. 859–879.

[*10*] Kirk, M. T., Waskey, J. P., and Dodds, R. H., "Procedure for Drop Tower Testing of Shallow Cracked Single Edge Notched Bend Specimens," in *ASTM STP 1130,* 1992, pp. 50–75.

[*11*] Sorem, W. A., Dodds, R. H., and Rolfe, S. T., "Effects of Crack Depth on Elastic Plastic Fracture Toughness," *International Journal of Fracture,* Vol. 47, 1991, pp. 105–126.

[*12*] Merkle, J. G., "An Examination of the Size Effects and Data Scatter Observed in Small-Specimen Cleavage Fracture Toughness Testing," U.S.N.R.C. NUREG/CR-3672, U.S. Nuclear Regulatory Commission, Washington, DC, 1984.

[*13*] Irwin, G. R., "Fracture Mode Transition for a Crack Traversing a Plate," *Journal of Basic Engineering,* Vol. 82, No. 2, 1960, pp. 417–425.

[*14*] Anderson, T. L. and Dodds, R. H., "Specimen Size Requirements for Fracture Toughness Testing in the Ductile-Brittle Transition Region," *Journal of Testing and Evaluation,* Vol. 19, 1991, pp. 123–134.

[*15*] Harrison, J. D. and Anderson, T. L., "Developments in the Application of the CTOD Approach to Fracture Assessment of Welded Construction," *Fracture Mechanics: Eighteenth Symposium, ASTM STP 945,* D. T. Read and R. P. Reed, Eds., American Society for Testing and Materials, Philadelphia, 1988, pp. 468–484.

[*16*] Shih, C. F., *Journal of Mechanics and Physics of Solids,* Vol. 29, 1981, pp. 305–326.

[*17*] Bertegon, C. and Hancock, J. W., "Two-Parameter Characterization of Elastic-Plastic Crack Tip Fields," *Journal of Applied Mechanics,* Vol. 58, March 1991, pp. 104–116.

[*18*] O'Dowd, N. P. and Shih, C. F., "Family of Crack-Tip Fields Characterized by a Triaxiality Parameter: Part II—Fracture Applications," *Journal of Mechanics and Physics of Solids,* in press.

[19] Herrens, J. and Read, D. T., "Fracture Behavior of a Pressure Vessel Steel in the Ductile to Brittle Transition Region," NISTIR 88-3099, National Institute for Standards and Technology, Boulder, CO, 1988.
[20] Larsson, S. G. and Carlsson, A. J., "Influence of Non-Singular Stress Terms and Specimen Geometry on Small-Scale Yielding at Crack Tips in Elastic-Plastic Materials," *Journal of Mechanics and Physics of Solids*, Vol. 21, 1973, pp. 263–277.
[21] Parks, D. M., "Engineering Methodologies for Assessing Crack Front Constraint," presented at the 1991 Spring Meeting of the Society for Experimental Mechanics, 1991.
[22] Tada, H., et al., *The Stress Analysis of Cracks Handbook*, Del Research Corp., St. Louis, 1985.
[23] Rice, J. R., "A Path Independent Integral and the Approximate Analysis of Strain Concentration by Notches and Cracks," *Journal of Applied Mechanics*, Vol. 35, 1968, pp. 379–386.
[24] Sumpter, J. D. G. and Hancock, J. W., "Shallow Crack Toughness of HY-80 Welds: An Analysis Based on T Stresses," *International Journal of Pressure Vessels and Piping*, in press.
[25] Sumpter, J. D. G. "J_c Determination for Shallow Notch Welded Bend Specimens," *Fatigue and Fracture of Engineering Materials and Structures*, Vol. 10, No. 6, 1987, pp. 479–493.
[26] Kirk, M. T. and Hackett, E. M., "An Evaluation of *J-R* Curve Testing Using Three-Point Bend Specimens," *Fracture Mechanics: Eighteenth Symposium, ASTM STP 945*, D. T. Read and R. P. Reed, Eds., American Society for Testing and Materials, Philadelphia, 1988, pp. 347–373.
[27] Dodds, R. H. and Lopez, L. A., "Software Virtual Machines for Development of Finite Element Systems," *International Journal for Engineering with Computers*, Vol. 13, 1985, pp. 18–26.
[28] Li, F. Z., Shih, C. F., and Needleman, A., "A Comparison of Methods for Calculating Energy Release Rates," *Engineering Fracture Mechanics*, Vol. 21, 1985, pp. 405–421.
[29] Shih, C. F., Moran, B., and Nakamura, T., "Energy Release Rate Along a Three-Dimensional Crack Front in a Thermally Stressed Body," *International Journal of Fracture*, Vol. 30, 1986, pp. 79–102.
[30] Sorem, W. A., "The Effect of Specimen Size and Crack Depth on Elastic Plastic Fracture Toughness of a Low Strength High Strain Hardening Steel," Ph.D. dissertation, University of Kansas, Lawrence, Kansas, 1989.
[31] Rice, J. R., Drugan, W. J., and Sham, T. L., "Elastic-Plastic Analysis of Growing Cracks," *Fracture Mechanics: Twelfth Conference, ASTM STP 700*, American Society for Testing and Materials, Philadelphia, 1980, pp. 189–221.

DISCUSSION

W. E. Pennell[1] *(written discussion)*—You have used the relative crack depth a/W as the correlation parameter in your study of the effects of crack depth on fracture toughness. I think a strong case can be made for the absolute crack depth a as a more appropriate correlation parameter. What was your rationale for selecting a/W rather than a as your correlation parameter? What would be the effect on your results and conclusions if a were substituted in place of a/W?

M. T. Kirk, K. C. Koppenhoefer, and C. F. Shih (authors' closure)—Plane strain finite element analyses of three SE(B) specimens were performed to gain insight into the effects of both absolute crack depth (a) and relative crack depth (a/W) on cleavage fracture toughness, J_c. The situations detailed in Table 2 were modelled (a Ramberg-Osgood strain-hardening coefficient of 4 was used in all analyses).

Figure 14 shows the variation of opening mode stress with distance from the crack tip along the crack line in each specimen at an applied J of 350 kPa · m. These data indicate that at a fixed a/W (0.5), the severity of conditions for cleavage fracture[2] increases with increasing a. However, Fig. 1 also shows that at a fixed a (25.4 mm), increasing a/W increases the opening mode stress and thereby the severity of conditions for cleavage fracture. Thus, neither simi-

[1] Oak Ridge National Laboratory, P.O. Box 2009, Oak Ridge, TN 37831-8056.
[2] Achieving a critically stressed volume of material in front of the crack tip triggers cleavage fracture [8]. Thus, the stress elevation ahead of the crack controls the severity of conditions for cleavage fracture.

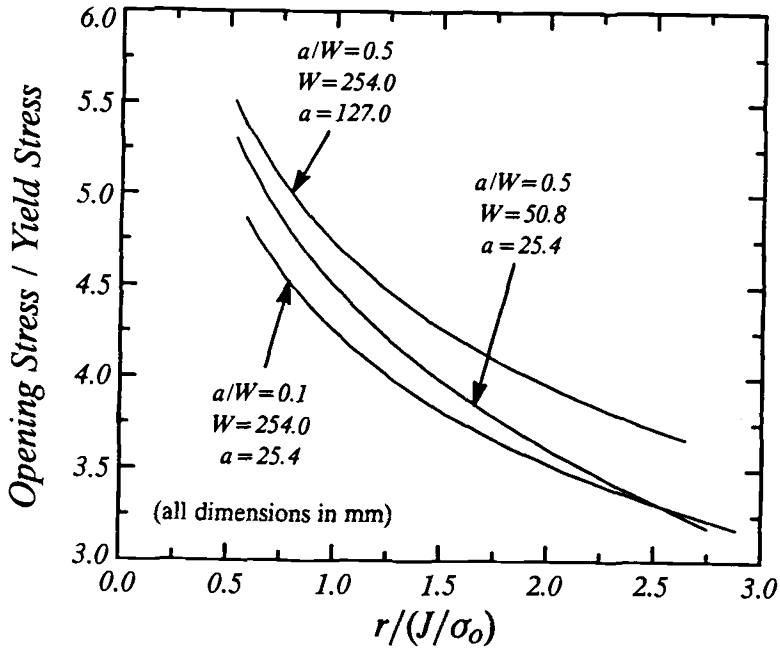

FIG. 14—*Variation of opening mode stress with distance from the crack tip at an applied* J *of 350 kPa · m for three different SE(B) specimens having a Ramberg-Osgood strain-hardening coefficient of 4.*

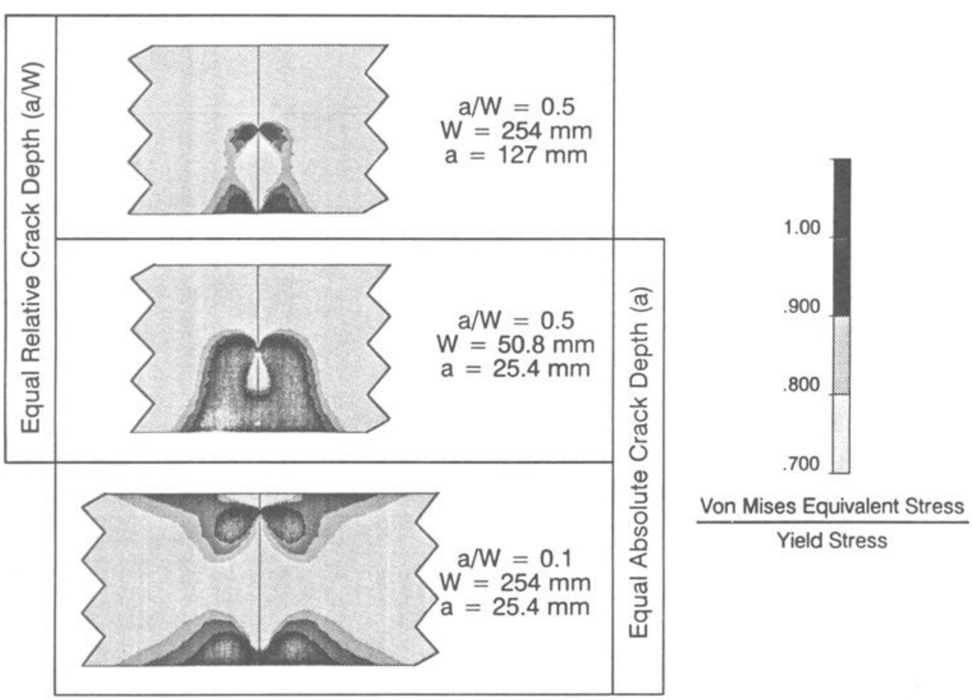

FIG. 15—*Effect of relative and absolute crack depth on plastic zone size. All three specimens loaded to an applied* J *of 350 kPa · m.*

TABLE 2—*Plane-strain finite element analyses of three single edge bending specimens.*

a/W	W, mm	a, mm
0.5	50.8	25.4
0.5	254.0	127.0
0.1	254.0	25.4

larity of a or of a/W ensures similarity of opening mode stress between SE(B) specimens of different overall size. The cause of these effects can be explained based on global deformation patterns. Figure 15 illustrates the plastic zones for the three SE(B) specimens analyzed with each specimen loaded to an applied J of 350 kPa · m. At an equivalent a/W (0.5), higher crack tip stresses occur ahead of the deeper crack (a = 127.0 mm) because yielding in this specimen is well confined within an elastic field. Conversely, the smaller specimen (a = 25.4 mm) has

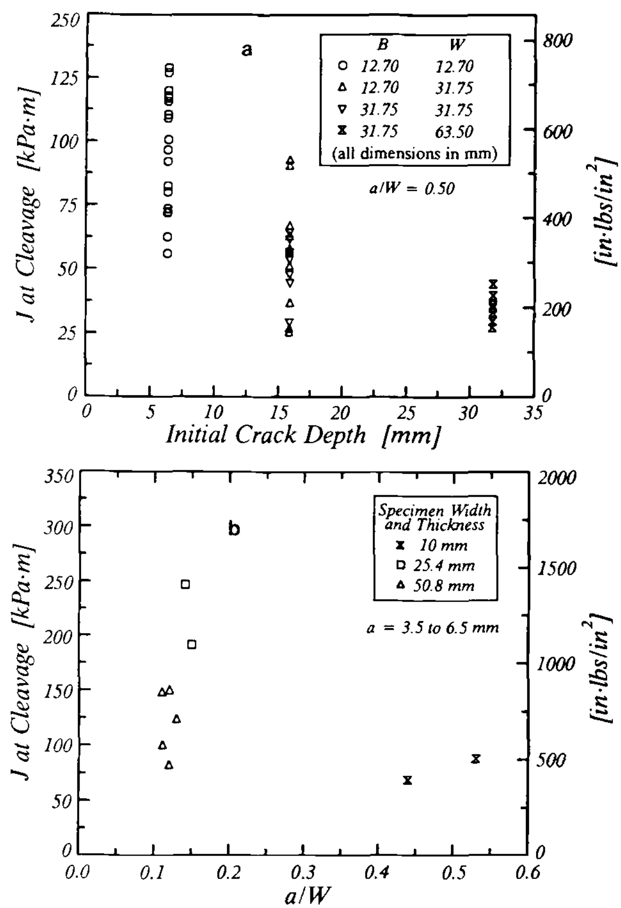

FIG. 16—(a) *Effect of absolute crack depth on the cleavage fracture toughness of A36 steel at −49°C.* (b) *Effect of relative crack depth on the cleavage fracture toughness of A515 Grade 70 steel at +20°C.*

formed a plastic hinge, thereby relaxing the stress elevation caused by the crack. At an equivalent a (25.4 mm), lower crack tip stresses occur ahead of the shallower crack ($a/W = 0.1$) because the stress concentration at the crack tip is relieved by the impingement of a global plastic zone characteristic of an uncracked beam in bending on the crack tip plastic zone. In the $a/W = 0.5$ specimen, the crack tip plastic zone is the only dominant feature.

In summary, these observations concerning opening mode stresses imply the following effects of a and a/W on cleavage fracture toughness (J_c):

1. At a fixed a/W, J_c should increase with reductions in a.
2. At a fixed a, J_c should increase with reductions in a/W.

Figure 16 provides experimental data, drawn from both this study and the work of Sorem on A36 steel [*30*], which substantiate these expectations. Thus, the combined numerical and experimental evidence indicates that neither similarity of a/W or of a ensures similarity of toughness between specimens of different overall size. However, as discussed in this paper, the micromechanics-based constraint correction proposed by Dodds and Anderson [*5,14*] for cleavage fracture accounts for both effects. As shown by the scaling relationships of Fig. 6*a*, a/W is accounted for by the different curves on the diagram, whereas a is accounted for by the presence of the remaining ligament ($b = W - a$) term in the axes normalization. These relations can be used to determine a specimen size independent cleavage fracture toughness, J_{SSY}, from any size specimen that fails by cleavage (Fig. 10). Alternatively, an appropriate cleavage fracture toughness for a specimen or structure could be estimated using these scaling relationships even if the specimen/structure has a relative and/or absolute crack depth different than that of available J_c data.

Timothy J. Theiss[1] *and John W. Bryson*[1]

Influence of Crack Depth on the Fracture Toughness of Reactor Pressure Vessel Steel

REFERENCE: Theiss, T. J. and Bryson, J. W., "**Influence of Crack Depth on the Fracture Toughness of Reactor Pressure Vessel Steel,**" *Constraint Effects in Fracture, ASTM STP 1171,* E. M. Hackett, K.-H. Schwalbe, and R. H. Dodds, Eds., American Society for Testing and Materials, 1993, pp. 104–119.

ABSTRACT: The Heavy Section Steel Technology Program (HSST) at Oak Ridge National Laboratory (ORNL) is investigating the influence of flaw depth on the fracture toughness of reactor pressure vessel (RPV) steel. Recently, it has been shown that, in notched beam testing, shallow cracks tend to exhibit an elevated toughness as a result of a loss of constraint at the crack tip. The loss of constraint takes place when interaction occurs between the elastic-plastic crack-tip stress field and the specimen surface nearest the crack tip. An increased shallow-crack fracture toughness is of interest to the nuclear industry because probabilistic fracture-mechanics evaluations show that shallow flaws play a dominant role in the probability of vessel failure during postulated pressurized-thermal-shock (PTS) events.

Tests have been performed on beam specimens loaded in three-point bending using unirradiated RPV material (A533 B). Testing has been conducted using specimens with a constant beam depth (W = 94 mm) and within the lower-transition region of the toughness curve for A533 B. Primarily two crack depths have been considered: a = 50 and 9 mm (a/W = 0.5 and 0.1). Three specimen thicknesses (B = 50, 100, and 150 mm) have been used to examine the influence of different out-of-plane constraint conditions on the test results. All tests resulted in cleavage failures. Test results indicate a significantly higher fracture toughness associated with the shallow flaw specimens compared to the fracture toughness determined using deep-crack (a/W = 0.5) specimens. The toughness increase is comparable with the toughness increase found at the University of Kansas using steels whose stress-strain properties bound those of A533 B. Test data also show little influence of thickness on the fracture toughness for the current test temperature (−60°C). The Irwin β_c correction has been modified to account for shallow flaws and was used to estimate the shallow-flaw toughness based on the results from the deep-crack specimens.

KEY WORDS: elastic-plastic fracture mechanics, constraint, shallow-crack fracture toughness, crack tip opening displacement (CTOD) testing, J-integral, reactor pressure vessel analysis, Irwin β_c correction

Nomenclature

a	Crack depth
B	Specimen thickness
CMOD	Crack-mouth opening displacement
CTOD	Crack-tip opening displacement
E	Elastic modulus
IPTS	Integrated-pressurized-thermal-shock
J_c	J-integral fracture toughness at unstable fracture
J_{el}	Elastic component of J-integral

[1] Engineers, Oak Ridge National Laboratory, P.O. Box 2009, MS-8056, Oak Ridge, TN 37831-8056.

J_{pl}	Plastic component of J-integral
K_{Ic}	Critical stress intensity factor, plane-strain fracture toughness
K_c	Fracture toughness not meeting plane-strain requirements
LLD	Load-line displacement
m	Constraint parameter
RPV	Reactor pressure vessel
PWR	Pressurized water reactor
PTS	Pressurized-thermal-shock
RT_{NDT}	Reference nil-ductility transition temperature
SENB	Single-edge-notch bend
RF	Rotation factor
T	Temperature
U_{pl}	Plastic energy or area under load versus load-line displacement curve
W	Specimen depth
σ_y	Yield strength
σ_f	Flow stress
ν	Poisson's ratio
β_c	Plastic-zone size parameter
β_{Ic}	Plane-strain plastic-zone size parameter
δ_c	Critical cleavage CTOD toughness
η_{pl}	Geometry dependent constant linking plastic J to plastic energy

Introduction

Recent investigations into the influence of crack depth on fracture toughness at the University of Kansas and elsewhere have shown a significant increase in toughness of steel specimens containing shallow flaws [*1,2*]. Similar experimental research is being jointly carried out by the Edison Welding Institute in the United States and the Welding Institute in the United Kingdom (Kirk et al. [*3*], and Sumpter [*4*]). The phenomenon of elevated shallow-crack fracture toughness appears to be caused by the relaxation of crack-tip constraint due to the proximity of a free surface. The elevated shallow-crack fracture toughness occurs in the lower transition range where cleavage fracture takes place but at temperatures above the lower shelf. Significant increases (factor of 2.5 to 4.0) in CTOD caused by shallow cracks were found for both A36 and A517 steel at the University of Kansas. A36 steel is a low-strength, high-strain-hardening material, while A517 is a high-strength, low-strain-hardening material. The strength and strain-hardening properties of reactor pressure vessel (RPV) material (A533 B) are between those of A36 and A517. It was anticipated, therefore, that a significant increase in the toughness of shallow flaws in A533 B would also take place [*5*].

Current reactor pressure vessel life assessments are strongly dependent on the ability of the vessel material to withstand load in the presence of a flaw (that is, sufficient fracture toughness). An accurate determination of the fracture toughness of an RPV is particularly important for pressurized-thermal-shock (PTS) loading. The fracture toughness used in RPV life assessments is a function of T-RT_{NDT} and to date has been determined using deep-notch specimens to provide conservative results. Probabilistic fracture mechanics evaluations of operating nuclear facilities in integrated pressurized thermal shock (IPTS) studies have shown that shallow, surface flaws rather than deep cracks in the reactor vessel contribute predominantly to the calculated probability of vessel failure [*6–8*]. The dominance of shallow rather than deep flaws in the probabilistic fracture mechanics evaluations is due in part to the higher density of shallow flaws assumed to exist in the vessel wall, the increased radiation damage near the inside surface, and the severity of the thermal shock on the vessel surface. IPTS studies indicate that roughly 95% of all the flaws that are predicted to initiate during the dominant transients for the three vessel models considered were 25 mm (1-in.) deep or less [6–8]. Moreover, the majority of these initiations took place at temperatures below RT_{NDT}. The temperatures of interest roughly correspond with the lower transition region of the toughness curve for A533 B material. In other words, a large number of the initiation events for an RPV in PTS analyses originate from shallow flaws and occur within the lower transition region where the shallow-flaw increase in fracture toughness has been shown to take place.

Preliminary estimates of the shallow-crack toughness for A533 B were made based on the results for A36 and A517, and these estimates were used to determine the impact of a shallow-flaw elevated toughness in PTS analyses. These analyses revealed that PTS analyses could potentially be significantly impacted by considering the shallow-crack toughness in RPV material [9]. The Heavy Section Steel Technology Program (HSST) is, therefore, investigating the influence of flaw depth on the fracture toughness of RPV steel [5,10].

The ultimate goal of the shallow-crack investigation is the generation of a limited database of elastic-plastic fracture toughness values appropriate for shallow flaws in a reactor pressure vessel and the application of these data to reactor vessel life assessments. To meet these objectives, the HSST experimental shallow-crack work is divided into two phases: a development phase and a production phase. Complementary analytical investigations are also in progress. During the experimental development phase, the laboratory techniques necessary for shallow-crack testing will be established and verified through several development beam tests. Once the testing capabilities are confirmed, the toughness of shallow cracks will be compared with the toughness measured using deep-crack specimens as a part of the production phase of the project. The test results reported in this paper are a part of the developmental phase. While the results to date have been encouraging, they should still be considered preliminary.

Specimens

The specimen configuration chosen for testing shallow cracks in the HSST shallow-crack project is the single-edge-notch-bend (SENB) specimen with a through-thickness crack (as opposed to surface crack). The bend specimen was considered to simulate the varying stress field in a reactor wall under PTS conditions. In addition, previous shallow-crack work has utilized SENB specimens [1,2]. The straight-through notch simulates an infinitely long, axially oriented crack in an RPV. To better simulate the conditions of a shallow flaw in the wall of a reactor vessel, the specimen depth W and thickness B should be as large as practicable. PWR vessel walls are nominally 200 to 280 mm thick (8 to 11 in.). A $\approx$100-mm-deep (4-in.) beam has been selected for use in the HSST shallow-crack project. The stress gradient produced in beams of this size when loaded in three-point bending is similar to the stress gradient produced in a flawed reactor vessel under PTS loading [6]. To maintain consistency with ASTM standards, the beams are being tested in three-point bending. All testing is being conducted on reactor material (A533 Grade B, Class 1) [11] with the cracks oriented in the L-S orientation to maintain consistency with the conditions of an RPV.

Pretest Analysis

A preliminary numerical study was conducted to help determine instrumentation requirements, to provide pretest analytical predictions of the global beam behavior, and to define the crack depth(s) that would be expected to exhibit an elevated shallow crack toughness. Crack depth to beam depth ratios (a/W) of 0.05, 0.10, 0.15, 0.20, and 0.50 were analyzed. The beam depth was held constant at 100 mm (4 in.); the span was set at 4 W. The ADINA-87 [12] finite-element code was used to perform plane strain, elastic-plastic (von Mises, isotropic hardening) analyses of the beams loaded in three-point bending (to the plane strain limit load). A multilinear stress-strain representation of A533 B material tensile properties at $T = -60°C$ ($-76°F$) was utilized.

Eight-noded isoparametric quadrilateral elements with reduced 2 by 2 integration order were employed throughout the modeling. Special collapsed quadrilaterals, that is, wedge elements, were used at the crack tip in order to simulate blunting and to provide a $1/r$ singularity at the crack tip. A total of 412 elements and 1335 nodes were used in the modeling for each of the five crack depths. A crack tip region that always had the same mesh structure was obtained by simply translating the block through the depth and renumbering the surrounding nodes and elements; hence, each model had roughly the same finite-element discretization.

Refinement of the finite element mesh in the crack tip region was insufficient for rigorous quantification of near-tip stresses and displacements; however, results of the numerical study indicated a fundamental difference in the nonlinear stresses surrounding the crack tip between the shallow and deep-crack geometries [*13,14*]. The elevated fracture toughness associated with shallow flaws is due to a loss of constraint, which is indicated by the nonlinear stresses surrounding the crack tip being influenced by the tension surface of the specimen [*1*]. The finite-element analyses indicated that because of the proximity of the tension surface at equivalent levels of CTOD toughness, the maximum opening stress decreases as the crack depth decreases. Also, examination of the plastic zone surrounding the crack tip at predicted failure load shows uncontained yielding for the crack depths of 5 and 10 mm [(0.2 and 0.4 in.) or $a/W = 0.05$ and 0.10]. Uncontained yielding is evidence of loss of constraint, and an elevation in the toughness would be expected. The plastic zone at predicted failure load surrounding the 15-mm (0.6-in.) crack was larger than the deep-crack case ($a/W = 0.5$), while the plastic zone surrounding the 20-mm (0.8-in.) crack depth was essentially identical to the deep-crack case. Based on the finite-element results, an elevated toughness was expected for the 5- and 10-mm (0.2- and 0.4-in.) crack depths in a 100-mm (4-in.) deep beam. An elevated toughness would not have been expected from the 20-mm (0.8-in.) deep crack, and no conclusion could be drawn about the extent of the toughness elevation for the 15-mm (0.6-in.) deep crack in a 100-mm (4-in.) beam.

Test Matrix

Two crack depths (one shallow and one deep) were tested during the development phase of the project. The nominal crack depth chosen was $a \approx 9$ mm ($a \approx 0.4$ in.), which is prototypic of the flaw depths that resulted in initiation in the IPTS studies [*6–8*] and would be expected to exhibit an elevated toughness. One specimen was tested with a flaw depth of 14 mm (0.55 in.) for comparison. Currently, the relative influence of absolute crack depth, a, or normalized crack depth, a/W, is not fully understood and will be further examined later in this study.

To transfer shallow-crack fracture toughness data to the RPV properly, the effect of out-of-plane constraint on the toughness must be well understood. To investigate the effects of out-of-plane constraint in the beams, the beam thickness was varied. Three thicknesses were used: $B = 50$, 100, and 150 mm (2, 4, and 6 in.) At least one deep-crack specimen and two shallow-crack specimens were tested using beams of each thickness. The span for the 50-mm-thick beam is $4W$ or 406 mm (16 in.). The spans for the 100- and 150-mm beams were increased to 864 mm (34 in.) to assure failure without exceeding the load capacity of the beam fixture.

The temperature for all developmental testing work is within the lower transition region for A533 B steel. RT_{NDT} for this material is $-35°C$ ($-30°F$) [*11*]. The testing temperature for all the tests except one was approximately $-60°C$ ($-76°F$). $T\text{-}RT_{NDT}$ was, therefore, $-25°C$

TABLE 1—*Test matrix for Heavy Section Steel Technology Program (HSST) development beams.*[a]

	Crack Depths, a/W			
Thicknesses	0.50	0.15	0.10	Total
50 mm	3 beams	1 beam	4 beams	8 beams
100 mm	1 beam	. . .	2 beams	3 beams
150 mm	1 beam	. . .	2 beams	3 beams
Total	5 beams	1 beam	8 beams	14 beams

[a] All beams were tested at $T \approx -60°C$ ($-7°F$) except one of the 50 mm, $a/W = 0.10$ beams, which was tested at $T \approx -35°C$ ($-30°F$). The nominal beam depth was 94 mm (3.7 in.).

($-46°F$). One test was run at RT_{NDT}. Table 1 gives a summary of the development phase test matrix, showing the number of tests performed at each condition. A total of 14 specimens have been tested in this phase.

Test Technique

Instrumentation is attached to the specimens to make possible J-integral and CTOD measurement of fracture toughness. The J-integral is determined from the load-line displacement (LLD) using the reference bar technique. CTOD is being determined from crack-mouth-opening displacement (CMOD) using clip gages mounted on the crack mouth of the specimen. Toughness data are primarily being expressed in terms of CTOD according to ASTM Test Method for Crack-Tip Opening Displacement (CTOD) Fracture Toughness Measurement (E 1290-89).

The plastic component of CTOD is determined experimentally from the plastic component of CMOD and the rotation factor. The plastic displacement of the crack flanks is assumed to vary linearly with distance from the plastic center of rotation. In this way, the plastic CMOD can be related to the plastic CTOD. The plastic center of rotation is located ahead of the crack tip a distance equal to the rotation factor (RF) multiplied by the remaining ligament (W-a) [*1*]. Numerous experimental and analytical techniques have been used to determine the RF [*1,2,15–19*], although no single technique seems to be universally accepted and the various experimental and analytical determinations sometimes appear contradictory [*4*], especially for shallow-crack specimens. The rotation factor in ASTM E 1290 is given as 0.4, but it is a function of specimen geometry and material.

In this study, two experimental methods were used to determine the RF. The first method was the use of dual clip gages located at different distances from the crack mouth. Clip gages were mounted directly on the mouth of crack and elevated 8.89 mm (0.35 in.) above the crack mouth. The second technique was to locate the neutral axis of the beam ahead of the crack tip using strain gages, assuming that the plastic center of rotation was located at the neutral axis of the beam. The RF relates the plastic component of CMOD to the plastic component of CTOD; therefore, only plastic strains were used to determine the RF. The dual clip gage technique produced values of the RF that varied significantly from 0.4 and were not constant as a function of load. However, the RFs determined the strain gage technique were close to 0.4 and were relatively insensitive to load once plastic strains became nontrivial. The RFs from strain gages were averaged for the deep and shallow-crack geometries and were used in the CTOD calculations. The average RF varied from 0.46 for the deep-crack specimens to 0.50 for the

TABLE 2—*Rotation factor data.*

HSST Beam Number[a]	a/W	Strain Gages	Dual Clip Gages
3	0.10	0.48	0.64
4	0.52	N/A	N/A
5	0.52	N/A	N/A
6	0.52	N/A	N/A
7	0.11	N/A	N/A
8	0.10	0.53	0.64
9	0.10	0.47	N/A
10	0.15	N/A	4.07
11	0.089	0.50	9.64
12	0.53	0.40	0.00
13	0.094	N/A	0.73
14	0.094	0.48	N/A
15	0.092	0.52	N/A
16	0.53	0.52	2.35
	Average deep	0.46	
	Average shallow	0.50	

[a] HSST = Heavy Section Steel Technology Program.

shallow-crack specimens. Individual values of the RF using both techniques are shown in Table 2.

Initial notches were inserted into the specimens using electron discharge machining (EDM). The notches were then fatigue precracked to produce sharpened initial flaws. Fatigue precracking was performed according to the guidelines detailed in ASTM Test Method for Plane-Strain Fracture Toughness of Metallic Materials (E 399-90). Crack growth was monitored by means of the change of crack mouth opening compliance, using the clip gage data and the equations for crack length in ASTM J_{Ic}, A Measure of Fracture Toughness (E 813-89). The equations in ASTM E 813 relating crack length to compliance are invalid for shallow-crack specimens. However, a change in compliance of 10 to 15% generally gave sufficient crack growth. In a few cases the fatigue growth did not exceed 1.3 mm (0.050 in.). Examination of the results from these cases revealed no noticeable variation in the toughness values. After fracture, fatigue crack growth was visually measured according to the nine-point method as outlined in ASTM E 813 or E 1290. The greatest difference between any two crack growth measurements for all the tests was less than 1.8 mm (0.070 in.). The average maximum difference in crack growth measurements was about 0.9 mm (0.035 in.). Crack growth met all remaining requirements in ASTM E 813 or E 1290 for crack profile and orientation.

Test Results

Load versus CMOD curves were generated and examined for each beam tested. In order to normalize the load between beams of different spans, thicknesses, and slightly different beam depths, the applied stress (rather than applied load) which would exist in an uncracked beam was plotted versus CMOD. The applied stresses for the test and analyses results were calculated from the applied loads and the beam geometries according to elastic strength of materials equations. The stress versus CMOD curves for the a/W = 0.50 and 0.10 tests are illustrated in Fig. 1 for beams tested at $T \approx -60°C$ ($-76°F$) and are compared with the analytical stress versus CMOD curve. The stress versus CMOD test data are consistent with each other and agree well with the analytical data providing additional confidence in the test data. The ana-

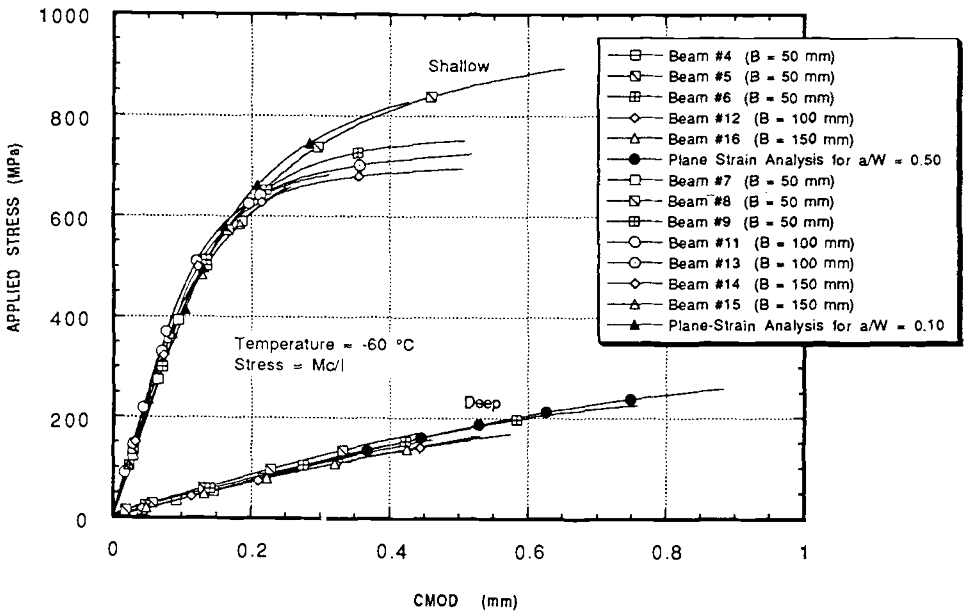

FIG. 1—*Applied stress versus CMOD for* a/W = *0.50 and* a/W = *0.10 beams.*

lytical stress versus CMOD curves were generated using a plane-strain elastic-plastic finite-element ADINA [*12*] model. The analytical results represent the behavior of a single specimen with idealized geometry and material properties. Small differences between test and analytical results in Fig. 1 are attributed to differences in geometry and material properties that inevitably occur. The test data represent beams of three different thicknesses. The consistency of the test data and the agreement with the plane-strain analytical data indicates little loss of out-of-plane constraint due to insufficient specimen thickness in the test data.

The toughness data expressed in terms of critical CTOD, δ_c, and temperature in Table 3 are shown in Fig. 2 along with the mean material characterization curve [*11*] determined in an earlier testing program. Data from three crack depths (a/W = 0.50, 0.15, and 0.10) and three thicknesses (B = 50, 100, 150 mm) are presented. The deep-crack toughness values are slightly higher than the material characterization curve and are consistent with previous compact-tension specimen data [*20*] from the same heat of material tested prior to this program. The trend of the results in Fig. 2 indicates a significant increase in the measured fracture toughness for shallow-crack specimens in the lower transition region. The a/W = 0.15 datum also appears to exhibit a shallow-crack toughness elevation. The ratio of the mean shallow-crack toughness to deep-crack toughness is 4.2 for the beams tested at −60°C (−76°F). The ratio of the shallow-to-deep lower-bound toughness is 2.9, which is consistent with the shallow-crack elevated toughness for A36 and A517 steel determined at the University of Kansas [*1,2*]. As indicated in Refs *1* and *2*, the shallow- and deep-crack toughness for A533 B is expected to converge on the lower shelf.

If it is assumed that the shallow-crack toughness curve has the same shape as the deep-crack toughness curve, the shallow-crack toughness increase can be expressed as a temperature shift. Previous A36 data supports this assumption [*1*]. The lower bound shallow-crack test results at T = −60°C (−76°F) and the single test results at T = −35°C (−30°F) are shifted 46 to 48°C (83 to 87°F) from the characterization curve, respectively. The lower bound deep-crack

TABLE 3—*HSST development beam data with CTOD toughness.*

HSST Beam No.	Temperature, °C	S, mm	B, mm	W, mm	a, mm	a/W	Measured Elastic Compliance, mm/kN	Failure Load, kN	Measured Failure CMOD, mm	Toughness CTOD, mm
3	−35.6	406	50.6	99.7	10.0	0.101	3.09×10^{-4}	600	0.808	0.59
4	−60.6	406	50.7	99.5	51.8	0.520	3.38×10^{-3}	128	0.461	0.048
5	−55.3	406	50.6	99.1	51.2	0.517	3.14×10^{-3}	140	0.442	0.049
6	−59.2	406	50.6	99.5	51.9	0.522	3.52×10^{-3}	185	0.758	0.12
7	−59.4	406	50.7	94.2	10.2	0.108	3.27×10^{-4}	483	0.250	0.14
8	−59.5	406	50.8	94.2	9.63	0.102	3.12×10^{-4}	657	0.652	0.48
9	−62.3	406	50.9	94.0	9.52	0.101	3.09×10^{-4}	552	0.508	0.35
10	−60.2	406	50.9	94.3	14.0	0.149	4.77×10^{-4}	489	0.434	0.24
11	−56.7	864	102	93.9	8.36	0.0890	3.08×10^{-4}	472	0.312	0.20
12	−56.7	864	102	94.7	49.8	0.526	4.44×10^{-3}	117	0.574	0.061
13	−59.6	864	102	94.0	8.81	0.0938	3.29×10^{-4}	502	0.514	0.36
14	−57.4	864	152	92.5	8.69	0.0939	2.25×10^{-4}	723	0.504	0.35
15	−58.5	864	153	94.5	8.66	0.0917	2.14×10^{-4}	684	0.257	0.15
16	−57.8	864	153	94.0	50.0	0.532	2.81×10^{-3}	170	0.530	0.060

Notes:
1. Rotation factors given in Table 2.
2. Yield Stress = 476 MPa at $T \approx -60$°C and 448 MPa at $T \approx -35$°C. The yield stress was estimated from room temperature values and adjusted for the lower temperatures.
3. E = 206 850 MPa, ν = 0.3.

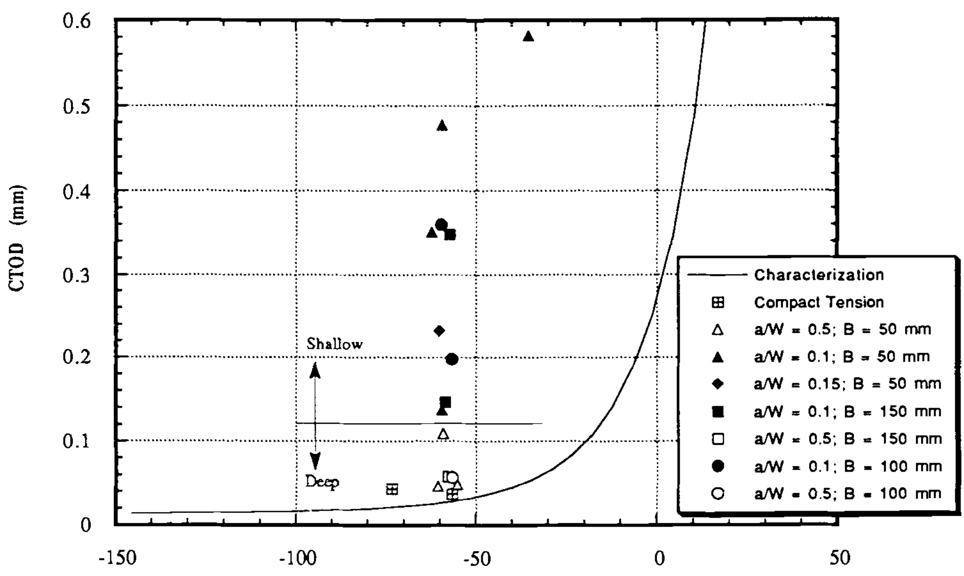

FIG. 2—*HSST test data with material characterization curve and previous compact tension data.*

datum is shifted about 16°C (28°F) from the characterization, which indicates a temperature shift for the shallow-crack specimens of 30°C (55°F).

Beams 50, 100, and 150-mm (2, 4, and 6-in.) thick were tested to investigate the influence of differing out-of-plane constraint levels on the toughness of shallow and deep-crack specimens. Toughness data are plotted as a function of beam thickness for all of the tests conducted at $T = -60°C$ ($-76°F$) in Fig. 3. As shown in Figs. 2 and 3, the toughness values for the shallow- and deep-crack specimens from the 100 and 150-mm (4 and 6-in.)-thick beams are generally consistent with the 50-mm (2-in.)-thick data. However, there appears to be slightly more data scatter associated with the 50-mm (2-in.)-thick beams than with the 100 and 150-mm (4 and 6-in.)-thick beams because more 50-mm (2-in.) specimens were tested. It is interesting to note that the lowest shallow and deep-crack toughness values were both from beams with the least thickness (B = 50 mm). Beams of three thicknesses were tested to select the appropriate beam size for the production phase testing. The testing temperature is expected to be greater for many of the beams tested in the production phase of the program. As the temperature increases, additional loss of out-of-plane constraint is anticipated. Therefore, even though the 50-mm beam thickness might be sufficient at lower temperatures, the 100-mm beam thickness was chosen for future testing because the greater thickness might be required at the higher temperatures.

Fracture toughness was determined for each beam in terms of the J-integral. Little or no crack growth took place in these tests, so ASTM E 813 is not strictly applicable. However, the critical J-integral toughness was determined according to Ref *4*

$$J_c = J_{el} + J_{pl} \tag{1}$$

where

$$J_{el} = K_c^2(1 - \nu^2)/E \tag{2}$$

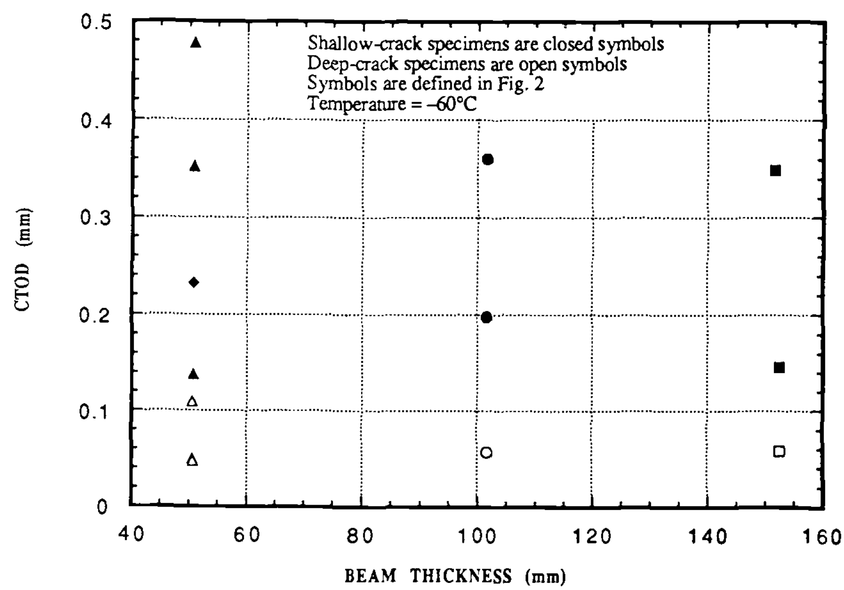

FIG. 3—*HSST test data at three thicknesses tested at −60°C.*

and

$$J_{pl} = \eta_{pl} U_{pl} / [B(W - a)] \tag{3}$$

Sumpter's formulation for η_{pl} was used [4]. J-integral toughness values are given in Table 4. Examination of the data in Table 4 shows that J_c toughness values are consistent with the δ_c calculations. The J_c ratio of the mean shallow-crack toughness to deep-crack toughness is 2.8 for the beams tested at −60°C (−76°F). The ratio of the shallow-to-deep lower-bound toughness is 2.0 which is consistent with the shallow-crack elevated toughness expressed in terms of CTOD.

Since J_c and δ_c are related according to $J_c = m \cdot \sigma_f \cdot \delta_c$ [21], comparison of J_c and δ_c allows m, the constraint parameter, to be determined as a function of crack depth. Plots of J versus CTOD show a linear relationship does exist between the two toughness expressions. The constraint parameter, m, for each test was determined using the critical toughness (J_c and δ_c) and the estimated flow stress, σ_f. Use of the critical toughness is in keeping with Sumpter's contention that η_{pl} is valid only for a perfectly plastic material after limit load [4]. Table 4 shows the constraint values calculated for each test. The average constraint parameter was 1.6 for deep-crack specimens and 1.1 for shallow-crack specimens.

Although the J-integral and CTOD toughness expressions are generally consistent with each other, the CTOD toughness was considered more reliable than the J-integral because the experimental load versus CMOD records were more consistent and repeatable than the load versus LLD records. For this reason, K_c was calculated from CTOD using the following relation [21]

$$K_c = \{m \cdot \sigma_f \cdot E' \cdot \delta_c\}^{1/2} \tag{4}$$

where

$m = 1.6$ and $E' = E/(1 - \nu^2)$ for deep crack specimens, and
$m = 1.1$ and $E' = E$ for shallow crack specimens.

TABLE 4—*J-Integral toughness and constant parameter,* m, *determination.*

HSST Beam Number[a]	Plastic Energy, kN-mm	η_{Pl}	J_c, MPa-mm	σ_f, MPa	m
3	752	1.13	260	525	0.87
4	4.6	2.00	42	558	1.6
5	4.1	2.00	48	550	1.8
6	26.5	2.00	100	556	1.6
7	114	1.16	92	556	1.2
8	673	1.14	280	556	1.1
9	372	1.13	170	561	0.89
10	187	1.34	140	557	1.1
11	376	1.07	100	552	0.97
12	16.9	2.00	50	552	1.5
13	1134	1.09	210	556	1.1
14	1876	1.09	230	552	1.2
15	400	1.08	85	552	1.1
16	10.7	2.00	46	556	1.4
				m (deep) =	1.6
				m (shallow) =	1.1

[a] HSST = Heavy Section Steel Technology Program.

TABLE 5—*Actual and "predicted" toughness values using modified Irwin β_c correction.*[a]

HSST Beam Number[b]	K_c Actual, MPa$\sqrt{m}$	K_{Ic}, MPa$\sqrt{m}$	K_c predicted, MPa$\sqrt{m}$
4	99	81	127
5	99	81	129
6	153	102	127
12	111	98	103
16	110	103	98
Average Deep-Flaw	114	93	117
7	131	74	235
8	244	93	246
9	211	88	245
10	172	91	181
11	156	75	282
13	212	86	265
14	208	85	271
15	135	103	271
Average Shallow-Flaw	184	87	250

[a] Average of deep-crack adjusted values was used to "predict" toughness for shallow-flaw specimens. Only tests conducted at $T \cong -60°C$ included.
[b] HSST = Heavy Section Steel Technology Program.

The plane-strain value of E' was used for the deep-crack specimens in spite of not meeting the validity requirements of ASTM E 399 because the experimental data in this program indicate little or no influence of beam thickness on the data. Table 5 gives the toughness of each beam in terms of K_c. The ratio of shallow-to-deep toughness in terms of K_c is equal to the square root of the ratio in terms of CTOD. The lower-bound shallow-crack toughness is ≈70% greater than the lower-bound deep-crack toughness at −60°C. The spread of the data is also reduced expressing the toughness in terms of K_c.

For comparison, K_c was calculated using the J-integral values in Table 4 and Eq 2 in addition to using CTOD and Eq 4. The two methods of determining K_c were very consistent. The maximum difference between K_c using the two techniques was 12%, the average difference was <5%.

Modified Irwin Correction

The goal of the shallow-crack program is to investigate toughness as a function of crack depth and apply the results to a reactor pressure vessel, which is a highly constrained application. The deep crack test results therefore should maintain plane-strain constraint or be adjusted to estimate the plane-strain toughness. Because specimens required to maintain plane-strain constraint are prohibitively large, the data taken from the deep-crack specimens have been adjusted for loss of out-of-plane constraint via Irwin's β_c correction [*22*]. The Irwin β_c correction is first applied by calculating β_c from the experimental data and then solving the following equation for β_{Ic}

$$1.4\beta_{Ic}^3 + \beta_{Ic} = \beta_c \tag{5a}$$

where

$$\beta_c = (K_c/\sigma_y)^2/B \tag{5b}$$

and

$$\beta_{Ic} = (K_{Ic}/\sigma_y)^2/P \tag{5c}$$

The adjusted, plane-strain toughness is then calculated according to

$$K_{Ic} = K_c\sqrt{(\beta_{Ic}/\beta_c)} \tag{6}$$

Application of the Irwin β_c correction reduces the average deep-crack critical toughness from 114 MPa$\sqrt{m}$ (104 ksi$\sqrt{in.}$) to a corrected plane-strain value of 93 MPa$\sqrt{m}$ (85 ksi$\sqrt{in.}$) as shown in Table 5. The magnitude of the reduction is relatively minor [22]. The small magnitude of the correction and the consistency between the data of different thicknesses indicate that little loss of out-of-plane constraint is present in the deep-crack data in spite of the fact that the ASTM E 399 validity requirements have not been met.

Relaxation of crack-tip constraint in either direction (in-plane or out-of-plane) has the effect of elevating the critical toughness. The Irwin β_c correction successfully accounts for loss of out-of-plane constraint, and therefore a modification (of the β_c correction) proposed by Merkle [23] to account for the loss of in-plane constraint associated with shallow flaws was applied. This modification is based on the assumption that the critical dimension in the constraint of a beam is the distance from the point of greatest constraint to the nearest free surface, not including the crack surface. In deep-crack beams, this distance is half the beam thickness; in shallow-crack specimens, the critical dimension is the crack depth. By using the appropriate critical dimension, the Irwin β_c correction can be modified to account for both loss of out-of-plane constraint (insufficient thickness) or loss of in-plane constraint (shallow-crack effect) [23]. As shown in Table 5 and Fig. 4, the modified Irwin correction applied to the HSST data adjusts both deep and shallow-crack toughness data to approximately the same value.

Since the shallow and deep-crack toughness data can be adjusted to the same value, the

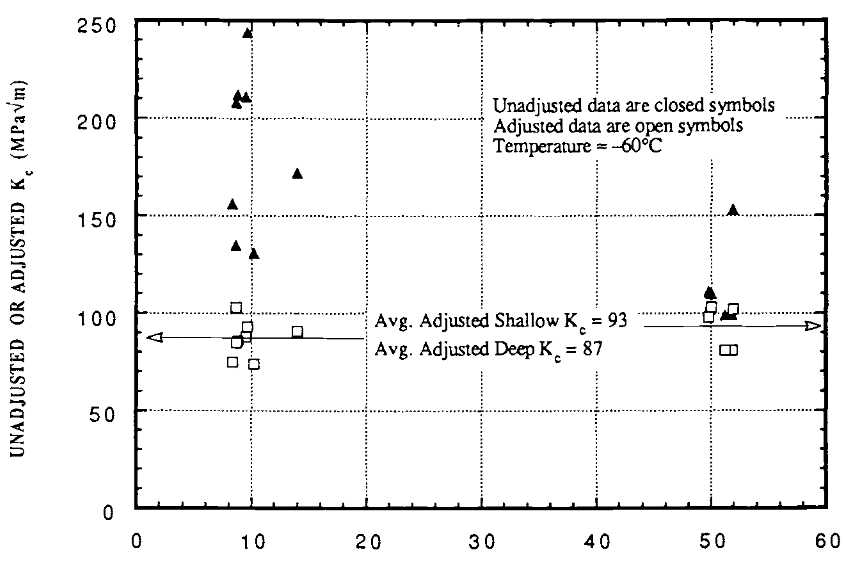

FIG. 4—*Application to modified Irwin β_c correction to deep and shallow-crack toughness data.*

modified correction could potentially be used to "predict" the shallow-crack fracture-toughness from deep-crack toughness data. Although the shallow-crack toughness data were available, the modified Irwin correction was applied to the data to see if "predictions" could be made of the shallow-crack toughness using only deep-crack data. The "predicted" shallow-crack toughness was determined using only the adjusted plane-strain, deep-crack toughness according to Ref *23*

$$K_c = K_{Ic} \cdot [1 + 1.4\beta_{Ic}^2]^{1/2} \tag{7}$$

$$\beta_{Ic} = (K_{Ic}/\sigma_y)^2/2a \tag{8}$$

where

$$K_{Ic} = 93 \text{ MPa}\sqrt{\text{m}} \ (85 \text{ ksi}\sqrt{\text{in.}})$$

The agreement between the "predicted" shallow-crack toughness estimated using the modified Irwin correction and the actual toughness from the shallow-crack specimens is reasonably good. The average "predicted" shallow-crack toughness using the deep-crack data with the modified Irwin β_c correction is 250 MPa$\sqrt{\text{m}}$ (228 ksi$\sqrt{\text{in.}}$); the average actual shallow-crack toughness is 184 MPa$\sqrt{\text{m}}$ (167 ksi$\sqrt{\text{in.}}$). A plot of the actual versus "predicted" toughness for each shallow-crack test (Fig. 5) shows reasonable agreement between the individual "predicted" and actual shallow-crack toughness values. The modified Irwin β_c correction tends to overestimate the actual shallow crack toughness. It should be noted that the modified Irwin

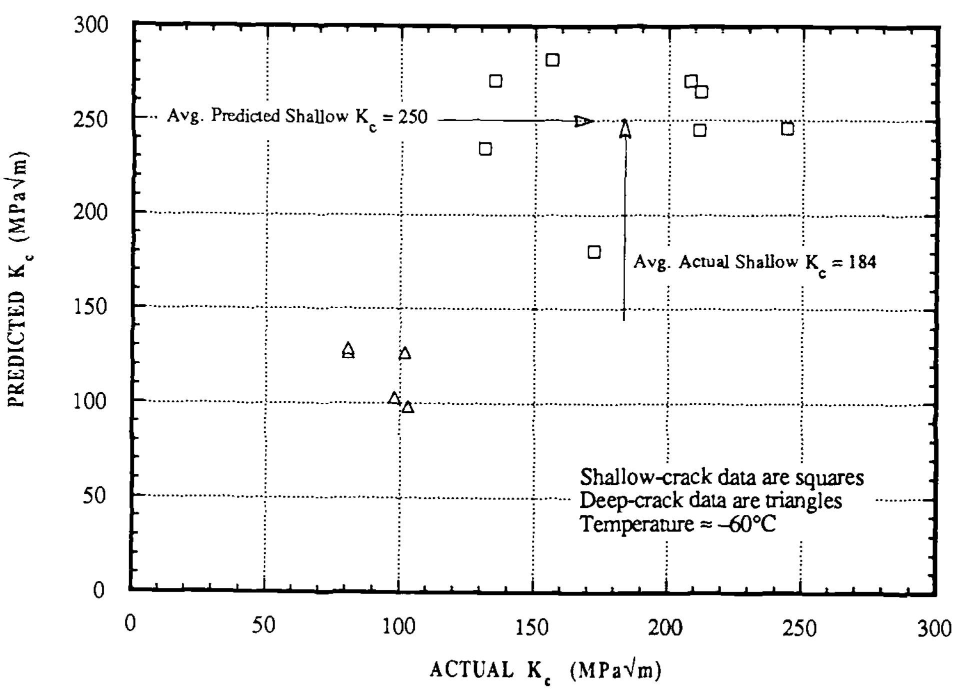

FIG. 5—*Agreement between actual and "predicted" toughness using modified Irwin β_c correction for shallow-crack specimens.*

correction "predicted" the shallow-crack toughness for crack depths ranging between a = 8.36 to 14.0 mm (0.329 to 0.553 in.). The "predicted shallow-crack toughness shows little scatter since the individual values only vary with the crack depth. The ability of the modified Irwin β_c correction to predict the elevated shallow-crack toughness from deep-crack data depends on similar out-of-plane constraint being present in the data of different thicknesses.

Future Work

The application of the shallow-crack fracture toughness data to reactor vessel analyses remains the final goal of the program. To reach that goal, more specimens should be tested with multiple crack depths and at several temperatures within the transition region. The results generated to date are encouraging but not conclusive as to how to apply the data to an RPV. Prior experimental work within the HSST program has included tests on thick-walled vessels which have contained relatively shallow flaws [*24*]. These tests offer a means to validate the technology of applying shallow-flaw toughness data to an RPV.

In addition, numerical analyses of the test specimen and the application (that is, an axially-oriented flaw in an RPV) need to be performed and interpreted. These analyses will provide a means for checking transferability of the test results to an RPV. The modified Irwin correction is being further evaluated and refined and is being considered as a relationship to account for flaw-depth in the fracture-toughness of reactor pressure vessel steels. The conditions under which the modified Irwin correction can be used in reactor vessel analyses need to be established.

Conclusions

Although the test results presented in this paper are preliminary, the data are encouraging and the following interim conclusions can be drawn.

1. Specimens tested with a shallow crack depth ($a \approx 9$ mm, in this case) exhibit a toughness that is significantly higher than the deep-notch toughness at temperatures in the lower transition region. The shallow-crack fracture toughness data determined for A533 B are consistent with the toughness elevation observed by others for shallow cracks in A36 and A517 steels.
2. The single specimen tested with a crack depth of 14 mm (0.6 in.) also appears to show a toughness elevation.
3. The shallow-crack toughness elevation from the 100 and 150-mm (4 and 6-in.)-thick beams is generally consistent with the 50-mm (2-in.)-thick data. The influence of out-of-plane constraint appears minimal in the test results.
4. The Irwin β_c correction, modified to account for loss of in-plane constraint, has been used to estimate the elevated shallow-crack fracture toughness from the deep-crack toughness data. The agreement between the estimated shallow-crack toughness estimated using the modified Irwin correction and the actual toughness from the shallow-crack specimens is reasonably good.

Acknowledgments

This work is sponsored through the Office of Nuclear Regulatory Research, U.S. Nuclear Regulatory Commission, and M. E. Mayfield is the technical monitor. The technical assistance of the HSST staff and subcontractors is gratefully acknowledged.

References

[1] Sorem, W. A., Dodds, R. H., Jr., and Rolfe, S. T., "An Analytical Comparison of Short Crack and Deep Crack CTOD Fracture Specimens of an A36 Steel," *WRC Bulletin 351*, Welding Research Council, New York, NY, February 1990.

[2] Smith, J. A. and Rolfe, S. T., "The Effect of Crack Depth to Width Ratio on the Elastic-Plastic Fracture Toughness of a High-Strength Low-Strain Hardening Steel," *WRC Bulletin 358*, Welding Research Council, New York, NY, November 1990.

[3] Kirk, M. T. and Dodds, R. H., Jr., "An Analytical and Experimental Comparison of J_i Values for Shallow Through and Part Through Surface Cracks," Report DTRC-SME-90/50, David Taylor Research Center, U.S. Navy, Annapolis, MD, June 1990.

[4] Sumpter, J. D. G., "J_c Determination for Shallow Notch Welded Bend Specimens," *Fatigue and Fracture in Engineering Materials and Structures*, Vol. 10, No. 6, 1987, pp. 479–493.

[5] Theiss, T. J., "Recommendations for the Shallow-Crack Fracture Toughness Testing Task Within the HSST Program," USNRC Report NUREG/CR-5554 (ORNL/TM-11509), U.S. Nuclear Regulatory Commission, Washington, DC, August 1990.

[6] Cheverton, R. D. and Ball, D. G., "Pressurized-Thermal-Shock Evaluation of the H. B. Robinson Nuclear Power Plant," USNRC Report NUREG/CR-4183 (ORNL/TM-9567/V1), U.S. Nuclear Regulatory Commission, Washington, DC, Sept. 1985, pp. 263–306.

[7] Cheverton, R. D. and Ball, D. G., "Pressurized-Thermal-Shock Evaluation of the Calvert Cliffs Nuclear Power Plant," USNRC Report NUREG/CR-4022 (ORNL/TM-9408), U.S. Nuclear Regulatory Commission, Washington, DC, Sept. 1985, pp. 201–44.

[8] Cheverton, R. D. and Ball, D. G., "Preliminary Development of an Integrated Approach to the Evaluation of Pressurized Thermal Shock as Applied to the Oconee 1 Nuclear Power Plant," USNRC Report NUREG/CR-3770 (ORNL/TM-9176), U.S. Nuclear Regulatory Commission, Washington, DC, May 1986, pp. 5.1–5.51.

[9] Dickson, T. L. and Theiss, T. J., "Potential Impact of Enhanced Fracture-Toughness Data on Pressurized-Thermal-Analysis," *Proceedings of the U.S. Nuclear Regulatory Commission, Eighteenth Water Reactor Safety Information Meeting*, Rockville, MD, 22–24 Oct., 1990, USNRC Report NUREG/CP-0014, U.S. Nuclear Regulatory Commission, Washington, DC, Vol. 3, April 1991, pp. 35–53.

[10] Theiss, T. J., Robinson, G. C., and Rolfe, S. T., "Preliminary Test Results from the Heavy-Section Steel Technology Shallow-Crack Toughness Program," *Proceedings of the ASME Pressure Vessel and Piping Conference*, PVP Vol. 213/MPC-Vol. 32, *Pressure Vessel Integrity*, American Society of Mechanical Engineers, New York, 1991, pp. 125–129.

[11] Naus, D. J., "SEN Wide-Plate Crack-Arrest Tests Using A 533 Grade B Class 1 Material: WP-CE Series," USNRC Report NUREG/CR-5408 (ORNL/TM-11269), U.S. Nuclear Regulatory Commission, Washington, DC, November 1989.

[12] Bathé, K. J., "ADINA-87, A Finite Element Program for Automatic Dynamic Incremental Nonlinear Analysis," MIT Report 82448-1, Massachusetts Institute of Technology, Cambridge, MA, 1975.

[13] Theiss, T. J., "Heavy-Section Steel Technology Program Semiannual Progress Report, April to Sept. 1990," USNRC Report NUREG/CR-4219, Vol. 7, No. 2 (ORNL/TM-9593/V7 and N2), U.S. Nuclear Regulatory Commission, Washington, DC, October 1991.

[14] Pennell, W. E., "Heavy-Section Steel Technology Program Overview," *Proceedings of the U.S. Nuclear Regulatory Commission Eighteenth Water Reactor Information Safety Meeting*, Rockville, Md., 22–24 Oct. 1990, USNRC Report NUREG/CP-0114, U.S. Nuclear Regulatory Commission, Washington, DC, April 1991, pp. 1–33.

[15] Cottrell, B., Li, Q.-F., Zhang, D.-Z., and Mai, Y.-W., "On the Effect of Plastic Constraint on the Ductile Tearing in a Structural Steel," *Engineering Fracture Mechanics*, Vol. 21, No. 2, 1985, pp. 239–244.

[16] Li, Q.-F., "A Study About J_i and δ_i in Three-Point Bend Specimens with Deep and Shallow Notches," *Engineering Fracture Mechanics*, Vol. 22, No. 1, 1985, pp. 9–15.

[17] Zhang, D.-Z. and Wang, H., "On the Effect of the Ratio a/W on the Value of δ_i and J_i in a Structural Steel," *Engineering Fracture Mechanics*, Vol. 26, No. 2, 1987, pp. 247–250.

[18] Matsoukas, G., Cottrell, B. and Mai, Y.-W., "On the Plastic Rotation Constant Used in Standard COD Tests," *International Journal of Fracture*, Vol. 26, No. 2, 1984, pp. R49–R53.

[19] Anderson, T. L., McHenry, H. I., and Dawes, M. G., "Elastic-Plastic Fracture Toughness Tests with Single-Edge Notched Bend Specimens," *Elastic-Plastic Fracture Test Methods: The User's Experience, ASTM STP 856*, E. T. Wessel and F. J. Loss, Eds., American Society for Testing and Materials, Philadelphia, 1985, pp. 210–229.

[20] Ayres, D. J., et al., "Material Characterization," Appendix G, *Tests and Analyses of Crack Arrest in Reactor Vessel Materials,* EPRI NP-5121SP, Electric Power Research Institute, Palo Alto, CA, April 1987.

[21] Barsom, J. M. and Rolfe, S. T., *Fracture and Fatigue Control in Structures,* Prentice-Hall, Englewood Cliffs, NJ, 1987.

[22] Merkle, J. G., "An Examination of the Size Effects and Data Scatter Observed in Small-Specimen Cleavage Fracture Toughness Testing," USNRC Report NUREG/CR-3672 (ORNL/TM-9088), U.S. Nuclear Regulatory Commission, Washington, DC, April 1984.

[23] Merkle, J. G., "An Approximate Method of Elastic-Plastic Fracture Analysis for Nozzle Corner Cracks," *Elastic-Plastic Fracture, ASTM 668,* J. D. Landes, J. A. Begley, and G. A. Clarke, Eds., American Society for Testing and Materials, Philadelphia, 1979, pp. 674–702.

[24] Cheverton, R. D., Iskander, S. K., and Ball, D. G., "Review of Pressurized-Water-Reactor-Related Thermal Shock Studies," *Fracture Mechanics: Nineteenth Symposium, ASTM STP 969,* T. A. Cruse, Ed., American Society for Testing and Materials, Philadelphia, 1988, pp. 752–766.

Yong-Yi Wang[1]

On the Two-Parameter Characterization of Elastic-Plastic Crack-Front Fields in Surface-Cracked Plates

REFERENCE: Wang, Y.-Y., "**On the Two-Parameter Characterization of Elastic-Plastic Crack-Front Fields in Surface-Cracked Plates,**" *Constraint Effects in Fracture, ASTM STP 1171,* E. M. Hackett, K.-H. Schwalbe, and R. H. Dodds, Eds., American Society for Testing and Materials, 1993, pp. 120–138.

ABSTRACT: Plane-strain elastic-plastic crack-tip fields at a constant J and various elastic T-stress levels were obtained in a modified boundary layer (MBL) formulation similar to that of Betegón and Hancock but with a slightly different power law hardening stress-strain law. The analyses were based upon small geometry change formulation and deformation theory plasticity. To verify the two-parameter characterization of elastic-plastic crack-tip fields, three-dimensional (3-D) elastic-plastic finite element (FE) analyses were performed on plates with deep ($a/t = 0.60$) and shallow ($a/t = 0.15$) semielliptical surface cracks under both remote tension and bending. Here t is the plate thickness and a is the maximum penetration of the crack through the plate thickness. In topological planes perpendicular to the semielliptical crack fronts, the crack-opening stress fields, normalized by the local J, were compared with the plane-strain MBL predictions based upon the local J and T. In all four cases studied, better than 94% agreement between the 3-D FE solutions and the plane-strain solutions was obtained for loads up to general yielding. This remarkable agreement held throughout all crack-front locations where the stress fields could be resolved accurately. Given the vastly different distributions of J, T, and crack-opening stress profiles along the collective set of respective crack fronts, the elastic T-stress appears to be a tractable, predictive parameter in quantifying elastic-plastic crack-front stress constraint.

KEY WORDS: crack-tip constraint, T-stress, two-parameter characterization, J-dominance, surface-cracked plates, three-dimensional finite element analysis

K_I-based linear elastic fracture mechanics (LEFM) assumes that the near crack-tip stress and deformation fields of an elastic-plastic material are characterized by the stress intensity factor, K_I, provided that certain conditions are satisifed [e.g., the ASTM Test Method for Plane-Strain Fracture Toughness of Metallic Materials (E 399-90)]. It is understood that if the crack-tip plastic zone is *much* smaller than any relevant specimen dimension, the stress state outside the plastic zone, but well away from the specimen boundary, can be characterized by the first singular term of the Williams [*1*] eigen-expansion

$$\sigma_{ij} = \frac{K_I}{\sqrt{2\pi r}} f_{ij}(\theta) \tag{1}$$

where r and θ are polar coordinates centered at the crack tip, and the functions f_{ij} describe the angular variations of the respective stress components. The plane-strain elastic-plastic finite element (FE) analysis of Larsson and Carlsson [*2*] revealed that the plastic zone sizes of some

[1] Senior research engineer, Edison Welding Institute, Columbus, OH 43212.

actual two-dimensional (2-D) specimens were substantially different from that of the boundary layer (BL) solution at the same K_I even within the ASTM limit. The BL solution was obtained by applying the traction boundary conditions corresponding to Eq 1 at large r (where r was much larger than the plastic zone size). In an attempt to resolve the difference, the traction boundary conditions corresponding to the stress fields of the first two terms in the Williams [1] eigen-expansion of near-tip elastic field

$$\begin{bmatrix} \sigma_{xx} & \sigma_{xy} \\ \sigma_{yx} & \sigma_{yy} \end{bmatrix} = \frac{K_I}{\sqrt{2\pi r}} \begin{bmatrix} f_{xx}(\theta) & f_{xy}(\theta) \\ f_{yx}(\theta) & f_{yy}(\theta) \end{bmatrix} + \begin{bmatrix} T & 0 \\ 0 & 0 \end{bmatrix} \tag{2}$$

were applied in a modified boundary layer (MBL) formulation. In Eq 2, the elastic T-stress is a tensile/compressive stress acting parallel to the cracked plane. Like K_I, the T-stress is a function of geometry and loading conditions, proportional to load amplitude. The crack-tip plastic zones of the MBL solutions with appropriate T were much closer to those of the corresponding actual specimens. Bilby et al. [3] also showed that the two-parameter (K_I and T) remote loading approach (Eq 2) characterizes the very near-tip elastic-plastic fields of a nonhardening blunted crack better than does K_I alone. More recently, Betegón and Hancock [4] applied the remote displacements dictated by K_I and T on the outer boundary of a semicircular domain simulating a crack-tip region. The ratios of K_I and T were chosen to match the biaxiality parameter B of certain 2-D specimens that were analyzed in full-field plane-strain FE solutions. The biaxiality parameter B is a dimensionless constant representing the ratio of T to K_I, nondimensionalized by an appropriate geometric parameter, e.g., the crack depth a. Since K_I and T are functions of geometry and loading conditions, so is B. The dependence of the crack-opening stress at a suitable normalized distance on the T-stress of the actual specimens closely matched that of the MBL prediction.

The dominance of J-based [5] HRR singularity fields [6,7] in a near crack-tip zone depends upon specimen geometry and loading conditions (e.g., Refs 8–11). The varied ability of attaining HRR dominance at crack tips of different specimens is attributed to the difference in crack-tip "constraint." One of the most widely used constraint parameter is the stress triaxiality, which is defined by the ratio of hydrostatic stress, $\sigma_m \equiv \frac{1}{3}\sigma_{kk}$, to the Mises equivalent tensile stress, σ_e [12,13]. High constraint is associated with high values of σ_m/σ_e. High crack-tip constraint is often found in specimens with sufficiently deep cracks under predominantly bending load and contained yielding. Low constraint is often associated with specimens of relatively shallow cracks under predominantly tensile loading. Low constraint generally manifests itself in high crack-tip ductility and high macroscopic toughness. Du and Hancock [14] found that positive T-stress causes the crack-tip region in a nonhardening material to exhibit the Prandtl stress field, which is the limiting case of the HRR stress field for nonhardening material. Negative T-stress reduces the hydrostatic stress, which in turn results in lower crack opening stress. Al-Ani and Hancock [15] analyzed plane-strain crack opening stress in edge-cracked specimens of various crack depths. Remote tension or bending loads, ranging from small-scale yielding (SSY) to large-scale yielding, were applied to simulate different levels of crack-tip constraint. The crack-opening stresses were in excellent agreement with the MBL prediction using the calculated elastic-plastic J of the specimen and elastically scaled T-stress. Similar agreement has been obtained by a number of other researchers [4] in a variety of plane-strain specimens. This indicates that the elastic T-stress can not only parameterize crack-tip constraint, but can also *quantitatively* predict the deviation of crack-tip fields from small-scale yielding solution.

We have built upon the above observations and extended them to more complicated 3-D crack geometries. First, elastic-plastic crack-tip fields in plane strain were analyzed using a slightly different material model from that of Ref 4. Three-dimensional elastic-plastic FE analyses were then carried out on plates having a variety of crack geometries and remote loading conditions using the same material model. These different crack geometries and loadings result in a wide range of continuously varying J and T distributions along the crack fronts of the surfaced-cracked plates (SCP). The local crack-front stress fields were then compared with the plane-strain MBL predictions using the calculated local J and elastically scaled T.

The T-Stress Effect, Plane-Strain Solutions

Formulation

Based upon a Ramberg-Osgood power law hardening material model and flow theory of plasticity, Betegón and Hancock [*4*] studied the T-stress effect using plane-strain MBL formulation by applying displacement boundary conditions dictated by K_I and T on a semicircular domain similar to that shown in Fig. 1. The crack-tip J was calculated by the domain integral method [*16,17*], which is an extension of the virtual crack extension method [*18*]. The calculated J was found to differ from the remote J^{far}, where $J^{far} = (1 - \nu^2)K_I^2/E$ (E is the Young's modulus, ν is the Poisson's ratio), even when the plastic zone was much smaller than the simulated domain. Our independent calculation based upon the same material hardening law and deformation theory plasticity revealed that the calculated J was significantly different from the applied J^{far} when $|\tau|$ (where $\tau \equiv T/\sigma_0$) was greater than 0.6, even though the calculated J was essentially path-independent (varying within 0.5%) in the entire domain.

Parks [*19*] suggested that the discrepancy between the calculated J and J^{far} at large $|\tau|$ is likely due to the nonlinear stress-strain relation in the Ramberg-Osgood material model when deformation theory plasticity is used. We use the same stress-strain relation as that of Ref *7* which, in one dimension (1-D), exhibits following relations

$$\frac{\epsilon}{\epsilon_0} = \begin{cases} \dfrac{\sigma}{\sigma_0} & \text{for } \sigma \leq \sigma_0 \\ \left(\dfrac{\sigma}{\sigma_0}\right)^n & \text{for } \sigma > \sigma_0 \end{cases} \tag{3}$$

Here σ_0 is the tensile yield stress, $\epsilon_0 = \sigma_0/E$, and $n (n > 1)$ is a material constant. The power law stress-strain relation of Eq 3 ($\sigma > \sigma_0$) can be tensorially generalized using J_2 deformation

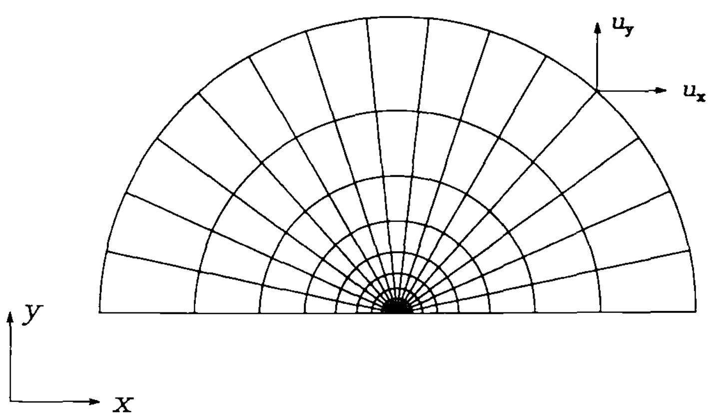

FIG. 1—*Schematic of the generalized plane mesh. Note that the actual number of fans in the circumferential direction is twice the number shown here.*

theory plasticity. Together with the tensorially generalized elastic stress-strain relation, Eq 3 can be expressed in a tensorial form as

$$E\epsilon_{ij} = \begin{cases} (1+\nu)s_{ij} + \dfrac{1-2\nu}{3}\sigma_{kk}\,\delta_{ij} & \text{for } \sigma_e \leq \sigma_0 \\ \dfrac{3}{2}\left[\left(\dfrac{\sigma_e}{\sigma_0}\right)^{n-1} - 1\right] s_{ij} + (1+\nu)s_{ij} + \dfrac{(1-2\nu)}{3}\sigma_{kk}\delta_{ij} & \text{for } \sigma_e > \sigma_0 \end{cases} \tag{4}$$

where ϵ_{ij} is the total strain (elastic plus plastic), s_{ij} is the stress deviator, $\sigma_e = \sqrt{3s_{ij}s_{ij}/2}$ is the Mises equivalent tensile stress, and δ_{ij} is the Kronecker delta. Equation 4 was incorporated into the ABAQUS [*20*] FE program through a user-defined material subroutine (UMAT). The discontinuous tangent modulus at ϵ_0 posed a problem in convergence. This was overcome by an introduction of a small circular arc near the transitional point, $\epsilon = \epsilon_0$, which tangentially intercepted the linear and power law part of the stress-strain curve. The two intercepting points were set at: $\sigma_{\text{linear}} = \beta \cdot \sigma_0$ and $\sigma_{\text{power}} = [1 + (1 - \beta)/n] \cdot \sigma_0$, where σ_{linear} was the intercepting point on the linear part of the curve, σ_{power} was on the power law part of the curve, and β was a parameter close to 1 that could be set in the UMAT (β was set to 0.95 for the present analysis). The strain energy density, which was used in calculating the J-integral, was reformulated accordingly. Using this material model, the calculated J was fully path-independent and consistent with the remote applied J up to the highest values of $|\tau|$ calculated ($|\tau|_{\max} = 0.9$). A set of material constants representing a low strain hardening material was chosen, namely, $\sigma_0 = 1$, $\epsilon_0 = 0.0025$, $n = 10$, and $\nu = 0.3$.

Mesh and Boundary Conditions

The crack tip was modelled by a semicircular domain shown in Fig. 1 with symmetry boundary condition imposed on the plane $y = 0$. There were 30 fans of elements circumferentially and 40 rings radially. The ratio of the outer boundary to the radius of the first ring elements was on the order of 10^7. Generalized plane strain, ten-node, reduced integration elements (ABAQUS element type GPE10R) were used. The two nodes added to the generalized plane strain elements with respect to conventional plane strain elements introduced three more degrees of freedom. Those degrees of freedom allowed the bounding planes of an element in the thickness direction to translate and rotate with respect to each other. The reason for using the generalized plane-strain elements will become clear later. For the moment, the elements can be considered as conventional plane-strain elements since the bounding planes were restricted from both translation and rotation for the present analysis.

In-plane displacement boundary conditions

$$u_i = \frac{K_{\text{I}}}{E}\sqrt{\frac{r}{2\pi}}f_i(\theta,\nu) + \frac{T}{E}rg_i(\theta,\nu) \tag{5}$$

were applied on the outer boundary of the domain shown in Fig. 1. Here $f_i(\theta,\nu)$ are the angular variations of the Cartesian displacement components of the elastic singular field, and $g_i(\theta,\nu)$ are the angular variations of the displacements due to the (plane-strain) T-term. Insofar as the two-parameter characterization is valid, the crack-tip fields of the MBL solution far from the outer boundary and outside the crack-tip blunting zone should represent those of any crack with the same values of K_{I} and T. Elastic-plastic crack-tip fields were obtained by systematically varying τ while keeping K_{I} constant. The maximum radius of plastic zone from the crack tip (at $\tau = -0.9$) was about $0.028R$, where R is the radius of the outer boundary. This ensured that the elastic-plastic crack-tip fields were surrounded by a large elastic domain.

Results

Figure 2 shows the variation of normalized crack-opening stress σ_{yy} ($\theta = 0$) versus normalized distance at various values of τ. Note that J/σ_0 can be taken as the only relevant length scale on the order of the crack-tip opening displacement (CTOD). The thick solid line at $\tau = 0$ is the stress profile at SSY. The stresses marked by the big circles are the HRR singularity fields with the same material constants. At any point outside the crack-tip blunting zone ($r > \sim J/\sigma_0$), the stress variations in terms of τ at any fixed normalized distance are essentially the same, which is consistent with the observation of Ref *4*. Substantial stress reduction is seen at negative τ. Moderate stress elevation is observed at positive τ, while the stresses seem to approach an asymptote at high positive τ. Similar stress profiles with r normalized by the remote applied $J^{\text{far}} = (1 - \nu^2)K_I^2/E$, using the Ramberg-Osgood material model and deformation theory plasticity, would show a greater τ-effect at both negative and positive τ.

Based upon the observation of Ref *4*, the plane-strain stress variation with respect to τ as shown in Fig. 2, at any normalized distance in the range $\sim 1 < r/(J/\sigma_0) < \sim 6$, was fitted in the following three-parameter form

$$\frac{\sigma_{yy}^{\text{MBI}}(r/(J/\sigma_0);\tau)}{\sigma_0} = \frac{\sigma_{yy}^{\text{SSY}}(r/(J/\sigma_0))}{\sigma_0} + A_n\tau + B_n\tau^2 + C_n\tau^3 \tag{6}$$

where A_n, B_n, and C_n are constants dependent upon the strain-hardening exponent n. The original two-parameter form of Eq 6 [*4*] fitted the low to middle range $\tau(|\tau| < 0.6)$ well. However, it was found that it could not match the asymptotic trend at high positive τ. Since this expression is purely a curve fit, the addition of one more parameter did not seem to be disadvantageous. The choice of normalized distance had little effect on the fitted constants as long as it was in the range $\sim 1 < r/(J/\sigma_0) < \sim 6$ [*4*]. However, since we subsequently intended to compare the stress at $r/(J/\sigma_0) = 2$, the stresses at this distance were chosen. The resulting fitted parameters were $A_n = 0.6168$, $B_n = -0.5646$, and $C_n = 0.1231$ for $n = 10$.

Figure 3 is the normalized equivalent plastic strain (ϵ^p) at $r = 1.22J/\sigma_0$. The thick solid line is the SSY solution ($\tau = 0$). Negative τ is associated with a large increase of peak ϵ^p and a shift of the peak to the forward section ($\theta < 90°$). A slight decrease of peak ϵ^p is observed at low

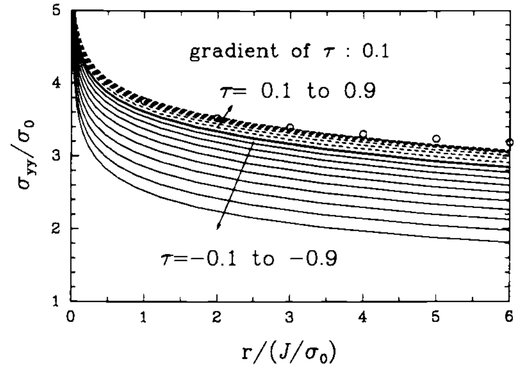

FIG. 2—*Normalized crack-opening stress distribution in plane strain at various values of $\tau \equiv T/\sigma_0$. The stresses marked with big circles are HRR singularity fields with same material constants.*

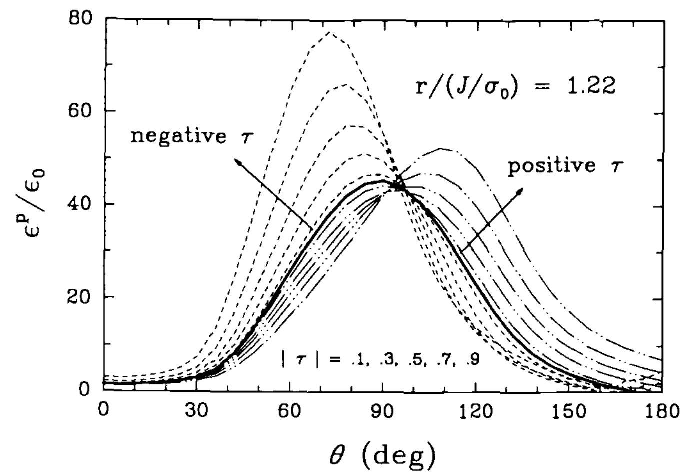

FIG. 3—*Circumferential normalized equivalent plastic strain distributions at* r = *1.22J/σ_0 in plane strain for various values of* τ.

values of positive τ, and a moderate increase of peak ϵ^p is seen at higher values of positive τ. The strain distribution is consistent with Shih and German's observation [*9*] that the equivalent plastic strain peak shifted to the forward sector ($\theta < 90°$) in the center-cracked panel (CCP), which has a negative T-stress under tensile loading (for example, Refs *2,3*). The change of the equivalent plastic strain distribution at various values of τ could have significant effects on ductile fracture process. However, we will focus on the τ effect on stress fields in the following sections.

Crack-Front Fields in Surface-Cracked Plates

Geometries and Meshes

Figure 4 is a schematic view of a plate with a part-through crack (only one quarter of the plate is shown because of the symmetry). The plate has a total length of $2h$, total width of $2b$, and a thickness of t. The semielliptical crack in the center of the plate has a surface length of $2c$ and maximum penetration of a. Note that two coordinate systems, the *global coordinate system* ($X - Y - Z$), and the *local coordinate system* ($x - y - z$) are used to locate a point in the plate. In the local coordinate system, the plane ($x - y$) is perpendicular to the crack front, and the z-axis is tangent to the crack front. The local polar coordinates ($r - \theta$) are in the plane of ($x - y$), and $\theta = 0$ when $y = 0$ and $x > 0$. The parametric angle ϕ, with $\phi = \cos^{-1}(Z/a)$ and $\phi = 0$ at $X = 0$, is used to locate position along the semielliptical crack-front locus $(X/c)^2 + (Z/a)^2 = 1$. The overall plate geometry was set to $h/t = 16$ and $b/t = 8$. Two crack geometries were analyzed, namely, $(a/c,a/t) = (0.24,0.60)$ and $(0.24,0.15)$.

Since an extremely fine mesh is required to resolve the detailed stress fields in the crack tip, the 3-D elastic-plastic FE analyses were performed through a two-stage, two-mesh analysis. The *global mesh,* with a moderately fine mesh along the crack front, modeled the entire one quarter of the plate. The solution from the *global mesh* was used to drive the *fine mesh,* which consists of the "tubular" region surrounding the crack front. The details of the meshes are explained below.

The global meshes were generated with an automatic FE mesh generator [*21*]. Reduced inte-

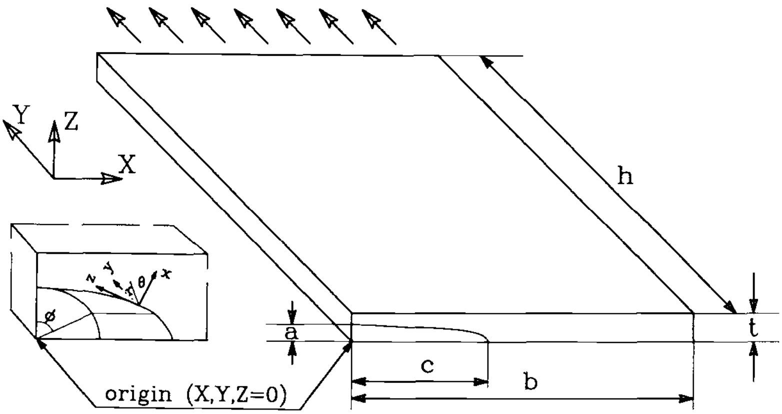

FIG. 4—*Schematic of one fourth of a surface-cracked plate. The inset at left shows the local Cartesian coordinate system (x-y-z system) with respect to global coordinate system (X-Y-Z system) and description of crack-front location parameter ϕ. Note that the drawing is not to scale.*

gration ($2 \times 2 \times 2$ Gaussian) 20-node isoparametric brick elements were used. Focused onto each of twelve segments (equal increments in ϕ) of the crack front were eight degenerate wedge-shaped elements. In the topological element "plane" locally normal to the crack front (plane $x - y$), there were six rings of elements in the radial direction with eight elements each in the circumferential direction. The wedge-shaped elements of the first ring had independent nodes located at the same point on the crack front. The global mesh had from 912 to 1152 elements, or about 12 000 to 15 000 degrees of freedom, depending upon the particular crack geometry and loading type. The radial extent of the first ring elements was of the order $10^{-2}t$. For details of the mesh generation, see Ref *21*.

The fine mesh consisted of the tubular regions surrounding the crack front. The exterior of the fine mesh coincided with the interelement boundary between the third and fourth rings of focused elements in the respective coarse meshes. The region inside the boundary was refined radially with eight to twelve rings of elements, instead of three rings in the global mesh. The fine mesh had from 768 ($8 \times 8 \times 12$) to 1152 ($8 \times 12 \times 12$) elements. The radial extent of the first ring of elements around the crack tip was of order $10^{-4}t$. The loading of the fine mesh was accomplished by applying the nodal displacements obtained from the nodes between the third and fourth rings of the coarse mesh. The procedure has proven effective and accurate in an earlier application [*11*]. Each iteration of the 912-element coarse mesh took about 20 min on a single processor of an Alliant FX-8; the 1152-element fine mesh run took about 90 min per iteration.

Boundary Conditions and Loading

Symmetry boundary conditions were applied on the planes $X = 0$ and $Y = 0$. Out-of-plane displacement (U_Z) of a single node was restrained to eliminate rigid body translation. In applying a remote tensile loading, uniform displacement U_Y on the remote plane $Y = h$ was imposed. The total remote tensile load was obtained by summing the Y-direction nodal forces on every node in the plane $Y = h$. The remote load level was defined as the ratio of the remote load to the remote limit load based upon the uncracked cross section, i.e., $\Sigma^\infty = \sigma^\infty/\sigma_0$, where the remote stress $\sigma^\infty = P/bt$ with P being the total tensile force applied on the plane $Y = h$ at $X \geq 0$.

In applying a remote bending moment, kinematic constraints were imposed on the nodes in the plane $Y = h$ so that the plane remained plane during loading. This was the only restriction applied; the plane was free to move in any other fashion. Two concentrated forces with the same magnitude and opposite signs were applied on two nodes, one on the top of the plate ($X = 0$, $Y = h$, and $Z = t$) and another on the bottom of the plate ($X = 0$, $Y = h$, and $Z = 0$). The loads were actually applied throughout the remote plane because of the kinematic constraints. The total moment on the remote plane was simply $M^{\infty} = P \cdot t$, where P was the magnitude of the concentrated load applied on the single node. The measure of the remote load level was defined as the ratio of remote moment to the remote limit moment, or $\Sigma^{\infty} = M/M_{\text{limit}}$, where $M_{\text{limit}} = \sigma_0 bt^2/4$, i.e., the moment at gross section yielding.

Data Reduction

In topological planes perpendicular to the crack front (plane $x - y$ in Fig. 4) where interfaces of elements exist, the nodal stresses of fine mesh were obtained from extrapolations of stresses at integration points of the surrounding elements. The extremely refined mesh ensured the accuracy of the extrapolated stresses. The radial distance, r, of each node from the local crack tip was calculated from the fine mesh nodal coordinates. Local $J(\phi)$ at each crack-front location was calculated using the domain integral method [*16,17*] in the entire domain of the fine meshes, which ranged from eight contours to twelve contours. Except for the first contour, which was inherently less accurate, the J-integral varied within 3%.

Crack-opening stress (σ_{yy} in the local coordinate system shown in Fig. 4) was plotted versus $r/(J(\phi)/\sigma_0)$ at various crack-front locations for each crack geometry and loading type. Stresses inside the blunting zone ($r < J/\sigma_0$) and outside the region of interest ($r > 6J/\sigma_0$) were deleted for a better curve fitting. The stress profiles were then fitted to a form, $\sigma_{yy}/\sigma_0 = Y_0 + L(r/(J/\sigma_0))^p$, where Y_0, L, and p are fitted constants depending upon crack-front location, crack geometry, and loading type. The fitted forms were then used to calculate stresses at any other normalized distance in the range. Sufficient data points and smooth variation of the stress profiles provided good fits. Eventually, stresses at $r/(J/\sigma_0) = 2$ were obtained from each fitted form to compare with the plane-strain MBL predictions.

The MBL solution was obtained from Eq 6. Following the notation of Parks [*22*], the normalized T-stress $\tau(\phi) \equiv T(\phi)/\sigma_0 = T(\phi)/\sigma^{\infty} \cdot \sigma^{\infty}/\sigma_0 = \hat{t}(\phi) \cdot \Sigma^{\infty}$, where $\hat{t}(\phi)$ is dependent upon crack geometry, loading type, and ν. Thus the T-stress at any point along the crack front is proportional to the remote load level Σ^{∞}. Recall that $\Sigma^{\infty} = 4M/\sigma_0 bt^2 = (4M/bt^2)/\sigma_0$ for plates under remote bending, so we have $\hat{t}(\phi) = T(\phi)/(4M/bt^2)$.

Using the line-spring model, Wang and Parks [*23*] have obtained $\hat{t}(\phi)$ distribution in a variety of SCPs under remote tension and bending. These results were in excellent agreement with $\hat{t}(\phi)$ estimates from extremely detailed 3-D elastic FE solutions. Similar results were obtained using a special domain integral method [*24*]. The $\hat{t}(\phi)$ distributions under remote bending were directly calculated from a fitted parametric form as a function of crack geometry and crack-front location [*23*]. Note that $\hat{t}(\phi) \equiv T(\phi)/(6M/bt^2)$ for plates under remote bending in Ref *23*, a factor of 1.5 in the value of $\hat{t}(\phi)$ should be realized in accordance with the present definition. Under remote tension, slightly different values of $\hat{t}(\phi)$ were obtained at crack-front locations $45° < \phi < 60°$ using the different methods mentioned above. Based upon the best estimates of the three methods, three data points at $\phi = 0, 45$, and $67.5°$ were chosen to fit the $\hat{t}(\phi)$ distribution into a quadratic polynomial, $\hat{t}(\phi) = a_0 + a_1\phi + a_2\phi^2$, where a_0, a_1, and a_2 were fitted constants dependent upon crack geometry. The resulting $\hat{t}(\phi)$ distributions under remote tension and bending are shown in Fig. 5. The results are not available at $\phi > 67.5°$ because the line-spring method is not accurate in these locations. More discussion on the limitation of the line-spring method is given in [*23*].

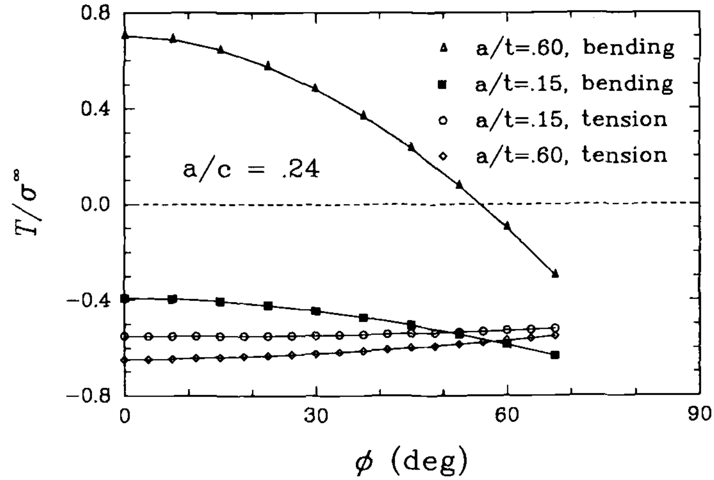

FIG. 5—*T-stress calibration factor* $\hat{t}(\phi) \equiv T/\sigma^{\infty}$ *of surface crack plates under remote tension and bending. Note that* $\sigma^{\infty} = 4M/bt^2$ *in bending.*

Comparison with the Plane-Strain Solutions

A number of comparisons can be made to verify the applicability of $J - T$ characterized MBL solution in predicting the 3-D crack-front stress fields. For instance, various stress and strain components at different ϕ, r, and θ, as well as plastic zone size and shape can be examined. However, the most important and obvious comparison is the stress directly ahead of the cracked plane ($\theta = 0$), both because of its relevance to the driving force of fracture processes and because of easy comparison with previous results [*8–11*].

Figure 6 shows the center plane ($\phi = 0$) crack opening stress normalized by HRR, SSY, and MBL solutions, respectively, plotted versus remote load level Σ^{∞} at normalized distance $r/(J/$

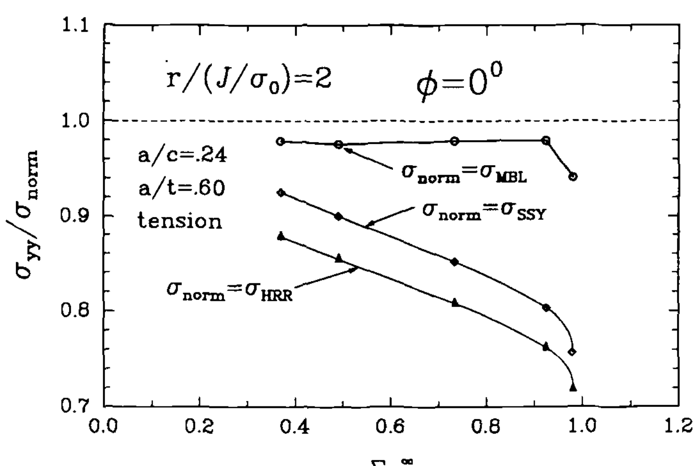

FIG. 6—*Center plane* ($\phi = 0°$) *crack opening stress at* $r = 2J/\sigma_0$, *normalized variously by the HRR, SSY, and MBL solutions at the same normalized distance for the deep-cracked plate under remote tension.*

$\sigma_0) = 2$ for the deep-cracked plate under remote tension. The radial distance from crack tip is about four CTODs, or $r = 2J/\sigma_0 = 2/d_n(\epsilon_0,n) \cdot d_n(\epsilon_0,n)J/\sigma_0 = 2/d_n(\epsilon_0,n) \cdot \text{CTOD} \doteq 4\,\text{CTOD}$, where $d_n = 0.51$ under plane strain for $\epsilon_0 = 0.0025$ and $n = 10$ [25]. The HRR and SSY solutions are invariants at $r = 2J/\sigma_0$, or $\sigma_{HRR} = 3.52\sigma_0$ and $\sigma_{SSY} = 3.34\sigma_0$ for the present material. The MBL stress, σ_{MBL}, was obtained from Eq 6 using the local calculated elastic-plastic $J(\phi = 0)$ and the elastically-calculated $T = \hat{t}(\phi = 0) \cdot \Sigma^\infty$, where $\hat{t}(\phi = 0)$ was taken from curves shown in Fig. 5. Stresses normalized by σ_{HRR} and σ_{SSY} show a steady deviation from unity as load level increases. If the curve normalized by σ_{SSY} was extrapolated back to $\Sigma^\infty = 0$, it would intercept the ordinate at unity, as it should. If similar extrapolation was made for the curve normalized by σ_{HRR}, it intercepts the ordinate at ~0.95, which reflects the limit of the ratio of SSY solution to the HRR solution at $r = 2J/\sigma_0$, or $0.95 \doteq \sigma_{SSY}/\sigma_{HRR} = 3.34\sigma_0/3.52\sigma_0$. The MBL solution is in better than 97% agreement with the 3-D FE results at load levels $\Sigma^\infty <$ ~0.92. Even at a remote load close to limit load, better than 94% agreement is obtained. At the same load, the 3-D result is about 76% of the SSY solution while the difference between the 3-D result and HRR solution is even greater. Given the elastic nature of the T calibration, the simple $J - T$ characterized MBL is remarkably accurate.

Figure 7 is the crack-opening stresses at $r = 2J/\sigma_0$, normalized by MBL solutions at the same normalized distance along the crack front for remote loads ranging from SSY to limit load. Data at $\phi > 67.5°$ are not included because both the 3-D FE solutions failed to produce sufficiently accurate stress at $r = 2J/\sigma_0$, nor was the elastic T calibration factor $\hat{t}(\phi)$ available at these locations. In any case, however, the crack front included in $67.5° < \phi < 90°$ is very small because of the low aspect ratio ($a/c = 0.24$). The 3-D FE stresses are normalized by σ_{MBL} using the local J and T at each crack-front location. It is seen that better than 98% agreement is obtained along (almost) the entire crack front for $\Sigma^\infty < 0.925$. Even at $\Sigma^\infty = 0.980$, the MBL prediction is still within 94% of the 3-D FE solution at all crack-front locations.

Figures 8 and 9 are similar to Figs. 6 and 7, respectively, except these are for the shallow-cracked plate under remote tension. The MBL solutions are in better than 97% agreement with the 3-D FE solutions at all crack-front locations for remote loads up to limit load. However, one should be cautious in making direct comparison between Figs. 9 and 7. The remote load parameter Σ^∞ is measured in terms of the remote load normalized by the limit load of the

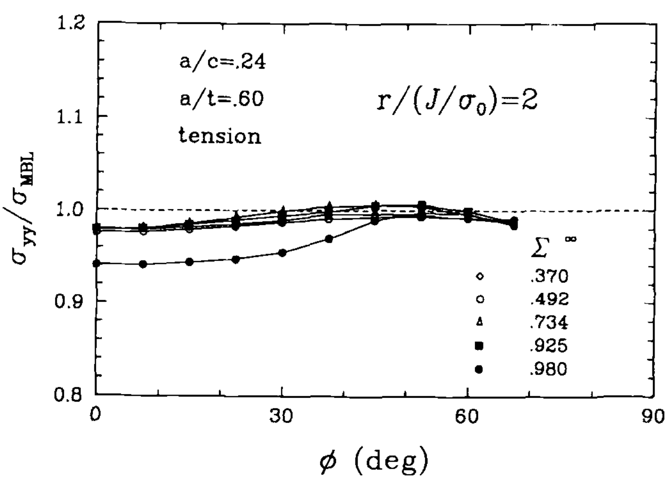

FIG. 7—*Crack-opening stress, normalized by the MBL solution, along the crack front of the deep-cracked plate under remote tension at various load levels.*

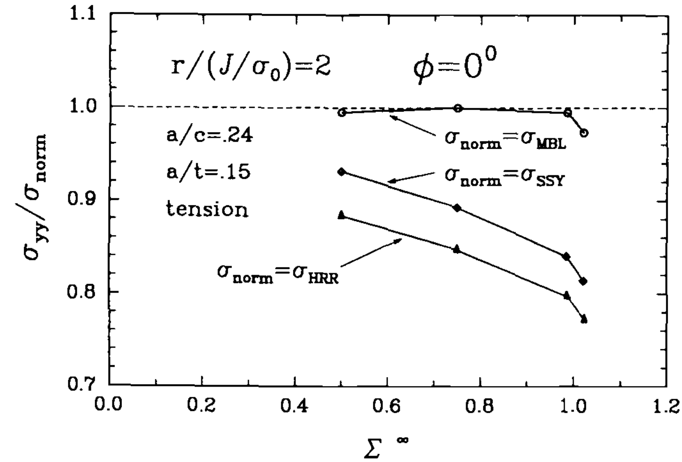

FIG. 8—*Center plane (ϕ = 0°) crack opening stress at* r = $2J/\sigma_0$, *normalized variously by the HRR, SSY, and MBL solutions at the same normalized distance for the shallow-cracked plate under remote tension.*

uncracked cross section. The cracked area of the shallow-cracked plate is much smaller than that of the deep-cracked plate. Indeed, if the limit loads were based up the uncracked ligament area of the respective plates, the load level corresponding to Σ^∞ = 1.022 of the shallow-cracked plate would be Σ^∞_{net} = 1.031, while Σ^∞_{net} = 1.149 at Σ^∞ = 0.980 for the deep-cracked plate. Thus, the load level of deep-cracked plate at the highest load level calculated here is actually greater than that of the shallow-cracked plate in terms of net-section yielding.

Figure 10 is the crack-opening stress at $r = 2J/\sigma_0$, normalized by HRR, SSY, and MBL solutions at the same normalized distance, respectively, plotted versus the remote load level for the shallow-cracked plate under remote bending. The stress normalized by σ_{HRR} and σ_{SSY} shows a nonlinear, gradual deviation from unity as load increases. The MBL solution agrees

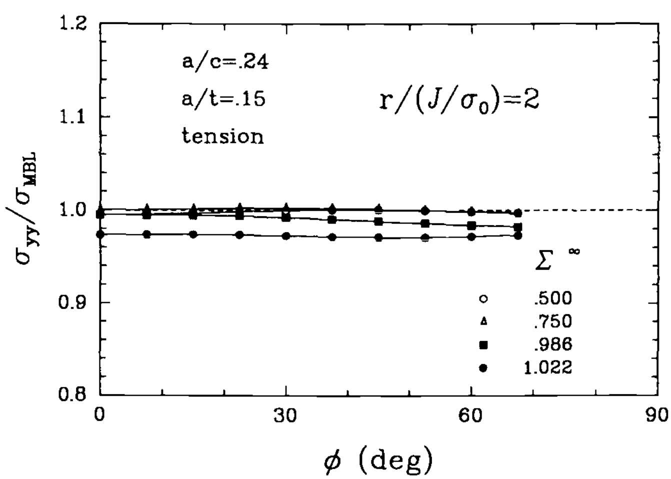

FIG. 9—*Crack-opening stress, normalized by the MBL solution, along the crack front of the shallow-cracked plate under remote tension at various load levels.*

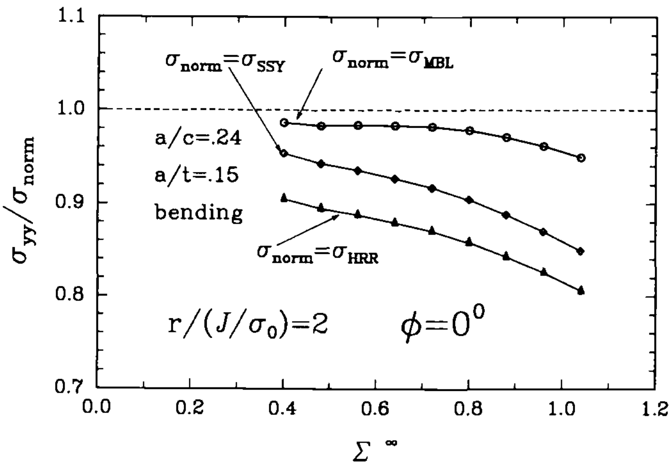

FIG. 10—*Center plane (ϕ = 0°) crack-opening stress at* r = $2J/\sigma_0$, *normalized variously by the HRR, SSY, and MBL solutions at the same normalized distance for the shallow cracked plate under remote bending.*

within 95% with the 3-D FE results at loads slightly over limit load. In Fig. 11, comparison is made along the crack front between the 3-D solutions and the MBL predictions for remote loads up to/over limit load. Referring to Fig. 5, the $\hat{t}(\phi)$ distribution of the shallow-cracked plate under remote bending shows a different trend from those plates under remote tension. Under remote bending, $\hat{t}(\phi)$ decreases with increasing ϕ. Nevertheless, the MBL solution prediction still has better than 95% accuracy at all crack-front locations for bending loads up to/over the limit load.

The $\hat{t}(\phi)$ distribution of the deep-cracked plate under remote bending, as shown in Fig. 5, is most interesting. The $\hat{t}(\phi)$ varies continuously from positive at ϕ = 0° to negative at ϕ = 67.5°.

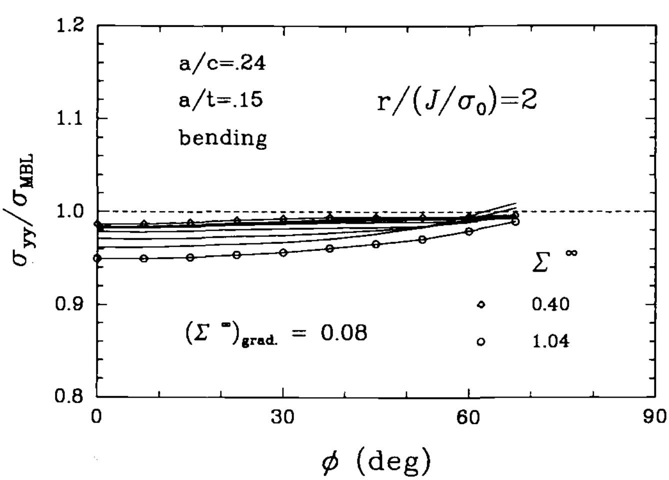

FIG. 11—*Crack-opening stress, normalized by the MBL solution, along the crack front of the shallow-cracked plate under remote bending. The normalized load level varies from 0.4 to 1.04 with a constant interval 0.08.*

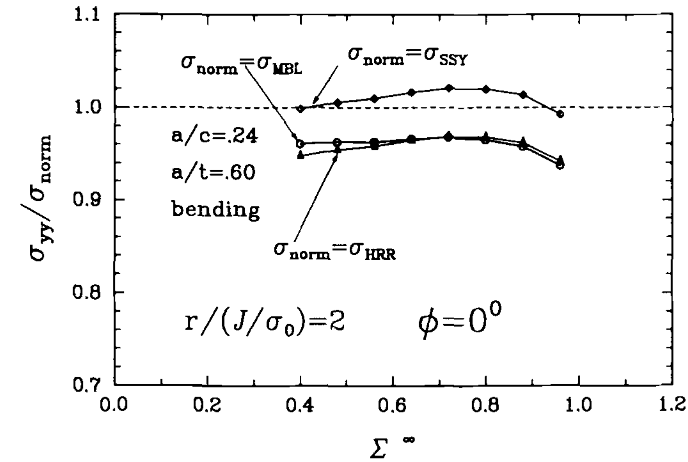

FIG. 12—*Center plane (ϕ = 0°) crack-opening stress at* r = $2J/\sigma_0$, *normalized variously by the HRR, SSY, and MBL solutions at the same normalized distance for the deep-cracked plate under remote bending.*

The qualitative prediction of Eq 6 suggests that, at appropriate load levels, the stresses at ϕ = 0° would be greater than the SSY result, while the stresses at ϕ = 67.5° would be less than the SSY result. This is indeed observed in Figs. 12 and 13, where the 3-D FE solutions at ϕ = 0° and ϕ = 67.5°, normalized by the HRR, SSY, and MBL solutions, respectively, are plotted versus remote load level. Later, it will be shown that the J at ϕ = 67.5° is greater than J at ϕ = 0° at same load. Nevertheless, normalized stress at ϕ = 67.5° is lower because of the negative τ. Qualitatively, the curve normalized by MBL solution at ϕ = 0° falls below that normalized by SSY solution, because σ_{MBL} is greater than σ_{SSY} at positive τ, whereas at ϕ = 67.5° (Fig. 13), the relative positions of the two curves are reversed. From Fig. 12, it appears that the SSY solution is a good prediction of the 3-D result, even at load up to the limit load. A similar

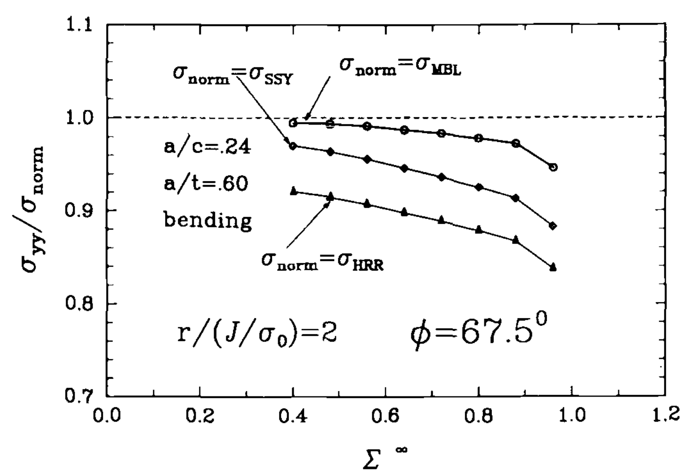

FIG. 13—*Crack-opening stress at* r = $2J/\sigma_0$ *and* ϕ = *67.5°, normalized variously by the HRR, SSY, and MBL solutions, for the deep-cracked plate under remote bending.*

conclusion was made elsewhere [4]. In any case, the MBL solution was within 94% of the 3-D result at both $\phi = 0°$ and $\phi = 67.5°$.

Figure 14 compares the MBL solution with the 3-D FE result along the crack front of the deep-cracked plate under remote bending. At loads up to $\Sigma^\infty < 0.88$, the agreement is better than 96%. At a higher load, $\Sigma^\infty = 0.96$, an appreciable drop of agreement is seen. Careful analysis of the crack opening stress profile, i.e., σ_{yy} versus $r/(J/\sigma_0)$, revealed that the global compressive stress on the ligament became a major contributing factor to the local crack-tip stress fields. Referring to Fig. 4, the neutral axis on the plane of $Y = 0$ is somewhere above the crack front, or $Z_{\text{neutral}} > a$. As load increased to a point near general yielding, J increases substantially. Since the radial distance at which the stress was compared is proportional to J, the stress at $r = 2J/\sigma_0$ was sampled at a distance sufficiently far away from the crack tip that the global negative stress gradient made the the stress lower than the MBL prediction. Similar features were noticed in Ref *15*.

Figure 15 shows the normalized J distribution along the crack front of a deep-cracked plate under remote bending. At $\Sigma^\infty = 0.96$, $J/\epsilon_0\sigma_0 t\Sigma^{\infty 2} = \sim 0.68$ inside $50° < \phi < 60°$, or $J/\sigma_0 t = \sim 0.02$. Within the range $50° < \phi < 60°$, crack depth $a(\phi)$ is about $0.5t$. Thus, $a/(J/\sigma_0) = (a/t)/(J/\sigma_0 t) \doteq 0.5/0.02 = 25$. Recalling that J/σ_0 is about two CTODs, one realizes that the CTOD is about $\frac{1}{50}$ of the crack depth. The CTOD is so great that it probably approaches the inherent fracture mechanics limit.

Concluding Remarks

To summarize the 3-D FE results, the crack opening stresses at $r = 2J/\sigma_0$ from $\phi = 0°$ to $\phi = 67.5°$ of four cases studied, shallow/deep, tension/bending, were plotted versus τ, as shown in Fig. 16. The thick solid line is the MBL prediction, or Eq 6, at $r/(J/\sigma_0) = 2$. The dashed line is a crack-opening stress level 5% below the MBL prediction. Almost all the 3-D results fall into the narrow band of the MBL prediction. The only stresses that fall outside of the 5% band are those from the deep-cracked plate under remote bending (marked with big diamonds) for the reasons explained before. In comparing these results, we ought to remember that the limit loads were based upon the remote uncracked sections. In fact, the cracked area of the deep-

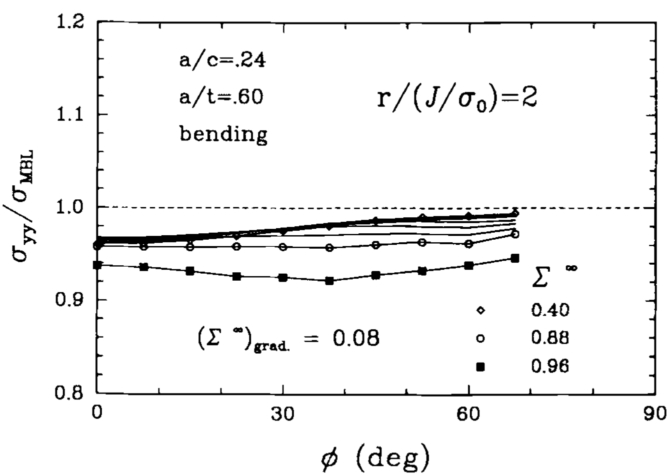

FIG. 14—*Crack-opening stress, normalized the MBL solution, along the crack front of the deep-cracked plate under remote bending. The normalized load level varies from 0.4 to 1.04 with a constant interval 0.08.*

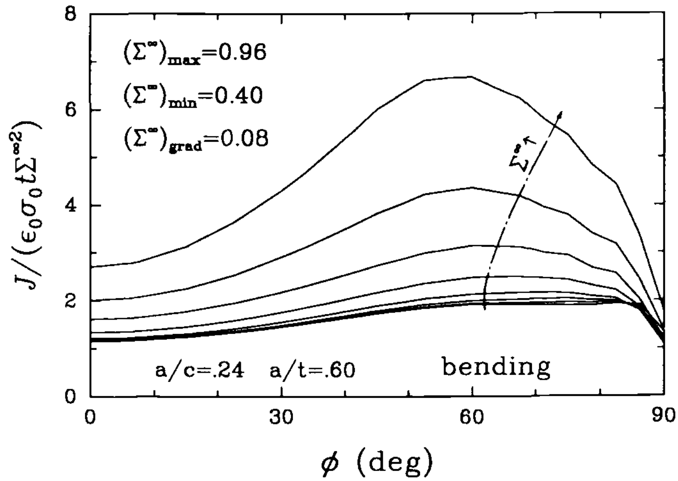

FIG. 15—*Normalized J along the crack front of the deep-cracked plate under remote bending. The normalized load level varies from 0.4 to 0.96 with a constant interval 0.08.*

cracked plate is $(0.60/0.15)^2$ = 16 times that of the shallow-cracked plate, or 14.7% of the gross section, compared with only 0.9% in the shallow-cracked plate. Figure 17 shows the value $\ell\sigma_0/J$, which can be interpreted as the ratio of relevant crack geometry scale ℓ to the CTOD, decreases rapidly as the remote load approaches limit load. Here ℓ is taken as the crack depth at $\phi = 0°$ for shallow cracks ($\ell/t = 0.15$), and remaining ligament at $\phi = 0°$ for deep cracks ($\ell/t = 0.4$). The inherent fracture mechanics limit, $\ell \gg$ CTOD, should always remain in effect

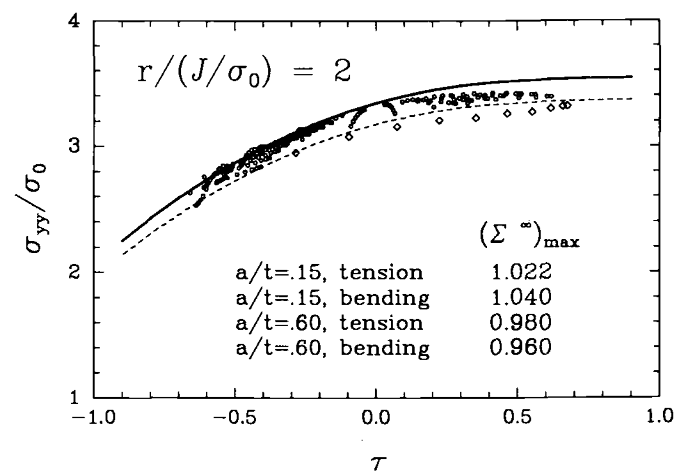

FIG. 16—*Comparison of various 3-D FE solutions with the MBL predictions at r = $2J/\sigma_0$. The solid line is the MBL solution, and the dashed line is 95% of the MBL solution. The 3-D FE results, marked by the open circles, include all four cases studied, shallow/deep cracks and tension/bending loads. The load levels are from SSY to the maximum values indicated on the figure. Data marked with large diamonds are those of the deep-crack plate under remote bending at Σ^∞ = 0.96.*

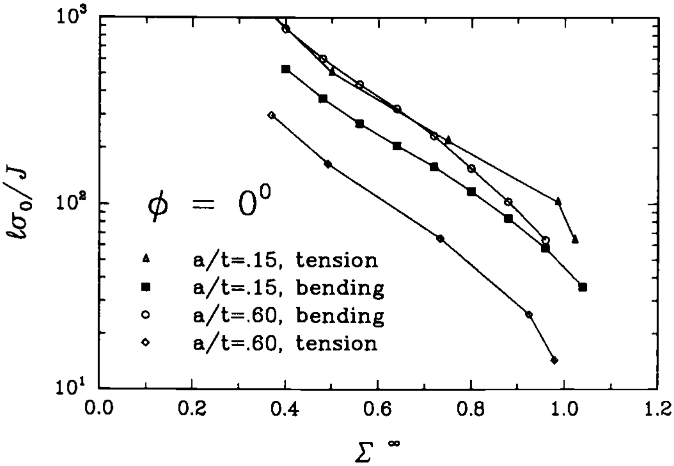

FIG. 17—*Center plane (ϕ = 0°) normalized* J *versus the normalized load level for various crack geometries and loading types.*

[*26*]. Therefore, one may not expect the two-parameter characterization to be good at load levels much greater than the limit load.

Returning to Fig. 16, the reason that the 3-D FE results are almost always below the MBL prediction can be partially explained here. Recall that the MBL solutions were obtained under plane-strain conditions. In a real 3-D SCP, the out-of-plane (local *zz* direction in Fig. 4) strain is generally negative along most of the crack front. For instance, our detailed 3-D elastic FE analysis [*27*] revealed that the out-of-plane strain at $\phi = 0°$ for deep-cracked plate under remote tension was about $\epsilon_{zz} = -0.55\epsilon_{YY}^{\infty}$, where ϵ_{YY}^{∞} is the remote strain near $Y = h$ in the tensile loading direction. Parks [*22*] suggested a generalized form of Eq 2 to express the linear elastic stress distribution in the vicinity of a crack front

$$\begin{bmatrix} \sigma_{xx} & \sigma_{xy} & \sigma_{xz} \\ \sigma_{yx} & \sigma_{yy} & \sigma_{yz} \\ \sigma_{zx} & \sigma_{zy} & \sigma_{zz} \end{bmatrix} = \frac{K_I}{\sqrt{2\pi r}} \begin{bmatrix} f_{xx}(\theta) & f_{xy}(\theta) & f_{xz}(\theta) \\ f_{yx}(\theta) & f_{yy}(\theta) & f_{yz}(\theta) \\ f_{zx}(\theta) & f_{zy}(\theta) & f_{zz}(\theta) \end{bmatrix} + \begin{bmatrix} T_{xx} & 0 & T_{xz} \\ 0 & 0 & 0 \\ T_{zx} & 0 & T_{zz} \end{bmatrix} \tag{7}$$

where T_{ij} represent constant tractions applied on a point around the crack front, and T_{xx} is the *T*-stress in Eq 2. The plane strain MBL formulation corresponds to a special case of $T_{xz} = T_{zx} = 0$ and $T_{zz} = \nu T_{xx}$. We analyzed another special case, where $T_{xz} = T_{zx} = 0$ and T_{zz} is finite, by varying the out-of-plane strain ϵ_{zz} at the same value of τ. The stress state simulated here is close to that at/near a symmetry plane such as at $\phi = 0°$ in SCP. Figure 18 shows the normalized crack opening stress at various values of ϵ_{zz}/ϵ_0 with a constant value of $\tau = 0$. Similar stress profiles were obtained at other values of τ. The relative variations in terms of ϵ_{zz}/ϵ_0 at various values of τ showed very little difference. Overall, the effect of out-of-plane strain on the crack opening stress is much smaller than that of the *T*-stress. At positive ϵ_{zz}, the ϵ_{zz} effect is negligible. For $\tau = 0$ and $\epsilon_{zz}/\epsilon_0 = -0.9$, the stress at $r = 2J/\sigma_0$ is below its plane strain stress by about $0.14\sigma_0$. A rough estimate for the deep-cracked plate under remote tension gives $\epsilon_{zz}/\epsilon_0 = \epsilon_{zz}/\epsilon_{YY}^{\infty} \cdot \epsilon_{YY}^{\infty}/\epsilon_0 \doteq -0.55 \cdot 1 = -0.55$ at $\sigma^\infty = 0.980$, where $\epsilon_{YY}^{\infty}/\epsilon_0 \doteq 1$ at this load. Assuming linear variation of crack opening stress between $\epsilon_{zz}/\epsilon_0 = 0$ and $\epsilon_{zz}/\epsilon_0 = -0.9$ at $r = 2J/\sigma_0$, the stress drop caused by ϵ_{zz} would be $0.55/0.90 \times 0.14\sigma_0 = 0.085\sigma_0$. This seems to be an

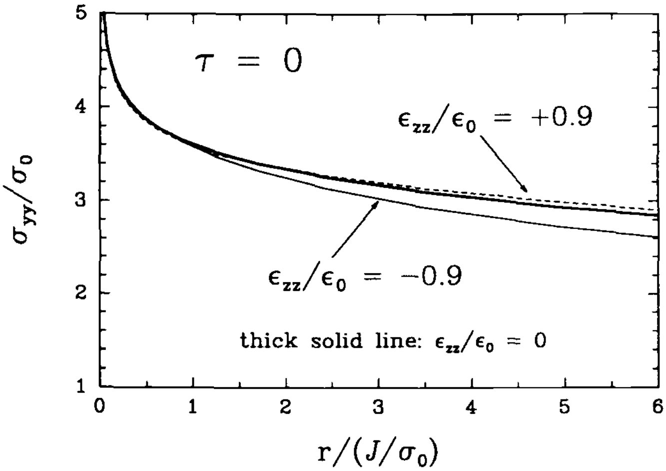

FIG. 18—*Normalized crack opening stress profiles in generalized plane strain at $\tau = 0$ and various values of ϵ_{zz}/ϵ_0.*

exceedingly small value until one considers that a 5% deviation from the plane-strain SSY solution ($\tau = 0$) at $r = 2J/\sigma_0$ is only about $0.16\sigma_0$. In other words, the stress drop induced by the negative out-of-plane strain could account for up to half of the 5% deviation. It is evident that the MBL predication is indeed accurate for loads up to limit load for the crack geometries studied here. Considering that the T parameter as used here is only an elastically scaled parameter, the accuracy of the MBL approach is indeed striking.

Having demonstrated the ability of the $J - T$ two-parameter approach in characterizing the elastic-plastic near crack-tip fields up to large-scale yielding, it should be emphasized that the elastic nature of the T-stress does pose some conceptual difficulties in understanding its usefulness in large-scale yielding. However, we feel that T-stress should not be looked at differently from other fracture parameters, such as the stress intensity factor K_I, and the J-integral. The K_I (or J) based one-parameter characterization is rigorous under SSY; so is the $J - T$ two-parameter characterization. The key is to establish the parametric limits of the $J - T$ two-parameter characterization, much like the parametric limit of HRR-dominance was once examined [*8,9*]. We have used the remote load level as our primary indicator of the extent of plastic deformation. This may be useful in engineering applications. However, other parameters, such as the ratio of the ligament/crack-depth to the CTOD, may be more relevant to the characterization of near crack-tip fields. Therefore, relations similar to those shown in Fig. 17 are very useful in defining the parametric limits of $J - T$ two-parameter characterization. The J-integral distributions along the crack fronts of SCPs studied here are given in [*27*] for load levels from SSY to general yielding.

Recently, O'Dowd and Shih [*28,29*] proposed a family of plane-strain elastic-plastic stress fields in a two-term form

$$\frac{\sigma_{ij}}{\sigma_0} = \left(\frac{\sigma_{ij}}{\sigma_0}\right)_{\text{HRR}} + Q\left(\frac{1}{r/(J/\sigma_0)}\right)^q \hat{\sigma}_{ij}(\theta) \tag{8}$$

where Q is the measure of the second term, and $\hat{\sigma}_{ij}(\theta)$ is the angular variation of the respective stress components. Physically, the second term is the difference between the complete stress fields and the HRR fields. O'Dowd and Shih found that the angular variation of the stress components in the forward sector ($\theta < 90°$) was very small, or $\hat{\sigma}_{ij}(\theta) \simeq \delta_{ij}$. Comparing with Eq 6 and neglecting the small difference between the HRR solution and the SSY solution at a point just outside the crack blunting zone, Q and τ can be related as

$$Q \sim A_n\tau + B_n\tau^2 + C_n\tau^3 \tag{9}$$

O'Dowd and Shih were able to show that the Q-family of stress fields represented the stress states of blunted cracks with a large range of crack-tip constraint. However, it appears that Q cannot be evaluated as easily as the T-stress. Other closely related approaches [*30,31*] seemingly have the same drawback. In contrast, an alternative characterizing parameter T can be readily evaluated from a moderately refined FE analysis. The recently developed interaction integral method [*24*] is capable of evaluating T as a function of crack geometry and loading type in general 3-D cracked geometries using standard domain integral techniques. The $J-T$ characterization appears to be a tractable, predictive methodology that provides both excellent qualitative and quantitative predictions of elastic-plastic crack-tip fields with variety of constraints.

Acknowledgments

The author would like to acknowledge many insightful discussions with his thesis advisor, David M. Parks. This work was supported by the Office of Basic Energy Sciences, Department of Energy, under Grant DE-FG02-85ER13331. Computations were performed on an Alliant FX-8 computer obtained under D.A.R.P.A. Grant N00014-86-K-0768, on Sun workstations obtained under ONR Grant 0014-89-J-3040, and on a Cray-2 at the MIT Supercomputer Facility. The ABAQUS finite element program was made available under academic license from Hibbitt, Karlsson, and Sorensen, Inc., Pawtucket, RI.

References

[*1*] Williams, M. L., "On the Stress Distribution at the Base of a Stationary Crack," *Journal of Applied Mechanics*, Vol. 24, 1957, pp. 111–114.

[*2*] Larsson, S. G. and Carlsson, A. J., "Influence of Non-Singular Stress Terms and Specimen Geometry on Small-Scale Yielding at Crack Tips in Elastic-Plastic Material," *Journal of the Mechanics and Physics of Solids*, Vol. 21, 1973, pp. 263–277.

[*3*] Bilby, B. A., Cardew, G. E., Goldthorpe, M. R., and Howard, I. C., "A Finite Element Investigation of the Effect of Specimen Geometry on the Fields of Stress and Strain at the Tips of Stationary Cracks," *Size Effects in Fracture*, Mechanical Engineering Publications Limited, London, United Kingdom, 1986, pp. 37–46.

[*4*] Betagón, C. and Hancock, J. W., "Two Parameter Characterization of Elastic-Plastic Crack Tip Fields," *Journal of Applied Mechanics*, Vol. 58, 1991, pp. 104–110.

[*5*] Rice, J. R., "A Path Independent Integral and the Approximate Analysis of Strain Concentration by Notches and Cracks," *Journal of Applied Mechanics*, Vol. 35, 1968, pp. 379–386.

[*6*] Hutchinson, J. W., "Singular Behavior at the End of a Tensile Crack in a Hardening Material," *Journal of the Mechanics and Physics of Solids*, Vol. 16, 1968, pp. 13–31.

[*7*] Rice, J. R. and Rosengren, G. F., "Plane Strain Deformation Near a Crack Tip in a Power Law Hardening Material," *Journal of the Mechanics and Physics of Solids*, Vol. 16, 1968, pp. 1–12.

[*8*] McMeeking, R. M. and Parks, D. M., "On Criteria for J-Dominance of Crack-Tip Fields in Large-Scale Yielding," *Elastic-Plastic Fracture, ASTM STP 668*, American Society for Testing and Materials, Philadelphia, 1979, pp. 175–194.

[*9*] Shih, C. F. and German, M. D., "Requirements for a One Parameter Characterization of Crack Tip Fields by the HRR Singularity," *International Journal of Fracture*, Vol. 17, 1981, pp. 27–43.

[*10*] Shih, C. F., "J-Dominance Under Plane Strain Fully Plastic Conditions: the Edge Crack Panel Sub-

ject to Combined Tension and Bending," *International Journal of Fracture*, Vol. 29, 1985, pp. 73–84.

[11] Parks, D. M and Wang, Y.-Y., "Elastic-Plastic Analysis of Part-Through Surface Cracks," *Analytical, Numerical, and Experimental Aspects of Three Dimensional Fracture Processes*, A. J. Rosakis, K. Ravi-Chandar, and Y. Rajapakse, Eds., ASME AMD-Vol. 91, American Society of Mechanical Engineers, New York, NY, 1988, pp. 19–32.

[12] Sommer, E. and Aurich, D., "On the Effect of Constraint on Ductile Fracture," *Defect Assessment in Components—Fundamentals and Applications, ESIS/EGF9*, J. G. Blauel and K.-H. Schwalbe, Eds., Mechanical Engineering Publications, London, United Kingdom, 1991, pp. 141–174.

[13] Brocks, W. and Künecke, G., "On the Influence of Triaxiality of the Stress State on Ductile Tearing Resistance," *Defect Assessment in Components—Fundamentals and Applications, ESIS/EGF9*, J. G. Blauel and K.-H. Schwalbe, Eds., Mechanical Engineering Publications, London, United Kingdom, 1991, pp. 189–201.

[14] Du, Z.-Z. and Hancock, J. W., "The Effect of Non-Singlar Stress on Crack Tip Constraint," *Journal of the Mechanics and Physics of Solids*, Vol. 39, 1991, pp. 555–567.

[15] Al-Ani, A. M. and Hancock, J. W., "*J*-Dominance of Short Cracks in Tension and Bending," *Journal of the Mechanics and Physics of Solids*, Vol. 39, No. 1, 1991, pp. 23–43.

[16] Li, F. Z., Shih, C. F., and Needleman, A., "A Comparison of Methods for Calculating Energy Release Rate," *Engineering Fracture Mechanics*, Vol. 21, 1985, pp. 405–421.

[17] Moran, B. and Shih, C. F., "Crack Tip and Associated Domain Integrals from Momentum and Energy Balance," *Engineering Fracture Mechanics*, Vol. 27, No. 6, 1987, pp. 615–642.

[18] Parks, D. M., "The Virtual Crack Extension Method for Nonlinear Material Behavior," *Computer Methods in Applied Mechanics and Engineering*, Vol. 12, 1977, pp. 353–364.

[19] Parks, D. M., personal communication, 1990.

[20] *ABAQUS User's Manual*, Version 4-7-1, Hibbitt, Karlsson, and Sorensen, Inc., Providence, RI, 1988.

[21] Wang, Y.-Y., "Analysis of Fracture Intitiation in Surface-Cracked Plates," S.M. Thesis, Department of Mechanical Engineering, Massachusetts Institute of Technology, Cambridge, MA, Aug. 1988.

[22] Parks, D. M., "Three-Dimensional Aspects of HRR-Dominance," *Defect Assessment in Components—Fundamentals and Applications, ESIS/EGF9*, J. G. Blauel and K.-H. Schwalbe, Eds., Mechanical Engineering Publications. London, United Kingdom, 1991, pp. 206–231.

[23] Wang, Y.-Y. and Parks, D. M., "Evaluation of the Elastic *T*-Stress in Surface-Cracked Plates Using Line-Spring Method," *International Journal of Fracture*, Vol. 59, 1992, pp. 25–40.

[24] Nakamura, T. and Parks, D. M., "Determination of Elastic *T*-Stress Along 3-D Crack Fronts Using an Interaction Integral," *International Journal of Solids and Structures*, Vol. 29, 1992, pp. 1597–1611.

[25] Shih, C. F., *Tables of Hutchinson-Rice-Rosengren Singular Field Quantities*, Brown University Report, Brown University, Providence, RI, 1983.

[26] Parks, D. M., "Engineering Methodologies for Assessing Crack Front Constraint," *Proceedings, SEM Spring Conference on Experimental Mechanics*, The Society for Experimental Mechanics, Inc., Bethel, CT, 1991, pp. 1–8.

[27] Wang, Y.-Y., "A Two-Parameter Characterization of Elastic-Plastic Crack Tip Fields and Applications to Cleavage Fracture," Ph.D. thesis, Department of Mechanical Engineering, Massachusetts Institute of Technology, Cambridge, MA, May 1991.

[28] O'Dowd, N. P. and Shih, S. F., "Family of Crack-Tip Fields Characterized by a Triaxiality Parameter: Part I—Structure of Fields," *Journal of the Mechanics and Physics of Solids*, Vol. 39, 1991, pp. 989–1015.

[29] O'Dowd, N. P. and Shih, S. F., "Family of Crack-Tip Fields Characterized by a Triaxiality Parameter: Part II—Applications," *Journal of the Mechanics and Physics of Solids*, Vol. 40, 1992, pp. 939–963.

[30] Li, Y. C. and Wang, T. Z., "High-Order Asymptotic Field of Tensile Plane-Strain Nonlinear Crack Problem," *Scientia Sinica (Series A)*, Vol. 29, 1986, pp. 941–955.

[31] Sharma, S. M. and Aravas, N., "Determination of Higher Order Terms in Asymptotic Eastoplastic Crack Tip Solutions," *Journal of the Mechanics and Physics of Solids*, Vol. 39, 1991, pp. 1043–1072.

Robert J. Bonenberger,[1] James W. Dally,[1] and George R. Irwin[1]

Lower-Bound Initiation Toughness with a Modified-Charpy Specimen

REFERENCE: Bonenberger, R. J., Dally, J. W., and Irwin, G. R., "**Lower-Bound Initiation Toughness with a Modified-Charpy Specimen,**" *Constraint Effects in Fracture, ASTM STP 1171*, E. M. Hackett, K.-H. Schwalbe, and R. H. Dodds, Eds., American Society for Testing and Materials, 1993, pp. 139–157.

ABSTRACT: Lower-bound initiation toughness of A533-B (UNS #K12539) reactor grade steel was determined over the temperature range from 0 to 57°C by using a modified-Charpy specimen. The lower-bound measurements were attained by utilizing the following procedures: (1) dynamic loading, (2) modification of the geometry of the specimen, and (3) axial precompression of the notch. The paper describes in detail the key features of the modified geometry, the method of precompressing the specimens, and the strain gage procedure. The dynamic initiation toughness K_{Id}, which correlates with the lower-bound toughness, was determined by analyzing strain-time records from the specimen. The results from a fractographic analysis were correlated with those from the strain-time analysis. An empirical correlation was developed relating K_{Id} to the energy absorbed (E_{cv}) during the fracture of the specimen. Finally, the lower-bound toughness from this study compared favorably with K_{Ia} and K_{Id} measurements from the same material, established in other programs.

KEY WORDS: Charpy specimen testing, fracture, fracture toughness (lower bound), impact testing, small specimen testing, steel (reactor grade).

Nomenclature

- B Thickness of specimen, mm
- B_n Thickness of specimen at side groove, mm
- K or K_I Opening-mode stress-intensity factor, $\text{MPa}\sqrt{\text{m}}$
- K_{II} Forward-shear-mode stress-intensity factor, $\text{MPa}\sqrt{\text{m}}$
- K_{Ia} Crack-arrest toughness, $\text{MPa}\sqrt{\text{m}}$
- K_{Id} Dynamic initiation toughness, $\text{MPa}\sqrt{\text{m}}$
- K_{IR} Lower-bound initiation toughness, $\text{MPa}\sqrt{\text{m}}$
- J_{Id} Dynamic, elastic-plastic initiation toughness, N/m
- ε_{yy} Strain along yy axis, m/m
- μ Shear modulus, MPa
- ν Poisson's ratio
- δ Axial deformation, mm
- RT_{NDT} Reference nil-ductility temperature, °C

[1] Graduate research assistant, professor, and professor, respectively, Mechanical Engineering Dept., University of Maryland, College Park, MD 20742.

Introduction

Lower-bound fracture toughness is an estimate of the lowest fracture toughness exhibited by a material when subjected to the most severe loading conditions at a specified temperature. The lower-bound toughness, designated K_{IR}, is often based on the lowest values of crack-arrest toughness K_{Ia} and dynamic initiation toughness K_{Id}, to give conservative estimates of fracture toughness. Prior measurements of K_{Ia} and K_{Id} have used large, plate-type fracture specimens at least 50-mm thick [*1,2*]. However, the current understanding of cleavage-fibrous behavior for nuclear reactor vessel steels suggests that a method of cleavage initiation testing with small specimens may provide the same lower-bound data with more efficiency.

The behavior that hinders slow-load, small-specimen testing to determine cleavage initiation toughness is the large amount of scatter observed in the test results [*3–5*]. The degree of scatter indicates that cleavage initiation along the crack front in a small specimen is a rare event. Only with a large number of small-specimen tests do the lowest observed values correspond with the toughness determinations from large specimens with long crack fronts. However, if the likelihood of cleavage initiation is enhanced by notch embrittlement, rapid loading, and geometric constraint, the scatter in the results is reduced significantly, which allows a good possibility for lower-bound toughness determinations. Recently, Dally et al. [*6*] have developed a testing procedure, utilizing relatively small, notched-round-bar specimens, for determining the lower-bound initiation toughness of reactor grade steels. This procedure was implemented by Irwin et al. [*7*] to determine the lower-bound initiation toughness for A533-B reactor grade steel over a range of temperatures in the ductile-to-brittle transition region. The results show less scatter than slow-load testing methods and agree quite well with toughness determinations from larger, plate-type specimens.

This paper presents a new procedure for determining the lower-bound toughness of A533-B reactor grade steel over a limited range of temperatures in the ductile-to-brittle transition region. The specimen employed was a modified form of a standard Charpy V-notch specimen. A critical factor in successful testing for the lower-bound initiation toughness with small specimens is an increase in the severity of the local stress adjacent to the precrack. By increasing these local stresses, it is possible to match more nearly the probability of cleavage initiation sites that occur in large specimens or in components with a long crack front.

The idea of using a Charpy-type specimen to determine K_{Id} is not new. Initial efforts to measure K_{Id} coincided with the development of the instrumented Charpy impact test [*8,9*]. In this approach, it is assumed that the response from strain gages on the tup characterizes the load-time response experienced by the specimen. The method for determining K_{Id} from these load-time traces was described by Radon and Turner [*10*] in 1969. This method was implemented by Server and Tetelman [*11*] to determine K_{Id} for a reactor grade steel. Both investigations employed standard-size Charpy specimens, which had been fatigue precracked and side-grooved. Later efforts [*12*] focused on developing procedures for improving the analysis of the load-time traces, such as the separation of the initiation energy from the total energy absorbed, the interpretation of oscillations on the traces, and the dynamic calibration of the tup/load cell. From the results of these studies, guidelines were developed [*13*] to determine K_{Id} and J_{Id}.

Very recently, MacGillivray and Cannon [*14*] developed a test method, using standard-size, precracked Charpy specimens for determining dynamic fracture toughness for metals. Unlike prior investigations, strain gages were placed on both the striking tup and the specimen. The strain gages on the specimen were calibrated to give the load imposed on the specimen, and this load was used to determine K_{Id}.

It is clear that the standard thickness of the Charpy specimen (10 mm) provides sufficient constraint to simulate plane-strain conditions only for very low toughness. The use of double-thickness Charpy specimens to increase constraint was proposed by Hoyt in 1938 [*15*], but further implementation of this proposal apparently did not occur. Another reason for increasing the thickness is to increase the number of potential cleavage initiation sites along the crack front. Also, studies have shown [*14,16*] that the signal from the instrumented tup does not accurately reflect the dynamic load acting on the specimen due to stress wave effects and specimen vibration. A simple solution is to mount strain gages directly on the specimens. This practice has been widely criticized because of costs and difficulties in implementation. However, instrumented specimens are preferable until a correspondence between the tup response and the specimen response is established.

The specimen used in this study is an oversized Charpy V-notch specimen, which has been modified to provide significant constraint with a large elevation of the flow stress. Impact loading and side-grooving of the specimen serve to further elevate the flow stress. Also, a small precrack is formed at the base of the V-notch by axial precompression. The axial compression closes a small segment at the root of the notch to form a pseudocrack, and upon release of the load, a small natural crack is formed at the tip of this pseudocrack. The precompression process also produces residual tensile stresses at the crack tip, which further elevates the local stresses, increasing severity and enhancing the probability of a lower-bound cleavage initiation.

This paper describes in detail the specimen geometry, the technique for axial precompression, and the testing procedure. Strain-time traces are included to characterize the response of the specimen to the impact loading. A data analysis process, using the strain-time traces, is given for determining K_{Id}, which corresponds to the lower-bound toughness. An interpretation of the fracture behavior of the specimen based on the strain-time response is described. Next, the results of a fractographic analysis are presented and correlated with the fracture behavior apparent in the interpretation of the strain-time traces. An empirical correlation is presented between K_{Id} values and the energy absorbed (E_{cv}) during the fracture of the specimen. Finally, the results for K_{Id} from this study are compared to K_{Ia} and K_{Id} measurements from the same material by independent evaluation programs.

Modified-Charpy Specimen

The purpose of using a modified-Charpy specimen in a dynamic fracture experiment is to match in a relatively small specimen the constraint present in a larger, plate-type specimen, such as a compact-tension specimen of twice the standard thickness. The specimen, defined in Fig. 1, is 64 mm long, 12.7 mm wide, and 19 mm thick. A 2-mm-deep notch, with a 45° included angle, was machined across the thickness of the specimen to produce a crack-plane orientation of *L-S*. The notch was cut with a tip radius of 0.13 mm. Side grooves 1.9 mm deep were machined on both faces of the specimen to increase constraint and to suppress multiple-plane cleavage fracture. Strain gages were mounted at several points on the faces of the specimen to measure the strains imposed during impact loading.

While the specimen is similar in appearance to the standard Charpy V-notch specimen, there are some marked differences. First, the thickness (19 mm) is approximately double that of the standard specimen (10 mm). This added thickness increases specimen constraint and promotes brittle rather than ductile fracture by elevating the flow stress. The inclusion of side grooves on the modified specimens increases the constraint even further. Finally, the radius at the notch tip is 0.13 mm as compared to 0.25 mm for the standard specimen. The sharp notch is employed so that a crack may be formed more easily at the notch tip by axial precompression. Essentially, these modifications transform a standard Charpy V-notch specimen into a fracture specimen of similar size, which can be used to measure fracture initiation toughness.

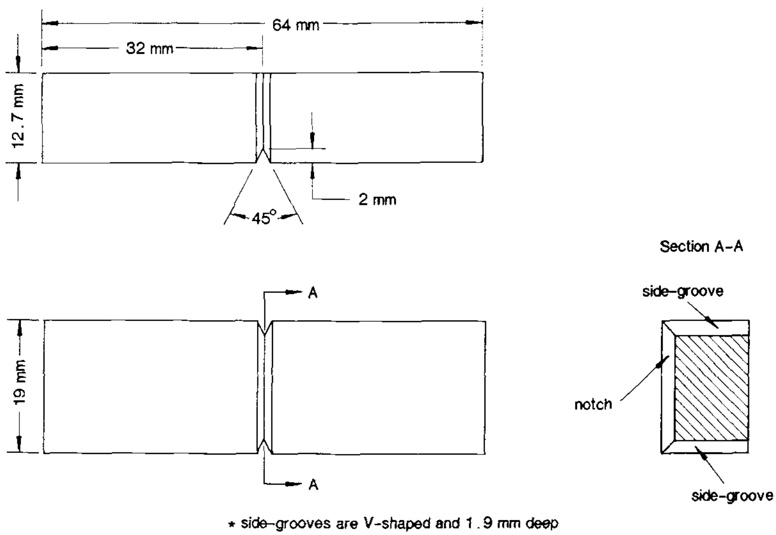

FIG. 1—*Dimensions of the modified Charpy specimen.*

Axial Precompression of Notch

Although the radius of the notch tip is only 0.13 mm, it is not sufficiently sharp to represent a crack and to initiate reliably a cleavage event in a fracture mechanics test. The notch was sharpened before testing by applying an axial compressive stress, which exceeded the yield strength of A533-B steel (482 MPa) by a factor of about 3. Yielding at the center of the specimen caused the sides of the notch to move together, as shown in Fig. 2. Note that the notch closes slightly during deformation, reducing the included angle to about 39°. Also, a short pseudocrack is formed at the base of the notch due to local yielding and the flow of material near the notch. Upon unloading, a short natural crack forms at a shallow angle to the pseudocrack. This crack is produced by the residual tensile stresses that form when the axial compressive load is removed from the specimen.

The effect of axial precompression on the mechanical properties of this steel is not known. During the precompression process, the material in the notch section is strained plastically to levels of 15 to 20%. One would normally expect some degree of work hardening from these large strains, except for the Bauschinger effect. Since the specimen is preloaded in compression and tested in tension, the Bauschinger effect should cause a reduction in the tensile yield strength and softening of the material in the notch section. It is believed these effects are small since the work hardening of low-carbon steels at these strain levels is not pronounced.

In this method of crack sharpening, it is essential to control both the uniformity and the extent of deformation. This control was accomplished by using a compression tube fixture where four specimens were placed back to back (notches facing outward). The amount of deformation, δ, was fixed by the difference between the specimen length and the height of the compression tube. Different amounts of deformation are imposed by varying the specimen length. For these experiments, δ varied from 1 to 1.5 mm.

Test Procedure

General purpose, bonded-foil resistance strain gages were used to measure the strains at selected points on the modified-Charpy specimen during impact. The gages employed had an

A

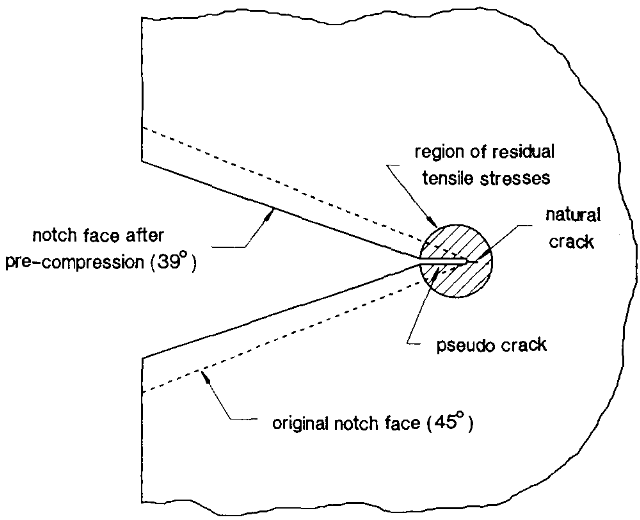

B

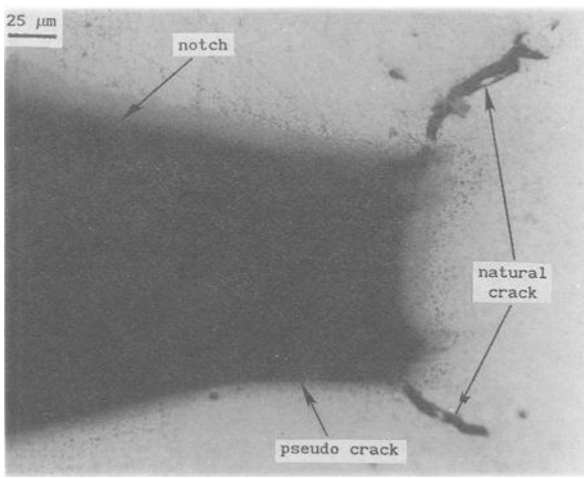

FIG. 2—*Pseudocrack formed due to axial precompression:* (a) *line drawing of pseudocrack;* (b) *polished section of specimen showing pseudocrack.*

active gage length of 1.6 mm and a nominal resistance of 350 Ω. In preliminary experiments, six gages were placed on the specimen at locations defined in Fig. 3*a* and will be referred to as the inclined gages, the 90° gages, and the midspan gages. The results from the initial experiments showed unexpected features in the strain-time records for the inclined and midspan gage sets. The strain indicated by both gage sets experienced pronounced oscillations. The inclined gages were oscillating out of phase, and the midspan gages indicated that the Charpy specimen was not acting like a simple beam in bending because the strains were not of equal magnitude and opposite sign.

To better define the stress-state in the modified Charpy specimen, a two-dimensional, static

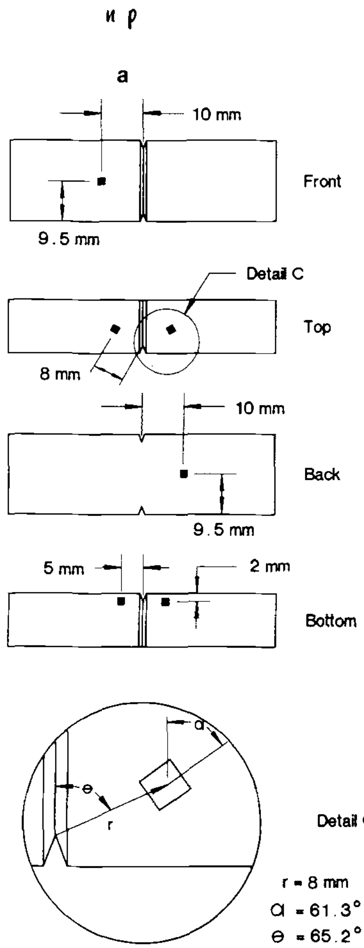

FIG. 3—*Strain gage positions on the modified Charpy specimen:* (a) *initial strain gage positions;* (b) *final strain gage positions.*

photoelastic analysis was conducted. As a result of that analysis, the gage placement was modified as shown in Fig. 3*b*. This gage configuration, which incorporates four 90° gages mounted 5 mm from the crack tip, was used in all subsequent experiments. The gages were connected to a single-active-arm Wheatstone bridge/amplifier unit, capable of 100 kHz, for appropriate signal conditioning.

A Type J, iron-constantan thermocouple was cemented in the notch to measure the testing temperature of the specimen. The output from the thermocouple was measured on a digital thermometer with a resolution of 0.1°C. Twenty-two specimens were tested over a range of temperatures from 0 to 57°C. Dry ice was used to cool the specimens, and a hot plate was used to heat the specimens.

The specimens were tested in a standard, Charpy impact testing machine. The only machine alteration was the installation of larger specimen shields to accommodate the 19-mm-thick specimens. All of the specimens were tested with a full-height hammer drop with an energy of 406 J and an impact velocity of 5.47 m/s. The strain rate in the specimen, estimated as the

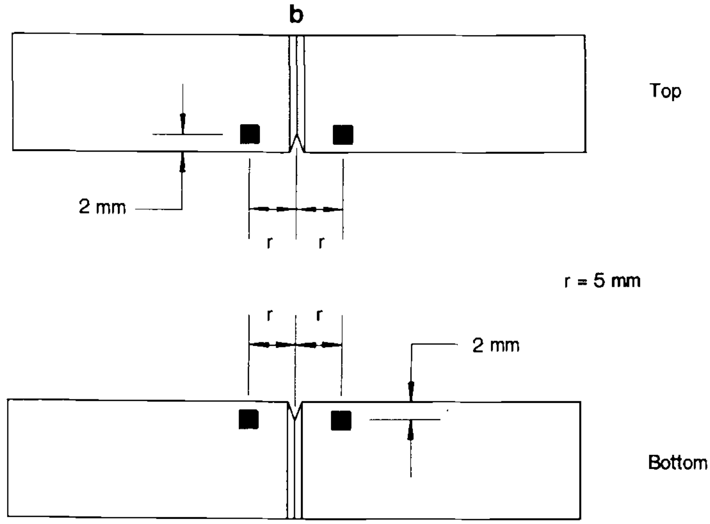

FIG. 3—*continued.*

ratio of the strain at fracture to the loading time to fracture, was about 15 s^{-1}. The capacity of the impact testing machine was sufficient to break all of the specimens over the range of temperatures investigated.

The voltage-time traces from each of the gages were recorded, on a common time base, on a pair of dual-channel, digital storage oscilloscopes. The analog-to-digital converter on each of the oscilloscopes was set to sample at a rate of 200 ns/point. After completing the test, the voltage-time traces were downloaded from the oscilloscope memories to a personal computer for further data processing.

Photoelastic Analysis

A static, two-dimensional photoelastic test was performed to determine the stress-state in the modified-Charpy specimen. The scale-model (three times actual size) was cut from a 6-mm-thick sheet of polycarbonate. The finished model was 191 mm long and 38 mm wide, with a 45°, 5-mm-deep notch. A 1-mm-deep saw cut was made at the base of the notch to simulate a crack.

The model, with a span of 120 mm, was placed in a circular polariscope and loaded in three-point bending. Light-field and dark-field fringe patterns representing the stress distribution are shown in Fig. 4. The fringe patterns show a complex, two-dimensional state of stress in the specimen rather than a uniaxial state of stress associated with three-point bending of a beam. Note in particular the absence of a neutral axis, which would appear as a straight horizontal fringe of zero order near the centerline of the specimen. The absence of the neutral axis confirmed that the specimen could not be characterized with simple beam theory. Since the usual analysis of the data from the midspan gages is based upon simple beam theory, this approach was discontinued.

Data from the light-field and dark-field fringe patterns included the fringe order N and the corresponding locations (x and y positions), relative to the origin at the crack tip, from about 160 data points in a region near the crack tip. Using a mixed-mode form of a series expansion for the stresses [*17*] and an over-deterministic solution [*18*], the unknown coefficients A_0, B_0,

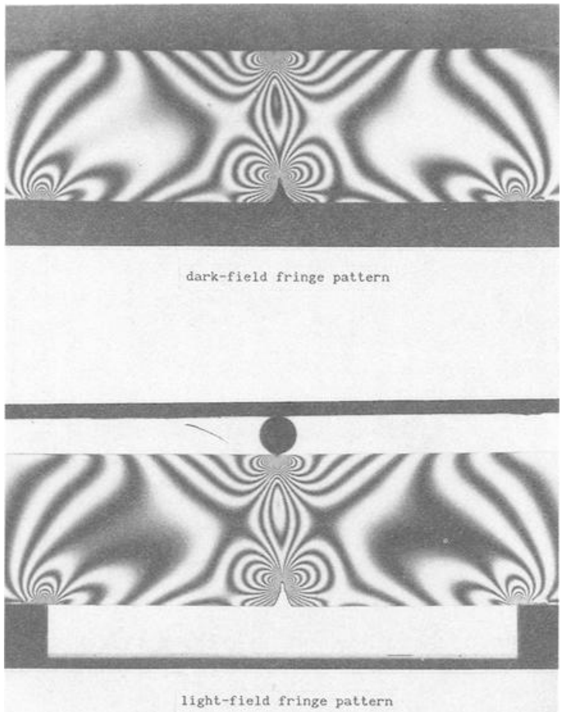

FIG. 4—*Isochromatic fringe patterns for the photoelastic model.*

C_0, etc. were determined. The two coefficients of main interest are A_0 and C_0 because they are related to the stress-intensity factors K_I and K_{II} by

$$K_I = A_0\sqrt{2\pi}$$

and

$$K_{II} = C_0\sqrt{2\pi} \tag{1}$$

It was observed that K_{II} was negligible compared to K_I, which confirms that the stress state at the crack tip was predominantly opening mode. The opening-mode coefficients A_0, B_0, and A_1, determined from the isochromatic patterns, were used in developing the analysis technique for determining K from strain-time traces from the 90° gages.

The photoelastic results obtained in this experiment agreed quite well with results by Corren et al. [*19*] that evaluated a standard Charpy V-notch geometry subjected to static and dynamic loadings. The results indicated differences between the dynamic and static loadings, due mainly to stress wave effects. Unfortunately, the scope of this investigation did not permit a dynamic photoelastic study of the modified-Charpy geometry, which is clearly needed to explain the oscillations occurring in the inclined gages as the stress field develops with time. Since the oscillatory behavior of these gages could not be explained by a static analysis, the use of the inclined gages was discontinued. The results obtained from this photoelastic analysis led to the adoption of the 90°-strain gage placement defined in Fig. 3.

Initiation Toughness Determinations from Strain Gages

The method used to determine the dynamic initiation toughness K_{Id} from strain-time records is based upon a static analysis. The analysis, developed by Dally and Sanford [20], uses a series representation of the generalized Westergaard equations to describe the strain field in the vicinity of a crack. The governing equation has the form

$$2\mu\varepsilon_{yy} = A_0 r^{-1/2}\{(k)\cos(\theta/2) + (1/2)\sin(\theta)\sin(3\theta/2)\} + B_0\{k - 1\}$$
$$+ A_1 r^{1/2}\cos(\theta/2)\{k - \sin^2(\theta/2)\} + B_1 r\{k - 1\}\cos(\theta) \quad (2)$$

where $k = (1 - \nu)/(1 + \nu)$ and K_I is given by Eq 1. With $\nu = 0.300$ for steel and $\theta = 90°$, Eqs 1 and 2 are combined to give

$$2\mu\varepsilon_{yy} = 0.2929 K_I r^{-1/2} - 0.4615 B_0 + 0.02720 A_1 r^{1/2} \quad (3)$$

Note that the influence of the B_1 term has vanished from Eq 3. To a first approximation, the contributions from the r^0 and $r^{1/2}$ terms are neglected by setting $B_0 = A_1 = 0$. Employing this approximation, and with $r = 5$ mm, Eq 3 can be rearranged as

$$K_I = 0.4828\mu\varepsilon_{yy} \quad (4)$$

A correction factor for the effect of side grooves is given by the relation

$$C_g = [B/B_n]^{1/2} = 1.118 \quad (5)$$

for $B = 19$ mm and $B_n = 15.2$ mm. Adjusting Eq 4 with C_g gives

$$K_I = 0.5397\mu\varepsilon_{yy} \quad (6)$$

where $\mu = 79.5$ GPa and K_I has units of MPa$\sqrt{\text{m}}$. If the strain ε_{yy} is the strain measured at initiation (ε_0), then Eq 6 gives the dynamic initiation toughness K_{Id}.

To develop Eq 6, it was necessary to arbitrarily assume the B_0 and A_1 coefficients were zero. To test the assumption, values of B_0 and A_1 determined from the photoelastic study were normalized with respect to K_I and inserted into Eq 3 to obtain

$$2\mu\varepsilon_{yy} = 0.2929 K_I r^{-1/2} + 0.3842 K_I + 0.1874 K_I r^{1/2} \quad (7)$$

For $r = 5$ mm, Eq 7 simplifies to

$$2\mu\varepsilon_{yy} = 4.142 K_I + 0.3975 K_I \quad (8)$$

The first term in Eq 8 is due to A_0, and the second term represents the error associated with neglecting the B_0 and A_1 coefficients. Rearranging Eq 8 and adjusting for the effect of side grooves gives

$$K_I = 0.4926\mu\varepsilon_{yy} \quad (9)$$

where K_I has units of MPa$\sqrt{\text{m}}$. A comparison between Eqs 6 and 9 reveals that the error introduced by neglecting the B_0 and A_1 coefficients is 9.6%. This result shows that the two-parameter solution of Eq 6 (A_0 and B_1) is capable of approximating a four-parameter solution (A_0,

A_1, B_0, and B_1), with a relatively small error. Even though Eq 6 overestimated K_I, this equation was used for simplicity and to offset partially other effects that were neglected, such as plastic behavior at the crack tip.

All of the equations were developed for static loading, and the applicability of this approach for dynamic loading may be questioned. Finite element studies conducted by Nakamura et al., concerning the determintation of J_{Id} for both notched-round-bar [21] and three-point-bend [22] specimens, indicate that the differences between static and dynamic solutions are very small for the loading rates present in the modified-Charpy specimens. Similarity in static and dynamic relations between K_I and strain has been verified by several investigations conducted at the University of Maryland [6,7,23,24], which employed static equations to predict K_{Id} successfully. The results of this study appear to agree with previous conclusions.

Strain-Time Records

Twenty-two specimens fabricated from A533-B steel were tested over a temperature range from 0 to 57°C. Of this group, 16 specimens failed with extensive quasicleavage and provided strain-time data suitable for a valid (acceptable) K_{Id} determination. The voltage-time records from the four gages on each specimen were imported into a commercial spreadsheet program, and strain-time traces were generated for each gage.

A preliminary observation of the traces indicated the mechanism of failure. Two types of failures were observed: (1) small amounts of ductile tearing followed by predominantly cleavage, or (2) extensive ductile tearing with little or no cleavage. The first mechanism yields data that permits a valid determination of K_{Id} from Eq 6, but the second mechanism does not.

Examples of valid and invalid strain-time traces are shown in Figs. 5 and 6, respectively. Three traces are shown in each figure: (1) the average of the bottom gages, (2) the average of

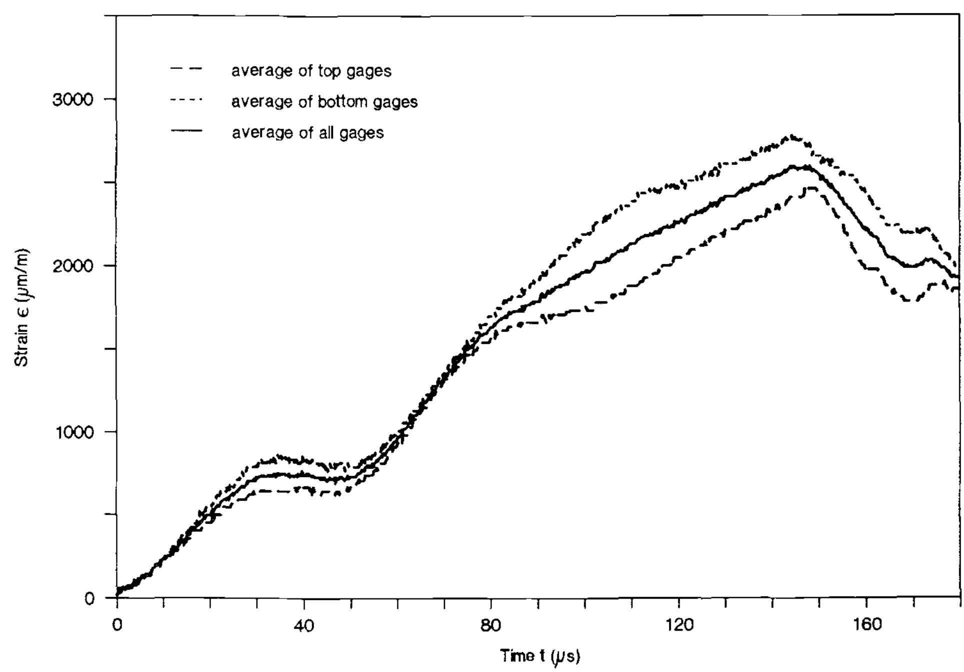

FIG. 5—*Strain-time traces for a valid test.*

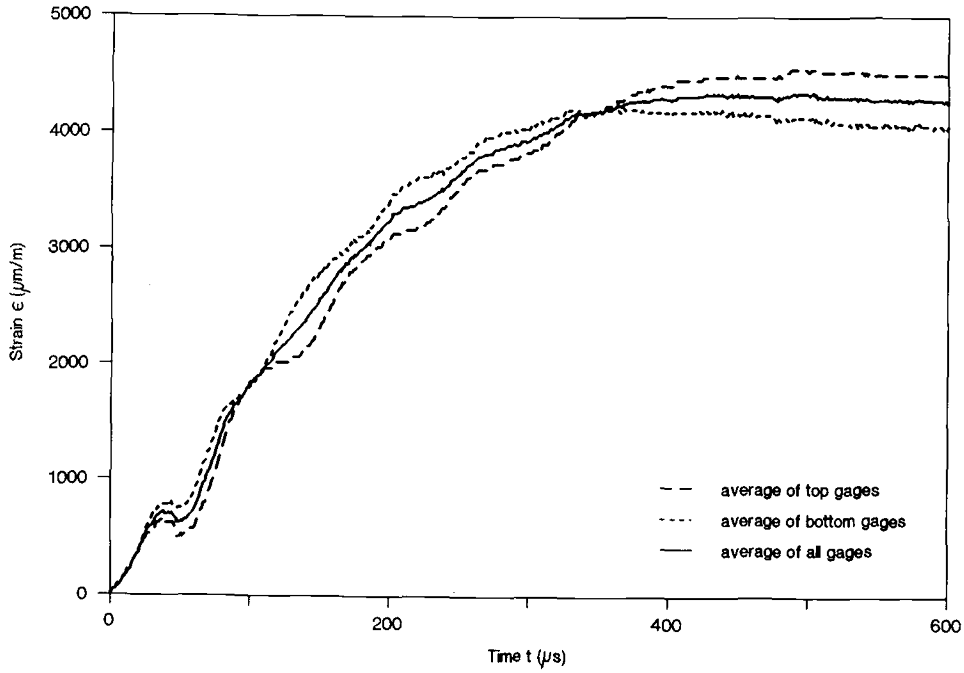

FIG. 6—*Strain-time traces for an invalid test.*

the top gages, and (3) the average of all the gages. For the valid test in Fig. 5, a single peak value of strain marked the initiation of the crack in the specimen. The strain increased monotonically with time for about 140 μs after the gage initially began to respond, with reasonable correspondence between the top and bottom gage sets. The small oscillations superimposed on the monotonic rise were attributed to stress wave effects and specimen vibration, resulting from the impact load. The response of all four gages to crack initiation was nearly simultaneous, and the strain decreased rapidly after initiation.

For the invalid test in Fig. 6, the strain monotonically increased to a very high value ($\approx$4300 $\mu\varepsilon$) and remained constant for several hundred microseconds. Again, close correspondence was noted between the gage sets. An observation of the fracture surface after the test indicated extensive ductile tearing (that occurs at low velocity) with almost no cleavage. These observations of the strain-time traces allowed immediate classification of specimens failing by primarily brittle cleavage from those failing due to ductile tearing (hole joining).

The maximum strain from the strain-time traces was used as the failure strain ε_0 for the 16 qualifying tests. Values of K_{Id} were calculated from the average of the peak values of the individual strain-time traces. The values of K_{Id} determined in this manner are shown as a function of temperature in a later section.

Fractographic Analysis

A fractographic analysis was conducted to verify that the values of initiation toughness determined with a modified-Charpy specimen were lower-bound values. To attain a minimum value of initiation toughness, the fracture surface must consist primarily of cleavage facets with very little prior ductile tearing (crack extension by microvoid coalescence). The features of the fracture surface were studied by using a scanning electron microscope (SEM). By analyzing the fractographs from the SEM in conjunction with the strain-time traces from the strain gages, the validity of the K_{Id} measurement was determined.

Common features appeared on all of the fracture surfaces from specimens giving valid K_{Id} results. From a macroscopic analysis, it was evident that the surfaces are generally flat, with the crack extension remaining in the plane of the side grooves. Microscopically, however, the typical fractograph (see Fig. 7) showed different mechanisms of fracture. The initial mechanism of failure was by ductile tearing, which appears as a thin, nearly uniform region extending along the base of the notch and, to a lesser extent, along the side grooves. As the fracture front moved inward from the base of the notch, cleavage was initiated from one or more sites along the crack front. A predominantly cleavage fracture extended over almost the entire fracture surface. However, the mode of failure was not pure cleavage because cleavage facets were surrounded by ductile tear ridges. This type of behavior is termed quasicleavage. A third failure mechanism occurred toward the end of the fracture, after the loss of constraint, and was due to shear rather than tensile stresses. The boundary between the quasicleavage and the shear regions is clearly seen at the bottom of the figure.

All of the specimens that provided data suitable for determining K_{Id} exhibited the features described in the previous paragraph. However, the fracture surface features changed with temperature. Representative fractographs, presented in Fig. 8, demonstrate the effect of temperature on the surface features. Fractographs from tests conducted at low (0°C), intermediate (27°C), and high (49°C) temperatures are included in the figure. It is observed that some characteristic features of the fracture surface changed with temperature. As temperature increased, the fracture generally became more ductile, as indicated by a widening of the initial tearing region and the increase in the number and area of tear ridges surrounding the cleavage facets. Also, the time to failure increased with increasing temperature, ranging from 79 μs at 0°C to

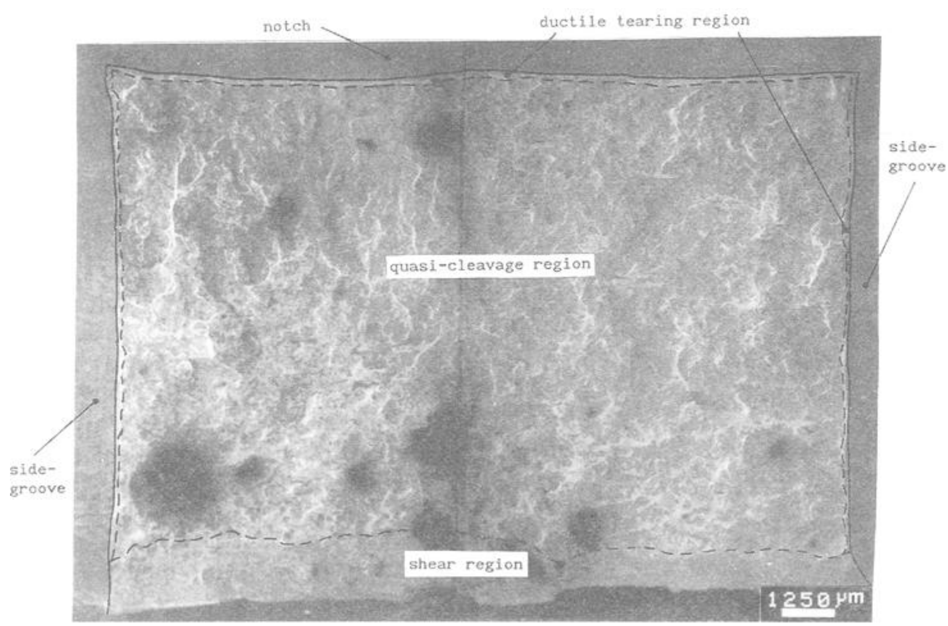

FIG. 7—*Fracture surface features for a valid test.*

147 μs at 49°C. It is believed that the increased time to failure is due to the greater amount of initial ductile tearing, which propagates at a much slower rate than cleavage fracture. This type of behavior is expected for steels exhibiting a ductile-to-brittle transition region. The gradual change from cleavage to hole joining, on a microscopic scale, produces an increase in fracture toughness with temperature.

Finally, a fractograph of a specimen that did not provide an acceptable K_{Id} value is shown in Fig. 9, and the corresponding strain-time traces for this specimen are presented in Fig. 6. The fracture surface appeared dull and exhibited primarily ductile tearing features (void formation and ductile hole joining) with no significant signs of cleavage. The failure was, therefore, classified as ductile rather than cleavage. Even with this ductile failure, the side grooves suppressed the formulation of appreciable shear lips, which commonly occur on standard Charpy V-notch specimens. This surface, and the corresponding strain gage records, should be contrasted with the results from the valid test shown in Figs. 7 and 5.

Discussion

Results for the initiation toughness of A533-B steel over the temperature range from 0 to 57°C are presented in Fig. 10 for both the modified-Charpy specimens and the notched-round-bar specimens. Included in this figure is additional data for K_{Ia} and K_{Id} due to independent measurements.[2] The data from sixteen valid tests agree well with other lower-bound determinations. The line labeled K_{IR} is the lower limit of fracture toughness, as given by the American Society of Mechanical Engineers (ASME) [*25*]. The modified-Charpy specimens tested at low temperatures produced results for K_{Id} that were slightly lower than the K_{IR} curve, indicating that the modified-Charpy test method gives a slightly conservative measure of K_{Id}. As seen from the figure, the tendency of previous K_{Ia} and K_{Id} determinations was to predict a lower toughness than the crack-arrest toughness measured by larger, compact-tension (CT) specimens given by the broken line labeled K_{Ia}. The modified Charpy test results match this tendency.

The following two factors were not considered in the analysis of the modified-Charpy data: (1) the influence of the B_0 and A_1 terms on the strain field, and (2) an adjustment for the plastic zone at the crack tip. The main contribution to the difference between Eqs 6 and 9 results from neglecting the B_0 coefficient, which is equivalent to neglecting the strain due to a uniform stress component parallel to the crack tip (commonly denoted σ_{0x}). The effect of considering the B_0 term in the analysis would have tended to lower the measured K_{Id} values. Conversely, any plastic-zone adjustment would tend to elevate the K_{Id} determinations. It is believed that the contributions from these effects tend to partially offest each other, resulting in useful K_{Id} determinations.

The use of strain gages on surveillance specimens is a disadvantage due to the time needed for gage mounting and the instrumentation required for recording the dynamic gage signals. Other parameters that were easier to measure were sought, from which K_{Id} could be inferred. The most common parameter is the energy absorbed (E_{cv}), as indicated on the Charpy testing machine. The relationship between E_{cv} and K_{Id} is presented in Fig. 11. Included in the figure are two of the more common empirical correlations, developed by Barsom [*26*] and Sailors and Corten [*27*] from standard Charpy V-notch specimens. The empirical correlation developed for the modified-Charpy specimen is given as

$$K_{Id} = 13\sqrt{E_{cv}} \tag{10}$$

[2]Note that the temperature in Fig. 10 is relative to the RT_{NDT}. For this particular A533-B steel, $RT_{NDT} = -2$°C.

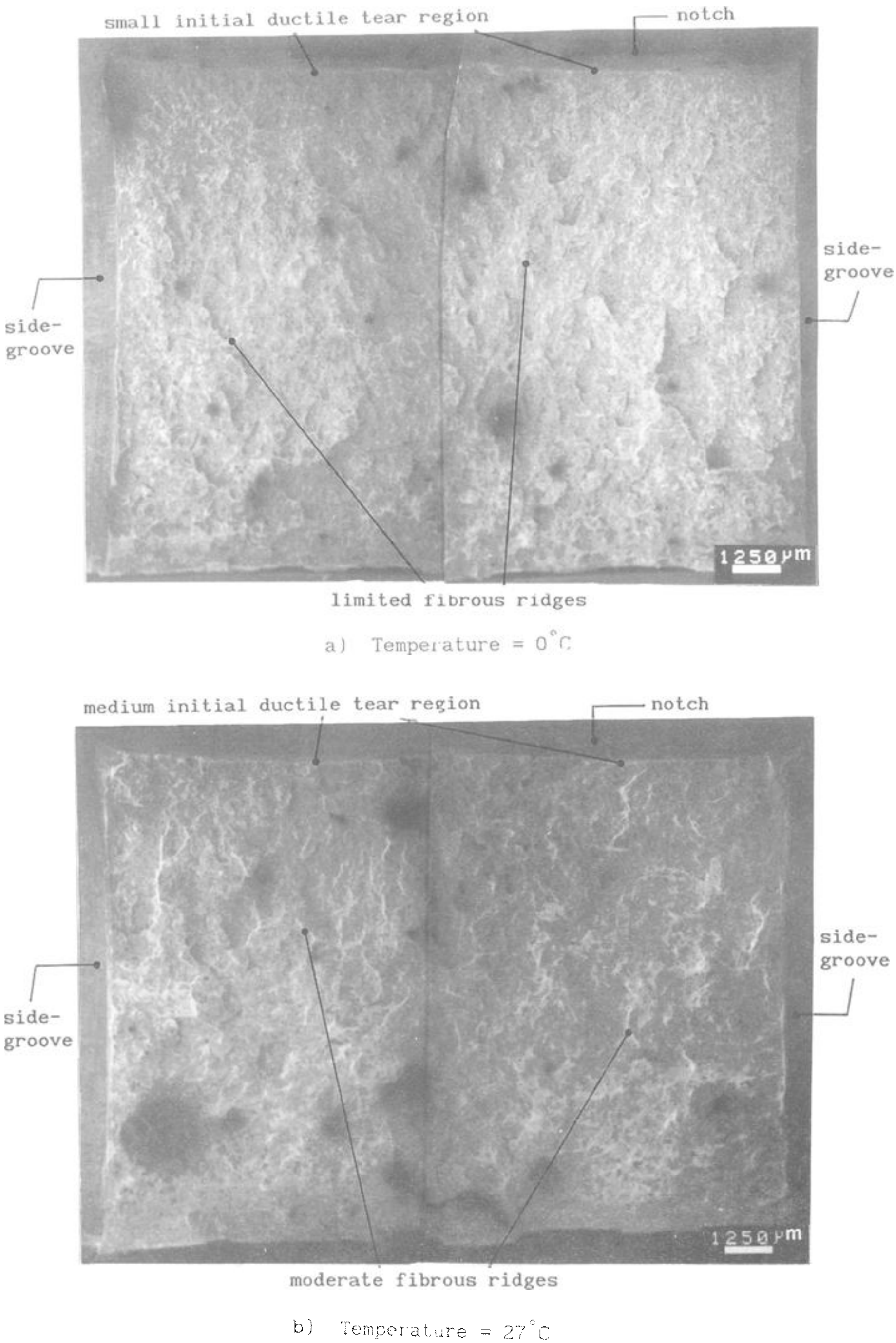

FIG. 8—*Effect of temperature on fracture surface features:* (a) *temperature = 0°C;* (b) *temperature = 27°C;* (c) *temperature = 49°C.*

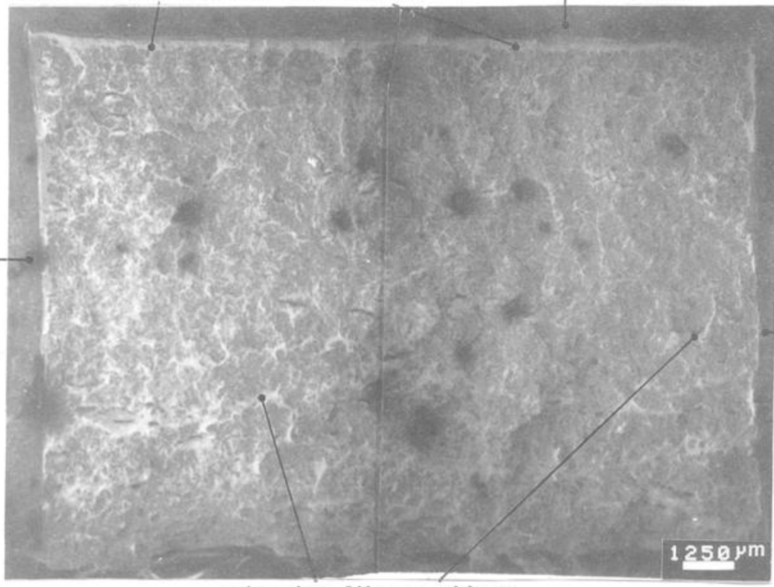

c) Temperature = 49°C

FIG. 8—*continued.*

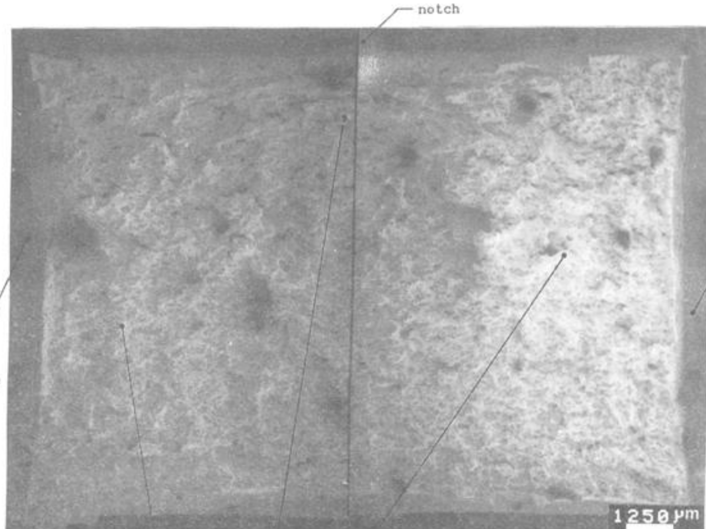

FIG. 9—*Fracture surface features for an invalid test.*

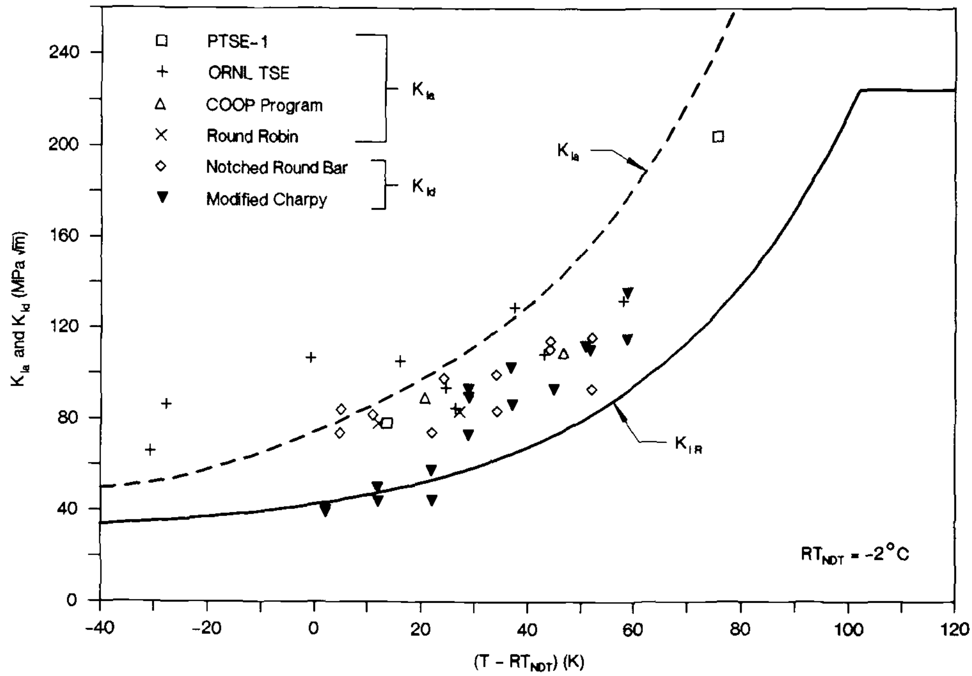

FIG. 10—*Comparison of lower-bound toughness determinations for A533-B reactor grade steel.*

where K_{Id} and E_{cv} have units of MPa$\sqrt{\text{m}}$ and J, respectively. Since the Barsom and Sailors-Corten equations were only intended for the lower part of the transition range, the equations are presented as broken lines beyond the limit of applicability ($\approx$54 J). A reason for the discrepancies between the K_{Id} predictions is that the previous correlations were developed for standard Charpy V-notch specimens, while Eq 10 was determined from modified-Charpy specimens. Clearly the energies absorbed by Charpy V-notch specimens differ from the energies absorbed by the modified-Charpy specimens.

The amount of precompression required to minimize ductile tearing is not known. Currently, the amount of axial precompression imposed on a specimen of a given material is determined from experience and observation of the degree of tearing observed in invalid tests. In general, a greater amount of precompression is required as temperature increases (that is, as the material exhibits higher toughness). Results from notched-round-bar testing indicated that excessive precompression produced K_{Id} values which were too low. It is conceivable that the conservative K_{Id} values from modified-Charpy specimens at low temperatures were due to excessive precompression for the test temperature. Clearly, a systematic study of the effect of the amount of axial precompression on both lower-bound toughness and the extent of crack extension by hole joining and by cleavage initiation is needed.

Conclusion

The results of this investigation indicate that modified-Charpy specimens can be employed to determine dynamic initiation toughness of reactor grade steels over an important range of temperatures (0 to 57°C). The toughness measurements agree with other lower-bound deter-

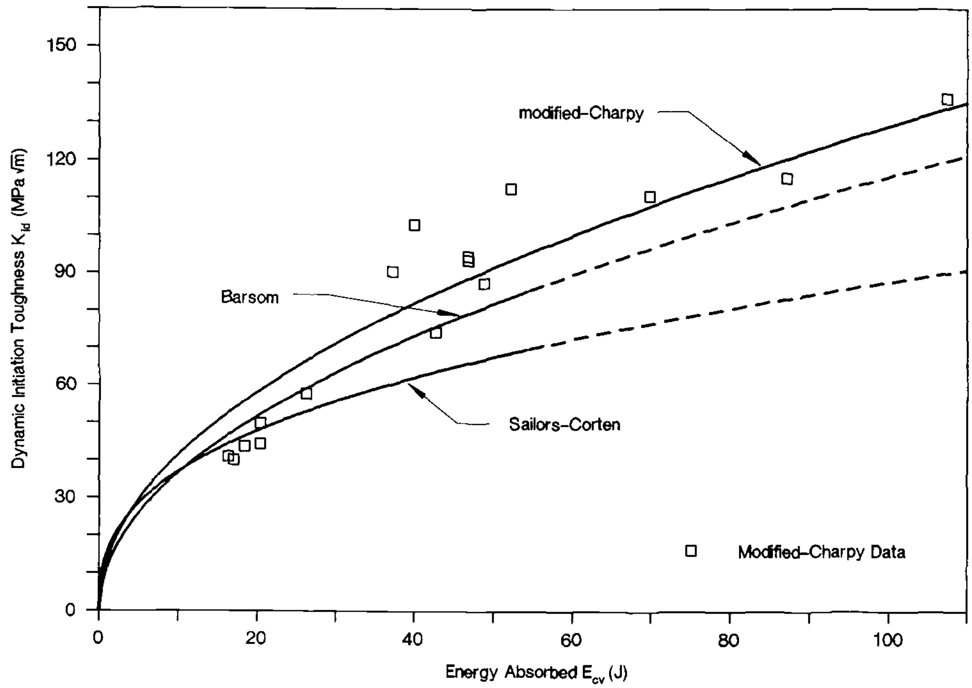

FIG. 11—*Comparison of* $K_{Id} - E_{cv}$ *correlations for Charpy-type specimens.*

minations from both crack-arrest (K_{Ia}) testing and rapid-load-initiation (K_{Id}) testing. The advantages of the modified-Charpy specimen are: (1) the small specimen size, which conserves material and simplifies handling, (2) the relatively low cost for machining the specimens, and (3) the possibility of automation of test procedures. These factors make the method attractive for use in a "hot-cell" environment to determine the properties of steels damaged by radiation.

Acknowledgments

The authors would like to thank X-J. Zhang for providing assistance in operating the SEM, and Y-M. Chen for his assistance with the photoelastic analysis. Research funding for this project was provided by Martin Marietta Energy Systems (ORNL) under Contract No. 19X-07778C.

References

[1] Crosley, P. B. and Ripling, E. J., "Crack Arrest Fracture Toughness of A-533 Class 1 Pressure Vessel Steel," HSSTP-TR-8, Materials Research Laboratory, Glenwood, IL, March 1970.

[2] Shabbits, W. O., "Dynamic Fracture Toughness Properties of Heavy Section A533 Grade B Class 1 Steel Plate," WCAP-6723, Westinghouse Electric Corp., Pittsburgh, PA, December 1970.

[3] Iwadate, T., Tanaka, Y., Ono, S., and Watanabe, J., "An Analysis of Elastic Plastic Fracture Toughness Behavior for J_{Ic} Measurements in the Transition Region," *Elastic-Plastic Fracture: Second Symposium, Vol. II: Fracture Resistance Curves and Engineering Applications, ASTM STP 803*, C. F. Shih and J. P. Gudas, Eds., American Society for Testing and Materials, Philadelphia, 1983, pp. 531-561.

[4] Merkle, J. G. "An Examination of the Size Effects and Scatter Observed in Small-Specimen Cleavage Fracture Toughness Testing," ORNL Report TM-9088, NUREG CR-3672, Oak Ridge National Lab., Oak Ridge, TN, 1984.
[5] Landes, J. D. and Schaffer, D. H., "Statistical Characterization of Fracture in the Transition Region," *Fracture Mechanics: 12th Conference, ASTM STP 700,* American Society for Testing and Materials, Philadelphia, 1980, pp. 368–382.
[6] Dally, J. W., Zhang, X-J., and Irwin, G. R., "Determining Lower Bound Dynamic Initiation Toughness from Notched Round Bars," *Symposium Dynamic Fracture Mechanics for the 1990's, PVP—Vol, 160,* H. Homma, D. Shockey, and G. Yagawa, Eds., American Society of Mechanical Engineers, New York, NY, 1989, pp. 47–54.
[7] Irwin, G. R., Dally, J. W., Zhang, X-J., and Bonenberger, R. J., "Lower Bound Initiation Toughness of A533-B Reactor Grade Steel," *Symposium on Rapid Load Fracture Testing,* San Francisco, CA, April 1990, ASTM, Philadelphia, 1990.
[8] *Impact Testing of Metals, ASTM STP 466,* ASTM, Philadelphia, 1970.
[9] *Instrumented Impact Testing, ASTM STP 563,* American Society for Testing and Materials, Philadelphia, 1974.
[10] Radon, J. C. and Turner, C. E., "Fracture Toughness Measurements by Instrumented Impact Test," *Engineering Fracture Mechanics,* Vol. 1, 1969, pp. 411–428.
[11] Server, W. L. and Tetelman, A. S., "The Use of Pre-Cracked Charpy Specimens to Determine Dynamic Fracture Toughenss," *Engineering Fracture Mechanics,* Vol. 4, 1972, pp. 367–375.
[12] Ireland, D. R., "Procedures and Problems Associated with Reliable Control of the Instrumented Impact Test," *Instrumented Impact Testing, ASTM STP 563,* American Society for Testing and Materials, Philadelphia, 1974, pp. 3–29.
[13] Server, W. L., "Impact Three-Point Bend Testing for Notched and Precracked Specimens," *Journal of Testing and Evaluation,* Vol. 6, No. 1, 1978, pp. 29–34.
[14] MacGillivray, H. J. and Cannon, D. F., "The Development of Standard Methods for Determining the Dynamic Fracture Toughness of Metallic Materials," *Symposium on Rapid Load Fracture Testing,* San Francisco, CA, April 1990, ASTM, Philadelphia.
[15] Hoyt, S. L., "Notched-Bar Testing and Impact Testing," *Proceedings, ASTM, Part II,* Vol. 38, ASTM, Philadelphia, 1938, pp. 141–156.
[16] Venzi, S., Priest, A. H., and May, M. J., "Influence of Inertial Load in Instrumented Impact Tests," *Impact Testing of Metals, ASTM STP 466,* American Society for Testing and Materials, Philadelphia, 1970, pp. 165–180.
[17] Chona, R., "The Stress Field Surrounding the Tip of a Crack Propagating in a Finite Body," Ph.D. dissertation, University of Maryland, College Park, MD, 1987.
[18] Sanford, R. J. and Dally, J. W., "A General Method for Determining Mixed-Mode Stress Intensity Factors from Isochromatic Fringe Patterns," *Engineering Fracture Mechanics,* Vol. 11, 1979, pp. 621–633.
[19] Corran, R. S. J., Mines, R. A. W., and Ruiz, C., "Elastic Impact Loading of Notched Beams and Bars," *International Journal of Fracture,* Vol. 23, 1983, pp. 129–144.
[20] Dally, J. W. and Sanford, R. J., "Strain-Gage Methods for Measuring the Opening-Mode Stress-Intensity Factor, K_I," *Experimental Mechanics,* Vol. 27, No. 4, 1987, pp. 381–388.
[21] Nakamura, T., Shih, C. F., and Freund, L. B., "Elastic-Plastic Analysis of a Dynamically Loaded Circumferentially Notched Round Bar," *Engineering Fracture Mechanics,* Vol. 22, No. 3, 1985, pp. 437–452.
[22] Nakamura, T., Shih, C. F., and Freund, L. B., "Analysis of a Dynamically Loaded Three-Point-Bend Ductile Fracture Specimen," *Engineering Fracture Mechanics,* Vol. 25, No. 3, 1986, pp. 323–339.
[23] Dally, J. W. and Barker, D. B., "Dynamic Measurements of Initiation Toughness at High Loading Rates," *Experimental Mehcanics,* Vol. 28, No. 3, 1988, pp. 298–303.
[24] Dally, J. W., Fourney, W. L., and Bonenberger, R. J., "Short Bar Measurements of Dynamic Initiation Toughness," *Dynamic Fracture Mechanics for the 1990's, PVP—Vol. 160,* H. Homma, D. Shockey, and G. Yagawa, Eds., American Society of Mechanical Engineers, New York, NY, 1989, pp. 39–46.
[25] Barsom, J. M. and Rolfe, S. T., *Fracture and Fatigue Control in Structures—Applications of Fracture Mechanics,* 2nd ed., Prentice-Hall, Inc., Englewood Cliffs, NJ, 1987, pp. 514–525.
[26] Barsom, J. M., "The Development of AASHTO Fracture Toughness Requirements for Bridge Steels," *Engineering Fracture Mechanics,* Vol. 7, No. 3, 1975, pp. 281–302.
[27] Sailors, R. H. and Corten, H. T., "Relationship Between Material Fracture Toughness Using Fracture Mechanics and Transition Temperature Results," *Fracture Toughness, Proceedings of the 1971 National Symposium on Fracture Mechanics, Part II, ASTM STP 514,* American Society for Testing and Materials, Philadelphia, 1972, pp. 164–191.

DISCUSSION

E. M. Hackett[1] *(written discussion)*—The transition time [*22*] should be calculated for the modified-Charpy specimen. Based on the presented times to fracture initiation (≈ 150 μs), it could be that the initiation is occurring in an inertial or kinetic energy dominated timeframe before the transition time. If such is the case, the fields controlling fracture would not be equivalent to the static case, and inertial considerations would have to be added to the K/J analysis.

Authors' Closure—Nakamura et al. [*22*] have presented a formula for the transition time of a standard ASTM three-point-bend specimen. This relation can be altered for a modified-Charpy specimen as

$$t_T = 23.3(S^*/S_s)H/c_0$$

where H is the width of the specimen, c_0 is the longitudinal wave speed in the bar, S_s is the shape factor of the standard ASTM specimen, and S^* is the shape factor of the modified-Charpy specimen. Using this equation gives the transition time for the modified-Charpy specimen as 36 μs. It is generally assumed that inertial effects can be neglected for times longer than $2t_T$, or 72 μs for the modified-Charpy specimen. Since crack initiations usually occurred around 150 μs, inertial considerations may be neglected.

The appearance of the strain-time records gives further evidence for employing a static analysis. As shown in Fig. 5, the strain-time trace exhibits a monotonic rise for about 150 μs, with the superimposed oscillations at 35 and 80 μs. These oscillations indicate the presence of inertial effects in the specimen. Note the reduced amplitude of the second oscillation as compared to the first, which demonstrates that inertial effects in the specimen are decreasing. Clearly all oscillations have vanished at the time of crack initiation at ≈ 150 μs. Therefore, the determination of K_{Id} by a static analysis seems appropriate.

[1] David Taylor Research Ctr., Code 2814, Annapolis, MD 21402.

Cedric E. Turner[1] *and Leda Braga*[1]

Energy Dissipation Rate and Crack Opening Angle Analyses of Fully Plastic Ductile Tearing

REFERENCE: Turner, C. E. and Braga, L., "**Energy Dissipation Rate and Crack Opening Angle Analyses of Fully Plastic Ductile Tearing,**" *Constraint Effects in Fracture, ASTM STP 1171,* E. M. Hackett, K.-H. Schwalbe, and R. H. Dodds, Eds., American Society for Testing and Materials, 1993, pp. 158–175.

ABSTRACT: The effects of geometry on the J_R-curve for ductile tearing toughness of a titanium alloy are investigated in a series of notch bend tests taken to large amounts of growth in the fully plastic regime. For this material there is a remarkably small effect of thickness over a nine-fold range from 4 to 35 mm, but for thicknesses of 17.5 mm and greater, the R-curves are lower for wider specimens. The results are then analyzed in terms of energy dissipation rate and crack opening angle. Both terms fall rapidly just after initiation and pass to a near steady-state regime after about 10% growth. In steady-state tearing the crack opening angle is substantially constant with growth, while the steady-state dissipation rate can be split into areal and volumetric components.

It is concluded that stable ductile tearing of this material at limit load conditions is controlled by processes of plastic deformation that, if expressed as conventional R-curves, show a definite dependence on width. However, interpretation by either crack opening angle or dissipation rate model is sensitive to how the data are analyzed. The dependence of the models on the degree of plane stress or plane strain is not yet clear so that extrapolation to other sizes of specimens is still uncertain.

KEY WORDS: toughness, R-curves, stable crack growth, crack opening angle, titanium

The object of fracture mechanics is to separate out at the macro-scale the inherent physical attributes of fracture from the effects of the geometry of a component. This is typified in linear elastic fracture mechanics (LEFM) by the concept of the plane-strain fracture toughness. G_{Ic} or K_{Ic}, which in principle gives a measure of the effective surface energy, $\gamma + w_p$, where γ is the true surface energy and w_p the very local plastic work that must be done before separation can occur on a macro-scale [*1,2*]. The same concept of determining a macro-fracture toughness has been carried over into elastic plastic fracture mechanics (EPFM). Most EPFM tests are conducted in general or uncontained yield so that meaning is encompassed within the term EPFM here. In EPFM the difficulty is in separating out the plastic work remote from the fracture from the Irwin-Orowan component, w_p, inherent to the fracture.

Two separate aspects of toughness soon emerged in EPFM as indeed they had in LEFM for other than plane strain, a value related to the initiation of tearing from a preexisting sharp crack and a subsequent measure of the continued resistance to tearing, a so-called resistance or R-curve. The measure of toughness used here will at first be J [*3*].

The object of the present work is to explore the geometry dependence of the J_R-curve for tearing toughness of metals, ductile in the micro-mode, when taken to amounts of growth large relative to the original ligament. The strong but varied pattern of geometry dependence of

[1] Professor and lecturer, Mechanical Engineering Dept., Imperial College, London, United Kingdom SW7 2BX.

conventional J_R-curves has been pointed out several times [*4–7*]. Some of these patterns were brought into a more unified perspective by examining the energy dissipation rate [*8*]. In this paper the data used will be from two series of tests on a particular titanium alloy, one at several thicknesses, another at various widths. The overall view that emerges from this and previous related studies is that the so-called-J-based R-curve simply reflects the accumulated work done and that the various different geometric trends seen in the literature are most likely to be understood in terms of the energy dissipation rate.

The paper is divided into three parts: (a) an overview of the new terms introduced and the J_R behavior patterns previously seen; (b) the experimental data; (c) models into which the results might fit.

It is important to note that all results discussed relate to the high in-plane constraint cases of deep notch bending or compact tension. No implication is made for results in either tension or shallow notch bending where loss of in-plane constraint is generally recognized. It should also be noted that the present work is not directly concerned with initiation of tearing for which J_{Ic} is the formalized measure. It is well known that it is difficult to define a precise measure of the initiation event other than in a practical though arbitrary way, such as ASTM Method for J_{Ic}, a Measure of Fracture Toughness (E 813-87). Here J_i is used to denote toughness "at" initiation, but a precise definition of J_i is not pursued.

An Overview of the Energy Dissipation Rate

As an aid to explaining the present viewpoint, an overview of the new terms introduced, see Refs *6–12*, is offered at this stage, in terms of conventional J notation. There are two steps; more exact definitions of the new terms are given later.

First, if no distinction is made between the various definitions of J_R found in the literature, then dissipation rate is related to $(b/\eta)(dJ/da)$, where b is ligament size and η is the factor that relates J to work per unit area. But it is the essence of the present argument that the relationship is more meaningful when stated the other way round, with dissipation as the physical term and dJ/da as a derived measure. For initiation the present measure of toughness is used, conceptually J_i, in practice, J_{Ic}. All the various measures used for J are based on

$$J = \eta U/Bb \tag{1a}$$

where U is the work done (that is, the area of the load-displacement diagram) up to the point of interest so that J is measured as a quantity of work normalized by η/Bb. (B is the specimen thickness.)

The practice over the last decade has been to modify Eq 1a after initiation to give

$$J_R = J_i + \Sigma dJ = J_i + \Sigma\eta dU/Bb + f[d(\eta U/Bb)] \tag{1b}$$

where the function selected to allow for growth has varied from time to time. It is now argued that (subject to the second step of the explanation that follows) dU/Bda is the term that is of more fundamental importance, being both more directly measured by experiment and more directly accounted for through physical understanding. From Eq 1b, neglecting the third function, it is seen that

$$dU/Bda = (b/\eta)(dJ/da) \tag{2}$$

so that dJ/da is simply some size-dependent multiple of the work rate.

The second step in the argument is that the work or energy rate used in Eq 2 should have a clear physical relationship with the characteristics of real elastic plastic (REP) material. As a consequence it must be accepted that much of the work input is dissipated in plasticity, which damages material adjacent to the crack but may or may not contribute directly to fracture. Some work input is stored as linear elastic strain energy, the later release of which contributes to the fracture process. Thus the term required, rather than dU/Bda, is more properly written

$$dU_{\text{dis}}/Bda = d(U - w_{el})/Bda \;(= D, \text{the dissipation rate}) \tag{3}$$

where U is external work as before and w_{el} is the conventional linear elastic strain energy, $w_{el} = Qq_{el}/2$, where Q is load and q_{el} is the linear elastic component of displacement.

Of course a related J_R-type formulation can be used if desired, by basing dJ/da in Eq 2 on Eq 3; this was indeed introduced in Ref *10*. Its relation to the original J-integral of Ref *3* is so remote that it might better be called dR/da, where R implies resistance.

$$dJ_{\text{dis}}/da \text{ (or better } dR/da) = \eta dU_{\text{dis}}/Bb_c \tag{4}$$

This definition uses the current ligament, b_c, but omits the term f{ } in Eq 2 on the grounds that because of the discontinuity at initiation, at least on the macro-scale used for U and J, a term such as dJ should be defined for REP material in the increment, rather than by differentiating a previous quantity, just as is done in the classical theory of incremental plasticity.

An interpretation was made in Ref *8* of data for D given by Watson & Jolles in Ref *13* (where it was called dU_{pl}/Bda but was clearly defined as in Eq 3). No R-curves were shown [*13*] nor final sizes given for shear-lips. The data were for 23-mm-thick HY130, with three widths of plain-sided specimens and a side-grooved specimen. From other tests in the literature, including Refs *14* and *15*, it is nearly certain that for the plain-sided specimens large shear lips would have developed. For the plain specimens the results for D show no decrease with growth but a very clear plateau behavior independent of Δa. For the side-grooved case a distinct decrease with growth was shown, similar to that for A533B shown in Ref *16* for reanalysis of tests originally reported in Ref *17*. In Ref *8* the plateau values of Ref *13* were broken into two terms, one dependent on area and one on volume

$$dU_{\text{dis}} = \gamma Bda + \rho c_1 c_2 da = \gamma Bda + \rho s^2 da \tag{5a,b}$$

where γ is energy dissipation rate per unit area and ρ is a mean dissipation rate per unit volume. The term s^2 implies a plane stress or shear-lip zone of equal dimensions, $c_1 = c_2 = s$, in the thickness and span-wise directions. Clearly the numerical value assigned to ρ will depend on the size of the volume over which the term is averaged, that is, whether s is an absolute or proportional dimension. The size of s might in general be controlled by an inherent toughness of material, s_m, or by geometry, s_g. The HY130 data from Ref *14* and Ref *15* are well fitted by $s_g = 0.2b_0$.

The Pattern of Geometry Dependence of Fully Plastic J_R *Curves in Bending*

It is emphasized that the patterns described here are not peculiar to titanium but have been found for other metals, both in-house and in the literature. Three main trends of R-curve behavior have been identified [*4–8*], although the passage from one to the other shows more cases and there may perhaps be other behaviors not yet properly perceived. The geometry dependence of R-curves has also be discussed recently by Atkins [*18*] and Kolednik [*19*]. The three main trends seen in the literature are:

1. "Wider-lower," that is, as the original ligament width, b_0, is increased at constant thickness the resulting R-curves fall below that for the previous size.
2. "Wider-higher," that is, as the original ligament width, b_0, is increased at constant thickness, the resulting R-curves rise above that for the previous size, and
3. "No trend with size," that is, as the size (both width and thickness) is increased to give geometrically similar pieces, the resulting R-curves are the same.

The increase in ligament width, b_0, may arise either from increasing the overall width W at constant a/W ratio or reducing the a/W ratio (still within the deep notch range, that is, $0.4 \leq a/W \leq 0.8$) at constant width, W, although some distinction will be made between these two cases later. An example of what might be called a sub-case is "wider–no trend," where data apparently lie between the first and second cases. Another is where some pieces with geometric similarity follow Trend 3 but then with a further change in absolute size, depart from it. The reason for these and other sub-trends will become apparent as the main data are discussed.

The scaling of the first wider-lower case to an abscissa of $\Delta a/b_0$ was noted in Refs *4* and *5*. It was also noted [*7*] that the data of Ref *16* followed the wider-lower trend and scaled to an abscissa of $(\Delta a/b_0)(S/b_0)$, where S equals the span for bend specimens, or the moment arm in compact pieces but as shown [*8*], that scaling does not extend to the "wider-higher" trend and of course none is needed for the "no trend with size" case. The basic reason for any scale effects in uncontained yield was seen [*6,8*] as an extension of the contained yield arguments for Rice, Drugan, and Sham [*20*]; indeed, they speculated that such scale effects would exist for the uncontained yield case.

The Present Tests; the Background

The starting point of the immediate tests was a series of deep notch bending tests on stable ductile tearing of a titanium alloy in the fully plastic range, reported [*9*] in terms of J_m. The main interest there was in the effect of width on the R-curves, since tests at 35 mm thick showed the "wider-lower" pattern of behavior. Tests of geometrically similar specimens from 10 by 10 mm to 40 by 40 mm also showed a "larger-lower" pattern that might at first sight be interpreted primarily as an effect of thickness. However, test data at constant width but various thicknesses showed a remarkably small effect of thickness so that the dominant effect again seemed to be the width. The "wider-lower" results were reanalyzed [*10*] in terms of D to give an R-curve that was a function of $\Delta a/b_0$ rather than just Δa; S/b_0 was constant for all those tests.

Since parts of the same plate of material were still available, several series of tests are now being conducted to examine further the size effects noted. Some experimental results for fully plastic deep notch bending of specimens of a given width, W, at four thicknesses, B, and further data from a series of four widths, W, at a given thickness [*12*] will be used here. Other series of tests will be reported on later. In related work [*14,15*], similar tests and analyses are being made on HY130 steel. It is already clear that there are both similarities and differences in the pattern of behavior of these two high-strength materials. Only the titanium data are discussed here.

The results will first be presented in terms of conventional J_R curves and then discussed in terms of the crack opening angle, COA, α, and the energy dissipation rate, D.

The material is a (6-2-1-1) titanium alloy containing 6% aluminium, 2% columbium, 1% tantalum, and 0.8% molybdenum. The mechanical properties are: Young's modulus: 123,000 MPa; 0.2% proof stress: 728 MPa; tensile strength: 828 MPa; (σ_{fl}: 778 MPa); elongation: 12%; hardness: 292 $\pm$ 8 VPN. The fracture parameters in Ref 9 are J_i = 0.17 $\pm$ 0.05 MN/m

(or $\delta_i = J_i/m\sigma_{fl} = 0.22 \pm 0.06$ mm if m is assumed to be unity) with $25J_i/\sigma_{fl} = 5.5 \pm 1.5$ mm as a minimum size criterion for conventional J testing.

The Test Results

The present tests are $S/W = 4$; $a/W = 0.55$ nominal; $W = 35$ mm; $B = 35$, 17.5, 8, and 4 mm, this last thickness being below the minimum size limit just quoted. The cases referred to in Ref *12* are $B = 17.5$ mm and $W = 25$, 30, 35, and 40 mm. Testing was in the T-L orientation (stress flow transverse, crack growth longitudinal to the rolling direction). The thinner pieces were cut from layers through the thickness. All were checked for hardness but the variations noted of ±8 VPN seemed random in relation to position in the thickness sense.

The specimens were prepared in accord with ASTM E 813-87, although the extent of crack growth is much larger than normally accepted so that selection of unloading points was sometimes dictated by individual test requirements rather than the recommendations of the standard. Since large growth rather than initiation toughness is the point of the present analysis, tests that were invalid on criteria related only to the specification of a formal J_{Ic} value were not, however, rejected.

For deep notch bend tests of conventional laboratory sizes, such as ligaments up to 50 mm, this material gives stable ductile tearing with full plasticity of the ligament when tested on the screw-driven machine used throughout. A typical load-deflection diagram for the unloading compliance test method is shown in Fig. 1*a*. This pattern of diagram, with a rather well-defined maximum load followed by a falling load, concave in shape, has been referred to as the "pagoda roof" type [*12*]. By contrast, an example of another type of diagram called the "round-house" type, convex in shape and also familiar in the conventional tensile test, is shown in Fig. 1*b* though not directly relevant to the present tests.

The R-curves for $B = 35$, 17.5, 8, and 4 mm with the common width $W = 35$ mm and $a/W = 0.55$ are shown in Fig. 2*a*. Two curves are shown for $B = 8$ mm, with slightly different a/W values from the fatigue precracking to illustrate the repeatability of the tests. The R-curves for the 17.5-mm-thick material at four widths, from Ref *12*, are shown in Fig. 2*b*. The use of J_0 (that is, Eq 1b with b taken as the original value, b_0, and no "correction" term $f\{\ \}$) may seem surprising in the light of all the suggestions that have emerged in the past decade, but for deep notch bending this value is practically identical to that recommended in the current ASTM standard method. The definition used for J does not affect the trends shown for the present data nor for any other deep notch bend data of various widths so far examined.

The load, Q, and increments in the displacement, q, are the raw data for dU and hence dJ, Eq 1b, and D, Eq 3. Load is shown as a function of Δa, Fig. 3*a*,*b*, in normalized form, L, where

$$Q = L\sigma_Y Bb_c^2/S \qquad (6)$$

so that at the limit load L would be expected to reach the value of the conventional plastic constraint factor. Displacements, q, are shown in Fig. 4*a* for the various thicknesses, with $W = 35$ mm, and Fig. 4*b* for the various widths with $B = 17.5$ mm. The data for displacement are later used to estimate the crack opening angle, COA, α, as a function of crack growth. Later in the paper the energy dissipation rates, D, will be discussed. These are formed from Eq 3 using the increments $dU = Qdq$ together with dw_{el}, which is known from load and change in elastic displacement from the compliance data. Example curves for U, U_{dis}, and w_{el} for one of the present tests are shown in Fig. 5.

It was observed that the size, s, of the shear lips formed was not more than 2 mm in width and height. A general description of size for these tests is $s = 0.1b_0$ to within about half a millimeter.

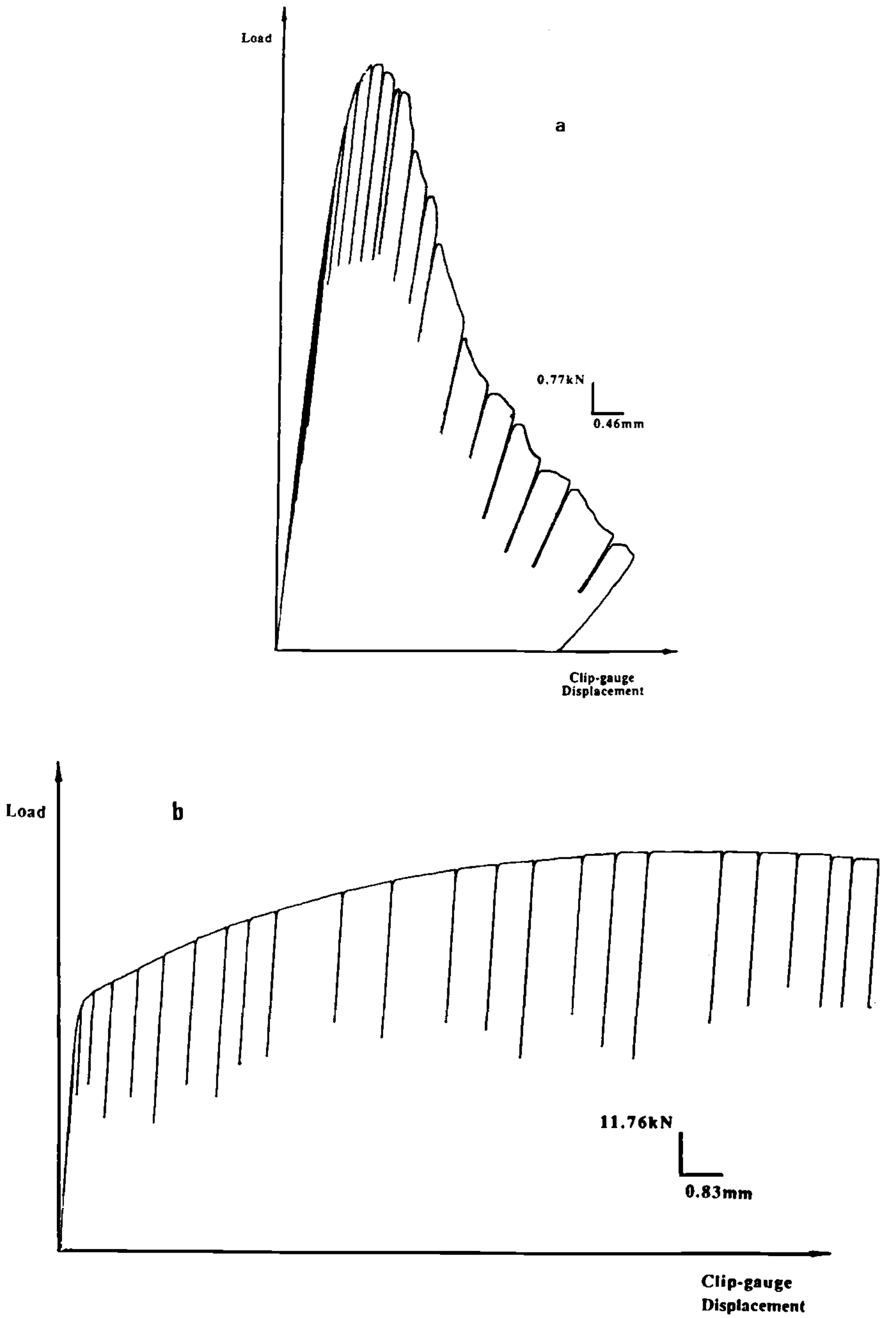

FIG. 1—*Typical load-displacement diagrams:* (a) *"pagoda-roof" type,* (b) *"round-house" type.*

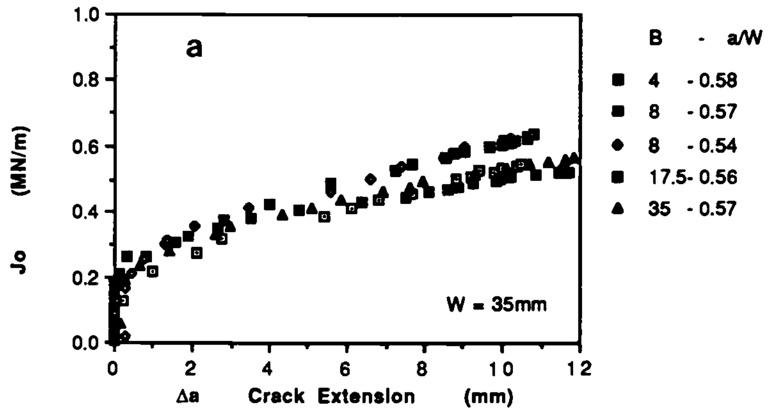

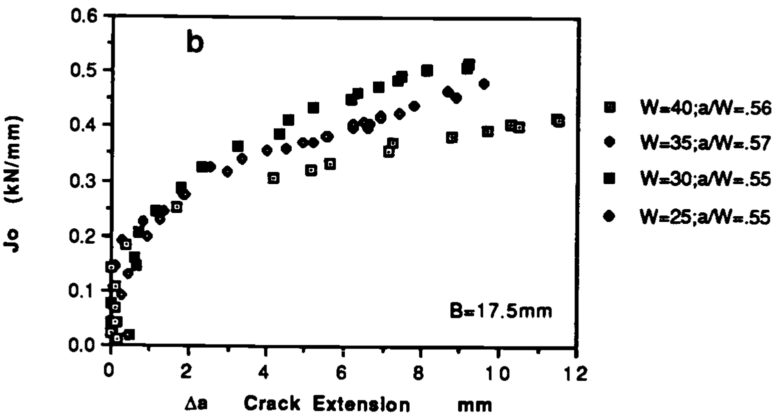

FIG. 2—*R-curves for titanium alloy expressed as* J_0: (a) W = *35 mm, various* B, (b) B = *17.5 mm, various* W.

Discussion of the Experimental Results

The *R*-curves of Fig. 2 clearly confirm the observation [*9*] that there is a very small effect of thickness in this material from 4 to 35 mm despite fracture being predominantly oblique in the former but flat in the latter. For this width, the shear lips grew to about 1.5 mm per side in thickness, leaving about a 1-mm groove between the two shear lips for the 4-mm specimen while at 35 mm there is about 32 mm of flat fracture.

The *R*-curves for various widths at 17.5-mm thick, Fig. 2*b*, show a "wider-lower" trend except for the narrowest specimen, $W = 25$ mm, which falls within the band of the other widths. After the results for this series were reported [*12*], a quite large group of inclusions was found in the ligament of that specimen, the only such defect so far noted. It is therefore not clear whether the reversal of trend is a genuine geometric effect or the consequence of the defect. A repeat test will be made.

The normalized loads or constraint factors, *L*, Figs. 3*a*,*b*, show an immediate rise over the first millimetre or so of growth to a value close to that expected in plane strain, about $2/\sqrt{3}$)(1.36), say 1.56, for the limit load of a mildly hardening material. The data are shown in two groups that do not coincide with the two series of tests; Fig. 3*a* is for cases $b > B$ and

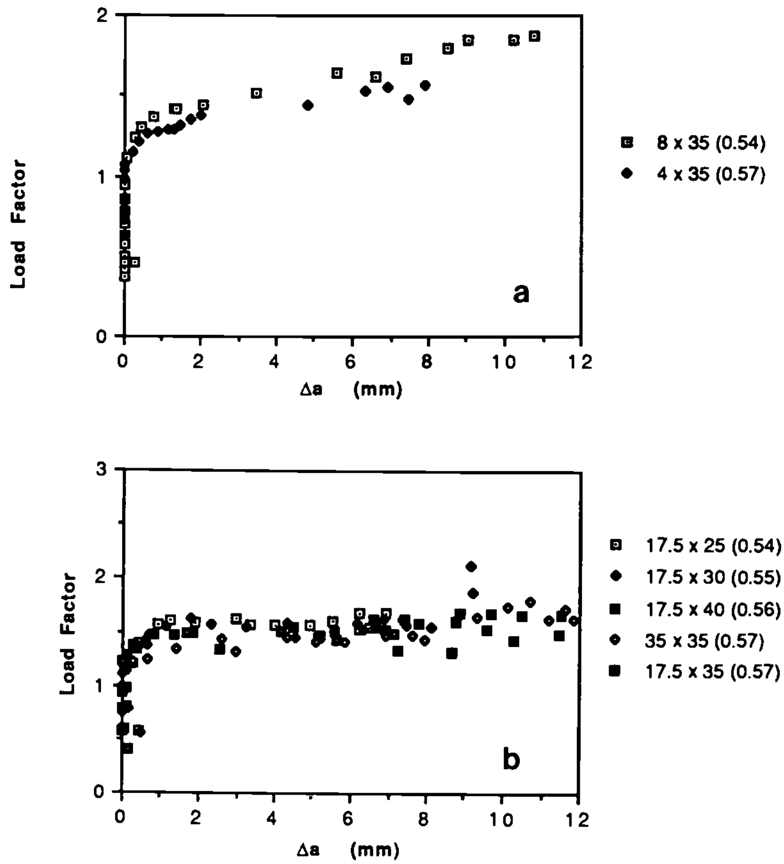

FIG. 3—*Normalized load vs crack growth:* (a) *various* B, W = *35 mm,* (b) *various* W, B = *17.5 mm. In Fig.* a, b > B; *in Fig.* b, b < B.

hence notionally in plane stress at the limit load, while Fig. 3*b* is for cases with $b < B$, notionally in plane strain. Although the thinnest specimen has the lowest value of L at initiation, Fig. 3*a*, consistent with it being more nearly in plane stress, the rise in value with small growth and the near linear rise thereafter takes the final values of L well above that expected for near plane stress behavior of a low-hardening material. The values in Fig. 3*b* for small growth are slightly higher, but then remain near constant in value. A rise, such as in Fig. 3*a*, was noted [*21*] for similar tests on HY130, also in cases with $b > B$. Finite element computations in Ref *22* showed that it was indeed a hardening effect that occurred only with tearing, that is, the constraint factor, L, and the corresponding maximum load for a hardening material became history dependent, according to whether a crack of certain length was taken to full plasticity at that length or by tearing it from a shorter length.

For both the COA and energy dissipation rate analyses, d/da rates are required. If rate values are formed incrementally, they will reflect the random errors in spot data that at some points are several fold. The extent to which that is due to conventional experimental errors or to irregularities in the mechanics of crack growth is not clear, but some form of smoothing process seems necessary if a macro-interpretation is to be found.

After the first millimetre or two of growth, the displacement data of Figs. 4*a*,*b* also show a

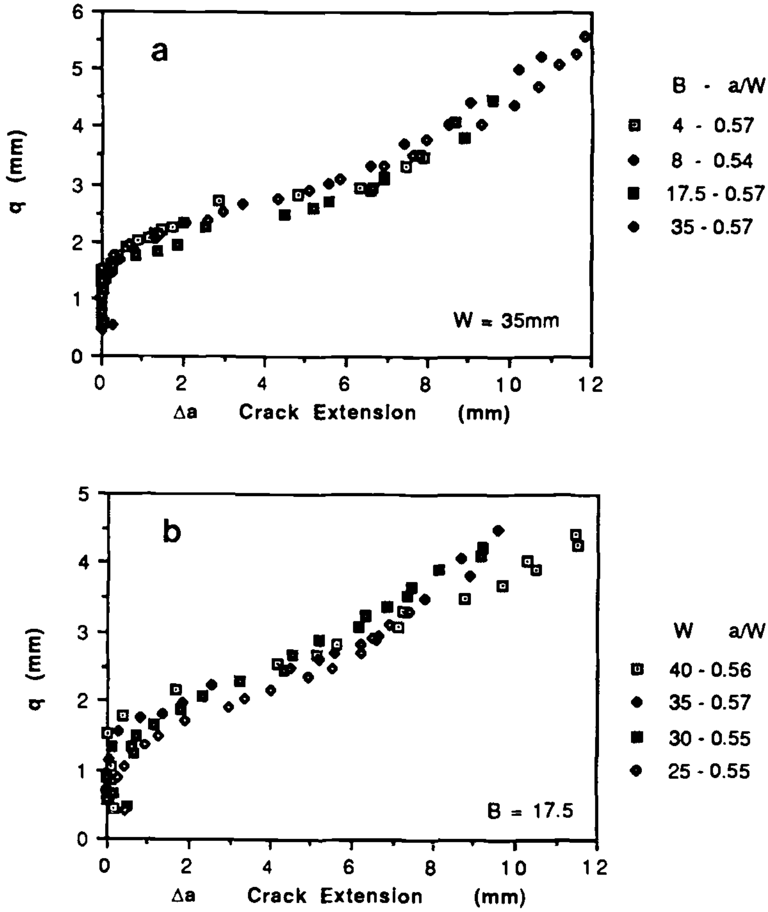

FIG. 4—*Displacements vs crack growth:* (a) *various* B, W = *35 mm,* (b) *various* W, B = *17.5 mm.*

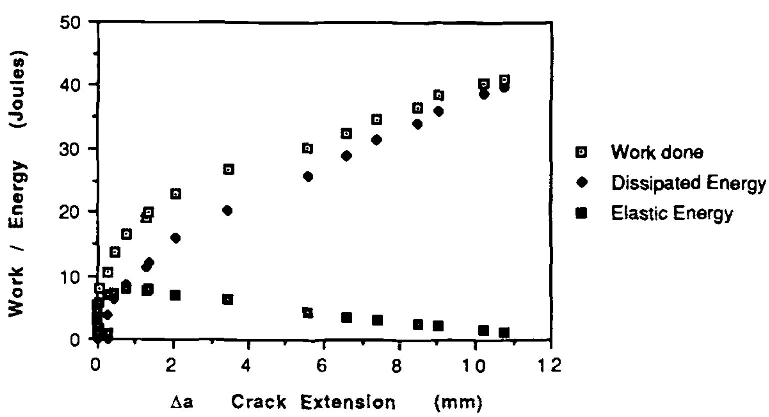

FIG. 5—*An example of work done,* U, *energy dissipated,* U_{dis}, *and elastic energy stored,* w_{el}, *for* B = *8 mm,* W = *35 mm.*

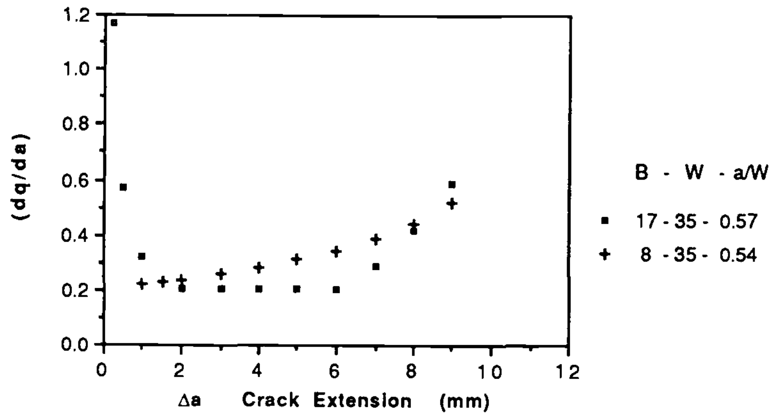

FIG. 6—*An example of rate of change of displacement with crack growth,* dq/da *versus* Δa, *for* B = *17.5 mm,* W = *35 mm, from raw data and for* B = *8 mm,* W = *35 mm from the analysis of Fig.* 7a..

near linear trend referred to here as the steady-state regime. There is, however, some upswing at larger growths, and an example of dq/da versus Δa, formed "by eye," is of "bathtub" form, as shown by the solid points, Fig. 6. A sample case is also plotted, Fig. 7*a*, in terms of q versus ln b_c, where b_c is the current ligament size, $b_0 - \Delta a$, for the steady-state regime only, that is, omitting the first few points corresponding to the rapid fall in Fig. 6. The result is satisfactorily linear so that dq/da is inversely proportional to b_c. The corresponding points are plotted as crosses on Fig. 6. A simple rigid plastic COA model fits the $1/b_c$ behavior very well. For span, S, using a center of rotation at rb_c (where r is often taken as about 0.45 for bending)

$$dq/da = S\alpha/4rb_c \tag{7}$$

This simple model neglects any elastic contribution to the COA but, if accepted, supports a constant COA criterion of growth, α, in the steady-state regime after, say, the first 10% of growth. The values of α so obtained are 2.1 ± 0.2°.

However, in the steady-state regime the data are equally well represented by a second power law in b_c, Fig. 7*b*, implying

$$dq/da = A_1 + A_2 b_c \tag{8}$$

with A_2 found to be negative, from which it seems that COA increases with growth. The values are closely comparable to those just quoted, but the first interpretation suggests that, subject to the scatter, COA is constant with growth (even though possibly a function of size, not determined here), whereas the second suggests that COA increases steadily with growth. In short, it seems that the present data allow more than one law to be stated for use with comparable sizes but cannot be used to state a general law sufficiently certain to allow extrapolation.

The energies in Fig. 5 show not only the general trend with growth but also illustrate the difference between work done and energy dissipated. Curves of the energy dissipation rates, D, are shown in Fig. 8*a,b* formed by taking slopes at uniform intervals from a smooth line drawn by eye through data for U_{dis}, as in Fig. 5. Because close attention has not been given here to initiation, the detailed shape of the curves in the blunting and first growth regions is not known. The interpretation starts here with some small growth, nominally 0.2 to 0.5 mm. There is then a clear regime of reducing values, again followed by a more or less steady state

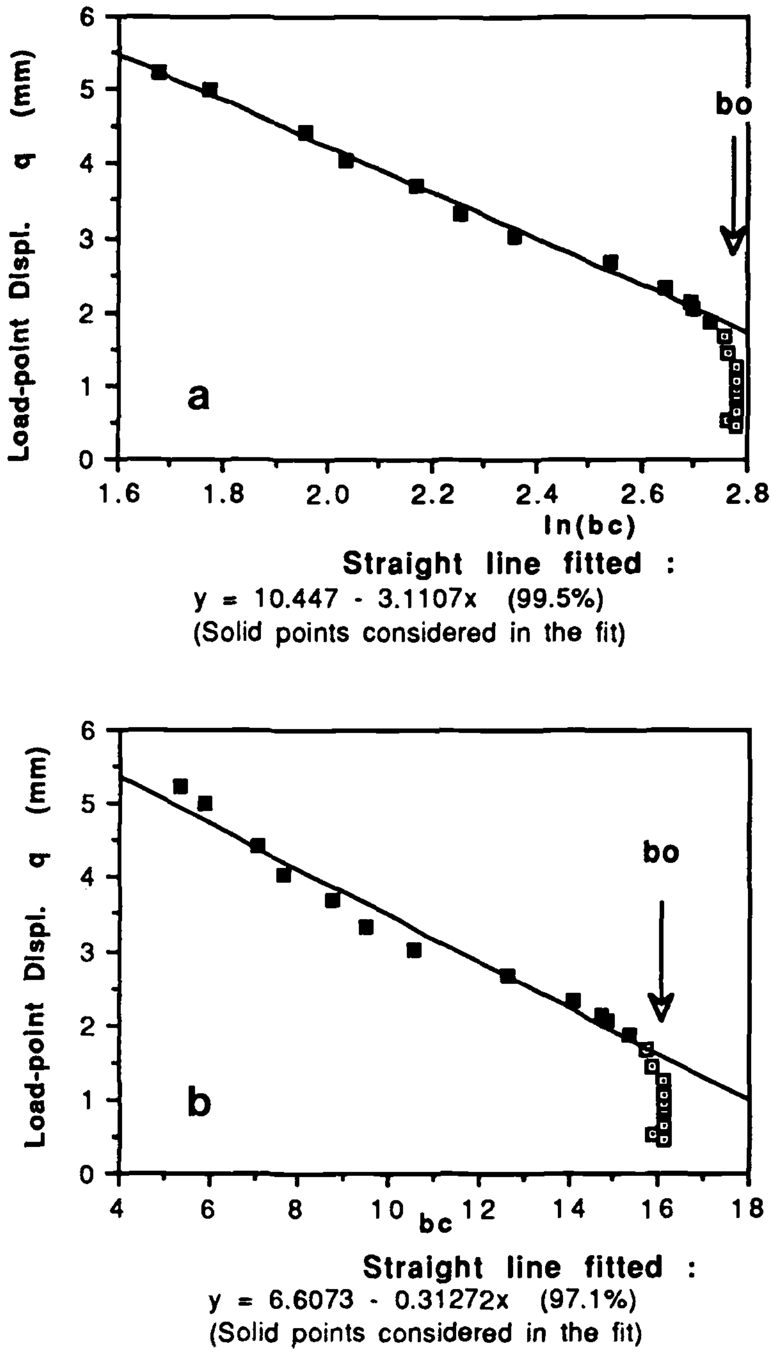

FIG. 7—*Displacement,* q, *in the steady-state regime:* (a) *as a function of ln* bc; (b) *as a second power function of* b_c, *for* B = *8 mm,* W = *35 mm.*

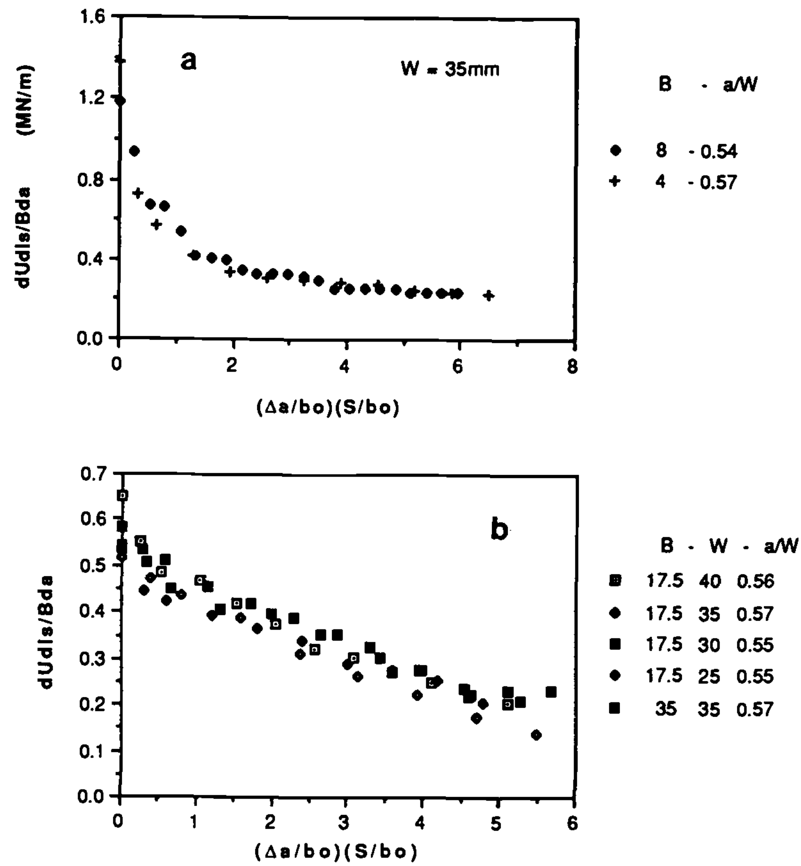

FIG. 8—*Energy dissipation rate,* D, *as a function of crack growth:* (a) *various* B, W = *35 mm,* (b) *various* W, B = *17.5 mm. In Fig.* a, b > B; *in Fig.* b, b < B.

after a millimetre or two of growth. However, in Fig. 8*a*, the steady state seems to come to a near constant or plateau value, whereas in Fig. 8*b* it seems to be a linear decrease. This behavior may be compared to data for side-grooved A533B [*16*] and mainly plain-sided data for HY130 in [*13*]. The former had a fine resolution and showed a rising regime near initiation, followed by the falling regime and an approach to a steady state that might not be reaching a plateau but was independent of ligament width; the latter showed only plateau behavior with neither rising nor falling regimes but with plateau values strongly width dependent.

Some of the present results were reexamined by taking U_{dis} as a second order function of b_c, omitting the first half millimetre or so of growth. One of the cases studied in detail, B = 8 mm, W = 35 mm, relates to Fig. 8*a* with an apparent steady-state plateau for D; the second with B = 17.5 mm, w = 35 mm, relates to Fig. 8*b* with an apparent steady-state decline. The example shown in Fig. 9 is representative of both and implies that the present data can be described by

$$U_{dis} = D_0 + D_1 b_c + D_2 b_c^2 \tag{9}$$

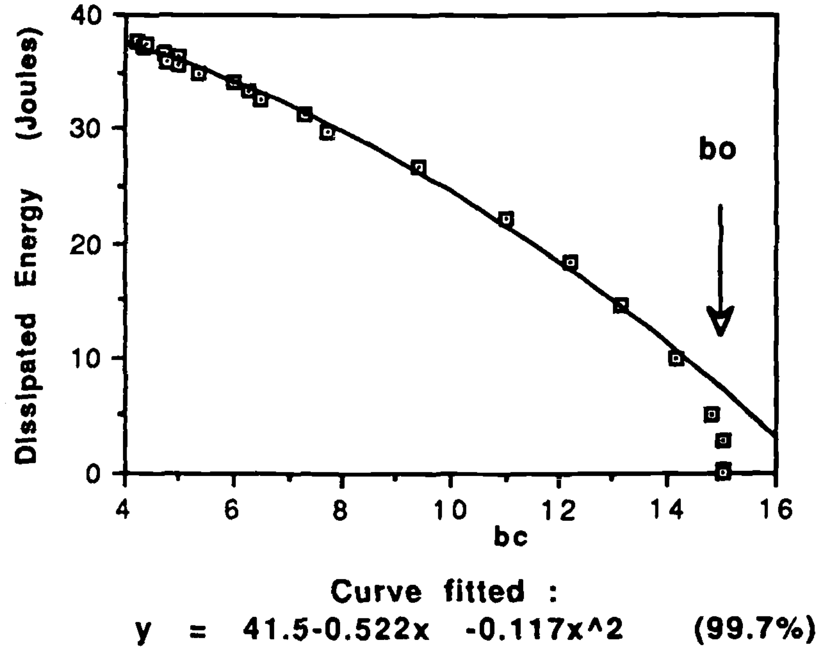

FIG. 9—*Energy dissipated,* U_{dis}, *as a second power function of* b_c *in the steady state regime;* B = *8 mm,* W = *35 mm.*

If the fitted curve is then differentiated to form $D = dV_{dis}/Bda$, it implies

$$-BD = D_1 + 2D_2b_c \tag{10}$$

A physical meaning to that model is outlined in the appendix. The immediate point is that it supports a ligament width-dependent trend with growth rather than a constant plateau for the present data. Nevertheless, if data are used for only the last several millimetres of growth, in all the cases examined it appears to follow a constant law rather than a decreasing law. Although not shown here, these same remarks apply to U as well as U_{dis}, and to dU/Bda as well as dU_{dis}/Bda. Just as for the COA interpretation, it does not seem possible to come to a firm conclusion on what law is being followed by the dissipation rate, the apparent law depending on the selection of data used.

As described by Eq 4, a J_R-curve type presentation of D can be made. The curves corresponding to Fig. 8*a* are shown in Fig. 10*a*; the curves corresponding to Fig. 8*b* are given in Fig. 10*b* from Ref *12*. Both can be presented on an abscissa of $\Delta a/b_0$ since S/b_0 is constant; in the former b_0 is also constant, but in the latter it is not. The differences in the initial values of D in Fig. 8*a* must translate to a slightly higher R-curve when the initial D value is high, thus supporting the previous suggestion in connection with Fig. 2 that there is a slight but definite increase of toughness with reduction in thickness, possibly peaking at about 8 mm thick.

Dissipation Rate and COA Models of Growth

The difference between dU/Bda and dU_{dis}/Bda, Eq 3, is dw_{el}/Bda. The form of the elastic contribution can be inferred from Fig. 5, and it is the only physical driving force that can make

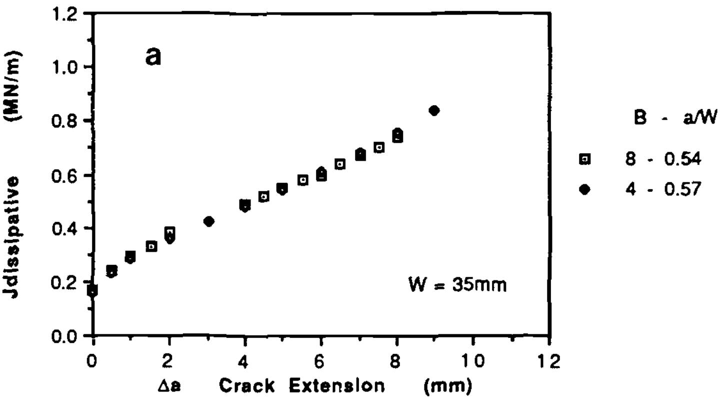

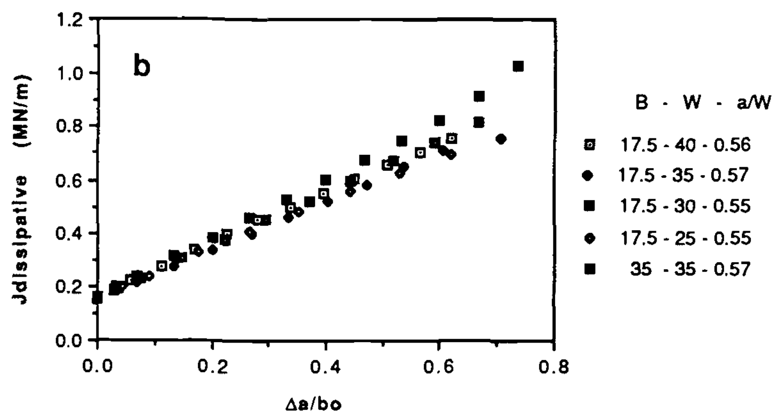

FIG. 10—R-*curves based on dissipation rate as a function of* $\Delta a/b_0$, (a) B = *8 mm*, W = *35 mm*, (b) B = *17.5 mm*, W = *35 mm. In Fig.* a, b > B; *in Fig.* b, b < B.

the actual separation of area at fracture. In the present tests the term dw_{el}/Bda is both nonzero and not equal to G. A comparison was shown for the series of various widths at $B = 17.5$ mm in Ref *12*. The lack of equality implies that dq_{el}/Bda is not quite zero. Reference *16* reports that $dw_{el}/Bda = G$. That implies dq_{el}/Bda was zero during growth.[2] In the authors' opinion, the case of dq_{el}/Bda being zero is not a generality of tearing behavior; it is speculated that its occurrence in Ref *16* may be a consequence of the use of side-grooved specimens and a very close approach to plane-strain behavior. In Ref *20*, a distinction is made between a rigid plastic case and the case where plasticity dominates over elastic terms. That distinction can now be seen in terms of dU and dU_{dis}. For rigid plastic behavior w_{el} is identically zero, and thus dw_{el} is always zero. So not only must dU and dU_{dis} be the same, but G is zero. For plastic domination, even though dw_{el}/Bda may in some case be zero, G will still exist. This distinction is here also relevant to the COA and the models used, Eq 7. That model is for rigid plastic material in which there is no elastic component of COA, but the data are for REP material with plastic

[2] Following discussion with one of the authors of Ref *16*, J. A. Joyce, it is now clear that the experimental value of dq_{el}/Bda was not zero but that, by intent, the corresponding change in w_{el} was not included in the evaluation of the particular energy rates reported in Ref *16*.

domination, in that reality elasticity causes the final separation and presumably alters the value of the COA formed. The elastic contribution to COA must exist *during* the actual process of growth, and the dq_{el} component will not scale directly with b_c as does the dominant component in Eq 7.

The term $Q\, dq/Bda$ is precisely dU/Bda and, subject to the influence of dw_{el}/da, sets the trend for D. It is supposed that the difference in the elastic component between this model and REP material is little more than the scatter of the data here. Using Eq 7 for a dominant plasticity model, DP

$$D(\text{DP}) = (L\sigma_Y b_c^2/S)dq/da \tag{11}$$

so that

$$D(\text{DP}) = (L\sigma_Y/4r)\alpha b_c \tag{12}$$

Thus, if α becomes constant for steady state tearing, D would be expected to reach a regime reducing with b_c, with slope $L\sigma_Y\alpha/4r$. Conversely, if D reaches a steady state plateau, as in Ref *13* and some of the present interpretations, then αb_c would be constant, implying α increases with growth. That is compatible with the possible trend discussed above, Eq 8, where, if not constant, α seemed to increase slightly. It is suggested that there is a consistency in the data despite the uncertainty in the way the d/da rates have been formed, the neglect of the elastic component of COA, and a genuine effect that the measurements are being taken on material that has suffered various degrees of damage during its loading history, according to its position ahead of the initial crack tip. It also seems from the R-curves that, in the sizes tested, this material is unusually insensitive to the effect of thickness so that separation of plane stress and plane strain effects is very uncertain. It is speculated that COA constant with growth and the reducing trend for D are attributes of plane strain, whereas the plateau behavior of D and an implied rising trend of COA are attributes of plane stress, but the present data neither completely confirm nor deny that inference.

As a final summary of the dissipation rate arguments, it is a requirement of the conservation of energy that, within the conventional approximations of engineering mechanics and also the neglect of internal energy of residual stresses, the dissipation rate must be both meaningful and identifiable. It is not surprising that the dissipation rate is a function of the remaining ligament rather than of the previous crack growth. Some history dependence may exist if rather different loading histories are experienced in different widths and thicknesses. What is more contentious is whether some portion of the dissipation rate, or a term related to it, can be identified as tearing toughness. The essence of the present analysis is that several candidates exist, namely:

1. The whole term D (which clearly contains a geometric plasticity component).
2. The elastic component, dw_{el}/Bda (which may be much less than G_{Ic} because plastic damage is preceding separation).
3. The areal and volumetric components of D (which may or may not prove to be geometry-dependent, see appendix).

However far removed these terms may be from the concept of toughness, they appear to offer insight into the process of tearing beyond that obtainable from a conventional R-curve. The choice between No. 1 and No. 2 was also discussed from a rather different approach in Ref *23*.

It may also be remarked that the so-called regime of J-controlled growth, often taken to extend up to $\Delta a/b_0 \leq 0.006$ [*24*], is here covered by the uncertainties near initiation and the region of rapid decrease of both dq/da, Fig. 6, and D, Fig. 8. That region is clearly not steady state. It is tentatively suggested that the physical basis for J-control, if it exists, is that the decreasing COA implied by the decrease in dq/da is a consequence of the plastic damage done by the dissipated energy. Thus, in so far as J is a function of work through Eq 1, J-control implies damage control. A more logical measure in dominant plasticity would thus seem to be J_{pl} or better, R as in Fig. *10b* from Eq 4. But that implies the control is a function not of Δa but of $\Delta a/b_0$ and would only change to Δa for contained yield [*11*], when control of the dissipation rate and associated damage passes to a material-dominated zone size [*20*], rather than the geometry-controlled zone size of uncontained yield.

Conclusions

For the present normal-sized laboratory specimens of 6-2-1-1 titanium alloy, tearing occurs with full plasticity, expressible as a nondimensional factor, L, of similar value for all cases, that rises for the first millimetre or so of growth. L then increases by some 20% for the cases $b > B$ but remains substantially constant for the cases $b < B$. It is inferred that although L reduces to the constraint factor for nonhardening limit behavior, for tearing with hardening it becomes history dependent. The conventional J_R-curves are a function of width but practically independent of thickness from 4 to 35 mm thick.

The stable plastic tearing of this material in bending can be expressed in terms of the energy dissipation rate, D, as a function of the remaining ligament, b_c. D can then be split into areal and volumetric components. Alternatively the tearing toughness for this material for plastic bending can be expressed as a constant crack opening angle, COA, of about 2.5° growth between about 10 and 50% of the ligament. Neither description can, however, be extrapolated to other sizes with certainty since different treatments of the same data allow the laws to be expressed in several different ways.

The conclusions are as yet limited strictly to the circumstances described in the paper. No investigation has been attempted of how the results or the method of analysis might apply to other configurations, and there is already other evidence to suggest that other regimes of deformation exist for other combinations of size and materials. Nevertheless, the separation of energy dissipation rate into areal and volumetric components and apparent relations to COA offers an insight into the interplay of several geometric size effects that merits further study.

Acknowledgment

One of the authors (CET) wishes to thank the Leverhulme Trust, London, United Kingdom, for a fellowship under which his contribution to this paper was made.

APPENDIX

The form of Eq 9 is not entirely empirical. In Ref *8* it was suggested that

$$dU_{\text{dis}} = \gamma B da + \tau s^2 da \tag{A1}$$

(modified version of Eq 5 in text)

where γ is a flat fracture energy per unit area and τ is a mean volumetric energy through the volume of the shear lips (the symbol ρ was used in Ref *8* but that now seems more appropriate for the term that follows). Equation A1 fitted well the HY130 data from Ref *13*, which at 20 mm thick was taken to have a strong plane stress (shear lip) component with s proportional to b_0. The arguments in the present paper that there sometimes seems to be a component of D that reduces with b_c, consistent with a constant COA, suggests that Eq A1 is incomplete and should be rewritten as

$$dU_{\text{dis}} = \gamma B da + \tau s^2 da + \rho B b_c da \tag{A2}$$

to give an extra term that accounts for the plane strain volumetric work all through the thickness B and extending a distance proportional to b_c along the span; s is again proportional to b_0 (at about 0.1 b_0 in the present tests and about 0.2 b_0 for HY130 [*16,17*]). A term representing a possible growth of plastic dissipation under rising load is still missing, but the use of the analysis omits the few points in that region in the present tests.

Thus, integrating Eq A2 up to Δa and writing $\Delta a = b_0 - b_c$

$$U_{\text{dis}} = (\gamma B b_0 + \tau b_0^3 + \rho B b_0^2/2 + U_{\text{dis},i}) - (\gamma B + \tau b_0^2) b_c - \rho B b_c^2/2 \tag{A3a}$$

where $U_{\text{dis},i}$ is the dissipative work up to just after initiation

$$U_{\text{dis},i} \approx J_{pl,i} B b_0/\eta \tag{A4}$$

Clearly the multiplicative constants in Eq A3 can be identified with D_0, D_1, and D_2 in Eq 9 so

$$U_{\text{dis}} = (b_0 D_1 + b_0^2 D_2 + U_{\text{dis},i}) + D_1 b_c + D_2 b_c^2 \tag{A5}$$

Thus ρ can be evaluated from D_2, $(\gamma B + \tau b_0^2)$ as D_1 whence $U_{\text{dis},i}$ can be found from D_0 since the other components of D_0 are multiples of D_1 and D_2. The present application of the analysis has been restricted to pieces of constant initial ligament width so that components of D_1 can only be separated if it is supposed that γ and τ are independent of thickness, that is, of the degree of plane strain. It remains open to question whether γ, τ, and ρ are independent of geometry. Certainly the shear lip component seems to include a material and geometry dependent size such as $s = xb_0$, where x is about 0.1 in the present work. It is not clear whether γ will depend on the thickness and ρ will prove to be geometry dependent, even in deep notch bending, since it is averaged through a poorly defined plastic volume, extending to about $0.4b_c$ for the slip line extent at the start of tearing but thereafter perhaps reducing.

The values obtained here are $\rho = 34.5$ MN/m^2; $(\gamma B + \tau b_0^2) = 234$ N (for $B = 8$ mm thick) and $\rho = 24.9$ MN/m^2; $(\gamma B + \tau b_0^2) = 636$ N (for $B = 17.5$ mm thick). Such values neglect the size factors, x, just mentioned as perhaps 0.1 and 0.4. If included, the more physically realistic values would be appreciably bigger than those just quoted. The values obtained for $J_{pl,i}$ from $U_{\text{dis},i}$ and Eq A4 in the two tests analyzed so far are 0.074 ± 0.005 MN/m, in good agreement with the value given in Ref *12* where the initiation toughness of 0.15 MN/m was broken into elastic and plastic components of $0.07 + 0.08$ MN/m, respectively.

References

[*1*] Orowan, E., "Fracture and Strength of Solids," *Rep Prog Phys,* Vol. 12, 1949, p. 185.
[*2*] Irwin, G. R., "Fracture Dynamics," *Fracturing of Metals,* American Society for Metals, Metals Park, OH, 1948.
[*3*] Rice, J. R., *Journal of Applied Mechanics,* Vol. 35, 1968, pp. 379–386.

[4] Etemad, M. R. and Turner, C. E., *International Journal of Pressure Vessels and Piping*, Vol. 20, 1985, pp. 1-5 and Vol. 26, 1986, pp. 79-86.
[5] Turner, C. E. and Etemad, M. R., *International Journal of Pressure Vessels and Piping*, Vol. 41, 1990, pp. 43-58.
[6] Wei, Y.-L., Etemad, M. R., John, S. J., and Turner, C. E., *Proceedings of the International Conference on Fracture and Fracture Mechanics*, C. Ouyang, Ed., Fudan University, Shanghai, China, 1987, pp. 60-72.
[7] Etemad, M. R. and Turner, C. E., in *Fracture Mechanics, 21st Symposium, ASTM STP 1074*, American Society for Testing and Materials, Philadelphia, 1990, pp. 289-306.
[8] Turner, C. E., in *Fracture Behaviour and Design of Materials and Structures*, EMAS, Warley, United Kingdom, 1990, Vol. I, pp. 933-968.
[9] John, S. J. and Turner, C. E., *Fatigue Fracture Engineering Materials and Structure*, Vol. 13, No. 2, 1990, pp. 95-107.
[10] John, S. J. and Turner, C. E. in *Defect Assessment in Components—Fundamentals and Applications (ESIS/EGF 9)*, Mech. Eng. Pub., 1991, pp. 299-318.
[11] Turner, C. E., "A Relationship between *R*-Curves in Uncontained and Contained Yield," presented, *22nd National Symposium Fracture* in Atlanta, 1990.
[12] Braga, L. and Turner, C. E., "Energy Changes during Ductile Tearing," *22nd National Symposium on Fracture*, held in Atlanta, 1990.
[13] Watson, T. J. and Jolles, M. I. in *Fracture Mechanics, 17th Volume, ASTM STP 905*, American Society for Testing and Materials, Philadelphia, 1986, pp. 542-558.
[14] Dagbasi, M., "Engineering Analysis of Cracked Bodies Using J-Integral Methods," Ph.D. thesis, University of London, London, United Kingdom, 1989.
[15] Xia, L., Ph.D. thesis, "Stable Crack Growth of Steel under Fully Plastic Bending," University of London, London, United Kingdom, 1991.
[16] Mecklenburg, M. F., Joyce, J. A., and Albrecht, P., in *Nonlinear Fracture Mechanics: ASTM STP 995*, American Society for Testing and Materials, Philadelphia, 1989, pp. 594-612.
[17] Vassilaros, M. G., Joyce, J. A., and Gudas, J. P., *Fracture Mechanics: Twelfth Conference, ASTM STP 700*, American Society for Testing and Materials, Philadelphia, 1980, pp. 251-270.
[18] Atkins, A. G., in *Fracture Behaviour and Design of Materials and Structures*, EMAS, Warley, United Kingdom, Vol. 1, 1990, pp. 1039-1046.
[19] Kolednik, O., *Engineering Fracture Mechanics*, Vol. 36, No. 8, 1991, pp. 403-412.
[20] Rice, J. R., Drugan, W. J., and Sham, T.-L., *Fracture Mechanics: Twelfth Conference, ASTM STP 700*, American Society for Testing and Materials, Philadelphia, 1980, pp. 189-219.
[21] Dagbasi, M. and Turner, C. E., *International Journal of Fracture*, Vol. 42, 1990, pp. R15-R18.
[22] Xia, L. and Turner, C. E., *Numerical Methods in Fracture Mechanics*, A. R. Luxmoore and D. R. J. Owen, Eds., Pineridge Press, Swansea, United Kingdom, 1990, pp. 79-90.
[23] Moran, B. and Shih, C. F., *Engineering Fracture Mechanics*, Vol. 27, No. 6, 1987, pp. 615-642.
[24] Shih, C. F., deLorenzi, H. G., and Andrews, W. R., *Elastic-Plastic Fracture, ASTM STP 668*, American Society for Testing and Materials, Philadelphia, 1979, pp. 175-194.

J. R. Gordon,[1] *R. L. Jones,*[2] *and N. V. Challenger*[3]

An Experimental Study to Determine the Limits of CTOD Controlled Crack Growth

REFERENCE: Gordon, J. R., Jones, R. L., and Challenger, N. V., "**An Experimental Study to Determine the Limits of CTOD Controlled Crack Growth,**" *Constraint Effects in Fracture, ASTM STP 1171,* E. M. Hackett, K.-H. Schwalbe, and R. H. Dodds, Eds., American Society for Testing and Materials, Philadelphia, 1993, pp. 176–194.

ABSTRACT: This paper presents the results of an experimental program to study size and geometry effects in CTOD R-curves. The results were obtained from room temperature unloading compliance R-curve tests on different-sized single-edge-notch-bend (SENB) specimens made from Ti-3Al-2.5V alloy, HY100 steel, and nickel-aluminum-bronze (NAB). The crack growth resistance was measured in terms of conventional CTOD, δ_0 (i.e., as defined in BS 5762), CTOD corrected for crack growth, δ_R, and CTOD derived using a double clip gage arrangement, δ_{dc}. It was found that all the CTOD R-curves exhibited upswings after crack extensions corresponding to approximately 15% of the initial uncracked ligament. Based on the results obtained in this study, it is postulated that the crack growth limit for CTOD controlled crack growth in R-curves is 15% of the initial uncracked ligament. This condition alone, however, is not sufficient to guarantee size/geometry independent results. It is also necessary to have the same level of specimen constraint.

KEY WORDS: fracture mechanics, fracture toughness, ductile fracture, CTOD, R-curves, J controlled crack growth, HY 100 steel, normalized R-curves

Nomenclature

a	Crack length
a_0	Initial crack length
Δa	Crack extension
B	Specimen thickness
B_n	Net thickness
W	Specimen width
b	Uncracked ligament
b_0	Initial uncracked ligament
E	Young's modulus
K	Stress intensity factor
V	Crack mouth opening displacement
V_e	Elastic component of V
V_p	Plastic component of V
z	Knife edge height
J	Fracture resistance J

[1] Manager of Engineering and Materials Department, Edison Welding Institute, 1100 Kinnear Road, Columbus, OH 43212.
[2] Head of Marine Structural and Engineering Metallurgy Section, United Kingdom Admiralty Research Establishment, Holton Heath, Poole, Dorset, United Kingdom.
[3] Research engineer, Engineering Department, The Welding Institute, Cambridge, United Kingdom.

δ_0 Conventional crack tip opening displacement (CTOD)
δ_R CTOD corrected for crack growth
δ_{dc} CTOD calculated using double clip gauge arrangement
ν Poisson's ratio
ρ, α, and ω Parameters for specifying the limits of J or CTOD controlled crack growth
σ_{YS} Yield strength
σ_{FLOW} Flow strength

Subscripts

k, k-1 unloading number
0 initial
u upper
l lower
e, el elastic
p, pl plastic

When a material exhibits fully ductile behavior, its resistance to crack extension is usually presented in the form of an elastic-plastic crack growth resistance curve (R-curve). In essence, the R-curve is a plot of the variation in crack growth resistance, generally expressed in terms of CTOD or J, during the process of stable crack extension.

Over the last few years, recommended test procedures have been published [*1–5*] which cover the measurement of J and CTOD R-curves using the multiple specimen method or the single specimen unloading compliance technique. Provided certain restrictions are satisfied, the resulting R-curves can be regarded as material properties. The purpose of the limitations is to ensure that J and CTOD remain valid characterizing parameters during the process of stable crack extension. If these conditions are satisfied, the crack growth process is frequently referred to as being either J or CTOD controlled, whichever is applicable.

It is generally accepted that the following conditions must be satisfied to ensure J-controlled crack growth [*6–8*]

$$B,b > \frac{\rho J}{\sigma_{FLOW}} \qquad \rho > 20\text{–}25 \text{ for bend specimens} \tag{1}$$

$$\Delta a \leq \alpha(W - a_0) \qquad \alpha = 0.06\text{-}0.1 \text{ for bend specimens} \tag{2}$$

$$\omega = \frac{b}{J}\frac{dJ}{da} \qquad \omega > 2.5\text{–}10.0 \text{ for bend specimens} \tag{3}$$

where

b, b_0 = current and initial uncracked ligaments,
a, a_0 = current and initial crack length,
a = crack growth, and
σ_{FLOW} = material flow strength.

Work conducted by Hellman and Schwalbe [*9*] on thin sheet material indicates that similar limits exist for CTOD, but that the restrictions are less severe than those for J. It should be stressed, however, that this program was primarily concerned with establishing plane stress R-curve limits rather than plane strain limits.

Nevertheless, based on the work by Hellman and Schwalbe, the following restrictions have been included in the European Group on Fracture (EGF) ductile fracture test procedure [4] for CTOD controlled crack growth under plane strain conditions

$$B, b > \rho\delta \; \rho = 50 \text{ for bend and compact specimens} \tag{4}$$

$$\Delta a \leq \alpha(W = a_0) \; \alpha = 0.1 \text{ for bend and compact specimens} \tag{5}$$

where

δ = CTOD.

This paper presents results from a large experimental program to study geometry and size effects in elastic-plastic crack growth resistance curves and in particular the limits of CTOD controlled crack growth. The test program included low, medium, and high toughness materials. The results obtained from the low toughness (Ti-3Al-2.5V alloy) and medium toughness (HY 100 steel) materials have been published previously [10–13]. This paper presents the results for the high toughness material (nickel-aluminum-bronze) and compares the trends obtained from all three materials.

The crack growth resistance was measured in terms of the following fracture parameters:

1. Standard CTOD (δ_0) based on the original crack tip location, i.e., as defined in BS 5762.
2. CTOD corrected for crack growth (δ_R).
3. CTOD derived from double clip gauge measurements (δ_{dc}).

Material

The high toughness material selected for this investigation was nickel-aluminum-bronze to DGS 8452 specification supplied in the form of a 110-mm-diameter bar. This alloy has a nominal yield strength of 310 N/mm^2 and a tensile strength of 680 N/mm^2. A summary of the tensile properties (including the Ramberg Osgood stress strain constants) of all three materials is presented in Table 1. It is evident that the NAB alloy has a much larger work-hardening capacity than the titanium alloy and HY 100 steel tested previously.

Test Program

General

The test program undertaken on the NAB material consisted of 15 room-temperature unloading compliance R-curve tests on single-edge-notch-bend (SENB) specimens of different sizes. Details of the NAB test matrix are presented in Table 2. The SENB specimens were side grooved by 20% after being fatigue precracked to provide initial crack length to specimen width ratios (a_0/W) of approximately 0.6. All the SENB specimens were tested with a loading span to specimen width ratio (S/W) of 4.0.

Five SENB specimen sizes were studied in this program corresponding to nominal thicknesses of 10, 20, 30, 40, and 50 mm. All the specimens had a width equal to twice the thickness ($B \times 2B$). For each specimen size, three room-temperature unloading compliance tests were performed.

The fracture toughness test program for the titanium and HY 100 materials was developed to enable independent studies of size and geometry effects. Details of the overall test matrixes are given in Tables 3 and 4. In the size effects programs, the specimen geometry was fixed at

TABLE 1—*Comparison of tensile properties.*

Property	NAB	HY 100	Ti-3Al-2.5V
Yield strength, N/mm^2	310	816	548
Tensile strength, N/mm^2	602	921	648
Young's modulus, kN/mm^2	126	196	95
ε_0	0.00238	0.004166	0.005914
σ_0	309	817	561
α	0.688	0.1452	1.285
η	8.72	24	22

NOTE: Ramberg Osgood Stress-strain relationship given by

$$\frac{\varepsilon}{\varepsilon_0} = \frac{\sigma}{\sigma_0} + \alpha\left(\frac{\sigma}{\sigma_0}\right)^{\eta}$$

TABLE 2—*Test matrix for NAB specimens: size effects program.*

Specimen Numbers	Specimen Thickness, mm	Specimen Width, mm	a/W Ratio
1–3	10	20	0.6
4–6	20	40	0.6
7–9	30	60	0.6
10–12	40	80	0.6
13–15	50	106	0.6

NOTE: All specimens sidegrooved by 20%.

TABLE 3a—*Test matrix for Ti-3Al-2.5V specimen: size effects program.*

Specimen Numbers	Specimen Thickness, mm	Specimen Width, mm	a/W Ratio
1–3	10	20	0.6
4–6	15	30	0.6
7–9	20	40	0.6
10–12	30	60	0.6
13–15	45	90	0.6

NOTE: All specimens sidegrooved by 20%.

TABLE 3b—*Test matrix for Ti-3Al-2.5V specimen: geometry effects program.*

Specimen Numbers	Specimen Thickness, mm	Specimen Width, mm	a/W Ratio
16–18	20	10	0.6
19–21	20	20	0.6
7–9	20	40	0.6
22–24	20	60	0.6
25–27	20	80	0.6

NOTE: All specimens sidegrooved by 20%.

TABLE 4a—*Test matrix for HY 100 specimens: size effects program.*

Specimen Numbers	Specimen Thickness, mm	Specimen Width, mm	a/W Ratio
1–3	15	30	0.6
4–6	30	60	0.6
7–9	45	90	0.6
10–12	60	120	0.6
13–15	75	150	0.6

NOTE: All specimens sidegrooved by 20%.

$B \times 2B$, but the specimen thickness was varied. In the geometry effects programs, the specimen thickness was fixed and the specimen width varied to give specimen geometries ranging from $B \times 1/2B$ to $B \times 4B$.

Test Details

The unloading compliance tests were conducted in broad agreement with the EGF R-curve test procedure [*4*]. Each test was terminated after the crack had grown by approximately 60% of the original uncracked ligament. At each unloading, the appropriate values of δ_0, δ_R, and δ_{dc} were calculated. All the SENB specimens were fitted with double clip gauge arrangements to permit the calculation of δ_{dc}.

Standard CTOD (δ_0)

The standard formula in BS 5762 [*14*] for calculating CTOD from an SENB specimen is given by

$$\delta = \frac{K^2(1 - \nu^2)}{2E\sigma_{YS}} + \frac{0.4(W - a_0)}{0.4W + 0.6a_0 + z} V_p \tag{6}$$

where

K = stress intensity factor,
σ_{YS} = yield strength,
ν = Poisson's ratio,
z = knife edge height,
V = crack mouth opening displacement, and
V_p = plastic component of crack mouth opening displacement ($V - V_e$) where the elastic component, V_e, is based on the initial slope of the load displacement record.

TABLE 4b—*Test matrix for HY 100 specimens: geometry effects program.*

Specimen Numbers	Specimen Thickness, mm	Specimen Width, mm	a/W Ratio
16–18	30	15	0.6
19–21	30	30	0.6
7–9	30	60	0.6
22–24	30	90	0.6
25–27	30	120	0.6

NOTE: All specimens sidegrooved by 20%.

The first term in Eq 6 represents the small-scale yielding component of CTOD, which is expressed as a function of the stress intensity factor. As the fracture toughness specimens tested in this investigation were side grooved, the stress intensity factors were determined using the following expression.

$$K = \frac{P}{(BB_n)^{1/2} W^{1/2}} F(a_0/W) \tag{7}$$

where

$F(a_0/W)$ = the stress intensity function given in BS 5762.

The second term in Eq 6 is the plastic component of CTOD, which is calculated from the plastic component of mouth opening displacement (V_p). This calculation assumes that a plastic hinge forms at a point of 0.4 ($W - a_0$) ahead of the initial crack tip. No account, therefore, is taken of the fact that the center of rotation of the plastic hinge may move as the crack extends. The general method of determining V_p involves measuring the slope of the load versus crack mouth opening displacement test record in the elastic regime, so that the elastic component of the crack mouth opening displacement at the point of interest can be subtracted from the total displacement. Note, since the construction procedure uses the slope of the initial elastic portion of the test record, which is a function of a_0, the calculation of V_p does not take crack growth into consideration.

CTOD Corrected for Crack Growth (δ_R)

The EGF ductile fracture test procedure [4] includes an expression for calculating CTOD which takes crack growth into account. The formula, which is applicable to both compact and SENB specimens, was originally proposed by Hellman and Schwalbe [9] and is given by

$$\delta_R = \frac{K^2(1 - \nu^2)}{2E\sigma_{YS}} + \frac{[0.6\Delta a + 0.4(W - a_0)]}{[0.6(a_0 + \Delta a) + 0.4W + z]} V_p \tag{8}$$

where

Δa = ductile crack extension.

Hellman and Schwalbe have shown that this correction for crack growth has to be applied to ensure agreement with the CTOD measured at the original crack tip. The principle behind this correction is that the plastic hinge forms $0.4[W - (a_0 + \Delta a)]$ ahead of the actual crack tip. The above equation, therefore, does not take account of the fact that the plastic hinge position changes with increasing crack growth. This problem, however, can be overcome if the plastic component of δ_R is rewritten in an incremental form. The resulting expression is given by

$$\delta_{R_K} = \frac{K_k^2(1 - \nu^2)}{2E\sigma_{YS}} + \delta_{pl_k} \tag{9}$$

where

$$\delta_{pl_k} = \delta_{pl_{k-1}} + \left[\frac{0.6(a_k - a_0) + 0.4(W - a_0)}{0.6a_k + 0.4W + z}\right] (V_{p_K} - V_{p_{K-1}})$$

δ_{R_k} = δ_R evaluated at crack length a_k,
δ_{pl_k} = plastic component of δ_R evaluated at crack length a_k
a_k = crack length at kth unloading.

In the above incremental equation, it is assumed that the instantaneous center of rotation of the plastic hinge is located 40% of the remaining ligament ahead of the current crack. In addition, the stress intensity factor and the plastic component of mouth opening displacement are based on the current crack length, i.e., the slope of the unloading line at the kth unloading is used to evaluate V_{p_k}.

CTOD Derived from Double Clip Gauge (δ_{dc})

The calculation of δ_R assumes that the instantaneous plastic hinge is located 40% of the remaining ligament ahead of the current crack. Previous work on a titanium alloy [11] has shown that this assumption is not always valid. In the case of the titanium alloy, it was found that the instantaneous plastic rotational factor increased from approximately 0.3 to 0.7 over 10 mm of crack growth in a 20 by 40 mm SENB specimen.

The problems associated with the assumption of a constant plastic rotational factor can, to some extent, be avoided by fitting a double clip gauge arrangement to the fracture toughness specimens. In such cases an estimate of the total CTOD (δ_{dc}) can be obtained using the following relationship

$$\delta_{dc} = \frac{K^2(1 - \nu^2)}{2E\sigma_{ys}} + \delta_{pl} \tag{10}$$

where

$$\delta_{pl} = V_p^u - \left[\frac{(V_p^u - V_p^l)(z_u + a_0)}{(z_u - z_l)}\right]$$

V_p^l = plastic mouth opening displacement associated with lower clip gauge,
V_p^u = plastic mouth opening displacement associated with upper clip gauge,
z_l = lower knife edge height, and
z_u = upper knife edge height.

In the above expression, the plastic component of δ_{dc} is calculated directly from the measured V_p's obtained from the two clip gages. The calculation assumes that δ_{pl} is given by a linear extrapolation of the upper and lower V_p's as illustrated in Fig. 1.

If necessary, Eq 10 can be reformulated to give the following incremental expression

$$\delta_{dc_k} = \frac{K_k^2(1 - \nu^2)}{2E\sigma_{ys}} + \delta_{pl_k} \tag{11}$$

where

$$\delta_{pl_k} = \delta_{pl_{k-1}} + (V_{p_k}^l - V_{p_{k-1}}) - \left[\frac{(V_{p_k}^u - V_{p_{k-1}}^u) - (V_{p_k}^l - V_{p_{k-1}}^l)(z_l + a_0)}{(z_u - z_l)}\right]$$

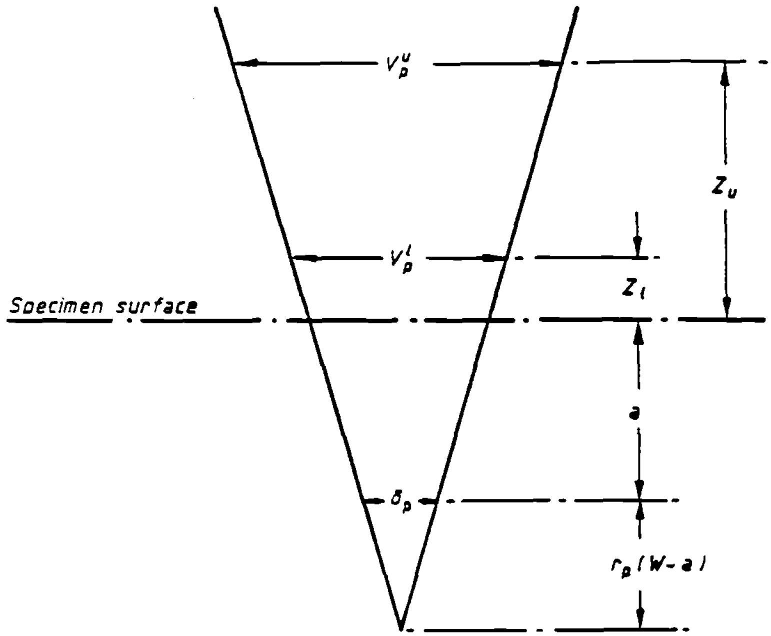

FIG. 1—*Measurement of plastic component of CTOD using double clip gauge arrangement.*

Results

General

All the unloading compliance CTOD *R*-curves (obtained from all three materials) satisfied the requirement that the difference between the measured and predicted crack growth should not exceed 10% [*1*]. Indeed, in the majority of tests the difference was less than 5%.

To give an indication of the variability of the NAB CTOD *R*-curve data, the δ_0 *R*-curves obtained for the 30 by 60 mm SENB specimens are compared in Fig. 2.

The materials tested in this program were selected to provide a range of *R*-curve behavior (i.e., high medium and low toughness). The CTOD *R*-curve behavior produced by the three materials is compared in Fig. 3. It is evident that the NAB alloy has a much higher toughness (i.e., steeper *R*-curve) than either the titanium alloy of the HY 100 steel.

The unloading compliance test data were also analyzed to determine the amount of stable crack growth that preceded the maximum applied load in each test. The average values of crack extension up to maximum load, Δa_m are compared with the Δa_m results obtained from the Ti-3Al-2.5V and HY 100 materials in Fig. 4. It is evident from Fig. 4 that for each material the crack extension up to maximum load increases with specimen size in approximately a linear fashion. Of the three materials studied, the NAB alloy produced the largest crack growth up to maximum load for a given specimen size.

NAB CTOD R-*Curve Results*

The CTOD *R*-curves obtained from the NAB alloy are presented in Figs. 5–7. In each case the CTOD *R*-curve presented for each specimen size represents the mean CTOD *R*-curve behavior obtained from a set of three specimens.

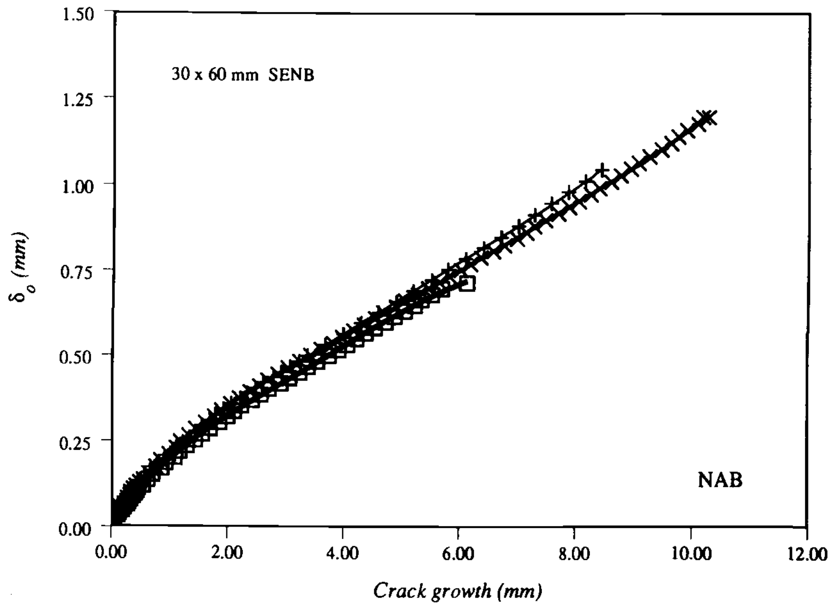

FIG. 2—*Comparison of NAB* δ_0 R-*curves from 30 by 60-mm SENB specimens.*

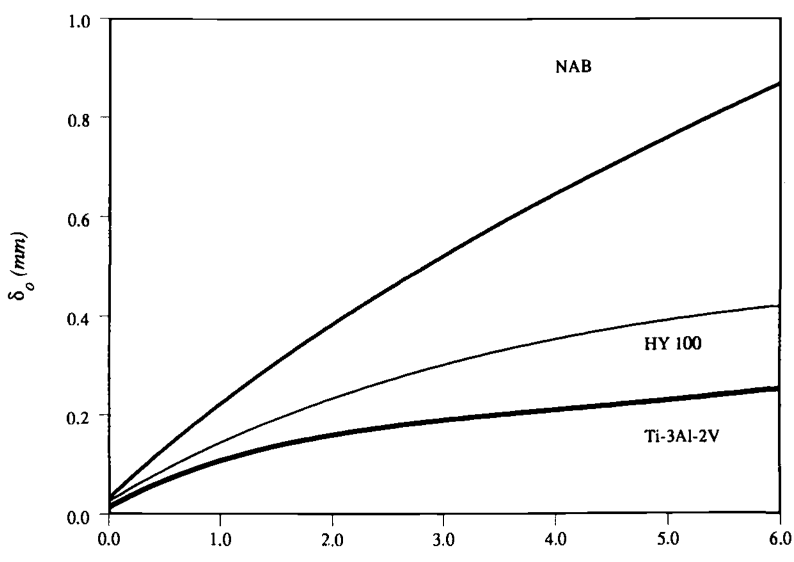

FIG. 3—*Comparison of* δ_0 R-*curves for Ti-3Al-2.5V, HY 100, and NAB.*

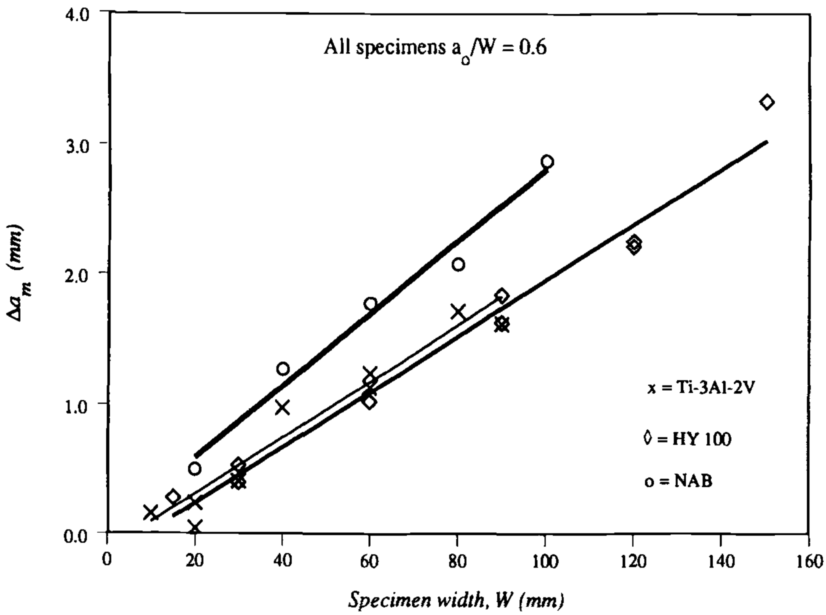

FIG. 4—*Plot of stable crack growth prior to maximum load against specimen width (W).*

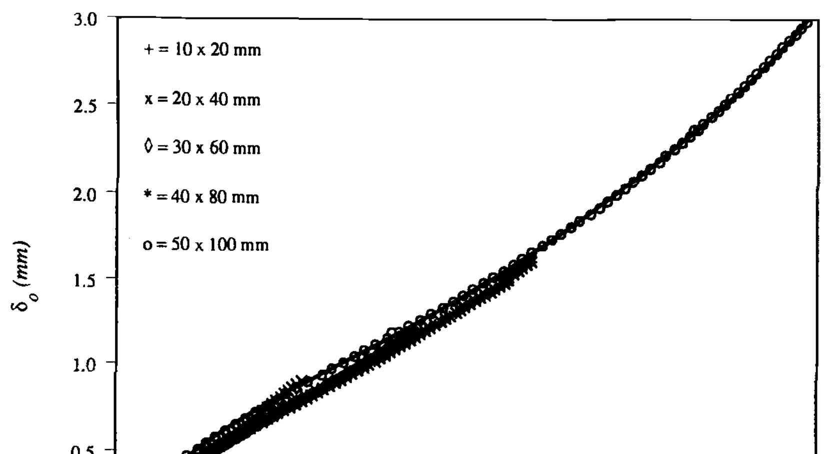

FIG. 5—*Comparison of NAB δ_0 R-curves (B $\times$ 2B SENB).*

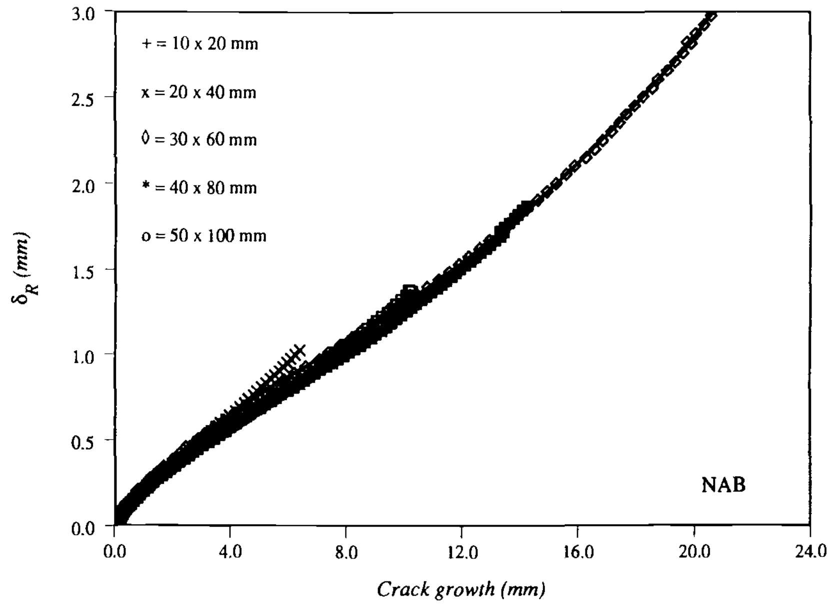

FIG. 6—*Comparison of NAB* δ_R R-*curves (*B × 2B *SENB).*

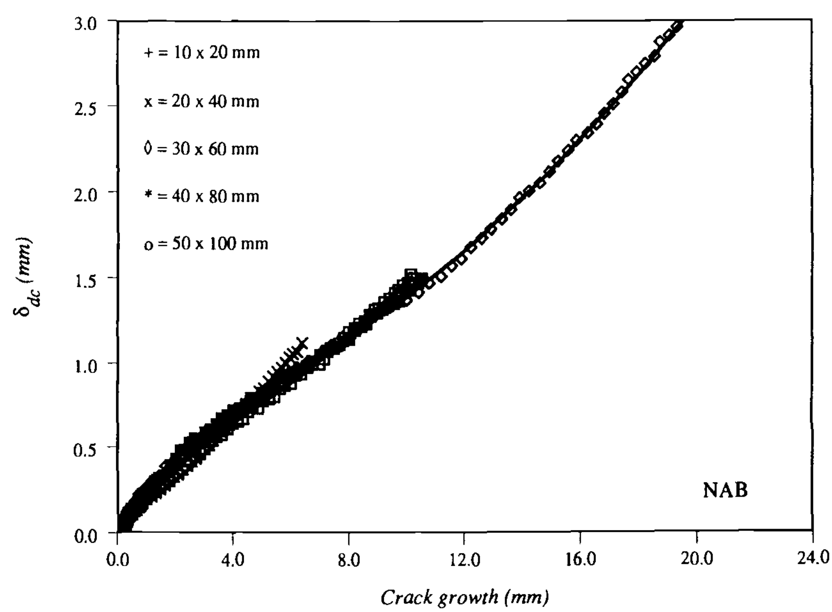

FIG. 7—*Comparison of NAB* δ_{dc} R-*curves (*B × 2B *SENB).*

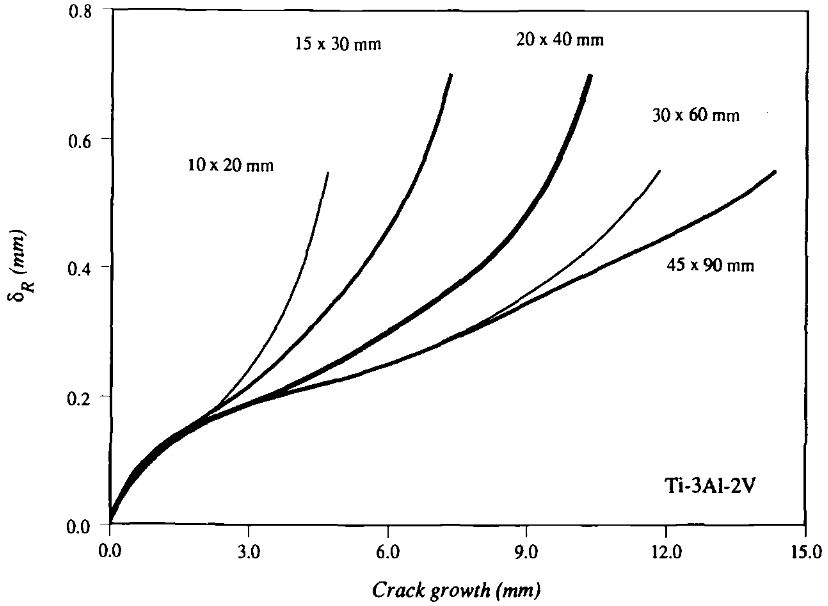

FIG. 8—*Comparison of Ti-3Al-2.5V δ_R R-curves (B $\times$ 2B SENB).*

It is evident from Figs. 5–7 that all three sets of R-curves (δ_0, δ_R, and δ_{dc}) exhibit excellent agreement. In each case the small specimen R-curves remain in excellent agreement with the large specimen R-curves throughout the crack growth range over which they were tested (approximately 50% of the initial uncracked ligament). The large specimens (50 by 100 mm) exhibited approximately 3.0 mm of stable crack growth prior to maximum load in comparison to approximately 0.5 mm for the small specimens (10 by 20 mm). This confirms that R-curves obtained from small specimens tested beyond maximum load can still give R-curves which are representative of much larger specimens (i.e., small specimen R-curves do not necessarily lose size independence beyond maximum load).

The CTOD R-curve behavior exhibited by the NAB alloy (i.e., excellent agreement throughout the entire crack growth range) is in marked contrast to the trends obtained from the Ti-3Al-2.5V alloy and HY 100 steel. In the case of the latter two materials, it was found that initially the R-curves obtained from the small specimens exhibited nominally identical behavior to the large specimen R-curves, but as crack growth continued the small specimen R-curves exhibited upswings. Moreover, the points at which the R-curves exhibited the upswings appeared to be dependent on specimen size, the smaller specimens displaying upswings at smaller values of crack extension. This behavior is illustrated in Figs. 8 and 9, which shows the δ_R R-curves obtained from the Ti-3Al-2.5V alloy and HY 100 steel size effects programs.

Discussion of Results

At the outset of this project it was hoped that it would be possible to estimate the limits of CTOD controlled crack growth from the CTOD R-curves by identifying the point at which the small specimen R-curves separate from the large specimen R-curves and evaluating the limiting values of ρ, α, and ω using the following expressions

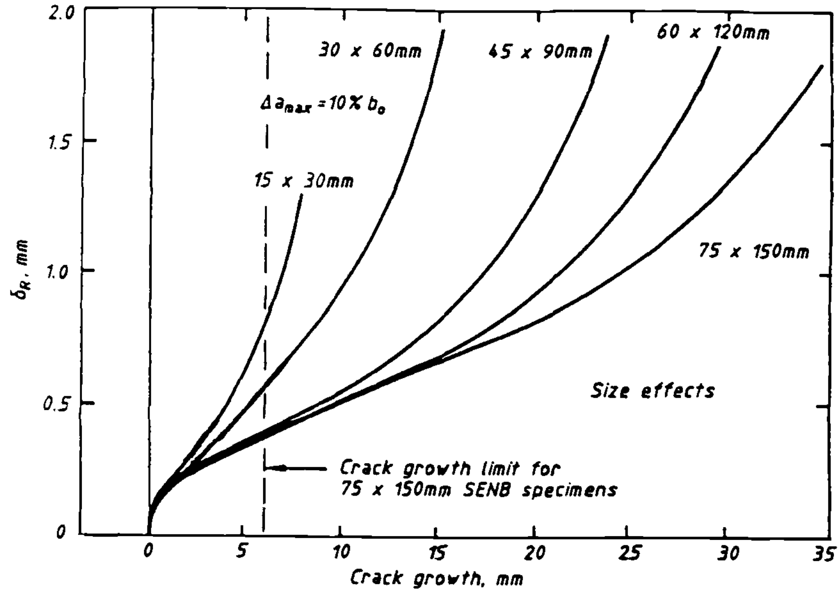

FIG. 9—*Comparison HY 100 δ_R R-curves (B × 2B SENB).*

$$\rho = \frac{B}{\delta_s}, \frac{b}{\delta_s} \tag{13}$$

$$\alpha = \frac{\Delta a_s}{b_0} \tag{14}$$

$$\omega = \frac{b}{\delta_s}, \frac{d\delta}{da} \tag{15}$$

where

Δa_s = crack growth at separation, and
δ_s = CTOD at separation.

Note: Since the ρ criterion is related to both ligament and specimen thickness, the ρ results have been further broken down to denote the specimen dimension used in the calculation (i.e., $\rho_b = \rho$ based on current ligament, $\rho_{b_0} = \rho$ based on initial ligament, etc).

However, as demonstrated from the previous work on the Ti-3Al-2.5V alloy and HY 100 steel, the breakdown of J and CTOD controlled crack growth is a gradual process, and consequently the R-curves do not always exhibit well-defined separation points. Although tentative values of ρ, α, and ω were proposed for the Ti-3Al-2.5V alloy and HY 100 steel, the CTOD R-curves obtained from the NAB alloy did not exhibit obvious separation points, and consequently it was not possible to determine values of ρ, α, and ω for this material.

It was found that the limiting values of ρ, α, and ω obtained from the various CTOD R-curves did not exhibit a consistent trend. This is perhaps indicative of the problems associated with identifying the separation points. In order to produce more accurate estimates of the limiting values of ρ, α, and ω, fifth order polynomials were fitted to the various CTOD R-curves by the method of least squares. For each specimen size, three fifth order polynomial fits were determined corresponding to δ_0, δ_R and δ_{dc} R-curve behavior. In all cases the fifth order polynomial expressions produced excellent fits. The subsequent polynomial expressions were then differentiated to produce plots of $d\delta/da$ versus Δa. Plots of $d\delta/da$ versus Δa are presented in Figs. 10–12 for the size effects R-curves obtained from the three materials. It is evident that in the case of the Ti-3Al-2.5V material the slopes of the R-curves reach a minimum at crack growths in the range of 12 to 17% of the initial uncracked ligament. Beyond this point the R-curves exhibit upswings. In the case of the HY 100 material, the slopes of the R-curves reach a minimum at crack extensions corresponding to 17% of the initial uncracked ligament. The HY 100 R-curves also exhibit a dramatic increase in slope at crack extensions corresponding to approximately 45% of the initial uncracked ligament. Finally, in the case of the NAB material, the slopes of the R-curves reach a minimum at crack extensions corresponding to approximately 15% of the initial uncracked ligament.

It should be noted that the trends exhibited in Figs. 10–12, including the crack extensions corresponding to the minimum R-curve slope, were produced by all three CTOD fracture toughness parameters studied in this project.

Based on the above trends it is postulated that the limiting value of α for Ti-3Al-2.5V alloy, HY100 steel and NAB CTOD R-curve data is approximately 0.15. Beyond this limit the CTOD R-curves exhibit upswings, which in the opinion of the authors is due to loss of crack tip constraint. Indeed, since a reduction in constraint is likely to result in large amounts of additional information being required to produce small amounts of crack extension, it is not unreasonable to expect an upswing in CTOD R-curves. Although a limiting α value of 0.15

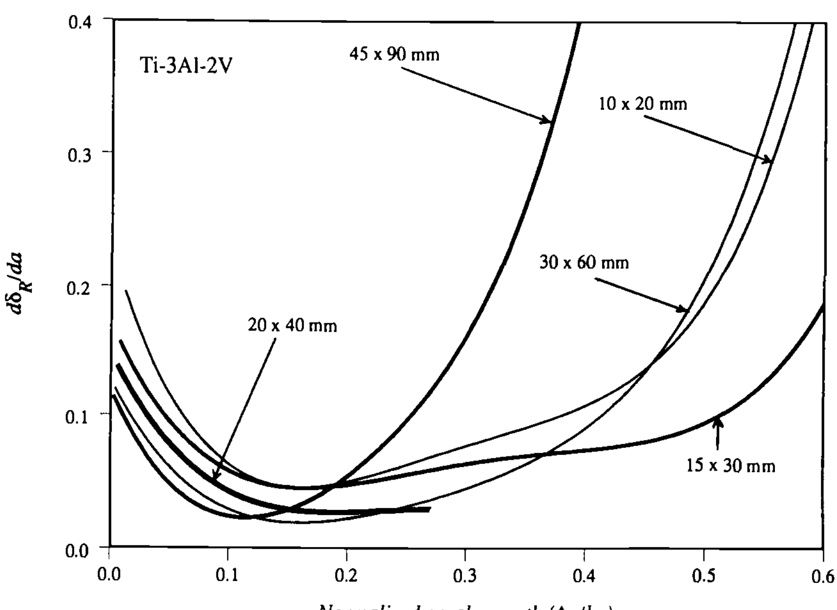

FIG. 10—*Plots of* $d\delta_R/da$ *versus normalized crack growth (Ti-3Al-2.5V).*

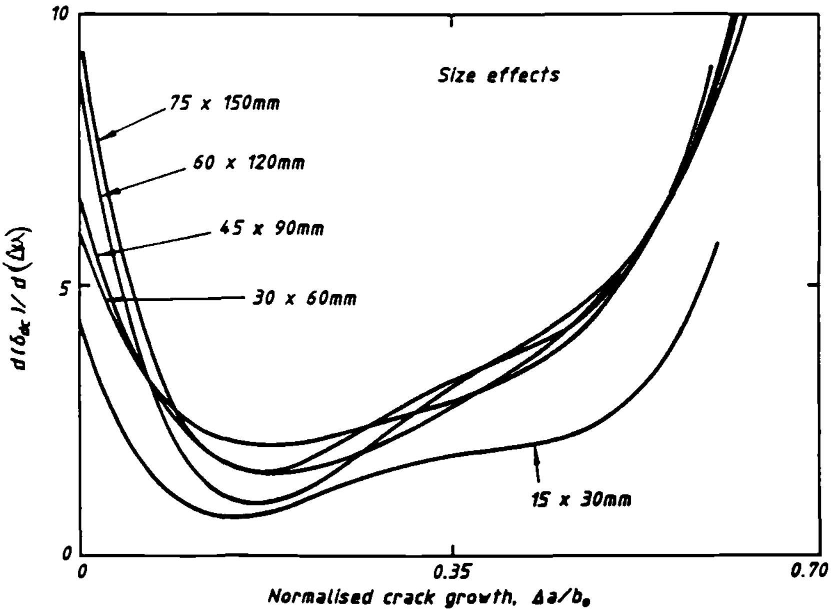

FIG. 11—*Plots of* $d\delta_{dc}/da$ *versus normalized crack growth (HY 100).*

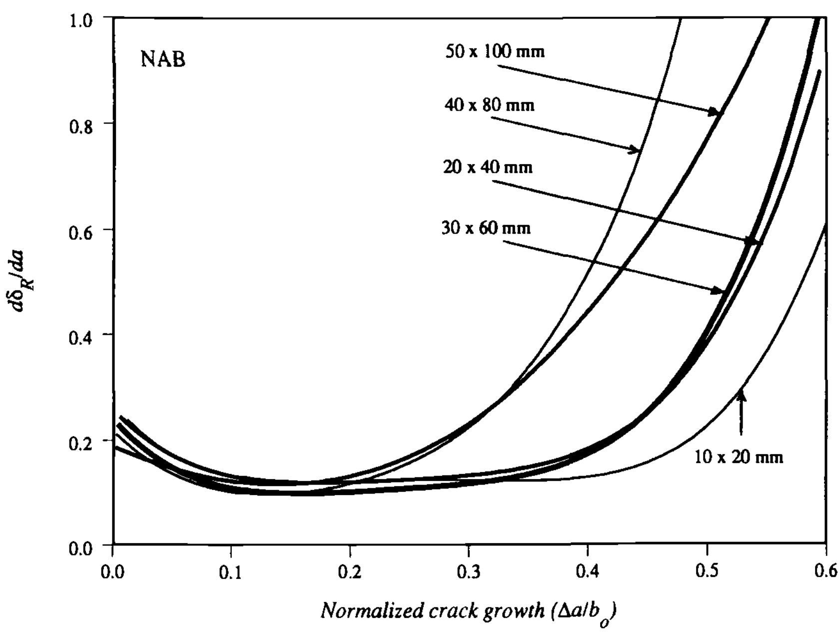

FIG. 12—*Plots of* $d\delta_R/da$ *versus normalized crack growth (NAB).*

appears to apply to all the CTOD *R*-curves obtained in this project, it does not necessarily guarantee size-independent *R*-curve behavior. Indeed, if the CTOD *R*-curves obtained in the HY 100 geometry effects program are compared to the corresponding CTOD *R*-curves obtained from the HY 100 size effects program, it is clear that most of the large specimen CTOD *R*-curves in the geometry effects program separate from the 75 by 150-mm SENB CTOD *R*-curve long before the $\alpha = 0.15$ limit. This implies that the 30-mm-thick specimens used in the geometry effects program are not sufficiently thick to produce plane strain conditions beyond CTOD levels of approximately 0.3 mm and crack extensions of 2.5 mm. This corresponds to a limiting ρ_B value of approximately 100, which is much larger than the limit specified in the EGF CTOD *R*-curve procedure, i.e., $\rho > 50$. It should be pointed out that this trend was not exhibited by the Ti-3Al-2.5V and NAB materials, which suggests that the ρ criterion was not invalidated for these materials. The results obtained from the latter materials indicate that the ρ limit could be as low as 20. These findings confirm that the limits of CTOD controlled crack growth are material dependent.

The use of a normalized abscissa in removing size and geometry effects beyond the limit of *J* controlled crack growth has been reported by Etemad and Turner [*15,16*]. The normalization takes the form $\Delta a/c$ where c is the parameter which inhibits the plastic work dissipation such as specimen thickness, ligament length, or material toughness. Throughout the size effects studies in this project, the specimens were geometrically identical (i.e., all B by $2B$) and were all precracked to an initial a/W ratio of 0.6. As a result the ligament should be the limiting geometric parameter for these specimens. A selection of normalized CTOD *R*-curves are presented in Figs. 13–15 for the three materials studied. It is evident that in the case of the HY 100 material the normalization procedure has produced a common curve with the exception of the *R*-curve obtained from the 15 by 30 mm specimen. However, in the case of the Ti-3Al-2.5V and NAB materials, the normalization procedure has not been successful.

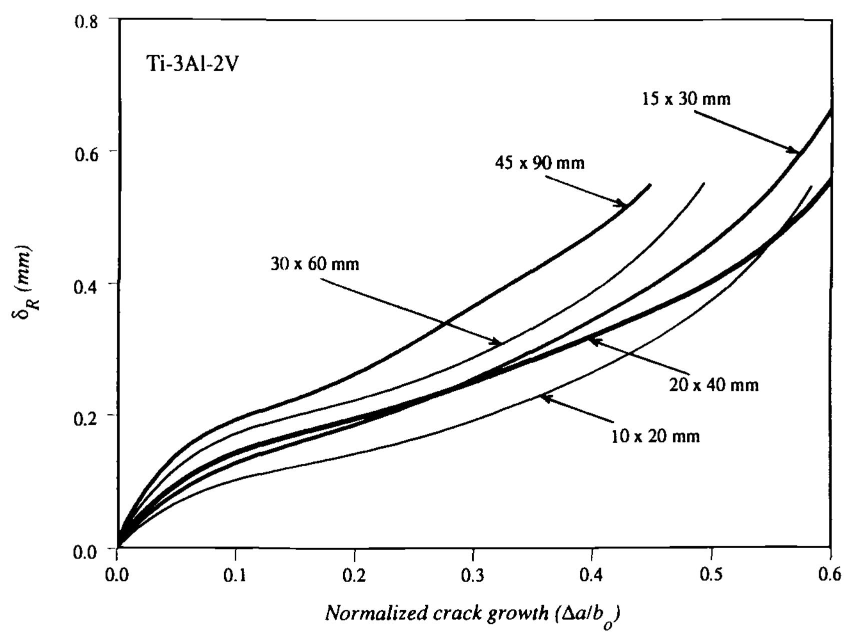

FIG. 13—*Normalized* δ_R R-*curves (Ti-3Al-2.5V).*

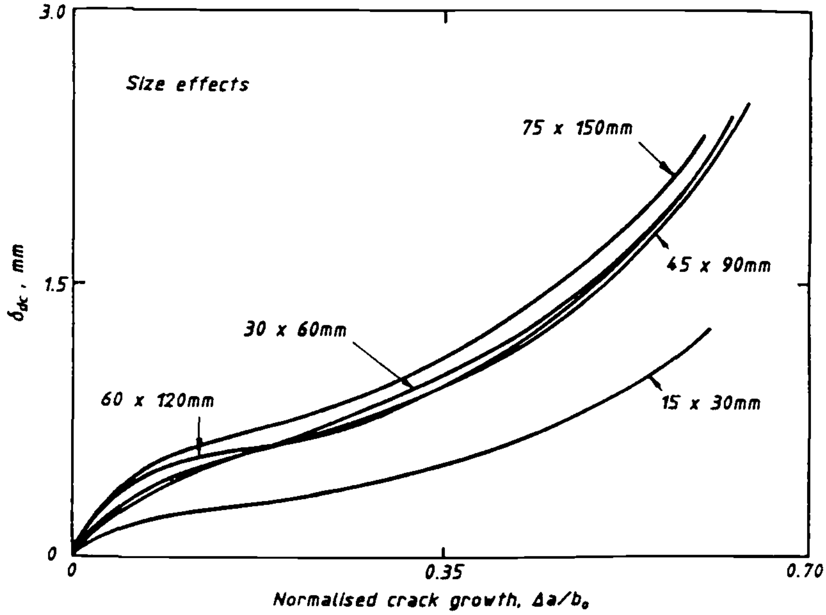

FIG. 14—*Normalized* δ_{dc} R-*curves (HY 100).*

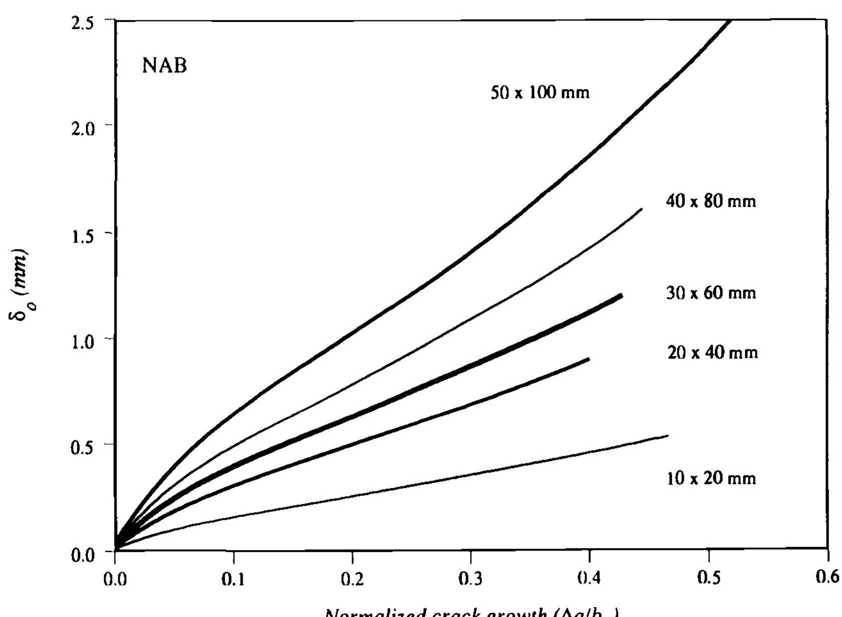

FIG. 15—*Normalized* δ_0 R-*curves (NAB).*

Conclusions

A series of unloading compliance R-curve tests have been performed on SENB specimens of different sizes made from Ti-3Al-2.5V alloy, HY100 steel, and nickel-aluminum-bronze (NAB) to study the CTOD R-curve behavior at large crack extensions. The crack growth resistance was measured in terms of conventional CTOD, δ_0, (as defined in BS 5762), CTOD corrected for crack growth, δ_R, and CTOD derived using a double clip gage arrangement, δ_{dc}. It was found that:

1. The limits of CTOD controlled crack growth are material dependent.
2. The δ_0 and δ_R R-curves exhibited size and geometry independence over approximately the same ranges of crack extension.
3. In general, the δ_{dc} R-curves exhibited size and geometry independence over slightly larger ranges of crack extension than the corresponding δ_0 and δ_R R-curves. For this reason it is recommended that CTOD R-curves should be based on the δ_{dc} parameter. This parameter also has the advantage that the calculation procedure does not assume a fixed value of 0.4 for the plastic rotational factor.
4. For specimens of a given thickness increasing the specimen width appears to increase the crack growth range over which the CTOD R-curves are in agreement. Nevertheless, this does not guarantee that the subsequent CTOD R-curve behavior exhibited over this crack growth range is size independent, i.e., it may be dependent on specimen thickness.
5. All the CTOD R-curves obtained in this study exhibited upswings. The upswings, in general, started at crack extensions corresponding to 15% of the initial uncracked ligament.
6. Based on the above observations, it is postulated that the crack growth limit for CTOD controlled crack growth in R-curves is 15% of the initial uncracked ligament. This condition alone, however, is not sufficient to guarantee size/geometry independent results. It is also necessary to have the same level of specimen constraint. The following values of ρ are proposed to ensure plane strain constraint:

$$\rho_B = 100$$

$$\rho_b = 50$$

References

[1] Gordon, J. R., "The Welding Institute Procedure for the Determination of the Fracture Resistance of Fully Ductile Metals," Welding Institute Report 275/1985, June 1985.

[2] Neale, B. K., Curry, D. A., Greene, G., Haigh, J. R., and Akhurst, K. N., "A Procedure for the Determination of the Fracture Resistance of Ductile Steels," *International Journal of Pressure Vessels and Piping*, Vol. 20, 1984, pp. 155–179.

[3] ASTM E1152: "Standard Method for Determining J R-Curves," 1987.

[4] European Group on Fracture (EGF) "EGF Recommendations for Determining the Fracture Resistance of Ductile Materials," 1990, pp. 1–90.

[5] ASTM E1290: Standard Test Method for Crack Tip Opening Displacement (CTOD) Fracture Toughness Measurement, 1989.

[6] Shih, C. F., and German, M. D., "Requirements for a One Parameter Characterization of Crack Tip Fields by the HRR-Singularity," *International Journal of Fracture*, Vol. 17, 1981, pp. 27–43.

[7] Hutchinson, J. W., "Fundamentals of the Phenomenological Theory of Non-Linear Fracture Mechanics," *Journal of Applied Mechanics*, Vol. 50, 1983, pp. 1042–1051.

[8] Landes, J. D., "Size and Geometry Effects on Elastic-Plastic Characterization," CNSI Specialists Meeting on Plastic Tearing Instability, NUREG/CP-0010, 1979, pp. 194–225.

[9] Hellman, D. and Schwalbe, K. H., "On the Experimental Determination of CTOD Based R-Curves," Workshop on the CTOD Methodology, GKSS, Geesthact, 1985.

[10] Gordon, J. R. and Jones, R. L., "The Effect of Specimen Size on the *J R*-Curve Behavior of a Titanium Alloy," *Fatigue and Fracture of Engineering Materials and Structures*, Vol. 12, 1989, pp. 295–308.

[11] Gordon, J. R. and Jones, R. L., "The Effect of Specimen Size on the CTOD *R*-Curve Behavior of a Titanium Alloy," *Fatigue and Fracture of Engineering Materials and Structures*, Vol. 12, 1989, pp. 309–321.

[12] Gordon, J. R. and Jones, R. L., "Specimen Size Requirements for Elastic-Plastic Crack Growth Resistance Curves," presented at the 2nd ASTM Symposium on Users Experience with Elastic-Plastic Test Methods, Lake Buena Vista, Florida, November 1989.

[13] Jones, R. L. and Gordon, J. R., "The Effect of Specimen Size and Geometry on the *J R*-Curve Behavior of HY 100 Steel," presented at the EGF Elastic-Plastic Fracture Mechanics Symposium, Freiburg, FRG, October 1989.

[14] BS 5762: Methods for Crack Opening Displacement (COD) Testing, British Standards Institution, 1979.

[15] Etemad, M. and Turner, C. E., "*R*-Curves with Normalized Axes," *International Journal of Pressure Vessels and Piping*, Vol. 26, 1986, pp. 79–86.

[16] Etemad, M. and Turner, C. E., "Unique Elastic-Plastic R-Curves, Fact or Fiction?" *Fracture Mechanics (21st Symposium), ASTM STP 1074*, 1990, pp. 289–306.

Allen L. Hiser, Jr.[1]

Specimen Size Effects on *J-R* Curves for RPV Steels

REFERENCE: Hiser, A. L., Jr., "**Specimen Size Effects on *J-R* Curves for RPV Steels,**" *Constraint Effects in Fracture, ASTM STP 1171*, E. M. Hackett, K.-H. Schwalbe, and R. H. Dodds, Eds., American Society for Testing and Materials, Philadelphia, 1993, pp. 195–238.

ABSTRACT: This study examined the effect of specimen size on *J-R* curves for reactor pressure vessel (RPV) steels. Overall comparisons for monolithic materials (base plate and forging) indicated that no significant size effect is apparent, using standard formulations for the *J*-integral within commonly accepted validity bounds. However, materials that are composite in nature, such as weld materials, or exhibit macro-scale inhomogeneities gave significant differences in *J-R* curve trends for different sizes of specimens.

KEY WORDS: fracture toughness, size effect, *J-R* curve, pressure vessel steel, *J*-integral

The *J*-integral proposed by Rice [*1*] is used as a fracture mechanics parameter for characterizing the elastic-plastic behavior of structural steels. For fully ductile upper shelf fracture behavior of such materials, the *J*-resistance curve (*J* as a function of slow stable crack growth) is used to characterize material fracture toughness. The *J-R* curve then provides a measure of the tearing resistance of the material under increasing load or displacement. This work examines the effect of specimen size on *J-R* curves. Implicit in this evaluation will be an assessment of the appropriateness of the various formulations of the *J*-integral available in the literature [*2–4*].

The laboratory evaluation of the *J-R* curve is normally accomplished using ASTM Standard Test Method for J_{Ic}, A Measure of Fracture Toughness (E 813) and Standard Test Method for *J-R* Curves (E 1152). For such evaluations, the specimens used are generally in the form of the compact tension, C(T), or the three-point bend, SE(B), geometries, with the use of C(T) specimens more prevalent in the technical community. If the *J-R* curve is a material property much as tensile strength is a material property, then one should be able to use specimens of different sizes and obtain the same *J-R* curve performance. In fact, various validity criteria have been developed to ensure that "*J*-dominance" occurs in the specimen [*5,6*].

From the standpoint of structural analysis, *J-R* curve data for crack growth of 25.4 mm (1 in.) or more is required in many instances to determine if the structure is safe for continued operation. *J-R* curve validity requirements for such large crack growth levels require quite large specimens, which tend to be costly from the standpoints of monetary and material consumption. Therefore, an ability to use smaller specimens, without sacrificing the integrity and usefulness of the resultant data, would provide a considerable advantage from several standpoints.

This work is focused on the effect of specimen size on *J-R* curve trends for several nuclear grade materials used in reactor pressure vessel (RPV) construction, including base materials

[1] Materials engineer, United States Nuclear Regulatory Commission, Mail Stop 217C NL/S, Washington, DC 20555 (formerly with Materials Engineering Associates, Inc., Lanham, MD).

and welds. Various formulations of the J-integral [*2–4*] are used to determine the appropriateness of each, with an emphasis on their ability to correlate the J-R curve trends from different size specimens to greater increments of crack growth.

Previous work in this area is not too extensive. McCabe and Landes [*7*] used specimens ranging in size by a factor of 20. This work led to the development of J_M by Ernst [*4*]. The other readily available work [*8–10*] used single specimen sizes from a planar view (either large or small), with specimen dimensions such as gross or net thickness and initial crack length varied in these works. In all cases, regions of correspondence between data from the various specimen configurations were found, and these regions were in some cases used as the bases for validity criteria development.

For the base materials in this study, the specimens are monolithic or essentially homogeneous, with large and small specimens composed of nominally the same material throughout. In contrast, for the weld materials, all of the specimens are composite specimens, composed of both weld and base metal. The crack propagation direction for the weld specimens is along the weld. The width of the weld region varies from 0.5 to 2 in. (12.7 to 51 mm), so that the small specimens are composed of predominantly weld metal, whereas the large specimens are predominantly base metal. The deformation characteristics of the weld and the base metals oftentimes are different, and the effect of these differences on the resultant J-R curves cannot be generally defined. In this study, the base metals consist of two heats exhibiting a "clean" fracture appearance and one heat exhibiting an extremely fibrous or inhomogeneous appearance. In contrast, the weld metals all exhibit a "clean" fracture appearance.

Test and Data Analysis Procedures

Specimen Designs and Test Procedures

The J-R curve tests were conducted using C(T) specimens ranging in size from 0.5T- to 6T-C(T). In general, the specimen designs are consistent with recommended proportionalities used in ASTM Standard Test Method for Plane-Strain Fracture Toughness of Metallic Materials (E 399), although for the small specimens [0.5T- and 1T-C(T)] the pinhole spacing was increased and the pinhole size was reduced for the 0.5T-C(T) specimens. The latter modifications, in conformance with ASTM E 813 and E 1152, permit measurement of load-line displacements in the standard position (i.e., between the loading pinholes).

Displacements were measured at several locations on the specimens (Fig. 1). In general, load-line displacement (measured between the pinholes, V_{LL}) was used for evaluations of crack length (via specimen compliance measurements) and J. For the 0.5T- and 0.8T-C(T) specimens of the weld metals, the load-line displacements used for J evaluations were measured external to the pinholes ($V_{LL'}$), as illustrated in Fig. 1. Discussion of the appropriateness of using $V_{LL'}$ measurements for evaluation of J is given in Ref *11*. Crack mouth or front-face displacement (V_M) was used for crack-size prediction via compliance evaluation in these cases.

The specimens were precracked in tension using cyclic loading. To facilitate initiation, the notch was loaded in precompression prior to the cyclic loading.

All specimens were side grooved by 20% of the total specimen thickness (B), 10% per side, using a Charpy-V (C_v) notch cutter (45° included angle and 0.25 mm, 0.01 in., root radius) after precracking. The resultant net specimen thickness (B_N) was then equal to 0.8 B.

The procedures used for these tests are in accordance with ASTM standards E 813 and E 1152. Specifically, the unloading compliance method was used to evaluate crack length during each test. Appropriate compliance expressions for the V_M and V_{LL} measurement positions were used in each case [*12*].

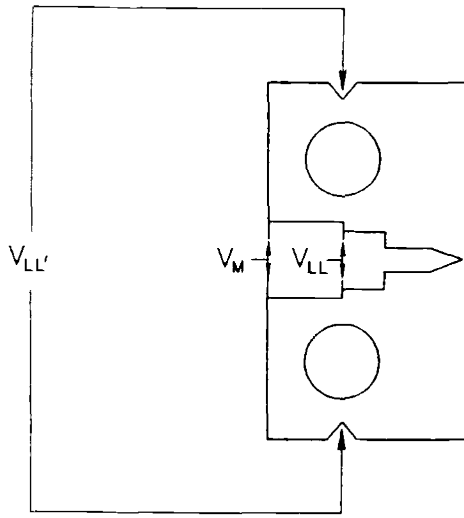

FIG. 1—*Displacements were measured at several locations on the compact tension specimens during these tests.*

J-Integral Evaluation Procedures

The J-integral values have been evaluated using three different formulations, specifically the Merkle-Corten form, J_{M-C} [*2*], the deformation theory form, J_D [*3*], and the "modified J", J_M [*4*].

The J_{M-C} formulation was developed to account for the axial force in the C(T) specimen and results in J values similar to values of G for the case of failure in the linear range of the load-displacement curve. The J_{M-C} formulation was not originally intended for growing cracks. As used in this paper, the initial crack length is not incremented for crack growth.

To account for crack growth in the evaluation of J, Ernst developed a crack growth correction procedure which preserves the conditions of a deformation theory of plasticity interpretation of J during crack growth; this formulation is termed here J_D [*3*] and is the form specified for use in ASTM E 1152. Evaluation of J_D-R curves for different sizes of C(T) specimens have demonstrated a specimen-size dependence as well [*4*].

For crack extension levels beyond the limit of 10% of $W - a_0$, one negative characteristic of J_D is a tendency towards a size effect, whereby smaller specimens give lower J-R curve levels than larger specimens, with negative J-R curve slopes resulting in some cases. To extend J measurements to greater crack extensions, Ernst introduced a new definition of J that appeared to satisfy the characteristics of a different type of J that Rice, Drugan, and Sham [*13*] had proposed was necessary for independence from crack growth, Δa. This new J-like value was termed "modified J" or J_M by Ernst [*4*]. The attributes of J_M cited by Ernst include a better accounting for the past history effects of deformation and crack growth in arriving at a given condition of load, displacement, and crack length. J_M allows for a large relaxation of the restrictions on the amount of crack extension and/or initial remaining ligament required to produce geometry-independent R-curves. The specimen size-independent characteristic of J_M was initially demonstrated in Ref *4* for an A 508 Class 2A steel using data from 0.5T- to 10T-C(T) specimens.

The J_D and J_M equations described above represent "total work done" forms of each whereby the area under the load-total displacement curve is used to evaluate J. Recent thinking indicates that a more appropriate way to evaluate J_D and J_M is to separate the elastic and plastic work portions of J, with J_{el} evaluated from ASTM Test Method for Plain-Strain Fracture Toughness of Metallic Materials (E 399), and J_{pl} evaluated using the area under the load-plastic displacement curve

$$J = J_{el} + J_{pl} \tag{1}$$

All of the data reported here are determined by separate consideration of elastic and plastic J as set forth in ASTM E 1152–87.

Material Evaluation

An additional comparison which will be used with these tests employs the "key curve" representation obtained from the test records (Refs *14* and *15*). The key curve for a test record compares normalized load (P_N, in units of stress) to normalized displacement, δ_N. The normalized displacement is dimensionless. For the compact specimen, these quantities are defined as

$$P_N = \frac{PW}{Bb^2g(a/W)} \tag{2}$$

$$\delta_N = \delta_{pl}/W = (\delta - PC)/W \tag{3}$$

with $g(a/W) = \exp[0.522(1 - a/W)]$, P and δ are the measured load and load-line displacement, respectively, and C is the elastic compliance (mm/kN or in./lb) corresponding to the current crack length. The key curve tends to have a shape similar to that of a true stress-strain record, with P_N levels continually increasing as δ_{pl}/W increases. The dimensions "a" and "b" (Eq 2) are updated for the crack growth which occurs during J-R curve testing. Therefore, correctly knowing the crack length (which is generally inferred from compliance measurements) permits comparison of the key curves from specimens of different overall size or different crack length. If the key curves for the different specimens are coincident, then the same deformation behavior is evident for each specimen. If the key curves do not coincide, then the deformation characteristics of the material(s) in the specimens being compared are not the same and one is effectively comparing different material for the different specimens. In contrast, coincident key curves do not ensure that the materials have the same ductile tearing characteristics (i.e., the same J-R curve toughness), since knowledge of the specimen load-displacement trend is required to completely define the material behavior. Conversely, noncoincident key curves do not ensure different J-R curves since the load-displacement-crack growth relationship may compensate for the key-curve differences.

Materials and Test Conditions

The materials used in this analysis are RPV steels, including two base plates, one forging, and several weld metals. The forging is an ASTM A 508 Class 2 forging (Code FP), whereas the base plates represent ASTM A 302 Grade B (Code V50) and ASTM A533 Grade B Class 1 (Code V8) steel plates. The forging and the Code V8 plate are relatively high-toughness materials exhibiting a clean fracture surface appearance. In contrast, the Code V50 plate is a much lower toughness material and exhibits an extremely rough, fibrous fracture surface appearance.

TABLE 1—*Chemical compositions of RPV steels.*

Description	Code	Chemical Composition, wt%									
		Cu	Ni	P	C	Mn	S	Si	Cr	Mo	V
A 533-B Plate	V8	...[a]	0.49	0.015	0.20	1.23	0.017	0.26	...[a]	0.52	...[a]
A 502-2 Forging	FP	...[a]	0.81	0.013	0.27	0.77	0.014	0.32	0.44	0.59	...[a]
A 302-B Plate	V50	0.059	0.23	0.010	0.21	1.46	0.021	0.24	0.06	0.54	0.012
Linde 80 Welds											
	61W	0.28	0.63	0.020	0.090	1.48	0.014	0.57	0.16	0.37	0.005
	62W	0.210	0.537	0.016	0.083	1.51	0.007	0.59	0.120	0.377	0.010
	63W	0.299	0.685	0.016	0.098	1.65	0.011	0.630	0.095	0.427	0.011
	64W	0.350	0.660	0.014	0.085	1.59	0.015	0.520	0.092	0.420	0.007
	65W	0.215	0.597	0.015	0.080	1.45	0.015	0.480	0.088	0.385	0.006
	66W	0.420	0.595	0.018	0.092	1.63	0.009	0.540	0.105	0.400	0.009
	67W	0.265	0.590	0.011	0.082	1.44	0.012	0.500	0.089	0.390	0.007

[a] Not determined.

The welds likewise have low toughness, but exhibit an extremely clean fracture surface appearance. The welds were made using Linde 80 flux, with a high copper content in each weld. High copper content causes high sensitivity to irradiation embrittlement, resulting in significant reductions in toughness after exposure to neutron irradiation [*16*]. The welds were made in either ASTM A 508 Class 2 forging or ASTM A 533 Grade B plate. These welds are coded as 61W through 67W.

The chemical compositions of these materials are given in Table 1. Pertinent uniaxial strength data are listed in Table 2. As indicated, the yield strength and ultimate strength levels

TABLE 2—*Uniaxial strength data for the RPV steels.*

Description	Code	Test Temperature		0.2% Offset Yield Strength		Ultimate Strength	
		°F	°C	ksi	MPa	ksi	MPa
A 533-B Plate	V8	200	93	63.3	436	83.3	575
A 508-2 Forging	FP	130	54	69.2	477	88.0	607
A 302-B Plate	V50	180	82	66.6	459	84.8	584
Linde 80 Welds							
Unirradiated	61W	550	288	60.0	418	77.4	533
Irradiated	61W	550	288	79.0	545	95.6	659
Unirradiated	62W	550	288	55.5	383	74.1	511
Irradiated	62W	550	288	75.7	522	91.1	628
Unirradiated	63W	550	288	59.2	408	76.4	527
Irradiated	63W	550	288	77.2	532	91.6	632
Unirradiated	64W	550	288	57.7	398	78.8	543
Irradiated	64W	550	288	75.4	520	93.7	646
Unirradiated	65W	550	288	59.9	413	79.5	548
Irradiated	65W	550	288	71.8	495	90.1	621
Unirradiated	66W	550	288	72.2	498	88.2	608
Irradiated	66W	550	288	83.7	577	98.8	681
Unirradiated	67W	550	288	62.1	428	81.2	560
Irradiated	67W	550	288	74.8	516	92.8	640

TABLE 3—*Charpy-V data for the RPV steels.*

Description	Code	Test Temperature °F	Test Temperature °C	Orientation[a]	Energy Level ft-lb	Energy Level J
A 533-B Plate	V8	200	93	C-L	134.5	182.4
		300	149	C-L	139.5	189.1
		200	93	L-C	75.0	101.7
A 508-2 Forging	FP	130	54	C-L	81.1	110.0
		USE[b]		C-L	85.7	116.1
		130	54	C-R	83.0	112.5
		USE		C-R	133.8	181.4
A 302-B Plate	V50	180	82	T-L	50.3	68.2
		USE		T-L	53.6	72.6
Linde 80 Welds						
Unirradiated	61W	USE		...[c]	67.9	92.0
Irradiated	61W	USE		...[c]	52.4	71.0
Unirradiated	62W	USE		...[c]	79.7	108.0
Irradiated	62W	USE		...[c]	59.0	80.0
Unirradiated	63W	USE		...[c]	70.8	96.0
Irradiated	63W	USE		...[c]	50.2	68.0
Unirradiated	64W	USE		...[c]	73.8	100.0
Irradiated	64W	USE		...[c]	55.3	75.0
Unirradiated	65W	USE		...[c]	79.7	108.0
Irradiated	65W	USE		...[c]	53.1	72.0
Unirradiated	66W	USE		...[c]	56.1	76.0
Irradiated	66W	USE		...[c]	42.8	58.0
Unirradiated	67W	USE		...[c]	76.0	103.0
Irradiated	67W	USE		...[c]	53.8	73.0

[a] Per ASTM standard E 616.
[b] Average upper shelf energy.
[c] Along the weld.

are quite similar for all of the materials. Charpy-V (C_v) energy levels are summarized in Table 3 for each material. The A 533-B plate and the A 508-2 forging have the highest C_v levels, whereas the A 302-B plate and the weld metals have lower C_v levels.

A 508 Class 2 Forging (Code FP)

This material (from a forged cylinder) was tested at 54°C (130°F) to match an intermediate test vessel (ITV) test conducted at Oak Ridge National Laboratory (ORNL). The test temperature was selected to be at the onset of the C_v upper shelf, as confirmed by the results listed in Table 3. *J-R* curve tests of this forging were made for the C-L and the C-R orientations (per ASTM standard E 399) to simulate the crack propagation directions in the ITV test. These orientations, which exhibit similar energy levels, are the low-toughness orientations for this forging, as indicated by C_v levels below 117 J (86 ft-lb) in contrast to the C_v level of 181 J (134 ft-lb) for the L-C orientation. *J-R* curves for this forging were evaluated using 0.5T-, 1.6T-, and 4T-C(T) specimens for the C-L orientation and 0.5T- and 1.6T-C(T) specimens for the C-R orientation. Additional information on this forging is given in Refs *17–19*.

A 533 Grade B Plate (Code V8)

As with the forging, this plate was evaluated at the same test temperature as an ORNL ITV test. In this case the test temperature was 93°C (200°F), the onset of the C_v upper shelf for this plate. The same orientations and specimens were used as for the forging evaluations. In this case, the C-L (and presumably the C-R) orientations are the high-toughness orientations (C_v energy of 186 J or 137 ft-lb), in contrast to the L-C orientation (102 J or 75 ft-lb). Additional information on this plate is given in Refs *19* to *21*.

A 302 Grade B Plate (Code V50)

This plate was fabricated as a 152-mm (6-in.)-thick plate. The heat treatment applied to the plate was determined from a review of the metallurgical histories of production A 302-B plates used in early RPV construction in an effort to match the final product used in early construction. The sulfur content of the ingot used to produce the plate was relatively high at 0.025 (wt%), but within the range of early production plates. In addition, a minimum of cross rolling was applied to this plate, which is in contrast to modern practices where near 1:1 cross rolling is generally used. As described later, the sulfur content and possibly the rolling characteristics of this plate result in a nonhomogeneous-appearing fracture surface.

In contrast to the Code V8 plate and the Code FP forging, this plate exhibited an extremely low C_v upper shelf, in this case 73 J (54 ft-lb) for the T-L orientation (per ASTM standard E 399). The *J-R* curve tests of this plate were evaluated at 82°C (180°F) at the onset of the C_v upper shelf. The specimens used from this plate were 0.5T-, 1T-, 2T-, 4T-, and 6T-C(T) specimens. Additional information on this plate is given in Refs *22* and *23*.

Linde 80 Welds (Codes 61W to 67W)

These seven weld metals exhibit fairly low C_v upper shelf energy levels in the unirradiated condition ranging from 76 to 108 J (56 to 80 ft-lb) and very low C_v upper shelf energy levels of 58 to 80 J (43 to 59 ft-lb) in the irradiated condition. These welds were tested at upper shelf temperatures ranging from 75 to 288°C (167 to 550°F). Specimen sizes were 0.5T-, 0.8T-, 1.6T-, and 4T-C(T), although not all specimen sizes were used in all cases. Due to the limited width of the welds (about 25 mm, 1 in.), these specimens are actually duplex specimens of weld and base metal. The yield strengths of the base metals were not evaluated, but were probably on the order of 10% less than that of the weld metals. Additional information on these weld metals is given in Ref *24*.

Results

The effect of specimen size for these materials will be evaluated by comparing the *J-R* curves from each specimen size. These comparisons will be made using the deformation and modified forms of the *J*-integral, J_D and J_M, respectively, as well as the Merkle-Corten formulation (J_{M-C}). The key curves will also be used to ascertain the relative deformation behavior of the various specimen sizes.

As described previously, the Code FP forging and the Code V8 plate exhibit relatively high toughness and a relatively clean fracture appearance. These two materials can be thought of as "monolithic/clean" materials since the characterization is essentially an accurate working model for those materials. Hence, one can argue that the theory behind the *J*-integral and its various formulations should be quite applicable to these two materials. The logic supporting this is that there are no macro-scale inhomogeneities internal to the specimen large enough to disrupt the stress-strain relationship surrounding the crack tip or to cause unusually large deviations from planar crack growth.

In contrast, the Code V50 plate has lower toughness and an inhomogeneous fracture appearance; this plate will be defined herein as a "monolithic/dirty" material. This plate is characterized by a nearly uniform distribution of macro-scale inhomogeneities which could perturb the stress-strain field or provide preferential crack growth planes exhibiting lower toughness than the bulk material of the plate.

The large specimens from the weld metals are composite specimens, with weld metal and base metal components, but also an intermediate zone or zones consisting of the fusion line and the heat-affected zone. In general one would expect all of these areas to have different deformation characteristics, with the stress-strain field (principally the plastic zone) in some of the larger specimens traversing this mixture of materials. Although these weld metals also exhibit a "uniform" fracture appearance, with the crack growth plane clearly defined, the J-integral theory may not be entirely applicable due to the lack of a homogeneous stress-strain field surrounding the crack tip.

Code FP Forging and Code V8 Plate

A large number of 0.5T-C(T) specimens (twelve from the C-L orientation and six from the C-R orientation) for each material were used to sample through-thickness variability of the J-R curves. Overall, the variability tends to be quite small using any of the J formulations. Comparing the results for the C-L orientation of each material (Figs. 2 and 3), the J_D-R curve results indicate a "peeling-off" trend whereby the slope of the J_D-R curve decreases rapidly for the 0.5T-C(T) specimens and the J levels themselves are somewhat reduced at large Δa levels. In contrast, the J_M-R curves indicate much improved correspondence between data for the various specimen sizes. However, the curves from the 0.5T-C(T) specimens tend to exhibit an inflection point, whereby the slope of the J_M-R curve increases instead of continuing to decrease with extensive crack growth. The use of J_{M-C} results in slightly improved correspondence between data from the small and the large specimens, in terms of the J levels, with no inflection of the curves at the end of the data for the 0.5T-C(T) specimens. Principally for the Code FP forging, the J_{M-C}-R curves for the large specimens appear to come directly out of the trend band for the 0.5T-C(T) specimen data.

The key curves for these materials are similarly quite well behaved (Fig. 4). As illustrated, excellent correspondence between the various specimen sizes occurs for each material, attesting to the similar deformation response for the large and the small specimens.

With these clean monolithic materials, the generally good correspondence found between results for the various specimen sizes at low Δa levels indicates that no inherent size effect results for the various J formulations within the validity range ($\Delta a \leq 0.1\ b_0$ and $J \leq b\ \sigma_f/25$). However, the use of J_M or J_{M-C} results in improved correspondence in the curves from different size specimens for greater levels of Δa.

Code V50 Plate

Six 0.5T-C(T) specimens were tested from this plate to sample through-thickness variability, which was found to be minimal. Comparison of the J_D-, J_M-, and J_{M-C}-R curves (Fig. 5) from all of the specimen sizes reveals a severe size effect, whereby increased specimen size results in significant reductions in toughness, including both J level and J-R curve slope.

a

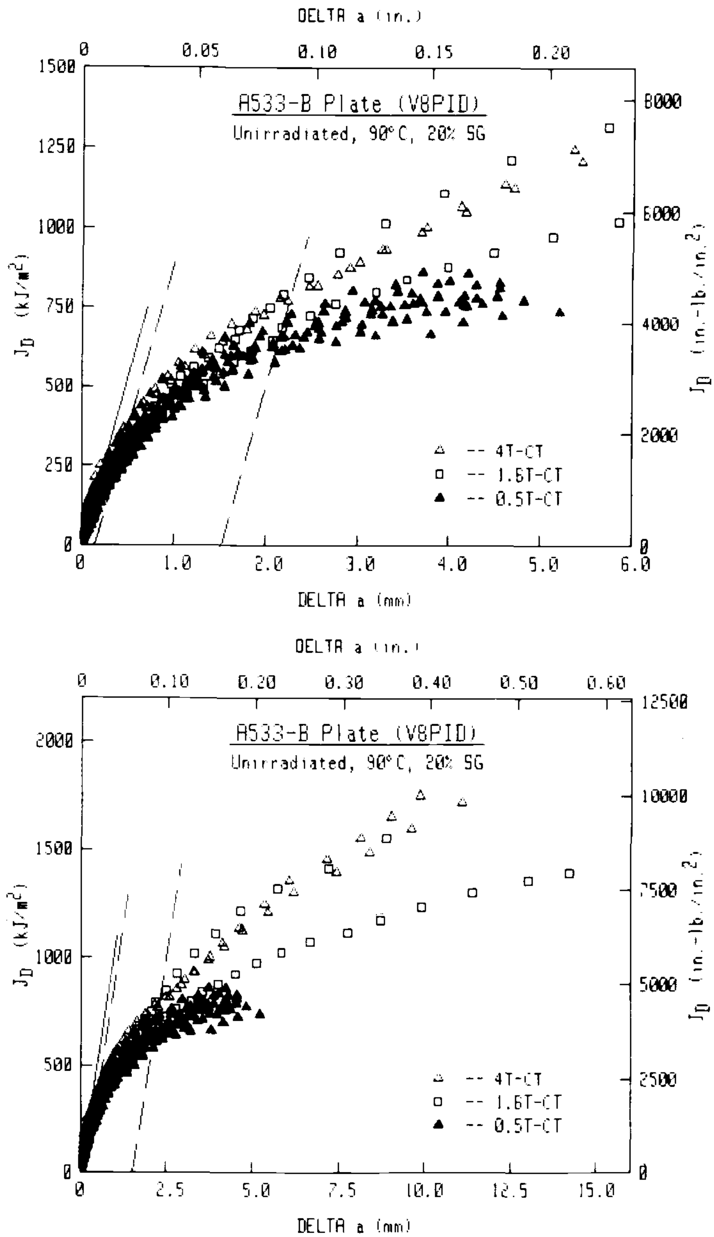

FIG. 2—*Comparison of* J-R *curves for the C-L orientation of the Code V8 plate at 90°C (194°F).* J_D (a), J_M (b), *and* J_{M-C} (c) *are illustrated, with the top graphs representing small crack growth levels and the bottom graphs representing large crack growth levels.*

b

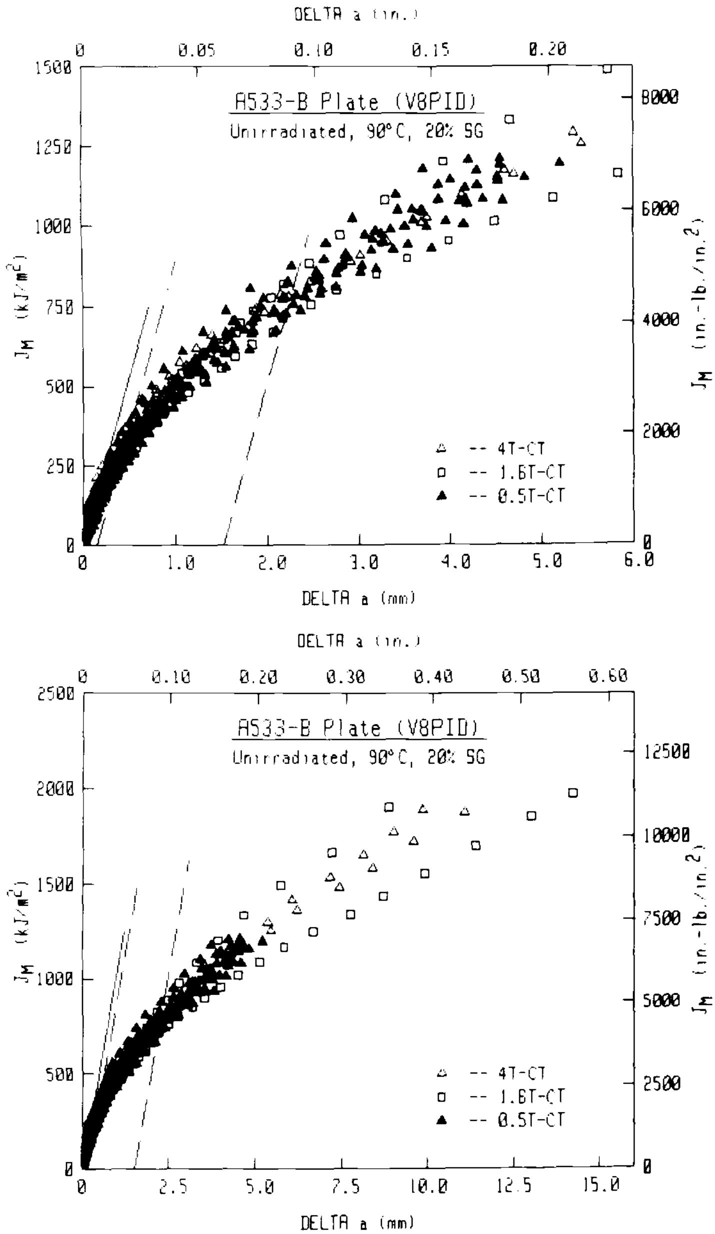

FIG. 2—*Continued*

c

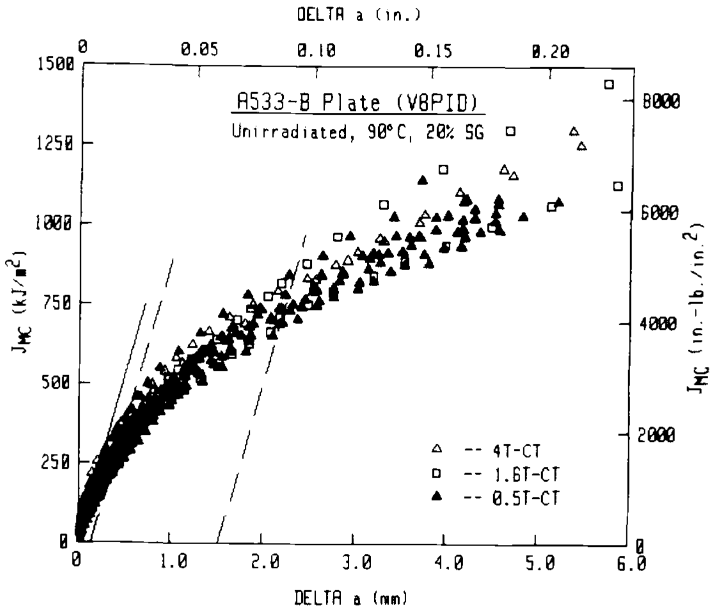

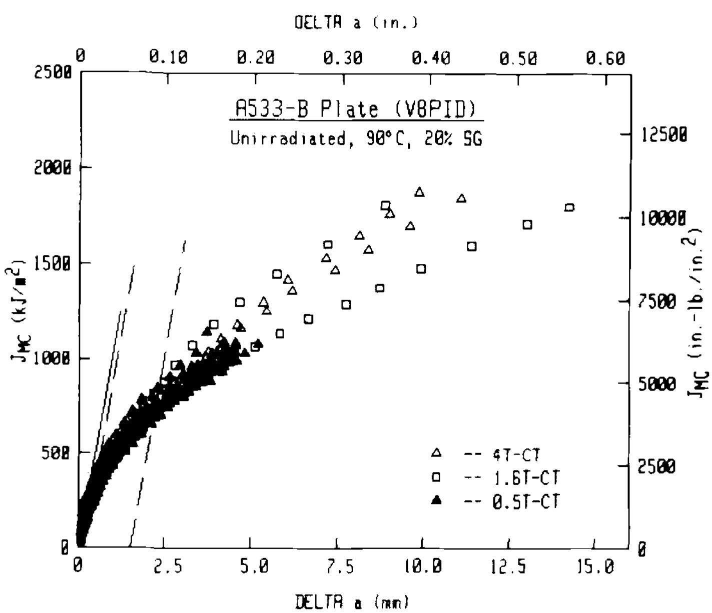

FIG. 2—*Continued*

a

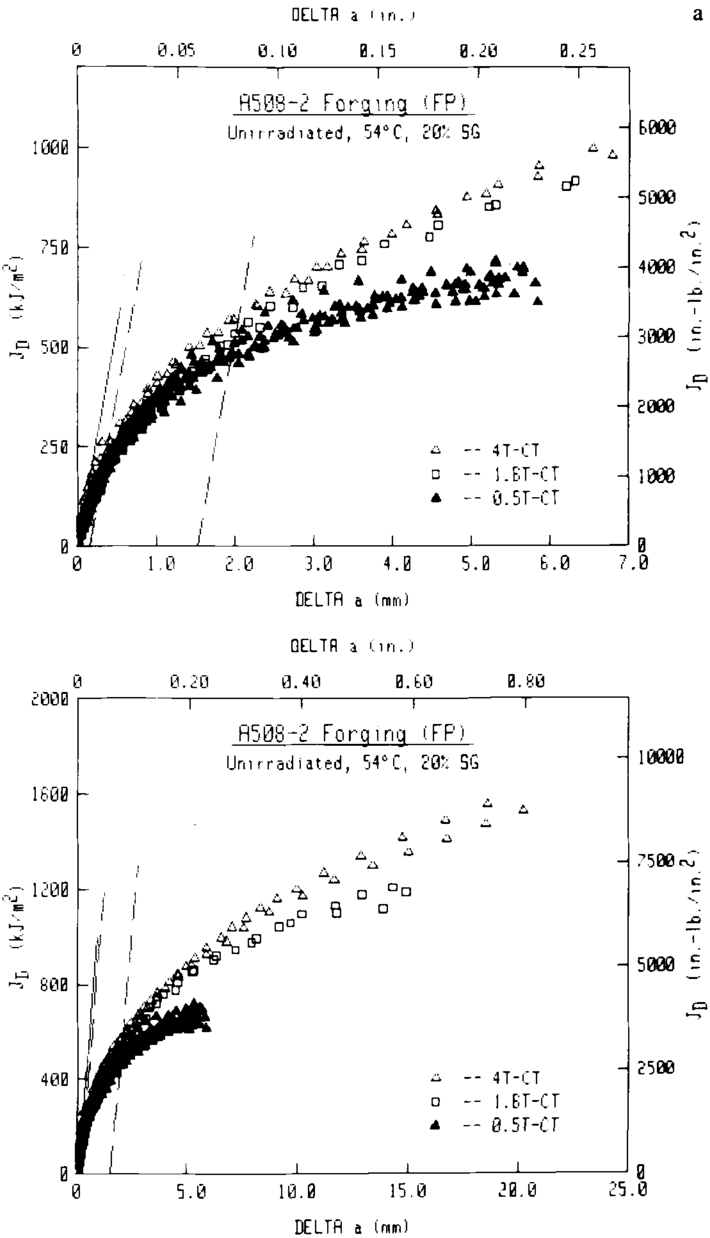

FIG. 3—*Comparison of* J-R *curves for the C-L orientation of the Code FP forging at 54°C (130°F).* J_D (a), J_M (b), *and* J_{M-C} (c) *are illustrated, with the top graphs representing small crack growth levels and the bottom graphs representing large crack growth levels.*

b

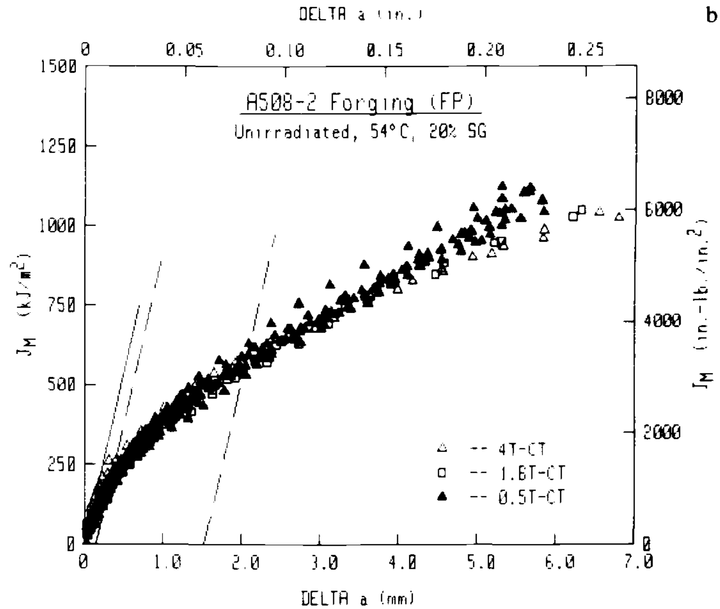

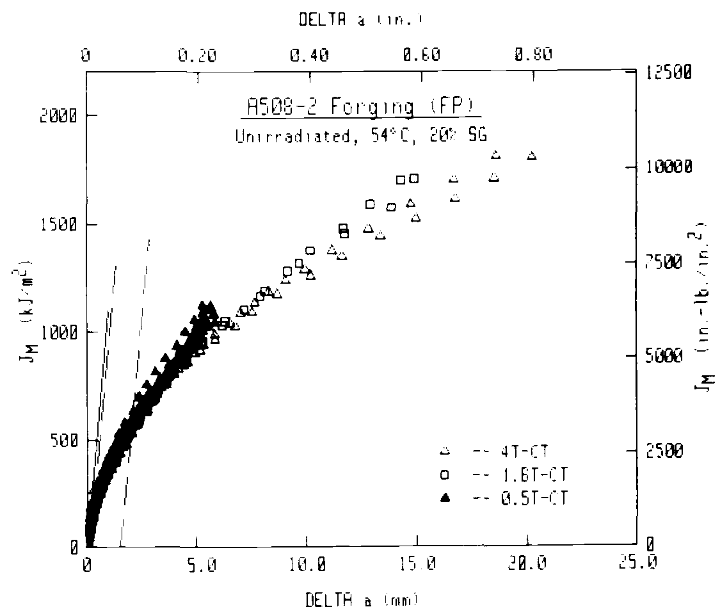

FIG. 3—*Continued*

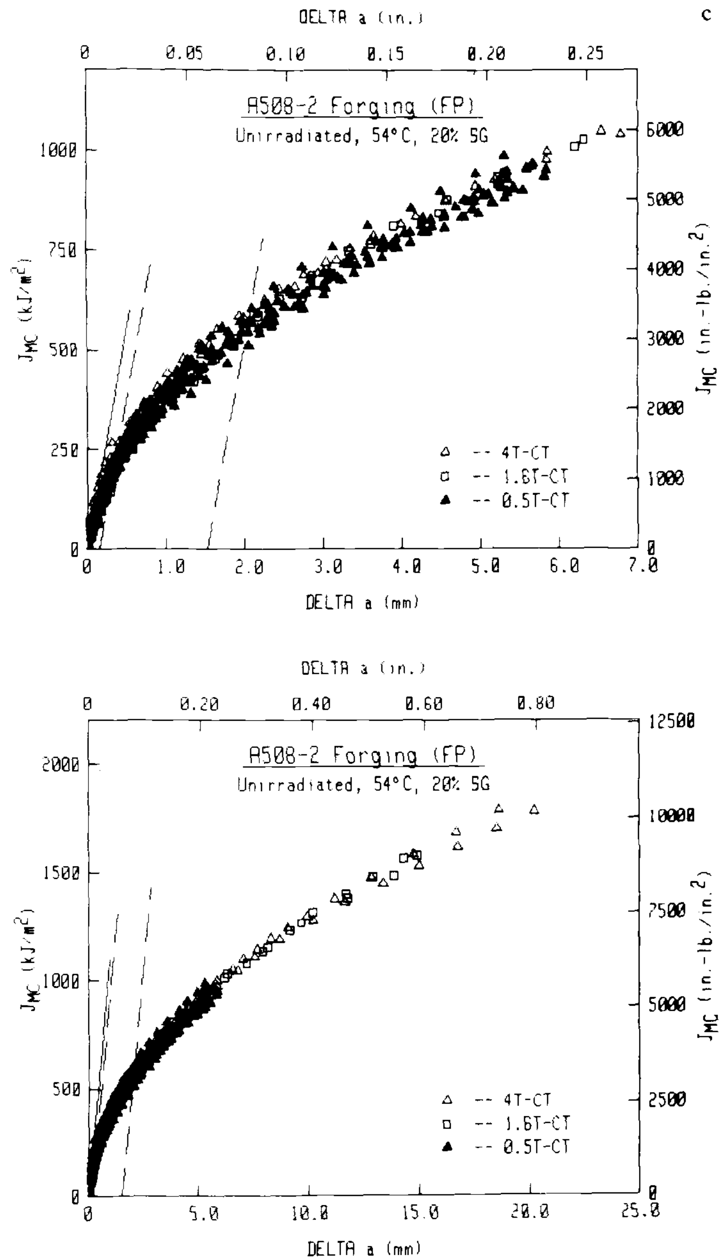

FIG. 3—*Continued*

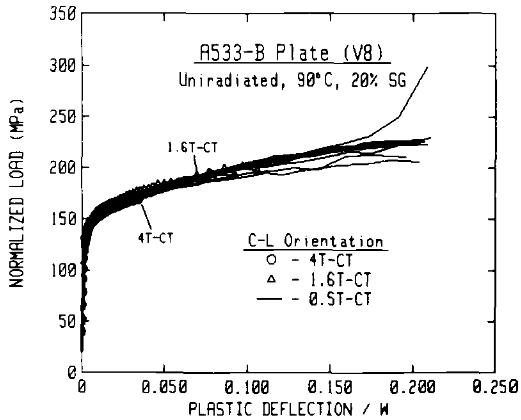

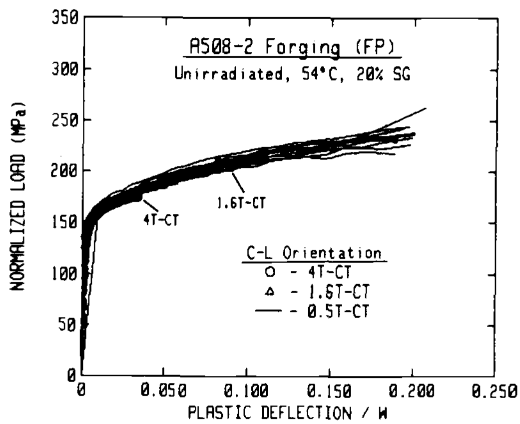

FIG. 4—*Key curves for the C-L orientations of Code V8 plate (*top*) and Code FP forging (*bottom*).*

The key curves (Fig. 6) likewise demonstrate a peculiar trend, as they generally tend toward a maximum value with an oscillatory behavior developing in the subsequent stages of slow-stable crack growth. The latter trend is most evident with the curves for the larger specimens. The near upper plateau on the key curve generally occurs at the first attainment of maximum load for the specimen, with the Δa levels ranging from 4.5 mm (0.177 in.) for the 6T-C(T) specimen down to near the J_{Ic} point for the small specimens. For the specimens larger than 1T in size, the *J-R* curves exhibit a severe decrease in slope following this point on the key curve.

The cause for the unusual key curves for (principally) the large specimens is thought to lie with poor correspondence between the actual crack sizes and those estimated from the unloading compliance method, as evidenced by large differences between the optical-method final crack length (at test termination) and that from the end-of-test compliance estimates. The causes for this poor correspondence are thought to center on the unusual fracture appearance for this material, characterized by a fibrous or "woody" appearance. The nonplanar nature of the features on these fracture surfaces resulted in contact between facets near the crack front during the unloading compliance measurements, yielding less measured compliance and hence reduced estimates of crack growth.

a

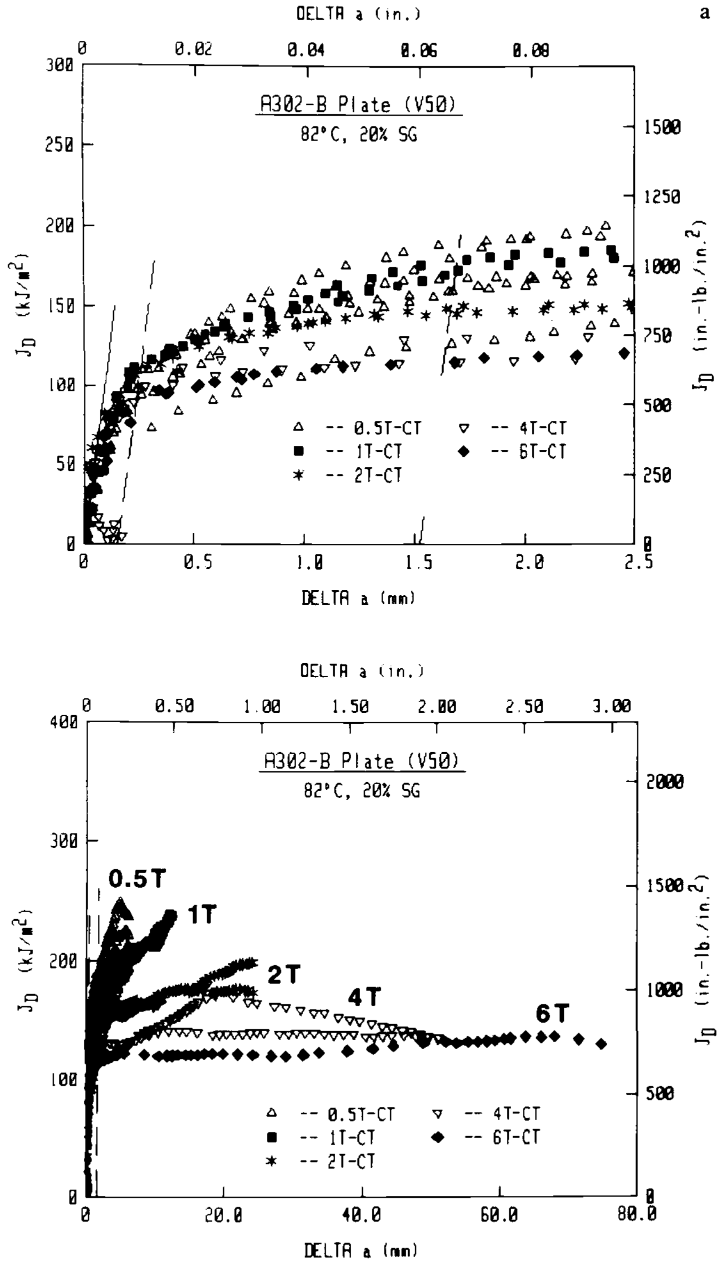

FIG. 5—*Comparison of J-R curves for the Code V50 plate at 82°C (180°F).* J_D (a), J_M (b), *and* J_{M-C} (c) *are illustrated, with the top graphs representing small crack growth levels and the bottom graphs representing large crack growth levels.*

b

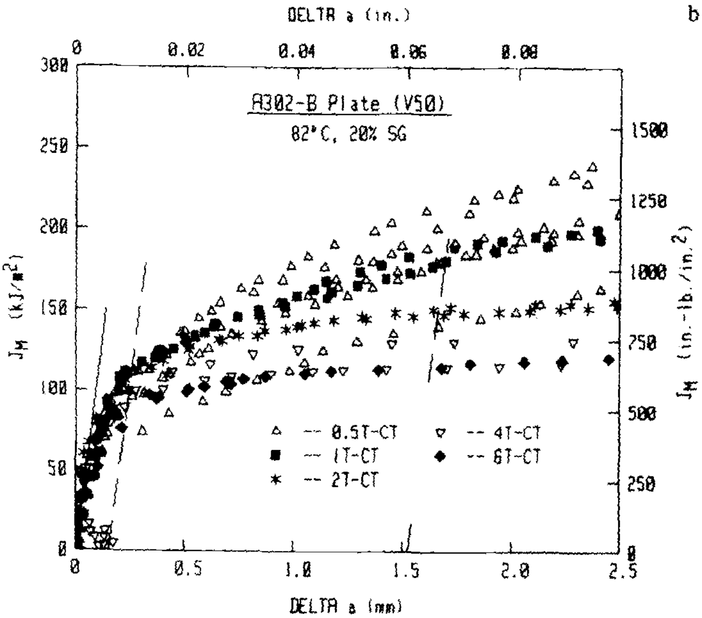

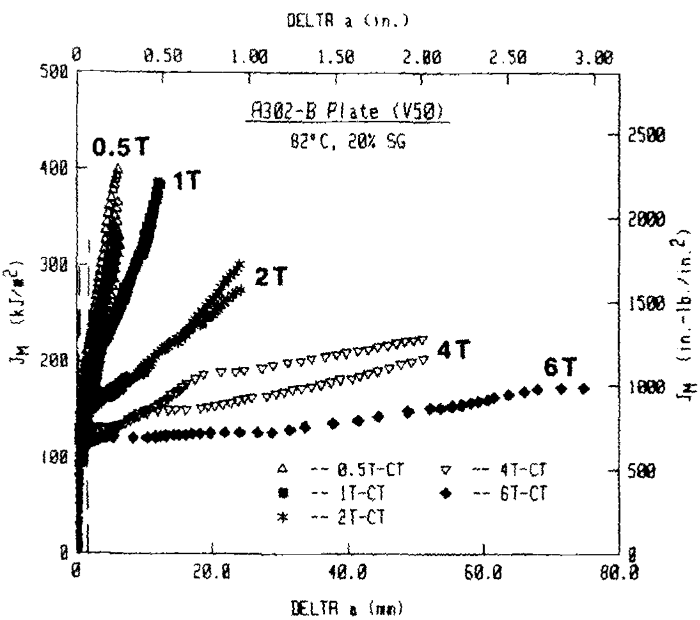

FIG. 5—*Continued*

c

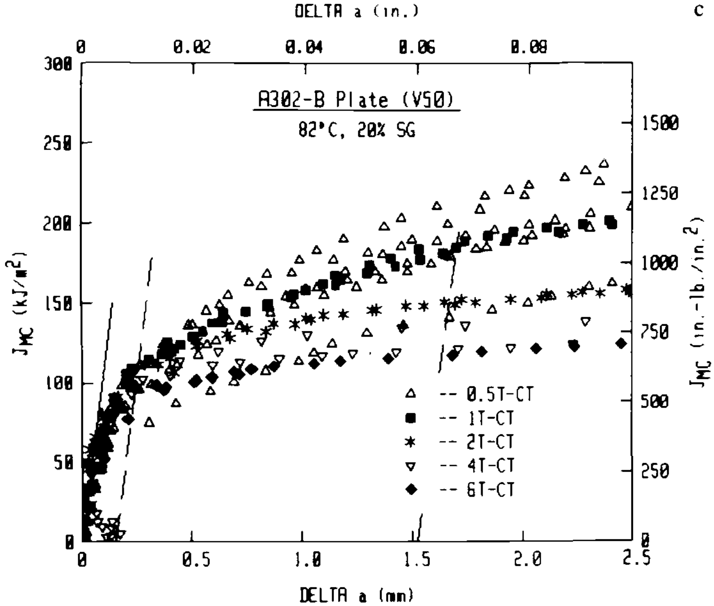

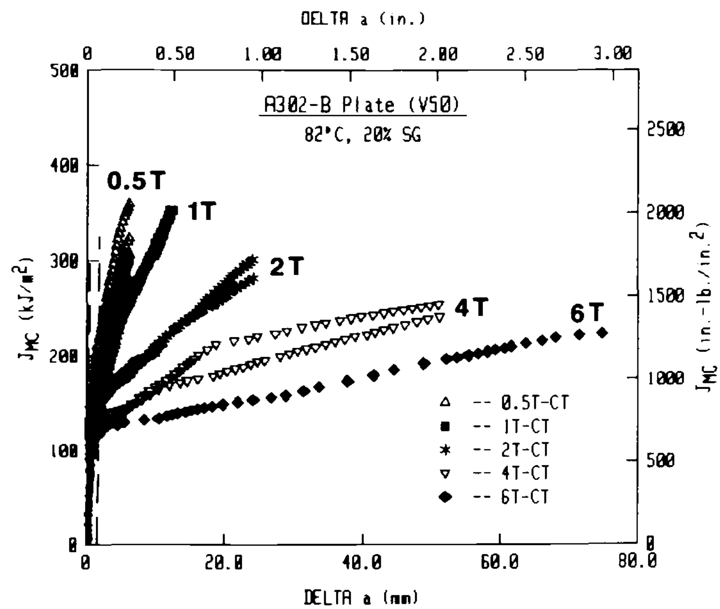

FIG. 5—*Continued*

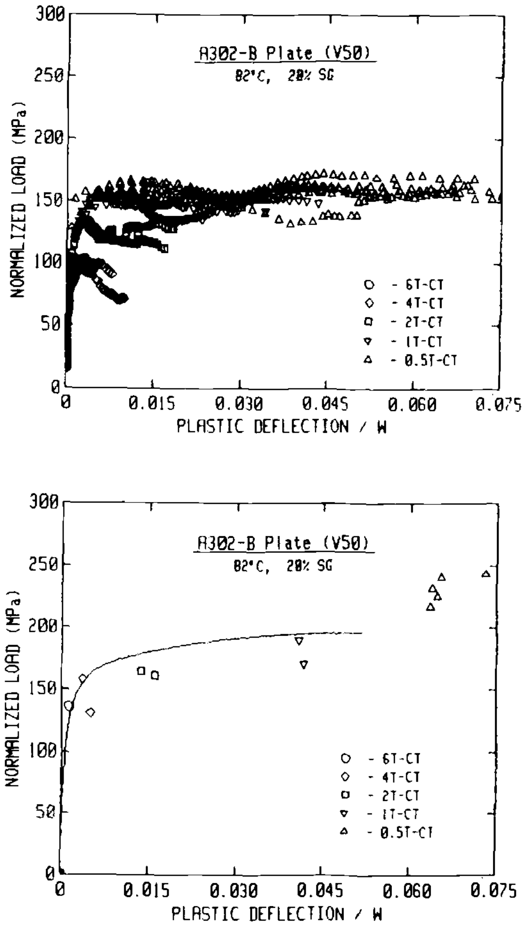

FIG. 6—*Key curves for the Code V50 plate using compliance measurements (*top*) and the final measured crack length (*bottom*).*

A blunt-notched 0.5T-C(T) specimen was used to develop an accurate key-curve representation of the deformation characteristics of this plate. As illustrated in Fig. 6, comparison of this key curve and the test termination point for the 6T-C(T) data indicates that the 6T-C(T) specimen did not have much plastic deformation and instead is dominated by elastic displacement.

Codes 61W to 67W Welds

A large number of *J-R* curves (160) are available for these seven weld metals, with specimen sizes including 0.5T-, 0.8T-, 1.6T-, and 4T-C(T). These data include both the unirradiated and the irradiated conditions, with results at several test temperatures. Although only a few cases will be presented here, in virtually every case a size effect was apparent whereby the largest specimens [4T-C(T)] yielded the highest *J-R* curves, and the smallest specimens [0.5T-C(T)] tended to yield the lowest *J-R* curves. Overall, the *J* levels tended to increase with specimen size, with the larger specimens tending to give the highest *J-R* curves.

As mentioned previously, the width of these welds typically ranged from 13 to 51 mm (0.5 to 2 in.). The 0.5T-C(T) specimens were typically composed of all weld metal, whereas each larger specimen size tended to have increasing amounts of base metal, at least on a proportional basis. Therefore, the small specimens are actually consistent with the monolithic materials exhibiting clean fracture surfaces, as with the Code V8 plate and the Code FP forging.

The materials and conditions presented in these comparisons (Figs. 7 to 13) are:

1. 62W, unirradiated condition at 200°C.
2. 63W, unirradiated condition at 171°C.
3. 67W, unirradiated condition at 288°C.
4. 65W, unirradiated condition at 200°C.
5. 65W, irradiated condition at 200°C.
6. 66W, unirradiated condition at 200°C.

Each of the *J-R* curve comparisons demonstrate a trend whereby the largest specimen size tends to give the highest curve and the smallest specimen tends to give the lowest *J-R* curve.

Among the three formulations of the *J*-integral, the J_D-R curves demonstrate a tendancy to approach a plateau level, with the *J* level at which a rapid reduction in slope occurs decreasing with decreasing specimen size. The result is a very strong size dependence. One advantage of using J_M is that the overall curvature and *J* levels of the J_M-R curves do not demonstrate the strong size dependence found with J_D. However, the J_M-R curves for (principally) the 0.5T-C(T) specimens typically demonstrate a slight inflection (or "hook-up" tendency) over the last several data points, resulting in an increasing slope near the end of those curves. In some cases, the curves for the small specimens cross those for the larger specimens. This inflection behavior probably indicates a breakdown in J_M validity (a limitation currently not quantified from any theoretical considerations). In contrast, the J_{M-C}-R curves tend to lie between the J_D- and the J_M-R curves, with the overall curvature of each data set not affected by either an inflection or a plateau behavior.

Comparison of the key curves for the specimens from one of these welds (Fig. 13) indicates only slight differences, as the curves for the 0.5T-C(T) specimens exhibit slightly higher key curves than those for the other specimens. The *J-R* curves for this weld are in Fig. 7. This type of a comparison is typical of that found with these welds. From the standpoint of interpretation of the key curves, a higher key curve would generally indicate slightly higher strength for that specimen, which is generally associated with reduced toughness.

Overall, the larger specimens tend to give the highest *J-R* curves. Using J_M does appear to improve the correlation between data from large and small specimens for greater crack growth levels than does J_D, up to the point at which inflection points apparently end the J_M validity. Overall, the use of J_{M-C} tends to give the best comparison for these welds (i.e., the curves do not exhibit plateau or inflection tendencies).

Microstructural and Fractographic Evaluations

From a macroscopic standpoint, these materials tend to exhibit fairly clean fracture appearances, except for the Code V50 plate. As illustrated in Fig. 14, photographs of the fracture surfaces for several of these broken specimens reveals the expected dimpled-rupture (microvoid coalescence) appearance of the Code FP forging, the Code V8 plate, and the welds, in contrast to the irregular appearance of the Code V50 plate. Further microstructural and fractographic work was then performed on the V50 plate to identify the cause(s) of the differences in toughness for the different specimen sizes and also the irregular appearance of these fracture surfaces [*22*].

a

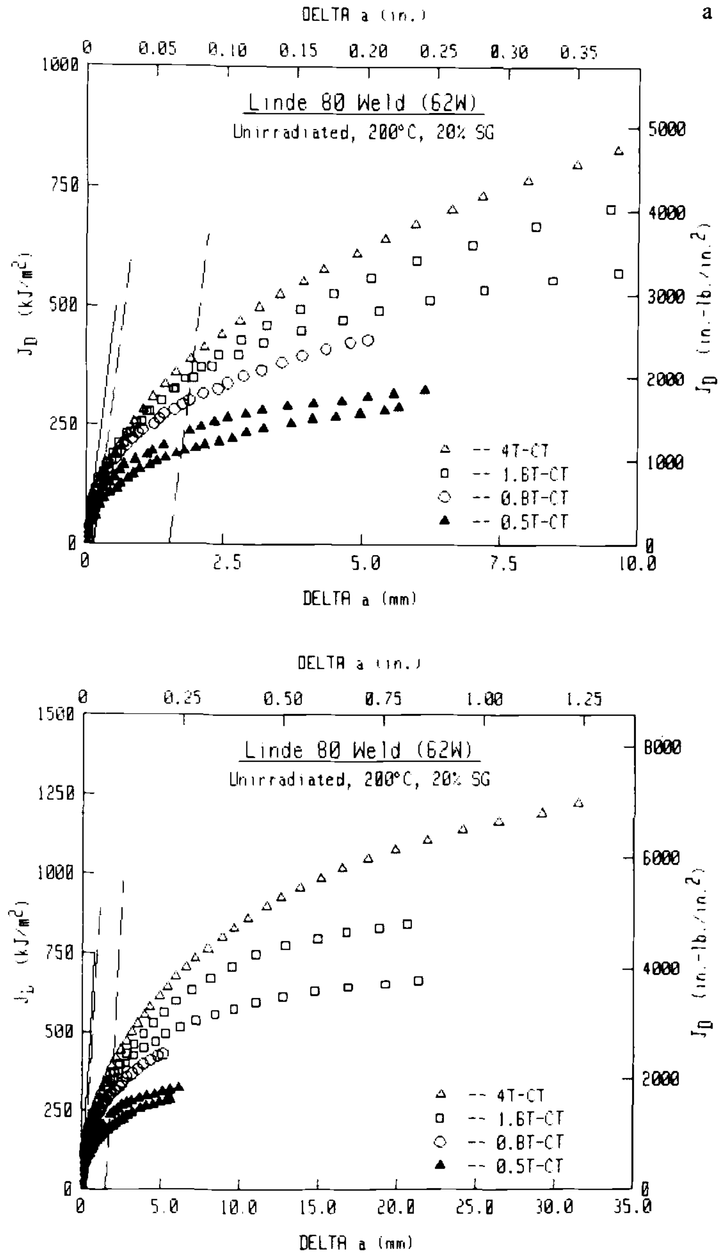

FIG. 7—*Comparison of* J-R *curves for the Code 62W weld, unirradiated condition at 200°C (392°F).* J_D (a), J_M (b), *and* J_{M-C} (c) *are illustrated, with the top graphs representing small crack growth levels and the bottom graphs representing large crack growth levels.*

b

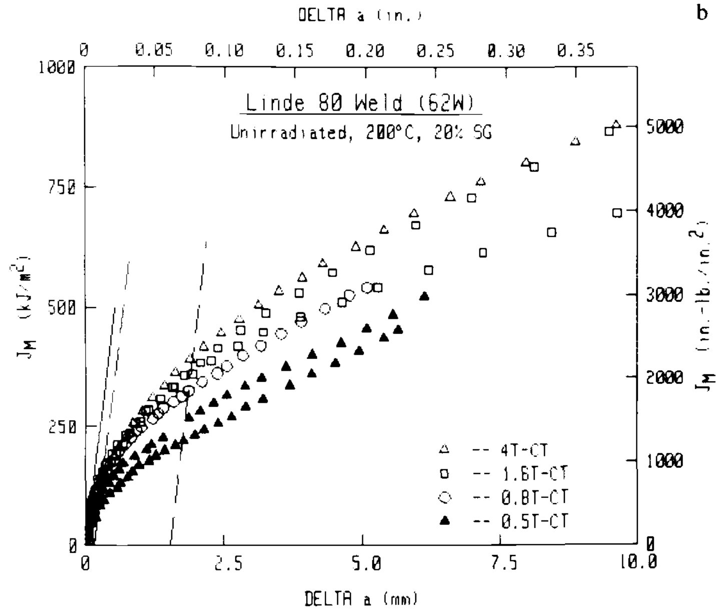

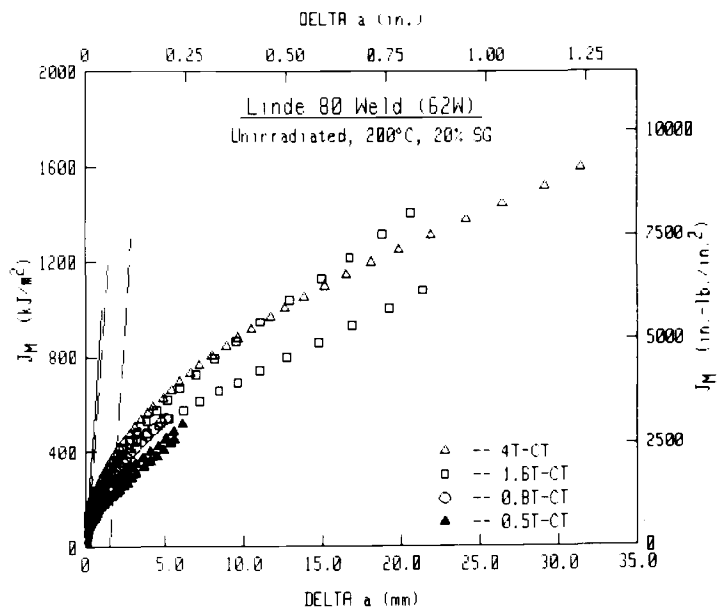

FIG. 7—*Continued*

c

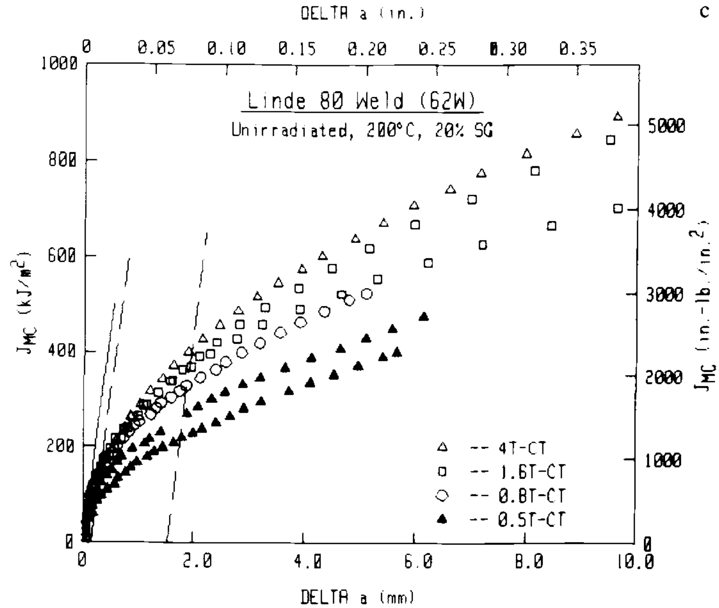

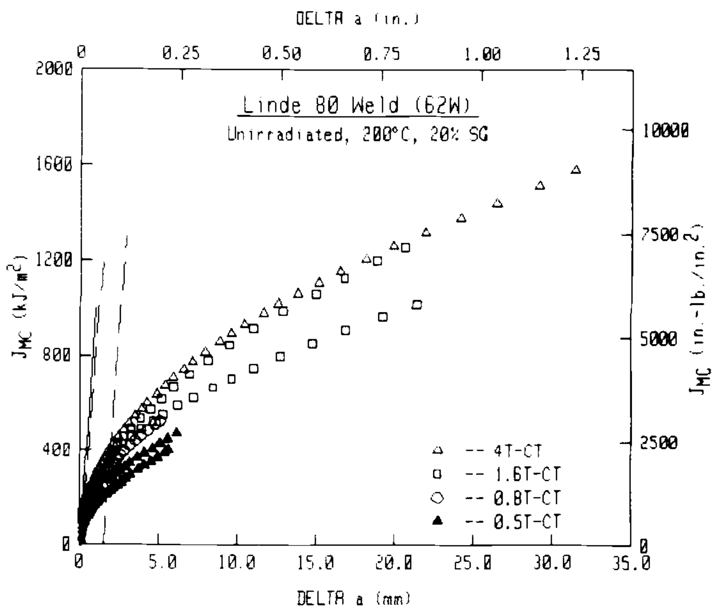

FIG. 7—*Continued*

a

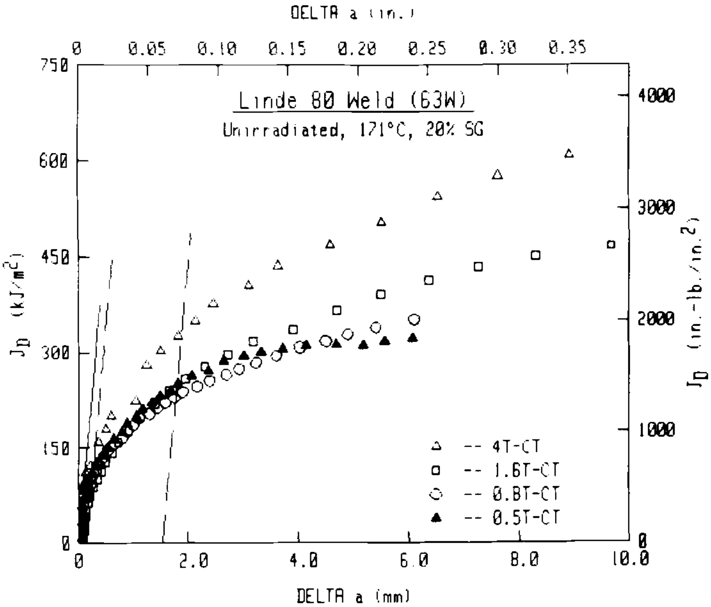

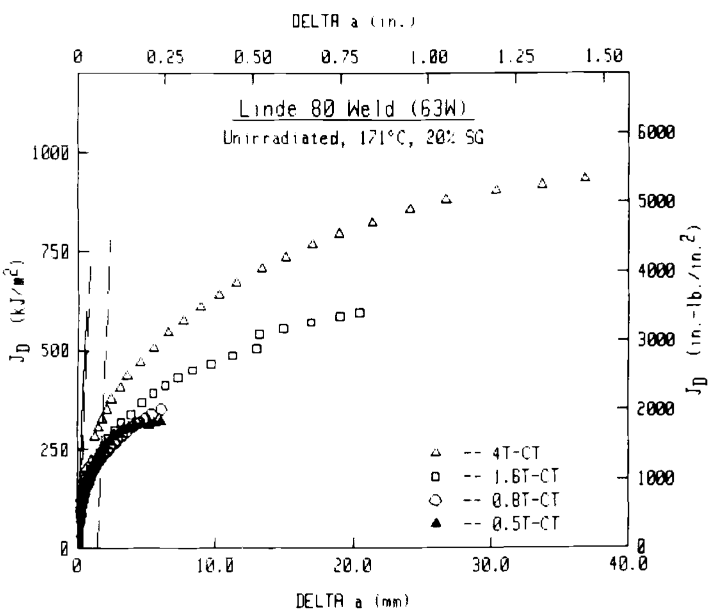

FIG. 8—*Comparison of* J-R *curves for the Code 63W weld, unirradiated condition at 171°C (350°F).* J_D (a), J_M (b), *and* J_{M-C} (c) *are illustrated, with the top graphs representing small crack growth levels and the bottom graphs representing large crack growth levels.*

b

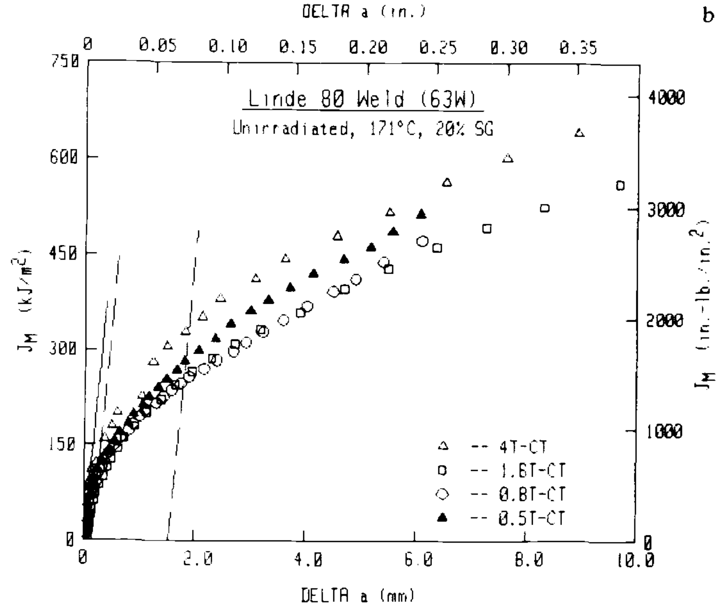

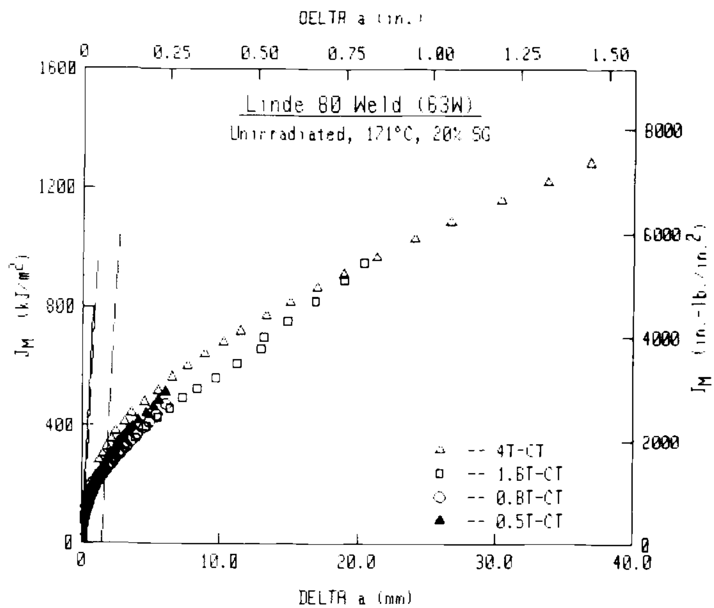

FIG. 8—*Continued*

c

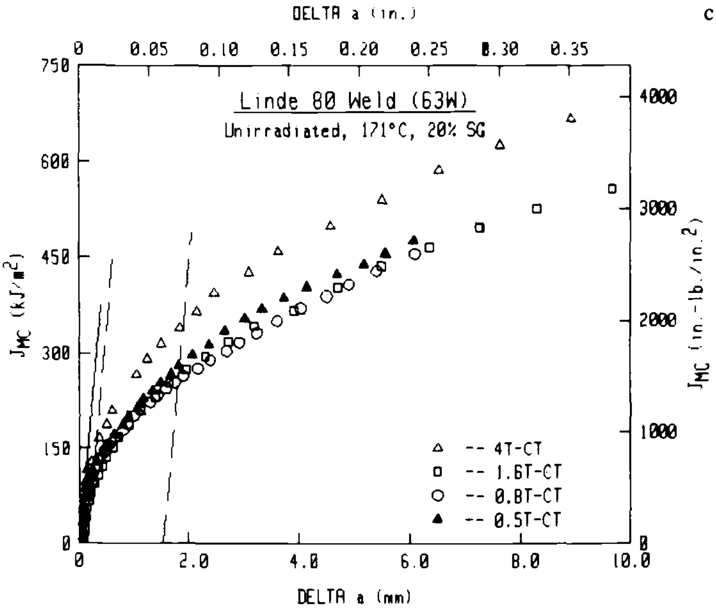

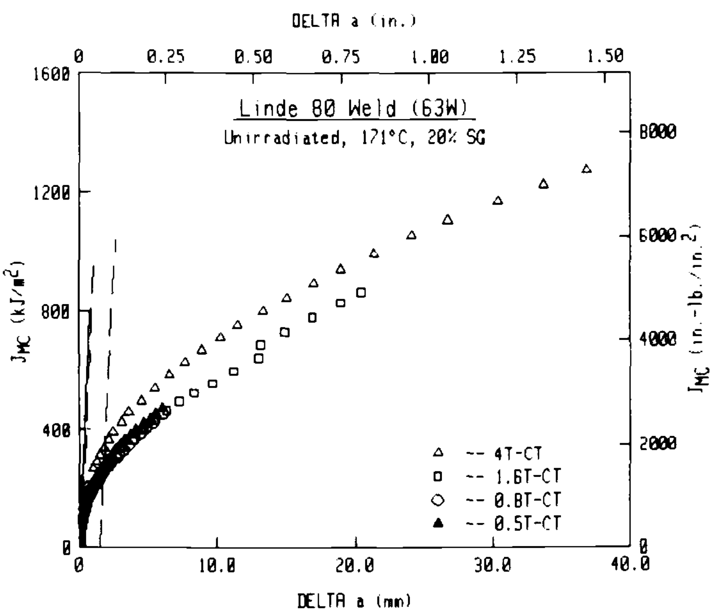

FIG. 8—*Continued*

a

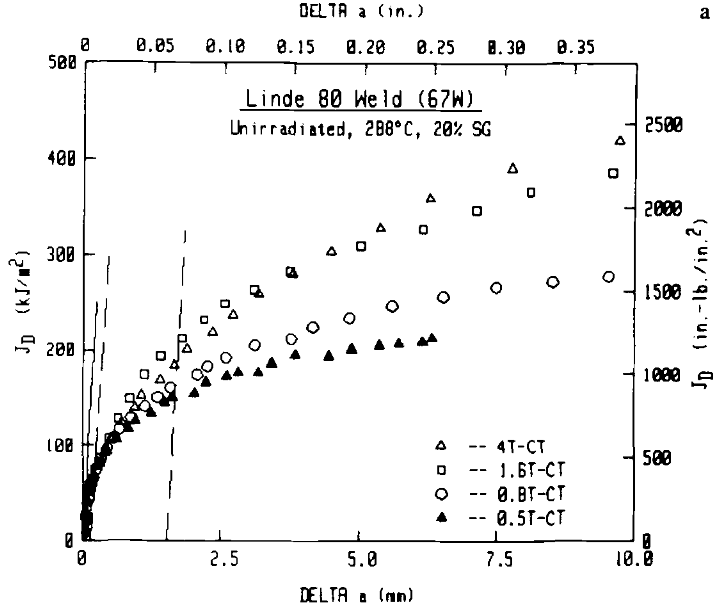

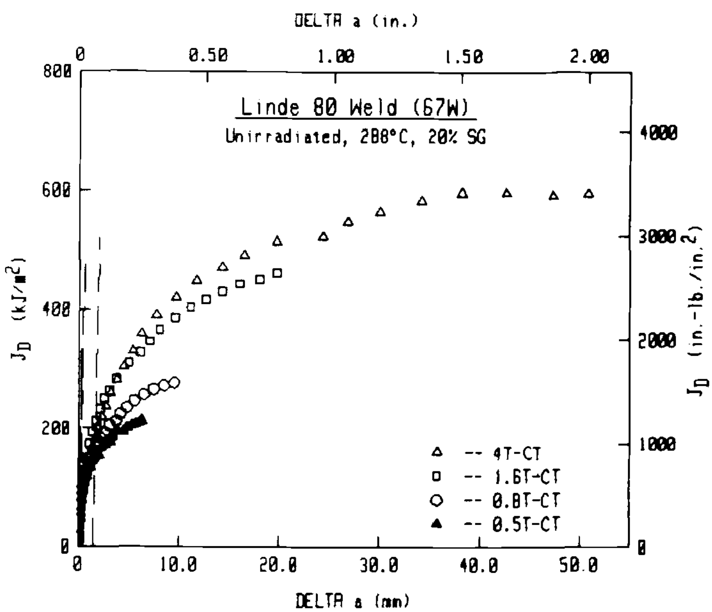

FIG. 9—*Comparison of* J-R *curves for the Code 67W weld, unirradiated condition at 288°C (550°F).* J_D (a), J_M (b), *and* J_{M-C} (c) *are illustrated, with the top graphs representing small crack growth levels and the bottom graphs representing large crack growth levels.*

b

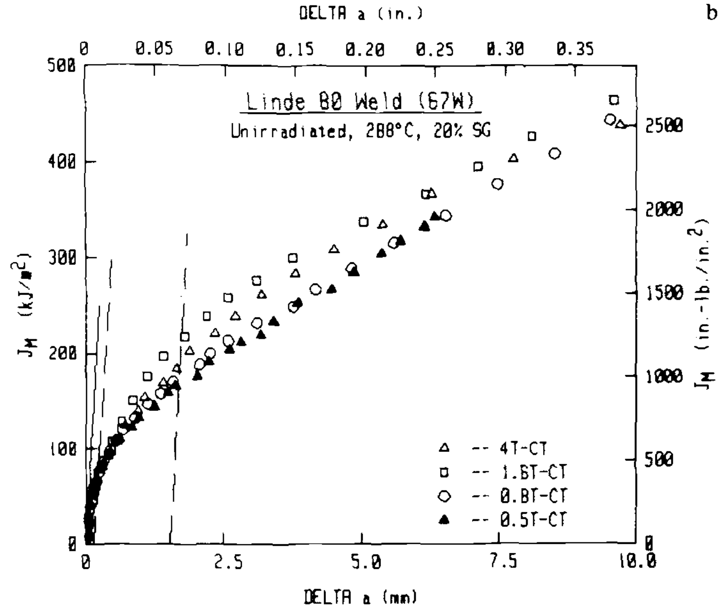

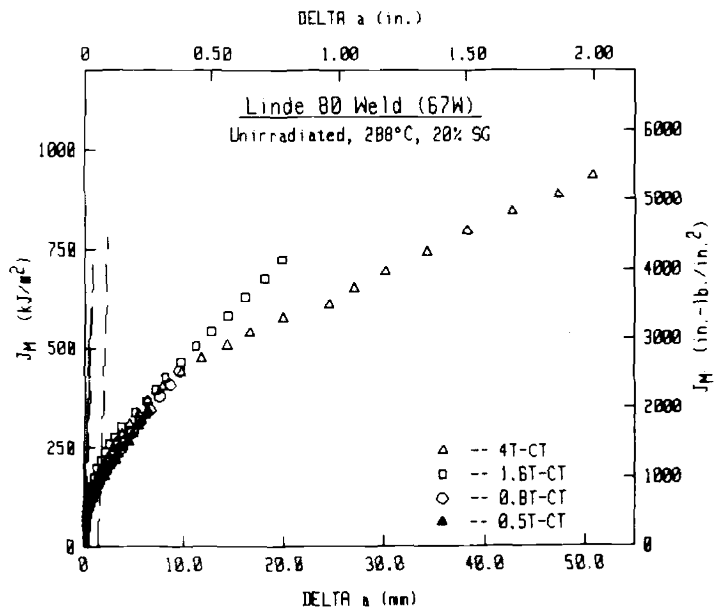

FIG. 9—*Continued*

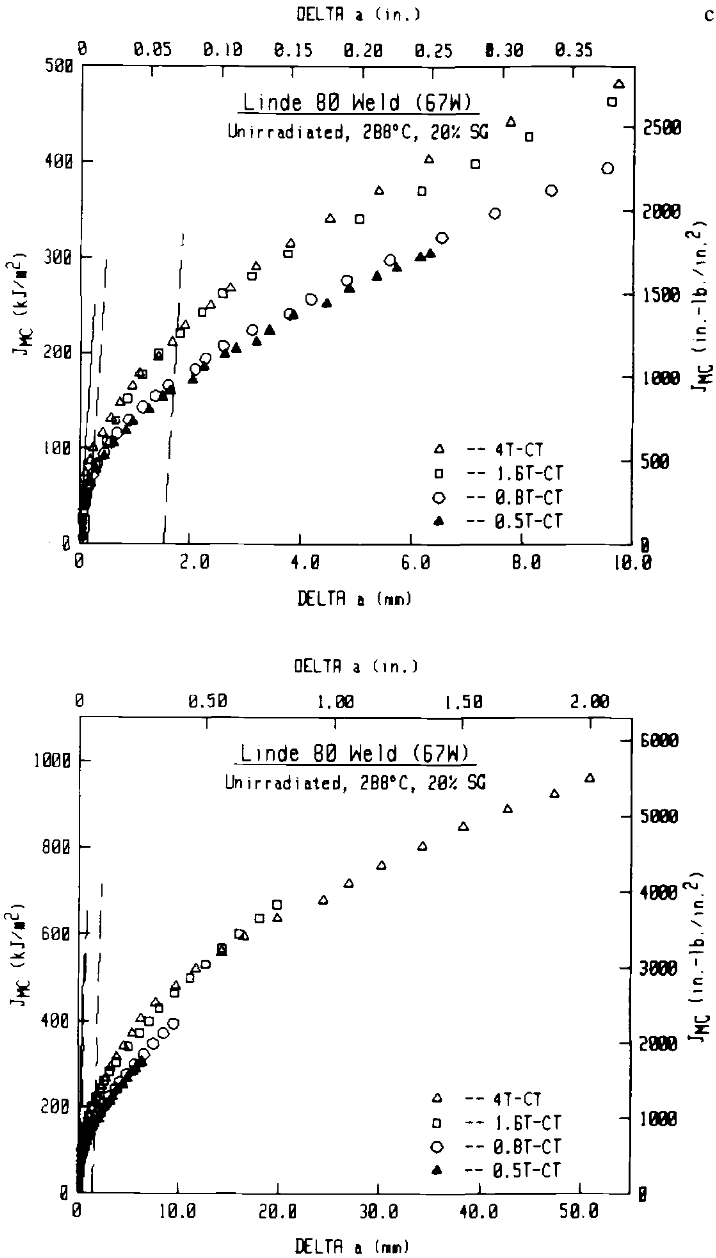

FIG. 9—*Continued*

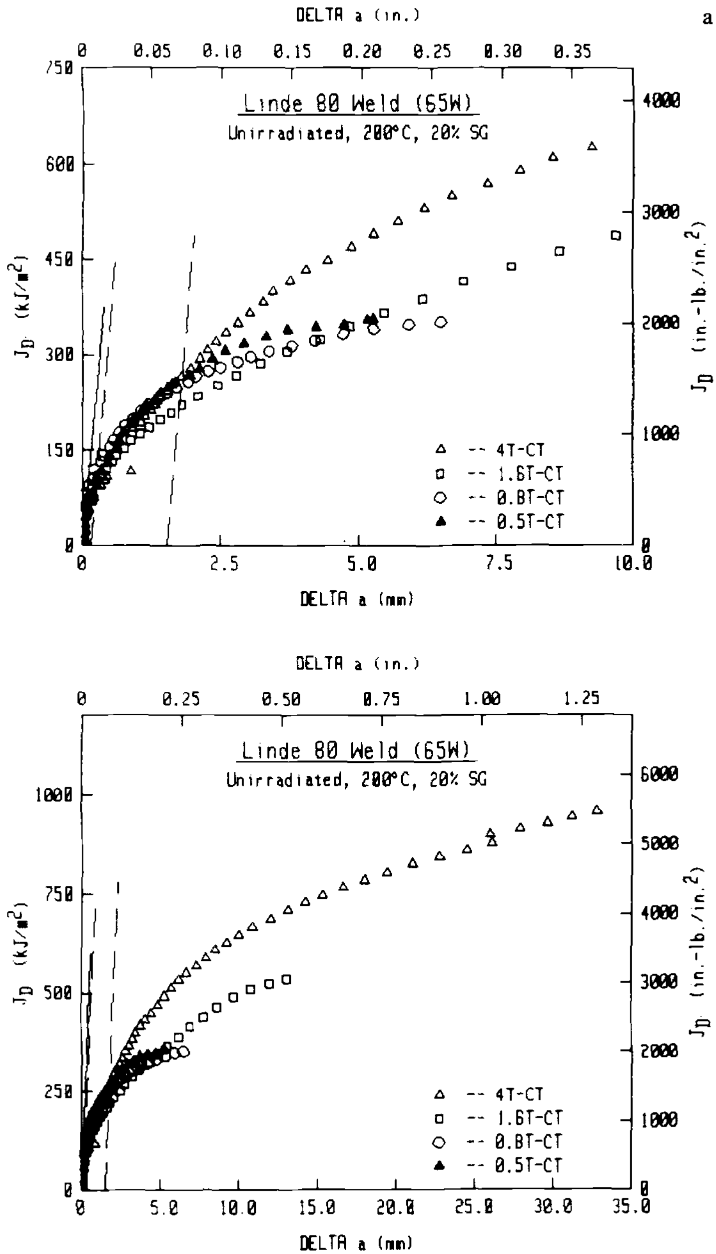

FIG. 10—*Comparison of* J-R *curves for the Code 65W weld, unirradiated condition at 200°C (392°F).* J_D (a), J_M (b), *and* J_{M-C} (c) *are illustrated, with the top graphs representing small crack growth levels and the bottom graphs representing large crack growth levels.*

b

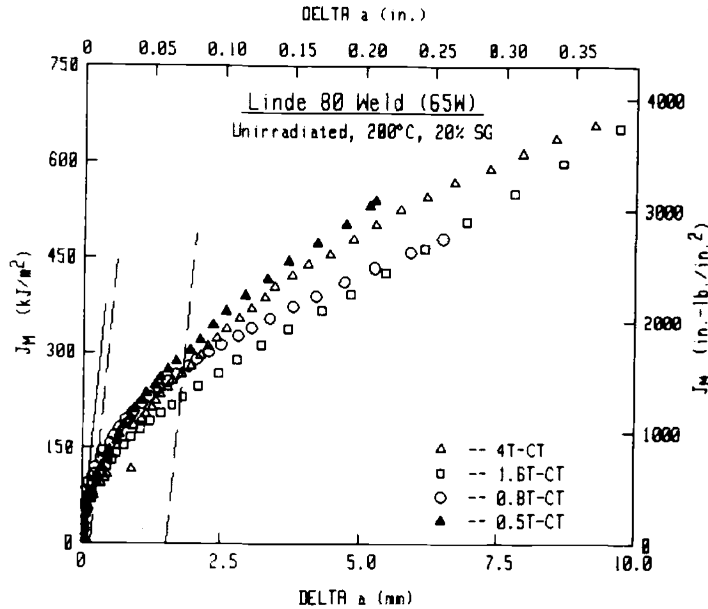

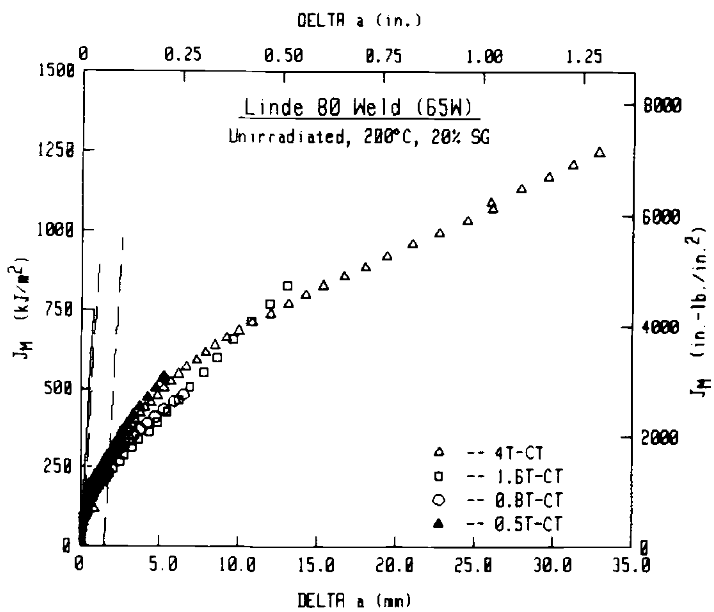

FIG. 10—*Continued*

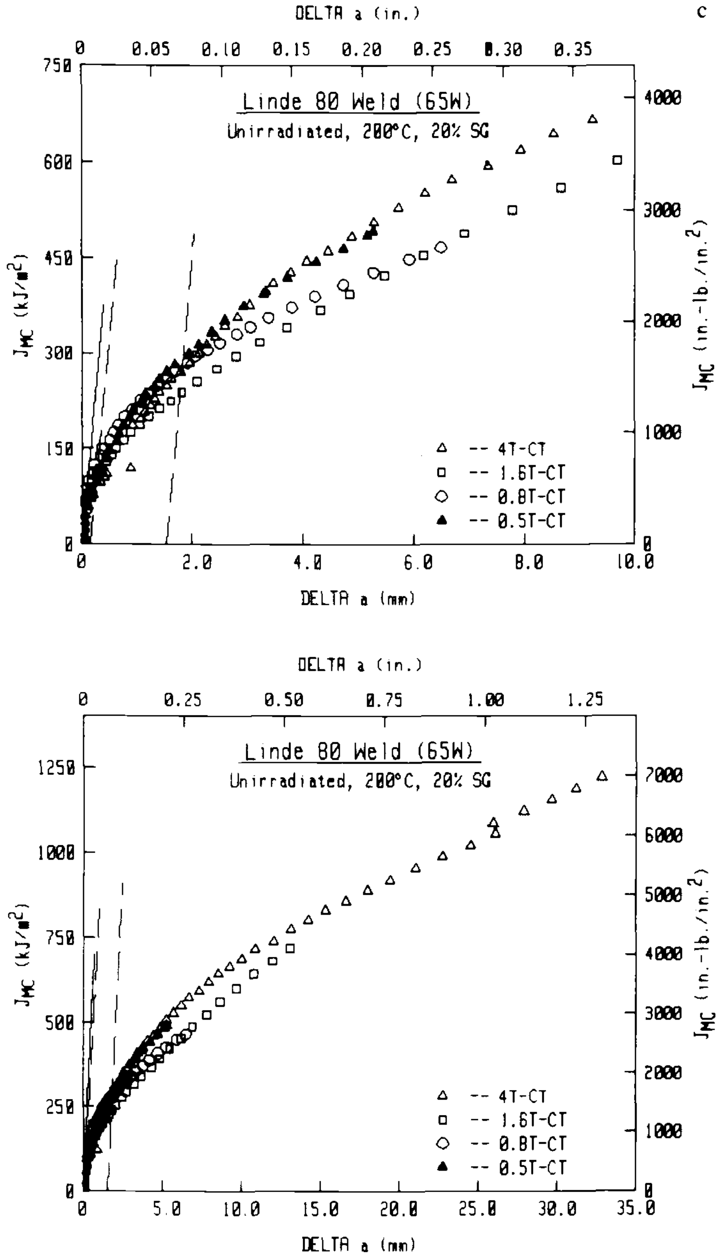

FIG. 10—*Continued*

a

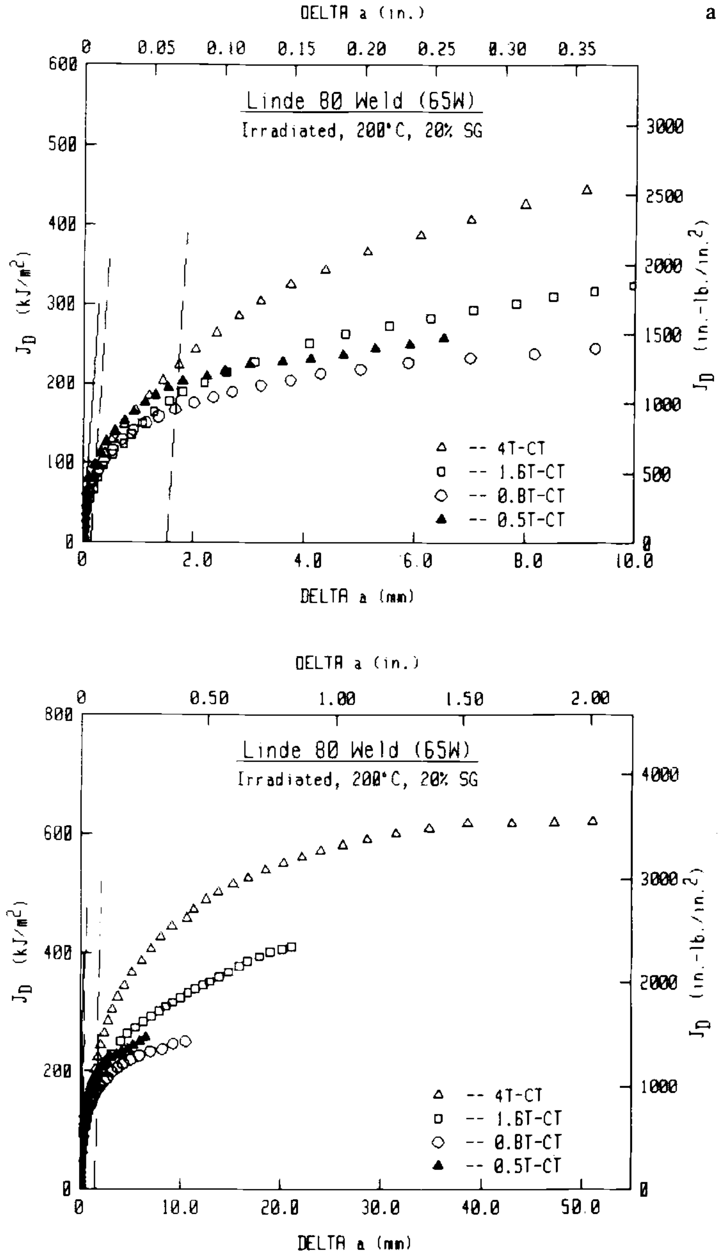

FIG. 11—*Comparison of* J-R *curves for the Code 65W weld, irradiated condition at 200°C (392°F).* J_D (a), J_M (b), *and* J_{M-C} (c) *are illustrated, with the top graphs representing small crack growth levels and the bottom graphs representing large crack growth levels.*

b

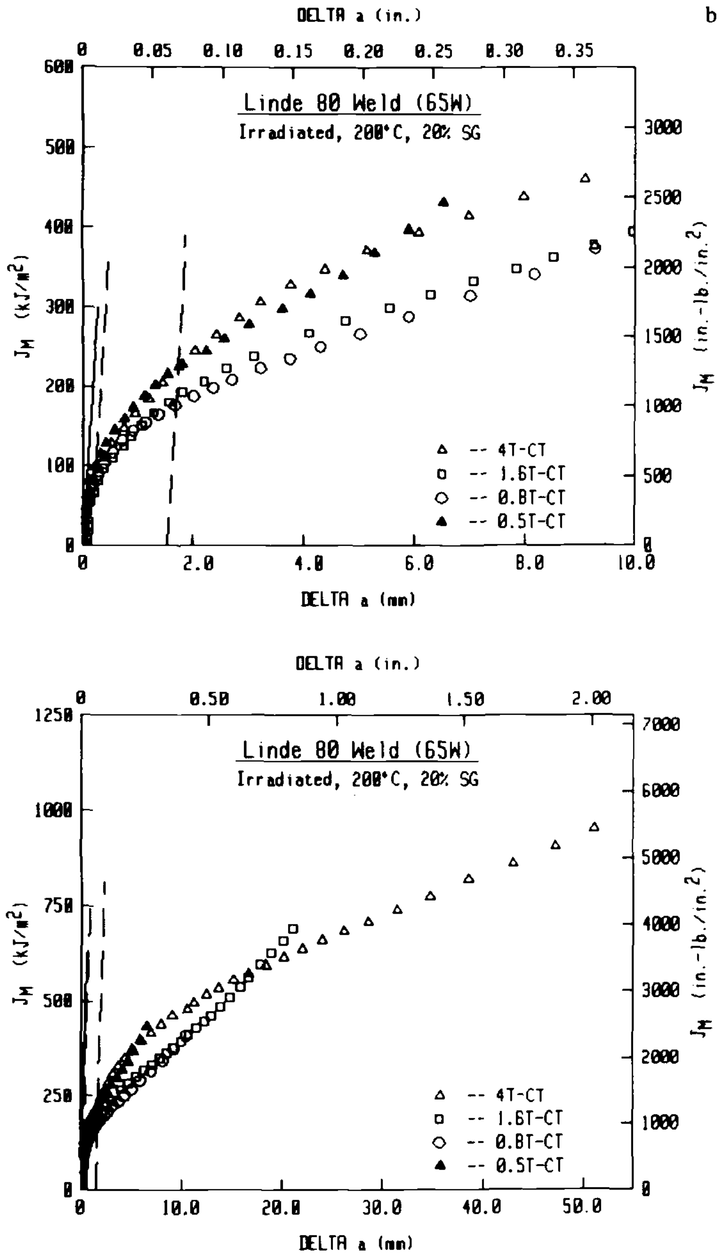

FIG. 11—*Continued*

c

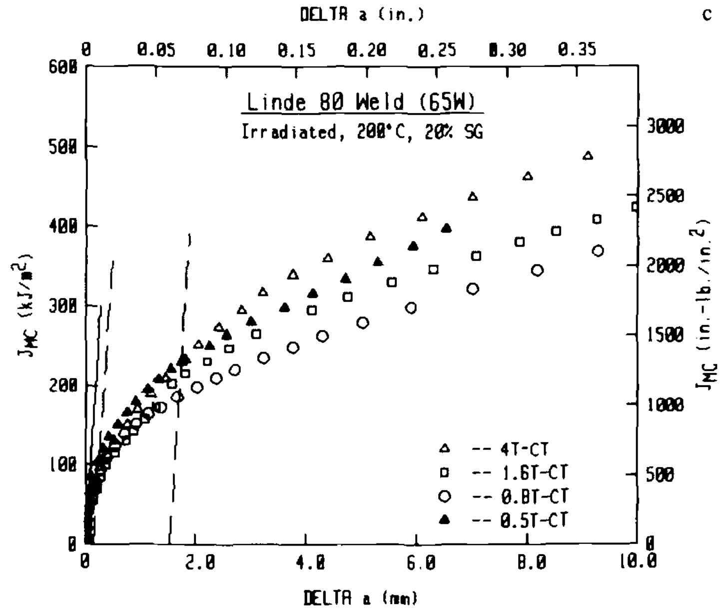

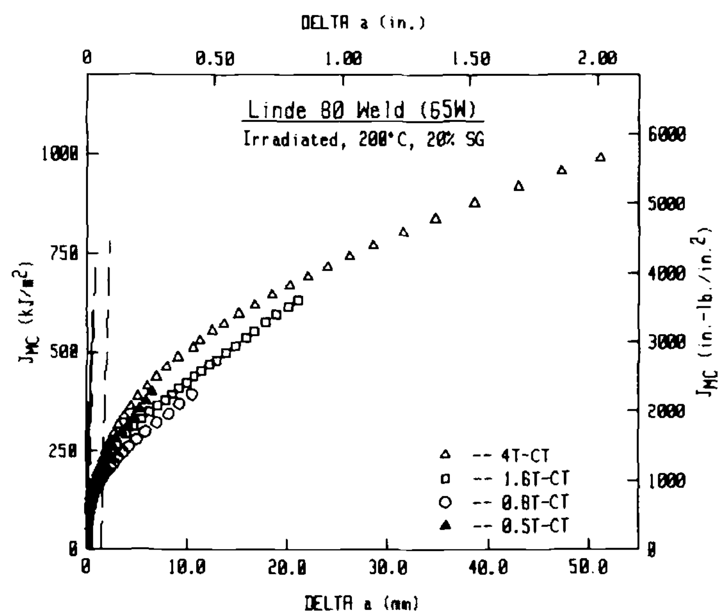

FIG. 11—*Continued*

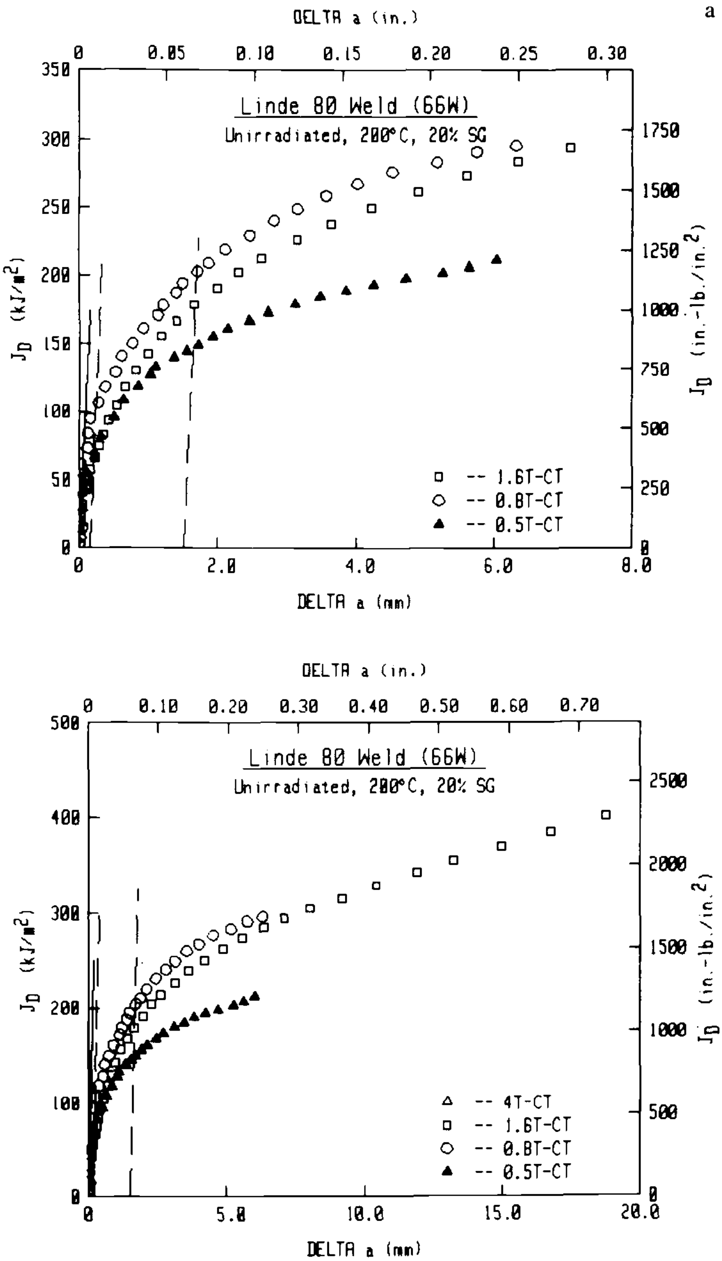

FIG. 12—*Comparison of* J-R *curves for the Code 66W weld, unirradiated condition at 200°C (392°F).* J_D (a), J_M (b), *and* J_{M-C} (c) *are illustrated, with the top graphs representing small crack growth levels and the bottom graphs representing large crack growth levels.*

b

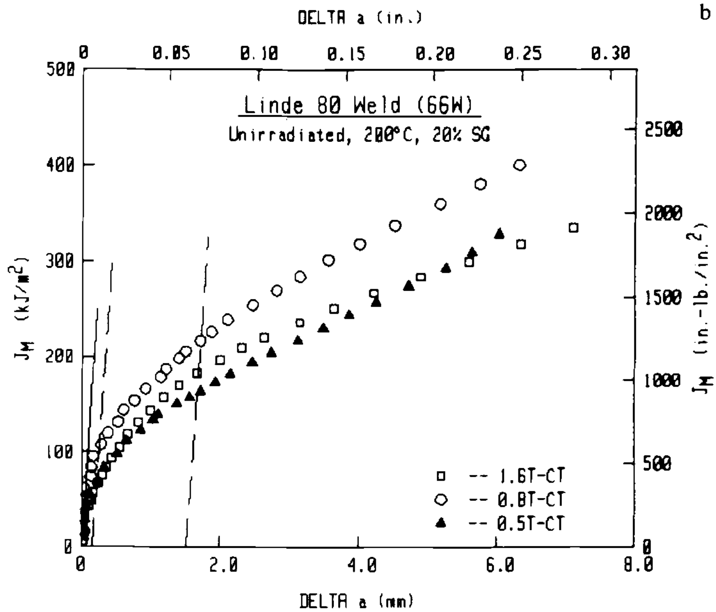

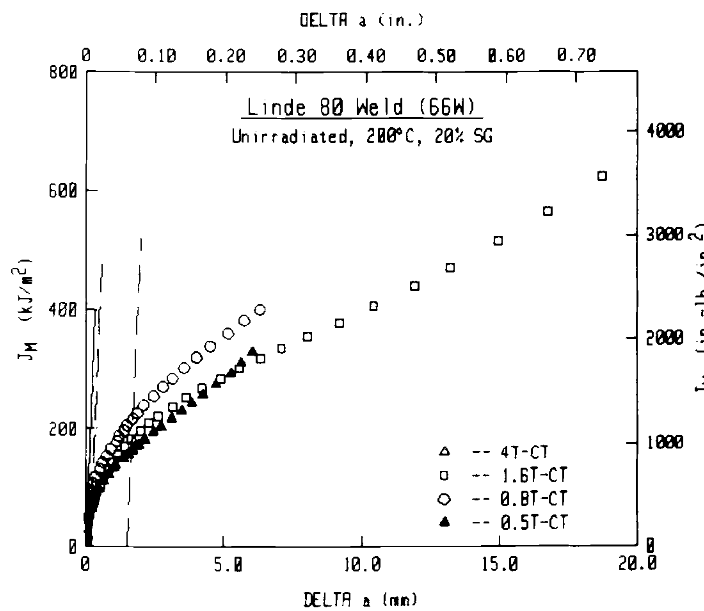

FIG. 12—*Continued*

c

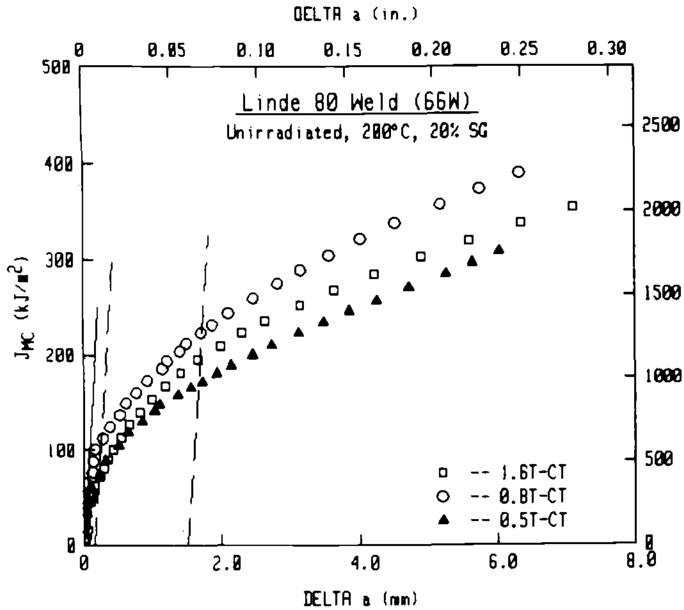

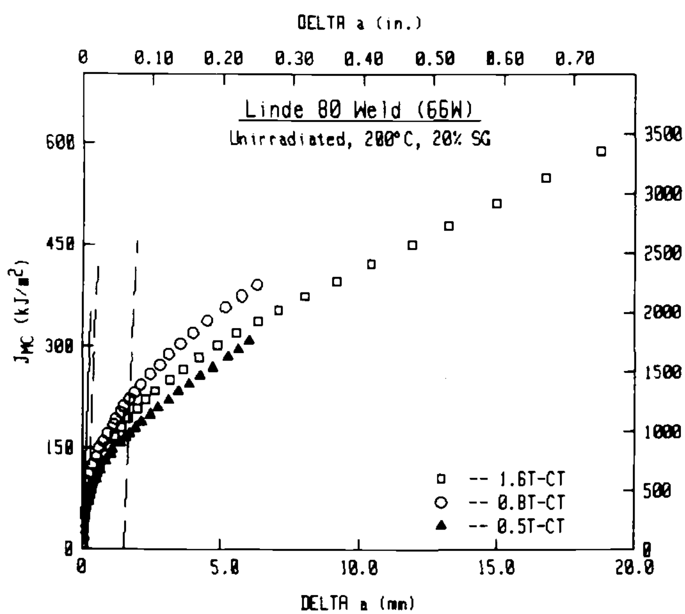

FIG. 12—*Continued*

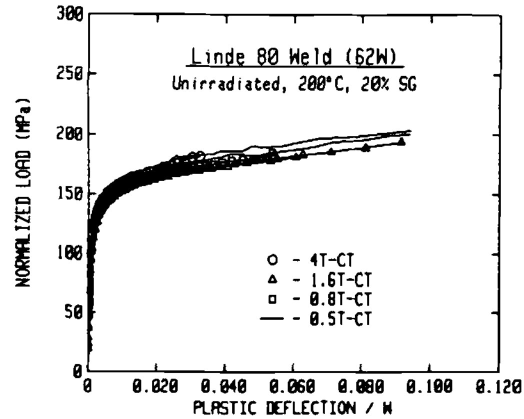

FIG. 13—*Key curves for the Code 62W weld, unirradiated condition at 200°C (392°F).*

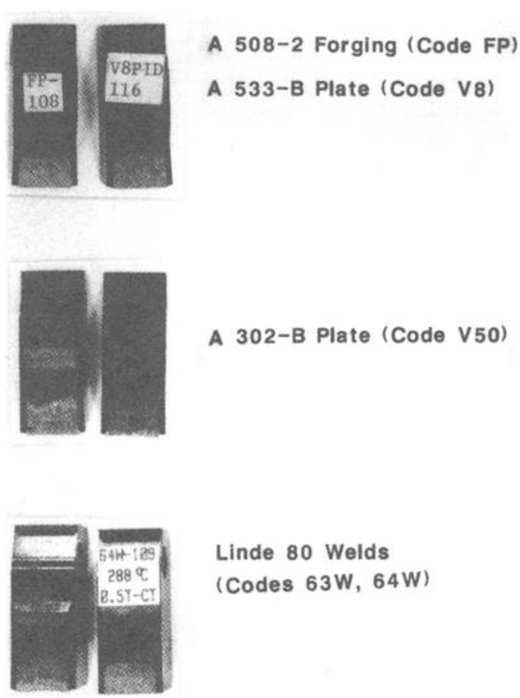

FIG. 14—*Comparison of fracture surfaces for several of the 0.5T-C(T) specimens from these materials. Only that from the Code V50 plate exhibits a nonhomogeneous appearance.*

Microstructural samples from one 0.5T-C(T) specimen and one 4T-C(T) specimen of the Code V50 plate were prepared by grinding and polishing selected surfaces to a 1.3-mm (0.05-in.) finish. The 0.5T-C(T) specimen was from the plate mid-thickness and yielded the lowest of the *J-R* curves from 0.5T-C(T) specimens. For the 4T-C(T) specimens, a piece representing the plate mid-thickness was used. Comparison of fracture surfaces from the 0.5T- and the 4T-C(T) specimens indicate no significant differences in characteristics for either specimen size (Fig. 15). Each of the fracture surfaces exhibit extensive laminated tearing, or splits, oriented in the direction of crack growth. These splits are the most prevalent feature on the fracture surfaces, with small amounts of microvoid coalescence found in the areas between the splits. The width, length, relative number, and relative distribution of the splits are generally the same for every specimen examined. These splits resulted from either: (a) separation of interfaces between the material bulk (composed of ferrite and fine pearlite) and the prolific volume of inclusions, and/or (b) the splitting of a more brittle, alloy-rich banded structure. Figure 16 compares the fracture surface with the inclusion distribution and the banded microstructure. Clearly, the distribution of splitting correlates with both the alloy-rich bands and the inclusions. Since this plate has a moderate sulfur level and plates of this variety are known to have an abundance of manganese-sulfide inclusions, these splits are thought to occur along these inclusions. The role of microstructure in explaining the discrepancy in fracture toughness of

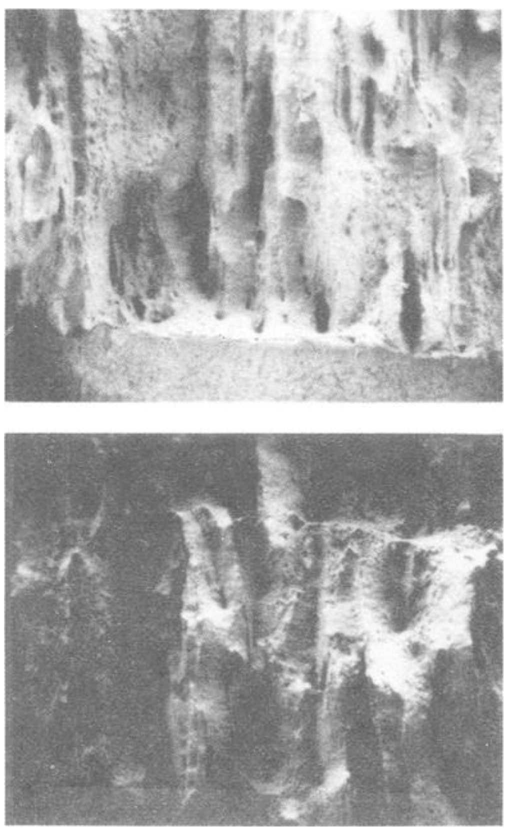

FIG. 15—*Fractograph of a high toughness 0.5T-C(T) specimen (*top*) and a low toughness specimen (*bottom*). Specimens were from the plate midthickness.* ×*30.*

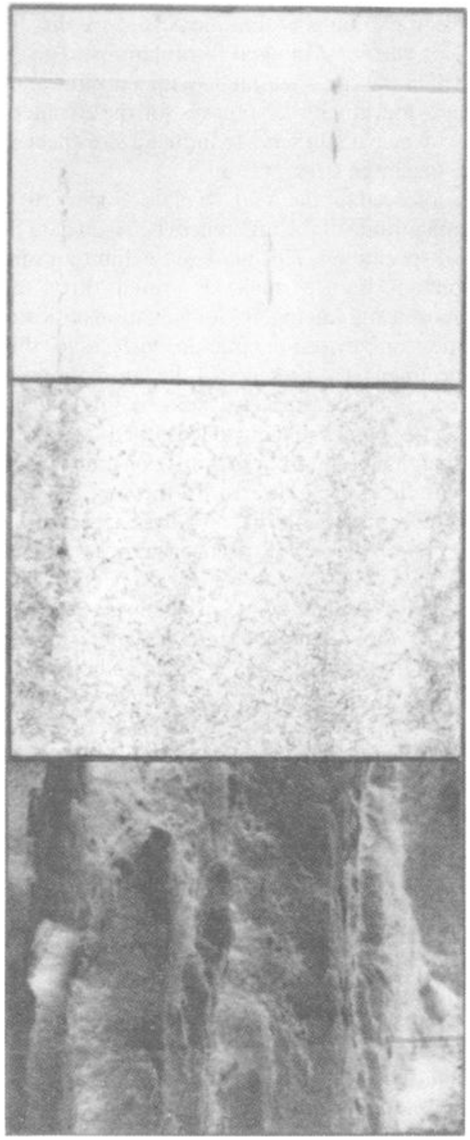

FIG. 16—*Visual correlation of the L-LT surface of the V50 plate, showing the inclusion distribution (*top*), microstructure with banding (*center*), and fracture surface with splits (*bottom*). Crack growth is from bottom to top.* $\times 100$.

these specimens is not clear, given in particular the similarities between fracture surfaces from low [4T-C(T)] and high [0.5T-C(T)] toughness specimens.

Discussion

Overall, the results for the clean/monolithic materials are quite encouraging, as excellent agreement between data from large and small specimens are apparent for these materials for all of the J formulations, in particular within the ASTM validity limits. This good agreement confirms the potential for current J-integral formulations to give reasonable assessments of material toughness, albeit in the cases of J_D and J_M for a limited amount of crack growth. Likewise, the good agreement found with key curves for these materials confirms the lack of a mechanical type of effect which could serve to induce a size effect simply due to the geometric differences between the specimen sizes.

The size dependence observed for the A 302-B plate (Code V50) was somewhat unexpected, in particular given the magnitude of the differences between data from small [0.5T-C(T)] and large [4T- and 6T-C(T)] specimens. This plate did exhibit an unusual fracture appearance, with a "woody" or fibrous appearance which was termed "dirty" for the purposes of this work. Although the microstructural and fractographic evaluation indicated no significant differences through the plate thickness or between the fracture surfaces for the high [0.5T-C(T)] and low [4T-C(T)] toughness specimens, the presence of the laminations or splits is undoubtedly the core cause for the size dependence. In Refs *25* to *27*, the deleterious effect of this splitting behavior on the C_v impact toughness of controlled-rolled steels was generally tied to a relative measure of the splits, such as the number of splits per unit thickness, or a separation index giving the length of separations per unit area. In these cases, an increase in the lamination parameter was readily tied to reductions in toughness. Development of such a parameter in the present work would probably not indicate any significant difference in expected toughness for the specimens from this A 302-B plate since the splits in this material tend to be fairly uniformly spaced, and each parameter would probably give the same value for both the large and the small specimens. Possibly the total number of splits, the total or average length of the splits, or the depth of the splits and not a relative parameter has the strongest influence on the specimen-size dependency. The characteristics of the splits (i.e., the length or the depth) could help to give lower toughness for the larger specimens in that more material (volumetrically) is exposed to the high stresses around the crack tip as the splits open. This increase in material under high stress would allow preferential cracking to occur along lower toughness planes, resulting in lower overall measured toughness for the large specimens. In contrast, the splits on the small specimens appear to be not as deep, with the result that cracking is limited to fewer possible planes, with a decreased probability that low toughness planes are accessed.

For the weld materials, the observed size effect generally results in lower J-R curves for smaller specimen sizes, with the 0.5T-C(T) specimens typically yielding the lowest J-R curves. Overall, the J_D-R curves demonstrate a "peeling-off" trend, whereby the curves for the smaller specimens tend to exhibit reduced slopes and J_D levels at relatively low a levels. In contrast, J_M does result in somewhat improved correspondence in the curves for the different specimen sizes, although in many cases the J_M-R curves exhibit an inflection point, indicating the end of J_M validity. The observed specimen size dependence is probably due to the composite nature of the large specimens, with the interaction of weld and base metals with intermediate fusion line and heat-affected zones. This hypothesis is reasonable due to the differences in key-curve trends which were generally found and the general trend of larger specimens to give higher J-R curve levels.

Conclusions

J-R curves from various sizes of specimens were compared for several steels. The specimen sizes ranged from 0.5T- to 6T-C(T), with intermediate sizes also used. For the materials studied, three categories were defined based upon the specimen makeup and the macroscopic fracture appearance. The categories include monolithic materials with clean or dirty macroscopic fracture appearances and composite (weld) metals which exhibit clean macroscopic fracture appearances.

Conclusions from this work include:

1. No significant size effect was found within the ASTM validity limits for two monolithic materials exhibiting homogeneous fracture surfaces.
2. J_D can give curves that tend to demonstrate a plateau behavior, with smaller specimens giving lower J levels than larger specimens. This behavior may indicate an end to validity of J_D.
3. J_M helps to improve correspondence in *J-R* curves for different sizes of specimens outside of the ASTM validity limits for the monolithic/clean materials, although curves for the smaller specimens frequently exhibit an inflection point at large crack growth levels. This behavior may indicate an end to validity of J_M.
4. J_{M-C} tends to give *J-R* curves intermediate to those using J_M and J_D without the adverse plateau behavior or inflection points. The lack of a change of curvature or excessive slope decrease results in no simple method for determining the end of validity of J_{M-C}.
5. The A 302-B plate (Code V50) under study exhibited a significant size effect, with smaller specimens giving much higher *J-R* curve levels than large specimens. However, J_{Ic} levels were similar for all specimen sizes.
6. The high content of manganese-sulfide inclusions and/or the banded regions of the microstructure are probably the key causes of the reduction in *R*-curve with specimen size observed for the A 302-B plate (Code V50). The fracture appearance is similar for both large (low-toughness) and small (high-toughness) specimens, but the length and depth of the splits that resulted from these planes of weakness increased with specimen size.
7. In many cases for the weld metals, a significant size effect was found, whereby larger specimen size tended to give higher *J-R* curve levels. This size dependency is probably due to the finite width of the welds, whereby the small specimens tend to be all weld metal and the larger specimens are a composite of weld and (predominantly) base metal.

References

[1] Rice, J. R., "A Path Independent Integral and the Approximate Analysis of Strain Concentration by Notches and Cracks," *Transactions of ASME, Journal of Applied Mechanics*, Vol. 35, June 1968, pp. 379–386.

[2] Merkle, J. G. and Corten, H. T., "A J-integral Analysis for the Compact Specimen, Considering Axial Force as Well as Bending Effects," *Transactions of ASME, Journal of Pressure Vessel Technology*, November 1974, pp. 286–292.

[3] Ernst, H. A. and Paris, P. C., "Techniques of Analysis of Load-Displacement Records by J-Integral Methods," NUREG/CR-1222, U.S. Nuclear Regulatory Commission, Washington, DC, January 1980.

[4] Ernst, H. A., "Materials Resistance and Instability Beyond J-Controlled Crack Growth," *Elastic-Plastic Fracture, ASTM STP 803*, Vol. I, ASTM, Philadelphia, 1983, pp. 191–213.

[5] Hutchinson, J. R. and Paris, P. C., "The Theory of Stability Analysis of J-Controlled Crack Growth," *Elastic-Plastic Fracture, ASTM STP 668*, ASTM, Philadelphia, March 1979, pp. 37–64.

[6] Shih, C. F., "An Engineering Approach for Examining Crack Growth and Stability in Flawed Structures," *Proceedings of CSNI Specialists Meeting in Plastic Tearing Instability*, NUREG/CP-0010, U.S. Nuclear Regulatory Commission, Washington, DC, January 1980.

[7] McCabe, D. E. and Landes, J. D., "J_R-Curve Testing of Large Compact Specimens," *Elastic-Plastic Fracture, ASTM STP 803*, Vol. II, ASTM, Philadelphia, PA, 1983, pp. 353–371.

[8] Shih, C. F., deLorenzi, H. G., and Andrews, W. R., "Studies on Crack Initiation and Stable Crack Growth," *Elastic-Plastic Fracture, ASTM STP 668*, ASTM, Philadelphia, March 1979, pp. 65–120.

[9] Vassilaros, M. G., Joyce, J. A., and Gudas, J. P., "Effects of Specimen Geometry on the J_I-R Curve for ASTM A533B Steel," *Fracture Mechanics: Twelfth Conference, ASTM STP 700*, ASTM, Philadelphia, 1980, pp. 251–270.

[10] Davis, D. A., Vassilaros, M. G., and Gudas, J. P., "Specimen Geometry and Extended Crack Growth

Effects on J_I-R Curve Characteristics for HY-130 and ASTM A533B Steels," *Elastic-Plastic Fracture, ASTM STP 803*, Vol. II, ASTM, Philadelphia, 1983, pp. 582–610.

[11] Hiser, A. L. and Loss, F. J., "Alternative Procedures for *J-R* Curve Determination," NUREG/CR-3402, U.S. Nuclear Regulatory Commission, Washington, DC, July 1983.

[12] Saxena, A. and Hudak, S. J., Jr., "Review and Extension of Compliance Information for Common Crack Growth Specimens," *International Journal of Fracture*, Vol. 14, No. 5, October 1978, pp. 453–468.

[13] Rice, J. R., Drugan, W. J., and Sham, T.-L., "Elastic-Plastic Analysis of Growing Cracks," *Fracture Mechanics: Twelfth Conference, ASTM STP 700*, ASTM, Philadelphia, 1980, pp. 189–221.

[14] Ernst, H., Paris, P. C., Rossow, M., and Hutchinson, J. W., "Analysis of Load-Displacement Relationships to Determine J-R Curve and Tearing Instability Material Properties," *Fracture Mechanics, ASTM STP 677*, ASTM, Philadelphia, 1979, pp. 581–599.

[15] Joyce, J. A., Ernst, H., and Paris, P. C., "Direct Evaluation of J-Resistance Curves from Load Displacement Curves," *Fracture Mechanics: Twelfth Conference, ASTM STP 700*, ASTM, Philadelphia, 1980, pp. 222–236.

[16] Hawthorne, J. R., "Significance of Nickel and Copper Content to Radiation Sensitivity and Postirradiation Heat Treatment Recovery of Reactor Vessel Steels," NUREG/CR-2948, U.S. Nuclear Regulatory Commission, Washington, DC, November 1982.

[17] Childress, C. E., "Fabrication and Mechanical Test Data for Acceptance of the First Six 6-Inch-Thick Intermediate Test Vessels of the Heavy-Section Steel Technology Program," ORNL/TM-4351, Oak Ridge National Laboratory, Oak Ridge, TN, October 1973.

[18] Derby, R. W. et al., "Test of 6-Inch-Thick Pressure Vessels, Series 1: Intermediate Test Vessels V-1 and V-2," ORNL-4895, Oak Ridge National Laboratory, Oak Ridge, TN, February 1974.

[19] Loss, F. J., Ed., "Structural Integrity of Water Reactor Pressure Boundary Components, Annual Report for 1983," NUREG/CR-3228, Vol. 2, U.S. Nuclear Regulatory Commission, Washington, DC, September 1984.

[20] Childress, C. E., "Fabrication and Mechanical Test Data for the Four 6-Inch-Thick Intermediate Test Vessels Made from Steel Plate for the Heavy-Section Steel Technology Program," ORNL/TM-5074, Oak Ridge National Laboratory, Oak Ridge, TN, January 1976.

[21] Merkle, J. G. et al., "Test of 6-Inch-Thick Pressure Vessels. Series 3: Intermediate Test Vessel V-7," ORNL/NUREG-1, Oak Ridge National Laboratory, Oak Ridge, TN, August 1976.

[22] Hiser, A. L. and Terrell, J. B., "Size Effects on J-R Curves for A 302-B Plate," NUREG/CR-5265, U.S. Nuclear Regulatory Commission, Washington, DC, January 1989.

[23] Loss, F. J., Ed., "Structural Integrity of Water Reactor Pressure Boundary Components, Progress Report Ending 29 Feb 1976," NRL Report 8006, Naval Research Laboratory, Washington, DC, 26 August 1976.

[24] Hiser, A. L., Loss, F. J., and Menke, B. H., "J-R Curve Characterization of Irradiated Low Upper Shelf Welds," NUREG/CR-3506, U.S. Nuclear Regulatory Commission, Washington, DC, April 1984.

[25] Emburg, J. D., Petch, N. J., Wraith, A. E., and Wright, A. E., "The Fracture of Mild Steel Laminates," *Transactions of the Metallurgical Society of AIME*, Vol. 239, January 1967, pp. 114–118.

[26] Miyoshi, E., Fukuda, M., Iwanaga, H., and Okazawa, T., "The Effect of Separation on the Propagating Shear Fracture," Paper 4, *Crack Propagation in Pipelines*, The Institute of Gas Engineers, March 1974.

[27] Poynton, W. A. and Christian, J. R., "An Experimental Study of Shear Fracture Propagation Using Small Scale Models," Paper 5, *Crack Propagation in Pipelines*, The Institute of Gas Engineers, March 1974.

James A. Joyce,[1] *Edwin M. Hackett,*[2] *and Charles Roe*[3]

Effects of Crack Depth and Mode of Loading on the *J-R* Curve Behavior of a High-Strength Steel

REFERENCE: Joyce, J. A., Hackett, E. M., and Roe, C., **"Effects of Crack Depth and Mode of Loading on the *J-R* Curve Behavior of a High-Strength Steel,"** *Constraint Effects in Fracture, ASTM STP 1171,* E. M. Hackett, K.-H. Schwalbe, and R. H. Dodds, Eds., American Society for Testing and Materials, Philadelphia, 1993, pp. 239–263.

ABSTRACT: This paper describes an experimental program which had the objective of developing a series of *J-R* curve data from laboratory specimens of varied constraint. Constraint was varied by testing specimens with different thicknesses, crack lengths, and mode of loading. All specimens were relatively small and were kept simple in geometry and loading to allow estimation of the applied J integral. Crack length-to-width ratios were varied dramatically from $a/W = 0.10$ to $a/W = 0.65$ and the mode of loading ranges from three-point bending of deeply cracked edge-notched bars to pure tensile loading of double edge-notched strips. All tests were conducted on a single material, a high-strength structural steel, at ambient temperature, which is well up on the ductile upper shelf for this alloy.

Results of these tests have shown that different constraint conditions can dramatically affect the J_{Ic} and the *J-R* curve for the full range of crack lengths and loading modes studied here, and these effects can be studied on relatively inexpensive laboratory specimens. Observed trends correspond to generally expected ideas of "increased constraint" or "decreased constraint" conditions, but since no factor is available to satisfactorily quantify constraint, an ability to utilize a data set such as this to predict the behavior of a material for a particular structural application is still lacking.

KEY WORDS: high-strength steel, *J-R* curves, J_{Ic}, SE(B), SE(T), DE(T), a/W effects

Objectives

J integral fracture toughness, as measured by ASTM standardized methods [ASTM Test Method for J_{Ic}, a Measure of Fracture Toughness (E 813); Test Method for Determining *J-R* Curves (E 1152); and Test Method for Crack-Tip Opening Displacement (CTOD) Fracture Toughness Measurement (E 1290)], utilizes deeply cracked bend-type specimens to assure lower bound, size-independent fracture toughness measures within the specified criteria. Application of these measures to real structures is often resisted with the justification that the real structure has only shallow cracks and thus the ASTM fracture toughness measures do not apply. A second argument is that the structural elements are predominantly loaded in tension, not in bending as is the case for the ASTM laboratory specimens.

An important objective is to develop data to address the effect of constraint on elastic-plastic fracture initiation and ductile crack growth. Several large-scale tests have been conducted

[1] Professor of mechanical engineering, U.S. Naval Academy, Annapolis, MD.
[2] Research engineer, U.S. Nuclear Regulatory Commission, Mail Stop NL/S 217C, Washington, DC 20555.
[3] Co-op engineer, David Taylor Research Center, Annapolis, MD 21402.

recently in the United States and in Europe which have shown that the J integral at initiation and the J-R curve in general are distinctly elevated for predominantly tensile loading in comparison with bending laboratory specimen results. Analyses of Betegon and Hancock [1], Al-Ani and Hancock [2], and O'Dowd and Shih [3] have proposed that an additional constraint parameter is needed, besides the J integral, to develop truly size and loading independent measures of ductile fracture toughness. Dodds and Anderson [4,5] have shown that in the lower transition range of ferritic steels, where fracture is cleavage dominated and hence stress controlled, a constraint correction can be applied which appears to develop a size-independent fracture initiation criteria for these conditions. Their methodology cannot be directly applied to the ductile fracture case since both stress and strain are controlling factors in ductile crack initiation and metallurgical aspects of fracture are more complex. A data set is required that covers a range of crack length, specimen sizes, and types of loading, a data set that hence covers a range of constraint conditions.

In this project a series of both deep and shallow cracked bend specimens have been tested with the objective of evaluating the difference between the measured fracture toughness of the shallow cracked geometries and those of standard ASTM configuration specimens. A typical high-strength structural steel alloy has been used for this experimental comparison. Additional specimens have been prepared which are predominantly tensile in loading. Standard specimens do not now exist for fracture testing using predominantly tensile loading. This has required the development of approximate equations for the evaluation of the J integral for tensile-loaded specimens as well as the development of crack length to compliance relationships that are accurate enough to allow single specimen, unloading compliance R curve evaluations. The two tensile geometries evaluated here are a single edge-notch tension specimen [SE(T)] and a double edge-notch tension specimen [DE(T)].

Experimental Details

Material Description

A high-strength structural steel was used for all tests, using SE(B), SE(T), and DE(T) geometries of various crack length-to-width (a/W) ratios. The material was originally 9 cm thick. All specimen crack planes were orientated in the T-L orientation as designated by ASTM Test Method for Plain-Strain Fracture Toughness of Metallic Materials (E 3990). The material tensile mechanical properties are shown in Table 1, and the chemical analysis is shown in Table 2.

Specimen Test Matrix

Table 3 shows a matrix of the specimens tested in this program. The first set of tests consisted of single edge-notched bend [SE(B)] specimens. These specimens were all 1T plan bend specimens according to ASTM E 813 with W = 2.0 in. (5.08 cm). They had a test thickness of 1.25, 2.5, and 5.0 cm. Samples were tested with and without side grooves; the side grooves, when present, were of 20% total thickness reduction and cut with a standard Charpy cutter. Two crack lengths were used, called deep and short in this document, with a/W ratios of nom-

TABLE 1—*Tensile mechanical properties of high-strength steel—material code FYO.*

Yield Stress, MPa (ksi)	Ultimate Stress, MPa (ksi)	% Elongation, 25 mm	% Reduction of Area
747 (109)	877 (128)	16.5	57

TABLE 2—*Chemical composition of high-strength steel (wt%)—material code FYO.*

C	Mn	P	S	Cu	Si	Ni	Cr	Mo	V	Ti
0.164	0.26	0.003	0.009	...	0.19	2.78	1.57	0.42	0.003	...

inally 0.6 and 0.13, respectively. The second set of tests included predominantly tensilely loaded specimens. Schematics of these two specimen types are shown in Fig. 1. The single edge-notched tension specimen [SE(T)] had a cross section of 2.5 in. (6.4 cm) by 1 in. (2.5 cm) and a length of 12 in. (30.5 cm). This specimen was loaded with a centered pin at a center distance of 9 in. (22.9 cm). Crack length-to-width ratios of 0.35 to 0.65 were investigated. The double edge-notched tension specimen [DE(T)] had the same size and shape as the SE(T) specimen, but an additional notch and precrack so that the test section was centered in the load line. The DE(T) specimens were tested with a/W ratios between 0.6 and 0.7. Both SE(T) and DE(T) were tested with side grooves with 20% total thickness reduction.

Specimen Precracking

All specimens tested in this program were precracked in bending using a three-point bend apparatus. The short cracks were obtained in the SE(B) specimens by starting with $W \approx 7$ cm and precracking until the desired crack length was achieved, then remachining the specimens

TABLE 3—*List of specimens.*

Specimen I.D.	Type	a/W	B, mm	B_n, mm	W, mm
FYO 1	SE(B)	0.66	50	40	50
FYO 2	SE(B)	0.66	50	50	50
FYO 3	SE(B)	0.66	50	40	50
FYO 4	SE(B)	0.63	50	50	50
FYO 5	SE(B)	0.66	50	50	50
FYO 21	SE(B)	0.14	50	40	50
FYO 23	SE(B)	0.13	50	50	50
FYO 25	SE(B)	0.13	25	25	50
FYO 26	SE(B)	0.13	25	20	50
FYO 27	SE(B)	0.14	25	20	50
FYO 150	SE(B)	0.61	25	20	50
FYO 151	SE(B)	0.61	25	20	50
FYO 153	SE(B)	0.61	25	25	50
FYO 154	SE(B)	0.61	25	25	50
FYO 155	SE(B)	0.60	12.5	12.5	50
FYO 157	SE(B)	0.60	12.5	12.5	50
FYO 158	SE(B)	0.60	12.5	10	50
FYO 159	SE(B)	0.62	12.5	10	50
FYO 160	SE(B)	0.11	12.5	10.0	50
FYO 161	SE(B)	0.11	12.5	10.0	50
FYO 162	SE(B)	0.11	12.5	12.5	50
FYO 2SB	SE(T)	0.40	25	20	64
FYO 3SB	SE(T)	0.47	25	20	64
FYO 4SA	SE(T)	0.65	25	20	64
FYO 10SA	SE(T)	0.35	25	20	64
FYO 11SB	DE(T)	0.68	25	20	32
FYO 12SA	DE(T)	0.61	25	20	32

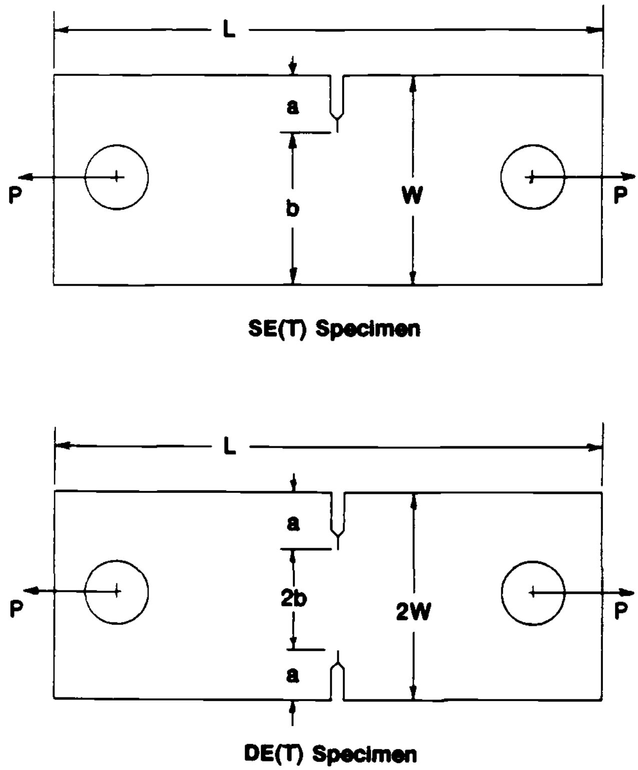

FIG. 1—*Schematic drawings of pin-loaded SE(T) and DE(T) specimens.*

until $W = 5$ cm for testing. The crack fronts obtained in this fashion for this material were found to be straight and accurate in all cases. The SE(T) specimens were precracked from initial machined notches with $a/W = 0.15$ without problems and grown by fatigue to a/W values of between 0.3 and 0.65 for testing.

The DE(T) specimens were also precracked in bending from initial notches with $a/W = 0.15$. Short notches were used here since a notch was present on both the compression and tensions sides while these specimens were being precracked. Once a crack was introduced on one side, the specimen was reversed and a second crack was grown from the other notch. Optical crack length monitoring was used to obtain approximately equal crack lengths, and then the specimen compliances were matched to achieve a final crack length agreement between the two sides of these specimens. Experience was a considerable factor in precracking the DE(T) specimens. All specimens were side-grooved after precracking.

Test Technique

All tests were conducted using a single specimen, computer interactive, unloading compliance test procedure which allowed monitoring the specimen crack length and the applied J integral during the course of the test. Equations are presented in later sections for the required K, η, γ factors and for the compliance relationships needed for each of the specimen geometries. In all cases, crack growth corrected J equations were used, similar to what is required by ASTM E 1152. All data were stored on magnetic media for subsequent reanalysis as needed.

Analysis

J Integral Analysis

The J integral is calculated here by separating it into elastic and plastic components and calculating the components separately. The elastic J component, J_{el}, is calculated from

$$J_{el} = \frac{K^2}{E'} \tag{1}$$

where K is the elastic stress intensity factor for the specimen, $E' = E/(1 - \nu^2)$, and E and ν are the elastic modulus and Poisson's ratio, respectively. The plastic J component, J_{pl}, is calculated using the standard E 1152 J_{pl} equation

$$J_{pli} = J_{pl(i-1)} + \frac{\eta_i}{b_i}\left[\frac{A_{pl(i)} - A_{pl(i-1)}}{B_N}\right]\left[1 - \frac{\gamma_i(a_i - a_{(i-1)})}{b_i}\right] \tag{2}$$

where

A_{pli} = area under the load versus plastic load line displacement curve to increment i,
B_N = net specimen thickness at the side groove roots,
η_i = the plastic η factor at crack length a_i,
b_i = the incremental remaining ligament,
W = the specimen width, and

$$\gamma_i = \left[\eta_i - 1 - \frac{b_i}{W}\frac{\eta_i'}{\eta_i}\right] \tag{3}$$

Formulas for the K's, η's, and γ's used for the SE(B), SE(T), and DE(T) specimens are presented in the next subsections.

SE(B) Analysis

Previous work by Joyce [6] has shown that unloading compliance can be used to evaluate J-R curves for short crack bend specimens. As the crack becomes very short, the compliance equation becomes less sensitive to crack length and the specimen limit load also increases, which increases the length of the allowed elastic unloading, and the total effective crack length measurement resolution is only slightly degraded. Results obtained by Joyce [6] appeared to be fully adequate for J_{Ic} and J-R curve testing to a/W ratios as small as 0.15. In this work similar success was found to a/W ratios as small as 0.1. To test in this a/W range, a new equation to estimate crack length from the specimen COD compliance is needed since the equation available in E 813 and E 1152 does not apply for a/W ratios below 0.4. Tada [7] supplies an equation for bend specimen compliance as a function of a/W that is good for all a/W. This equation is

$$\frac{\delta}{P} = \frac{24(a/W)}{\left[\dfrac{BWE'}{S/4}\right]}\left[0.76 - 2.28(a/W) + 3.87(a/W)^2 - 2.04(a/W)^3 + \frac{0.66}{[1 - a/W]^2}\right] \tag{4}$$

where

δ = crack mouth opening displacement at the specimen edge,
P = load,
B = specimen thickness,
S = specimen span.

An equation has been proposed by Kapp et al. [8] to give a/W as a function of δ/P across the full a/W range, but it has been found to be too inaccurate ($\pm 4\%$) for use for unloading compliance crack length estimates. A reverse fit was obtained by Joyce [6] using a standard fifth order polynomial by restricting the a/W range to between 0.05 and 0.45 which was accurate to within 0.06%, which is acceptable for the unloading compliance method. The Joyce relationship is

$$a/W = [1.01878 - 4.5367u + 9.0101u^2 - 27.333u^3 + 74.4u^4 - 71.489u^5] \quad (5)$$

and has been used for the short crack SE(B) specimens presented below. The standard equation of ASTM E 1152 was used for the deep cracked bend specimens analyzed below.

For the deep cracked SE(B) specimens, the η and γ factors of ASTM E 1152, namely that $\eta = 2.0$ and $\gamma = 1.0$ can be used in Eq 2 to evaluate J. For the short crack specimens, however, these coefficients must be changed to accurately evaluate J. This problem was looked at by Haigh and Richards [9], Sumpter [10], and by Joyce [6]. A comparison of various estimates of η is shown in Fig. 2 which includes results of the above authors and results derived by Joyce [6] from the EPRI Handbook [11]. The ABAQUS results were obtained by Joyce [6] using a two-dimensional incremental elastic plastic analysis. In the work that follows, the polynomial function developed by Sumpter [10] is used for all short-cracked SE(B) specimens with $a/W < 0.282$. This polynomial expression is

$$\eta = 0.32 + 12(a/W) - 12(a/W)^2 + 99.8(a/W)^3 \quad (6)$$

This equation gives $\eta < 2.0$ if $a/W < 0.282$. Sumpter switches to $\eta = 2.0$ when the specimen exceeds $a/W = 0.282$. In this work the short crack specimens were started and completed with $a/W < 0.282$.

The γ factor is calculated from η using Eq 3. For the short crack specimens γ was obtained by differentiating Eq 7 to give

$$\gamma = \frac{\begin{gathered}[-12.22 + 106.7\,(a/W) + 362.2(a/W)^2 - 924.6(a/W)^4 \\ - 1292(a/W)^4 - 988(a/W)^5 + 9960(a/W)^6]\end{gathered}}{[0.32 + 12(a/W) - 49.5(a/W)^2 + 99.8(a/W)^3]}$$

SE(T) Analysis

For unloading compliance testing of SE(T) specimens, equations are required for K, η, and γ as functions of a/W and for a/W as a function of the specimen COD compliance. The equations used for this are presented in the following sections.

SE(T) K *Expression*

Since the SE(T) specimens tested here had pin loading, the K expressions available in the Tada Handbook [7], developed for fixed end loading, were checked with ABAQUS finite element analysis. A total of 14 different SE(T) finite element grids were developed with $0.12 \leq$

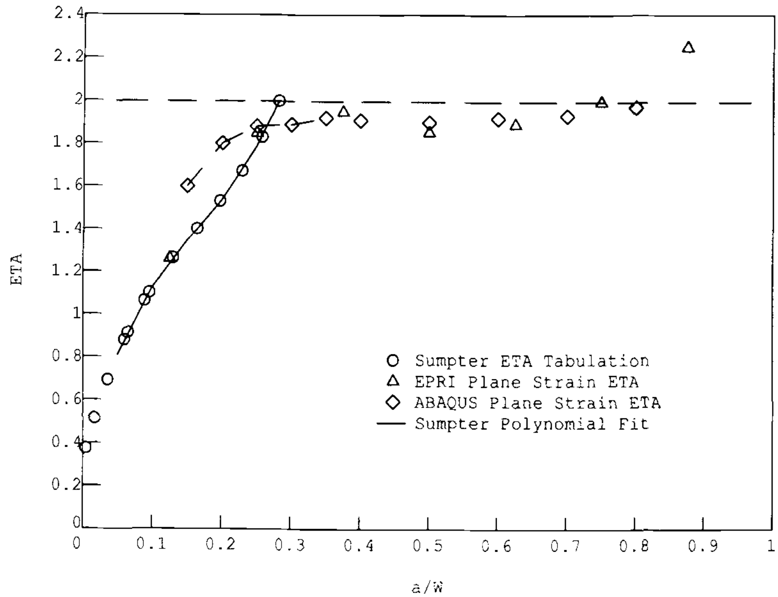

FIG. 2—*Predicted plastic η factors for short-cracked three-point bend specimens.*

$a/W \leq 0.80$. These grids were used to develop both the elastic stress intensity factor K and also the plastic η factor as described below. The stress intensity factor relationship was assumed to have the form

$$K = \sqrt{\pi a}\,\frac{P}{WB}\,F(a/W) \tag{8}$$

and $F(a/W)$ was fit with a polynomial to give

$$F(a/W) = -0.0917 + 22.392(a/W) - 141.96(a/W)^2 + 449.72(a/W)^3 - 645.59(a/W)^4 + 363.52(a/W)^5 \tag{9}$$

This equation fit the ABAQUS results within $\pm 2\%$ over the a/W range from 0.12 to 0.80. A comparison is presented in Fig. 3 with the ABAQUS results and a standard form taken from the Tada Handbook [*7*]. Clearly the Tada equation, the polynomial fit, and the ABAQUS results agree almost exactly in the range of $0.12 \leq a/W \leq 0.80$. In the experimental work presented below, the polynomial form for $F(a/W)$ presented in Eq 10 has been used for all SE(T) specimens.

SE(T) η Factor

Two methods were used here to calculate the plastic η factor for the SE(T) specimen. The first method uses the ABAQUS finite element analysis described above, except that the loading was extended into the elastic-plastic regime. The second method used the EPRI Handbook [*11*] approach. Additional estimates of η by Shang-Xian Wu et al. [*12*] and Sharobeam et al. [*13*] are presented for comparison.

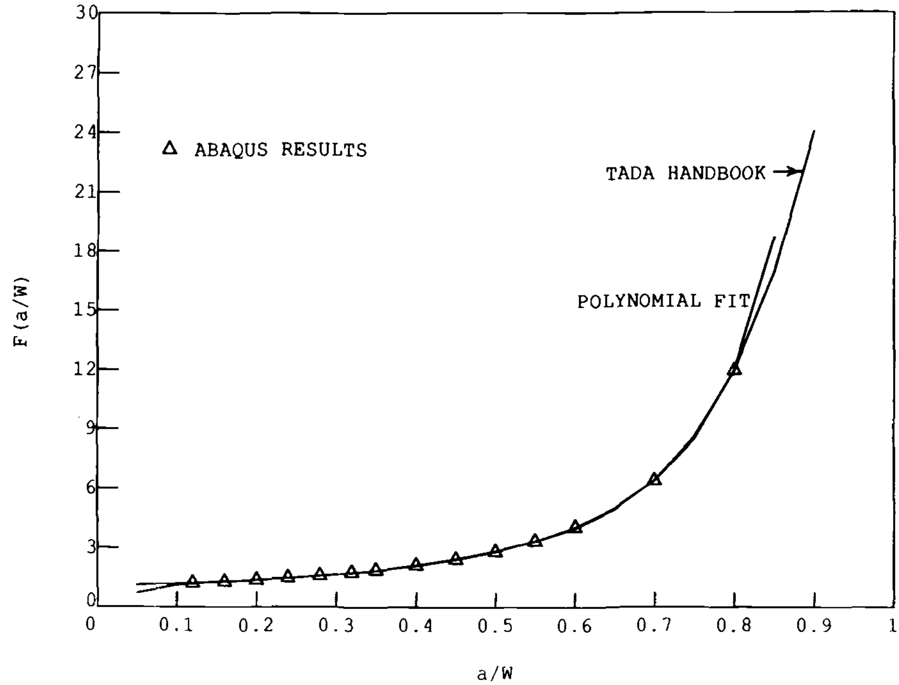

FIG. 3—*Comparison of stress intensity factor relationships for the SE(T) specimen geometry.*

The finite element method involved running each of the 14 SE(T) grids with different a/W ratios to obtain predicted load, displacement, and J integral information. Plane strain modeling was used with material properties obtained from the stress strain curve of the high-strength steel described above. Piecewise linear stress strain modeling was used along with incremental strain theory and the Von Mises yield criterion. The results of each analysis were used to generate a spreadsheet calculation of the plastic η factor as shown for one case in Table 4. The η value was taken as the average of the last few load increments. The results of this process are shown in Fig. 3 for all 14 analyses.

The EPRI Handbook [*11*] contains relationships that can be used to develop an analytical expression for η in terms of the tabulated h functions given in the handbook. For the SE(T) specimen geometry the EPRI result is

$$\gamma = \frac{\sigma_0}{P_0}\frac{b^2}{W}\left[\frac{(n+1)}{n}\right]\frac{h_1}{h_3} \tag{10}$$

where

P_0 = specimen limit load,
σ_0 = material yield stress,
n = material strain hardening exponent,
h_1, h_3 = EPRI Handbook functions of a/W, n, and specimen geometry.

TABLE 4—*Spreadsheet for η evaluation—SE(T) specimen.*

	SEN Case SEN7	$a = 0.7$ $b = 1.8$	$W = 2.5$	$B = 1$	$B_n = 1$	C(COD) 7.89E-08 C(LL) 1.86E-07	$f = 0.9488$	$E =$ 2.90E + 07	$Nu = 0.3$			
Load Increment	Load, lb	D_{el}-COD, in.	D_{el}-LP, in.	A_{tot}, in.-lb	A_{el}, in.-lb	A_{pl}, in.-lb	J_{tot}, lb/in.	J_{el}, lb/in.	J_{pl}, lb/in.	N_{tot}	N_{el}	N_{pl}
	0	0	0	0	0	0	0	0	0			
1	53670	0.00426	0.0105	281.7675	267.8836	13.88389	82.2	81.3684301	0.831569	0.5251137	0.546741	0.107810
2	101200	0.00838	0.0293	1737.545	952.4539	785.0915	310.5	289.303555	21.19644	0.3216606	0.546741	0.048597
3	150710	0.01406	0.0691	6750.554	2112.355	4638.198	819.3	641.618512	177.6814	0.2184620	0.546741	0.068954
4	184350	0.0223	0.126	16283.01	3160.597	13122.41	1682	960.017235	721.9827	0.1859361	0.546741	0.099034
5	191970	0.0253	0.1494	20685.95	3427.280	17258.67	2005	1041.02096	963.9790	0.1744661	0.546741	0.100538
6	198410	0.02844	0.174	25487.62	3661.087	21826.54	2348	1112.03859	1235.961	0.1658216	0.546741	0.101927
7	205280	0.0334	0.2078	32309.99	3919.008	28390.98	2887	1190.38110	1696.618	0.1608357	0.546741	0.107566
8	212830	0.041	0.2578	42762.74	4212.584	38550.15	3737	1279.55346	2457.446	0.1573004	0.546741	0.114744
9	220610	0.538	0.3188	55982.66	4526.195	51456.46	5213	1374.81143	3838.188	0.1676126	0.546741	0.134263
10	229030	0.0748	0.394	72889.12	4878.290	68010.83	7663	1481.75872	6181.241	0.1892381	0.545741	0.163595
11	239180	0.1049	0.4996	97610.61	5320.257	92290.35	11422	1616.00414	9805.995	0.2106287	0.546741	0.191252
12	242450	0.1155	0.542	107821.1	5466.726	102354.4	12829	1660.49328	11168.50	0.2141713	0.546741	0.196408

For the plane strain model, the EPRI Handbook takes

$$\frac{\sigma_0}{P_0} = \frac{1}{1.455Bb} \tag{11}$$

with

$$\beta = \left[1 + \left[\frac{a}{b}\right]^2\right]^{1/2} - \frac{a}{b} \tag{12}$$

and thus

$$\eta = \frac{0.687b}{\beta W}\left[\frac{n+1}{n}\right]\frac{h_1}{h_3} \tag{13}$$

An additional term is added to this model by Shang-Xian Wu et al. [*12*] to account for a no-crack load point displacement component giving a corrected equation as

$$\eta^* = \frac{0.687b}{\beta W}\left[\frac{n+1}{n}\right]\left[\frac{h_1}{h_3 + h_{30}}\right] \tag{14}$$

with

$$h_{30} = \frac{\sqrt{3}(1 - a/W)}{a/W}[1.26\beta(1 - a/W)]^n \tag{15}$$

These predictions for η are shown and compared to the finite element results on Fig. 4. Also shown on Fig. 4 are results from the EPRI Handbook and a result obtained experimentally by Sharobeam et al. [*13*]. A strain-hardening coefficient of 10 was used for all evaluations where it was required.

In the experimental work that follows, the dashed bilinear relationship shown in Fig. 4 was used to evaluate η_i at each crack length a_i. This form also allowed calculating γ_i from Eq 3, which is also needed to calculate J_{pl} using Eq 2. For the experimental work described below, the equations used for the SE(T) specimen to evaluate η_i and γ_i are thus

$$\eta_i = 5.71(a_i/W) \qquad 0 < a_i \leq 0.417 \tag{16}$$

$$\eta_i = 2.38 \qquad 0.417 < a_i/W \leq 1.0 \tag{17}$$

$$\gamma_i = 1.38 \qquad 0.417 < a_i/W \leq 1.0 \tag{18}$$

$$\gamma_i = \eta_i - 1 - (b_i/W)\left[\frac{5.71}{\eta_i}\right] \qquad 0 < a_i/W \leq 0.417 \tag{19}$$

SE(T) Crack Length Estimation

Since the SE(T) specimen is of a rather short length and has the load applied through the centered pin holes, the compliance equations in standard fracture mechanics handbooks like

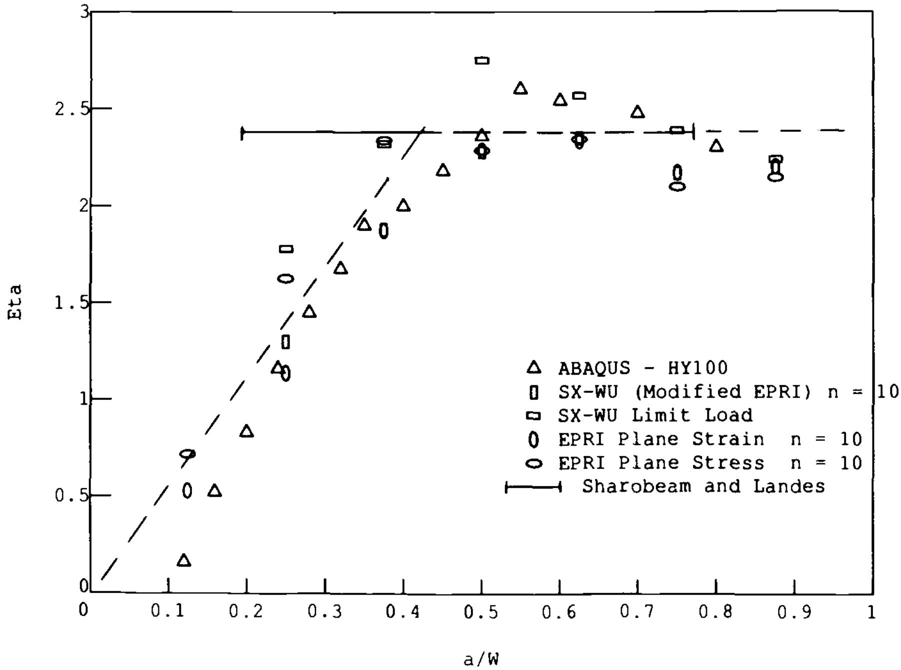

FIG. 4—*Predicted plastic η factors for the SE(T) specimen geometry.*

the Tada Handbook [7] are not necessarily applicable. The standard forms available assume uniform stresses at the loading edges, and the SE(T) configuration used here was not initially thought to be long enough to allow the direct use of equations based on the uniform stress assumption. The finite element analysis described above was used to determine the suitability of the standard compliance equation forms to the SE(T) specimen used here. A comparison of the Tada Handbook compliance equation and the results of the 14 elastic finite element analyses are shown in Fig. 5. Also shown in Fig. 5 is a polynomial fit to the results of the finite element analyses which had the form

$$a/W = 1.012525 - 2.95323u'^1 + 6.68u'^2 - 17.1954u'^3 + 25.3571u'^4 - 12.9747u'^5 \tag{20}$$

$$u' = \frac{1}{1 + \sqrt{\dfrac{E'B\delta}{P}}} \tag{21}$$

For side-grooved specimens, the thickness B is replaced by B_e where

$$B_e = B - \frac{(B - B_n)^2}{B} \tag{22}$$

where B_n is the net specimen thickness at the side groove roots. This substitution is consistent with ASTM E 813 and E 1152.

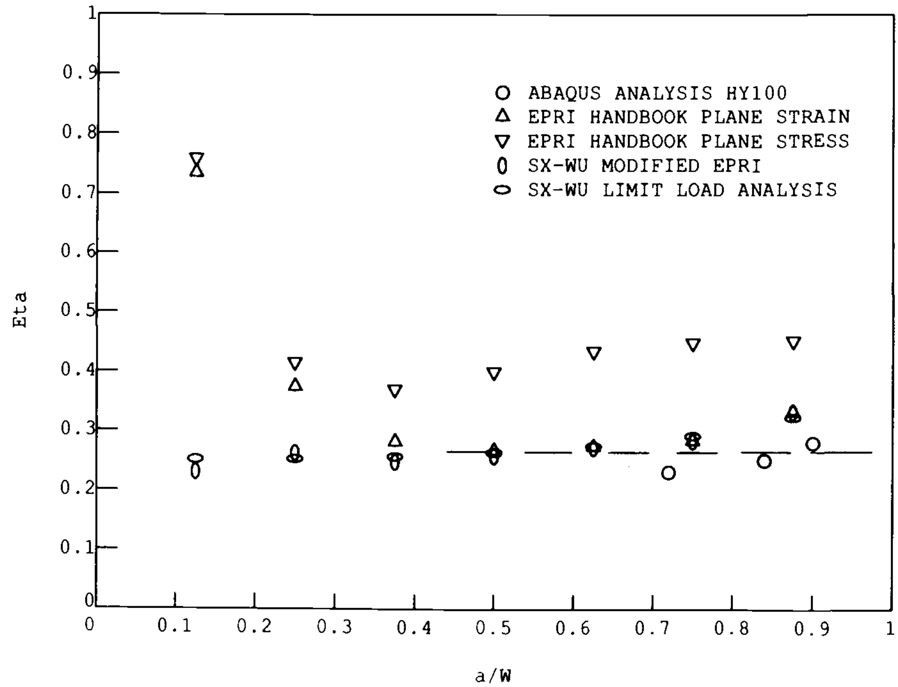

FIG. 5—*Comparison of ABAQUS and handbook compliance results for the SE(T) specimen geometry.*

DE(T) Analysis

For unloading compliance testing of the DE(T) specimens, equations are required for calculation of K, η, and γ as functions of a/W and for a/W as a function of the COD compliance, δ/P. The equations used for this project are presented in the following sections.

DE(T) K *Expression*

The K equation for the DE(T) specimen with a deeply cracked geometry can be taken directly from the Tada Handbook. The equation used has the form

$$K = \sqrt{\pi a}\left[\frac{P}{2WB}\right] F(a/W) \tag{23}$$

with

$$F(a/W) = \frac{\left[1.122 - 0.561\left[\frac{a}{W}\right] + 0.205\left[\frac{a}{W}\right]^2 + 0.471\left[\frac{a}{W}\right]^3 - 0.19\left[\frac{a}{W}\right]^4\right]}{\sqrt{1 - a/W}} \tag{24}$$

This equation should be accurate to $\pm 0.5\%$ for any a/W, but is limited to $a/W > 0.6$ by the pin hole loading. Three ABAQUS two-dimensional finite element grids were developed, which included the specimen dimensions and the pin hole loading and run with $a/W = 0.72$, 0.84, and 0.9, and the results were found to agree within $\pm 2\%$ with the prediction of Eq 24. This agreement is not surprising since the relatively deep notches reduce the effect of the remote loading differences on the resulting stress intensity factor.

DE(T) η and γ Factors

The DE(T) specimen η factor was obtained from both elastic-plastic ABAQUS analysis and from the EPRI Handbook. The η factor used here is taken to relate the J integral at each crack to the *total* plastic work applied to the specimen, i.e.

$$J_{pl} = \frac{\eta A_{pl}}{Bb} \tag{25}$$

where

A_{pl} = plastic area under the specimen load versus plastic load line displacement plot,
b = specimen half remaining ligament,
B = specimen thickness, and
η = plastic η factor.

Analytical work by Shang-Xian Wu et al. [*12*], based on limit load theory, shows that η should be nearly constant for the DE(T) specimen over the a/W range of interest here. A value of approximately 0.27, instead of the usual 2.0, is also predicted in Wu et al. [*12*] with only a very slight dependence on strain hardening. These predictions are confirmed here by both the finite element analysis and the EPRI analysis.

The three deeply notched DE(T) finite element grids described above were run using an ABAQUS elastic-plastic analysis to evaluate the plastic η factors for the $a/W = 0.72, 0.84$, and 0.9 cases. A typical spreadsheet analysis used to obtain the η value is shown in Table 5. The results are shown in Fig. 6 and compared to the results of Wu et al., and the correspondence is clearly excellent.

Use of the EPRI Handbook analysis method gives a equation for the plastic η factor for the DE(T) specimen in the form

$$\eta = \left[\frac{n+1}{n}\right] Bb \left[\frac{h_1}{h_3}\right] \frac{\sigma_0}{P_0} \tag{26}$$

For the plane strain case

$$\frac{\sigma_0}{P_0} = (0.72W + 1.82b)B \tag{27}$$

and

$$\eta = \left[\frac{n+1}{n}\right] \frac{h_1}{h_3} \left[\frac{b/W}{0.72 + 1.82b/W}\right] \tag{28}$$

Again the work of Shang-Xian Wu et al. [*12*] adds a small correction term to this to account for the component of load point displacement of a specimen without a crack, to give

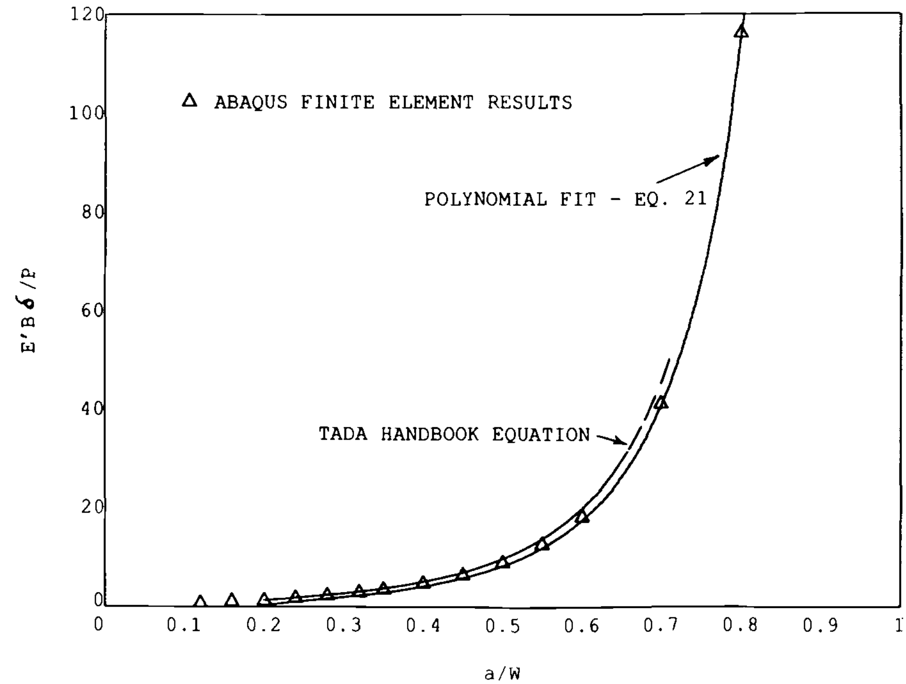

FIG. 6—*Predicted plastic η factors for the DE(T) specimen geometry.*

$$\eta^* = \left[\frac{n+1}{n}\right]\left[\frac{b/W}{0.72 + 1.82b/W}\right]\left[\frac{h_1}{h_3 + h_{30}}\right] \tag{29}$$

with

$$h_{30} = \frac{\sqrt{3}}{b/W}[0.433(0.72 + 1.82b/W)]^n \tag{30}$$

These results are shown in Fig. 6 and compared to the previous results obtained by finite elements.

For the experimental work described below, a constant value of η was used for all tests. DE(T) specimens were restricted to $0.6 \leq a/W \leq 0.9$, and for all tests η was set equal to 0.27 while γ was taken as $(\eta - 1)$ or -0.73. The negative γ did not have a strong effect on these tests because of the small amount of crack extension investigated using the DE(T) specimen.

DE(T) Crack Length Estimation

The DE(T) specimen is tested with a small remaining ligament, generally in the range of $0.6 \leq a/W \leq 0.9$. In this range, the Tada Handbook compliance equation would be very accurate even for the pin-loaded specimen used here. The compliance equation used has the form

TABLE 5—*Spreadsheet for η evaluation—DE(T) specimen.*

		DENT Case DENT1	$a = 1.8$	$W = 3$ $b = 1.2$	$B = 1$	$B_n = 1$	C(COD) 5.62E-08 C(Load Line) 8.55E-08	$f = 0.495$	$E =$ 290E + 07	$Nu = 0.3$		
Load Increment	Load, kips	D_{el}-COD, in.	D_{el}-LP, in.	A_{tot}, in.-lb	A_{el}, in.-lb	A_{pl}, in.-lb	J_{tot}, lb/in.	J_{el}, lb/in.	J_{pl}, lb/in.	N_{tot}	N_{el}	N_{pl}
	0	0	0	0	0	0	0	0	0			
1	120	0.00678	0.0128	768	404.928	363.072	109.7	110.7175	−1.017503	0.171406	0.328110	−0.00336
2	240	0.01378	0.0208	2208	1619.712	588.288	447.6	442.8700	4.7299862	0.243260	0.328110	0.009648
3	282	0.0165	0.0249	3278.1	2236.214	1041.885	643.6	611.4374	32.162587	0.235599	0.328110	0.037043
4	330	0.01934	0.0291	4563.3	3062.268	1501.032	884.7	837.3011	47.398880	0.232647	0.328110	0.037893
5	399	0.0268	0.04	8536.35	4476.732	4059.617	1777	1224.051	552.94880	0.249802	0.328110	0.163448
6	422.4	0.0338	0.0497	12520.14	5017.219	7502.920	2642	1371.834	1270.1658	0.253224	0.328110	0.203147
7	444	0.0452	0.065	19148.1	5543.464	13604.63	4088	1515.722	2572.2773	0.256192	0.328110	0.226888
8	456	0.0516	0.0734	22928.1	5847.160	17080.93	4872	1598.760	3273.2392	0.254988	0.328110	0.229957
9	468	0.059	0.083	27363.3	6158.954	21204.34	5808	1684.013	4123.9867	0.254706	0.328110	0.233385

$$\delta/P = \frac{24a}{E'}\frac{V(a/W)}{WB} \tag{31}$$

with

$$V(a/W) = \left[\frac{1}{u^*}\right] [0.454 \sin(u^*) - 0.065 \sin^3(u^*) - 0.007 \sin^5(u^*) + \cosh^{-1} (\sec(u^*))] \tag{32}$$

where

$$u^* = \frac{\pi a}{2W} \tag{33}$$

This equation must be inverted to be used for unloading compliance. This inversion can be performed in a standard fashion to give a polynomial compliance equation of the form

$$a/W = [0.0955026 - 0.097503v' + 0.245981v'^2 - 0.115274v'^3 + 0.0205763v'^4 - 0.0013593v'^5] \tag{34}$$

with

$$v' = \frac{E'B\delta}{p} \tag{35}$$

Discussion

Accuracy of Crack Extension Estimates

The deeply cracked, side-grooved specimens [SE(B), SE(T), and DE(T)] were accurately tested using unloading compliance. Table 6 shows a comparison of both the predicted initial and final crack lengths and the predicted and estimated crack extensions for these specimens. In the SE(B) case the accuracy is within $\pm 5\%$, while for the SE(T) and DE(T) specimens the accuracy is within $\pm 15\%$. For the shallow-cracked specimens [(SE(B) and SE(T)] nearly the same accuracy was found for both the initial and final crack lengths and for the resulting crack extensions.

The application of unloading compliance to the deeply cracked but not side-grooved specimens does not give accurate final crack lengths. This result has been demonstrated by many authors over the past 15 years. In all cases the unloading compliance method underestimates the measured nine-point average crack extension on the nonside-grooved specimens resulting in elevated *J-R* curves. This effect is more dramatic for the thinner specimens where the degree of crack tunneling is most pronounced. Figure 7 shows photographically the crack tip tunneling that occurred in the 1.25, 2.5, and 5.0 cm specimens when they were tested with and without side grooves.

When crack extensions are inaccurate and crack fronts are uneven the resulting *J-R* curves are incorrect for two reasons. First the incorrect crack extension estimate causes direct error on the *J-R* curve, but also because the two-dimensional *J* integral calculation obtained according to Eqs 1 and 2 is incorrect for the highly irregular three-dimensional crack front geometry.

TABLE 6—*Crack estimation results.*

		Estimated by Compliance			Measured Post Test				
Specimen I.D.	Specimen Type	a_0, mm	a_f, mm	Δa, mm	a_0, mm	a_f, mm	Δa, mm	% Difference	Side Grooves
FYO 1	SE(B)	33.73	37.57	3.84	33.91	37.90	3.99	3.8	Y
FYO 2	SE(B)	33.60	37.36	3.76	34.09	38.33	4.24	11.3	N
FYO 3	SE(B)	33.71	38.43	4.72	33.91	38.66	4.75	0.6	Y
FYO 4	SE(B)	31.72	35.53	3.81	32.46	37.16	4.70	18.9	N
FYO 5	SE(B)	33.60	37.57	3.97	34.14	38.68	4.54	12.6	N
FYO 21	SE(B)	7.06	12.32	5.26	7.16	12.17	5.01	−5.0	Y
FYO 23	SE(B)	6.53	11.76	5.23	6.43	11.45	5.02	−4.2	N
FYO 25	SE(B)	6.63	11.35	4.72	6.65	13.06	6.41	26.3	N
FYO 26	SE(B)	6.71	9.55	2.84	6.65	9.14	2.49	−13.9	Y
FYO 27	SE(B)	6.78	11.46	4.68	6.88	11.86	4.98	4.0	Y
FYO 150	SE(B)	31.04	33.76	2.72	31.01	33.68	2.67	−1.9	Y
FYO 151	SE(B)	31.22	33.91	2.69	31.29	33.83	2.54	−5.8	Y
FYO 153	SE(B)	30.91	33.53	2.62	31.19	34.77	3.58	26.9	N
FYO 154	SE(B)	31.01	33.58	2.57	31.39	34.72	3.33	22.9	N
FYO 155	SE(B)	30.63	33.12	2.49	30.68	34.49	3.81	34.5	N
FYO 157	SE(B)	30.73	33.25	2.52	30.68	34.39	3.71	32.1	N
FYO 158	SE(B)	30.81	33.48	2.67	31.04	33.45	2.41	−10.7	Y
FYO 159	SE(B)	31.45	34.11	2.66	31.93	34.95	3.02	11.9	Y
FYO 160	SE(B)	5.66	10.64	4.98	6.03	11.02	4.99	0.2	Y
FYO 161	SE(B)	5.38	10.24	4.85	5.66	10.31	4.65	4.1	Y
FYO 162	SE(B)	5.59	9.60	4.01	5.83	10.68	4.86	−21.2	N
FYO 2SB	SE(T)	25.4	30.15	4.75	25.43	...[a]	...	...	Y
FYO 3SB	SE(T)	29.87	33.12	3.25	29.44	33.20	3.76	−15.7	Y
FYO 4SA	SE(T)	40.49	49.78	9.29	41.09	51.32	10.20	−10.1	Y
FYO 10SA	SE(T)	21.31	24.41	3.10	21.27	...[a]	...	...	Y
FYO 11SB	DE(T)	21.65	24.48	1.83[b]	21.2	22.8	1.607	−12.2	Y
					20.5	22.3	1.802	−1.5	
FYO 12SA	DE(T)	25.0	26.65	1.65[b]	26.1	27.3	1.15[c]	−30.3	Y

[a] Test terminated by ductile tearing instability.
[b] Average growth on each side.
[c] Only one side exposed by posttest cold cleavage.

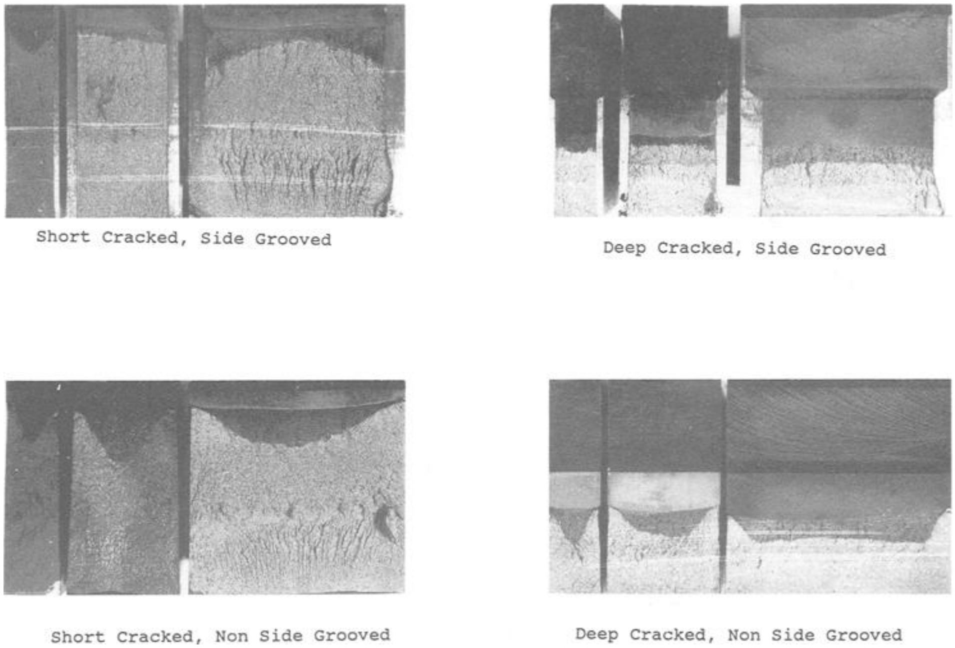

FIG. 7—*Photographs showing the heat tint zones for short and deep cracked SE(B) specimens.*

SE(B) Results

Comparison of η's for J *Calculation*—As described above, the short crack SE(B) specimens require distinctly different η and γ factors from the standard values of 2.0 and 1.0 used by the deep cracked specimens of standard fracture toughness methods like E 813 and E 1152. It was of interest here to evaluate how large a correction was involved in the use of the short crack η and γ factors for the short crack SE(B) specimens tested here. Figure 8 shows a comparison of the standard deep crack J analysis and the Sumpter [*10*] modified analysis for one of the short-cracked 20% side-grooved specimens. Clearly little effect of the changed η factor analysis is demonstrated on the resulting J-R curve. This is somewhat surprising initially since the η factor is reduced by about 80%, and the γ factor is dramatically changed from 1.0 to ≈ -4.5. A little investigation showed, however, that it is correct. Basically, for the short-cracked specimen, the elastic J component is providing the largest part of the J calculation, and this component is not affected by the η and γ factors. As the crack grows, the effects of the plastic J component increase, but the η factor effect is now largely canceled by the crack growth γ factor effect, and little change results on the J-R curve. This same result was previously reported by Joyce [*6*] for somewhat longer SE(B) test results of another steel alloy. In all results below, the Sumpter [*10*] short crack analysis is used for the short crack specimens.

Comparison of Short Crack and Deep Crack SE(B) Results—The data presented in Fig. 9 is taken by the authors as the baseline data for all comparisons made in the following sections. These data are the deep-cracked, side-grooved results from specimens of thickness from 1.25 to 5.0 cm. As shown in Fig. 9, these data form a tight band of results, and these results will

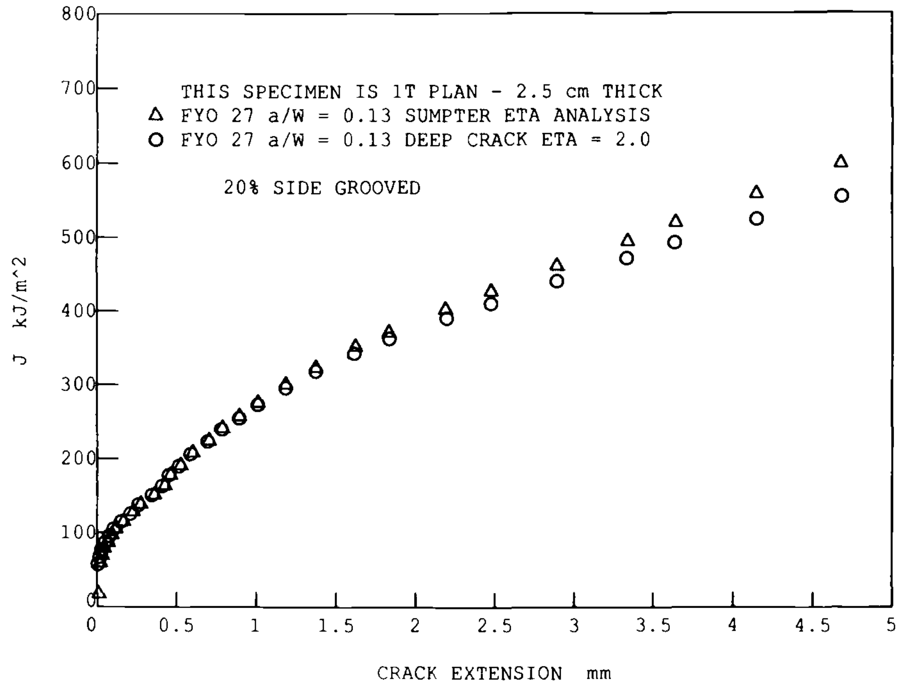

FIG. 8—*Comparison of an application of the Sumpter η analysis and the standard deep crack η factor analysis for a short-cracked three-point bend specimen.*

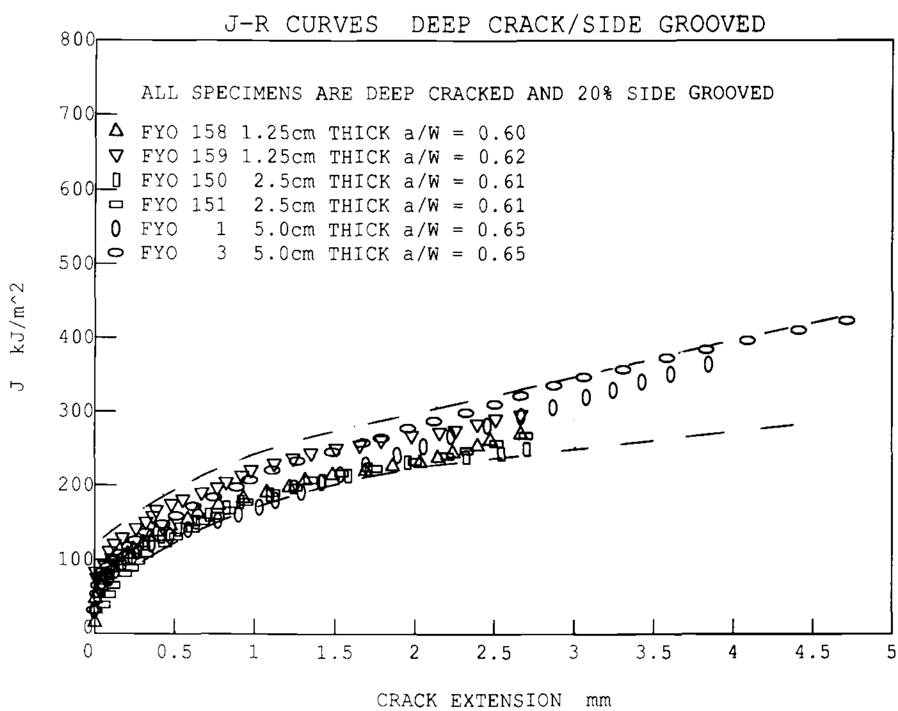

FIG. 9—*Baseline* J-R *curves for the structural steel alloy obtained from side-grooved, deep-cracked, single edge-notched, bend specimens.*

generally form the lower bound of short crack SE(B), SE(T), and DE(T) specimen results that are discussed below. The dashed lines on Fig. 9 will be carried to later figures for comparison.

Results for the short crack specimens tested here are shown in Fig. 10 and compared to the band of baseline data. The bifurcation shown in this data set is not fully understood but is thought to correspond to a failure of the side grooves in two of these specimens to keep the crack growing uniformly across the thickness. The two specimens that demonstrate the increased fracture toughness are two of the thickest specimens, and it appears that the short crack has acted here to release the side groove effect, allowing uneven crack advance and hence apparently higher fracture toughnesses in these specimens. Whatever the case, however, no fracture toughness increase is present in these specimens near crack initiation, and beyond initiation the fracture toughness increase due to the short cracks is limited at best. Figure 11 shows a comparison of the deep-cracked, nonside-grooved results with the baseline data band. Here the nonside-grooved data are initially very similar to the side-grooved results, but as the crack tunneling develops, rather striking deviations from the baseline data set occur. This deviation occurs first for the thin specimens which tunnel most dramatically, though all specimens are shown to run high compared to the baseline data as crack extension continues. A very distinct increase in fracture toughness is shown by the short crack, nonside-grooved results of Fig. 12. As discussed above, some of the apparent fracture toughness elevation is due to inaccuracy of the unloading compliance crack length estimate, but even at crack initiation the fracture toughness is dramatically increased in these specimens.

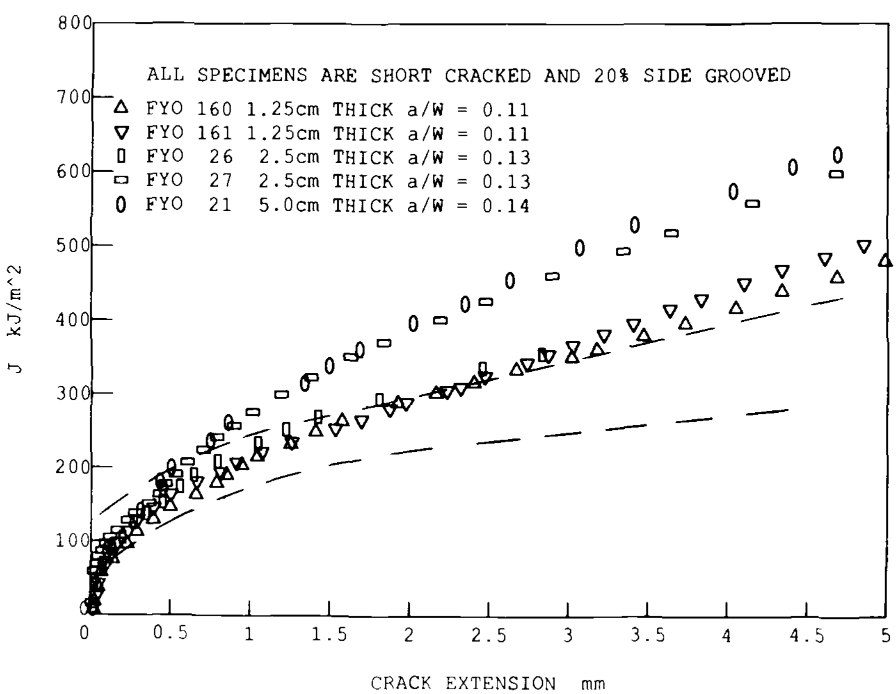

FIG. 10—*Comparison of the baseline* J-R *curve data and data from short-cracked, side-grooved specimens of three thicknesses.*

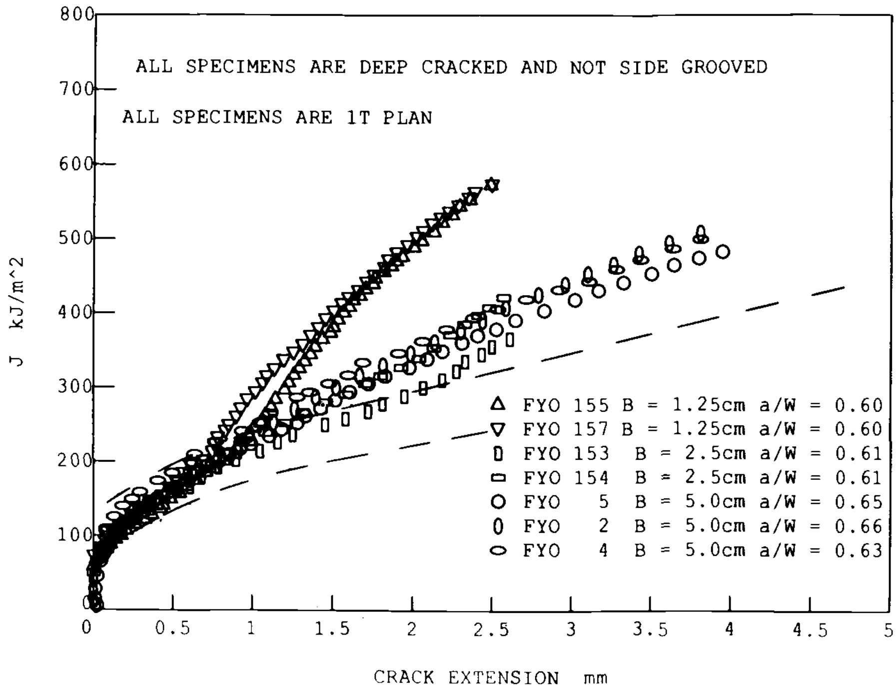

FIG. 11—*Comparison of nonside-grooved, deep-cracked bend specimen data to the baseline* J-R *curve data.*

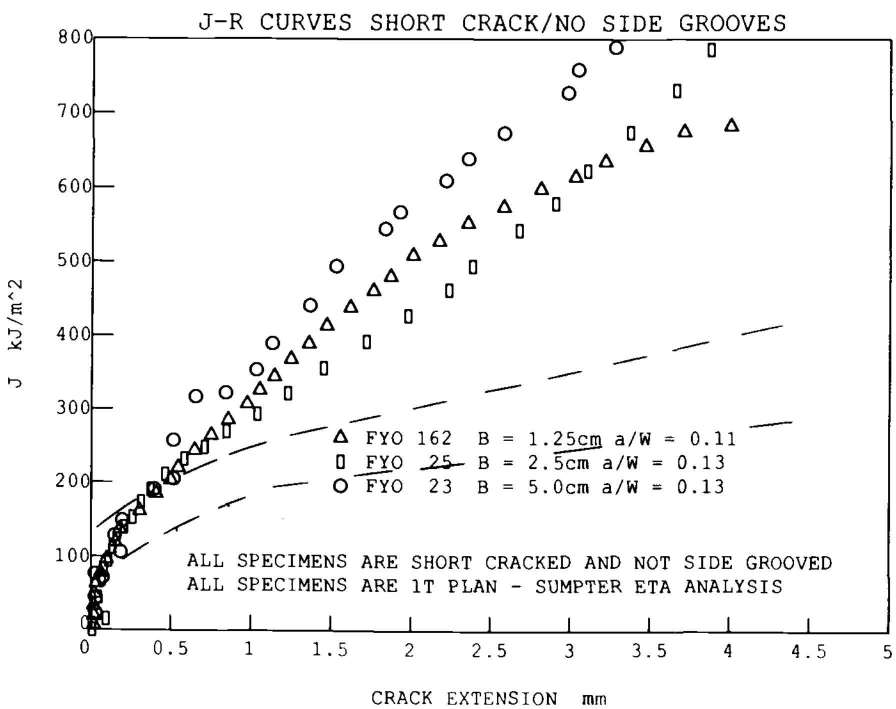

FIG. 12—*Comparison of nonside-grooved, short-cracked, bend specimen data to the baseline* J-R *curve data.*

SE(T) Results

J-R curves from four SE(T) specimens with different crack length ratios are shown in Fig. 13 and compared to the baseline band. These four SE(T) specimens were all 20% side-grooved and appear to have given reasonably accurate crack length estimates during testing by unloading compliance. The measured crack extensions were somewhat larger than the unloading compliance estimates as shown in Table 6, but this small error would not greatly modify the results shown in Fig. 13. Clearly the SE(T) geometry demonstrates an elevated toughness behavior in comparison with the deep-cracked SE(B) baseline data band at crack initiation and throughout the ductile crack growth region. This result has been inferred by large-scale tests of pressurized and thermally shocked cylinders [*14,15*], but has not previously been demonstrated by simple geometry, laboratory-scale specimens.

A rather surprising result demonstrated by Fig. 13 is that the crack length appears to have so little effect on the measured *J-R* curves. It was felt that increasing the a/W ratio from 0.35 to 0.65 would result in a dramatic drop of the resulting *J-R* curve toward the baseline SE(B) results. A small effect is shown by the data, but not the large reduction that was expected as the loading was changed from predominantly tensile to a mixture of tension and bending. This is apparently a result of the pin hole loading which allows the specimen halves to rotate so that the load line is nearly centered over the remaining ligament, providing a predominantly tensile loading even in the case of the deeply cracked geometry.

DE(T) Results

J-R curves from two DE(T) specimens are shown on Fig. 14 and compared with the baseline deep crack SE(B) data. These specimens are fully tensile in mode of loading, but have a high level of constraint, at least if the fully plastic slip line field is considered. The resulting *J-R* curves clearly correspond very well to the deep crack SE(B) baseline data. These results are clearly demonstrating that the mode of loading is not the dominant factor elevating the apparent fracture toughness for the SE(T) specimens of the previous section, but rather some more complex measure of crack tip "constraint" is truly required.

The maximum net section stress demonstrated by these specimens was approximately 1400 MPa, which is approximately 1.5 times the material's ultimate strength. This compares with a factor of about 2.97 predicted by Hill [*16*] from a limit load analysis for fully plastic plane strain material behavior.

Overall Comparison of Results

Figure 15 shows a comparison of some of the side-grooved SE(B), SE(T), and DE(T) specimen *J-R* curves developed in this program. Initially the DE(T) specimens compare well with the SE(B) specimen results, but later they start to become elevated, apparently as the side grooves start to fail to control the crack front straightness. As discussed above, increasing the crack lengths of the SE(T) specimens seems ineffective in lowering the resulting *J-R* curves toward the SE(B) baseline data; on the other hand, very short-cracked SE(B) specimens do not become elevated in fracture toughness, i.e., they do not start to act like the SE(T) specimens.

Conclusions

The work described above leads to the following conclusions:

1. Unloading compliance methods can be used to develop *J-R* curves from nonstandard specimens of varied constraint. In this study, short crack single edge-notched bend spec-

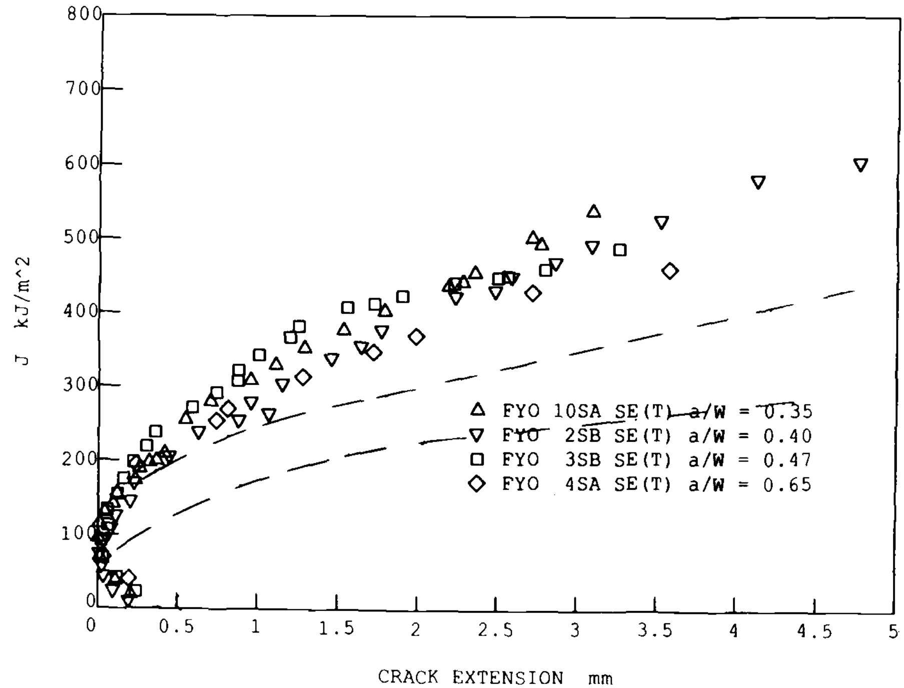

FIG. 13—*Comparison of SE(T) specimen data of four* a/W *ratios to the baseline* J-R *curve data.*

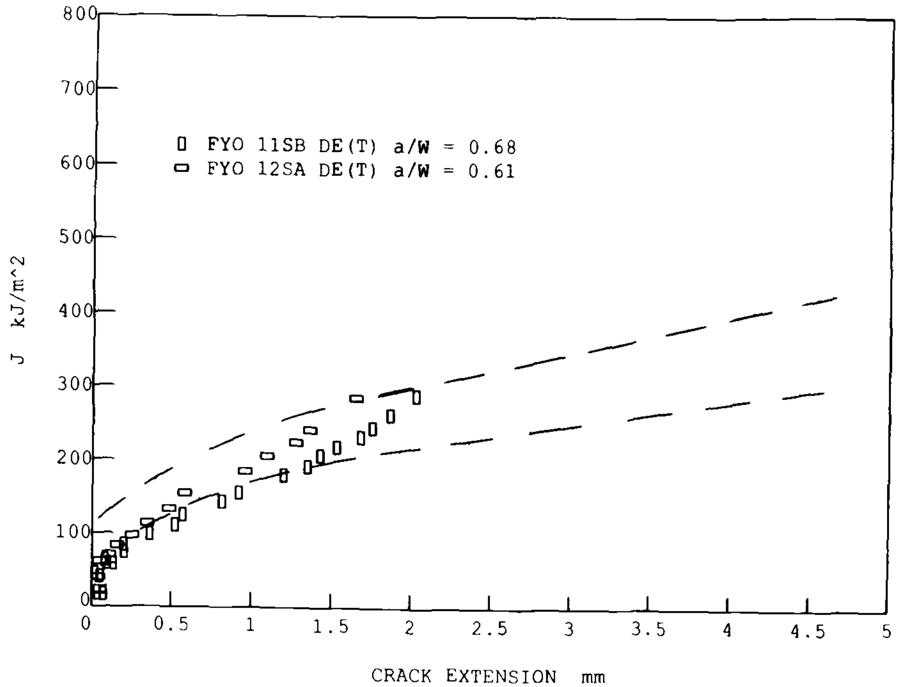

FIG. 14—*Comparison of DE(T) specimens data of two* a/W *ratios to the baseline* J-R *curve data.*

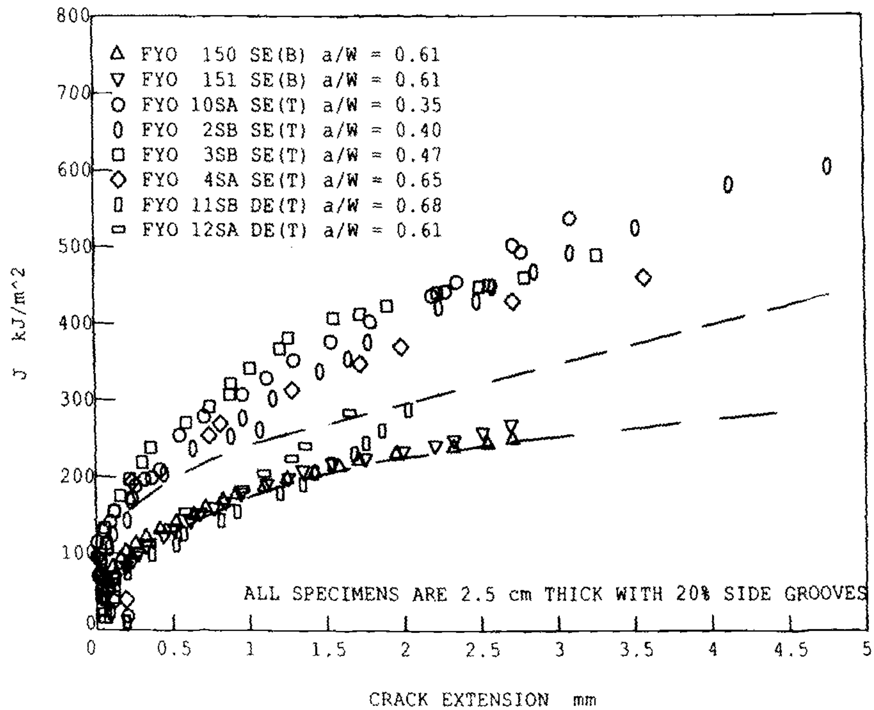

FIG. 15—*Comparison of SE(B), SE(T), and DE(T)* J-R *curves with various crack lengths. All specimens are 2. 5 cm thick with 20% side grooves.*

imens were tested successfully as well as single edge-notched tension specimens and double edge-notched tension specimens. Adequate compliance, the stress intensity factor, and η equations were developed using two-dimensional finite element results or obtained from the literature.

2. When deep and short-cracked SE(B) specimens are side grooved, the apparent fracture toughness of short-cracked SE(B) ($a/W \approx 0.12$) was only slightly higher than that of standard deep-cracked specimens.
3. The initiation fracture toughness of nonside-grooved SE(B) specimens is not measurably higher than the initiation fracture toughness of side-grooved specimens for this material when both sets of specimens are deeply cracked. As the nonside-grooved specimens develop tunneled crack fronts, the apparent fracture toughness increases, i.e., the *J-R* curve becomes elevated in comparison with the side-grooved results.
4. Nonside-grooved, short-cracked SE(B) specimens act in a much tougher fashion than side-grooved deep-cracked specimens, both at crack initiation and throughout the *R* curve.
5. Single edge cracked, side-grooved, tensilely loaded SE(T) specimens demonstrated dramatically increased fracture toughness in comparison with standard deep-crack bend specimens. This was true at crack initiation and during subsequent crack growth.
6. Single edge crack, side-grooved, tensile SE(T) specimens were not very sensitive to the crack length ratio over the range $0.3 \leq a/W \leq 0.65$. The deeper cracked specimens were slightly less tough than the shorter crack specimens, but remained much tougher than the baseline SE(B) *R* curves.

7. The side-grooved, single edge-notched tensile SE(T) specimens were consequently much tougher than the side-grooved short-crack bend specimens.
8. The side-grooved, double edge-cracked, tensile DE(T) specimens were identical in fracture toughness to the baseline, deeply cracked, side-grooved bend specimens. This appeared true at both initiation and for some initial crack extension. For larger amounts of crack growth, i.e., $\gtrsim 1.5$ mm the double edge-cracked bar started to demonstrate elevated fracture toughness. This is thought to be due to a failure of the side grooves to control the crack straightness.
9. An important final conclusion is that a variation in constraint can be developed in laboratory scale specimens, and these data should be useful in evaluating newly developed, analytical, constraint factors.

References

[*1*] Betegon, C. and Hancock, J. W. , "Two Parameter Characterization of Elastic-Plastic Crack Tip Fields," to appear in *Journal of Applied Mechanics*, 1991.

[*2*] Al-Ani and Hancock, J. W., "J-Dominance of Short Cracks in Tension and Bending, Department of Mechanical Engineering, University of Glasgow, Glasgow, Scotland, 1990.

[*3*] O'Dowd, N. P. and Shih, C. F., "Family of Crack-Tip Fields Characterized by a Triaxiality Parameter: Part I—Structure of Fields," Division of Engineering Report, Brown University, Providence, RI, June 1990.

[*4*] Dodds, R. H., Jr. and Anderson, Ted L., "Numerical Correlation of Size Effects on Elastic-Plastic Fracture Toughness (J_c) in SE(B) Specimens," UILU-ENG-90-2002, Department of Civil Engineering, University of Illinois, Champaign, IL, January 1990.

[*5*] Anderson, T. L. and Dodds, R. H., Jr., "Specimen Size Requirements for Fracture Testing in the Transition Region," MM-6586-90-5, Mechanics and Materials Center, Texas A & M University, College Station, TX, May 1990.

[*6*] Joyce, J. A., "J Resistance Curve Testing of Short Crack Bend Specimens Using Unloading Compliance," presented at the 22nd National Symposium on Fracture, Atlanta, GA, 19–21 June 1990.

[*7*] Tada, H., Paris, P. C., and Irwin, G. R., "The Stress Analysis of Cracks Handbook," Paris Productions, Inc., St. Louis, MO, 1985.

[*8*] Kapp, J. A., Leger, G. S., and Gross, B., "Wide-Range Displacement Expressions for Standard Fracture Mechanics Specimens," *Fracture Mechanics: 13th Conference, ASTM STP 743*, American Society for Testing and Materials, Philadelphia, 1981, pp. 476–502.

[*9*] Haigh, J. R. and Richards, C. E., "Yield Point Loads and Compliance Functions of Fracture Mechanics Specimens," CEGB Report RD/L/M461, Central Electricity Generating Board, Aisley, UK, 1974.

[*10*] Sumpter, J. D. G., "J_c Determination for Shallow Notch Welded Bend Specimens," *Fatigue and Fracture of Engineering Materials and Structures*, Vol. 10, No. 6, 1987, pp. 479–493.

[*11*] Kumar, V., German, M. D., and Shih, C. F., "An Engineering Approach for Fracture Analysis," Electric Research Power Institute, Palo Alto, CA, 1981.

[*12*] Wu, S.-X., Mai, Y.-W., and Cotterell, B., "Plastic η-Factor Specimens with Deep and Shallow Cracks," *International Journal of Fracture*, Vol. 45, 1990, pp. 1–18.

[*13*] Sharobeam, M. H., Landes, J. D., and Herrera, R., "Development of Eta Factors in Elastic-Plastic Fracture Testing Using a Load Separation Technique," Elastic-Plastic Fracture Test Methods, Second Volume: The User's Experience, ASTM STP 1114, American Society for Testing and Materials, Philadelphia, 1991, pp. 114–132.

[*14*] Sievers, J., "Ductile Fracture Mechanical Analysis of Thermal Shock Experiments," *Proceedings*, 9th Structural Mechanics in Reactor Technology (SMIRT) Conference, Vol. G, 1987, pp. 361–368.

[*15*] Bryan, R. H., et al., "Pressurized Thermal Shock Test of 6 in. Thick Pressure Vessels: PTSE-2: Investigation of Low Tearing Resistance and Warm Prestressing," NUREG-CR-4888, U.S. Nuclear Regulatory Commission, Washington, DC.

[*16*] Hill, R., *The Mathematical Theory of Plasticity*, Oxford University Press, London, 1950.

Kim Wallin[1]

Statistical Aspects of Constraint with Emphasis on Testing and Analysis of Laboratory Specimens in the Transition Region

REFERENCE: Wallin, K., "**Statistical Aspects of Constraint with Emphasis on Testing and Analysis of Laboratory Specimens in the Transition Region,**" *Constraint Effects in Fracture, ASTM STP 1171,* E. M. Hackett, K.-H. Schwalbe, and R. H. Dodds, Eds., American Society for Testing and Materials, Philadelphia, 1993, pp. 264–288.

ABSTRACT: The effect of specimen thickness, side grooving, large-scale yielding of the ligament, and ductile tearing upon the probability of cleavage fracture initiation is examined within the framework of a general statistical model for cleavage fracture initiation. First, a derivation of the statistical model is presented, and then the model is used to explain the effects of different factors affecting the cleavage fracture probability. As a result, a specimen size requirement for elastic-plastic cleavage fracture toughness testing with bend-type specimens is obtained. Additionally, a simple correction function to validate invalid test results with insufficient ligament size and prior ductile tearing is presented.

KEY WORDS: cleavage fracture initiation, constraint, statistical modelling, fracture toughness testing, transition region

Fracture toughness testing in the ductile-brittle transition region has been problematic for a long time. In this temperature region both the K_{Ic} and J_{Ic} standards are inapplicable. Only crack tip opening displacement (CTOD) standards cover the transition region. However, these do not treat testing in the transition region any differently than in the fully brittle or ductile regimes.

Earlier, when having to rely on linear-elastic fracture mechanics, testing in the transition regime was difficult mainly due to plasticity effects. The evolution of the elastic-plastic fracture mechanics theory made it possible to reduce this problem. Unfortunately, another problem appeared, that is, it was found that the scatter in the measured fracture toughness grew very large in the transition region. Often some amount of ductile tearing was found to precede brittle fracture. The amount of the ductile tearing was not constant but showed a similar scatter as the fracture toughness. The question arose as to why the scatter grew large and what was the role of ductile tearing in the fracture process.

First, it was attempted to explain the findings based solely on constraint effects. It was proposed that ductile tearing somehow increased the stress levels ahead of the crack, thus causing the fracture mode to change into cleavage. The scatter would then be due to differences in the material's resistance to ductile fracture. Later, an explanation, based on weakest link statistics, for the behavior of fracture toughness in the transition region was presented. According to this

[1] Senior advisor, Technical Research Center of Finland (VTT), Metals Laboratory, P.O. Box 26 (Kemistintie 3), SF-02151 Espoo, Finland.

explanation, the effect of ductile tearing would be one of increasing the sampling volume, thus increasing the fracture probability. In reality, both the statistical effect as well as the constraint effect are acting simultaneously.

In this paper the effect of constraint on cleavage fracture toughness in the elastic-plastic regime is examined. The constraint effect is combined with statistical cleavage fracture theory so that the effect of prior ductile tearing is included. As a result, a specimen size requirement for elastic-plastic cleavage fracture toughness testing with bend-type specimens is obtained. Additionally, a simple correction function to validate invalid test results with insufficient ligament size and prior ductile tearing is presented.

Theory

To be able to examine the effect of constraint, first the derivation of the statistical model must be performed. The model is very general and makes no assumptions regarding what the cleavage fracture initiators are. The model is derived in the following.

General Statistical Model for Cleavage Fracture Initiation

The basis of the statistical model is as follows [1]. It is assumed that the material in front of the crack contains a distribution of possible cleavage fracture initiation sites, that is, cleavage initiators. The cumulative probability distribution for a single initiator being critical can be expressed as $P(\xi \geq \xi_c)$, where ξ describes the level of severity of the controlling feature of the initiators and ξ_c is the critical value. $P(\xi \geq \xi_c)$ is a complex function of the initiator size distribution, stress, strain, grain size, temperature, stress, strain rate, and so on. The shape and origin of the initiator distribution is not important in the case of a "sharp" crack. The only necessary assumption is no global interaction between initiators. This means that interactions on a local scale are permitted. Thus, a cluster of cleavage initiations may be required for macroscopic initiation. In such a case the cluster forms the critical initiator and can be treated as a single event. Also, the assumption does not cause any restrictions on whether initiation or propagation is most critical. All the above factors can be implemented into the initiator distribution, and they are not significant as long as no attempt is made to determine the shape of the distribution. Only if an additional, conditional crack arrest criterion is assumed is the treatment affected.

The cumulative failure probability of a volume element, with a uniform stress state, can be expressed as

$$P_f = 1 - [1 - P(\xi \geq \xi_c)]^{N_v \cdot V} \tag{1}$$

where N_v is the number of initiators in unit volume and V is the volume of the element.

Equation 1 can also be rewritten as

$$P_f = 1 - \exp\{V \cdot \ln[1 - P(\xi \geq \xi_c)]^{N_v}\} \tag{2}$$

In the case of several independent homogeneous volume elements, with size V_i having different states of stress, the total cumulative failure probability becomes

$$P_f = 1 - \exp \sum_{i=1}^{n} V_i \cdot \ln[1 - P_i(\xi \geq \xi_{ci})]^{N_v} \tag{3}$$

where n is the number of volume elements.

Equation 3 needs one restricting assumption, that is, that the volume elements are homogeneous so that the number of initiators in a volume element is defined as: $N = N_v \cdot V$. In reality the initiators are randomly distributed, which causes N to be not constant but Poisson distributed [2]. If we mark the mean number of initiators with $\overline{N}$, the probability P_N of having N initiators in a volume element is

$$P_N = \frac{\overline{N}^N \cdot \exp(-\overline{N})}{N!} \tag{4}$$

The probability of initiation in one volume element becomes

$$P_f = 1 - \sum_{N=0}^{\infty} [1 - P(\xi \geq \xi_c)]^N \cdot P_N \tag{5}$$

Performing the summation one obtains

$$P_f = 1 - \exp\{\overline{N} \cdot [1 - P(\xi \geq \xi_c)]\} \cdot \exp(-\overline{N}) \tag{6}$$

which reduces to

$$P_f = 1 - \exp\{-\overline{N} \cdot P(\xi \geq \xi_c)\} \tag{7}$$

Thus, the form of Equation 3, when assuming randomly distributed initiators, is

$$P_f = 1 - \exp \sum_{i=1}^{n} \{-\overline{N}_v \cdot V_i \cdot P_i(\xi \geq \xi_{ci})\} \tag{8}$$

where $\overline{N}_v$ is the mean number of initiators per unit volume.

If the probability of an initiator being critical is smaller than 0.1, Eqs 3 and 8 are practically identical. Because the probability of an initiator being critical is usually much smaller than 0.1, it is arbitrary which form to use. Otherwise, the above expressions contain no approximations.

For a "sharp" crack in small-scale yielding, the stresses and strains are described by the Hutchinson-Rice-Rosengren (HRR) field [3,4]. One property of the HRR field is that the stresses have an angular dependence. Thus, the stress field can be divided into small fan-like elements with an angle increment $\Delta\theta$. In this case the cumulative failure probability becomes

$$P_f = 1 - \exp \sum_{\theta=0}^{2\pi} \left\{ \sum_{x=0}^{x_p} - \overline{N}_v \cdot B \cdot \Delta x \cdot x \cdot \sin(\Delta\theta) \cdot P(\xi \geq \xi_c) \right\} \tag{9}$$

where B is the thickness of the element, x is the distance from the crack tip, and x_p marks the extent of the plastic zone in direction θ. The volume element, defined by $B \cdot \Delta x \cdot x \cdot \sin [\Delta\theta]$, must be clearly larger than the initiator size. The double summation indicates that the summation is performed over the whole plastic zone.

Due to the properties of the HRR field, it is possible to normalize the distance with the stress intensity factor

$$U = \frac{x}{(K_I/\sigma_y)^2} \tag{10}$$

When Eq 10 is inserted into Eq 9 the cumulative failure probability becomes

$$P_f = 1 - \exp\left\{B \cdot \sin(\Delta\theta) \cdot \frac{K_I^4}{\sigma_y^4} \cdot \sum_{\theta=0}^{2\pi}\left(\sum_{U=0}^{U_p} - \overline{N}_v \cdot U \cdot \Delta U \cdot P(\xi \geq \xi_c)\right)\right\} \tag{11}$$

The result of the double summation is always negative and independent of K_I. This enables us to write

$$P_f = 1 - \exp[-\text{const.} \cdot B \cdot K_I^4] \tag{12}$$

It is seen that the scatter of fracture toughness is really independent of the cleavage initiator distribution. The result contains no approximations. The only assumption is that the initiators are independent on a global scale. In other words, it is assumed that the volume elements are independent for a constant K_I. Only, if it is assumed that a certain fraction of the crack front must experience critical initiations to cause macroscopic failure, then the result will differ from Eq 12. In the derivation, the cleavage fracture process zone was assumed to be equal to the plastic zone. Equation 12 is, however, not sensitive to the definition of the process zone as long as it is assumed that the process zone size correlates with K_I, CTOD, or J. It is interesting to note that Eq 12 is identical to the Weibull distribution function with a fixed value for the shape parameter. The result is not, however, related to Weibull statistics in any way but to assume a weakest link-type failure mechanism.

Equation 12 would imply that an infinitesimal K_I value might lead to a finite failure probability. This is not true in reality. For very small K_I values the demand for Δx to be clearly larger than the initiator size is violated. Also, for very small K_I values the stress gradient becomes so steep that even if cleavage fracture can initiate it will almost immediately arrest, thus causing a stable type of fracture. This is an effect often seen with ceramics. Finally, the prefatiguing process causes a warm prestress effect. All these factors lead to a lower limiting K_{min} value below which cleavage fracture is impossible. It is not clear which of the factors are dominant for K_{min}, but for steels in the ductile-to-brittle transition region it seems likely to be the microscopic crack arrest effect.

The addition of K_{min} into Eq 12 is problematic. At first glance it would seem natural to write the equation as

$$P_f = 1 - \exp[-\text{const.} \cdot B \cdot (K_I^4 - K_{min}^4)] \tag{13}$$

This form does not, however, describe the true fracture behavior quite correctly. The stress distributions at different K_I levels are overlapping, and this will cause the effect of K_{min} to be more complicated. Actually, it does not seem possible to come up with a simple closed form exact solution for the effect of K_{min}, but is has been proposed [5] that the effect can well be approximated by the form

$$P_f = 1 - \exp[-\text{const.} \cdot B \cdot (K_I - K_{min})^4] \tag{14}$$

This approximate expression has later also been suggested by Stienstra [6] based on modelling of the microscopic crack arrest effect.

Allowing for K_{min} the equation describing the fracture toughness scatter can thus be written as

$$P_f = 1 - \exp\left[-\frac{B}{B_0} \cdot \left\{\frac{K_I - K_{min}}{K_0 - K_{min}}\right\}^4\right] \tag{15}$$

In Eq 15, B_0 and K_0 are normalization constants. The normalization thickness B_0 can be made equal to any desired reference thickness. The scale parameter K_0 corresponds to a 63.2% fracture probability, for thickness B_0, and is approximately given by $K_0 = 1.1 \cdot K_{mean}$.

Determination of K_{min}

The determination of K_{min} is problematic. Practically the only way to estimate it is based on statistical analysis of experimental K_{IC} data. There exist a number of possible estimation algorithms, for example, maximum likelihood, least squares, moments, and GLUEs (good linear unbiased estimator). Unfortunately, all the algorithms are to varying degrees biased and have different accuracies. The two types of algorithms best suited to analyze an expression such as Eq 15 are maximum likelihood and least squares. Out of these, the estimate based on maximum likelihood is less scattered but is on the other hand strongly biased to higher values. It is possible to make a bias correction on the maximum likelihood estimate with the equation

$$K_{min} \approx (N \cdot \hat{K}_{min} - \hat{K}_0)/(N - 1) \tag{16}$$

where $\hat{K}$ is the estimated value and N is the number of tests. Unfortunately, the bias correction of the maximum likelihood estimate of K_{min} makes it much more scattered so that it is no better than least square algorithms.

Linear test square algorithms are the simplest to use, and they are also well-suited for censored data sets where only part of the data is used in the analysis. In order to use least squares one must determine the cumulative probabilities that correspond to the rank-ordered fracture toughness data. There exist several different equations for approximating the median rank probability, all being of the type

$$P = (i - C)/(N + 1 - 2 \cdot C) \tag{17}$$

where i is the rank number, N is the total number of tests, and C is a constant in the range $0 \leq C < 1$. The most accurate description of the median rank probability is obtained with $C = 0.3$, but unfortunately this value is not ideal for the estimation of K_{min}. A better value of a has been found to be 0.5, which when used with Eq 15 in the linearized form

$$\{-\ln(1 - P)\}^{0.25} = (\hat{K}_0 - \hat{K}_{min})^{-1} \cdot K_{IC} - \hat{K}_{min}/(\hat{K}_0 - \hat{K}_{min}) \tag{18}$$

yields an only slightly biased estimate of $\hat{K}_{min}$ and practically an unbiased estimate of $\hat{K}_0$. An approximate bias correction for $\hat{K}_{min}$ is of the form

$$K_{min} \approx (\hat{K}_{min} - 0.3 \cdot [N - 1]^{-2} \cdot \hat{K}_0)/(1 - 0.3 \cdot [N - 1]^{-2}) \tag{19}$$

It should be pointed out that the least square analysis must be performed in the form described by Eq 18. If the equation is turned around, the result is unreliable and considerably biased.

Even the bias corrected estimate of K_{min} is not very accurate. The lower 5% confidence limit of K_{min} can, for $N > 2$, be approximated by

$$K_{min}^{5\%} \approx K_{min} - (K_0 - K_{min}) \cdot 1.22/\sqrt{N - 1} \tag{20a}$$

and the upper 95% confidence limit, for $N > 2$, by

$$K_{min}^{95\%} \approx K_{min} + (K_0 - K_{min}) \cdot 1.05/\sqrt{N - 1} \tag{20b}$$

Equations 20a and b show that even with 50 specimens one can achieve only roughly a 15% accuracy with respect to $K_0 - K_{min}$. This means that an experimental determination of K_{min} is possible only when K_{min} is very close to K_0. This is by no means the case in the ductile-to-brittle transition region, and therefore an experimental determination of K_{min} in the transition region is practically impossible. Because of this it is better to assume K_{min} to be some constant value that is likely to be on the conservative side. Based on a large number of analyses, it has been proposed that a value of $K_{min} = 20$ MPa$\sqrt{m}$ might be used for ferritic steels [5].

Large-Scale Yielding of the Ligament

The above treatment is valid only for small-scale yielding situations where J or K_I describe the stress distribution unconditionally. In cases of large-scale yielding of the ligament, the treatment becomes more complex [7].

Brittle cleavage fracture is a critical stress-controlled local fracture process. The possible cleavage fracture initiators are randomly distributed, and this causes cleavage fracture to be a statistical event. A prerequisite for cleavage fracture is local plasticity at the site of fracture initiation. Therefore, the process zone for cleavage fracture must be smaller than or equal to the plastic zone size. Because cleavage fracture is stress controlled and because the HRR field predicts a stress maximum, the probability of cleavage fracture initiation is largest close to this stress maximum. Statistical modelling indicates that with a 95% probability, cleavage fracture will initiate closer to the crack tip than approximately three to five times the distance from the crack tip to the stress maximum. This can be taken as an effective process zone for cleavage fracture initiation. Outside this region, cleavage fracture is still in theory possible within the plastic zone, but the probability of fracture as compared to the fracture probability closer to the stress maximum is essentially negligible.

The J-integral or K_J describes cleavage fracture initiation as long as it describes the stresses within the process zone with an adequate accuracy. McMeeking and Parks [8] showed with their FEM calculations that, at increasing J-levels, the stresses start to deviate from the small-scale yielding calculations. They plotted their results in the form of the normalized distance $x/(J/\sigma_0)$ to be able to make the comparison with the small-scale yielding results. With increasing J the stresses deviated from the small-scale yielding results at smaller values of normalized distance. When the process zone is defined with the normalized distance, it is possible to determine the ligament size and J-level at which the stresses no longer describe the process zone correctly. Based on the McMeeking Parks results, Wallin [7] has deduced that the size restriction $b \geq \alpha \cdot (J/\sigma_f)$ might be $b \geq 50 \cdot (J/\sigma_f)$. It should be pointed out that the size restriction for cleavage is not the same as the standard size restriction for ductile fracture ($\alpha \approx 25$) because the fracture process zone for ductile fracture is smaller than for cleavage fracture initiation. Later, Anderson and Dodds [9] have proposed that $\alpha \approx 200$ (based on a similar treatment as by Wallin of their own FEM calculations). These α values are so far apart that a closer examination of their meaning is in order.

Wallin [7] bases his argument on an obtainable upper effective J-level from a cleavage fracture point of view. Above a certain load level the stress distribution saturates and becomes practically independent of J. This means that beyond a certain critical J-value the effective J from a cleavage fracture point of view becomes constant. Anderson and Dodds [9] base their viewpoint on the J-level where the stress distribution starts to deviate from the small-scale yielding stress distribution. Thus the Anderson and Dodds size restriction is much more severe than the one proposed by Wallin. Thanks to their refined FEM analysis, Anderson and Dodds were able to determine the relation between the measured J and the effective J (defined by Anderson and Dodds as J_{ssy}), for several crack lengths and material properties. For an a/W of 0.5 their results can roughly be approximated by

$$J_{ssy} \approx J/\{1 + [A \cdot J/(a \cdot \sigma_y)]^B\} \tag{21}$$

where σ_y is the yield stress, $A = 38.1 \cdot \ln(N/3.14)$ and $B = 1.27 + N/104$ for $5 \leq N \leq 50$. For comparison, the simplified Wallin relation has been compared with the more refined Anderson and Dodds relations in Fig. 1. In Fig. 1, Eq 21 has been evaluated in terms of the flow stress (σ_f) instead of σ_y [9] because Wallin based his relation on σ_f. It can be seen from the figure that especially for the higher strain-hardening material the two relations are actually quite close. Thus, the big difference in α is more apparent than actual.

The large-scale yielding correction described through Eq 21 is preferable in relation to the simplified Wallin relation because it is much more accurate in the beginning of large-scale yielding. An α value of 200 seems, however, too severe a criterion for when to perform the large-scale yielding correction. Based on Fig. 1, a value closer to $\alpha = 100$ would seem adequate to guarantee essentially small-scale yielding behavior. The criterion should not, however, be used to assess single results but instead the whole data set. If all results fulfill the size criterion the large-scale yielding correction can be omitted, but if any results exceed the criterion then the whole data set should be corrected for large-scale yielding.

With the foregoing discussions in mind, the following assumptions regarding the effect of ligament size on cleavage fracture toughness are proposed:

1. The J-integral (or K_J) describes the cleavage fracture initiation event as long as $b \geq 100 \cdot (J/\sigma_{flow})$.
2. At higher load levels, the effective load parameter J_{ssy} saturates and is described by Eq 21 for a deep crack.
3. When J_{ssy} saturates, ductile tearing is likely to precede cleavage fracture initiation.

Effect of Ductile Crack Growth

When ductile tearing precedes cleavage fracture initiation, two additional effects have to be accounted for: first, the statistical sampling effect due to the crack advancement and second, the possible effect that the crack growth may have on the stress distribution.

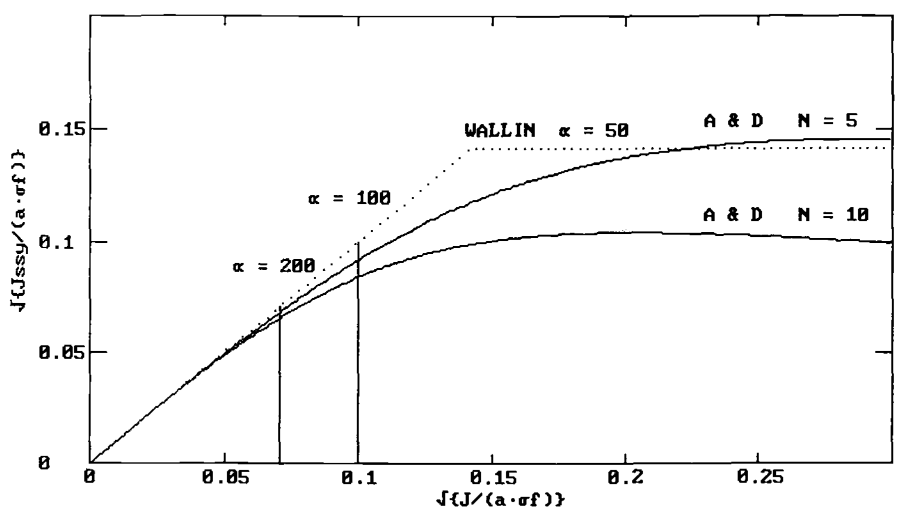

FIG. 1—*Comparison of Wallin's* [7] *simplified LSY relation with Anderson and Dodds* [9] *FEM calculations.*

Statistical Ductile Crack Growth Correction (DCG)

The basic assumptions for the DCG correction are presented elsewhere [*10*]. The distance parameter $\beta \sim x \cdot \sigma_f^2/K_I^2$ defines the cleavage fracture process zone size. In the derivation it is assumed that there exists a specific fracture toughness K_i, corresponding to ductile crack growth initiation and that the lower limiting fracture toughness K_{min} is zero. The sampling volume is presented as having a wedge shape with an active angle θ. The value of the angle and even the exact shape of the sampling volume is arbitrary. It is only used to show that the stress and strain distributions have an angular dependence. The stress distribution within the wedge in front of the crack is assumed to be insensitive to the crack growth.

Considering the fact that Eq 12 actually describes a volume, we can rewrite the equation as

$$P_f = 1 - \exp\left[-\left\{\frac{V}{V_0}\right\}\right] \tag{22}$$

The volume increment due to both increase in loading parameter as well as crack growth is, when written as a function of Δa and neglecting second order terms,

$$\partial V = \frac{V_i}{K_i^4} \cdot \{4 \cdot f(\Delta a)^3 \cdot f'(\Delta a) + 2 \cdot f(\Delta a)^2 \cdot \sigma_f^2/\beta\} \cdot \partial\, \Delta a \tag{23}$$

where $K_I = f(\Delta a)$.

Integrating Eq 23 and combining it with Eq 22, the Δa correction becomes

$$\ln \frac{1}{1 - P_f} = \frac{f(\Delta a)^4}{K_0^4} + \frac{2 \cdot \sigma_f^2}{K_0^4 \cdot \beta} \cdot \int_0^{\Delta a} f(\Delta a)^2 \cdot \partial\, \Delta a \tag{24}$$

for $K_I > K_i$.

The ductile crack growth correction presented here is not unique. Another DCG correction has been presented by Brückner and Munz [*11*]. They have previously derived an expression for the ductile crack growth correction based on normal weakest link type Weibull statistics. When fixing the Weibull slope to be equal to 4, their expression becomes

$$\ln \frac{1}{1 - P_f} = \frac{K_i^4}{K_0^4} + \frac{1}{K_0^4 \cdot W_1} \cdot \int_0^{\Delta a} f(\Delta a)^4 \cdot \partial\, \Delta a \tag{25}$$

where W_1 is a constant, describing the size of the active volume in mm.

Comparing Eq 25 with Eq 24, it is seen that they are rather similar. The difference is that the expression based on the general model assumes that the effective active volume continues to grow as a function of $(K_I^2)^2$ even after the ductile crack growth begins, whereas Brückner and Munz assume that the size of the active volume becomes constant when ductile crack growth starts.

The fitting capability of the two crack growth corrections is practically identical [*10*], but here the assumption of the active volume being a function of $(K_I^2)^2$ is assumed because it seems logical to assume the plasticity to grow with increasing loading.

Both Eqs 24 and 25 have a drawback. They require that the crack growth integrals are solved. This means that the actual R-curve up to cleavage fracture for each specimen must be known. Because scatter usually exists in the ductile tearing R-curves, the application of Eqs 24 and 25 is either very laborious or demands the use of some mean approximation of the R-curves. To overcome this difficulty a simplified form of the crack growth correction is required.

If the ductile crack growth is independent of K_I the crack growth correction is much simplified. It can be written as

$$\left(\ln \frac{1}{1-P_f}\right)^{1/4} = \frac{K_i}{K_0}\left(1 + \frac{2 \cdot \Delta a \cdot \sigma_f^2}{K_i^2 \cdot \beta}\right)^{1/4} \tag{26}$$

When the crack growth is small $\approx$ 1 mm or the R-curve is relatively flat or both, Eq 26 can be used to approximate Eq 24, by insertion of K_I in place of K_i. If the relative process zone size is proportional to the location of the stress maximum, β is more or less proportional to σ_f^2. This enables one to define a parameter $\Omega^2 = \sigma_f^2/\beta$. Using Ω and accounting for specimen thickness and a lower limiting fracture toughness the approximate correction can be written as

$$\left(\ln \frac{1}{1-P_f}\right)^{1/4} = \frac{K_I - K_{min}}{K_0 - K_{min}} \cdot \left(\frac{B}{B_0}\right)^{1/4} \cdot \left(1 + \frac{2 \cdot \Delta a \cdot \Omega^2}{K_I^2}\right)^{1/4} \tag{27}$$

Ductile Tearing and Constraint

The effect of ductile tearing on the tensile stress distribution in front of the crack is somewhat controversial. FEM studies by Sham [*12*] indicate a negligible effect, whereas FEM studies by Van den Horn et al. [*13*] indicate a clearer effect. According to the Van den Horn results, the stress distributions are identical outside the stationary crack stress maximum, but the stress maximum of the growing crack is higher and occurs closer to the crack tip. In both cases it appears possible to normalize the stress distributions by J or K_I^2. If the process zone size is approximately three to five times the distance from the crack tip to the stress maximum of the stationary crack, the effect of the stress elevation occuring very close to the crack tip may.not be too severe. The main effect of the stress elevation would be to diminish the cleavage fracture process zone size, that is, increase the value of Ω. In any case, Eq 27 can be used to describe the effect of ductile tearing on cleavage fracture initiation.

Effect of Specimen Thickness and Side Grooving

Besides causing the statistical effect, specimen thickness also affects the stress triaxiality of the specimen. As long as the specimen remains in small-scale yielding and the specimen is of a standard geometry, the effect of the specimen thickness upon the stress state does not seem important [*14*]. Side grooving of the specimen will cause an elevation of the stress state, but at the same time the specimen net thickness diminishes. These two factors yield effects that are opposite in nature, and it has been proposed that for moderate amounts of side grooving ($\approx$ 20%), the sum effect will be negligible [*14*]. In the large-scale yielding region, the loss of constraint in a nonside-grooved specimen may become large, thus pronouncing the specimen thickness effect. It is possible that side grooves on the specimen may inhibit the loss of constraint to some degree, but unfortunately there exists at present no quantitative description of the specimen thickness effect for the large-scale yielding case. To be on the safe side, it seems advisable to use side-grooved specimens for fracture toughness testing in the ductile-to-brittle transition region. In such cases Eq 27 should yield sufficient accuracy.

Verification

The experimental verification consisted of 105 K_{Jc} tests with identical specimens of a single material. The material used was a 2¼ Cr 1 Mo steel taken from a 20-year-old hydrogenating reactor pressure vessel. The room-temperature 0.2% proof strength and ultimate strength were $R_{p0.2} = 300$ MPa and $R_u = 532$ MPa. The specimens were 25-mm-thick compact tension (CT) specimens with 20% side grooves. Details of the test procedure and material are presented elsewhere [15]. All specimens were tested at room temperature, and the value of the J-integral at cleavage fracture initiation as well as the amount of ductile tearing, measured by scanning electron microscopy (SEM), were recorded. The results are presented as a multispecimen J-R-curve in Fig. 2 and tabulated in Appendix I. Seven of the specimens failed to initiate cleavage before the test was terminated. These specimens are included in Fig. 2, but they were omitted from the statistical analysis so that a censored data set was used.

The analysis was performed by using Eq 27 and by applying K_{jssy} in place of $K_I \cdot K_{jssy}$ was calculated from K_j by application of an equation like Eq 21. Because the a/W of the specimens was approximately 0.6, the J was normalized by the ligament (b) and flow stress instead of a and σ_y. Because of this it was decided to fit the parameter A. The parameter B was fixed as 1.32, corresponding to a strain-hardening exponent of $N = 5$. A best fit of all the data yields $K_{min} \approx 20$ MPa$\sqrt{m}$, $K_0 \approx 240$ MPa$\sqrt{m}$, $A \approx 24.7$, and $\Omega \approx 4700$ MPa.

The results of the analysis are presented in Fig. 3. In the figure the 5 and 95% confidence limits of the rank-based probabilities are included [16]. The data are seen to be well described through the large-scale yielding and crack growth corrections. The standard deviation of the estimates of rank probabilities is 0.023.

For a strain-hardening exponent of 5, the relation between flow stress and yield stress is approximately $\sigma_f \approx 1.5 \cdot \sigma_y$. When the parameter A is corrected to correspond to σ_y, we obtain $A \approx 16.5$. This value is really quite close to the value based on the Anderson and Dodds analysis ($A \approx 17.7$). Thus it appears that for deep cracks with $a/W > 0.5$, Eq 21 can be applied directly with the crack length replaced by the ligament size.

Another interesting set of data has been presented by Morland [17]. He performed fracture toughness tests at different temperatures with varying specimen thicknesses and amount of side grooves. Here, his data have been reanalyzed using Eqs 21 and 27. Based on his tension test results and the expression for N presented by Anderson and Dodds [9], it would seem

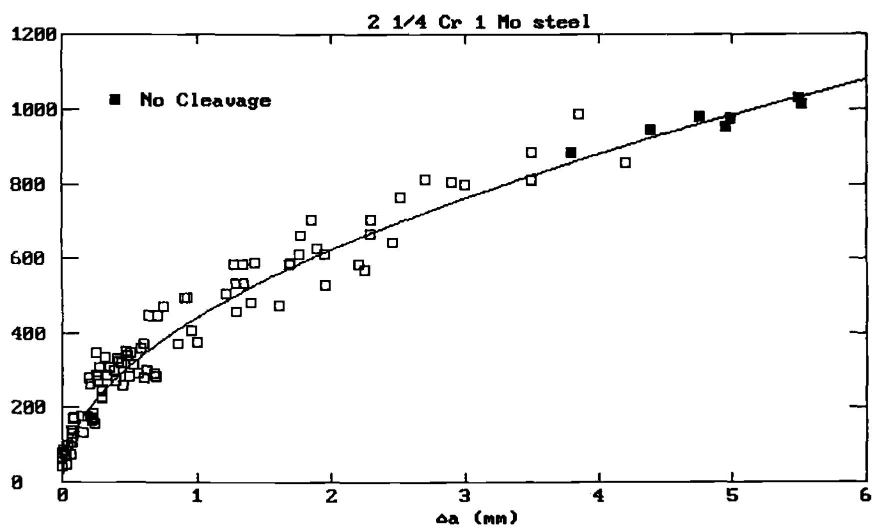

FIG. 2—*Multispecimen* J-R-*curve based on ductile crack growth value at cleavage initiation for 105 specimens.*

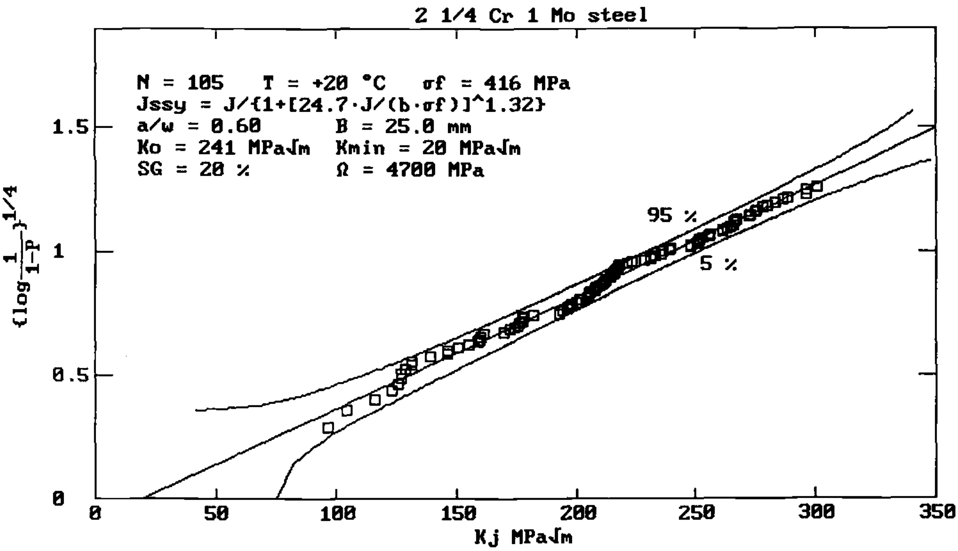

FIG. 3—*Failure probability diagram.* K_j *corrected for ductile crack growth and large-scale yielding.*

appropriate to take the work-hardening exponent as $N = 10$ but this overpredicted the large-scale yielding effect. The possibility that the overprediction might be the result of assuming a too low K_{min} value for this material was examined by trying out higher K_{min} values, but the result remained the same. Instead, a value of $N = 5$ was used. This value is based on an experimental correlation between yield ratio and strain-hardening exponent [*18*]. The reanalyzed Morland data are presented graphically in Appendix II in the form of failure probability diagrams. All the K_0 values cited in the Appendix refer to an effective specimen thickness of 25 mm. The thickness correction was performed on the nominal thickness and not the net thickness of the specimens. The reason for this was that it was assumed that the side grooving increases the stress triaxiality so as to compensate for the decrease in crack front length [*14*]. In addition to the Morland data, Ingham et al. [*19*] have presented three-point bending results obtained with apparently the same material. Their data included square section specimens without side grooves with thicknesses in the range 10 to 230 mm. The Ingham data that were tested at the same temperatures as the Morland data were thus included in the analysis. For all cases the normalizing fracture toughness K_0 corresponding to an effective specimen thickness of 25 mm was determined based on a maximum likelihood estimation. At each temperature the mean $\overline{K}_0$ for all cases was determined, and the individual K_0 values were normalized with this mean value. The results for the different temperatures are presented in Fig. 4.

Included in Fig,. 4 are also the theoretical 5 and 95% confidence limits for a K_0 estimate based on ten specimens. The value of 10 was chosen, as the majority of cases consisted of ten specimens. It is seen that the scatter in K_0 estimates is clearly larger than if it was only due to statistical variation. Furthermore, clear trends can be seen. At higher temperatures (that is, higher toughness) the small specimens predict a lower toughness than the large specimens. Actually, if the 25-mm-thick specimens at -10 and $+10$°C and the 10-mm-thick specimens at -70 and -50°C are omitted from the analysis, all estimates will lie roughly within the theoretical confidence lines. It appears that the large-scale yielding correction becomes overconservative for high loading levels where the large-scale yielding is extensive. This does not directly impede on the use of Eq 21. It actually verifies that the large-scale yielding correction

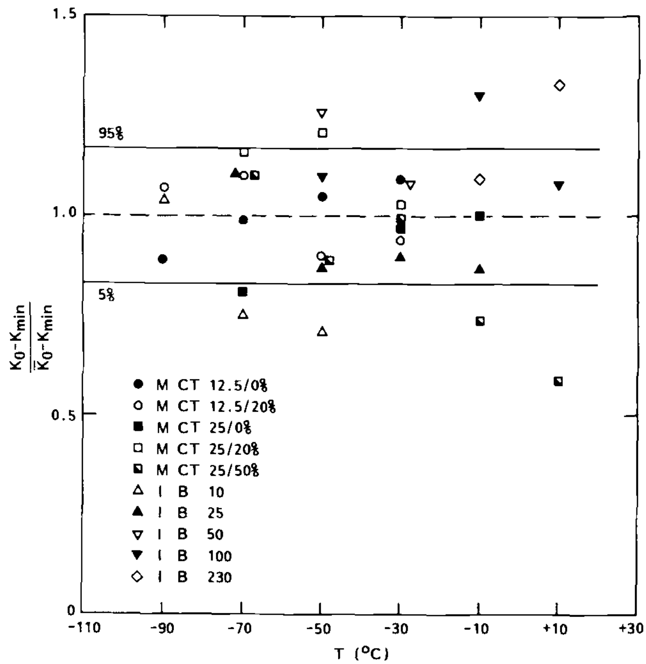

FIG. 4—*Effect of specimen geometry on* K_0.

produces safe estimates of the fracture behavior for quite small specimens. Another point to be seen from Fig. 4 is that there appears to be no clear effect of side grooving, thus confirming the methodology of analysis of side-grooved specimens adopted here.

Summary and Conclusions

Based on a statistical treatment of constraint effects on fracture toughness results from laboratory specimens in the ductile-to-brittle transition region, the following can be concluded:

1. The J-integral (or K_J) describes the cleavage fracture initiation event as long as $b \geq 100 \cdot (J/\sigma_{flow})$.
2. Large-scale yielding of the ligament, possible ductile tearing, and varying specimen thicknesses can successfully be corrected for by the equation

$$K_{Icorr.} = K_{min} + \{K_I - K_{min}\} \cdot \left(\frac{B}{B_0}\right)^{1/4} \cdot \left(1 + \frac{2 \cdot \Delta a \cdot \Omega^2}{K_I^2}\right)^{1/4} \tag{28}$$

   where K_I has been corrected for large-scale yielding with the approach adopted by Anderson and Dodds [9].
3. The large-scale yielding correction has a tendency to become overconservative for high loading levels where large-scale yielding is extensive.
4. Moderate side grooving of the specimen does not appear to have a significant effect on fracture toughness as long as B is described with the nominal thickness of the specimen.

Acknowledgment

This work is a part of the Nuclear Power Plant Structural Integrity Programme performed at the Technical Research Centre of Finland (VTT) and financed by the Ministry of Trade and Industry in Finland.

APPENDIX I

TABLE 1.

Code	a_0 mm	Δa mm	J_C, kJ/m^2	Comment
A-4	30.16	0.064	109	
A-5	30.45	0.25	290	
A-6	30.78	0.28	308	
A-7	31.11	0.255	347	
A-8	30.53	0.93	492	
A-9	30.87	4.40	945	No Cleavage
A-10	30.90	0.39	300	
A-11	30.36	0.44	318	
A-12	30.92	0.625	299	
A-13	31.07	0.066	140	
A-14	30.91	0.027	77	
A-15	30.89	1.28	581	
A-16	31.14	1.21	503	
A-17	30.25	1.78	662	
A-20	30.64	0.23	171	
A-21	30.82	1.70	587	
A-22	30.60	0.28	308	
A-23	31.00	0.326	290	
A-24	30.70	0.08	170	
A-25	30.85	0	66	
A-26	30.17	2.90	808	
A-27	30.77	3.80	886	No Cleavage
A-28	30.87	1.69	581	
A-29	30.94	4.95	950	No Cleavage
A-30	30.57	1.95	528	
A-31	31.07	0.61	281	
A-32	30.98	0.185	178	
A-33	30.71	0.202	280	
A-34	30.93	0.40	273	
A-35	30.25	0.567	293	
A-36	30.44	3.50	886	
A-37	30.25	0.91	492	
A-38	30.24	5.50	1030	No Cleavage
A-39	31.04	2.30	703	
A-40	30.39	0.082	140	
A-41	30.75	0.70	285	
A-42	30.33	0.01	88	
A-43	30.84	0.47	350	
A-44	30.85	0.264	274	
A-45	30.84	4.20	858	
A-46	30.78	3.00	≈800	
A-47	31.05	1.77	611	
A-48	30.81	3.85	987	
A-49	30.27	5.00	976	No Cleavage
A-50	30.92	0.21	265	
A-20.1	30.95	0.41	331	
A-30.1	30.90	0.51	346	
A-40.1	30.75	5.52	1015	No Cleavage

TABLE 1.

Code	a_0 mm	Δa mm	J_C, kJ/m^2	Comment
A-50.1	30.33	1.85	706	
A-51	30.93	0.034	78	
A-52	30.11	0.295	249	
A-53	30.66	3.50	811	
A-54	30.60	1.61	474	
A-55	30.51	1.44	587	
A-56	29.85	1.95	612	
A-57	30.85	0.49	341	
A-58	30.44	1.00	373	
A-59	30.51	0.15	134	
A-60	30.72	0.22	167	
A-61	31.57	0.353	307	
A-62	30.79	0.22	175	
A-63	30.19	1.29	459	
A-64	30.88	0.684	291	
A-65	30.88	0.228	188	
A-66	30.99	0.642	445	
A-67	30.63	0	44	
A-68	31.04	2.25	568	
A-69	30.49	0.50	286	
A-70	30.99	0.061	130	
A-71	30.59	0.705	447	
A-72	30.28	0.14	179	
A-73	30.78	0.036	72	
A-74	30.99	1.40	479	
A-75	30.33	0.415	323	
A-76	30.69	0.30	224	
A-77	30.94	0.59	360	
A-78	30.05	2.21	583	
A-79	31.02	0.068	141	
A-80	31.10	4.75	979	No Cleavage
A-81	30.75	0.035	85	
A-82	31.17	0.091	176	
A-83	30.84	0.045	98	
A-84	30.97	0.07	118	
A-85	30.86	2.47	641	
A-86	30.77	0.86	371	
A-87	30.47	1.29	530	
A-88	30.46	1.35	530	
A-89	31.07	0.24	158	
A-90	30.85	2.52	765	
A-91	30.41	0.526	316	
A-92	30.67	0.75	467	
A-93	30.83	0.96	407	
A-94	30.86	0.32	336	
A-95	30.73	0.061	78	
A-96	30.90	0.036	49	
A-97	30.62	0.455	262	
A-98	30.96	0.30	229	
A-99	31.15	1.35	581	
A-100	30.45	1.90	626	
A-101	30.64	0	82	
A-60.1	30.56	0.082	107	
A-70.1	30.66	2.30	665	
A-80.1	31.03	2.70	813	
A-90.1	30.55	0.30	245	
A-100.1	30.59	0.61	372	

APPENDIX II

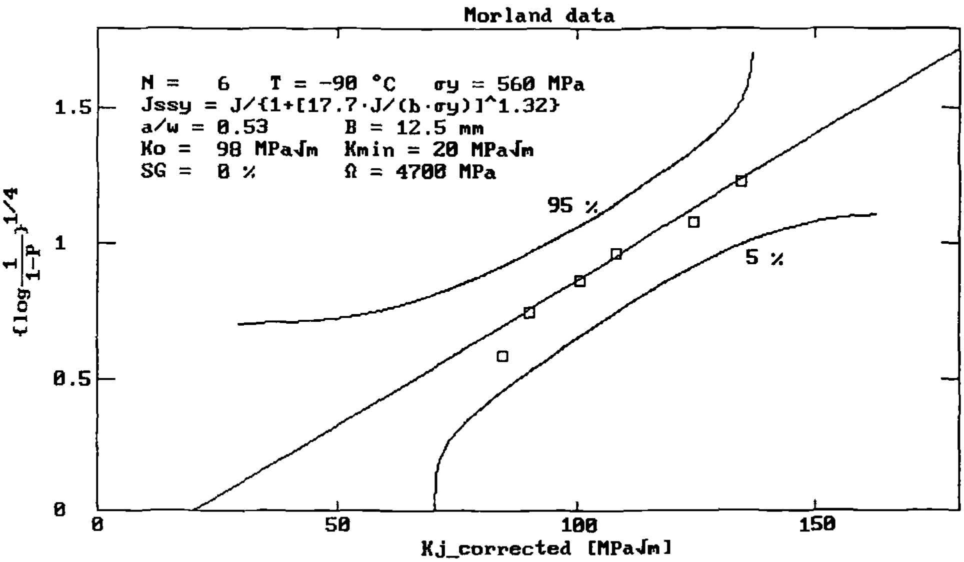

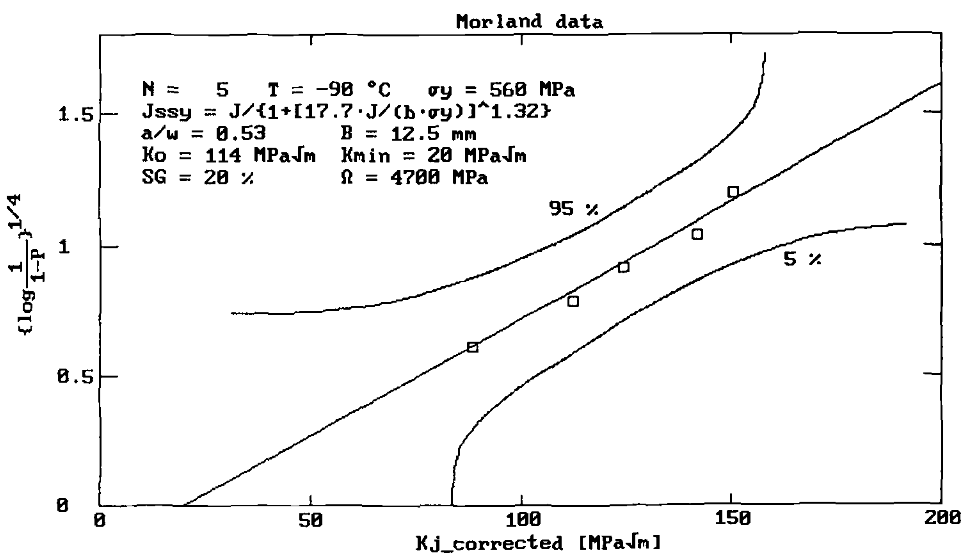

FIG. A1—*Failure probability diagrams of LSY and DCG corrected Morland data* [17].

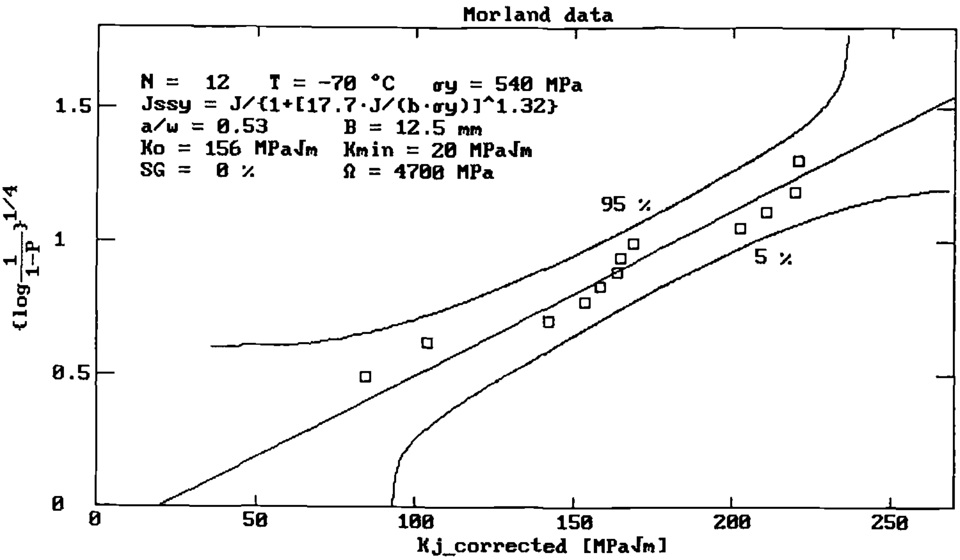

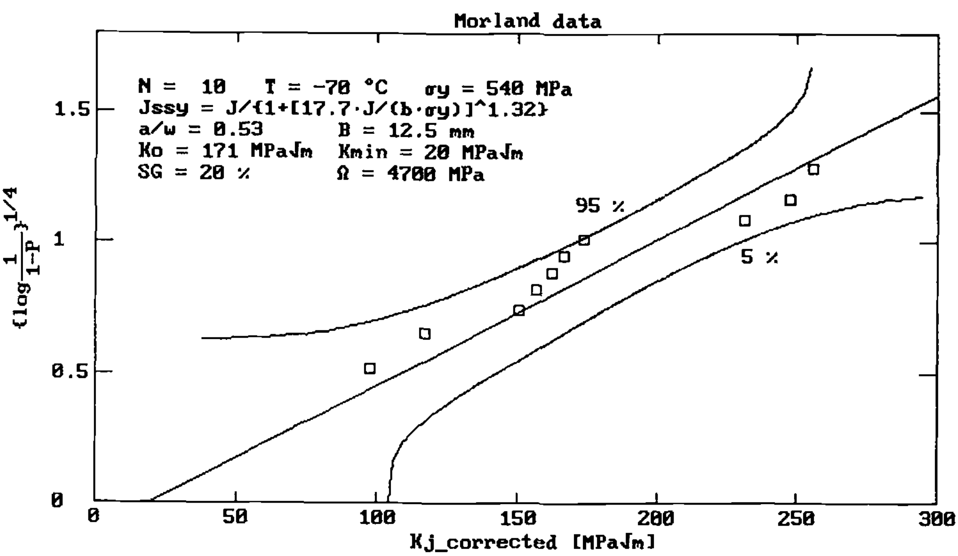

FIG. A1—*Continued*

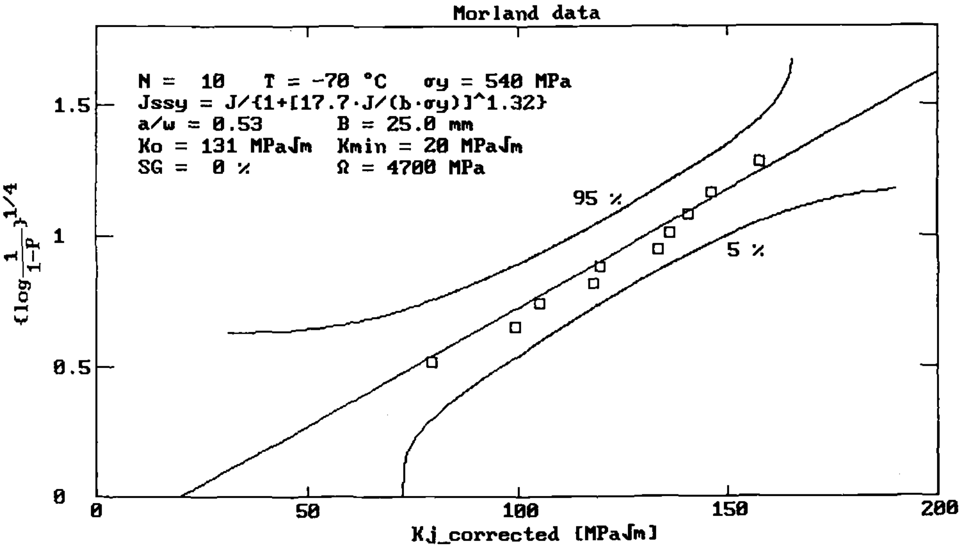

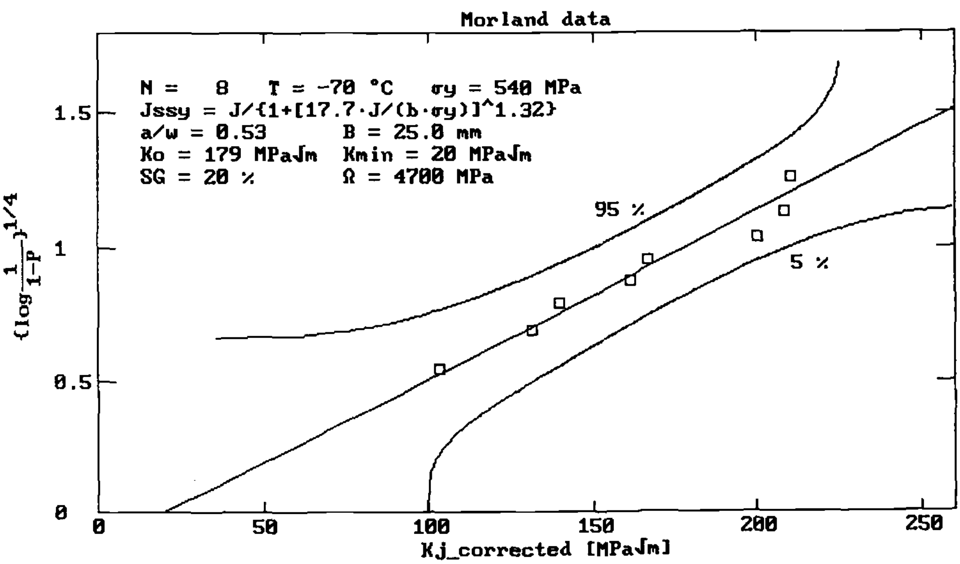

FIG. A2—*Failure probability diagrams of LSY and DCG corrected Morland data* [17].

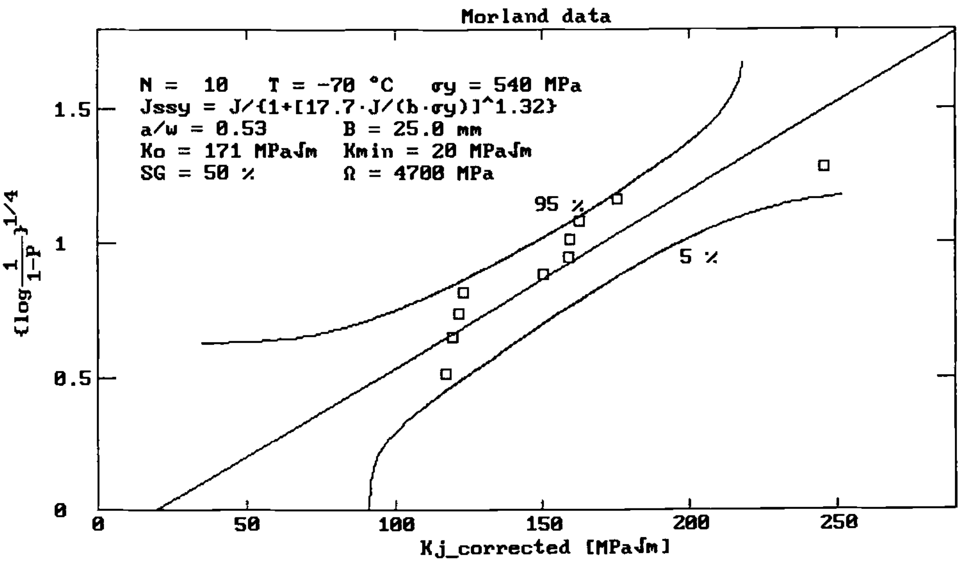

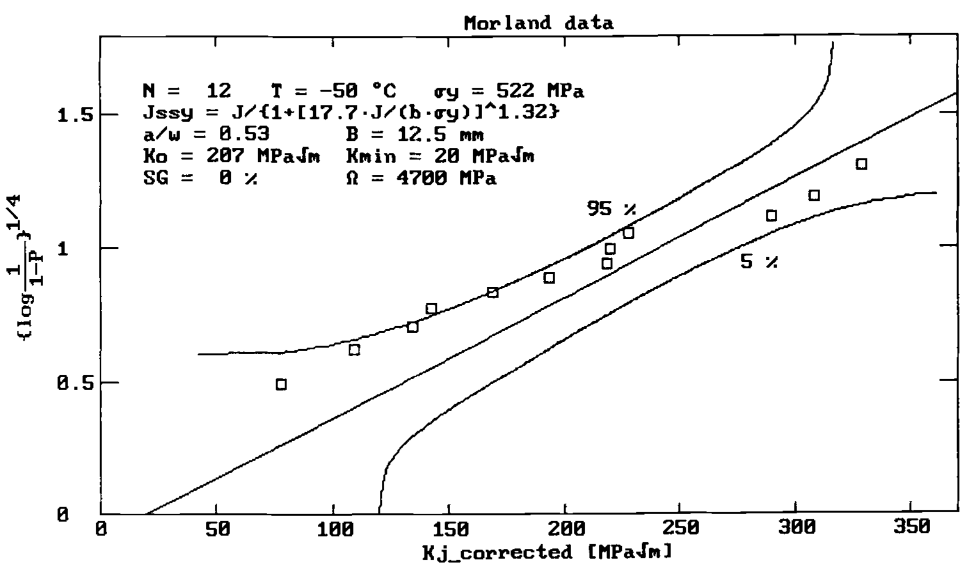

FIG. A2—*Continued*

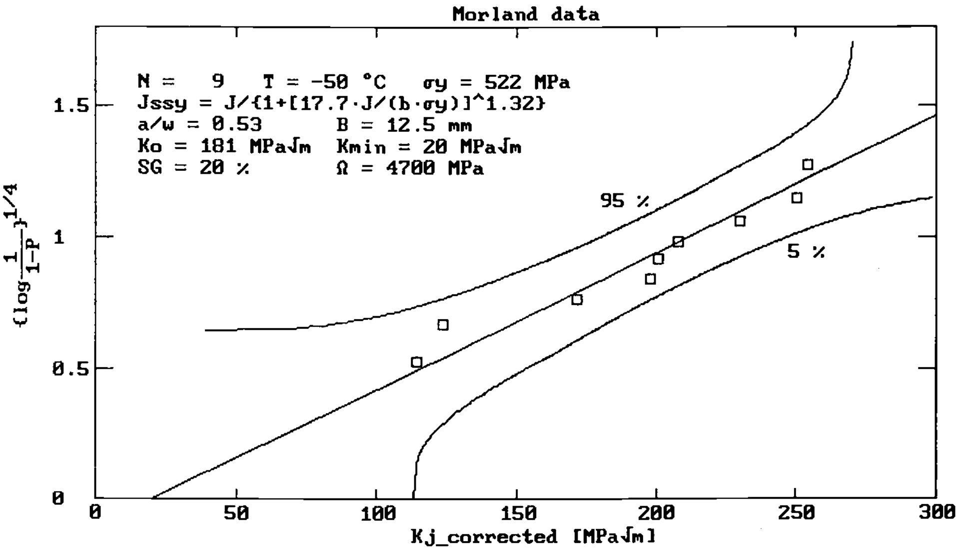

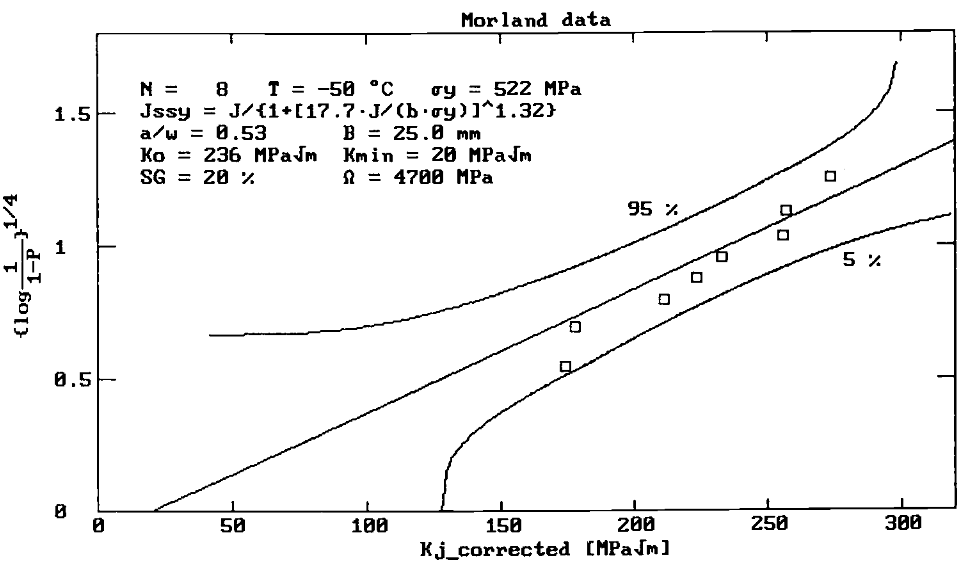

FIG. A3—*Failure probability diagrams of LSY and DCG corrected Morland data* [17].

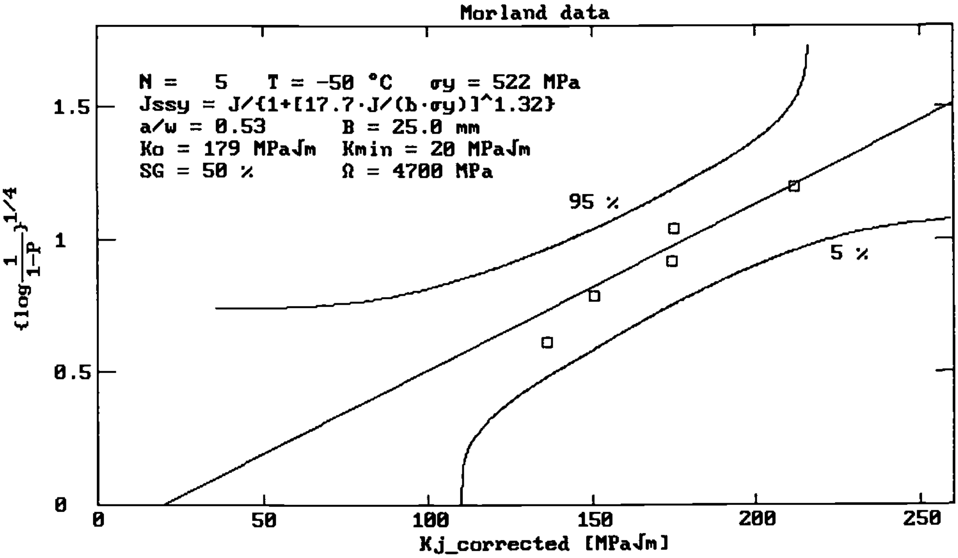

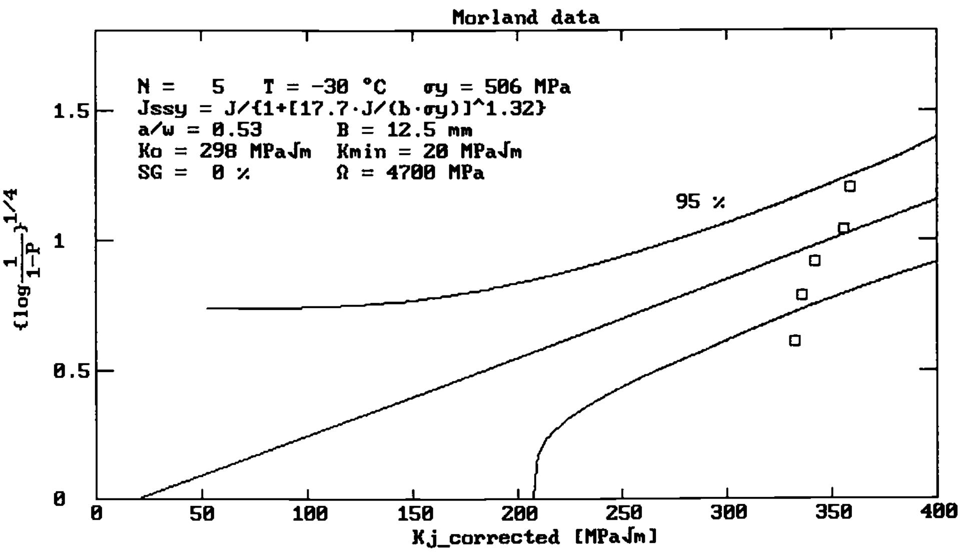

FIG. A3—*Continued*

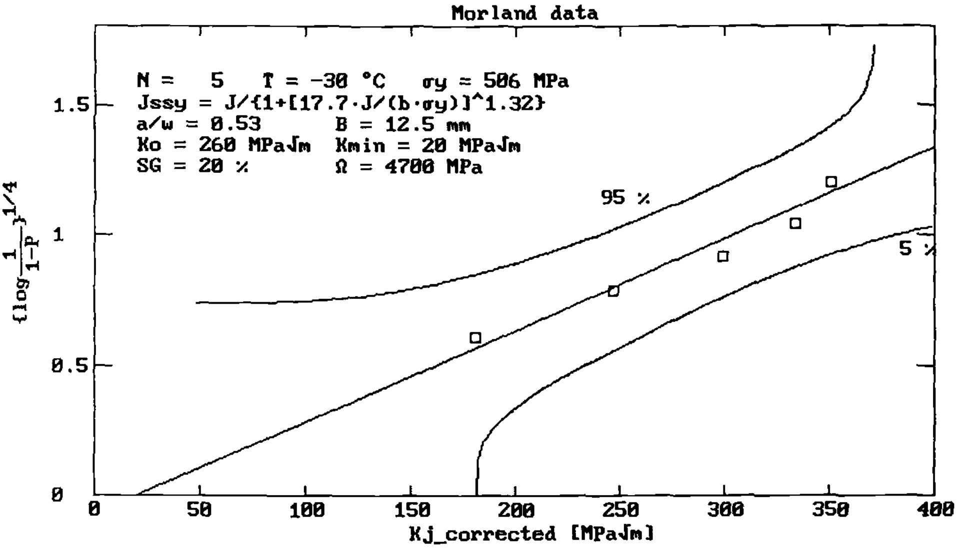

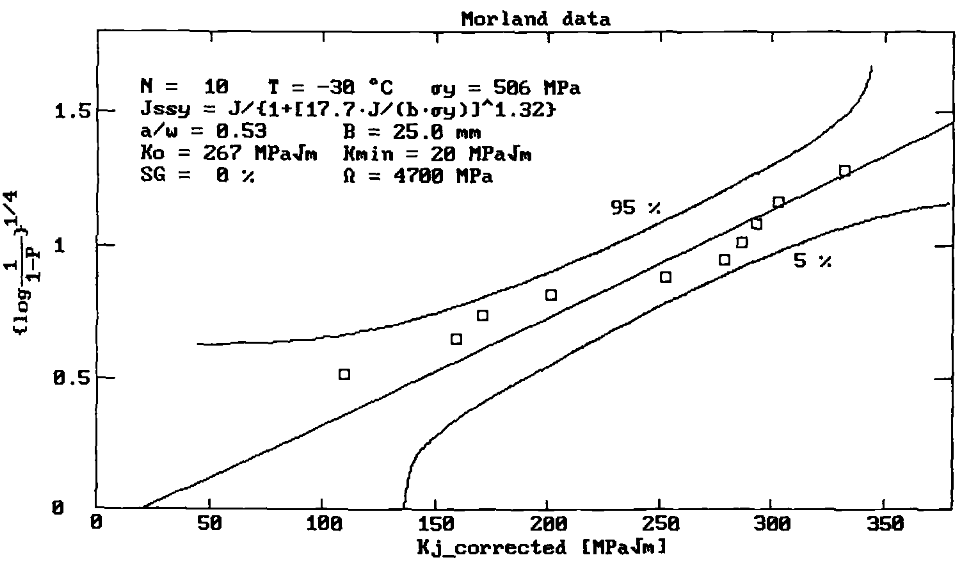

FIG. A4—*Failure probability diagrams of LSY and DCG corrected Morland data* [17].

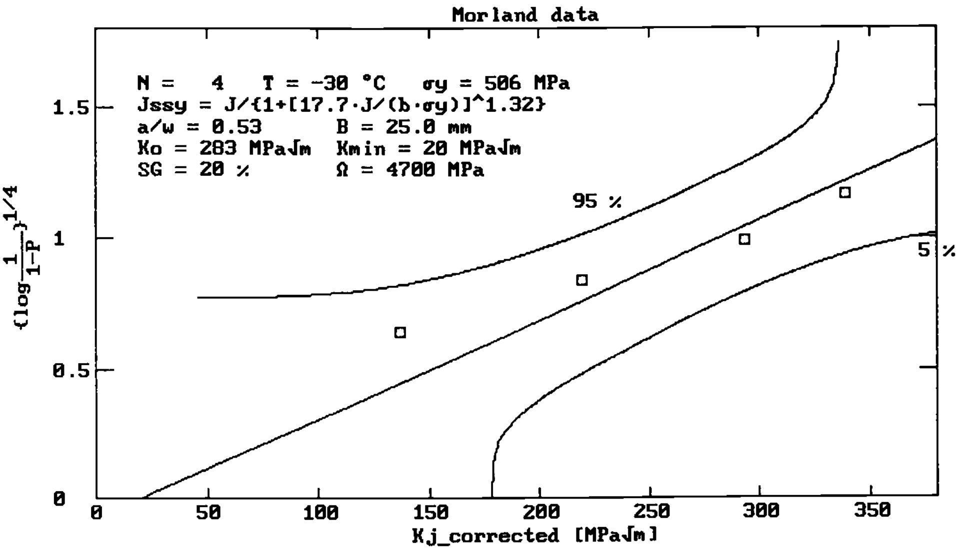

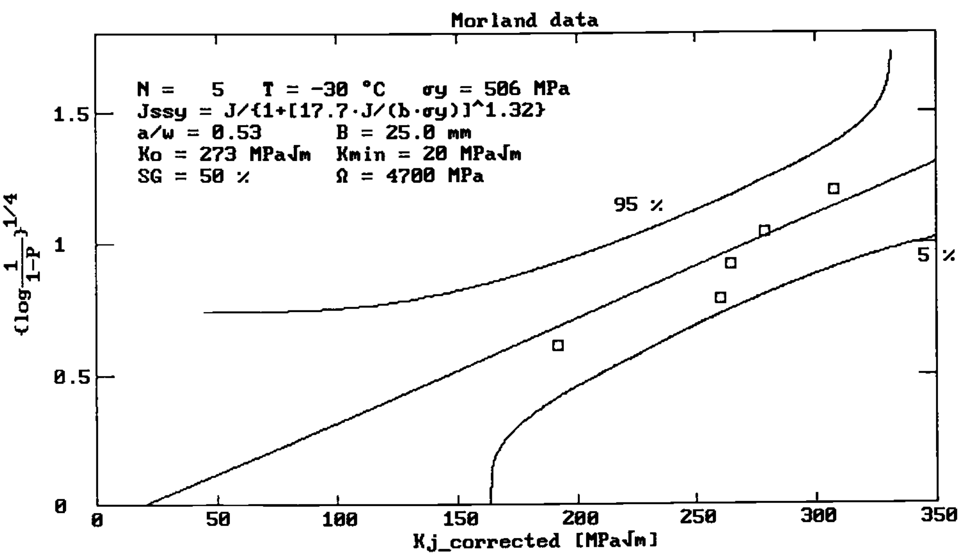

FIG. A4—*Continued*

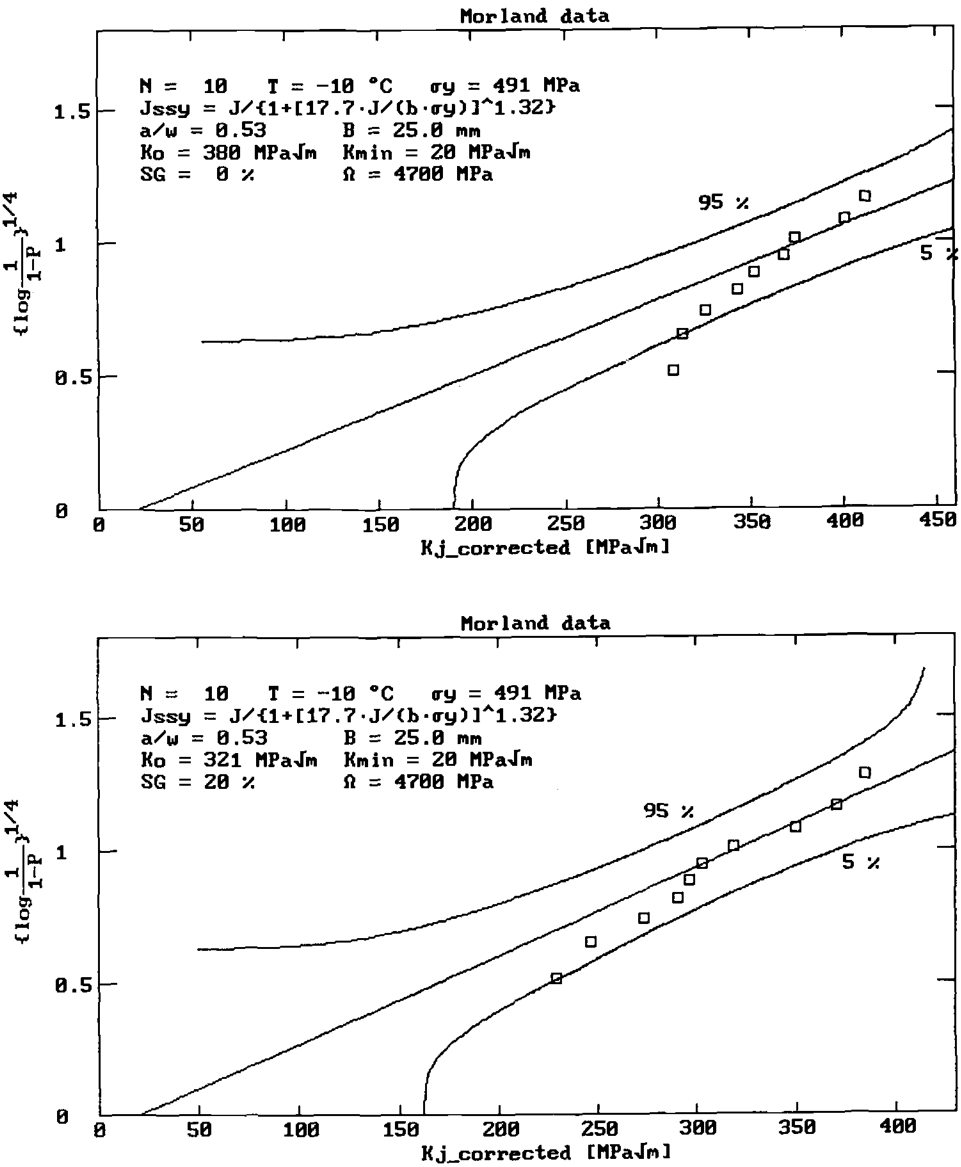

FIG. A5—*Failure probability diagrams of LSY and DCG corrected Morland data*]17].

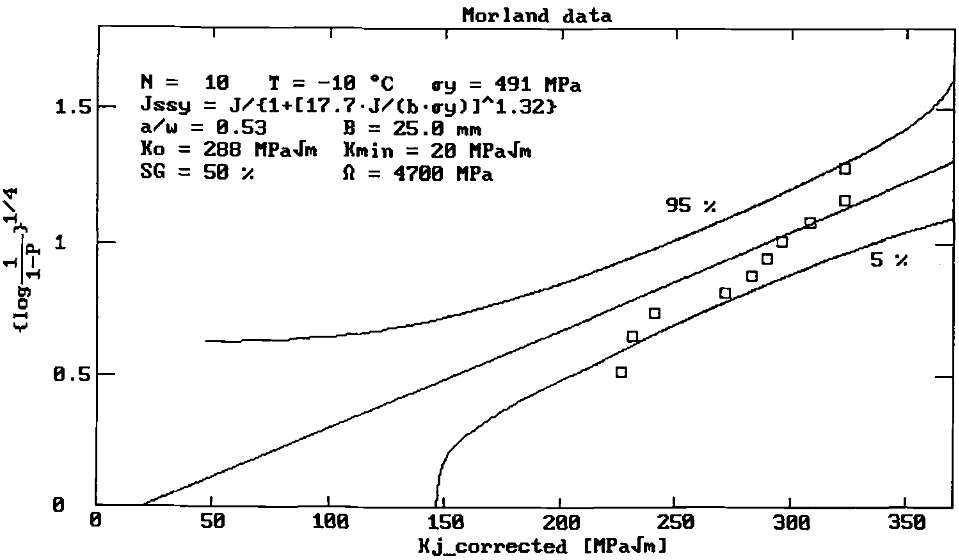

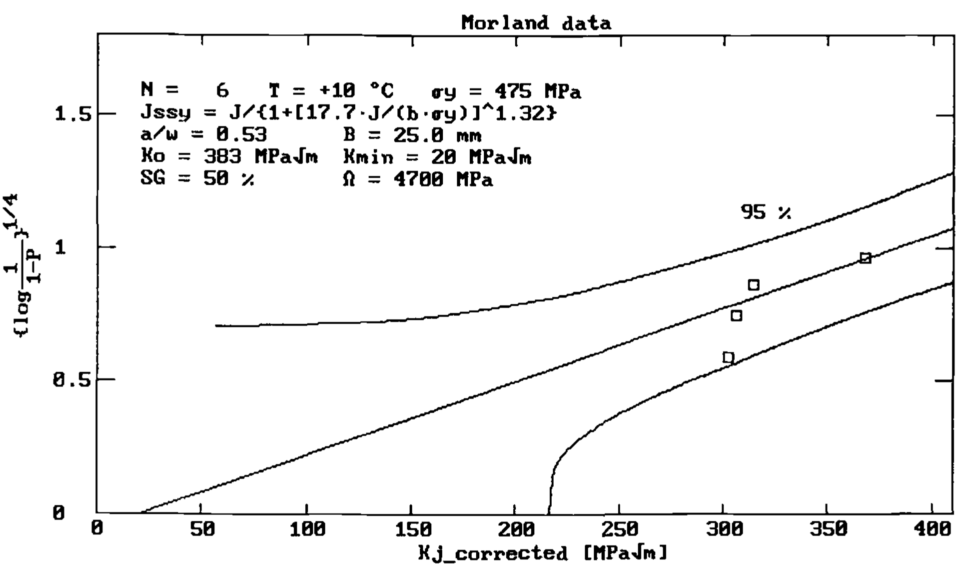

FIG. A5—*Continued*

References

[1] Wallin, K., "Statistical Modelling of Fracture in the Ductile to Brittle Transition Region," *European Symposium on Elastic-Plastic Fracture Mechanics: Elements of Defect Assessment*, Freiburg, Germany, 1989.

[2] Brückner-Foit, A., Munz, D., and Trolldenier, B., "Intermediate Report Over DFG Project, Brittle Fracture, MU466/14-1, for the time period 1.07.1987-31.12.1988," in German, Institute for Reliability and Failure Analysis, University of Karlsruhe (TH), Karlsruhe, Germany, 1989.

[3] Hutchinson, J. W., "Singular Behavior at the End of a Tensile Crack in a Hardening Material," *Journal of the Mechanics and Physics of Solids*, Vol. 16, 1968, pp. 13-31.

[4] Rice, J. R. and Rosengren, G. F., "Plane Strain Deformation near a Crack Tip in a Power-Law Hardening Material," *Journal of the Mechanics and Physics of Solids*, Vol. 16, 1968, pp. 1-12.

[5] Wallin, K., "The Scatter in K_{IC}-Results," *Engineering Fracture Mechanics*, Vol. 19, 1984, pp. 1085-1093.

[6] Stienstra, D. I. A., "Stochastic Micromechanical Modeling of Cleavage Fracture in the Ductile-Brittle Transition Region," Ph.D. dissertation, Texas A&M University, College Station, TX, August 1990.

[7] Wallin, K., "The Effect of Ligament Size on Cleavage Fracture Toughness," *Engineering Fracture Mechanics*, Vol. 32, 1989, pp. 449-457.

[8] McMeeking, R. M. and Parks, D. M., "On Criteria for *J*-Dominance of Crack-Tip Fields in Large Scale Yielding," *Elastic-Plastic Fracture, ASTM STP 688*, J. D. Landes, J. A. Begley, and G. A. Clarke, Eds., American Society for Testing and Materials, Philadelphia, 1979, pp. 175-194.

[9] Anderson, T. L. and Dodds, R. H., "Specimen Size Requirements for Fracture Toughness Testing in the Transition Region," *Journal of Testing and Evaluation*, Vol. 19, 1991, pp. 123-134.

[10] Wallin, K., "The Effect of Ductile Tearing on Cleavage Fracture Probability in Fracture Toughness Testing," *Engineering Fracture Mechanics*, Vol. 32, 1989, pp. 523-531.

[11] Brückner, A. and Munz, D., "Scatter of Fracture Toughness in the Brittle-Ductile Transition Region of a Ferritic Steel," *Advances in Probabilistic Fracture Mechanics—PVP, Vol. 92*, The American Society of Mechanical Engineers, New York, NY, 1984, pp. 105-111.

[12] Sham, T-L., "A Finite-Element Study of the Asymptotic Near-Tip Fields for Mode I Plane-Strain Cracks Growing Stably in Elastic-Ideally Plastic Solids," *Elastic-Plastic Fracture: Second Symposium, Volume I: Inelastic Crack Analysis, ASTM STP 803*, C. F. Shih and J. P. Gudas, Eds., American Society for Testing and Materials, Philadelphia, 1983, pp. I-52-I-79.

[13] Van den Horn, B. A., Braam, H., and Van Kranenburg, M. A. C., "Two-Dimensional Elastic-Plastic Finite Element Analysis of a SENB4 with a Growing Crack," Report ECN-I—90-023, Netherlands Energy Research Foundation, Petten, The Netherlands, 1990.

[14] Wallin, K., "The Size Effect in K_{IC}-Results," *Engineering Fracture Mechanics*, Vol. 22, 1985, pp. 149-163.

[15] Toivonen, J., "The Effect of Mechanical Loading on Acoustic Emission in a Fracture Toughness Test," in Finnish, M.Sc. Thesis, Helsinki Technical University, Espoo, Finland, 1987.

[16] Wallin, K., "Optimized Estimation of the Weibull Distribution Parameters," Research Report 604, Technical Research Centre of Finland, Espoo, Finland, 1989.

[17] Morland, E., "Fracture Toughness in the Transition Regime for A533B-1 Steel: The Effect of Specimen Sidegrooving," *Fracture Mechanics: Twenty-First Symposium, ASTM STP 1074*, J. P. Gudas, J. A. Joyce, and E. M. Hackett, Eds., American Society for Testing and Materials, Philadelphia, 1990, pp. 215-237.

[18] Auerkari, P., "On the Correlation of Hardness with Tensile and Yield Strength," Research Reports 416, Technical Research Centre of Finland, Espoo, Finland, 1986.

[19] Ingham, T., Knee, N., Milne, I., and Morland, E., "Fracture Toughness in the Transition Regime for A533B Steel: Prediction of Large Specimen Results from Small Specimen Tests," *Fracture Mechanics: Perspectives and Directions: Twentieth Symposium, ASTM STP 1020*, R. P. Wei and R. P. Gangloff, Eds., American Society for Testing and Materials, Philadelphia, 1989, pp. 369-389.

D. Firrao,[1] R. Doglione,[1] and E. Ilia[2]

Thickness Constraint Loss by Delamination and Pop-In Behavior

REFERENCE: Firrao, D., Doglione, R., and Ilia, E., "**Thickness Constraint Loss by Delamination and Pop-In Behavior,**" *Constraint Effects in Fracture, ASTM STP 1171*, E. M. Hackett, K.-H. Schwalbe, and R. H. Dodds, Eds., American Society for Testing and Materials, 1993, pp. 289–305.

ABSTRACT: Fracture toughness of aluminum-lithium 8090-T8 alloy has been investigated. *J-R* and *K-R* curves tests have been performed on compact tension (CT) samples machined from a 12-mm-thick plate, both in longitudinal transverse (LT) and transverse longitudinal (TL) directions. Sample thickness and width varied in order to assess the dependence of constraint on the geometry. It was found that, owing to delaminations occurring perpendicular to short transverse direction and local fracture path deviation from Mode I, a relaxation of the degree of thickness constraint inside the material takes place. Large pop-in phenomena ensue, thus hampering the *J-R* curves interpretation. Metallographic structure and fracture surfaces were investigated to clarify the micromechanisms of fracture and to ascertain the possibility to single out unequivocally the critical event for J_{Ic} significant determinations. Also, *K-R* curves have been explained on the basis of the results of fracture mechanisms and microstructure. The extent to which J_{Ic} and *K-R* curves are representative and size independent, as well as the inapplicability of ASTM Test Method for Plane-Strain Fracture Toughness of Metallic Materials (E 399-83), have been discussed.

KEY WORDS: Al-Li 8090-T8 alloy, delaminations, pop-in, recrystallization, J_{Ic}, *K-R* curves, thickness constraint, fracture surface roughness

Among aluminum-lithium (Al-Li) alloys, Aluminum Alloy (AA) 8090 is particularly attractive for aeronautical purposes, coupling a 10% reduction in density with an 11% increase in Young's modulus. This alloy, classified as having medium strength and low density, will be deemed indeed successful only if it is applied in the direct replacement of components without redesign. This is because economical considerations tend to limit its application: costs are from two to four times higher than those of conventional alloys, and the production of components as well as scrap recovery need particular processes and plants. Thus, the substitution of conventional alloys by the lighter and more rigid Al-Li alloys is considered possible only if all the mechanical and other physical properties are equal or better.

For the Alloy 8090, the T8 thermomechanical treatment is the most attractive; it yields quite high tensile properties so that 8090-T8 can be considered as a substitute for the 2214-T6, 7075-T7, and 7475-T7 alloys. From the point of view of fracture resistance properties, it has been shown that 8090 is characterized by LT and TL fracture toughness values (K_{Ic}) of the same order of the alloys referenced above, namely 30 MPa$\sqrt{m}$ or slightly higher. However, unlike

[1] Full professor and assistant professor, Dipartimento di Scienza dei Materiali e Ingegneria Chimica, Politecnico di Torino, Corso Duca degli Abruzzi 24, 10129, Turin, Italy.

[2] Assistant professor, Universiteti Politeknik i Tiranes, Fakulteti i Inxhinierise Mekanike, Tirana, Albania.

the classical alloys, 8090 possesses particularly low short transverse fracture toughness values (13 to 15 MPa$\sqrt{m}$) [*1,2*].

In spite of these K_{Ic} values, there are doubts on how to identify on the *R*-curves the critical event for significant fracture properties determination, the peculiar thickness effect in this alloy playing an unusual role. First of all, many researchers have found, during TL and LT fracture toughness tests, a particular behavior characterized by a great number of delaminations along high-angle grain boundaries parallel to the rolling plane. This gives rise to a local internal loss of thickness constraint along delaminations, which is reflected in multiple local plane stress conditions ahead of the crack tip, with at times coupled plane strain zones between them [*1*]. Therefore, the crack front is characterized by an alternation of plane stress and plane strain zones, giving rise to the question of whether the K_{Ic} value, determined according to the ASTM Test Method for Plane-Strain Fracture Toughness of Metallic Materials (E 399-83), is a valid plane strain one [*3*]. Another and more general question is whether a classical (continuum mechanics) plane strain condition may ever exist at fracture in this kind of alloy.

A certain number of publications deal with the effect of delaminations on long and long transverse fracture toughness of 2090-T8 and 8090-T8 alloy plates at room and cryogenic temperatures [*3–6*]. Cryogenic temperature tests have indicated a slight increase of LT fracture toughness upon decreasing the test temperature below room temperature; S-T fracture toughness, instead, follows the usual path and decreases with the temperature [*4,5*]. The results indicate that the delaminations relieve through-thickness constraint and stresses in a thick sample, which is transformed in a laminate-like subsample system, the more marked the lower the temperature. Furthermore, the critical stress intensity factor is thickness independent at least down to thicknesses of the order of one tenth or less of those foreseeable on the basis of the ASTM E 399-83 standard. Considering these results, one can deduce that plane strain conditions are restricted from the full thickness of the plate to the center of each ligament between delaminations.

The occurrence of pop-ins in Al-Li alloys is rarely mentioned in literature, probably because they complicate the application of the current standards for J_{Ic} determination, which explicitly exclude, for the sake of validation, events of this kind. Yet, they are clearly visible in the *R*-curves and may hide the critical event. Thus, the matter is still open for discussion. As for the 8090-T8 alloy, the pop-in behavior has already been quoted in Ref *6* and more explicitly discussed by the authors [*7*].

Another problem, which makes difficult the interpretation of fracture data, is the high degree of roughness of the fatigue precracked surfaces. This peculiarity has been already pointed out in many recent works on Al-Li fatigue crack propagation: at intermediate (ΔK) values, where the Paris law should be obeyed, a plateau in the da/dN-ΔK curves is often observed together with darkened areas on the sample fracture surface (see for instance, Ref *8*). The above-mentioned phenomena have been attributed to roughness-induced crack pinning and closure, which are able to alter the elastic part of the load-displacement (P-COD) diagram of a fracture test.

Summarizing, three main problems, namely delaminations, pop-in behavior, and precracked surface roughness, make difficult a reliable and unequivocal identification of the critical fracture event both on the *J-R* and *K-R* curves. There are additionally two characterizing aspects of the P-COD records in both TL and LT directions: a pronounced nonlinearity even at low load levels and the appearance of very small pop-ins well before P_{max}, Fig. 1. The diagram nonlinearity was already cited [*9*] but not explained; yet it contradicts the standard implicit hypothesis that the nonlinearity caused by plasticity or fracture propagation is confined to high load levels close to the critical event. This assumption is reflected in the requirement to determine P_Q by drawing a 95% offset slope line. In the 8090-T8 alloy case, the standard requirement shifts the critical event towards very low *K* values, which is reflected by the

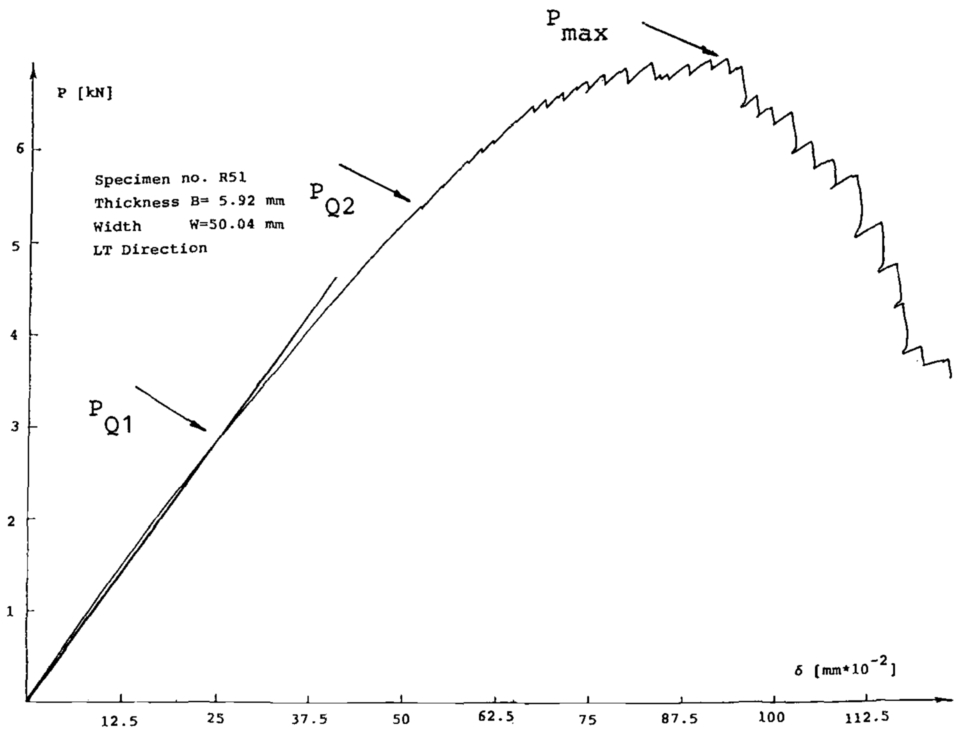

FIG. 1—*A typical example of a P-COD diagram showing nonlinearity and possible locations of the critical event.*

fact that P_{max}/P_Q will be mostly greater than 2. As already clarified [*3,7*], these values do not represent the real physical critical event. Moreover, this kind of nonlinearity is not reproducible and consequently results in a broad scatterband for K_Q values.

As already reported [*3*], the identification of P_Q at the first pop-in allows a significant reduction in the K_Q values' scatterband. Nevertheless, the K_Q values determined at the first pop-in are still too low, since the real critical event (onset of tearing), as determined by the J analysis [*7*], Fig. 1, is located at higher load levels.

In conclusion, in the case of the 8090-T8 alloy, in both TL and LT directions, the ASTM E 399-83 does not yield a meaningful criterion for a valid K_{Ic} determination. It is necessary to reexamine more thoroughly the whole problem of the fracture toughness of Al-Li alloys, giving special consideration to the microstructure of the alloy and its influence on the fracture micromechanisms.

Experimental Procedures

The material tested was provided by the Pechiney Co. in the form of AA 8090-T851 with a 12-mm thickness, B. The average chemical composition is shown in Table 1; chemical analyses were checked at four different locations in the plate, namely at the surface, at a distance of $B/6$ from it, at $B/3$, and at the core. The deviation in the chemical composition from the average was found not significant.

Experimental investigations on the microstructure were effected by metallographic analyses

TABLE 1—*Chemical composition of AA 8090 alloy (wt %).*

Li	Cu	Mg	Fe	Si	Zr	Al
2.38	1.39	0.74	0.2	0.1	0.12	balance

and X-ray diffraction tests. The former were carried out on the short transverse (ST) and short longitudinal (SL) planes, which are the fracture planes of specimens tested in the LT and TL directions, respectively. Optical micrographs were also taken from sections perpendicular to the fracture surfaces of the fracture toughness samples in order to evaluate the delamination spacings and, qualitatively, the degree of stress relieving near them. The X-ray analyses were performed by a Rigaku system, making possible the assessment of the existence of various kinds of precipitates and the investigation of the degree of recrystallization by texture analysis.

Tension and fracture tests and fractographic analyses were also performed. Both LT and TL direction CT specimens were machined from the plates. Fracture toughness (K_{Ic} and J_{Ic}) as well as K-R curves tests were carried out at room temperature, as specified by ASTM E 399-83; ASTM Test Method for J_{Ic}, a Measure of Fracture Toughness (E 813-88); and ASTM Practice for R-Curve Determination (E 561-83), using an MTS servohydraulic system under strain control. The crack growth was determined employing the unloading compliance single specimen technique. Four values of specimen thickness, B = 4, 6, 10, and 12 mm, with two values of width, W = 50 mm, for specimens with B = 6 mm and B = 10 mm, and W = 26 mm for the rest, were adopted for J tests, whereas, for K_{Ic} as well as for K-R curves tests, additional CT samples with B = 2, 8, and 10 mm and W = 26 mm width were used. Thinner samples (B = 2 and B = 4 mm) were machined from the plate's outer part. The CT samples fracture surfaces were observed by an ISI scanning electron microscope.

Experimental Results and Discussion

Microstructure of the 8090-T851 Alloy

The 8090-T8 is a peak-aged Al-Li alloy; the thermomechanical heat treatment consists of solubilization for 2 h at 535°C, water quenching, 3% stretch, and aging for 16 h at 190°C. The alloy shows a highly anisotropic, mostly unrecrystallized grain structure at the center of the plate, with pancake-shaped grains elongated in the rolling direction where the crystals are coarse, about 1- or 2-mm long, 350 μm wide and 20 μm thick (Fig. 2*a*). On the surface, Fig. 2*b*, an anisotropic recrystallized structure exists; due to the zirconium action, recrystallization was possible only during solubilization and was restricted almost entirely to the surface of the plate, more stretched than the interior during rolling. The intermediate plastic deformation during the T8 treatment was so limited (3% stretching) that it left the microstructure roughly unchanged, increasing the dislocation density but not altering the number and the shapes of the grains.

This fact was confirmed by X-ray analysis; both at the surface and at the center of the plate, the crystallographic structure is highly textured. The different state of crystallographic orientation between the surface and the core is shown in Table 2, where the diffraction pattern intensity of some crystallographic planes of the Al lattice is reported. The core, mainly unrecrystallized, which had undergone a severe amount of deformation before the solubilization, develops a preferred orientation which gives rise to the strongest diffraction intensity along the (220) plane instead of the (111) one, the aluminum maximum density plane. On the surface, the recrystallization of the stretched metal during solubilization produces a preferred orientation different from that existing in the core [*10*]. The recrystallization texture, which has not

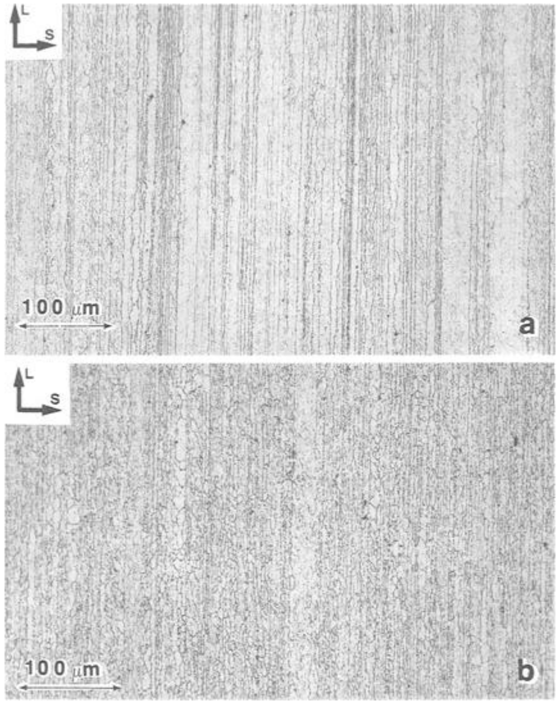

FIG. 2—(a) *Comparison between unrecrystallized core and* (b) *recrystallized surface part (etchant: Keller's reagent).*

been modified by the weak stretching during the T8 treatment, gives the strongest diffraction intensity along the (200) plane.

It is well known from the literature [*11*] that on aging 8090 to a peak strength T8 condition, one sees the formation of the following precipitates:

1. δ'-(Al_3Li) metastable, coherent, ordered, spherical-shaped, strengthening; it nucleates homogeneously in the Al matrix or heterogeneously on existing β' particles.
2. S'-(Al_2CuMg) metastable, semicoherent, lathlike-shaped, strengthening; it nucleates heterogeneously along the matrix dislocations produced during the T8 stretching, low-angle grain boundaries, or other structural inhomogeneities.

TABLE 2—*Aluminum crystallographic planes diffraction patterns in the tested Al-Li alloy: comparison between intensity at the surface and at the core. Annealed aluminum values are reported for reference.*

Plane	(111)	(200)	(220)	(311)
$(I/I_{max})_{surface}$	0	100	13	9
$(I/I_{max})_{core}$	3	6	100	2
$(I/I_{max})_{Al}$	100	47	22	24

3. T_1-(Al_2CuLi) equilibrium, lathlike-shaped particle, strengthening; it nucleates heterogeneously on dislocations, low-angle grain boundaries and other structural inhomogeneities.
4. β'-(Al_3Zr) coherent particle, dispersoid, suppressing recrystallization.
5. T_2-(Al_6CuLi_3) equilibrium particle, displaying five-fold icosahedral symmetry; it nucleates mainly on high-angle grain boundaries, with reduction of ductility and fracture toughness.
6. δ-(AlLi) equilibrium particle, precipitates heterogeneously at grain boundaries after high temperatures or long aging times.

In the present case, the X-ray diffraction analysis excluded the presence of δ, confirming that the alloy was not overaged. Also, the presence of T_2 is excluded, according to the fact that its presence is possible only in the very thick sections [*12*] where the cooling rates during quenching may be low in the core, which is not the present case because the plate is only 12-mm thick. Instead, T_1 particles were detected, but only in traces, and the same situation holds also for β' particles: in fact, these precipitates do not represent the major volumetric fraction. The major precipitate constituent, apart from δ', which is always present, resulted as being S'.

The precipitation occurs quite uniformly throughout the Al matrix. However, aging produces a preferential precipitation, mainly of δ', at the grain boundaries, with consequent formation of PFZs (precipitate-free zones).

Tensile Properties

The tensile properties of the 8090-T851 alloy are reported in Table 3. The values show clearly that this is a medium-high-strength alloy, even better than 2214-T651 and 7075-T73, whose tensile properties are 50 MPa lower. Even more, the strength level of 8090-T851 is comparable to that of 7475-T7351 plate.

J-R *Curves*

J-R curves, for both the TL and LT directions (Figs. 3 to 6), show local broad scatterbands, mainly at low *J* levels. In these conditions, it is quite impossible to recognize a straight line, corresponding to the blunting stage. However, a stretched zone was identified by fractography (Fig. 7), proving that a blunting phenomenon does indeed exist, but it is masked by another phenomenon already cited in the introduction: the roughness of the fracture surface, produced by fatigue propagation, which results in an alternate crack closure and opening during the initial unloading-reloading sequence. Compliance data thus do not reflect actual crack lengths. This behavior is further complicated by partial delaminations and subsequent formation of alternate plane strain and plane stress zones. This causes a marked increase of COD at constant load and hence compliance, its amount being dependent on the total fraction of resisting plane stress ligaments [*7*]. When the actual crack front evens out after a certain degree of crack

TABLE 3—*Tensile properties of AA 8090-T851.*

Crack Plane Orientation Code	σ_{YS}, MPa	σ_{TS}, MPa	e_f, %
LT	474	547	6.2
TL	482	543	7.5

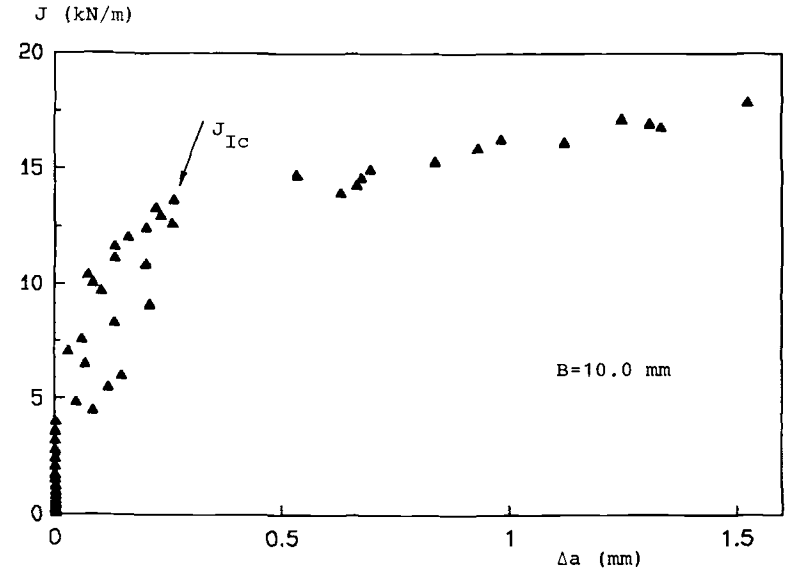

FIG. 3—J-Δa *curve for a 10-mm-thick TL sample, showing the location of the critical event.*

growth and prevailing plane strain conditions are resumed, the compliance reduces somehow, resulting in an apparent crack healing in the J-Δa diagrams. When further delaminations appear at higher loads, the phenomenon is repeated up to the time that they are well enough established to constantly control the fracture process. Both these phenomena (crack roughness and delaminations) are also present after the critical crack growth event, but now, due to the higher load levels, the surface roughness plays a minor role, and so the scatterband is narrower.

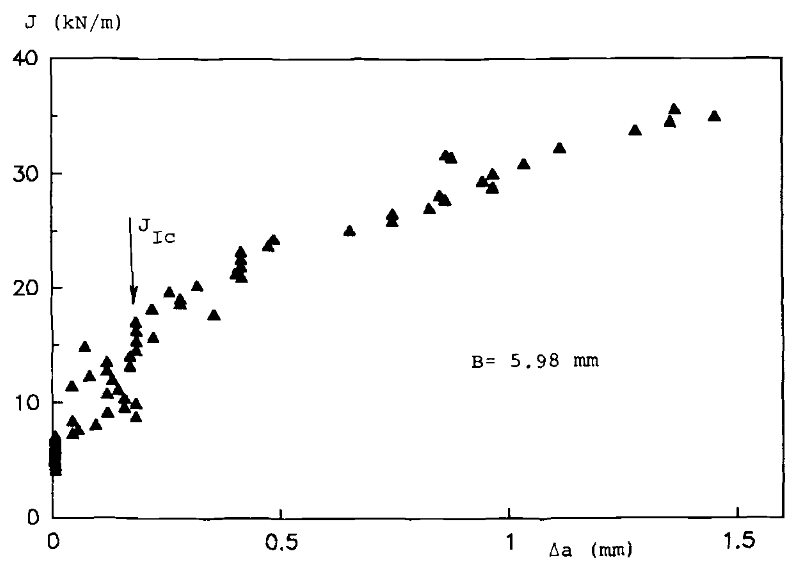

FIG. 4—J-Δa *curve for a 6-mm-thick LT sample, showing the location of the critical event.*

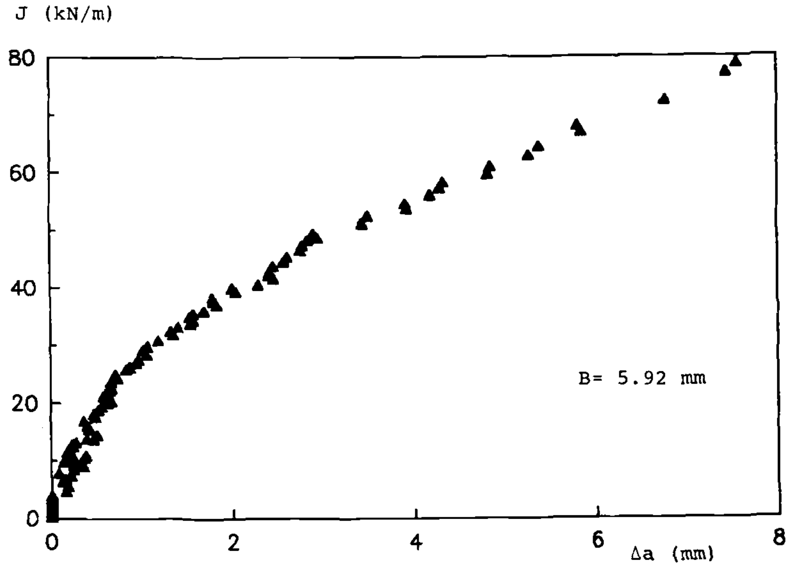

FIG. 5—*Complete* J-Δa *curve for a 6-mm-thick LT sample.*

Even in the presence of these difficulties, and even if the load-COD diagrams show numerous pop-ins, sometimes quite large (see for instance, the figures in Ref 7), which exclude the applicability of the existing standards on the fracture toughness J_{Ic} determination, a critical event is always recognizable on the *J-R* curves as the onset of tearing (see arrows in Figs. 3 and 4). The above conflicting statements are further discussed below.

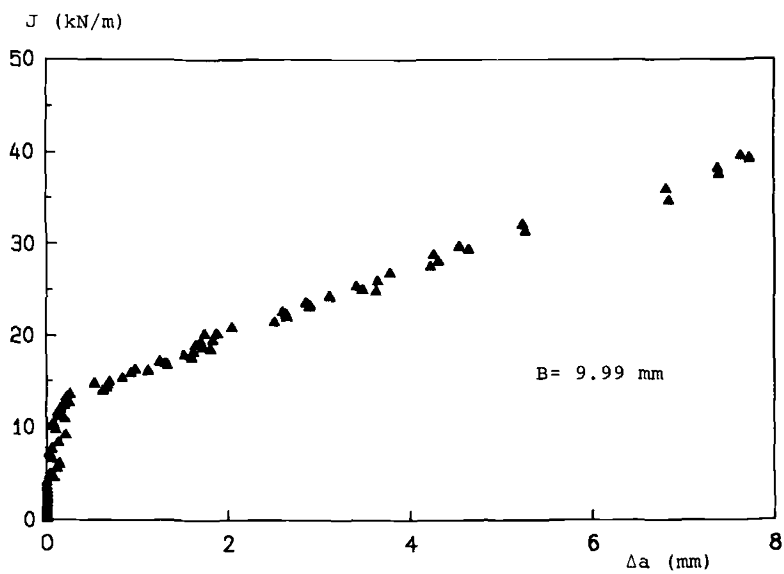

FIG. 6—*Complete* J-Δa *curve for a 10-mm-thick TL sample.*

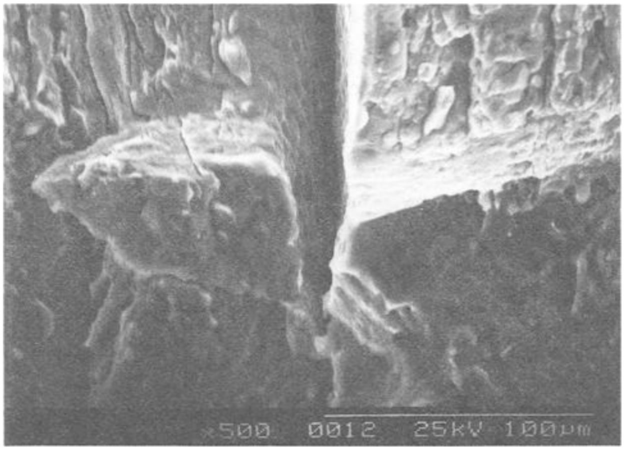

FIG. 7—*A delamination originating in the fatigue precracking zone (bottom) passing through the stretched zone.*

The inapplicability of existing standards for J_{Ic} determination is stated in different terms in each of them; ASTM E 813-87 specifies that the critical event to be singled out is the "initiation of slow stable crack growth," while the new ESIS Recommendations for Determining the Fracture Resistance of Ductile Materials (P 1-90) specifically excludes materials which exhibit a pop-in behavior.

On the other hand, taking into account the already given explanation of the pop-in behavior [7], which linked large pop-ins with the sudden failure of the resisting plane stress ligaments formed after the delamination occurring, a consistent response of the alloy to increasing stress concentrations at the crack tip yielding a regular tearing curve is reached only when delaminations are stably formed and are propagated well beyond the process zone. Having recognized that the first portion of what is usually termed "blunting line" ends at too low J-values [7], which are without engineering significance, it was decided to locate the critical event at the onset of the tearing portion of the J-R curve, which corresponds to a significant slope variation (Figs. 3 and 4). Thus, it is possible to determine the critical value of the J-integral, which was found well reproducible and with no more than $\pm 9.4\%$ dispersion for TL and $\pm 5.3\%$ dispersion for LT direction around the average value, Table 4.

The fracture toughness J_{Ic} was found to be thickness and width independent at least in the tested ranges. Values of 16.9 kN/m for the LT direction and of 13.8 kN/m for the TL direction were determined.

K-R *Curves*

K-R curves were also determined for each thickness, width, and direction (for example, see Figs. 8 to 10). Due to the already cited roughness and delamination phenomena, these curves show a certain degree of scatter, too, although to a lesser extent than in the case of J-R curves. A typical feature of the K-R curves (Fig. 8) is that its first portion does not follow the classical trend, often showing unpredictable changes in concavity. Moreover, the presence of pop-ins in the load-COD diagrams, as already signaled, often accompanied by sudden crack propagations, gives rise to singularities in K-R curves and to a peculiar points distribution in groups.

Upon examining Fig. 8, it can be seen that the classical shape of the K-R curve in the blunt-

TABLE 4—*Results of* J_{Ic} *tests.*

Specimen Index Code	Specimen Width, mm	Specimen Thickness, mm	Orientation Code	J_{Ic}, kN/m	K_{JIc}, MPa$\sqrt{m}$
R 27	26.03	3.96	LT	17.0	38.6
R 77	26.07	4.07	LT	17.6	39.3
R 47	50.20	5.96	LT	16.0	37.4
R 51	50.04	5.92	LT	17.0	38.6
R 62	49.88	5.98	LT	17.0	38.6
R 71	50.57	10.00	LT	16.2	37.7
R 44	50.00	10.00	LT	17.0	38.6
R 17	26.04	11.87	LT	17.0	38.6
R 21	26.09	11.85	LT	17.5	39.2
R 76	26.17	3.97	TL	13.1	33.3
R 55	50.22	5.98	TL	12.5	32.5
R 79	50.90	5.99	TL	14.5	35.0
R 50	49.96	10.02	TL	14.0	34.4
R 52	50.17	10.01	TL	15.0	35.6
R 54	50.15	9.99	TL	14.0	34.4
R 12	26.08	11.62	TL	13.5	33.8

ing stage is not respected. There are two main factors that affect and modify the shape of the first part of the *K-R* curves for the 8090-T8 alloy. The first factor, whose influence is more pronounced in the lower part, is the surface roughness produced during the fatigue precracking. It is located in the unrecrystallized zones in the core of the original plate. After fatiguing, the samples were unloaded and then reloaded during the fracture test. In the first loading stages, the crack behaves as a shorter one because of the roughness-induced crack closure. As the applied K approaches the value of K_{max} applied in the final fatigue cycles, the crack begins to open, with the apparent crack length being still smaller than the real one. Owing to the surface morphology, the crack opening is not continuous, with discrete jumps determined by

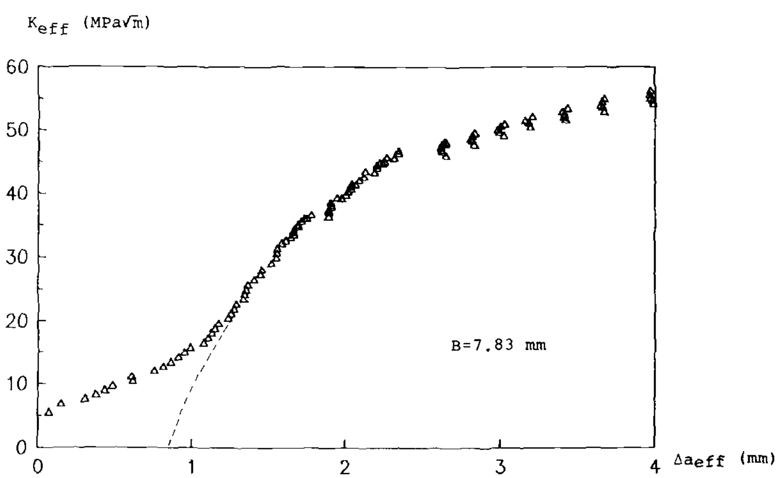

FIG. 8—K_{eff} – Δa_{eff} *curve for an 8-mm-thick LT sample. The dashed line represents an approximation of the real blunting stage.*

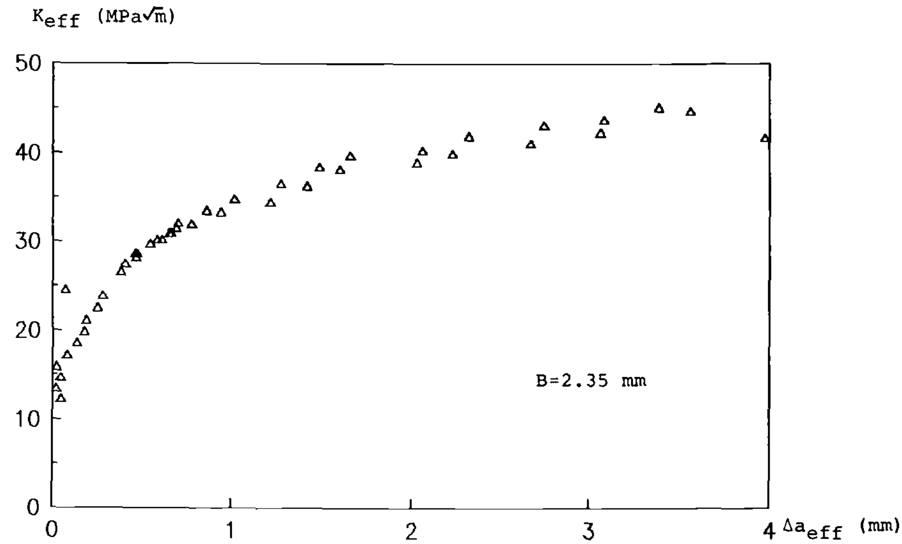

FIG. 9—*Normalized* K_{eff} — Δa_{eff} *for a 2-mm-thick TL sample.*

sudden unlocking of large surface portions, thus generating a pop-in behavior at low load levels. In these conditions, there is no real correspondence between initial sample compliance and the true crack length obtained by fatiguing. Calculations performed without taking into consideration this fact yield an initial compliance which indicates an apparent crack length lower than the real one, thus overestimating the effective crack propagation. Referring to Fig. 8, this

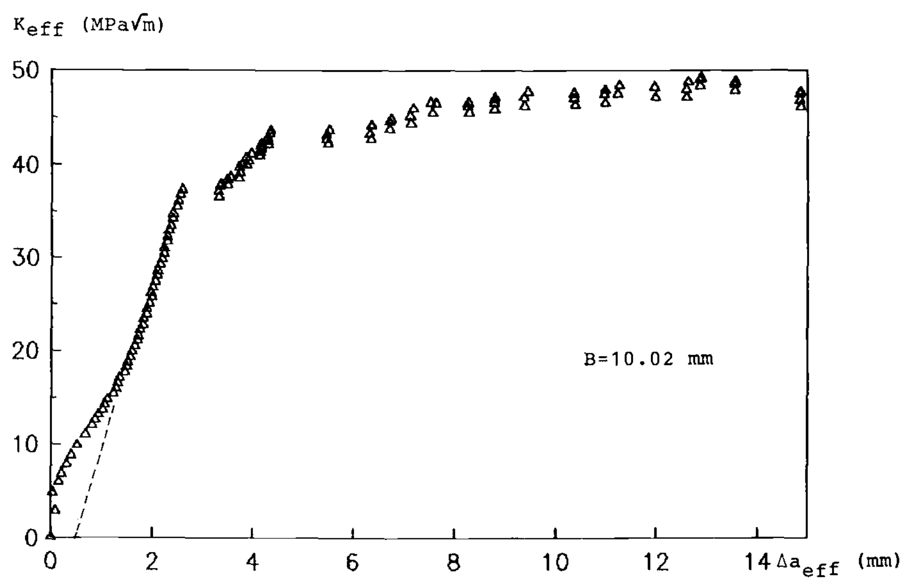

FIG. 10—K_{eff} — Δa_{eff} *curve for a 10-mm-thick TL sample, The dashed line represents an approximation of the real blunting stage.*

phenomenon is represented by the first, low-slope part of the K-R curve, which is consequently only a virtual one.

In the thinner samples, mainly consisting of recrystallized material, taken from the outer part of the plate, there is little surface roughness, crack closure is not manifested, and the apparent K-R curve coincides with the real one (Fig. 9).

The second factor affecting the blunting shape of the K-R curves is the delaminations, which begin to occur even during fatigue precracking (Fig. 7). Such a phenomenon, producing local plane-stress states inside the sample, relaxes thickness constraint and gives rise to a local increase in plastic zone size and consequent increase in the effective crack length. Thus, the apparent changes in concavity and the sometimes low slopes of the K-R curves before the critical event may be justified.

A further phenomenon may cause another difficulty in the interpretation of the K-R curves (Fig. 10). Often, at the end of the first reblunting stage, K_{eff} values follow a straight line. This is related to the fatigue surface morphology, which, in these cases, shows an extremely pronounced elevation in the unrecrystallized material. Thus, the fatigue front does not lie on an average flat surface, giving rise to a local mixed fracture Mode I, II, III on the crack tip during blunting. In these cases, the critical event occurs by pop-in, resulting in a discontinuity of the K-R curve (Fig. 10). After the critical event, the crack plane flattens and the fracture surface becomes similar to that observed on the other samples. Sometimes, when crack branching occurs, the situation is even more complicated. This phenomenon has already been reported and investigated [*13*]. Crack branching is always located in the unrecrystallized central part of the sample, in the fatigue surface (Fig. 11), immediately before or in the stretched zone. Secondary cracks appear to be shallow and finely dispersed. Severe bifurcation of the crack is usually seen in underaged Al-Li alloys, where the ordered δ' particle, inducing slip planarity, deviates the propagation along intense shear bands in the plastic zone during the onset of quasistatic fracture [*13*]. Alloy 8090-T8 is peak-aged, and so the branching that occurs at high K levels a little before fracture initiation is not related to δ' particle deviation effect but rather to the strong crystallographic texture. These secondary cracks influence the blunting stage because they give rise to energy absorption and diminish the stress concentration at the main crack tip.

All these particular fracture surface features suggest that the stress-strain state and the degree of constraint at the crack tip is not strictly reproducible from one sample to another. The loss

FIG. 11—*Branching of the crack on the fatigue surface in the plate core unrecrystallized zone. On the right, fatigue striations are visible.*

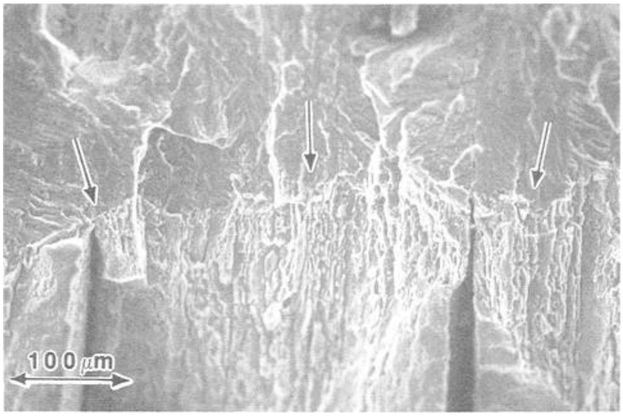

FIG. 12—*Transition from the fatigue surface (top) to the fracture surface (bottom). Arrows indicate the end of the fatigue propagation. In the lower part, two delaminations are clearly visible as well as the beginning of the shear lips.*

of thickness constraint is reproducible in the material near the surface of the plate (Fig. 12), where delaminations occur with a regular interspace and with development of shear lips. Since the crack is located in recrystallized material, the degree of constraint varies independently of the sample thickness, depending only on the delamination interspace. When the crack is located in the unrecrystallized material, the delaminations are less pronounced and the spacings are not regular (Fig. 13).

Taking into consideration the criteria that the standards prescribe about the determination and the validation of K_Q as K_{Ic}, and the difficulties during their application and in the identification of the critical event, it is likely that a unique K_{Ic} value (ASTM E 399) does not exist for Alloy 8090-T8. On the other hand, as already proved [7], in the case of J tests the results were well reproducible and independent of thickness, leading to K_{JIc} values equal to 34.2 MPa$\sqrt{m}$ for TL direction and 38.5 MPa$\sqrt{m}$ for LT direction.

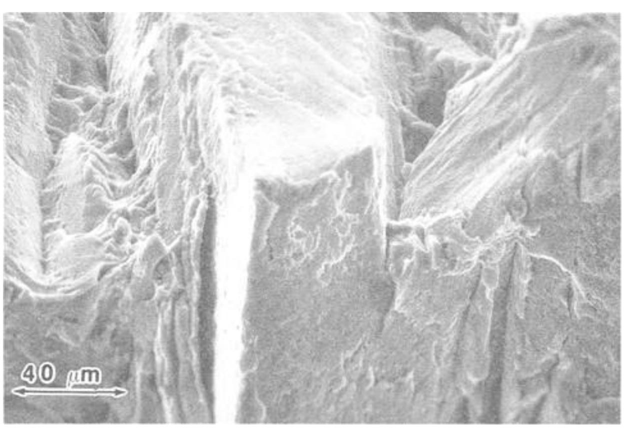

FIG. 13—*Stretched zone in the plate core unrecrystallized part. Delaminations are fairly evident; a change in surface orientation occurs, advancing from the fatigue to the fracture zone.*

On the basis of the previous considerations, the explanation of this independence remains difficult. Perhaps there exists a kind of compensation between the variable degree of thickness constraint in different samples and the nonplanarity of the crack surface in the unrecrystallized material at the onset of the quasistatic fracture. The mainly unrecrystallized material at the plate core, undergoing mixed mode fracture, is characterized by a lesser degree of Mode I thickness constraint and is therefore less stressed in the thickness direction: σ_z will consequently be lower and the same will occur for the tendency to the delamination. This assumption is reinforced by the results of the metallographic analysis. In fact (Fig. 14), it was seen that the tendency to delaminate depends only on the σ_z levels and not on the material state (recrystallized or not) because the intergranular decohesion occurs always at the prior high-angle grain boundaries.

Furthermore, owing to all the previous explained problems, it is possible to show that the *K-R* curve, apart from the blunting stage, possesses a good thickness independence. This is possible if the initial apparent compliance phenomenon, which is crack-closure dependent and variable from a sample to another, is taken into proper consideration. Since a low slope in the first part of the *K-R* curve (Fig. 8) is to be considered virtual, without physical representativity, it can be ignored by extrapolating to zero the high slope blunting part of the curve. The extrapolation criteria are surely affected by some degree of arbitrariness, but in this way it is possible to translate roughly the curve to more physically based Δa_{eff} values and to eliminate the overestimate in K_{eff} caused by the overestimate in Δa_{eff}. The results of the normalization process of the *K-R* curves are reported in Figs. 15 and 16 for TL and LT directions, respectively. Only the curves corresponding to thickness values B of 2, 6, and 10 mm are reported for clarity reasons. As can be seen, there exists a good overlapping of the representative curves of different thickness values. Except for the mixed mode fracture case, shown in Fig. 15, corresponding to thickness $B = 10$ mm, where the blunting part of the curve is roughly linear instead of curved, the overlapping is good also in the blunting stage.

Another interesting reproducible feature of these curves is their tendency to reach a plateau, whose level is roughly located at 40 MPa $\sqrt{m}$ for TL and 50 MPa $\sqrt{m}$ for LT directions. These plateau levels can be interpreted as corresponding to a saturation value and coincide with the P_{max} and the zone immediately after on the load-COD diagram. The plastic zone size remains

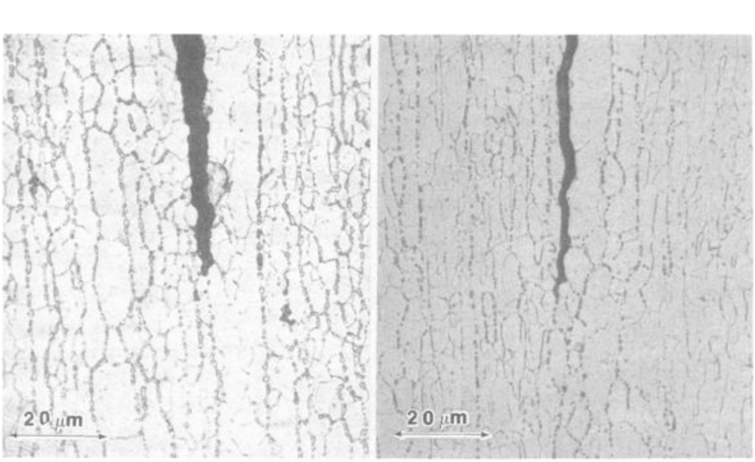

FIG. 14—*Delamination along high-angle grain boundaries, on the left for the recrystallized surface, on the right for the unrecrystallized core. In both cases, the delamination is located at the prior high-angle grain boundaries.*

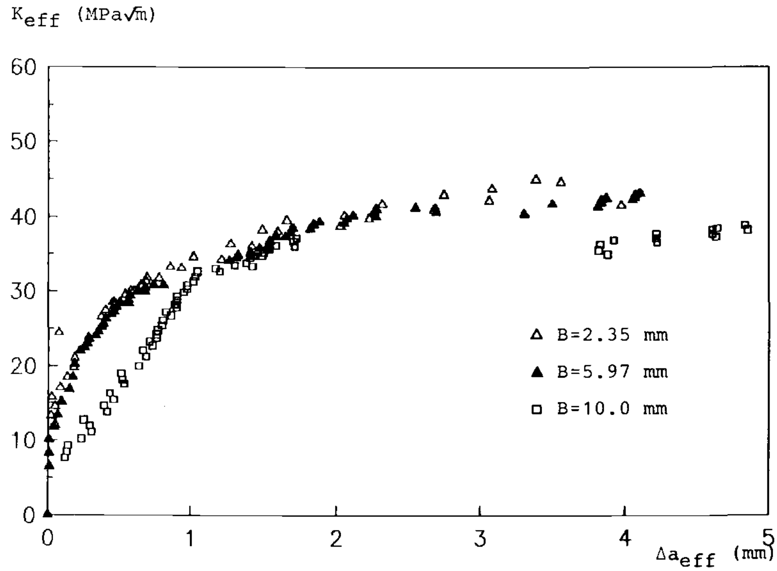

FIG. 15—*Superimposition of various K_{eff} — Δa_{eff} curves corresponding to different thickness values for TL samples. Apart from the blunting stage, a good overlapping is verified on the rest of the curves.*

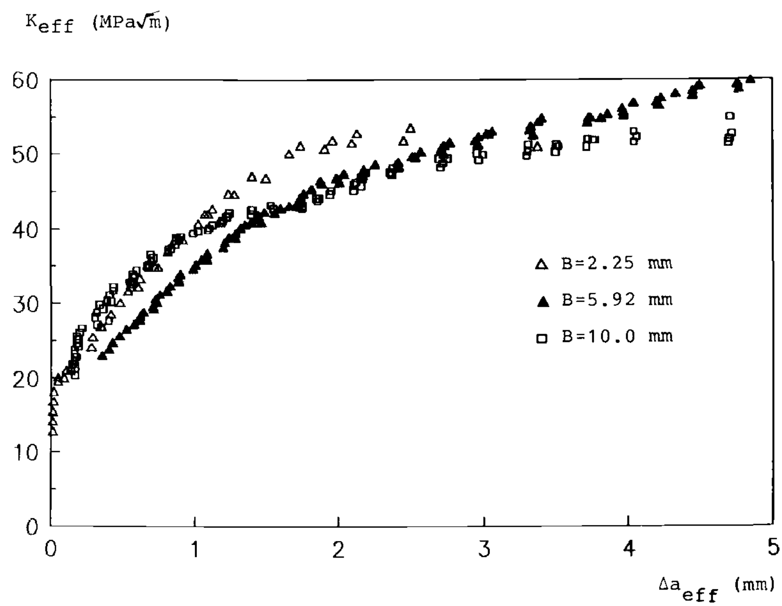

FIG. 16—*Superimposition of various K_{eff} — Δa_{eff} curves corresponding to different thickness values for LT samples. A good overlapping is verified.*

constant (does not grow further); the crack propagates physically. At this stage, the physical crack increase does not alter noticeably the total crack length as compared to the sample geometry, and the propagation is compensated by slight load decrease beyond P_{max}. The examination of the TL and LT fracture surfaces after the onset of propagation reveals that slant fracture zones ratio to sample thickness agrees quite well irrespective of the thickness, ranging around 60%. This observation agrees with the hypothesis that plastic zone size remains approximately constant. Correspondingly, the slope of the J-Δa curve is nearly constant [*14*] as shown in Figs. 5 and 6. A further confirmation results from the particular point distribution in the plateau: it yields grouped points, spaced by pop-ins. In each points group the crack does not grow, so giving rise to a new little-pronounced high K level blunting.

Finally, on the basis of the previous considerations, from an engineering point of view, it can be considered that K_{JIc} values are material characteristics and thickness independent. The difference between LT and TL values can be explained by the deeper extent of delaminations in the former case (Fig. 17). Remembering that the crystal dimensions perpendicular to the fracture plane are larger in the LT direction as compared to the TL one, a more pronounced intergranular short transverse fracture means a more complete σ_z relaxation, leading to larger plastic zones.

Conclusions

The fracture toughness resistance of AA 8090-T8 rolled plate has been assessed. J_{Ic}, K_{JIc}, and K-R curves for LT and TL directions were determined. Problems related to fatigue surface roughness, to the loss of thickness constraint due to delaminations, and to a peculiar pop-in behavior made difficult the application of the current fracture toughness standards. Nevertheless, the following was proved.

1. J_{Ic} values are well reproducible and size independent.

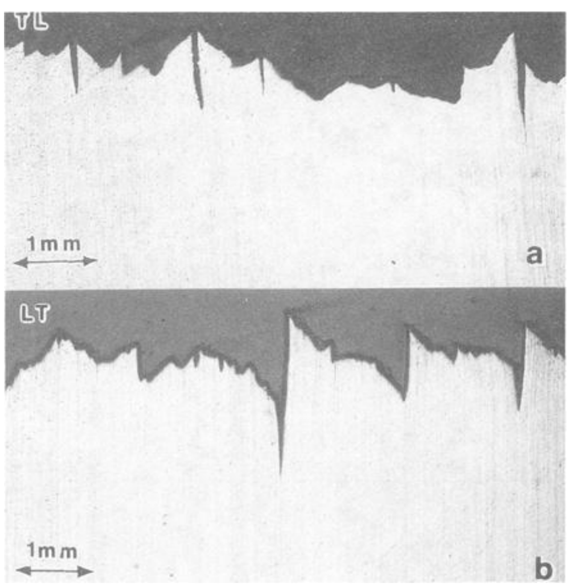

FIG. 17—*Micrographs of sections perpendicular to the fracture plane: comparison between the depth of delaminations.*

2. K_{JIc} values are representative of the linear elastic fracture toughness, which cannot be determined in a straightforward manner via the ASTM E 399 standard.
3. Delaminations and mixed mode fracture during blunting enhance the fracture resistance relaxing thickness constraint.
4. *K-R* curves are thickness independent and overlap well within the entire range of crack propagation, if misleading information from the initial apparent compliance is discounted.
5. Owing to the described loss of thickness constraint, an intrinsic geometry independence is always reached.

Acknowledgment

Work partially funded by Italian Ministry for university and scientific research (60%).

References

[*1*] Rao, K., Venkateswara, T., and Ritchie, R. O., "Mechanical Properties of Al-Li Alloys, Part 1: Fracture Toughness and Microstructure," *Material Science and Technology*, September 1989, Vol. 5, pp. 882–895.

[*2*] Morrison, J. and Karisallen, K. J., "Orientation Dependence of Fracture Toughness in 8090 Aluminum Alloy Plate Using Chevron Notched Specimens," *ECF8-Fracture Behaviour and Design of Materials and Structures*, D. Firrao, Ed., Engineering Materials Advisory Service, Warley, United Kingdom, 1990, Vol. 1, pp. 327–333.

[*3*] Doglione, R., Ilia, E., and Firrao, D., "L'effetto dello spessore sulla tenacità a frattura K_{Ic} della lega alluminio-litio 8090-T8," *Proceedings*, VI Conv. Naz. Gruppo Italiano Frattura, A. Corvi, Ed., Ancona, Italy, 1990, pp. 181–196.

[*4*] Rao, K., Venkateswara, T., and Ritchie, R. O., "Influence of Extrinsic Crack Deflection and Delamination Mechanisms on the Cryogenic Toughness of Aluminum-Lithium Alloy 2090: Behavior in Plate (T81) vs. Sheet (T83) Material," *Aluminum-Lithium Alloys V*, T. H. Sanders, Jr. and E. A. Starke, Jr., Eds., Materials and Component Engineering Publications, Ltd., Birmingham, United Kingdom, 1989, pp. 1501–1512.

[*5*] Rao, K., Venkateswara, T., Yu, W., and Ritchie, R. O., "Cryogenic Toughness of Commercial Aluminum-Lithium Alloys: Role of Delamination Toughening," *Metallurgical Transactions A*, Vol. 20A, March 1989, pp. 485–497.

[*6*] Rao, K., Venkateswara, T., and Ritchie, R. O., "Mechanism Influencing the Cryogenic Fracture-Toughness Behavior of Aluminum-Lithium Alloys," *Acta Metallurgica et Materialia*, Vol. 38, No. 11, 1990, pp. 2309–2326.

[*7*] Doglione, R., Ilia, E., Scavino, G., and Firrao, D., "On the Applicability of J_{Ic} Standards to the Pop-In Behaviour of an Al-Li 8090-T8 Alloy," *ECF8-Fracture Behaviour and Design of Materials and Structures*, Vol. II, D. Firrao, Ed., Engineering Materials Advisory Service, Warley, United Kingdom, 1990, pp. 1052–1058.

[*8*] Peters, M., Welpmann, K., McDarmaid, D. S., and Hart, W. G. J., "Fatigue Properties of Al-Li Alloys," *New Light Alloys, Proceedings*, Conference No. 444, AGARD, Neuilly Sur-Seine, France, 1989, pp. 6-1 to 6-18.

[*9*] Chan, K. S., "Confirmation of a Sheet Toughening Mechanism and Anisotropic Fracture in Al-Fe-X Alloys," *Metallurgical Transactions A*, Vol. 20A, November 1989, pp. 2337–2344.

[*10*] Dieter, G. E., *Mechanical Metallurgy*, 3rd Ed., McGraw-Hill, New York, 1986, pp. 237–239.

[*11*] Starke, E. A., Jr. and Quist, W. E., "The Microstructure and Properties of Aluminum-Lithium Alloys," *New Light Alloys, Proceedings*, Conference No. 444, AGARD, Neuilly Sur-Seine, France, 1989, pp. 4-1 to 4-23.

[*12*] Lewis, R. E. and Starke, E. A., Jr., et al., "Microstructure and Properties of Al-Li-Cu-Mg-Zr (8090) Heavy Section Forgings," *Proceedings*, 4th International Al-Li Conference," *Journal de Physique*, C3, Tome 48, September 1987, pp. C3-643 to C3-652.

[*13*] Suresh, S., Vasudévan, A. K., Tosten, M., and Howell, P. R., "Microscopic and Macroscopic Aspects of the Fracture in Lithium-Containing Aluminum Alloys," *Acta Metallurgica*, Vol. 35, No. 1, 1987, pp. 25–46.

[*14*] Kolednik, O., "On the Physical Meaning of the J-Δa Curves," *Engineering Fracture Mechanics*, Vol. 38, No. 6, 1991, pp. 403–412.

Bernard Faucher[1] *and William R. Tyson*[1]

Size Limits for Brittle Fracture Toughness of Bend Specimens

REFERENCE: Faucher, B. and Tyson, W. R., "**Size Limits for Brittle Fracture Toughness of Bend Specimens,**" *Constraint Effects in Fracture, ASTM STP 1171*, E. M. Hackett, K.-H. Schwalbe, and R. H. Dodds, Eds., American Society for Testing and Materials, Philadelphia, 1993, pp. 306–317.

ABSTRACT: Fracture toughness data obtained previously from three-point-bend 10-mm, 20-mm, and 50-mm-thick side-grooved specimens and from 10-mm-thick plain-sided specimens are reanalyzed with respect to constraint. The test temperatures were low enough for the grade of steel used to ensure brittle fracture without any initiation of ductile tearing; nevertheless, extensive crack-tip blunting was observed at the highest temperatures, resulting in a highly non-linear load-deformation behavior. Fracture toughness was evaluated from the J-integral value at the onset of brittle fracture, J_c. An equivalent stress intensity factor K_J was then obtained from the relation $K_J^2 = E'J_c$. The elastic stress intensity factor, K_c, is shown to be equal to K_J for specimen thicknesses down to half the size requirements of ASTM E 399. The macroscopic constraint, defined from the load-carrying capacity of the specimens, is independent of thickness for side-grooved specimens over the range of thicknesses studied in this work; however, it decreases slightly for plain-sided specimens. The results indicate that even when the validity limits for plane-strain fracture toughness evaluation as specified in ASTM E 399 are largely exceeded, it is still possible to measure plane-strain toughness of brittle materials using the J-integral. The results suggest that the validity limits of ASTM E 813 for measurement of cleavage fracture toughness should be increased by a factor of about two.

KEY WORDS: brittle fracture, constraint, side grooves, thickness effects, ferritic steel, fracture toughness

At low ("lower shelf") temperatures, cleavage of ferritic steels is initiated on a plane normal to the principal tensile stress from micro-cracks, often inclusions or particles, when the local stress exceeds the Griffith stress [*1*]. The fracture toughness is low enough to be characterized by the critical value of the plane-strain stress intensity factor, K_{Ic}, for practical thicknesses. At high ("upper shelf") temperatures, plastic flow occurs at stresses well below the fracture stress, which promotes the formation and growth of cavities leading eventually to ductile tearing. The fracture toughness may be characterized by the critical value of the J-integral for initiation of tearing, J_{Ic}. There is, therefore, a well-known transition range, where the toughness increases rapidly with the temperature. For modern clean steels containing few inclusions, cavities are widely spaced and micro-void coalescence occurs only after extensive deformation. For these steels, in the lower part of the transition range, cleavage may be preceded by extensive plastic flow without any ductile tearing. Because there is cleavage, but also extensive plasticity without tearing, the choice of the appropriate fracture toughness parameter is ambiguous.

Cleavage, which is normally observed only at low values of fracture toughness, is associated with plane-strain fracture. Plane-strain conditions are obtained with a thick specimen. It is

[1] Research scientist and program coordinator, respectively, Metals Technology Laboratories, CANMET, Energy, Mines and Resources, 568 Booth Street, Ottawa, K1A 0G1, Canada.

more difficult to observe cleavage in a thin specimen where plane-stress conditions prevail because the value of the principal tensile stress to cause plastic flow is smaller than for the plane-strain state [2]; the constraint is low, and large shear lips are observed on the fracture surface. Because the formation of the shear lips by plastic flow absorbs much more energy than cleavage, this results in the well-known effect of thickness on fracture toughness: the toughness decreases as the thickness increases. However, there is another valid explanation for the effect of thickness on brittle fracture toughness, based on "weakest-link" statistics. The probability of initiating cleavage increases with the thickness because of the increased probability of having a "weak spot."

ASTM standards impose very strict size limitations for the specimens used to measure fracture toughness. The ASTM Standard Test Method for Plane-Strain Fracture Toughness of Metallic Materials (E 399-90) requires the net thickness, B_N, (and the ligament) to be such that:

$$B_N \geq 2.5(K_{Ic}/\sigma_y)^2 \tag{1}$$

which for a steel with a yield strength $\sigma_y = 450$ MPa and a toughness of 200 MPa$\sqrt{\text{m}}$ demands a thickness larger than 500 mm. On the other hand, the ASTM Standard Test Method for J_{Ic}, a Measure of Fracture Toughness (E 813-89) requires only that

$$B_N \geq 25 J_{Ic}/\sigma_y \tag{2}$$

which for the same steel and using the plane-strain relation

$$J = K^2(1 - \nu^2)/E \tag{3}$$

with the elastic modulus $E = 207$ GPa, and Poisson's ratio $\nu = 0.3$ would demand the thickness be larger than 10 mm only, a reasonable specimen size. Therefore, it has become popular to evaluate fracture toughness from standard E 813 and use Eq 3 to obtain an equivalent stress intensity factor, usually called K_j. Although ASTM E 813 defines an effective yield strength to be used in Eq 2, which is the average between yield and ultimate tensile strength, only the yield strength has been used in both Eqs 1 and 2 in this study; for the steel used, the difference is of the order of 15%.

In addition to considerations of constraint, size limitations arise also from the conditions required for the fracture mechanics parameters to describe adequately the stress and strain fields ahead of a sharp crack. In linear elastic fracture mechanics, it is required that the plastic zone size, which is proportional to $(K/\sigma_y)^2$, would be only a small fraction of the specimen dimensions: the empirical requirements of ASTM E 399, Eq 1, correspond to a thickness about 50 times larger than the plane-strain plastic zone size. The question then arises: "Is the size limitation a result of loss of constraint which affects fracture micro-mechanism, or simply of loss of linear-elastic behavior?"

Based on former results, this paper will try to shed some light on the effect of size on constraint and linear elastic behavior for "brittle" steels failing by cleavage.

Experimental Details

All the specimens were cut from one 75-mm-thick steel plate that was partially controlled-rolled and normalized [3]. The chemical composition is given in Table 1, and the yield strength values indicated in Table 2 correspond to the strain-rate at the elastic-plastic boundary at the crack tip of a bend specimen at general yield [4].

TABLE 1—*Composition of the steel used.*

Element	Weight %	Element	Weight %
Carbon	0.12	Chromium	0.17
Silicon	0.28	Copper	0.25
Manganese	1.39	Molybdenum	0.001
Phosphorus	0.017	Nickel	0.15
Sulfur	0.011	Niobium	0.041
Aluminum	0.027	Vanadium	0.053

Fracture toughness tests were carried out on standard, $B \times 2B$, three-point-bend (TPB) specimens of different thicknesses, B. The specimens were fatigue precracked to a depth, a, of about 60% of their width, W, and most had V-grooves machined on each side to 10% of B. Typical fracture surfaces are shown in Fig. 1. The tests were run at low strain rates (crosshead speed/thickness < 0.005/s) and over a large temperature range.

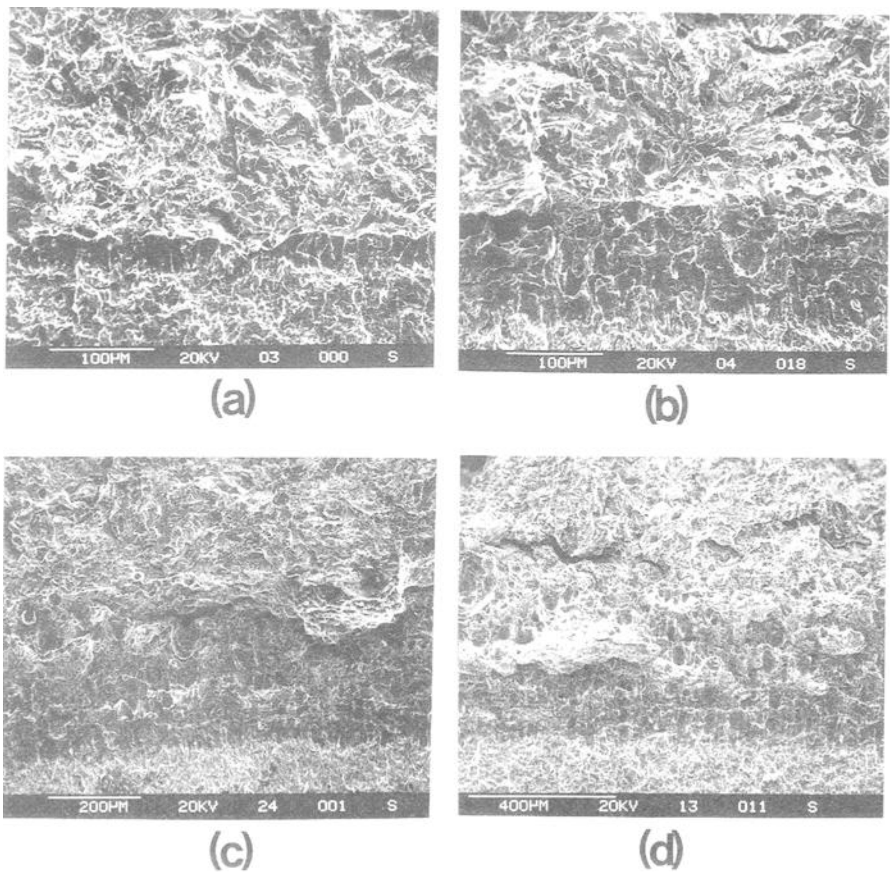

FIG. 1—*Scanning electron micrographs of fracture surfaces showing fatigue precrack, stretch zone, and cleavage area:* (a) *50-mm-thick specimen,* K_J = *91 MPa$\sqrt{m}$ at −100°C;* (b) *20 mm, 192 MPa$\sqrt{m}$ at −100°C;* (c) *10 mm, 317 MPa$\sqrt{m}$ at −100°C;* (d) *50 mm, 296 MPa$\sqrt{m}$ at −60°C* [4].

Experimental Results

All experimental fracture toughness values have been reported already in relation to the yield strength [3–5]. A set of data obtained with plain-sided (PS) specimens [6] is also included. All specimens failed by cleavage after more or less pronounced blunting (Fig. 1), depending on the testing conditions. Ductile dimples could be observed only at a few locations along the stretch zone for the toughest specimens (Figs. 1*c* and 1*d*).

Fracture toughness was evaluated at the onset of cleavage. In addition to the previously reported values of K_j, obtained from the value of J, values of K, calculated from the load at cleavage and initial crack length according to ASTM E 399, are also included as K_c in Table 2. Values of K_c do not satisfy the requirements of ASTM E 399, but they are related to the elastic part of the J-integral through Eq 3. Table 2 indicates also the lower yield strength associated with the testing conditions and the initial crack length. It can be easily verified that, except for the few specimens tested at the lowest temperatures, the validity requirements for size of ASTM E 399, Eq 1, are not met.

Most of the data have been used to obtain the parameters of a statistical model [1] giving the fracture toughness at a probability of failure, Φ, as [4]

$$\ln K = 40.35 + 0.248 \ln(50/B) - 5.74 \ln \sigma_y + 0.248 \ln \ln[1/(1\text{-}\Phi)] \tag{4}$$

where K is expressed in MPa$\sqrt{\text{m}}$, B in mm, and the lower yield stress, σ_y, in MPa. Equation 4 describes the temperature and strain rate dependence of the fracture toughness through the temperature and strain rate dependence of the lower yield stress. The effect of specimen thickness on the measured fracture toughness is also predicted by the statistical model, as seen in Fig. 2 [4].

The macroscopic constraint factor, L, is usually defined from the load, P, carried by a bend specimen as [2]

$$P = L\sigma_y(W - a)^2 B_N/(4W) \tag{5}$$

where B_N is the net section thickness. The normalized load, $PW/(W - a)^2B_N$, has been plotted as a function of the load-line-displacement (normalized by the width) in Fig. 3 for a few results. The normalized load is proportional to the constraint factor; however, to differentiate the curves at the two temperatures, the load values are not normalized by the yield strength. From each test result, a value of L was obtained at a value of the plastic crack-mouth-opening displacement of 0.002 W. The average values of L measured for the different geometries are given in Table 3. The constraint factor is independent of temperature. It is also independent of thickness for side-grooved specimens, but it is significantly lower for plane-sided specimens at 10-mm thickness.

Figure 3 shows that the specimens tested in this work fracture after general yield, although the micro-mechanism is cleavage. Figure 3 illustrates also that thick specimens fracture at a smaller deformation than thin ones.

Discussion

Size Effects

Constraint at the microscopic scale is usually characterized by the stress triaxiality, that is, the ratio of the hydrostatic stress to the equivalent stress, σ_m/σ_{eq}. Change of triaxiality with specimen geometry is of concern for the measurement of ductile fracture toughness: J_{Ic} is influenced by constraint since the crack tip field loses J-dominance at smaller deformation with

TABLE 2—*Yield strength, fracture toughness, and initial crack size for several specimen geometries: side-grooved specimens, unless otherwise indicated.*

B = 10 mm				
T, °C	σ_y, MPa	K_J, MPa$\sqrt{m}$	K_C, MPa$\sqrt{m}$	a_0, mm
−120	530	81	68	11.82
−120	530	101	71	11.04
−120	530	106	70	11.39
−120	530	108	75	10.61
−120	530	119	64	12.86
−120	530	124	61	13.99
−120	530	125	67	12.27
−120	530	126	69	11.77
−120	530	133	71	10.92
−120	530	141	69	11.78
−120	530	145	69	12.02
−120	530	145	63	13.27
−120	530	155	70	11.37
−120	530	165	74	11.13
−120	530	167	74	10.97
−120	530	192	73	11.74
−120	530	198	77	10.51
−120	530	198	77	10.95
−120	530	212	70	12.69

B = 10 mm				
T,°C	σ_y, MPa	K_J, MPa$\sqrt{m}$	K_C, MPa$\sqrt{m}$	a_0, mm
−90	456	320	66	11.68
−90	456	373		11.40
−80	431	347	75	11.62
−80	431	390		11.47
−80	431	407	76	11.69
−80	431	290	64	12.32
−80	431	361	66	11.66

B = 10 mm Plain Sided				
T, °C	σ_y, MPa	K_J, MPa$\sqrt{m}$	K_C, MPa$\sqrt{m}$	a_0, mm
−120	530	92	61	14.11
−120	530	99	66	11.80
−120	530	114	66	11.68
−120	530	116	67	12.16
−120	530	122	65	12.65
−120	530	128	66	12.57

B = 20 mm				
T,°C	σ_y, MPa	K_J, MPa$\sqrt{m}$	K_C, MPa$\sqrt{m}$	a_0, mm
−160	579	47	47	23.63
−160	579	81	78	25.33
−160	579	51	51	25.97
−140	521	91	77	26.82
−140	521	98	82	25.13
−140	521	100	85	23.79
−140	521	125	82	27.70
−140	521	133	97	21.55
−120	463	117	74	26.62
−120	463	118	82	23.72
−120	463	166	74	25.96
−120	463	193	84	24.03
−120	463	234	82	25.76
−100	413	230	84	23.06
−100	413	284	82	25.21
−100	413	321	84	25.83
−100	413	473	91	23.71
−80	387	443	90	23.80
−80	387	451	92	23.44

−120	530	275	78	11.12
−120	530	288	79	10.77
−160	628	30	29	10.84
−160	628	34	33	10.45
−150	604	48	46	11.15
−150	604	26	26	10.92
−140	579	40		11.10
−140	579	101	67	13.00
−140	579	37	37	10.72
−140	579	124	74	10.69
−130	554	123	71	10.64
−130	554	98	68	10.79
−120	530	78		11.02
−120	530	137	69	11.19
−120	530	71	60	10.48
−120	530	106	66	10.72
−110	505	201		11.32
−110	505	226	68	11.04
−110	505	146	64	11.38
−110	505	221	66	11.75
−110	505	258	66	10.71
−100	481	343	69	11.91
−100	481	403	71	11.23
−100	481	455	77	11.69
−100	481	232	63	12.34
−100	481	317	70	10.86

−120	530	132	70	12.04
−120	530	146	56	13.72
−120	530	150	69	10.59
−120	530	170	69	10.88
−120	530	207	69	12.81

B = 50 mm

T, °C	σ_y, MPa	K_J (MPa$\sqrt{m}$)	K_C (MPa$\sqrt{m}$)	a_0, mm
−140	576	40	40	60.11
−120	527	76	76	59.98
−100	477	91	88	60.72
−90	452	97	90	60.96
−80	427	101	96	60.85
−80	427	148	120	61.61
−80	427	182	116	61.14
−80	427	250	122	61.03
−70	412	240	123	61.20
−70	412	282	125	61.53
−60	398	296	122	61.30
−60	398	307	120	61.29
−60	398	322	121	60.90
−60	398	355	134	60.72
−60	398	385	121	60.90

−140	570	64	64	22.57
−130	554	69	68	26.13
−120	530	67		27.80
−120	530	122	94	22.74
−110	505	81	74	26.60
−110	505	120	91	24.26
−100	481	112	82	25.84
−100	481	192	92	22.04
−90	456	110	75	27.13
−90	456	171	75	28.45
−80	431	179	88	22.55
−80	431	181	84	23.62
−75	421	175	82	23.93
−75	421	468	98	22.26
−70	413	312	84	26.39
−70	413	381	67	25.25

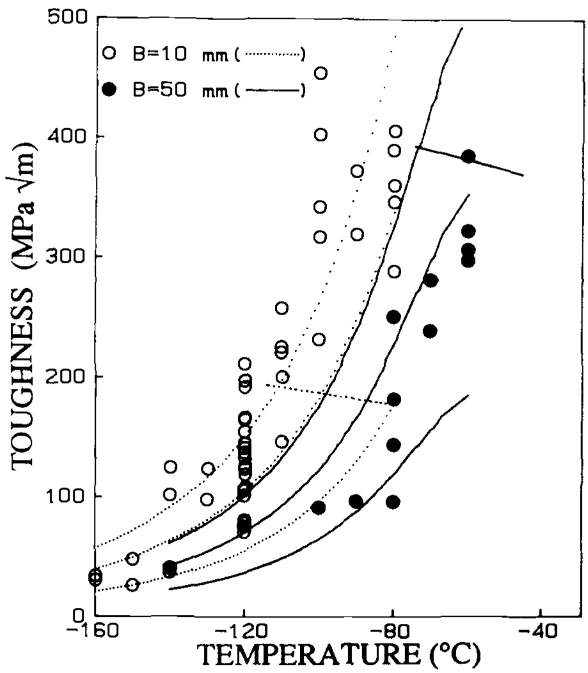

FIG. 2—*Comparison of experimental results with the predictions of the statistical model for 10 and 50-mm-thick SG specimens. The curves have been calculated at 5, 50, and 95% probability of failure* [4], *and the short lines correspond to the limits given by Eq 2 (limit of validity by ASTM E 813) for* B_N = *8 and 40 mm.*

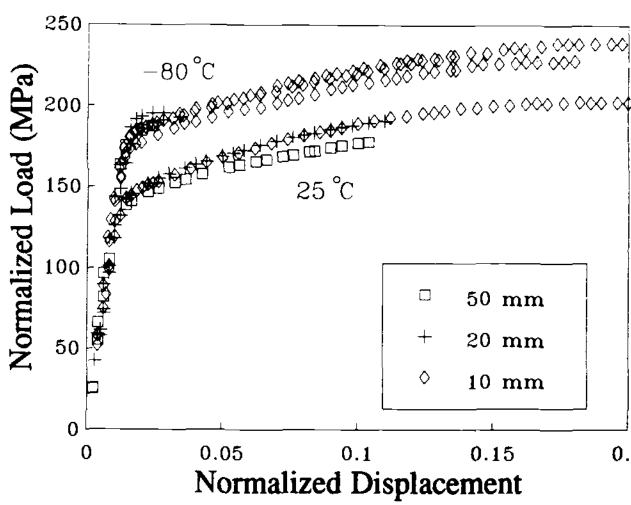

FIG. 3—*Normalized load,* $PW/(W - a)^2B_N$, *as a function of load-line-displacement normalized by the specimen width for SG specimens of various thicknesses at two temperatures. The specimens tested at 25°C did not fracture.*

TABLE 3—*Average value and standard deviation of the constraint factor for various side-grooved (SG) and plane-sided (PS) specimens of different thickness at a crack-mouth-opening displacement of 0.002 W.*

Specimen	50 mm, SG	20 mm, SG	10 mm, SG	10 mm, PS
L	1.60 ± 0.03	1.57 ± 0.06	1.57 ± 0.04	1.42 ± 0.05

geometries with low constraint than with high constraint [*7–8*]. Cleavage, however, is controlled locally by the principal tensile stress, σ_1, which, especially for deeply-cracked TPB specimens, is close to the value given by the HRR field [*9*] for plane-strain conditions [*7,8*].

Three-dimensional finite-element modelling of compact tension specimens [*10–11*] and three-point-bend specimens [*12*] have shown that side grooves promote a uniform state of stress close to plane strain along the crack front. Side grooves introduce additional out-of-plane constraint, which suppresses the formation of shear lips on the specimen sides independently of the specimen size. The results shown in Fig. 3 and Table 3 confirm at the macroscopic level that there is no loss of constraint for SG bend specimens as the thickness decreases from 50 to 10 mm; but, as indicated in Table 2, the constraint is lower for plain-sided than for SG specimens.

Size affects the brittle fracture toughness also through the statistical (weakest link) effect. The results presented here are adequately described (Fig. 2) by the statistical model of Eq 4, as long as the size requirements of ASTM E 813 are satisfied. This indicates that most of the size effect in the present work results from statistical sampling. Also, because the statistical model of Eq 4 is based on the J description of the stress field, the present results indicate that the microscopic constraint remains constant for side-grooved specimens when their size stays within the validity limits of ASTM E 813. The change of constraint with thickness is not significant when specimens are side grooved, even though the specimens do not meet the size requirements of ASTM E 399.

Thickness Effects

The fracture toughness may be expressed either in terms of K or J through Eq 3. When the material behavior is no longer linear elastic, as seen in Fig. 3, the crack-tip stress field cannot be described by K; it must be described by J. Hence, because brittle fracture is a stress-controlled phenomenon, the fracture toughness must be determined from the critical value of J in plastically deformed specimens.

To compare K_c and K_j, their ratio has been plotted as a function of the normalized thickness in Fig. 4. The normalizing thickness, B_{E399}, is defined from the ASTM standard E 399 as

$$B_{E399} = 2.5(K_J/\sigma_y)^2$$

All the points in Fig. 4 fall on the same curve, and $K_c = K_j$ down to approximately $B = 0.5B_{E399}$. This indicates a linear elastic behavior down to a size about half the size requirements of ASTM E 399 for bend specimens. The ratio K_j/K_c at a given value of KJ increases as the thickness decreases in the elastic-plastic range. That is, the amount of plastic deformation in specimens of similar geometry increases as the thickness of the specimen decreases for a given J value, even if the constraint remains the same. This is consistent with the behavior shown in Fig. 3.

Size requirements for J-integral evaluation are much less restrictive than for K_{Ic} measurement. According to ASTM standard E 813, the stress field at the crack tip in a bend specimen

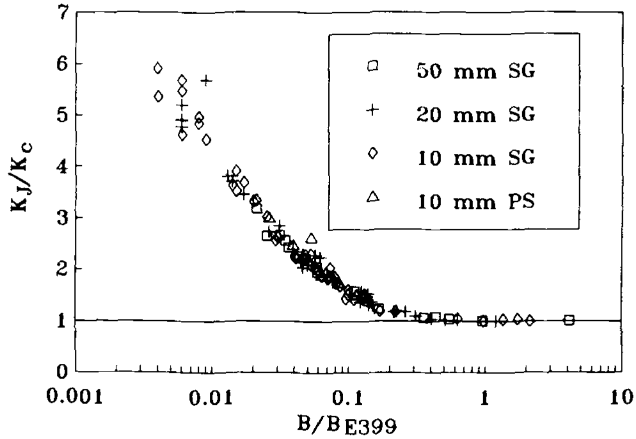

FIG. 4—*Ratio* K_c/K_j *as a function of the ratio of the specimen thickness to the minimum thickness of ASTM E 399.*

is described by J as long as Eq 2 is satisfied for the ligament and the thickness. Defining the minimum thickness, B_{min}, from Eq 2, the toughness results of Table 1 are plotted in Fig. 5 as a function of the ratio of the thickness to B_{min}. The toughness values have been normalized with the toughness corresponding to a probability of failure $\Phi = 0.5$, obtained from Eq 4. This normalization takes into account the statistical size effect and the temperature dependence. The lines calculated with Eq 4 at a probability of failure of 1 and 99% are also drawn. Because the model leading to Eq 4 was based on the HRR stress field obtained from the J-integral, the toughness values (98% of them) are expected to be scattered between these two lines. It is seen that this is verified as long as the thickness is larger than about twice the minimum value of ASTM E 813. When the thickness does not satisfy Eq 2 ($B < B_{min}$), the measured toughness K_j can greatly exceed the values predicted by the model of Eq 4. This may be attributed to a loss of J dominance, the process zone being too large compared to the specimen size; the microscopic stress field ahead of the crack tip is no longer described by J, although the curves in Fig. 3 do not indicate a loss of macroscopic constraint, even at large deformation.

Ligament Effects

Even if there is no loss of macroscopic constraint (change of L value) with the small SG specimens tested, there seems to be a loss of J dominance when the size is below the requirements of ASTM E 813: The stress field is no longer described by the J-integral, and the micro-mechanical model described by Eq 4 fails. This loss of J dominance may be related to a loss of in-plane constraint because the low thickness specimens have also a small ligament. Anderson and Dodds [*13*] have calculated, by finite element method in plane-strain condition, the maximum principal stress contours ahead of a crack in three-point-bend specimens. The probability of rupture by cleavage being a function of the volume under stress (micro-mechanical model), they have shown that the value of J obtained with specimens with short cracks would be different from J_{ssy}, the value obtained with specimens satisfying small-scale-yielding conditions. Their results for a work-hardening coefficient $n = 10$ (which is reasonable for the steel used in this study, the statistical analysis in Eq 4 yielding a value of 11.5) can be approximated by the relation

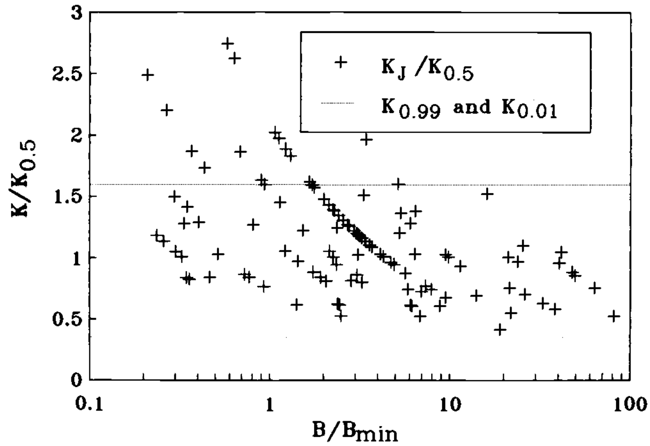

FIG. 5—*Toughness normalized by the toughness at a probability of failure of 50% from Eq 4 as a function of the ratio of the specimen thickness to the minimum thickness given by ASTM E 813 size requirements.*

$$J/J_{ssy} = 0.817 + 0.0002a\sigma_y/J - 28.4(a\sigma_y/J)^{-0.779}\ln(a/W) \quad (7)$$

Although these results were obtained for crack lengths only up to 0.5 W, Eq 7 has been used to obtain J_{ssy} for all the present results even if some crack lengths exceed 0.6 W. The K_{ssy} values thus obtained are approximate. Nevertheless, when they are plotted, similarly to Fig. 5, as a function of B/B_{min}, they all fall within the expected scatter band of the statistical model, without any consideration of size limit (Fig. 6). The corrections obtained from Eq 7 at a crack length a = 0.6 W and for twice the size limit of ASTM E 813 for a 10-mm-thick specimen (b = 50 J/σ_y) indicate that the value of J obtained with a 50-mm-thick specimen at the same J_{ssy}

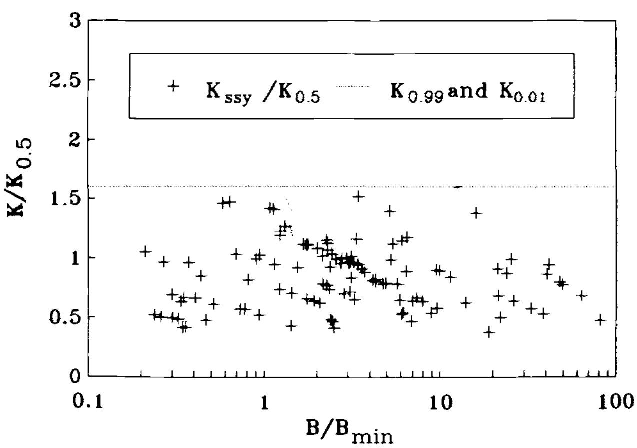

FIG. 6—*Estimated small-scale-yielding toughness (corrected according to FEM calculations of Anderson and Dodds* [13]*) as a function of the ratio of the specimen thickness to the minimum thickness given by ASTM E 813 size requirements.*

value would be about 14% lower than the value obtained with a 10-mm-thick specimen. The difference would be only 4% at four times the size limit of ASTM E 813. The micro-mechanical model of Eq 4 gives a difference of about 50% for the same size ratio. These observations confirm that most of the thickness effect for cleavage for the present results should be attributed to statistical effect. The micro-mechanical model remains valid for specimen sizes larger than approximately twice the ASTM E 813 limit.

Conclusions

From experimental results obtained with side-grooved specimens of a low carbon steel, in the lower part of the transition temperature curve, it may be concluded that:

1. Side grooving promotes a state of plane strain. The macroscopic constraint of SG specimens is independent of the thickness for the steel tested in this work for thickness down to 10 mm.
2. For side-grooved specimens, the stress intensity factor K loses its validity when nonlinear behavior becomes significant (at about half the size limitations of ASTM E 399), not because of a change of constraint. ASTM E 399 limits are required for this reason, whether or not there is any change of crack-tip constraint. For small specimens, toughness can be measured by J.
3. For side-grooved deeply-cracked bend specimens, ASTM E 813 size limits for the evaluation of J are related to a loss of in-plane constraint. The ASTM E 813 size limit for the ligament should be increased by a factor of about 2.
4. The effect of thickness on brittle fracture toughness result essentially from the statistical effect as long as the size satisfies twice the ASTM E 813 minimum requirements.

Acknowledgment

This report is part of a research project on the effect of thickness on fracture toughness, partially funded by PERD from the Department of Energy, Mines and Resources Canada.

References

[1] Tyson, W. R. and Marandet, B., "Cleavage Toughness Variability and Inclusion Size Distribution of a Weld Metal," *Fracture Mechanics: Eighteenth Symposium, ASTM STP 945*, D. T. Read and R. P. Reed, Eds., American Society for Testing and Materials, Philadelphia, 1988, pp. 19–32.
[2] Knott, J. F., *Fundamentals of Fracture Mechanics*, John Wiley & Sons, New York, 1973, p. 32.
[3] Faucher, B. and Tyson, W. R., "A Study of Variability, Size, and Temperature Effects on the Fracture Toughness of an Arctic Grade Steel Plate," *Fracture Mechanics: Eighteenth Symposium, ASTM STP 945*, D. T. Read and R. P. Reed, Eds., American Society for Testing and Materials, Philadelphia, 1987, pp. 164–178.
[4] Faucher, B., Wang, K. C., and Bouchard, R., "Relationship between Strain-Rate Sensitivity of Yield Stress and Transition Temperature of an Arctic Grade Steel," *Proceedings of the International Symposium on Fracture Mechanics*, W. R. Tyson and B. Mukherjee, Eds., Pergamon Press, New York, 1988, pp. 133–144.
[5] Faucher, B. and Tyson, W. R., "A Statistical Description of the Effect of Strain Rate, Thickness and Temperature on the Brittle Fracture Toughness of an Arctic Grade Steel," *Strength of Metals and Alloys*, P. O. Kettunen, T. K. Lepistö, and M. E. Lehtonen, Eds., Pergamon Press, Oxford, 1988, pp. 1077–1082.
[6] Faucher, B. and Tyson, W. R., "Statistical Analysis of the Effect of Side-Grooving on the Measurement of Brittle Fracture Toughness," *International Journal of Fracture*, Vol. 43, 1990, pp. 175–184.
[7] Yun, S., Zengjie, D., Zhonghua, L., and Mingjing, T., "Effect of Stress Triaxiality in Crack Tip Field on Validity of J-Dominance," *Engineering Fracture Mechanics*, Vol. 34, No. 3, 1989, pp. 637–643.

[8] Al-Ani, A. M. and Hancock, J. W., "J-Dominance of Short Cracks in Tension and Bending," *Journal of Mechanics and Physics of Solids*, Vol. 39, No. 1, 1991, pp. 23–43.
[9] Hutchinson, J., "Singular Behavior at the End of a Tensile Crack in a Hardening Material," *Journal of Mechanics and Physics of Solids*, Vol. 16, 1968, pp. 13–31; Rice, J. and Rosengren, G., "Plane Strain Deformation Near a Crack Tip in a Power Law Hardening Material," *Journal of Mechanics and Physics of Solids*, Vol. 16, 1968, pp. 1–12.
[10] deLorenzi, H. G. and Shih, C. D., "3-D Elastic-Plastic Investigation of Fracture Parameters in Side-Grooved Compact Specimen," *International Journal of Fracture*, Vol. 21, 1983, pp. 195–220.
[11] Kikuchi, M. and Miyamoto, H., "The Thickness Effect of Side Grooved CT Specimens," *International Journal of Pressure Vessels & Piping*, Vol. 16, 1984, pp. 1–16.
[12] Imai, Y. and Matake, T., "Effect of Side Grooves for Three-Point Bending Fracture Toughness Specimens—Three-Dimensional Elastic-Plastic Finite Element Analysis," *Bulletin of the Japanese Society of Mechanical Engineers*, Vol. 27, No. 227, May 1984, pp. 909–916.
[13] Anderson, T. L. and Dodds, R. H., Jr., "Specimen Size Requirements for Fracture Toughness Testing in the Transition Region," *Journal of Testing and Evaluation*, JETVA, Vol. 19, No. 2, 1991, pp. 123–134.

Charles W. Schwartz[1]

Influence of Out-of-Plane Loading on Crack Tip Constraint

REFERENCE: Schwartz, C. W., **"Influence of Out-of-Plane Loading on Crack Tip Constraint,"** *Constraint Effects in Fracture, ASTM STP 1171*, E. M. Hackett, K.-H. Schwalbe, and R. H. Dodds, Eds., American Society for Testing and Materials, Philadelphia, 1993, pp. 318–340.

ABSTRACT: The strains parallel to the crack front for a circumferential flaw in a pressure vessel are tensile, as opposed to zero (plane strain) or compressive (plane stress). It is reasonable to expect that this tensile strain condition may influence the constraint at the tip of the circumferential flaw. A series of axisymmetric nonlinear finite element analyses have been performed to investigate the nature of the crack tip stress fields and constraint for the limiting case of a continuous inner circumferential flaw, with an emphasis on comparing these fields and constraint levels to those in a plane strain configuration having the same geometric configuration and subjected to axial loading only. The focus of these investigations is on constraint implications for cleavage initiation in the lower transition region at realistic pressure vessel load levels; in addition, the results provide some insight into constraint implications for ductile fracture under higher load levels. Constraint is quantified using: (a) the extent of the yielded zone, (b) a hydrostatic stress triaxiality factor, (c) the elastic second-order stress term (T-stress) and the near tip elastic-plastic second-order stress term (Q-stress—O'Dowd and Shih, 1991 [*24*]). The analysis results suggest that the cleavage-relevant constraint measures for the circumferential flaw under combined internal pressure, crack face, and axial loading are comparable in magnitude to those in the corresponding plane strain condition at low J values; at higher J values, however, the circumferential flaw under combined loading exhibits significantly lower constraint levels than those in the plane strain reference condition. The reduction in constraint at higher J values in the circumferential flaw case is found to be caused principally by the negative in-plane stress biaxiality induced by the internal vessel pressure loading rather than by the out-of-plane tensile strain influence.

KEY WORDS: elastic-plastic fracture, cleavage fracture, crack tip stress fields, constraint, circumferential flaws, pressure vessels

The Mode I crack tip stress and strain conditions for a circumferential flaw in a pressure vessel differ from those in conventional laboratory fracture specimens in one potentially significant aspect: the strains parallel to the crack front are tensile as opposed to zero (plane strain) or compressive (plane stress). This tensile out-of-plane strain condition might be colloquially termed "super" plane strain (although it is more correctly termed a case of generalized plane strain). It is reasonable to hypothesize that this condition may influence the constraint at the crack tip and, as a consequence, the resistance of the material to crack initiation. The question to be addressed is then: "Given that fracture toughness in plane strain is lower than in plane stress, is the fracture toughness in the 'super' plane strain condition even lower?" The answer to this question is of some importance to the evaluation of the fracture integrity of welds in ring forged nuclear reactor pressure vessels, which contain only circumferential welds.

The variation of cleavage fracture toughness with constraint within the range between plane

[1] Associate professor, University of Maryland, Department of Civil Engineering, College Park, MD 20742.

stress and plane strain conditions is well known [1–3]. Conceptually, constraint is a secondary characteristic of the crack tip stress and strain fields (the primary characteristic being the singularity in the fields) that promotes fracture mechanisms within the fracture process zone (e.g., increases crack opening stresses) and inhibits energy-absorbing plastic flow within the region surrounding the fracture process zone. Constraint is usually associated with high triaxiality of the crack tip stress fields. Under ideal plane strain conditions, this triaxiality develops because the contraction parallel to the crack front is prevented, producing tensile stresses parallel to the crack front in addition to the tensile in-plane stresses. In sufficiently thick laboratory fracture specimens, contraction within the crack tip plastic zone is inhibited by the surrounding elastic material, planes normal to the crack front remain essentially plane, and tensile stresses are induced parallel to the crack front. In a circumferentially flawed pressure vessel, not only do the radial-axial planes remain plane during deformation (at least for the limiting case of a continuous circumferential flaw), but the hoop stresses further increase the tensile strains acting parallel to the crack front.

Loss of constraint is associated with: (a) decreasing specimen thickness; (b) crack length (very short cracks or very short ligaments); (c) increased load/yield levels; and (d) loading configuration (tension instead of bending). Specimen thickness influences the in-plane crack tip fields through its effect on the out-of-plane stresses and strains, while the other three factors influence the in-plane fields more directly. The effects of these factors on constraint underlie the minimum specimen size requirements in the ASTM specifications Test Method for Plane-Strain Fracture Toughness of Metallic Materials (E 399) and Test Method for J_{Ic}, a Measure of Fracture Toughness (E 813). In fracture configurations possessing "sufficient" constraint, the plastic crack tip stress and strain fields can be characterized by a single parameter, J [4–7]. In configurations with insufficient constraint, a multiparameter fracture characterization may be required.

This paper reports the results of an analytical investigation into the nature of the crack tip constraint for a circumferential flaw in comparison with that in the corresponding plane strain condition. The flaw geometry considered here is an idealized continuous inner circumferential flaw in a cylindrical pressure vessel, which is the limiting case for a finite length circumferential surface flaw. The primary practical focus of this study is on cleavage initiation in the lower transition region under realistic pressure vessel load magnitudes. However, the results also provide some insights into the constraint conditions at higher load levels relevant to ductile fracture propagation.

Analysis Model

In this study, a circumferentially flawed pressure vessel was simulated using two-dimensional nonlinear finite element analyses. The vessel was treated as a cylinder having an internal radius, r_i, of 2171.7 mm (85.5 in.) and a wall thickness, W, of 215.9 mm (8.5 in.); these dimensions are typical for reactor pressure vessels. The circumferential flaw was assumed continuous around the inner beltline of the vessel with a crack length, a, equal to 53.975 mm in the radial direction ($a/W = 0.25$). No crack extension was considered in the analyses.

Three different loading configurations were analyzed: a reference plane strain condition under axial loading only; axisymmetric conditions under axial loading only; and axisymmetric conditions under combined internal pressure, crack face pressure, and axial loading. All loads were applied incrementally from values corresponding to essentially linear, very small-scale yielding conditions to levels just beyond general yielding of the vessel wall.

The finite element model of the assumed geometry as generated using the PATRAN [8] pre-/post-processing system is illustrated in Fig. 1. Only the upper symmetric half of the vessel was considered. The mesh consisted of 1727 nodes and 536 eight-node reduced (2 by 2) inte-

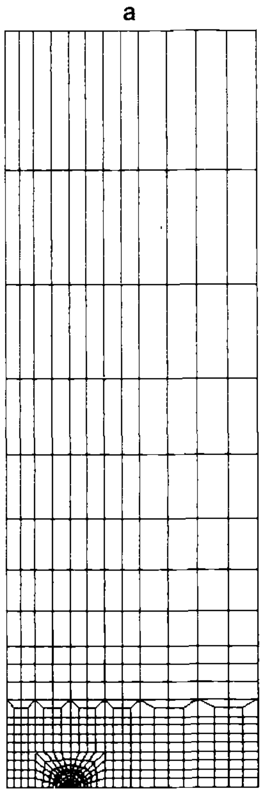

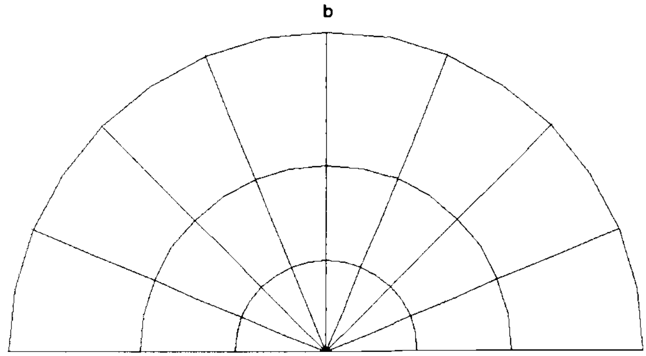

FIG. 1—*Finite element mesh for all analyses:* (a) *overall mesh;* (b) *detail of crack tip region.*

gration isoparametric elements. Eight fans of elements converge on the crack tip (Fig. 1*b*); the 17 initially coincident crack tip nodes are free to deform independently during the analysis. The discretization is sufficiently fine to permit adequate resolution of the stresses and strains within distances on the order of ten crack tip opening displacements (CTODs) from the crack tip; the radial dimension of the elements at the crack tip is approximately 0.02 mm (r/W = 0.000124). All finite element calculations were performed using the ABAQUS analysis code [*9*].

The ends of the vessel were not modeled explicitly in the analyses. Instead, the mesh was truncated above the crack plane at a distance equal to three times the wall thickness, and the axial loads were applied as uniform normal tractions along this boundary. In the combined loading case, appropriate normal tractions were also applied to the internal wall of the vessel and to the crack face. The rotational restraint provided by the vessel ends was approximated by restricting all rotation of the top of the mesh through displacement constraint equations. This was felt to be a better representation of the actual restraint provided by the vessel ends than the opposite extreme of uninhibited rotation. The effect of the rotational restraint on the crack plane is moderate; for LEFM plane strain conditions, the computed J values for the bounding cases of no restraint (i.e., a conventional SENT configuration) and full restraint differed by 19%.

The material stress-strain behavior was modeled using the Ramberg-Osgood constitutive relation

$$\epsilon/\epsilon_o = \sigma/\sigma_o + \alpha(\sigma/\sigma_o)^n \tag{1}$$

The following values of the material constants were used in all analyses: elastic modulus $E = \sigma_o/\epsilon_o = 300$; Poisson's ratio $\nu = 0.3$; $\sigma_o = 1$; $\alpha = 1$; and $n = 10$. A small strain formulation was employed in all analyses. Although the small strain formulation cannot correctly model the stress and strain fields and crack tip blunting in the very high strain region immediately surrounding the crack tip, the stress and strain fields predicted by small strain and large strain formulations are similar at distances greater than approximately 3 CTODs from the crack tip under plane strain conditions [*10,11*].

J-integral values were computed using the virtual crack extension algorithm as implemented in ABAQUS [*9,12*]. Ten contours were evaluated to establish path independence for the *J*-integral value.

Results

The computed *J*-integral values and hoop strains ϵ_ϕ as a function of load level are summarized in Fig. 2 for all three configurations analyzed. Load level is quantified by p_a/σ_o, in which p_a is the remote axial stress applied at the top of the analysis model. For the axisymmetric/combined load case, p_a is a function of the vessel pressure p_i applied normal to the inner surface of the vessel

$$p_a = -p_i r_i^2/(r_o^2 - r_i^2) = -4.792 p_i \tag{2}$$

in which r_i and r_o are the inner and outer radii of the vessel. For easy reference in conjunction with later figures in this paper, Table 1 summarizes the $J/(a\sigma_o)$ values corresponding to p_a/σ_o for each output load step in the analyses. General yield of the wall thickness occurred at loads above approximately $p_a/\sigma_o = 0.8$ for the plane strain and axisymmetric/axial load configurations and above approximately $p_a/\sigma_o = 0.4$ for the axisymmetric/combined load case. A value of $p_a/\sigma_o = 0.3$ corresponds to the practical upper limit for the loading in a pressure vessel (axisymmetric/combined load case). As shown in the lower half of Fig. 2, the hoop strain ϵ_ϕ varies in an essentially linear fashion with load up to the point of general yield. As expected, ϵ_ϕ is compressive in the axisymmetric/axial load case and tensile with a higher magnitude in the axisymmetric/combined load case.

The extent of the yielded zone is defined by the effective stress contour $\sigma_{\text{eff}} = \sigma_o$, where

$$\sigma_{\text{eff}} = \{(1/2)[(\sigma_1 - \sigma_2)^2 + (\sigma_2 - \sigma_3)^2 + (\sigma_3 - \sigma_1)^2]\}^{1/2} \tag{3}$$

TABLE 1—*Normalized* J $(a\sigma_o)$ *values corresponding to load levels* p_a/σ_o *for all three loading configurations.*

	J/($a\sigma_o$)		
Load Level, p_a/σ_o	Plane Strain	Axisymmetric/Axial Load	Axisymmetric/Combined Load
0.10	1.78E-4	1.68E-4	2.43E-4
0.15	4.02E-4	3.80E-4	5.48E-4
0.20	7.18E-4	6.79E-4	9.78E-4
0.25	1.13E-3	1.07E-3	1.54E-3
0.30	1.64E-3	1.56E-3	2.25E-3
0.35	2.27E-3	2.14E-3	3.18E-3
0.40	3.02E-3	2.86E-3	4.48E-3
0.60	7.91E-3	7.83E-3	4.06E-2
0.80	2.26E-2	2.58E-2	...
1.00	1.01E-1	1.20E-1	...

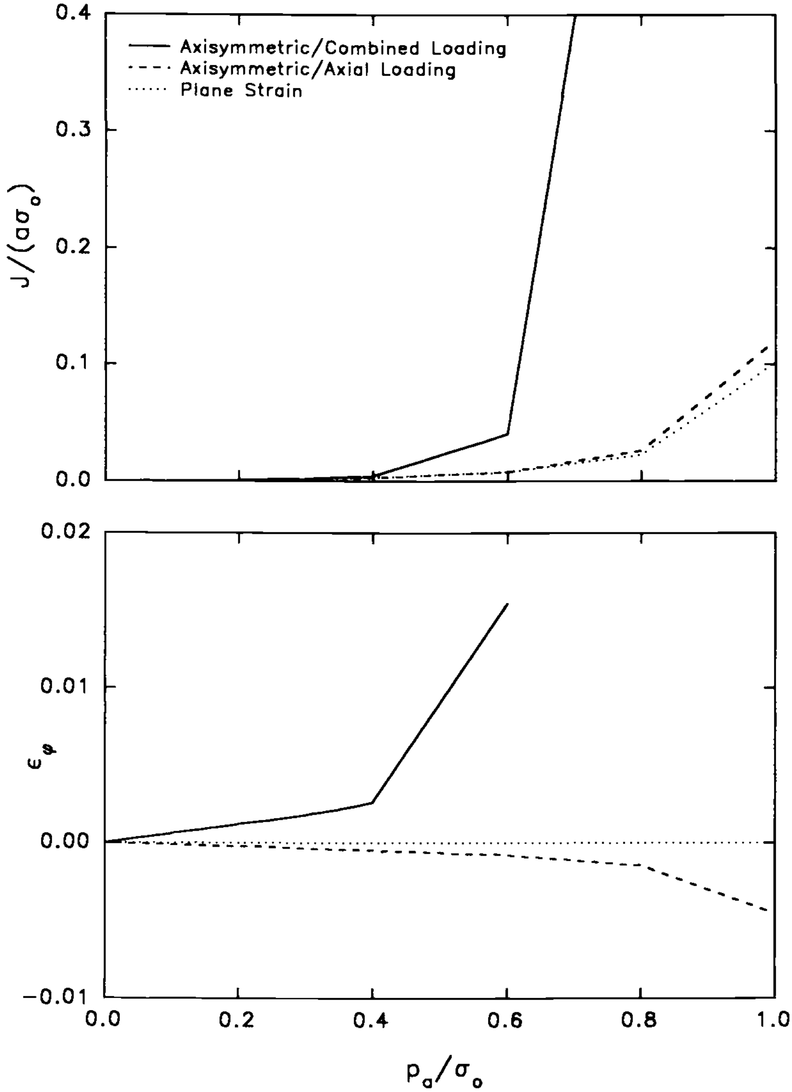

FIG. 2—*Normalized* J, $J/(a\sigma_o)$, *and hoop strain,* ϵ_ϕ, *as functions of load level,* p_a/σ_o, *for all three configurations.*

Figure 3 summarizes the extent of the crack tip yielded zones at various load levels for the plane strain configuration; the corresponding results for the axisymmetric/axial load and axisymmetric/combined load configurations are given in Figs. 4 and 5, respectively. The largest contour in all three figures corresponds to the largest output load step still under contained yield conditions. The shapes of the yielded zones are qualitatively similar for all three loading configurations. The maximum extent of the contained yield zone at the last output step prior to general yield was $r/a \cong 0.2$, $z/a \cong 0.33$ for the plane strain and axisymmetric/axial load configurations and $r/a \cong 0.1$, $z/a \cong 0.2$ for the axisymmetric/combined load case, where r and z are the radial and axial distances from the crack tip. Note that although the contours in

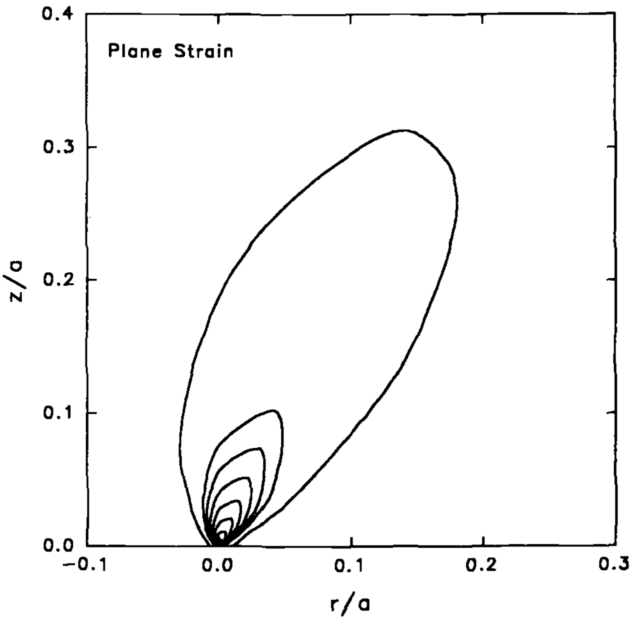

FIG. 3—*Extent of yielded zones for plane strain configuration under axial loading. Contours (from largest to smallest) correspond to load levels* p_a/σ_o = *0.60, 0.40, 0.35, 0.30, 0.25, 0.20, 0.15, 0.10.*

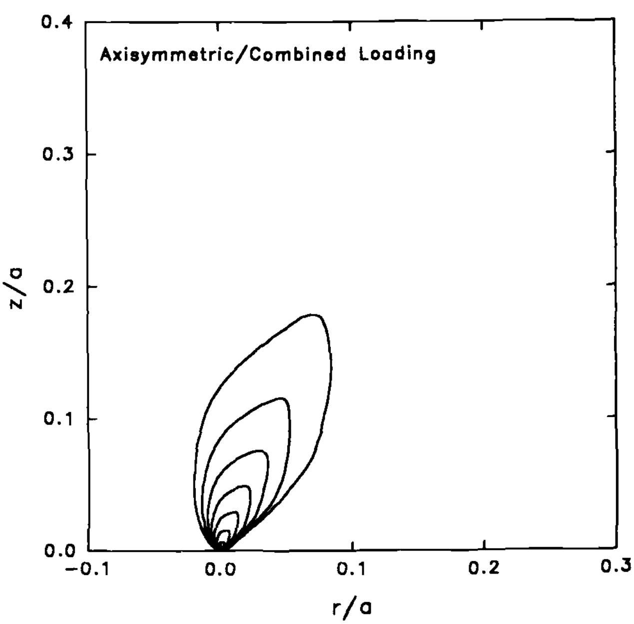

FIG. 4—*Extent of yielded zones for axisymmetric configuration under axial loading only. Contours (from largest to smallest) correspond to load levels* p_a/σ_o = *0.60, 0.40, 0.35, 0.30, 0.25, 0.20, 0.15, 0.10.*

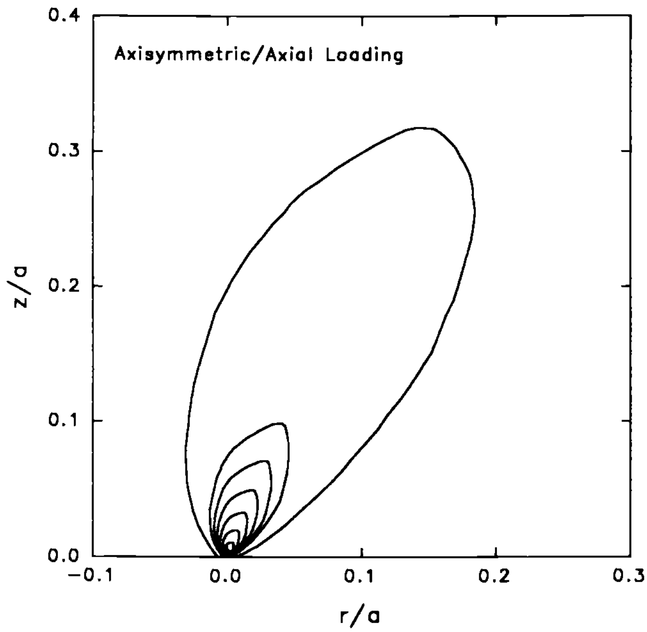

FIG. 5—*Extent of yielded zones for axisymmetric configuration under combined loading. Contours (from largest to smallest) correspond to load levels* p_a/σ_o = *0.40, 0.35, 0.30, 0.25, 0.20, 0.15, 0.10.*

Figs. 3 through 5 correspond to similar p_a/σ_o values, the corresponding $J/(a\sigma_o)$ values differ among the three loading configurations (see Table 1).

The extent of yielding for all three loading configurations can be compared directly in terms of the area of the yielded zones. Figure 6 summarizes the normalized yield zone area for contained yield as a function of load level for all three configurations. The yield zone area, A_o, is defined as the area contained within the $\sigma_{eff} = \sigma_o$ contour. The normalizing factor for the yield zone area is a measure of the yield extent under small scale yielding (SSY) conditions, as follows. Using the Irwin estimate for the extent of the plastic zone r_p under SSY conditions

$$r_p \propto (K_I/\sigma_o)^2 \tag{4}$$

or

$$r_p \propto JE/\sigma_o^2 \tag{5}$$

An estimate of the yield zone extent under small-scale yielding, $A_{o,SSY}$, can then be expressed as

$$A_{o,SSY} \propto r_p^2 \tag{6}$$

or

$$A_{o,SSY} \propto (JE/\sigma_o^2)^2 \tag{7}$$

Thus, the normalizing factor is proportional to the estimate of the yield zone area under SSY, and a rise of $A_o/(JE\sigma_o^2)^2$ with increasing load indicates increasing deviation from SSY condi-

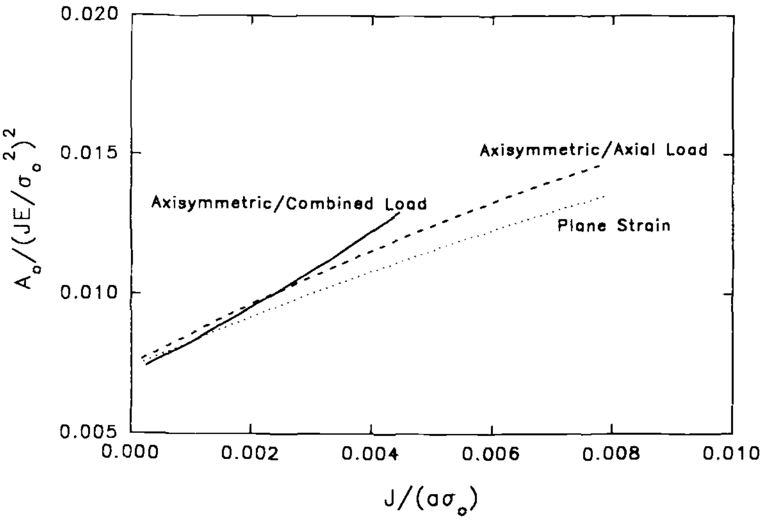

FIG. 6—*Normalized yield zone area,* $A_o/(JE/\sigma_o^2)^2$, *versus* $J/(a\sigma_o)$ *for all three loading configurations.*

tions. Note that the ordinate intercepts of the curves in Fig. 6 do not (and should not) equal zero. In the limit of $J/(a\sigma_o) \to 0$, $A_o \to A_{o,SSY}$ and the ordinate intercept therefore represents the implicit proportionality constant in Eq 7.

Several trends can be observed in the data presented in Fig. 6. At low J values, all three configurations produce similar yield zone areas. At higher J values and following the argument outlined above, all three configurations exhibit increasing deviation from SSY yield conditions with increasing load level. Assuming that higher constraint is associated with reduced yielding at a given J value, then the curves in Fig. 6 at low J values give a very weak indication of slightly higher constraint in the axisymmetric/combined load configuration and slightly lower constraint in the axisymmetric/axial load case as compared to the reference plane strain configuration. At higher J values, however, the differences among the three configurations are more pronounced. The larger yield zones computed for the axisymmetric/axial load case as compared to the reference plane strain configuration are consistent with the expected lower constraint levels for this case. However, the axisymmetric/combined load case produced the largest yield zones at higher J values, suggesting that it exhibits the lowest constraint level of all three configurations. This is contrary to what would be expected under the "super" plane strain argument.

And alternate and common way of quantifying constraint in the crack tip region is through the hydrostatic stress triaxiality parameter h

$$h = \sigma_m/\sigma_{\text{eff}} \tag{8}$$

in which σ_m is the mean or hydrostatic stress. Studies of ductile fracture processes dominated by cavity growth and coalescence have shown that the cavity growth rate increases sharply with increasing hydrostatic stress triaxiality [*13,14*]; h has also been used to quantify the effects of constraint on *J-R* curves for ductile crack extension [*15*]. Although the practical focus of the present study is on cleavage initiation, computation of the h parameter from the analysis results provides some insights for ductile fracture.

The variation of h with radial distance along the crack plane for the plane strain, axisymmetric/axial load, and axisymmetric/combined load configurations are summarized in Figs.

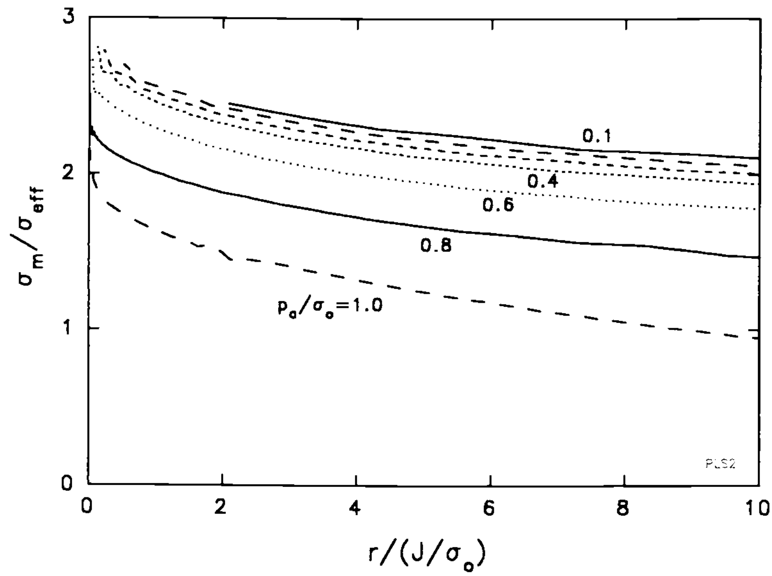

FIG. 7—*Hydrostatic stress constraint factor, σ_m/σ_{eff}, versus radial distance along the crack plane for the plane strain configuration under axial loading. Load levels p_a/σ_o = 0.1, 0.2, 0.3, 0.4, 0.6, 0.8 correspond to contained yield, and 1.0 corresponds to general yield.*

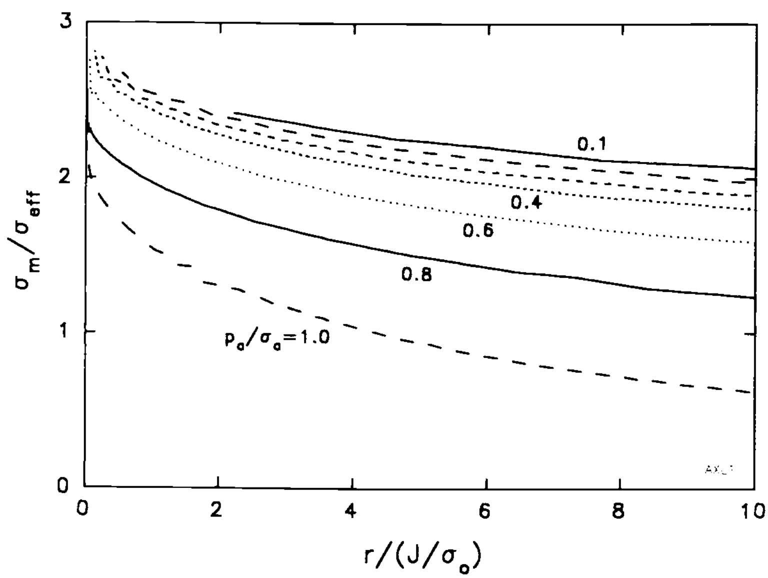

FIG. 8—*Hydrostatic stress constraint factor, σ_m/σ_{eff}, versus radial distance along the crack plane for the axisymmetric configuration under axial loading. Load levels p_a/σ_o = 0.1, 0.2, 0.3, 0.4, 0.6, 0.8 correspond to contained yield, and 1.0 corresponds to general yield.*

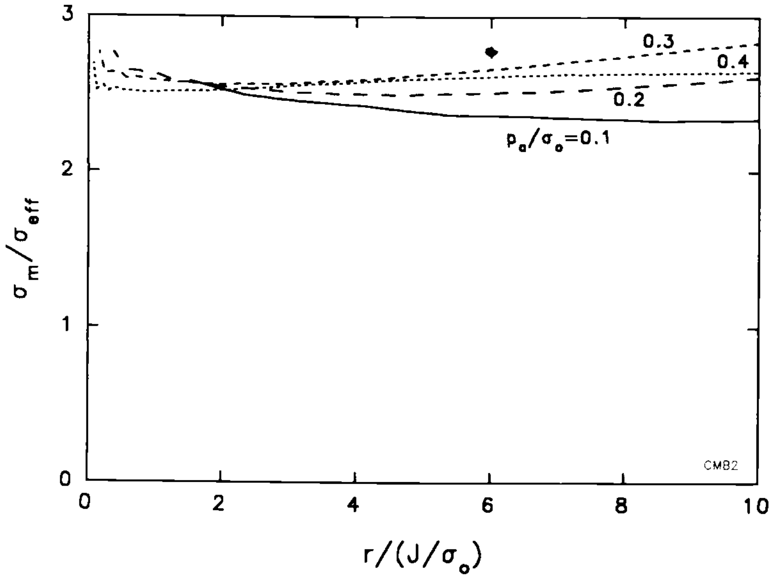

FIG. 9—*Hydrostatic stress constraint factor, σ_m/σ_{eff}, versus radial distance along the crack plane for the axisymmetric configuration under combined loading. Contained yield conditions obtain at all load levels shown in the figure.*

7, 8, and 9, respectively. Note that the curves in Figs. 7 and 8 for p_a/σ_o = 1.0 correspond to general yielding; all other curves in these two figures, plus all of the curves in Fig. 9, correspond to contained yield. Radial distance in these figures is normalized by J/σ_o, which is the only length scale for a crack in an infinite region [*16,17*]; although the finite geometry configurations analyzed here do have other length scales, it is still convenient to normalize length in terms of J/σ_o. When interpreting the stress distributions in Figs. 7 though 9, recall that the small strain formulation employed in these analyses gives physically incorrect results for the stresses and strains within a few CTODs of the blunted crack tip. CTOD can be estimated as

$$\delta_t = d_n J/\sigma_o \tag{9}$$

in which δ_t is the CTOD and d_n is a function of the material properties n and σ_o/E [*18*]. For the material property values in these analyses, $d_n \cong 0.5$ and

$$\delta_t \cong 0.5J/\sigma_o \tag{10}$$

Consequently, the stresses in Figs. 7 though 9 for $r/(J/\sigma_o)$ less than approximately 1.5 are not accurate representations of the true values under large strain conditions.

The trends in the hydrostatic constraint factor for the plane strain (Fig. 7) and axisymmetric/axial load (Fig. 8) configurations are quite similar. The constraint parameter h is only slightly dependent upon radial distance over the range $2 \leq r/(J/\sigma_o) \leq 10$, and at any given distance h decreases with increasing load. A close comparison of the two figures shows that the axisymmetric/axial load case exhibits slightly lower values for h and thus less constraint than in the plane strain configuration at the same distance and J value. The axisymmetric/combined load case (Fig. 9) shows markedly different behavior, however. First, the values for h in the axisymmetric/combined load case are relatively insensitive to load level. More significantly, however, the values for h in the axisymmetric/combined load case are substantially higher than those in the other two loading configurations; this is a direct consequence of the high tensile hoop stresses in the pressurized cylinder. This result is shown even more dramatically in contour plots of h in the near tip region, which are given in Figs. 10, 11, and 12 for the plane strain, axisymmetric/axial load, and axisymmetric/combined load configurations, respectively. The contours for higher values of h—i.e., h greater than about 2—enclose a substantially larger volume of the crack tip region in the axisymmetric/combined load case as compared to the other two loading configurations. Consequently, cavity growth may occur at a higher rate and over a larger volume in the axisymmetric/combined loading case.

On the basis of hydrostatic stress triaxiality, the axisymmetric/combined load case exhibits constraint levels significantly higher than those under plane strain conditions. Note that this contradicts the conclusions drawn from consideration of yield zone extents (Fig. 6), suggesting perhaps that the constraint phenomenon for ductile fracture may be more complex than is represented by either h or yield extent alone. However, for cleavage-dominated fracture in the lower transition region, which is the practical focus of the present study, it is not triaxiality itself that is important, but rather the *effect* that this triaxiality may have on reducing yielding and, in particular, on increasing the crack opening stresses ahead of the tip that are critical for cleavage initiation. One approach toward quantifying the effect of constraint on the crack tip fields under SSY conditions has been based on the two-parameter "T-stress" expansion for the

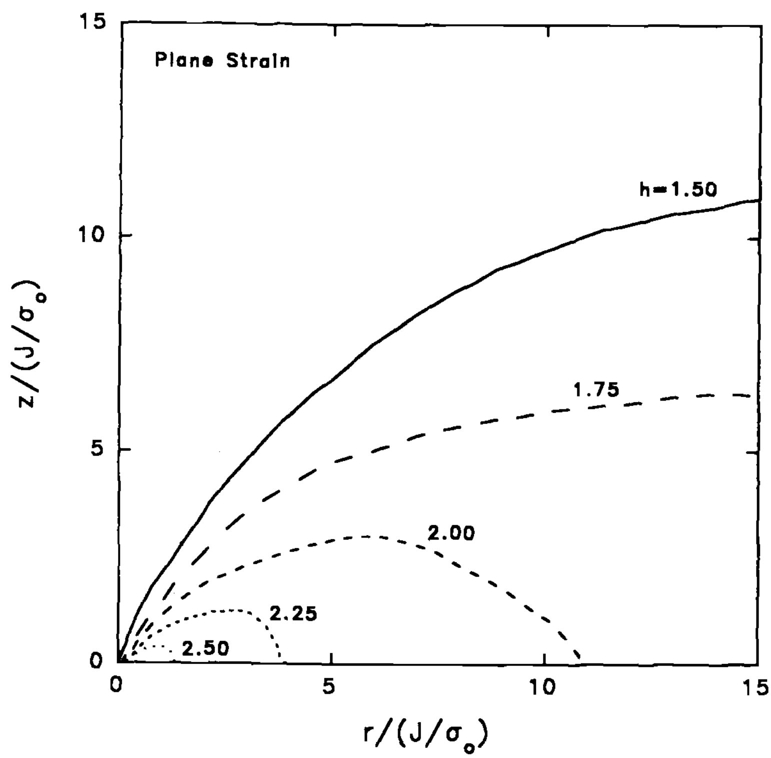

FIG. 10—*Contours of hydrostatic stress constraint factor, σ_m/σ_{eff}, in the crack tip region for the plane strain configuration under axial loading. Contours correspond to load level p_a/σ_o = 0.25 (contained yield).*

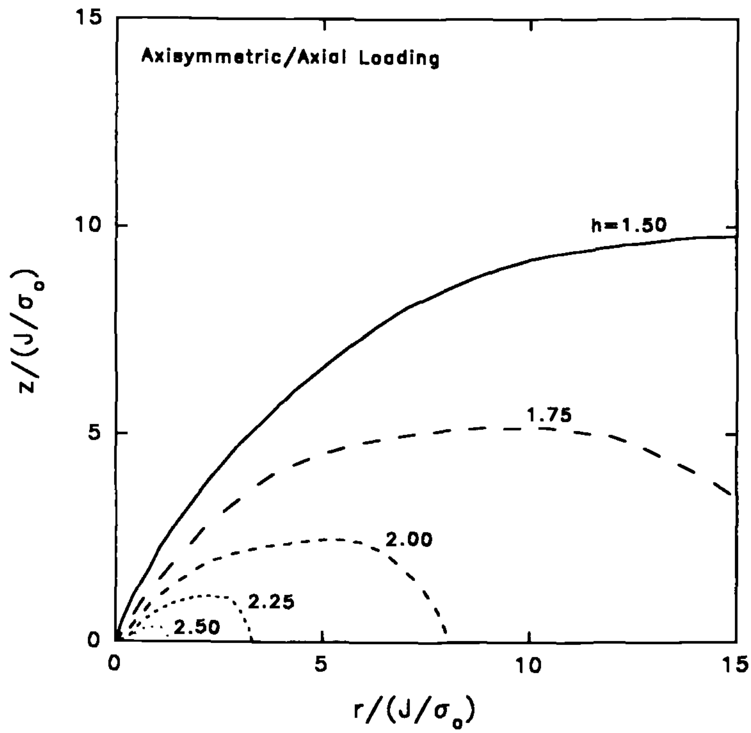

FIG. 11—*Contours of hydrostatic stress constraint factor, σ_m/σ_{eff}, in the crack tip region for the axisymmetric configuration under axial loading. Contours correspond to load level p_a/σ_o = 0.25 (contained yield).*

remote elastic stress field (i.e., at distances many times greater than the dimension of the yielded zone) [19]

$$\sigma_{ij} = (K_I/(2\pi r)^{1/2})f_{ij}(\theta) + T\delta_{1i}\delta_{1j} + \text{higher order terms} \tag{11}$$

in which r and θ are the usual in-plane polar coordinates originating from the crack tip, the $f_{ij}(\theta)$ functions capture the θ-variation of the stress field, and T represents the magnitude of the remote in-plane stress component acting parallel to the crack plane. The effect of the remote T-stress term on the details of small-scale yielding has been demonstrated through finite element boundary layer solutions by Larsson and Carlsson [20] for small strain assumptions in a nonhardening material; by Bilby et al. [21] for large strain assumptions in a nonhardening material; and by Betegón and Hancock [22] for small strain assumptions in a power law hardening material.

The original T-stress approach considers only in-plane constraint influences—i.e., constraint influences that can be incorporated into the in-plane T-stress term. For the circumferential flaw problem, it is essential to also include the out-of-plane constraint influences. Although the T-stress expansion can be generalized to include out-of-plane normal and shear T-stress terms [23], multiple constraint parameters must now be quantified. As an alternative approach, O'Dowd and Shih [24] have extended the two-parameter expansion approach to the *near*-tip elastic-plastic stress fields in a power law hardening material.

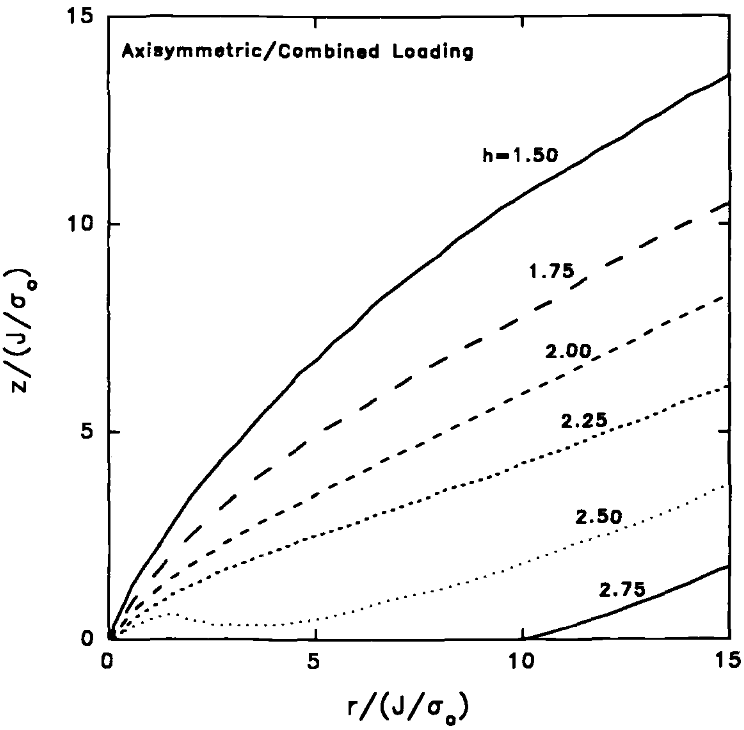

FIG. 12—*Contours of hydrostatic stress constraint factor, σ_m/σ_{eff}, in the crack tip region for the axisymmetric configuration under combined loading. Contours correspond to load level p_a/σ_o = 0.25 (contained yield).*

$$\sigma_{ij}/\sigma_o = [J/(\alpha\epsilon_o\sigma_o I_n r)]^{1/(n+1)}\tilde{\sigma}_{ij}(\theta) + Q[r/(J/\sigma_o)]^q\hat{\sigma}_{ij}(\theta) \\ + \text{higher order terms} \tag{12}$$

The first term represents the usual HRR singularity [*16,17*] with amplitude equal to J. The second order term has the dimensionless parameter Q as its amplitude; Q captures *all* constraint influences on the near-tip stress fields, regardless of whether these influences are the results of in-plane or out-of-plane factors. The functions $\tilde{\sigma}_{ij}(\theta)$ and $\hat{\sigma}_{ij}(\theta)$ represent the angular variation of the stress fields and are expected to depend also upon the material hardening; the $\hat{\sigma}_{ij}(\theta)$ functions are normalized such that $\hat{\sigma}_{\theta\theta}$ equals 1 at $\theta = 0$. Note that the second order expansion in Eq 12 assumes a small strain formulation, as it is based upon the HRR solution. The material parameters α, n, ϵ_o, and σ_o have been defined previously (Eq 1), and values for I_n and $\tilde{\sigma}_{ij}(\theta)$ are tabulated graphically in Refs *2* and *16*.

The second order stress field for a crack in an infinite region can be extracted by subtracting the HRR solution from a two-parameter boundary layer numerical solution at the same J value. The parameters Q, q, and $\hat{\sigma}_{ij}(\theta)$ can then be evaluated. Based on the results of this procedure, O'Dowd and Shih make the following arguments: (a) the variation of the second order stress fields with radial distance is very weak, hence $|q| << 1$; (b) the $\hat{\sigma}_{ij}(\theta)$ functions vary weakly with θ over $|\theta| \leq \pi/2$; (c) $\hat{\sigma}_{r\theta}(\theta)$ terms are very small, thus the $\hat{\sigma}_{rr}(\theta)$ and $\hat{\sigma}_{\theta\theta}(\theta)$ terms correspond to the principal stresses of the second order stress field; and (d)$\hat{\sigma}_{rr}(\theta)/\hat{\sigma}_{\theta\theta}(\theta) \cong 1$ for $|\theta| \leq \pi/4$—i.e., the second order fields closely approximate a state of hydrostatic stress in this sector. As a consequence of the above arguments, Eq 12 can be reasonably approximated within the sector $|\theta| \leq \pi/4$ as follows

$$\sigma_{ij}/\sigma_o \cong J/(\alpha\epsilon_o\sigma_o I_n r)^{1/(n+1)}\tilde{\sigma}_{ij}(\theta) + Q\delta_{ij}\hat{\sigma}_{ij}(\theta) \tag{13}$$

The constant Q is in essence a triaxiality parameter, but for the *second order* fields. O'Dowd and Shih also applied this procedure to a variety of finite geometry crack configurations under different loading conditions, where the second order fields were extracted by subtracting the HRR solution from full-field numerical solutions. The computed Q values ranged between approximately -2 and 0 in all of their analyses. Furthermore, Q decreased as the extent of plastic yielding increased. The Q value reached a steady-state value when fully plastic conditions were attained, and this steady-state Q value is considered a characteristic of the crack geometry.

Following O'Dowd and Shih's approach, the second order crack tip fields along the crack plane $\theta = 0$ have been extracted from the computed stresses for the three loading configurations analyzed in the present study. These stresses are given in Figs. 13 and 14 for the plane strain configuration, Figs. 15 and 16 for the axisymmetric/axial load case, and Figs. 17 and 18 for the axisymmetric/combined load case; in each pair of figures, the first is for the tangential or crack opening normal stresses and the second is for the radial normal stresses, and in all figures (*a*) summarizes the total computed stresses and (*b*) gives the second order component only. The curves for $p_a/\sigma_o = 1.0$ in Figs. 13 through 16 correspond to general yielding; all other curves in Figs. 13 through 18 correspond to contained yield conditions. The results shown in these figures are very similar to those found by O'Dowd and Shih. There is a slight variation of the second order stresses with radial distance—perhaps somewhat more than observed by O'Dowd and Shih, but still quite small. Q is always negative for the three loading configurations considered here and becomes more negative with increasing load level and consequent yielding.

It is difficult to compare the different loading configurations directly using Figs. 13 through 18 because the p_a/σ_o levels correspond to different $J/(a\sigma_o)$ values in each specimen. Additionally, the radial variation of the second order stresses complicates a direct comparison. However, if we define

$$Q^* = Q[r/(J/\sigma_o)]^q \tag{14}$$

then $Q^* = Q$ at $[r/(J/\sigma_o)]^q = 1$. Note that for the small strain formulation employed in these analyses, $[r/(J/\sigma_o)]^q = 1$ is within the large strain region where the computed stresses are an inaccurate representation of the actual stresses. For comparison purposes, however, a straightforward approach is to simply extrapolate the linear portion of the $Q^*\hat{\sigma}_{\theta\theta}$ versus (J/σ_o)—e.g., the region $1.5 \leq r/(J/\sigma_o) \leq 10$—back to $r/(J/\sigma_o) = 1$ and use this extrapolated value as an estimate of Q. The results of this procedure are summarized in Fig. 19 for all three loading configurations. The Q values for all configurations and load values are always negative, with smaller—i.e., more negative—values indicating lower constraint. The constraint in the axisymmetric/axial load configuration is slightly less than that for the plane strain reference case at all load levels. This is consistent with the conclusions drawn from consideration of yield zone extents (Fig. 6) and hydrostatic constraint factor (Figs. 7 and 8). The constraint in the axisymmetric/combined load case, however, is substantially less than in both of the other two configurations. Although this is again consistent with the observed yield zone extents, at least at higher J values (Fig. 6), it contradicts the trends of the hydrostatic constraint factor (Figs. 7 through 9).

If we accept the argument that for cleavage-dominated fracture it is not triaxiality *per se* that

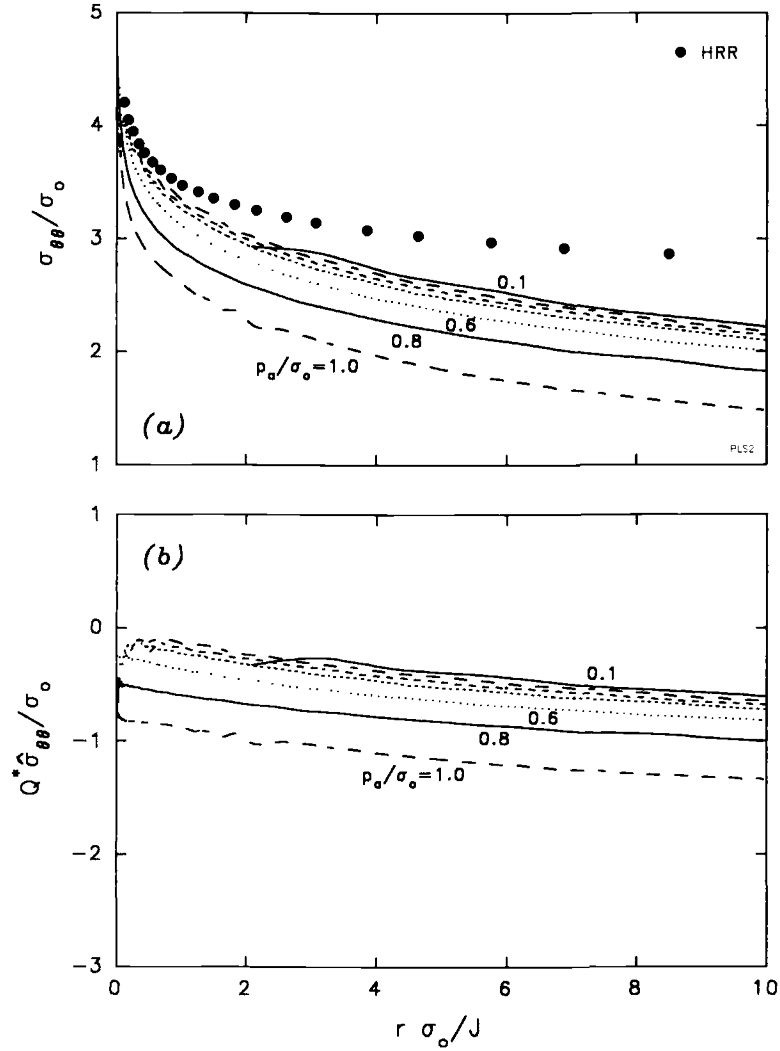

FIG. 13—*Total and second order tangential normal stresses (i.e., crack opening stresses) along the crack plane* $\theta = 0$ *for the plane strain loading configuration. Contours correspond to load levels* p_a/σ_o = *0.1, 0.2, 0.3, 0.4, 0.6, 0.8 (contained yield), and 1.0 (general yield).*

is important but rather the *effect* that triaxiality has on the crack opening stress fields, then the results in Fig. 19 clearly show that the axisymmetric/combined load configuration exhibits less constraint than the reference plane strain condition at all but the smallest J values. This is quite the opposite of what would be expected under the "super" plane strain argument. However, other evidence supports the lower constraint in the axisymmetric configuration. Our attention thus far has focused on the out-of-plane aspects of the axisymmetric configuration. In the axisymmetric/combined loading case there are also radial compressive stresses acting parallel to the crack plane that are not present in either the plane strain or axisymmetric/axial load con-

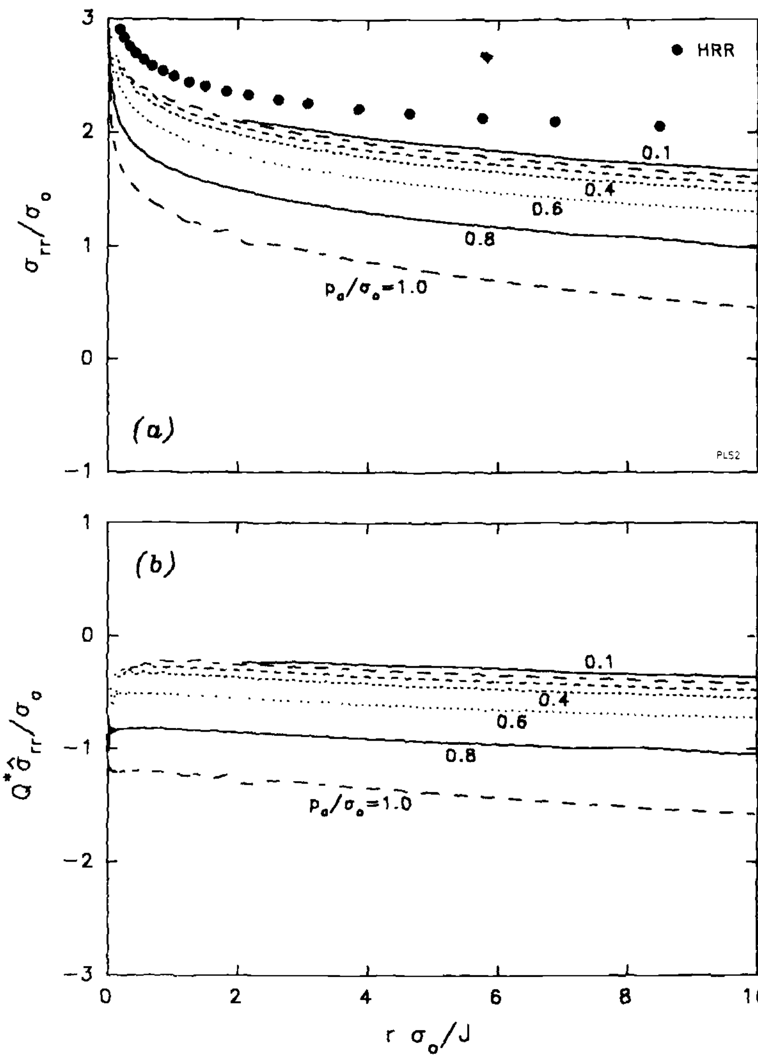

FIG. 14—*Total and second order radial normal stresses along the crack plane $\theta = 0$ for the plane strain loading configuration. Load levels p_a/σ_o = 0.1, 0.2, 0.3, 0.4, 0.6, 0.8 correspond to contained yield, and 1.0 corresponds to general yield.*

figurations; these stresses are due to the internal pressure loading of the vessel. In addition, there are crack face pressures in the axisymmetric/combined loading case that may influence in-plane constraint—particularly after crack tip blunting, when the crack face pressures at the blunted tip generate radial compressive stresses (note that this effect cannot be modeled in the small-strain analyses performed in this study). Compressive radial stresses correspond to lower or negative T-stresses, which in turn are associated with lower constraint.

To quantify the in-plane constraint influences, the T-stresses can be extracted from the present analyses by subtracting the singular LEFM stress distributions from the full field solution

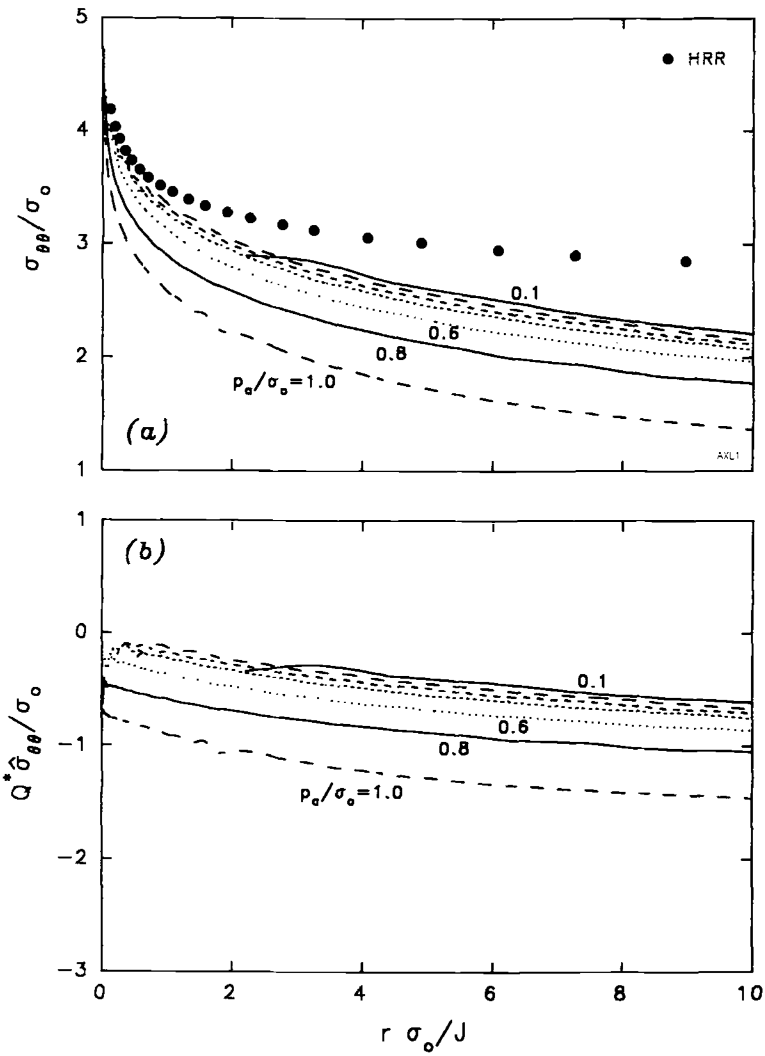

FIG. 15—*Total and second order tangential normal stresses (i.e., crack opening stresses) along the crack plane $\theta = 0$ for the axisymmetric/axial load configuration. Load levels* p_a/σ_o = *0.1, 0.2, 0.3, 0.4, 0.6, 0.8 correspond to contained yield, and 1.0 corresponds to general yield.*

along a contour remote from the crack tip (i.e., at a distance many times the yielded zone extent). The magnitude of the T-stress can be quantified in terms of a dimensionless biaxiality parameter B [*25*]

$$B = T(\pi a)^{1/2}/K_I \tag{15}$$

For the plane strain configuration, the computed value for B is -0.33. This value is approximately 20% larger (less negative) than that computed by Leevers and Radon [*25*] for an SENT configuration having the same a/W ratio. This discrepancy may be due to the rotational

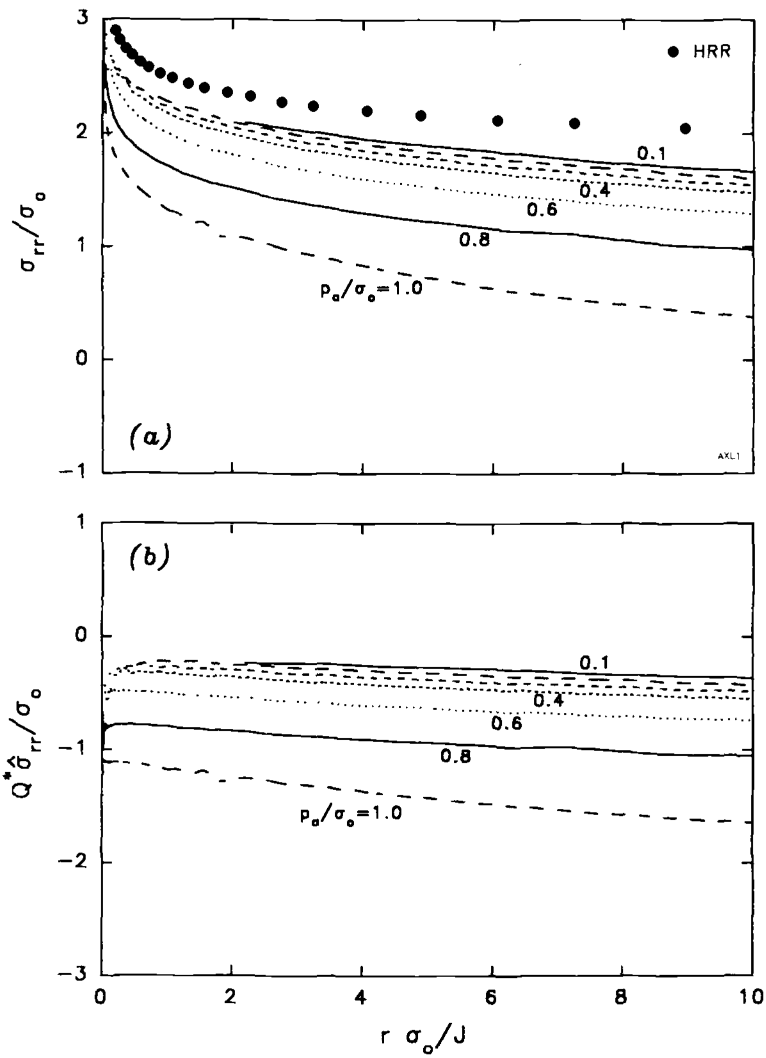

FIG. 16—*Total and second order radial normal stresses along the crack plane $\theta = 0$ for the axisymmetric/axial load configuration. Load levels* p_a/σ_o = *0.1, 0.2, 0.3, 0.4, 0.6, 0.8 correspond to contained yield, and 1.0 corresponds to general yield.*

restraint at the top of the finite element model in the plane strain configuration considered here. The computed B value for the axisymmetric/axial load case is approximately 1% smaller (more negative) than that for the reference plane strain configuration; this is consistent with the slightly lower constraint indicated in Fig. 19. The computed B value for the axisymmetric/combined load configuration is −0.43, or 30% smaller than that for the reference plane strain case; this is consistent with the significantly lower constraint indicated for this configuration in Fig. 19.

Other recent work substantiates the conclusion that the out-of-plane strain has only a secondary influence on crack tip constraint for the circumferential flaw problem. Wang [*26*] per-

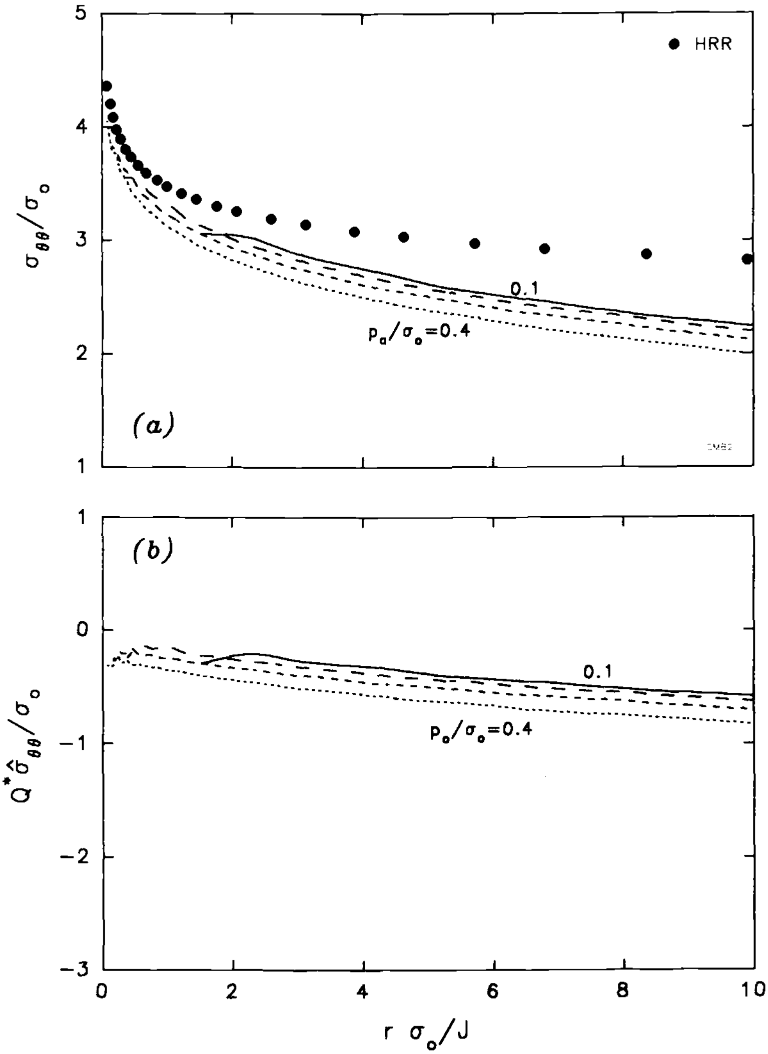

FIG. 17—*Total and second order tangential normal stresses (i.e., crack opening stresses) along the crack plane θ = 0 for the axisymmetric/combined load configuration. Contained yield conditions obtain at all load levels shown.*

formed a series of generalized plane strain modified boundary layer solutions in which the out-of-plane strain level varied from −90% to +90% of the uniaxial yield strain; his results indicate that the near-tip in-plane stress fields are insensitive to the out-of-plane strain level. Similar observations have been made by Parks [*23*] and by Hancock [*27*] for out-of-plane strain levels on the order of the yield strain or less. A remaining unresolved question is whether out-of-plane strain control (generalized plane strain) produces the same effect on the in-plane stress fields as does out-of-plane stress control (generalized plane stress); a related question is which condition (out-of-plane strain versus out-of-plane stress control) is the closer approximation to the conditions at the crack front for a finite width circumferential surface flaw.

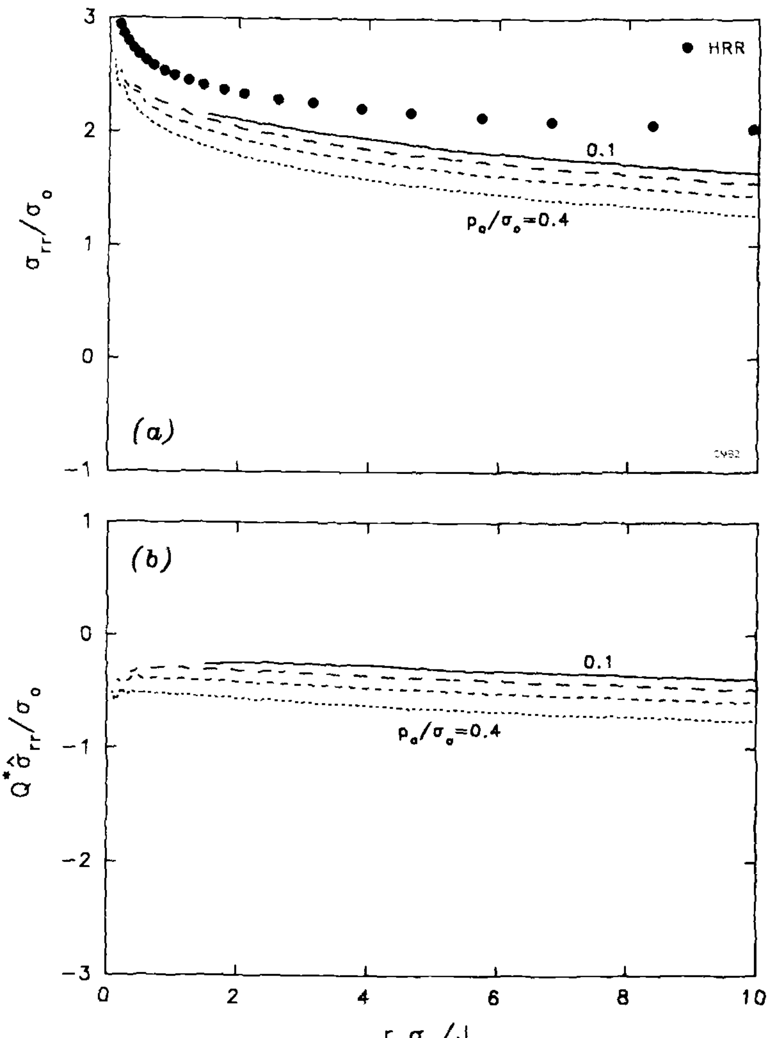

FIG. 18—*Total and second order radial normal stresses along the crack plane $\theta = 0$ for the axisymmetric/combined load configuration. Contained yield conditions obtain at all load levels shown.*

Conclusions

The analyses in this study have quantified the crack tip constraint for a continuous inner circumferential flaw in a pressure vessel under a pure axial loading and a combined internal pressure, crack face pressure, and axial loading as compared to the constraint for a corresponding reference plane strain configuration having the same geometry and subjected to axial loading only. The primary focus of this study is cleavage initiation in the lower transition region under realistic pressure vessel loading conditions.

For the case of a circumferential flaw under axial loading, the constraint is slightly less than that under plane strain conditions for all load levels and constraint measures considered. On

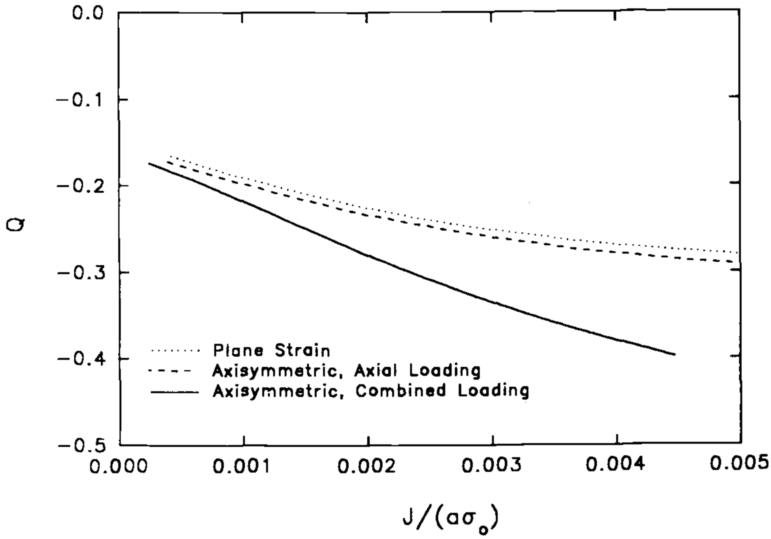

FIG. 19—*Variation of* Q *with load level for all three loading configurations under contained yield conditions.*

the basis of yield zone extent and the second order near-tip elastic plastic stresses (Q-stresses), the constraint for the circumferential flaw under combined loading is at most only comparable to that in the plane strain condition at low J values, and at higher J values is significantly less than that in the plane strain condition. However, examination of hydrostatic stress triaxiality constraint factor $h = \sigma_m/\sigma_{\text{eff}}$ leads to the opposite conclusion of significantly increased constraint for this case; it appears that the high tensile hoop stresses in the combined loading case affect h disproportionately more than they influence yield zone extent or the in-plane crack tip stress fields.

Of the quantitative constraint measures considered in this study, the Q-stress approach is the most rigorous and appropriate for cleavage-dominated fracture as it is focused on the details of the near-tip stress fields, and in particular on the crack tip opening stresses. By this measure, the constraint at the tip of a shallow circumferential flaw in a pressurized vessel is always less than that in an equivalent plane strain condition under axial loading only. However, this difference in constraint is due more to in-plane than out-of-plane effects. Specifically, it is due to the more negative in-plane stress biaxiality (T-stress biaxiality) resulting from the radial pressure applied to the inner surface of the vessel. This stress biaxiality effect will be greatest for shallow flaws, whose tips are nearest the inner surface where the radial compressive stresses are the largest. Thus, shallow flaws in pressure vessels, which already exhibit higher toughness simply because they are shallow, will exhibit an additional toughness elevation because of stress biaxiality.

Although cleavage-dominated fracture intiation was the primary focus of this study, the findings regarding the hydrostatic stress triaxiality factor have significant implications for ductile crack extension. The magnitude and volumetric extent of the high-triaxiality region in the circumferential flaw/combined loading case suggest that cavity growth may be significantly accelerated by the tensile hoop stresses.

Additional analyses are required before a definitive answer can be given regarding the precise nature of the crack tip stress fields and constraint magnitudes for circumferentially flawed pressure vessels under all realistic geometry and load conditions. Constraint can be expected to change with a/W ratio (e.g., because of the different T-stresses), hardening and other material properties, and the ratio of vessel internal radius to wall thickness (which changes the hoop stress and strain magnitudes). Finite width surface flaws must also be considered, particularly under pressurized thermal shock loading conditions and thermal streaming [*28*].

Acknowledgments

Funding for this investigation was provided by the U.S. Nuclear Regulatory Commission through the Oak Ridge National Laboratory, which is operated for the U.S. Department of Energy by Martin Marietta Energy Systems, Inc. Computer time for this study was provided by the San Diego Supercomputer Center, which is sponsored by the National Science Foundation and administered by General Atomics, Inc. Additional computational resources were provided by the College of Engineering and the Computer Science Center at the University of Maryland.

References

[*1*] Broek, D., *Elementary Engineering Fracture Mechanics*, 3rd ed., Martinus Nijhoff Publishers, The Hague, The Netherlands, 1982.

[*2*] Kanninen, M. F. and Popelar, C. H., *Advanced Fracture Mechanics*, Oxford University Press, New York, NY, 1985.

[*3*] Barsom, J. M. and Rolfe, S. T., *Fracture and Fatigue Control in Structures*, 2nd ed., Prentice-Hall, Inc., Englewood Cliffs, NJ, 1987.

[*4*] Rice, J. R., "A Path Independent Integral and the Approximate Analysis of Strain Concentration by Notches and Cracks," *Journal of Applied Mechanics*, Vol. 35, 1968, pp. 379–386.

[*5*] McMeeking, R. M. and Parks, D. M., "On Criteria for J-Dominance of Crack-Tip Fields in Large Scale Yielding," *Elastic-Plastic Fracture Mechanics, ASTM STP 668*, American Society for Testing and Materials, Philadelphia, 1979, pp. 175–194.

[*6*] Shih, C. F. and German, M. D., "Requirements for a One-Parameter Characterization of Crack Tip Fields by the HRR Singularity," *International Journal of Fracture*, Vol. 17, 1981, pp. 27–43.

[*7*] Hutchinson, J. W., "Fundamentals of the Phenomenological Theory of Nonlinear Fracture Mechanics," *Journal of Applied Mechanics*, Vol. 50, 1983, pp. 1042–1051.

[*8*] *Patran Plus User Manual—Release 2.4*, PDA Engineering, Inc., Costa Mesa, CA, 1989.

[*9*] *ABAQUS User Manual—Version 4.8.5*, Hibbit, Karlsson, and Sorenson, Inc., Providence, RI, 1989.

[*10*] Rice, J. R. and Johnson, M. A., "The Role of Large Crack Tip Geometry Changes in Plane Strain Fracture," *Inelastic Behavior of Solids*, Kanninen et al., Eds., McGraw-Hill, New York, NY, 1970, pp. 641–670.

[*11*] McMeeking, R. M., "Finite Deformation Analysis of Crack Tip Opening in Elastic-Plastic Materials and Implications for Fracture," *Journal of the Mechanics and Physics of Solids*, Vol. 25, 1977, pp. 357–381.

[*12*] Parks, D. M., "The Virtual Crack Extension Method for Nonlinear Material Behavior," *Computer Methods in Applied Mechanics and Engineering*, Vol. 12, 1977, pp. 353–364.

[*13*] McClintock, F. A., "A Criterion for Ductile Fracture by the Growth of Holes," *Journal of Applied Mechanics*, Vol. 14, June 1968, pp. 363–371.

[*14*] Rice, J. R. and Tracey, D. M., "On the Ductile Enlargement of Voids in Triaxial Stress Fields," *Journal of the Mechanics and Physics of Solids*, Vol. 17, 1969, pp. 201–217.

[*15*] Kordisch, H., Sommer, E., and Schmitt, W., "The Influence of Triaxiality on Stable Crack Growth," *Nuclear Engineering Design*, Vol. 223, 1989, pp. 27–35.

[*16*] Hutchinson, J. W., "Singular Behavior at the End of a Tensile Crack in a Hardening Material," *Journal of the Mechanics and Physics of Solids*, Vol. 16, 1968, pp. 13–31.

[*17*] Rice, J. R. and Rosengren, G. F., "Plane Strain Deformation Near a Crack Tip in a Power-Law Hardening Material," *Journal of the Mechanics and Physics of Solids*, Vol. 16, 1968, pp. 1–12.

[*18*] Shih, C. F., "Relationship Between the J-Integral and the Crack Opening Displacement for Stationary and Extending Cracks," *Journal of the Mechanics and Physics of Solids*, Vol. 29, 1981, pp. 305–326.

[19] Rice, J. R., "Limitations to the Small-scale Yielding Approximation for Crack Tip Plasticity," *Journal of the Mechanics and Physics of Solids*, Vol. 22, 1974, pp. 17–26.
[20] Larsson, S. G. and Carlsson, A. J., "Influence of Nonsingular Stress Terms and Specimen Geometry on Small-Scale Yielding at Crack Tips in Elastic-Plastic Material," *Journal of the Mechanics and Physics of Solids*, Vol. 21, 1973, pp. 263–277.
[21] Bilby, B. A., Cardew, G. E., Goldthorpe, M. R., and Howard, I. C., "A Finite Element Investigation of the Effect of Specimen Geometry on the Fields of Stress and Strain at the Tips of Stationary Cracks," *Size Effects in Fracture*, Mechanical Engineering Publications Ltd., London, 1986, pp. 37–46.
[22] Betegón, C. and Hancock, J. W., "Two-Parameter Characterization of Elastic-Plastic Crack Tip Fields," *Journal of Applied Mechanics*, Vol. 58, 1991, pp. 104–110.
[23] Parks, D. M., "Three-Dimensional Aspects of HRR-dominance," *Symposium on Elastic-Plastic Fracture*, European Group on Fracture, Freiburg, West Germany, October 1989.
[24] O'Dowd, N. P. and Shih, C. F., "Family of Crack-Tip Fields Characterized by a Triaxiality Parameter: Part I—Structure of Fields," *Journal of the Mechanics and Physics of Solids*, Vol. 39, 1991, pp. 93–115.
[25] Leevers, P. S. and Radon, J. C., "Inherent Stress Biaxiality in Various Fracture Specimen Geometries," *International Journal of Fracture*, Vol. 19, 1982, pp. 311–325.
[26] Wang, Y. Y., "On the Two-Parameter Characterization of Elastic-Plastic Crack-Front Fields in Surface Cracked Plates," presented at the *ASTM Symposium on Constraint Effects in Fracture*, Indianapolis, IN, May 1991.
[27] Hancock, J. W., personal communication.
[28] Pennell, W. E., "Heavy-Section Steel Technology Program: Semiannual Progress Report for October 1989-March 1990," Report No. NUREG/CR-4219 (ORNL/TM-9593/V7&N1), Oak Ridge National Laboratory, Oak Ridge, TN, Vol. 7, No. 1, March 1991.

Karl Kussmaul,[1] *Karl Maile,*[2] *and Wilhelm Eckert*[3]

Influence of Stress State and Specimen Size on Creep Rupture of Similar and Dissimilar Welds

REFERENCE: Kussmaul, K., Maile, K., and Eckert, W., **"Influence of Stress State and Specimen Size on Creep Rupture of Similar and Dissimilar Welds,"** *Constraint Effects in Fracture, ASTM STP 1171,* E. M. Hackett, K.-H. Schwalbe, and R. H. Dodds, Eds., American Society for Testing and Materials, 1993, pp. 341–360.

ABSTRACT: Small-scale tension specimens taken transversely from similar weldments of 12% Cr steel as well as small- and large-scale specimens from dissimilar weldments of 12% Cr/1% CrMoV with 12% Cr deposit were tested to obtain creep rupture data at 550°C. For the similar weld, the rupture time of the specimens was considerably longer than the rupture time determined in uniaxial creep tests of the weakest heat-affected zone (HAZ) microstructure. Results of finite element analyses have shown that this is caused by a constraint imposed on the weakest HAZ by the surrounding microstructures with higher creep strength. For the dissimilar weld, the creep rupture strength of large-scale specimens is higher than that of small-scale specimens. Finite element analyses have shown differences in the stress states developing in small- and large-scale specimens, which lead to different rupture times.

KEY WORDS: creep, weldments, finite element analysis, HAZ properties, Type IV cracking

Welded joints are among the most important construction elements in fossil power plants; a number of 40 000 to 50 000 weldments for a 300-MW unit is estimated [*1*]. Safe and reliable service of welds is, therefore, of crucial importance for the performance of power and other plants. Électricité de France has, for example, reported that approximately 40% of the damage in boilers that they found in 1987 and 1988 was caused by failure of weldments [*2*].

With respect to assessing welds, a specific problem for fossil power plants is the behavior of welds at high temperatures. Creep rupture tests of small-scale specimens taken transversely from the weld have shown that at high stress levels rupture occurs in the base metal or deposit for the majority of welded joints made of creep-resistant ferritic steels, whereas at low stress levels premature failure takes place in the heat-affected zone (HAZ). This type of failure in the fine-grained HAZ, the so-called Type IV-cracking, was also observed in components of which the main loading direction is perpendicular to the weld as for instance in the case of pipes with longitudinal seams [*3*].

To investigate the creep behavior of welds and to explain the migration of rupture position observed in tests and service, a series of research projects [*4–6*] were carried out at Staatliche Materialprüfungsanstalt (MPA) Stuttgart; some experimental and numerical results therefrom are presented below.

[1] Director, [2]head of department, and [3]research engineer, respectively, Staatliche Materialprüfungsanstalt (MPA), Pfaffenwaldring 32, 7000 Stuttgart 80, Germany.

TABLE 1—*Investigated welds.*[a]

Joint	Heat Input[d]	Base Metal 1	Base Metal 2
B1	8	1% CrMoV[b]	12% Cr[c]
A	16	12% Cr	12% Cr
B3	24	1% CrMoV	12% Cr

[a] Deposit: 12% Cr
[b] Cast, German Standard GS-17 CrMoV 5 11.
[c] Forging, German Standard X 20 CrMoV 12 1.
[d] In kJ/cm.

Investigated Welds

The investigations within the above-mentioned research projects concentrated on similar welds of 12% Cr (German standard X 20 CrMoV 12 1) steel and dissimilar welds between 12% Cr and 1% CrMoV (German standard GS-17 CrMoV 5 11) steel, Table 1, where different welding procedures and different heat inputs were considered. These welds are representative, for

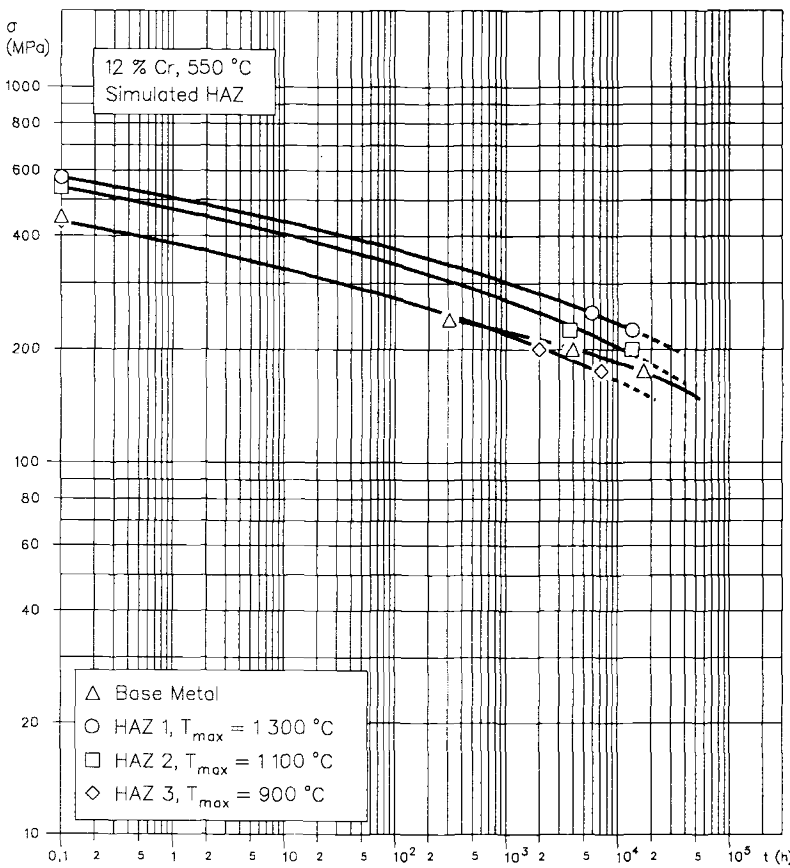

FIG. 1—*Creep rupture strength of 12% Cr base metal and simulated HAZ.*

example, for circumferential welds in 12% Cr piping, respectively, of the connection between 12% Cr piping and 1% CrMoV turbine casing.

HAZ Properties of 12% Cr Steel

As was already mentioned, in experiment and service a migration of the rupture location from the base metal or deposit into the fine-grained HAZ is observed with decreasing stress. It is assumed that this shift is caused by the interaction between adjacent material zones displaying different material properties in the HAZ. To quantify these differences, three microstructures typical for the HAZ were produced by means of weld simulation. With simulation peak temperatures of 1300, 1100, and 900°C, respectively, these three microstructures approach the whole variety of microstructures developing in the HAZ. The creep rupture strength of the simulated HAZ materials is depicted in Fig. 1 and compared with the base metal. Evidently, the creep rupture strength of HAZ 1 (peak temperature 1300°C) and HAZ 2 (peak temperature 1100°C) lies beyond the creep rupture strength of the base metal at least for times up to 50 000 to 60 000 h, whereas the creep rupture strength of HAZ 3 is clearly below the creep rupture strength of the base metal even in the case of short times; the distance between these two increases with increasing creep rupture time.

The minimum creep rate of HAZ, base metal, and deposit as a function of nominal stress is given in Fig. 2. The order of ascending minimum creep rate corresponds exactly to the order of descending creep rupture strength. The results given in Figs. 1 and 2 show a distinct variation of material properties within the HAZ so that interactions between adjacent zones and subsequently a considerable influence on the creep and failure behavior must be expected.

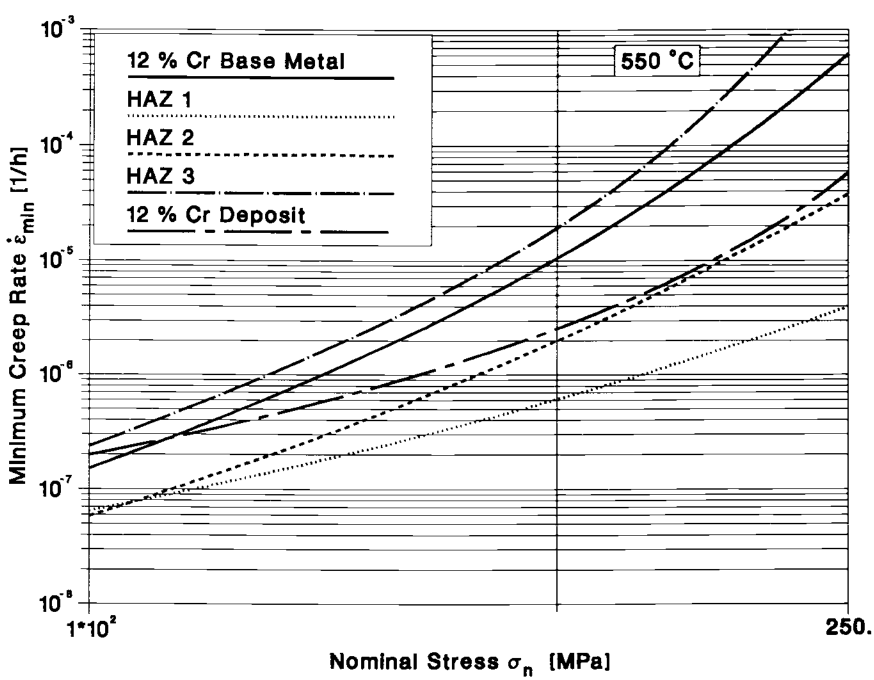

FIG. 2—*Minimum creep rate of 12% Cr base metal, simulated HAZ and deposit.*

Experimental Results from Similar Welds of 12% Cr

To determine experimentally the behavior of similar welds of 12% Cr steel, round tension specimens of Type 3 (see Fig. 3) were taken from Joint A (see Table 1); specimens of Type 4 were taken from joints B1 and B3. The results of creep rupture tests at different stress levels are shown in Fig. 4. Tests at nominal stress $\sigma_n = 201$ MPa with specimens of Type 4 fall beyond the scatterband of the base metal. The influence of the laboratory where the tests were carried out (specimens of Types 3 and 4 were tested at different laboratories) cannot be excluded; also, inhomogeneities of the material may have caused these results (these will therefore not be taken into account in the following discussion).

At a nominal stress of 200 MPa, the tested Type 3 specimen fails in the base metal at a rupture time that is explicitly longer than is expected from the results of HAZ 3 at the same nominal stress. At 171 MPa, all specimens failed in the HAZ; the time to rupture was, however, almost identical to the rupture time expected for the base metal at the same stress and considerably longer than expected for HAZ 3. A significant decrease in rupture time compared with the base metal is found for the specimens tested at 141 MPa; the creep rupture strength is, then, still beyond HAZ 3, but with an obvious tendency towards HAZ 3. For all stress levels, the results of the specimens from Points B1, A, and B3 are located within a small scatterband; for this reason, only results of specimens taken from Joint A are discussed below.

Results of Finite Element Calculations of Specimens taken from Joint A

To evaluate the effects leading to the experimental results, extensive finite element calculations were conducted. It was assumed that the material behavior is characterized by linear-elastic and creep behavior, that is, von Mises equivalent stress is always lower than the yield strength. This assumption was verified by the results of the calculations. The materials' creep behavior was described by a Graham-Walles type creep law

$$\varepsilon_c = A \cdot t^{1/3} + B \cdot t + C \cdot t^{3.75}$$

describing primary, secondary, and tertiary creep

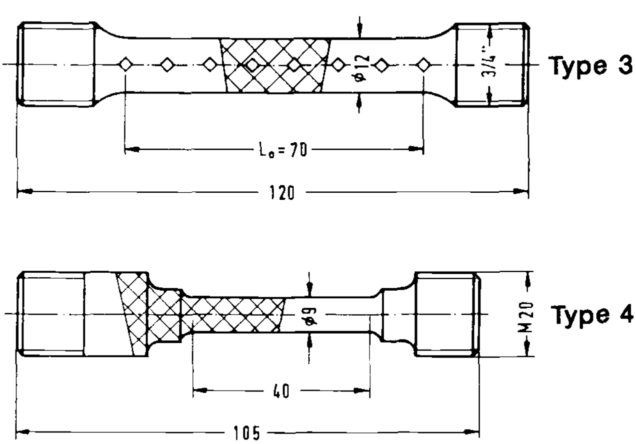

FIG. 3—*Dimensions (mm) of small-scale specimens.*

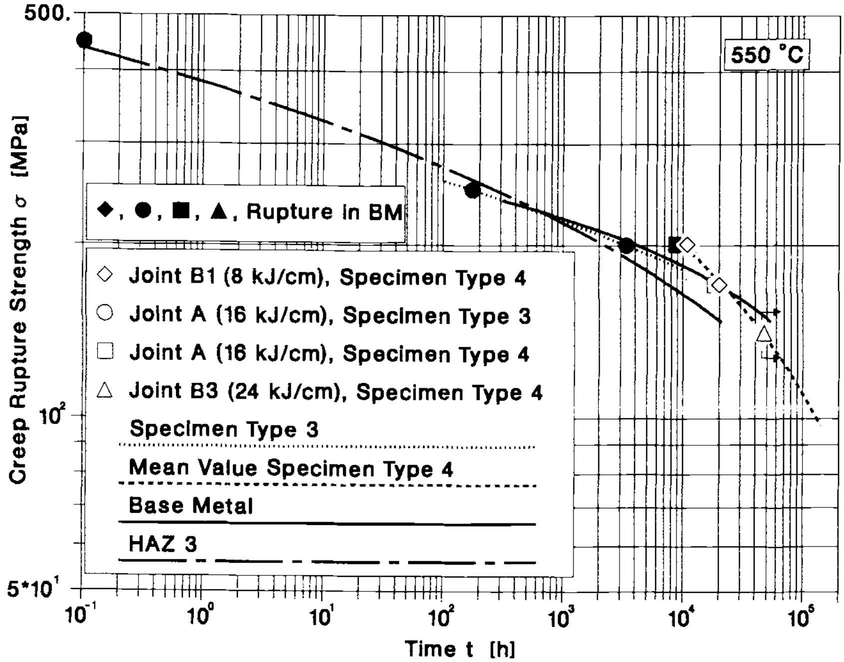

FIG. 4—*Creep rupture strength of small-scale specimens taken from similar welds.*

where

ε_c = creep strain,
$A = a_0 \cdot \exp(a_1 \cdot \sigma + \ldots + a_n \cdot \sigma^n)$,
$B = b_0 \cdot \exp(b_1 \cdot \sigma + \ldots + b_n \cdot \sigma^n)$,
$C = c_0 \cdot \exp(c_1 \cdot \sigma + \ldots + c_n \cdot \sigma^n)$, and
σ_n = nominal stress.

The coefficients a, b, and c were fitted to the results of uniaxial creep tests carried out on base metal, weld metal, and the three different HAZ microstructures, respectively.

The uniaxial creep law thus determined was implemented as a user subroutine into the finite element program ABAQUS [7]. This user subroutine calculates the creep strain increment as a function of time and strain (that is, it uses a strain-hardening formulation) and delivers it as an input to the main program of ABAQUS.

The finite element mesh is depicted in Fig. 5; material properties of base metal, deposit, and the three zones of the HAZ were taken into account. Figure 6 shows a comparison between measured and calculated elongation of specimens from Joint A; again, the results of the test at 201 MPa with a specimen of Type 4 do not fit, whereas for all other results the coincidence between experimental and numerical results is satisfying.

Assuming that von Mises equivalent stress σ_v or, more generally spoken, the second invariant of the deviatoric stress tensor correlates with the creep rupture time at high stress levels even for multiaxial stress states, the maximum von Mises equivalent stress for each of the materials taken into account in the finite element calculation was evaluated. The values normalized by the nominal stress are shown in Fig. 7 for a specimen tested at 200 MPa nominal

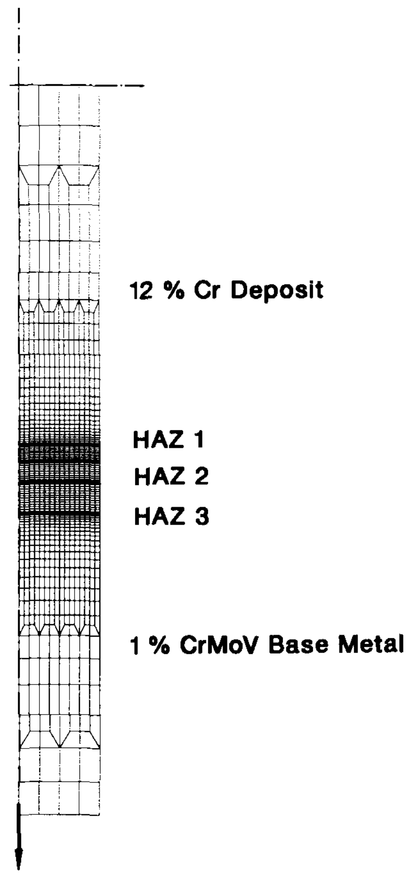

FIG. 5—*Finite element mesh for calculation of dissimilar welds.*

stress. While the maximum von Mises equivalent stress is approximately identical to the nominal stress for the base metal, the maximum value lies beyond the nominal stress for HAZ 3. At first glance, this is a surprising effect for a smooth round bar under uniform tension. The effect is, however, understood if the values of radial stress σ_r, axial stress σ_a, and hoop stress σ_h are depicted. This is done for one section of the specimen in HAZ 3, Fig. 8. As can be seen there, positive radial and hoop stresses emerge, and the increase of σ_r and σ_h is higher than that of σ_a so that σ_v falls below the value of the nominal stress over the whole section (Fig. 9). The multiaxiality of the stress state can be quantified by a simplified multiaxiality quotient h^*, which is defined as

$$h^* = \frac{\sigma_1 + \sigma_2 + \sigma_3}{\sigma_v}$$

where for uniaxial tension $h^* = 1$ and for the hydrostatic stress state $h^* \rightarrow \infty$. As can be seen from Fig. 9, a multiaxial stress state develops over the whole section under consideration.

The distribution of σ_a, σ_v, and h^* at the outside of the specimen is shown in Fig. 10; the maximum values of σ_a and σ_v occur in HAZ 1, which does, however, not fail due to its high

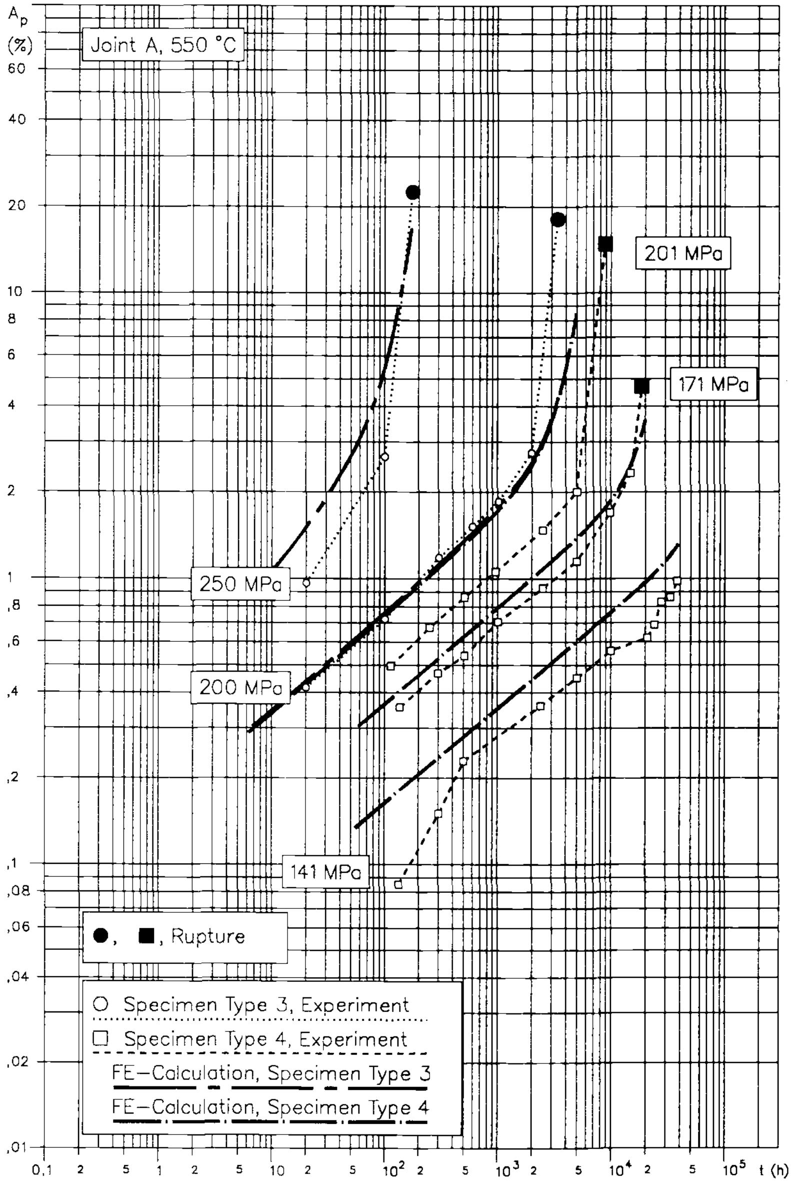

FIG. 6—*Comparison of experimental and numerical results for specimens taken from Joint A.*

creep rupture strength. The maximum value of h^* occurs in HAZ 3. At the border between two materials, the material with the higher minimum creep rate has a higher value of h^* and a lower value of σ_v.

The decrease of σ_v in HAZ 3 caused by the development of a triaxial stress state is the reason for rupture in the base metal at a time beyond that expected for HAZ 3 at a nominal stress of 200 MPa.

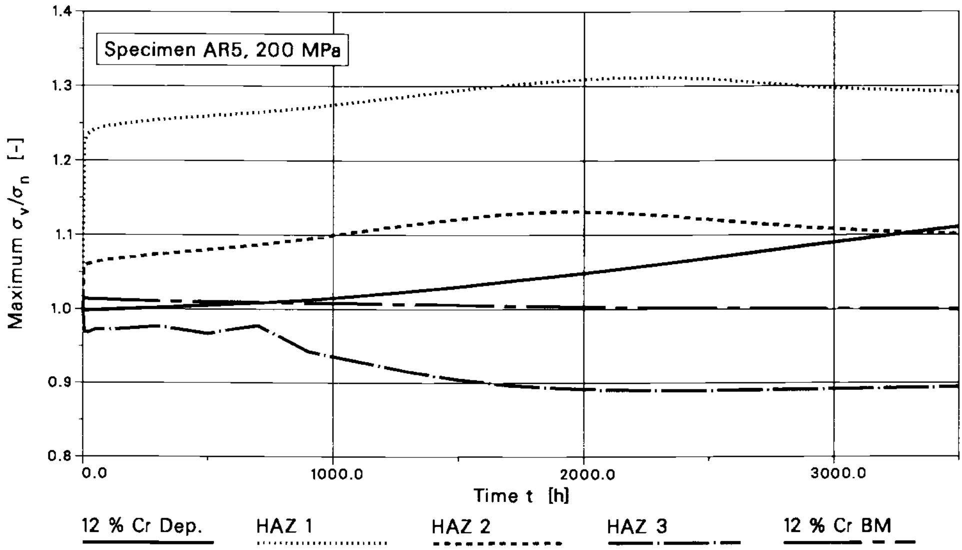

FIG. 7—*Maximum σ_v/σ_n of a small-scale specimen taken from Joint A, nominal stress 200 MPa.*

The situation changes, however, with decreasing nominal stress. The variation of maximum axial stress within the materials decreases, whereas the difference in the maximum von Mises stress in HAZ 3 and base metal increases slightly, Fig. 11. The maximum value of h^* is around the same as for 200 MPa nominal stress in HAZ 3 and decreases for all other materials. Despite the fact that σ_v in HAZ 3 is even lower in relation to the base metal than it is at a nominal stress of 141 MPa, failure is predicted in the HAZ since the decrease of the creep rupture strength of HAZ 3 compared to the base metal becomes more distinct with longer time to rupture. Indeed, rupture occurred in HAZ 3 in the experiment. As the damage mechanism changes from transgranular to intergranular, the rupture location can however only be predicted by application of σ_a.

Experimental Results from Dissimilar Welds of 12% Cr and 1% CrMoV Steel

Creep rupture tests of round small-scale specimens (Type 3, see Fig. 3) and flat large-scale specimens, Fig. 12, from a dissimilar weld of 12% Cr and 1% CrMoV steel (Joint B3, see Table 1) were carried out in order to characterize the influence of specimen size on creep rupture. Creep curves of small- and large-scale specimens are depicted in Fig. 13. As can be seen, large-scale specimens exhibit longer times to creep rupture than small-scale specimens.

A comparison of creep rupture strength of small-scale specimens, large-scale specimens, and HAZ 3 is shown in Fig. 14. The values for HAZ 3 were determined in Ref *8* for a heat of 1% CrMoV base metal with a higher creep rupture strength than that of the base metal from Joint B3. One can, however, assume that differences in the HAZ properties of both base metals diminish for long-term creep. For stresses higher than 70 MPa, small- and large-scale specimens fail in HAZ 1 near the fusion line. The creep rupture strength of the large-scale specimens is beyond that of small-scale specimens and HAZ 3.

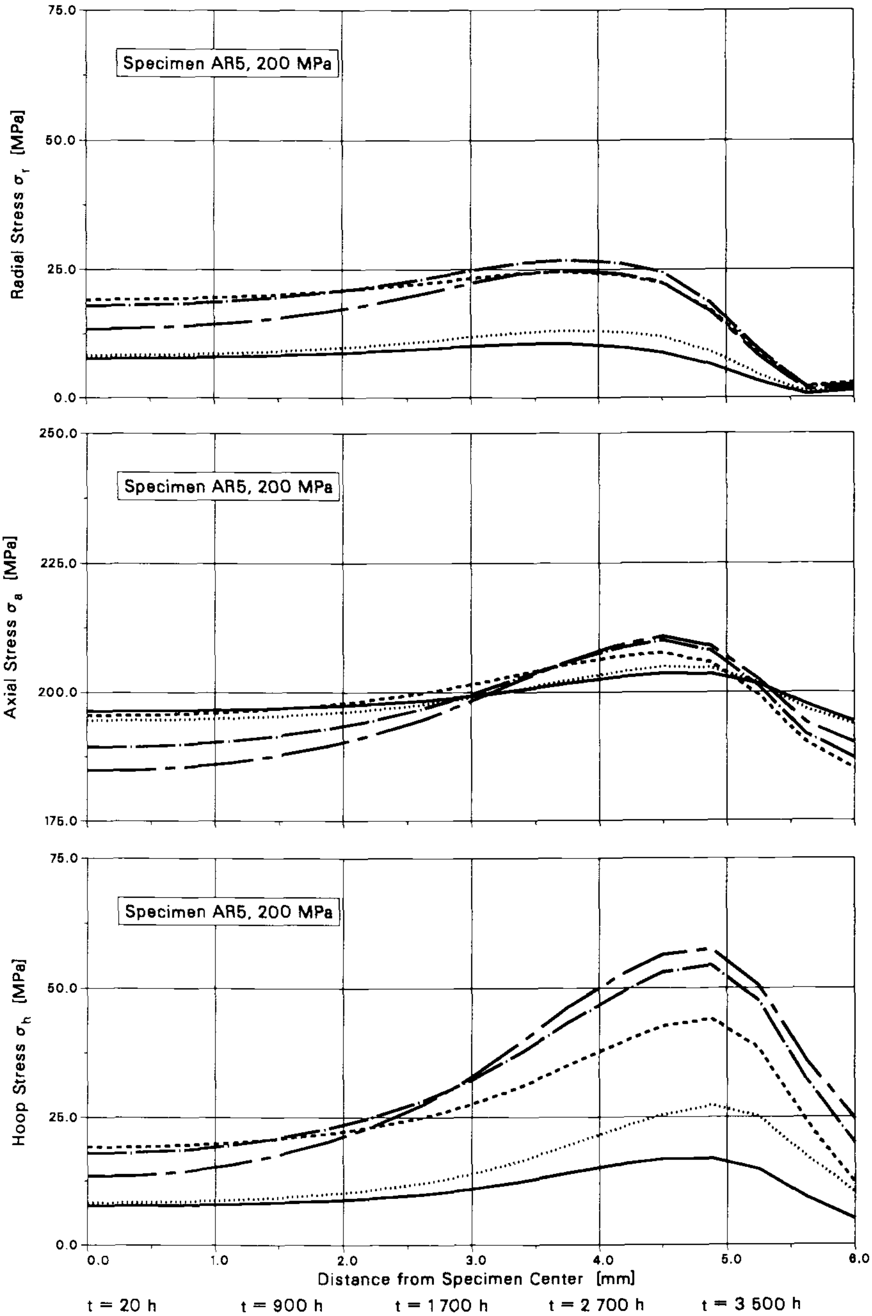

FIG. 8—*Stress components in a section in HAZ 3 of a small-scale specimen taken from Joint A, distance from fusion line 2.29 mm, nominal stress 200 MPa.*

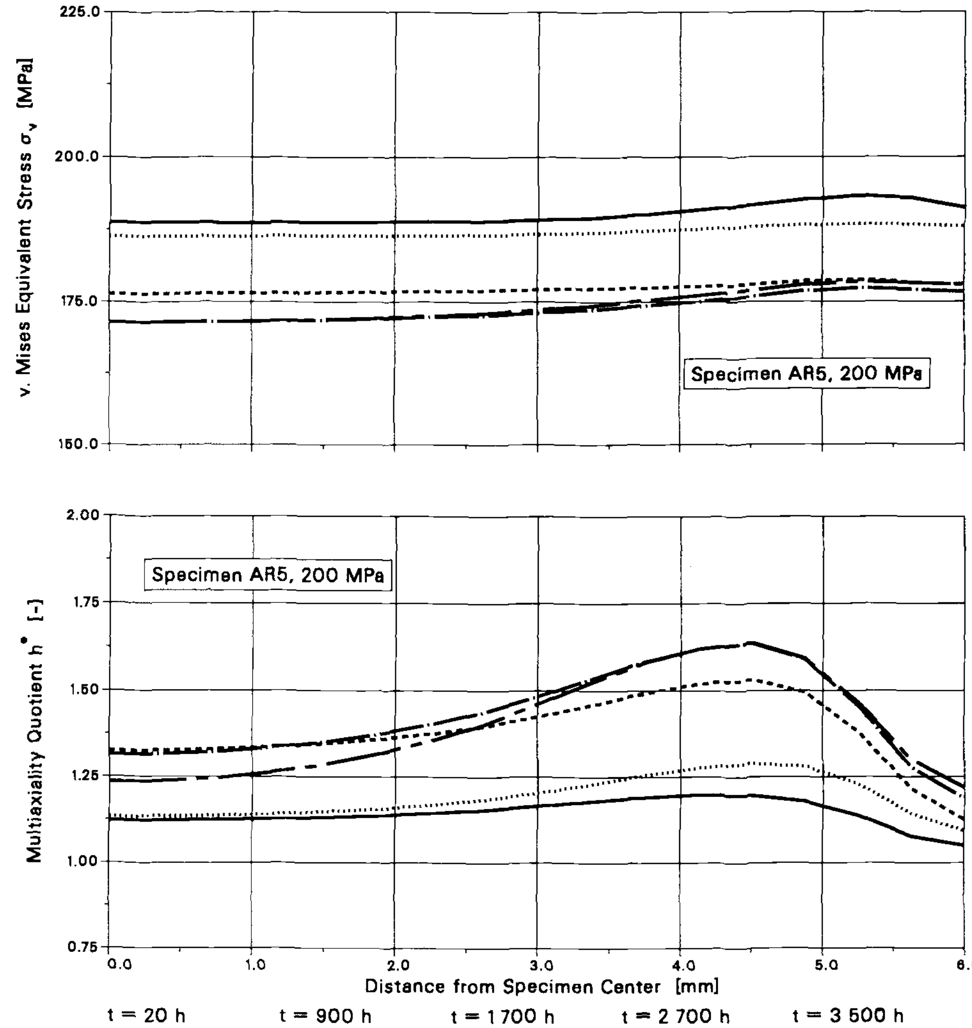

FIG. 9—σ_v *and* h* *in a section of HAZ 3 of a small-scale specimen taken from Joint A, distance from fusion line 2.29 mm, nominal stress 200 MPa.*

Results of Finite Element Calculations of Specimens from a Dissimilar Weld

Finite element calculations taking into account creep properties of base metals, weld metal, and HAZ were carried out to explain the different rupture time of small- and large-scale specimens. A comparison of measured and calculated elongation of small- and large-scale specimens is given in Figs. 15 and 16, respectively. Again, the coincidence between experimental and numerical values is good; for large-scale specimens, plain strain calculations give better results than plain stress calculations.

Normalized values of σ_a, σ_v, and h^* for small- and large-scale specimens tested at 200 MPa nominal stress are shown in Figs. 17 and 18. The stress concentration for σ_a in HAZ 1 is higher than for the similar weld; this is caused by the differences between 12% Cr deposit and 1%

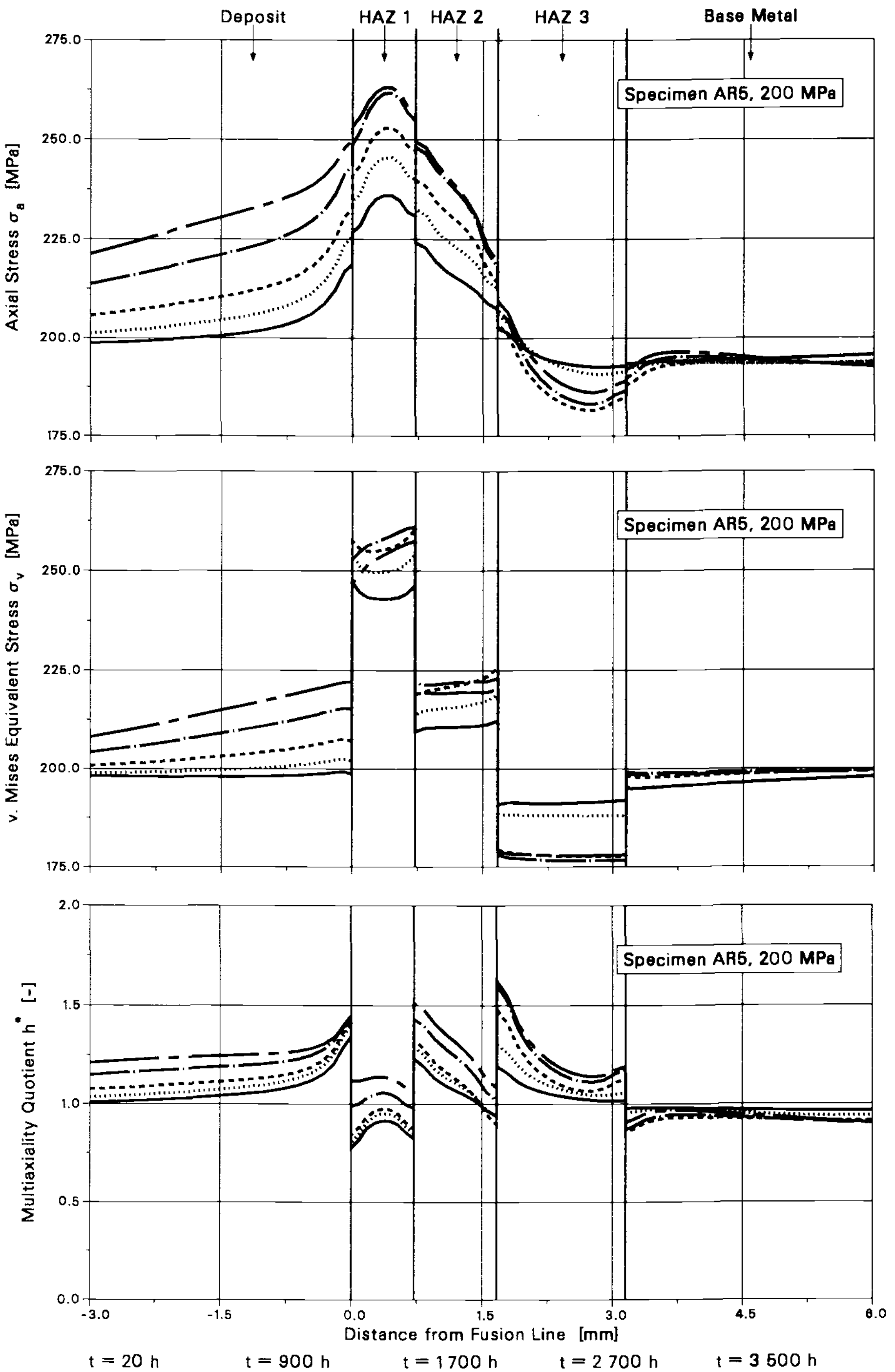

FIG. 10—σ_a, σ_v *and* h* *at the outside of a small-scale specimen taken from Joint A, nominal stress 200 MPa.*

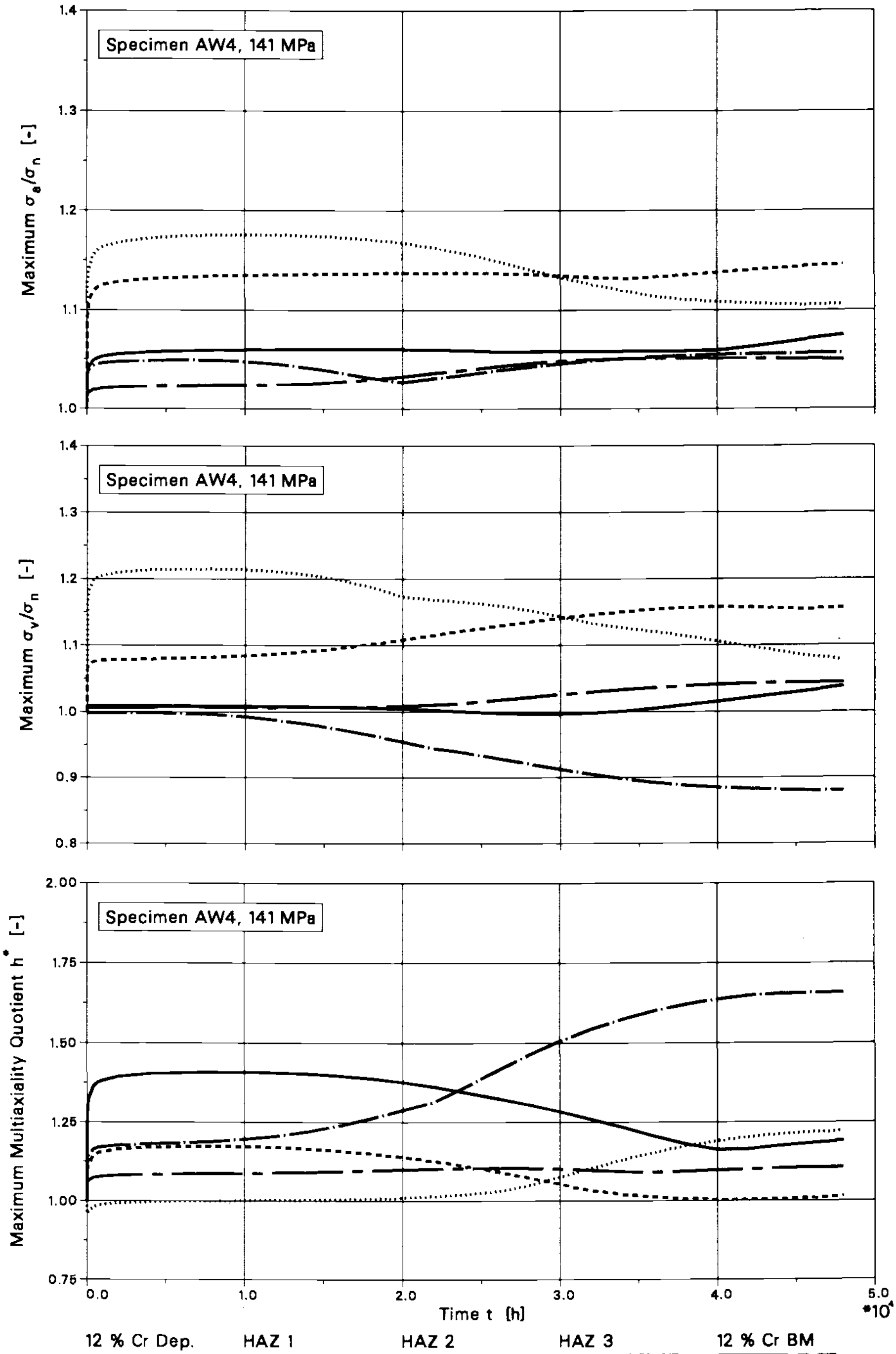

FIG. 11—*Maximum values of* σ_a/σ_n, σ_v/σ_n *and* h* *of a small-scale specimen taken from Joint A, nominal stress 141 MPa.*

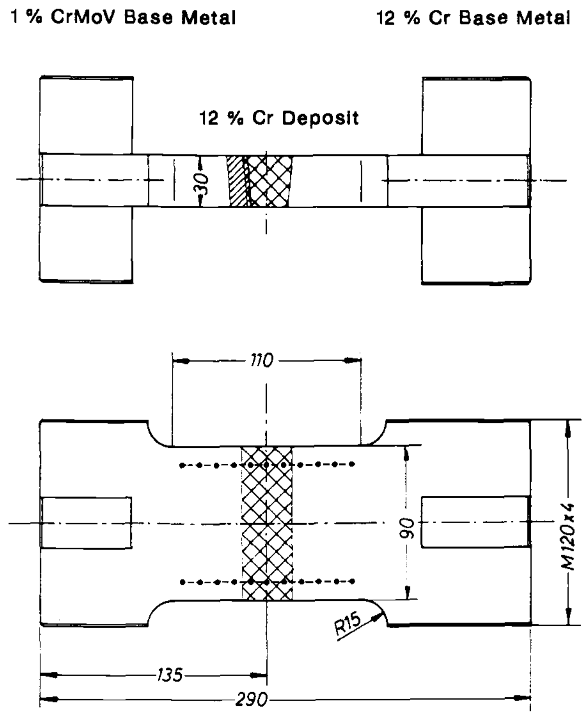

FIG. 12—*Dimensions (mm) of large-scale specimens.*

CrMoV HAZ. This stress concentration is also observed for σ_v. For the same test duration, the maximum values of σ_a and σ_v are higher in the small-scale specimen than in the large-scale specimen. The reason for this is a slower stress- and strain-redistribution in the large-scale specimen due to the higher constraint, which finally leads to longer rupture times for the large-scale specimen.

Again, the results of the finite element calculations make possible a prediction of rupture location and rupture time by taking into account multiaxial stress states originating from different creep properties of adjacent microstructures in the transition deposit-HAZ-base metal.

Summary

Small-scale specimens taken transversely from similar weldments of 12% Cr steel as well as small- and large-scale specimens taken from dissimilar weldments 12% Cr/1% CrMoV with 12% Cr deposits were tested in creep rupture tests at 550°C. For the similar welds, a migration of the rupture location from base metal into the fine-grained HAZ was observed with decreasing nominal stress; the creep rupture strength of the welded joint was, however, beyond that of the weakest HAZ microstructure. This effect is caused by the multiaxial stress state in the weakest HAZ, which develops due to a constraint imposed by the surrounding microstructures with lower creep rate and higher creep rupture strength. For dissimilar welds, the large-scale

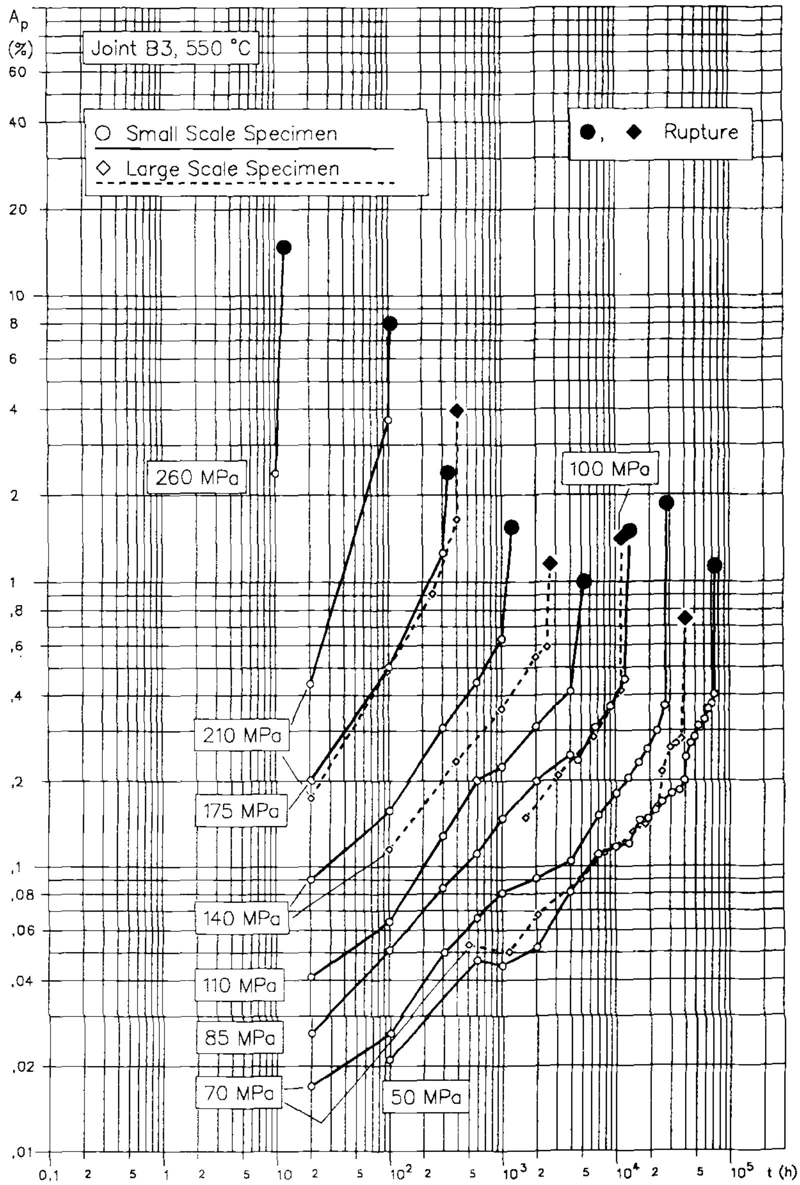

FIG. 13—*Creep curves of small-scale and large-scale specimens taken from Joint B3.*

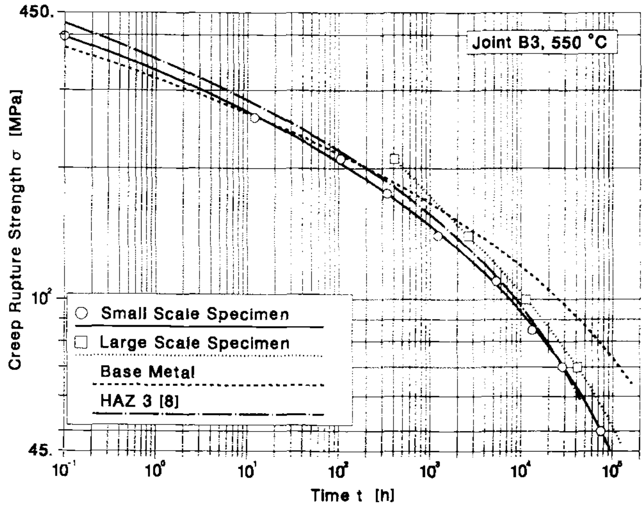

FIG. 14—*Creep rupture strength of small-scale and large-scale specimens taken from Joint B3.*

specimens tested exhibit longer creep rupture times than the small-scale specimens. Results of finite element calculations show that in large-scale specimens the stress- and strain-redistribution due to creep is slower than in small-scale specimens, which is caused by a higher constraint in large-scale specimens.

By means of finite element calculations, it was possible to make safe but not overconservative predictions of the creep rupture time and the rupture location if different creep properties in the HAZ of similar and dissimilar welds were taken into account.

Acknowledgment

The work has been sponsored by the Federal Minister of Trade and Commerce within the scope of the industrial joint research program (Research Project AIF-Nr. 7030). The Arbeitsgemeinschaft Warmfeste Stähle contributed the testing material. The authors express their sincere thanks for this support.

References

[*1*] Ruttmann, W., Bettzieche, P., Jahn, E., Müller, E.-O., and Schieferstein, U., "Zeitstandversuche an Schweißverbindungen zwischen warmfesten Stählen," *Schweißen und Schneiden, Vol. 21,* 1969, No. 1, pp. 8/17.

[*2*] Thoraval, G., "The Behaviour of Welds in EdF Fossil-fired Power Plants," *Proceedings: Life of Welds at High Temperatures,* Institute of Mechanical Engineers, London, 12–13 June 1990, London, United Kingdom, 1990.

[*3*] Gooch, D. J. and Kimmins, S. T., "Type IV Cracking in ½Cr½Mo¼V/2¼Cr1Mo-Weldments," *International Conference on Creep and Fracture of Engineering Materials and Structures,* Swansea, United Kingdom, 1987.

[*4*] Maier, G., Theofel, H., and Maile, K., "Einfluß der Wärmeeinbringung beim Schweißen auf die Zeitstandfestigkeit und das Kriechverhalten von Schweißverbindungen, untersucht an warmfesten CrMoV-Stählen mit 1% und 1% Chrom," Final Report, Research Project AIF-Nr. 4566, MPA, University of Stuttgart, Stuttgart, Germany, 1983.

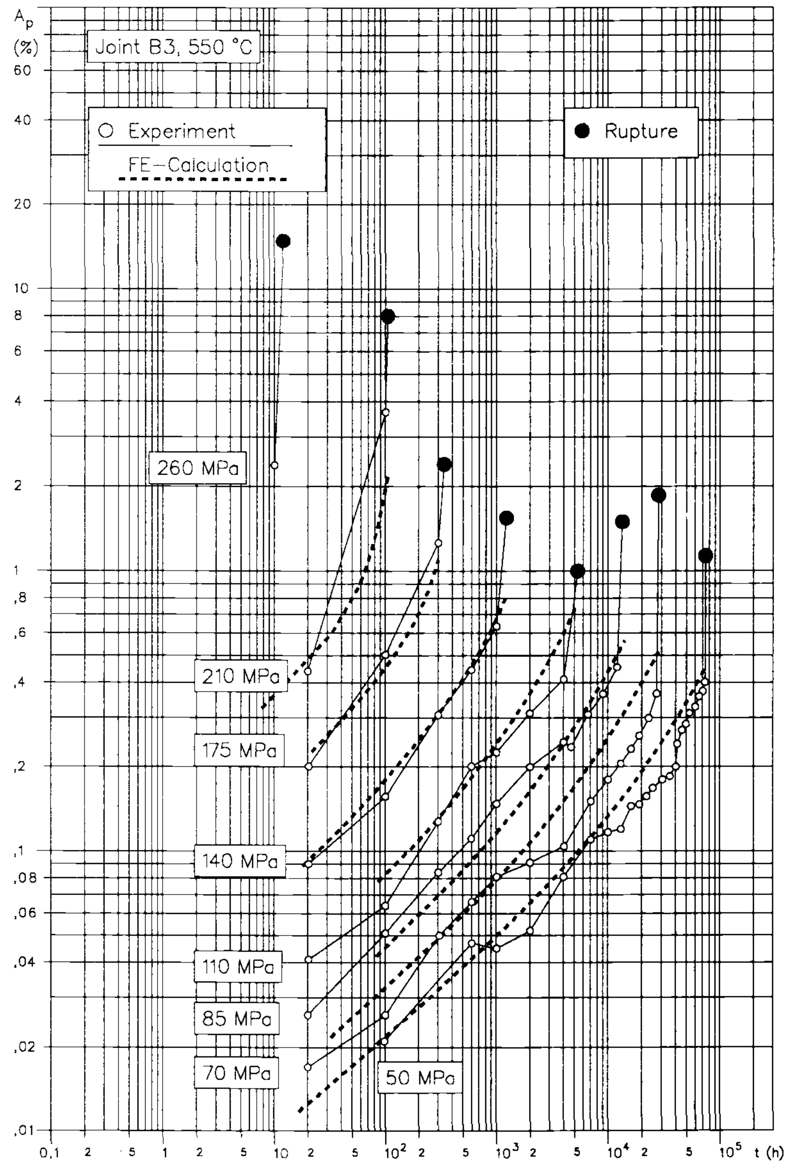

FIG. 15—*Comparison of experimental and numerical results for small-scale specimens taken from Joint B3.*

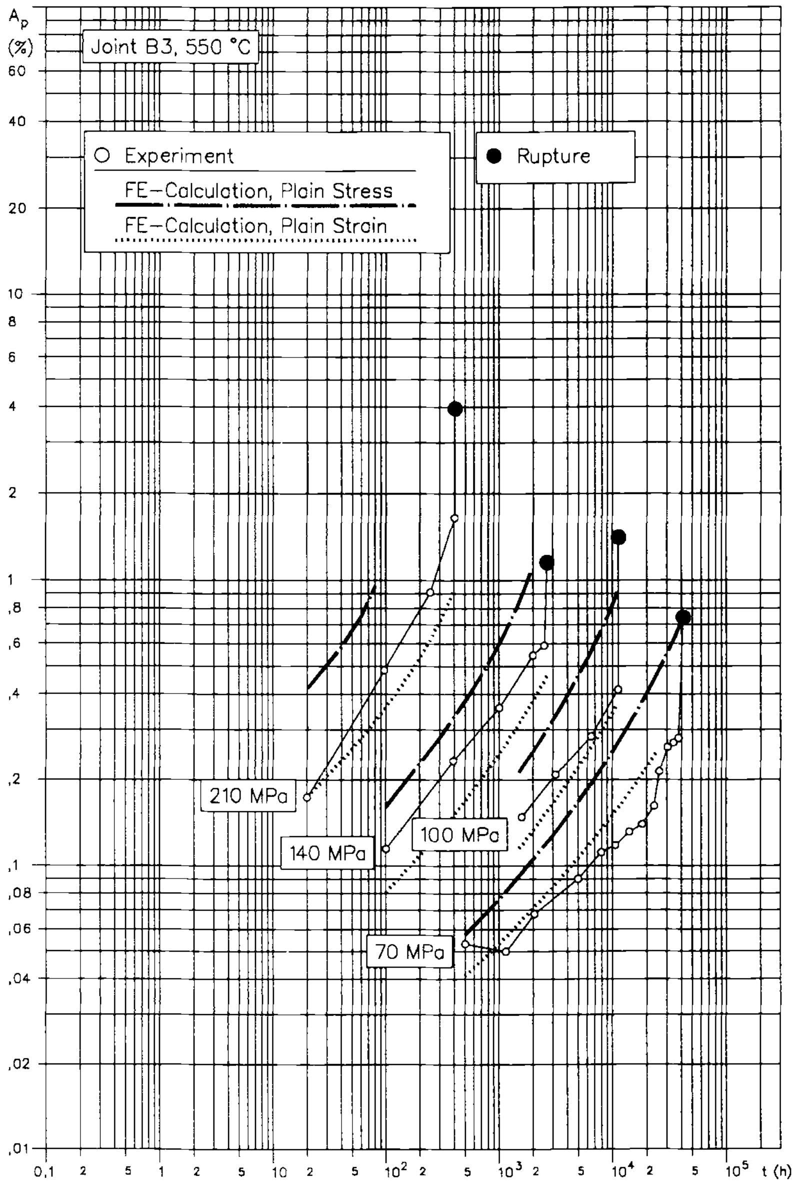

FIG. 16—*Comparison of experimental and numerical results for large-scale specimens taken from Joint B3.*

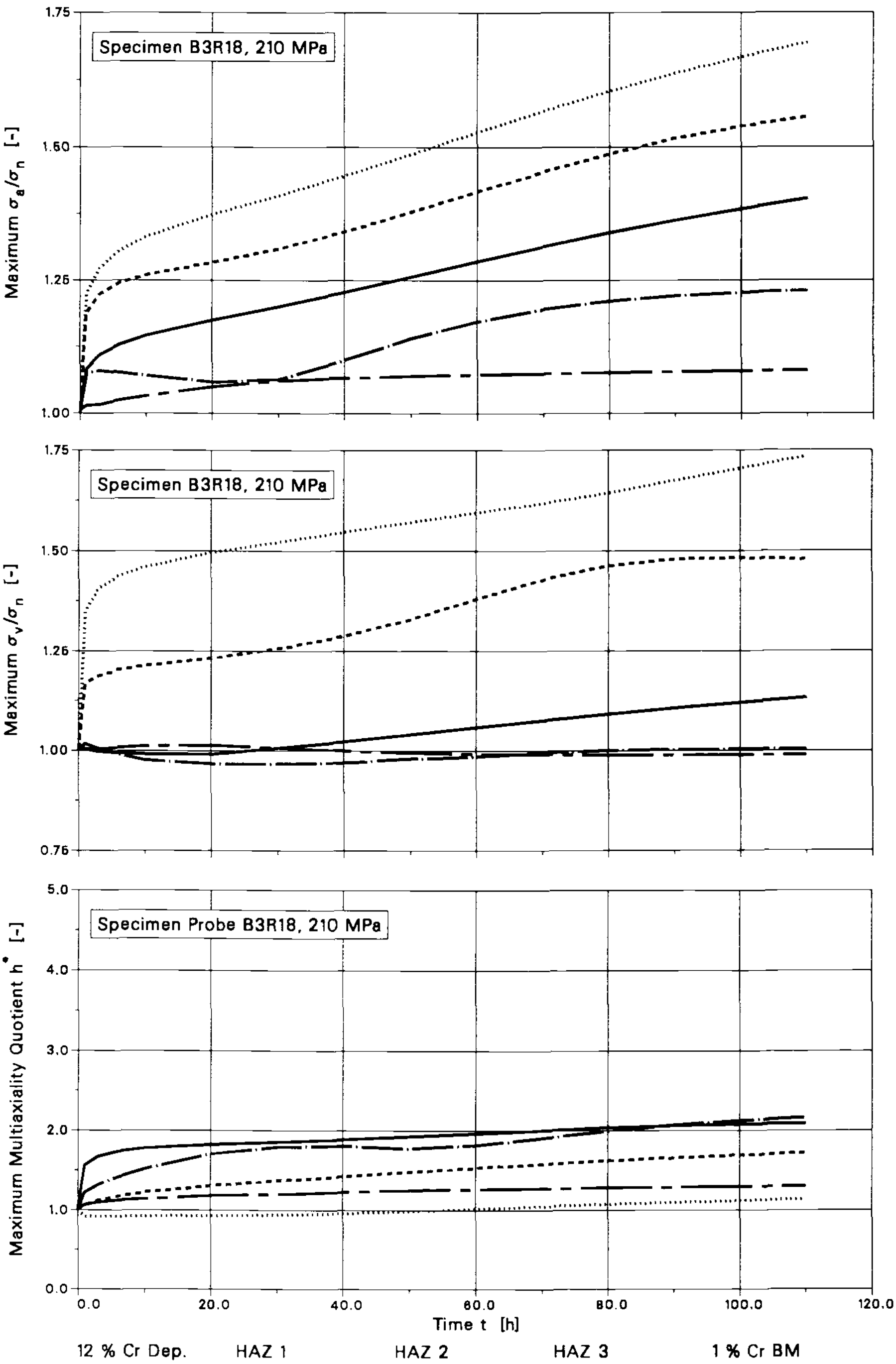

FIG. 17—*Maximum values of* σ_a/σ_n, σ_v/σ_n *and* h* *of a small-scale specimen taken from Joint B3, nominal stress 210 MPa.*

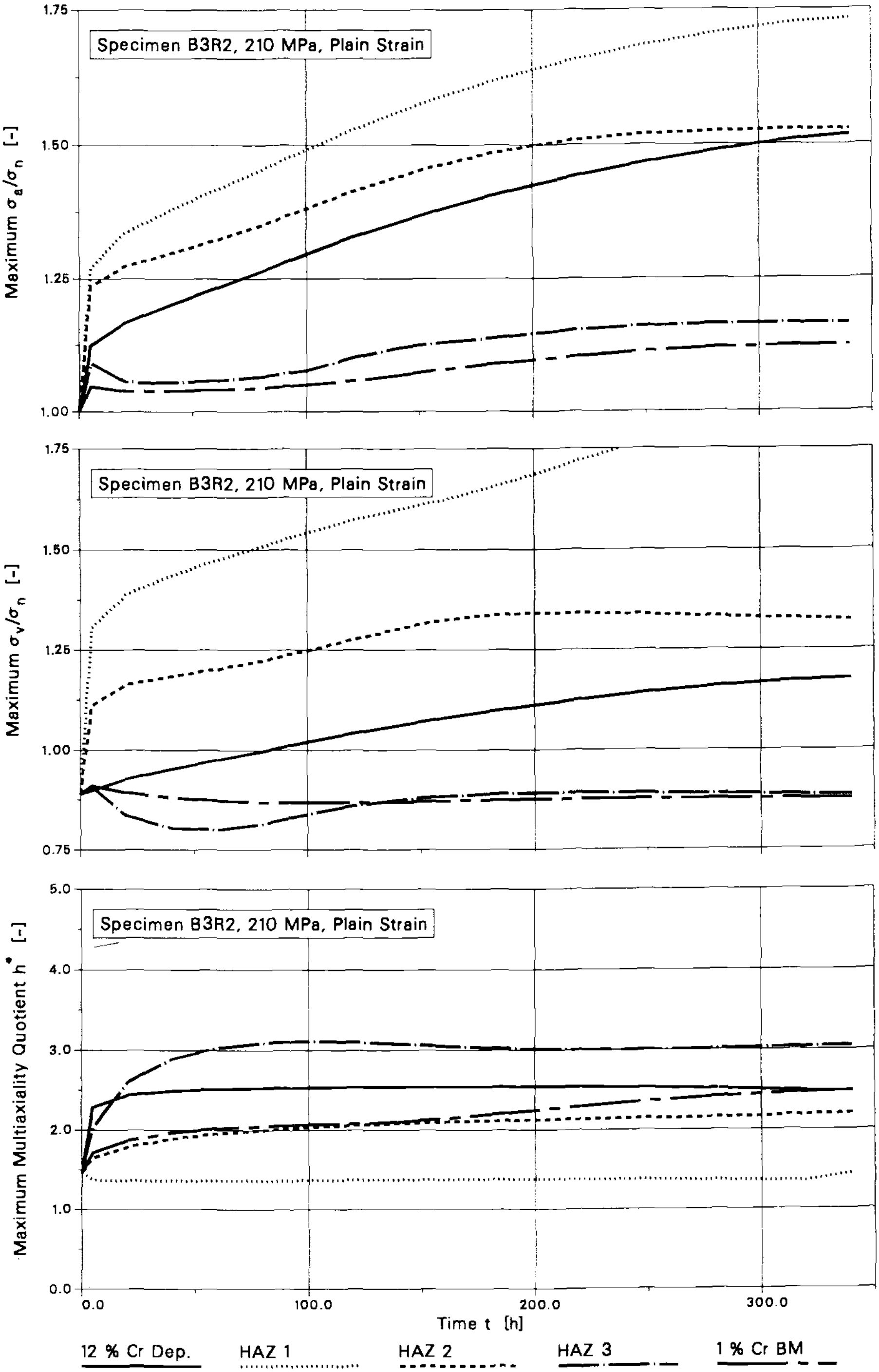

FIG. 18—*Maximum values of* σ_a/σ_n, σ_v/σ_n *and* h* *of a large-scale specimen taken from Joint B3, nominal stress 210 MPa.*

[5] Theofel, H. and Maile, K., "Einfluß der Wärmeeinbringung beim Schweißen auf die Zeitstandfestigkeit und das Kriechverhalten von Schweißverbindungen, untersucht an warmfesten CrMoV-Stählen mit 1% und 12% Chrom," Final Report, Research Project AIF-Nr. 5710, MPA, University of Stuttgart, Germany, 1987.
[6] Eckert, W. and Maile, K. "Langzeitstandversuche und numerisch-analytische Untersuchungen zur Ermittlung der Zeitstandfestigkeit und des Kriechverhaltens von Schweißverbindungen aus warmfesten CrMoV-Stählen," Final Report, Research Project AIF-Nr. 7030 MPA,, University of Stuttgart, Germany, 1991.
[7] ABAQUS User's Manual, Version 4.8, Hibbitt, Karlsson & Sorensen Inc., Providence, RI, 1988.
[8] Theofel, H., "Investigation of the Structural Formation, Toughness and Strength of the Heat Affected Zone by Means of Weld Simulated Specimens of 1% CrMoV Steel," Final Report, COST 505 Project D 17, MPA, University of Stuttgart, Germany, 1988.

Roland deWit,[1] *Richard J. Fields,*[1] *and George R. Irwin*[2]

Use of Thickness Reduction to Estimate Fracture Toughness

REFERENCE: deWit, R., Fields, R. J., and Irwin, G. R., "**Use of Thickness Reduction to Estimate Fracture Toughness,**" *Constraint Effects in Fracture, ASTM STP 1171,* E. M. Hackett, K.-H. Schwalbe, and R. H. Dodds, Eds., American Society for Testing and Materials, Philadelphia, 1993, pp. 361–382.

ABSTRACT: To help predict the behavior of a nuclear pressure vessel undergoing pressurized thermal shock, values of the arrest toughness are required. The purpose of the work described here is to show how toughness values can be calculated from the thickness reduction (TR) of the tested specimens and then used as "lower-bound" estimates. In the NIST wide-plate crack-arrest test program, 16 single edge-notched tension specimens were fractured, using the 26.7 MN universal testing machine. The first series of tests used HSST A533 Grade B Class 1 quenched and tempered steel, while the second series used a low upper-shelf 2¼ Cr-1 Mo steel. For each specimen the TR was measured on the two halves of the broken specimen and a contour map was constructed. The thickness reduction, TR, along the crack propagation plane can be related to the toughness, K, by the relationship $K^2 = E \cdot \sigma_Y \cdot \text{TR}$, where E is Young's modulus and σ_Y an estimate of the tension effective yield strength adjusted for temperature, strain-rate, and constraint. The results show good agreement with values of K for arrest and reinitiation computed from a finite-element generation-mode analysis. Therefore, the indication of plastic work rate provided by the thickness reduction near the fracture plane is a useful preliminary assessment of the fracture toughness.

KEY WORDS: crack arrest, dynamic fracture, fracture mechanics, temperature gradient, toughness, wide-plate testing

To predict the behavior of a nuclear pressure vessel undergoing pressurized thermal shock, certain information on dynamic crack propagation and arrest is required. In particular, it is desirable to know the crack-arrest toughness values, K_{Ia}, as a function of the operating temperature. The purpose of the work described here is to show how the use of thickness reduction (TR) measurements can assist the interpretations of fracture experiments.

The TR near the fracture plane can serve as an indication of plastic work rate for a crack traversing a plate. Nearly all of the energy loss rate, G, produces plastic strains in the plastic zone ahead of the apparent crack front and behind it during separation of late-breaking ligaments. Therefore a correlation between G and some measure of plastic strain intensity would be expected and a direct proportionality is plausible.

The idea of relating the TR of a plate-type fracture specimen to the crack-tip opening displacement (CTOD) or the toughness, K, while not new, has received no significant attention in technical publications. An experimental trial by F. M. Burdekin at the Welding Institute in Abington, England, circa 1964, indicated a near equality between CTOD values and the TR measured close to the notch root. He used a single-edge notched bend specimen. The mea-

[1] Physicist and metallurgist, respectively, Mechanical Properties and Performance, National Institute of Standards and Technology, Gaithersburg, MD 20899.
[2] Professor, Department of Mechanical Engineering, University of Maryland, College Park, MD 20742.

surements of CTOD and TR were made at a series of loadings prior to significant crack extension. The specimen was taken from an air-cooled mild steel plate, and the applied loads were too large for use of linear-elastic analysis.

Subsequently, trials of TR in relation to values of K were made at the Frankford Arsenal by C. C. Carman. Large center-cracked plates of high-strength 7075-T6 Al alloy were used. The TR was measured after a small amount of stable crack extension from the sharp root notch. In place of direct CTOD measurements, the comparison was made to inferred values of CTOD using the equation $K^2 = EG = E \cdot \sigma_{YS} \cdot \mathrm{CTOD}$, where E is Young's modulus and σ_{YS} the uniaxial tension yield strength. Accurate measurements were difficult. A wide-yoke micrometer, fitted with rounded contact points, was used. The average result from several measurements supported the idea of a near equality between TR (close to the crack front) and the inferred CTOD. From current viewpoints σ_{YS} should be replaced by an estimate of the effective yield strength (or flow stress), σ_Y, but the effect of this modification would be small for the aluminum alloy.

Recently, Irwin and Zhang [1] made comparisons of TR to values of CTOD, inferred from fracture surface topography, using a side-grooved specimen of A710 steel. The test conditions caused initiation of cleavage from a fatigue pre-crack after a very small amount of void-joining separation. A near equality was observed with the topographic estimate of CTOD being about 10% smaller than the TR. It was noted that the TR measurements were not significantly different, using measurements across contact of the side grooves with the fracture, and using TR across the contacts of side grooves with the specimen surfaces. The side grooves reduced the net section by 20%.

The above considerations lead to the following significant relationships

$$K^2 = E \cdot \sigma_Y \cdot \mathrm{CTOD} \tag{1}$$

$$\mathrm{CTOD} = \mathrm{TR}\ (\text{thickness reduction}) \tag{2}$$

Equation 1, where σ_Y is an estimate of the tension effective yield strength (plastic flow stress), has often been used to relate CTOD values to values of K. TR in Equation 2 is the thickness reduction measured across the fracture surface close to the crack plane.

For moderate cleavage crack speeds, the portion of the energy loss rate which can be ascribed to damping of kinetic energy is not significant. With regard to K-from-TR values for a running crack, in the 1946–1956 period, a large number of wide-plate fracture tests of 25 and 19-mm-thick ship steel plates were conducted in connection with brittle fractures of welded cargo ships. Tests with center-notched wide plates at −18°C (0°F) produced cleavage crack speeds in the range of 0.3 to 0.5 of the sound velocity. It was noted that a TR of about 0.5% occurred near the fracture plane. A value of 331 MPa (48 ksi) can be assumed as an appropriate low strain rate value of σ_Y. However, a factor of 10^6 increase in loading rate causes about a 207 MPa (30 ksi) increase of the flow stress [2]. Then a TR value of 0.13 mm (0.005 in.) leads to a K-estimate of 119 MPa$\sqrt{\mathrm{m}}$ (108 ksi$\sqrt{\mathrm{in.}}$). Figure 6 in Ref *2* shows that this K value lies on the upper plateau of the crack speed versus K relationship, i.e., it is a reasonable estimate of the dynamic K.

Background of Wide-Plate Testing Program

The primary objective of the crack-arrest technology studies under the Heavy-Section Steel Technology (HSST) Program conducted by the Oak Ridge National Laboratory (ORNL) for the Nuclear Regulatory Commission (NRC) is to generate data for an understanding of crack-arrest behavior at temperatures near and above the onset of the Charpy upper-shelf region.

The program goals include: (1) extending the existing K_{Ia} data bases to temperatures beyond those associated with the upper limit in Section XI of the American Society of Mechanical Engineers (ASME) Boiler and Pressure Vessel Code; (2) clearly establishing that crack-arrest occurs prior to fracture mode conversion; (3) observing the relationship between arrest data and machine/specimen compliance behavior; and (4) validating the predictability of crack arrest, stable tearing, and/or unstable tearing sequences for reactor pressure vessel materials. Additionally, the tests and analyses provide bases for obtaining and interpreting dynamic-fracture data (with relatively long crack runs) and bases for validation of viscoplastic fracture models and analysis methods.

Early studies of crack arrest utilized a small specimen method which provided useful results only at temperatures near or below the NDT temperature. In addition, this test method used a crack-driving force that decreased with crack extension. Under the HSST program, crack-arrest data have been generated at ORNL over an expanded temperature range through tests involving large thermally shocked cylinders, which also provide data under multiaxial transient and high-restraint loading. The program then undertook the performance of a series of wide-plate tests as an opportunity to obtain a more significant number of data points at affordable costs.

The HSST wide-plate crack-arrest tests were designed to provide fracture-toughness measurements at temperatures approaching or above the onset of the Charpy upper-shelf regime, in a rising toughness region, and with an increasing driving force. The tests were performed at the National Institute of Standards and Technology (NIST) [formerly National Bureau of Standards (NBS)] using the 26.7-MN capacity (in tension) universal testing machine. In total, four series of tests were planned: (1) WP-1 series (A533 Grade B Class 1 material), (2) WP-2 series (low upper-shelf base material), (3) WP-3 series (low upper-shelf weld material), and (4) WP-CE series (A533 Grade B Class 1 material supplied by Combustion Engineering, Inc.[3]). The data and observations concerning high-temperature run/arrest behavior are needed to further the understanding of potential light-water reactor pressure vessel behavior under certain thermal-shock scenarios. In addition to providing K_{Ia} data from finite-element calculations, the wide-plate tests also provide information on dynamic fracture (run and arrest) processes that are being used by researchers at ORNL, Southwest Research Institute, and the University of Maryland to develop and evaluate improved fracture-analysis methods.

A detailed description of the whole wide-plate test program is given in Refs *3–7*. A summary of the program can be found in Refs [*8–10*].

Summary of Wide-Plate Testing Program

Over the five-year period from 1984 to 1988, all the tests except for Series WP-3 have been completed, giving a total of sixteen tests, eight utilizing specimens fabricated from HSST plate 13A of A533 Grade B Class 1 steel (WP-1 series), two fabricated from a second heat of A533 Grade B Class 1 steel supplied by Combustion Engineering, Inc. (WP-CE series), and six utilizing specimens fabricated from a low upper-shelf base material (WP-2 series). Table 1 lists the complete set. With the exception of tests WP-1.7, WP-1.8, WP-2.1, WP-2.2, WP-2.3, and WP-2.6, which employed a 0.15-m-thick specimen, each test utilized a single-edge notched (SEN) plate specimen approximately 1 by 1 by 0.1 m. Each specimen was side-grooved by about 12.5% on each side with an angle of 45 ± 5°. The machined notch was precracked by hydrogen charging an electron-beam (EB) weld located at the base of the notch.

ORNL prepared the specimens and shipped them to NIST, where they were welded to two

[3] Trademarks and company names are reported only to describe more fully the experimental conditions and do not imply an endorsement by NIST.

TABLE 1—*Wide-plate testing program.*

Test	Thickness	Date	Quality	Problem
WP-1.1	101.5 mm	9/27/84	NA	Too much out-of-SG
WP-1.2	101.8 mm	1/17/85	Good	Substantially out-of-SG
WP-1.3	99.5 mm	5/9/85	Better	
WP-1.4	101.4 mm	7/19/86	Good	Moderately out-of-SG
WP-1.5	101.7 mm	10/9/86	Best	
WP-1.6	101.8 mm	2/12/86	Better	
WP-1.7	152.4 mm	7/23/87	Good	Moderately out-of-SG
WP-1.8	152.4 mm	3/29/88	NA	Too much out-of-SG
WP-CE-1	101.7 mm	9/14/87	NA	Not dynamic, slanted front
WP-CE-2	101.8 mm	5/12/88	Good	Substantially out-of-SG
WP-2.1	152.6 mm	9/24/86	Better	
WP-2.2	152.2 mm	6/16/88	Best	
WP-2.3	152.1 mm	5/28/87	Good	Undercutting above 37° C
WP-2.4	101.7 mm	8/22/86	NA	Too much out-of-SG
WP-2.5	101.3 mm	1/8/87	Better	
WP-2.6	152.4 mm	9/22/88	Better	

NA = Not analyzed because the fracture surface conditions deviated too far from the criteria for a good thickness reduction calculation.

pull-plates making assemblies that were about 10 m long. Figure 1 shows the specific dimensions of WP-1.3, which is typical of each specimen. For the test an attempt was made to establish a linear thermal gradient across the plate and along the plane of crack propagation, i.e., the side-grooved plane. The actual temperature profiles at the approximate time of the crack initiation and arrest events for the WP-2 series are shown in Fig. 2. The temperature profiles of the other series lay about 100°C lower; for tests WP-1.1 through WP-1.6 they can be found in Refs *3* or *8*, for WP-1.7 and WP-1.8 in Ref *4*, and for WP-CE-1 and WP-CE-2 in Ref *5*. The precracked notch tip was approximately at the 20-cm location. The specimen was then pulled in tension until a crack started propagating from the notch. After initiation of crack propagation in cleavage, several arrests and reinitiations generally occurred until the crack ran by ductile tearing through the high-temperature region to the edge of the specimen. During each test, strain and temperature measurements were made as functions of position and time. Load and crack mouth opening displacement were also obtained as functions of time.

After each test the thickness of the plate was measured in the vicinity of the crack plane. Some typical results are shown in Fig. 3. In these figures the dots represent the points at which the final thickness was measured with a wide-yoke micrometer. From these data the reduction-in-thickness contour maps were drawn.

Calculation of Fracture Toughness from Thickness Reduction

The purpose of this paper is to calculate the fracture toughness, K, from the thickness reduction, TR, by Eqs 1 and 2. These equations were used without a constraint correction because the degree of plane strain constraint was negligible for most of the calculated K values. We shall illustrate the method of the K-from-TR calculation in detail for test WP-2.6, and then just present the results for the other tests. We used the following room temperature value of Young's modulus for steel

$$E = 206.9 \text{ GPa} \tag{3}$$

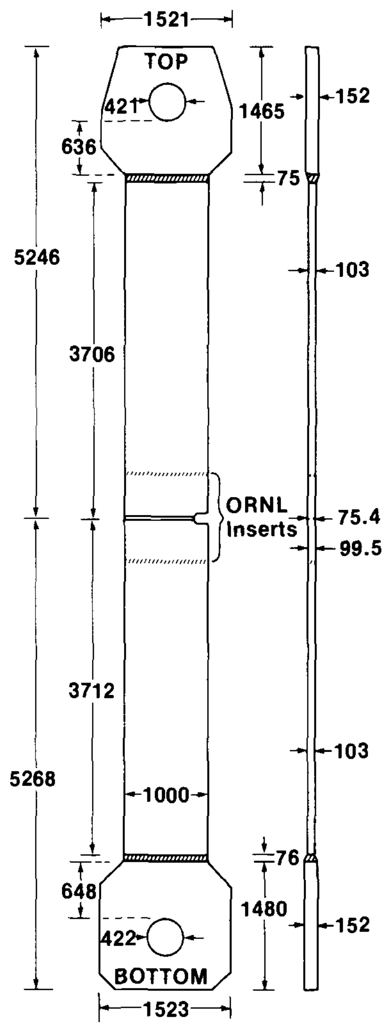

FIG. 1—*Overall dimensions of the third wide-plate crack-arrest specimen and pull plates, WP-1.3. All dimensions are in millimeters ± 2 mm.*

Young's modulus varies only slightly for the temperature ranges investigated here. The tension effective yield strength, σ_Y, was adjusted for the rapid deformation of the material by a modest increase of 138 MPa (20 ksi) over the static value [*2*]

$$\sigma_Y = \sigma_Y(\text{static}) + 138 \text{ MPa} \tag{4}$$

The static value was taken as the average of the 0.2% offset yield strength, σ_{YS}, and the ultimate tension strength, σ_{UT}, as follows

$$\sigma_Y(\text{static}) = \tfrac{1}{2}(\sigma_{YS} + \sigma_{UT}) \tag{5}$$

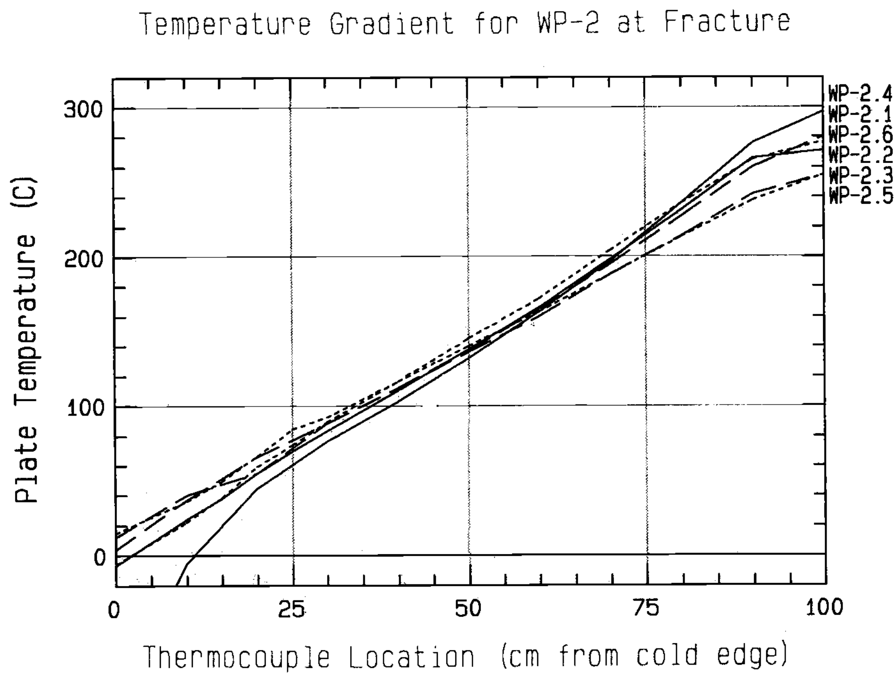

FIG. 2—*Transverse temperature profiles at approximate time of crack initiation-arrest events for test series WP-2, tests WP-2.1 through WP-2.6.*

The values of σ_{YS} and σ_{UT} had already been determined for the three materials as a function of temperature [*3–7*]. The existing data can be represented by the following expressions

$$\sigma_Y(\text{static}) = 530 - 0.668\,T + 0.00291\,T^2 - 0.0000033\,T^3 \quad \text{for WP-1 in the range } -73°\text{C} < T < 315°\text{ C} \tag{6a}$$

$$\sigma_Y(\text{static}) = 506 - 0.753\,T + 0.00479\,T^2 - 0.000007675\,T^3 \quad \text{for WP-CE in the range } 24°\text{C} < T < 121°\text{C} \tag{6b}$$

$$\sigma_Y(\text{static}) = 473 - 0.951\,T + 0.00315\,T^2 - 0.00000238\,T^3 \quad \text{for WP-2 in the range } 23°\text{C} < T < 300°\text{C} \tag{6c}$$

The temperature at any crack length was determined from the temperature profiles, such as those shown in Fig. 2. The temperature dependence of the fracture properties for different materials are often compared to each other with respect to a reference nil ductility temperature, RT_{NDT}. For the wide-plate materials these are

$$\begin{aligned} RT_{NDT} &= -23°\text{C} && \text{for WP-1} \\ RT_{NDT} &= -34°\text{C} && \text{for WP-CE} \\ RT_{NDT} &= 60°\text{C} && \text{for WP-2} \end{aligned} \tag{7}$$

Using these data the values of TR were then obtained as a function of $T - RT_{NDT}$ from the thickness measurements, such as those presented in Fig. 3, by a combination of two methods: (1) from the plotted contours, and (2) from the original measurement points.

K-from-TR Using the Contours

From the intersections of the contours with the crack plane (Fig. 3) an average value of TR was determined between the top and bottom half of the specimen as a function of position. The position was then related to the temperature from the temperature profiles (Fig. 2), and the toughness was calculated from Eqs 1–6. The result for WP-2.6 is plotted in Fig. 4 as a function of $T - RT_{NDT}$.

K-from-TR Using the Measurement Points

From the measurement points closest to the crack plane (Fig. 3) an average final thickness was determined between the top and bottom half of the specimen as a function of position. The TR was obtained by subtracting this final thickness from the original thickness listed in Table 1. When the TR is small, this is the difference between two large numbers and is therefore subject to a large amount of measurement error. To emphasize the uncertainty in the original thickness, we assumed three different values for it and then calculated the corresponding toughnesses as shown in Fig. 5 for WP-2.6. It is seen that the lower K the larger the uncertainty in its value. In fact, for temperatures where cleavage fracture occurred the measurement error was larger than the calculated value of the TR, and therefore these points were not used. These are the temperatures between the cross and the lowest solid symbols in Fig. 5.

Toughness Calculation from Initiation Load

The initial value of K, shown as the cross in Figs. 4 and 5, represents a calculation (see Appendix) based upon the initiation load, crack size, specimen dimensions, and the 25% reduction of the crack front due to the side grooves. This point serves as a low-K tie-point for the TR data. From an inspection of Fig. 5 it was decided that the best choice for the original thickness was 152.4 mm for specimen WP-2.6.

Smooth K-from-TR Curves

Comparing Figs. 4 and 5 we see that for test WP-2.6 the values of K from the contour plots agree well with K from the measurement points. Therefore we fitted a smooth curve through all these data, including the initiation toughness, as shown in Fig. 6.

Wide-Plate Test Quality Assessment

To use the K-from-TR calculations to select best "lower-bound" estimates for crack arrest, it is also important to grade the fracture appearance and conditions of the tests. The criteria for good results are: that the crack surface be flat, in the side-grooved plane, and that the crack front be straight. Therefore, before proceeding with the remaining TR calculations we made a quality assessment of the whole wide-plate testing program by examining the fracture surfaces. A summary of our conclusions is given in Table 1. Four tests were disqualified because they deviated too far from the criteria. The acceptable tests were graded in three categories as good, better, and best. The good tests generally still had some serious problems, such as the

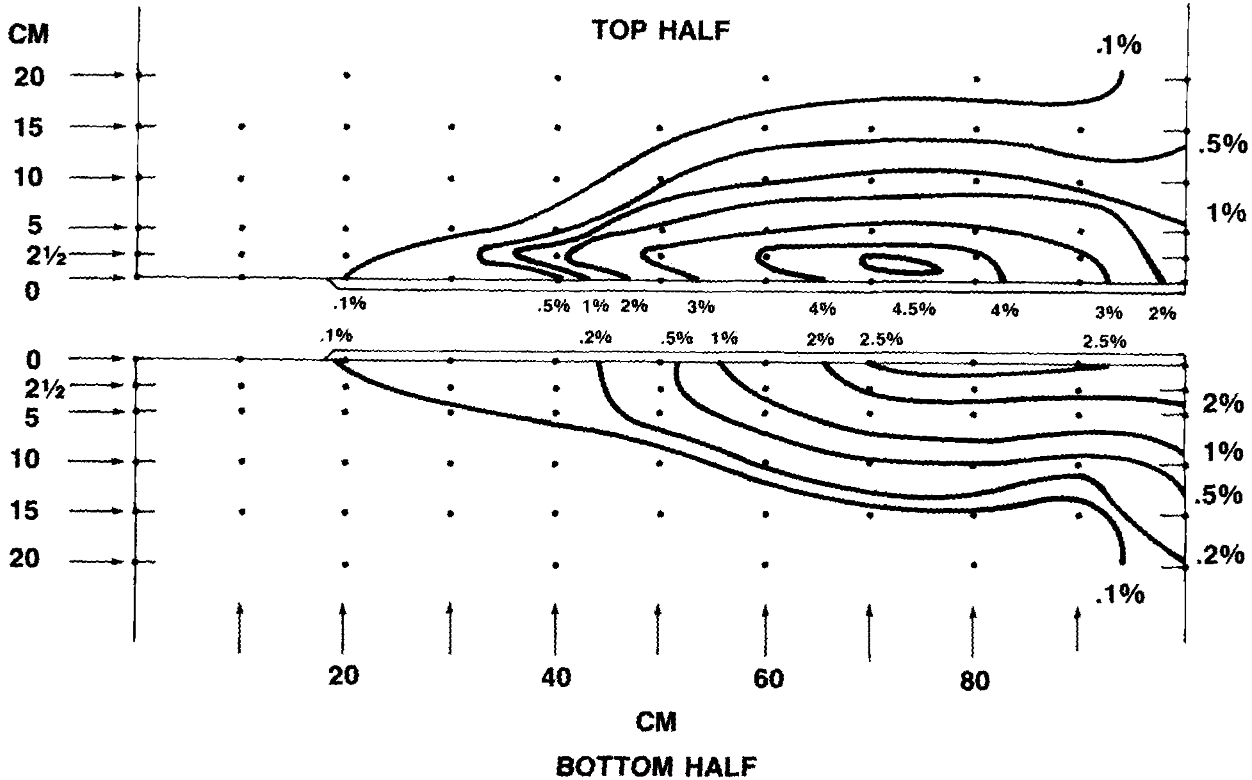

FIG. 3—*Reduction-in-thickness contour maps for specimen* (a) *WP-1.8, which had a high degree of asymmetry and was not analyzed,* (b) *WP-2.3, a good test,* (c) *WP-2.6, a better test, and* (d) *WP-1.5, which had a high degree of symmetry and was a best test. The solid circles represent the measurement points.*

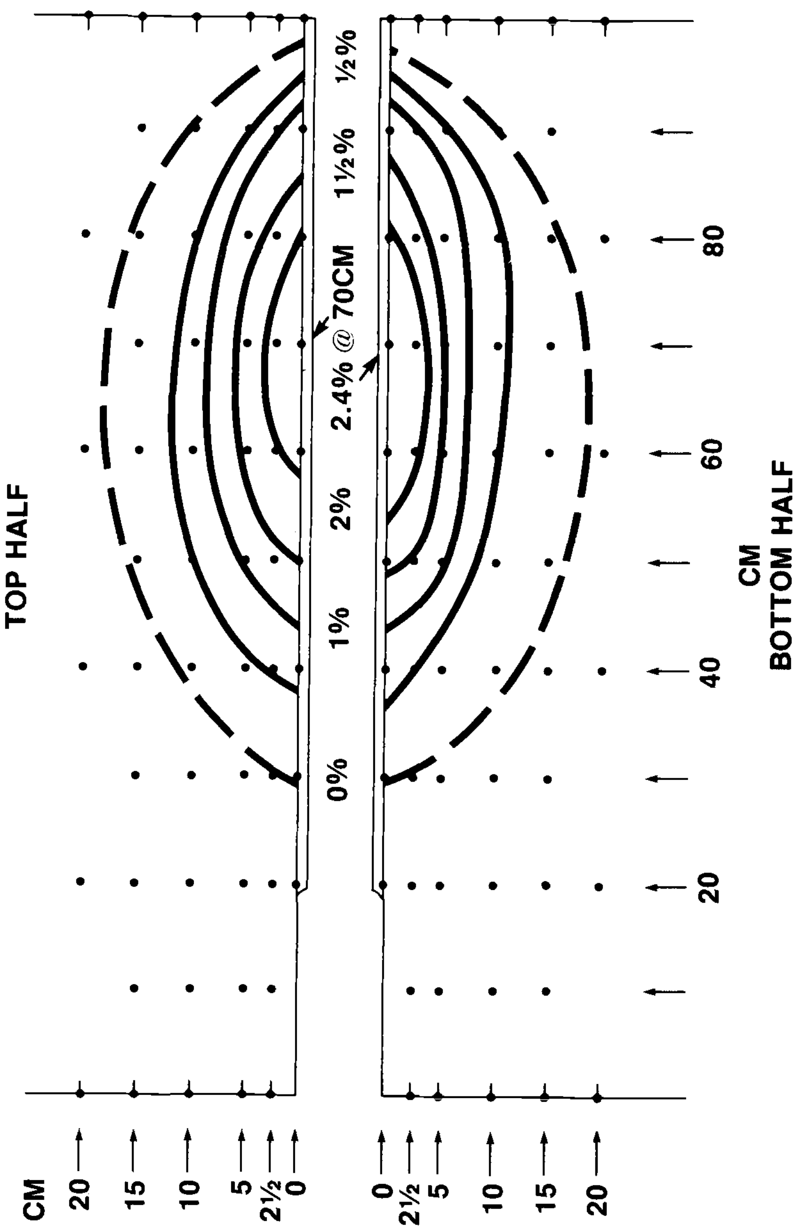

FIG. 3—*Continued*

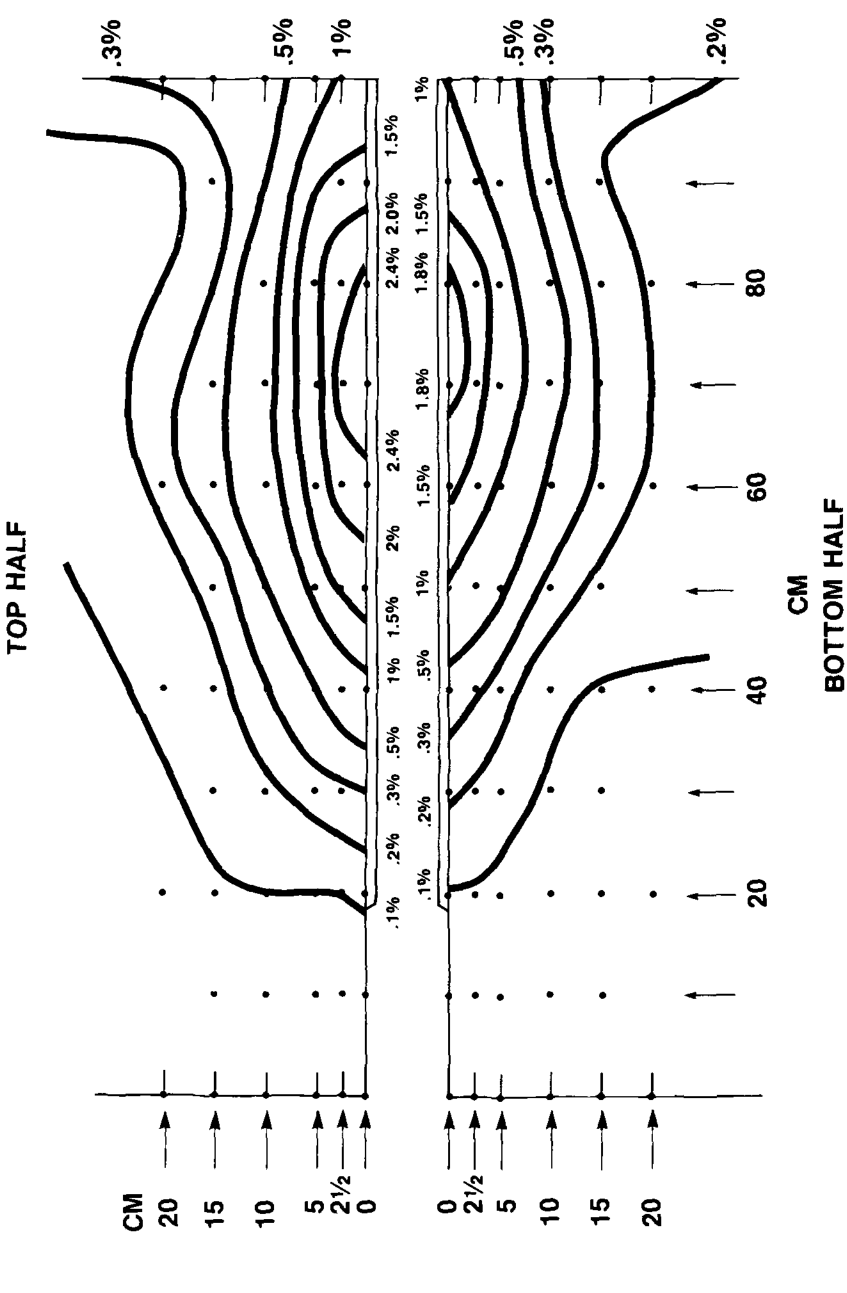

FIG. 3—*Continued*

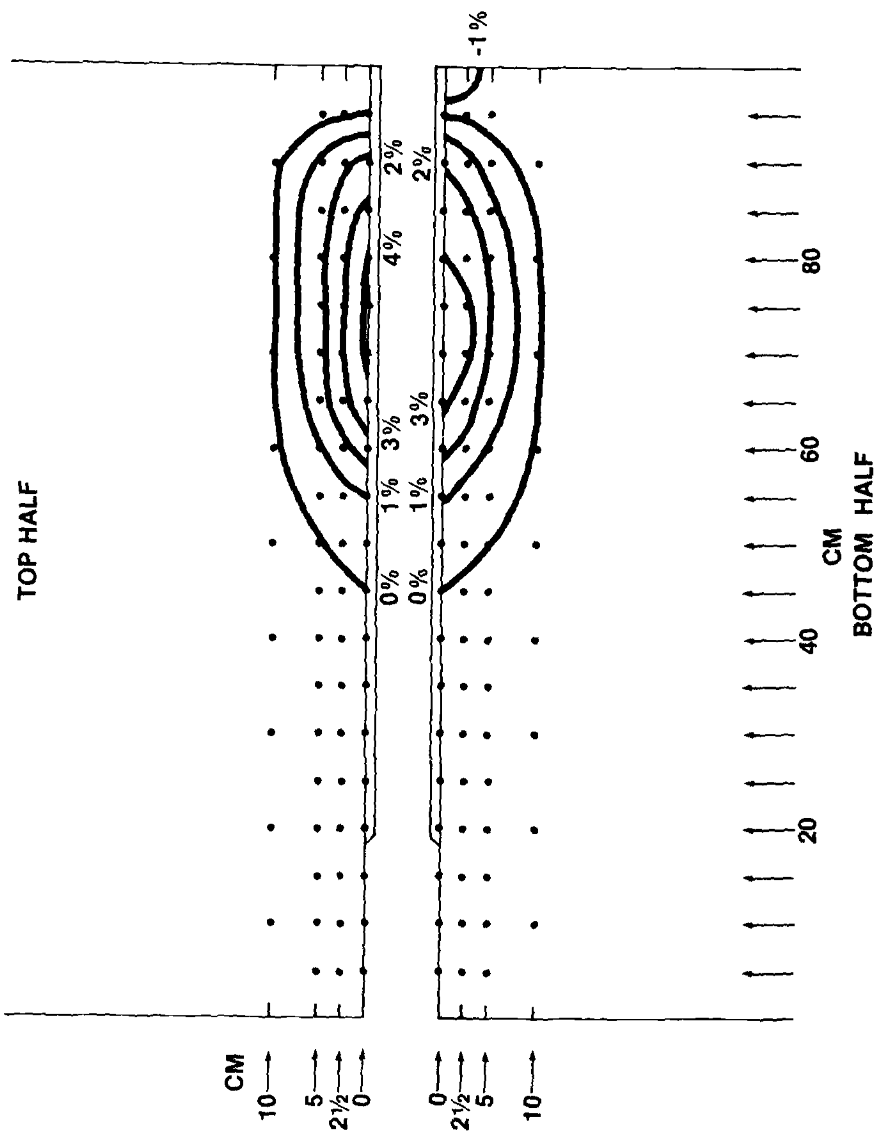

FIG. 3—*Continued*

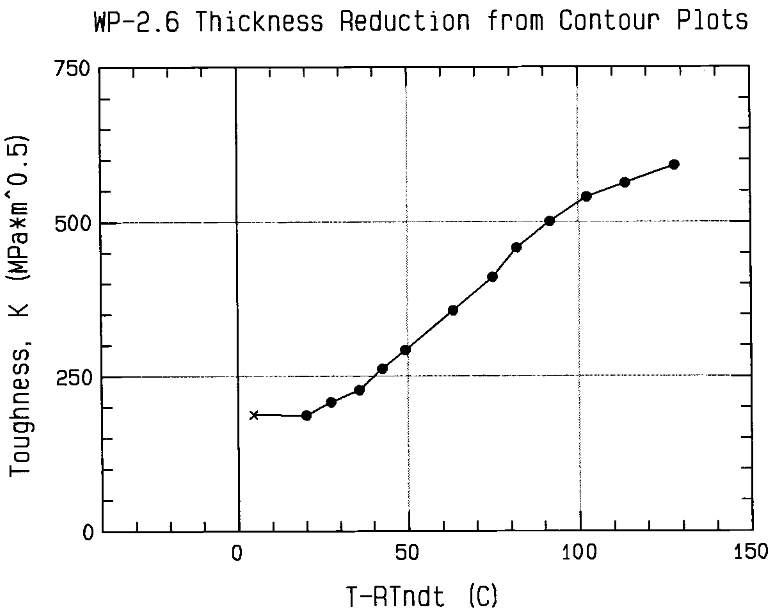

FIG. 4—*Fracture toughness,* K, *deduced from the contour plots, as a function of temperature for WP-2.6. The circles represent calculations from the TR determined by the contour plots in Fig.* 3c *and the cross a calculation from the initiation load and crack size given in the Appendix.*

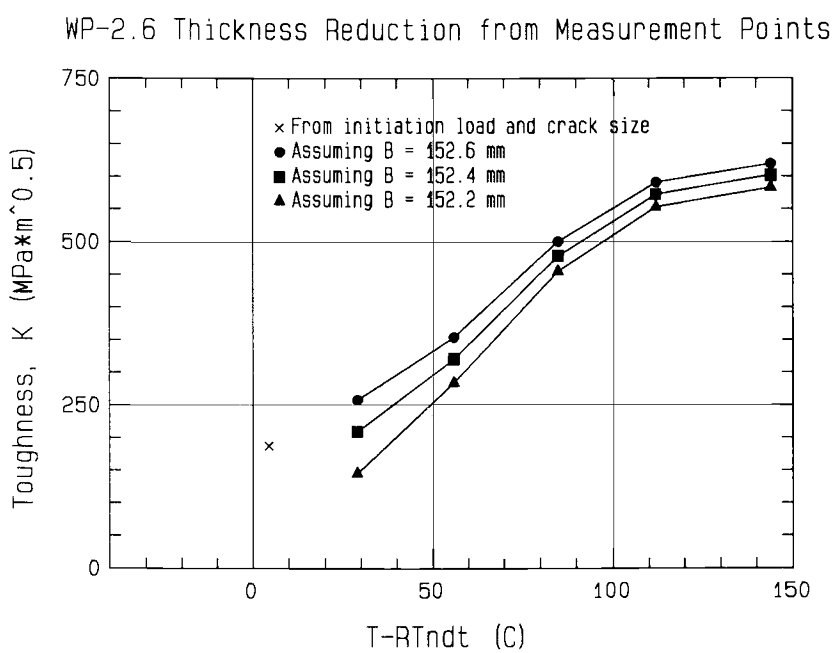

FIG. 5—*Fracture toughness,* K, *deduced from measurement points, as a function of temperature for WP-2.6. The solid symbols represent calculations from the TR determined by the measurement points in Fig.* 3c *and the cross a calculation from the initiation load and crack size given in the Appendix. The circles, squares, and triangles represent calculations based on assuming different original thicknesses.*

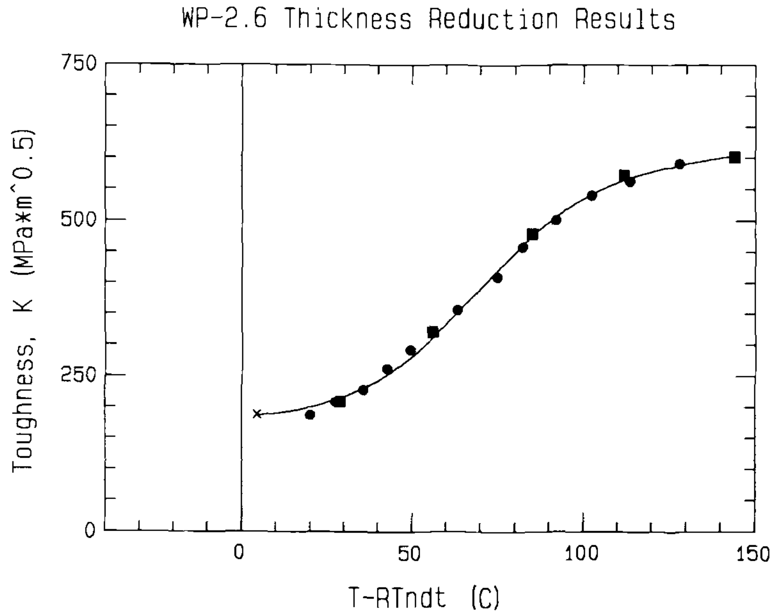

FIG. 6—*Smooth K-from-TR curves for WP-2.6 using the data from Figs. 4 and 5.*

crack surface was rough and curved, it was out of the side-grooved plane, and the crack front was curved and slanted to one side. The better tests had relatively few of these problems. The best tests were the closest to the desirable criteria, but no test was perfect, i.e., had a completely flat surface, lay exactly in the side-grooved plane, and had a straight-edge crack front from one side to the other.

Smooth K-from-TR curves were calculated for all the acceptable tests, using both the thickness contours and the measurement points (Fig. 3), as explained above.

Comparison with Finite-Element Analyses

ORNL conducted post-test analyses for each wide-plate crack-arrest test, except the first. Two-dimensional (2-D) elastodynamic generation-mode finite-element analyses were carried out using the ADINA/VPF dynamic crack analysis code. The results of this analysis is shown together with the smooth K-from-TR trend for test WP-2.6 in Fig. 7. A summary of all the acceptable K-from-TR curves together with the ORNL finite element arrest analyses is given in Fig. 8. In this figure the good TR data is shown by dotted curves, the better by dashed, and the best by solid curves. The open symbols represent finite element analyses for which no TR trend was calculated.

Visual Inspection and Analysis of Each Test

Each test was examined as to the crack surface flatness, whether it was in the plane of the side grooves, the shape of the crack front, and the behavior during the test (arrest, tearing, etc.). Based on this assessment, it was possible to judge whether the test met the criteria for analysis. The more the test deviates from the basic criteria, the higher will be the results of the TR calculations.

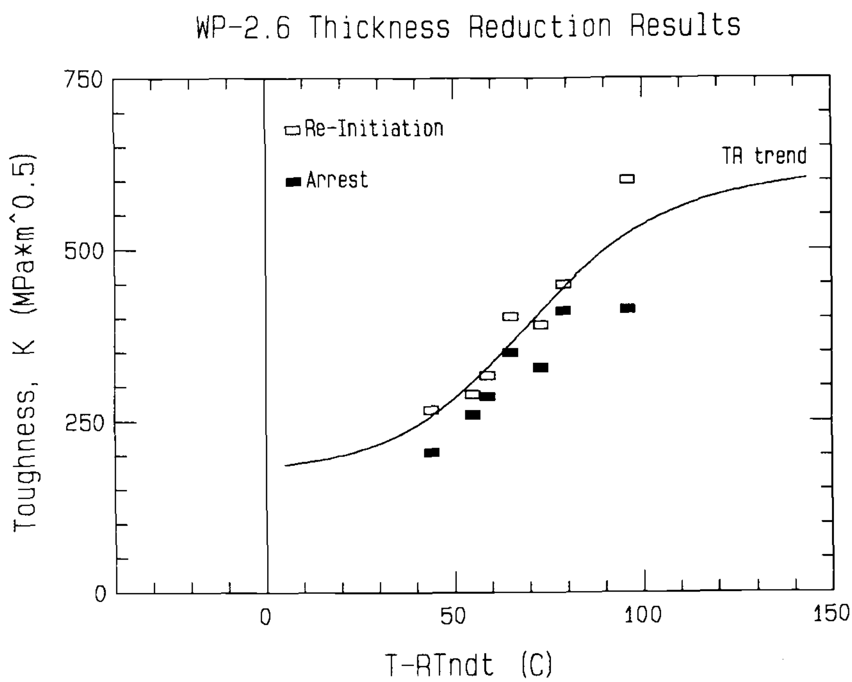

FIG. 7—*Smooth* K*-from-TR trend (solid curve) and ORNL finite-element crack reinitiation and arrest analyses (points) versus temperature for WP-2.6.*

WP-1.1—In this first wide-plate test the cleavage portion of the fracture surface left the side-grooved plane completely early in the crack run and extended at a significant angle (20 to 30°) into the full thickness part of the plate. There was also evidence of crack branching. During the ductile tearing the fracture returned to the side-grooved plane in an extremely jagged way, and the surface did not approach flatness until the crack had almost reached the edge of the plate. These conditions did not permit a meaningful calculation to be made.

WP-1.2—For this test the out-of-side groove features are substantial, but better than for WP-1.1. So the test was considered good, and we made a comparison of the K-from-TR trend to the estimated K_a values, which can be seen in Fig. 8*a* as the dotted curve and solid circles. This figure shows that all estimates from this test are moderately too high relative to a "lower-bound."

WP-1.3—The fracture surface was rough at initiation. Near crack arrest, the crack plane was nearly in-plane with the side grooves. The results are better than WP-1.2, and Fig. 8*a* shows that the K-from-TR trend and the K_a estimates are of interest as close to "lower-bound" behavior.

WP-1.4—This test used a pillow-jack to apply additional pressure to the notch at crack initiation. There was moderate out-of-side groove behavior and so K_a estimates are of questionable value, but deserve retention as above "lower-bound" values.

WP-1.5—This test closely meets all the criteria for a good analysis and so was classified as one of the best tests. Symmetry of the TR between the top and bottom of the specimen (Fig. 3*d*) indicates relatively little deviation of the crack plane from the side grooves, as observed. As seen in Fig. 8*a* this test has the lowest K-from-TR values prior to $T - RT_{NDT} = 110$°C. The K_a estimate at the first arrest ($T - RT_{NDT} = 79$°C) is acceptable and agrees well with the K-

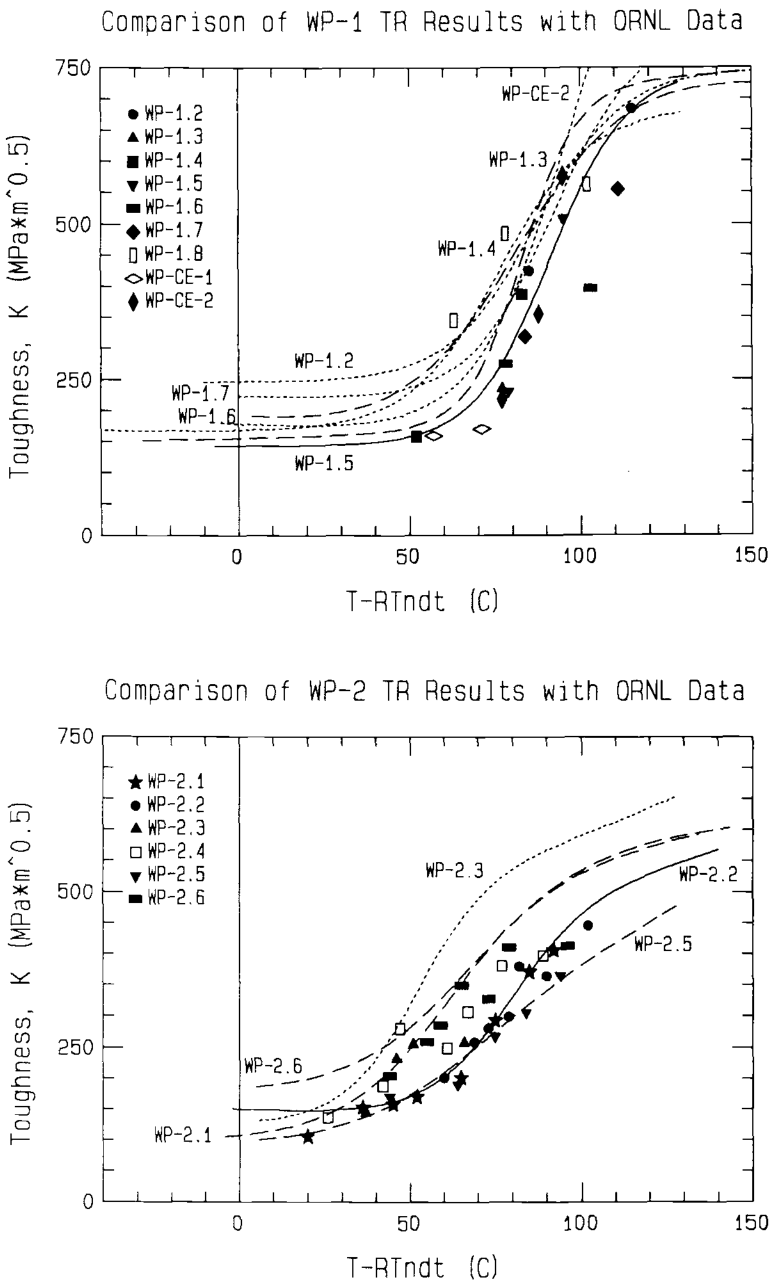

FIG. 8—*Summary of smooth* K*-from-TR trends (curves) and ORNL elastodynamic generation-mode crack-arrest analyses (points) for* (a) *WP-1 series and* (b) *WP-2 series. The good TR data are given by the dotted curves, the better by the dashed, and the best data by the solid curves. The open symbols represent finite-element data for the tests that were disqualified for TR calculations.*

from-TR trend, whereas the K_a estimated at the second arrest ($T - RT_{NDT} = 95°C$) is at the start of tearing, where the TR for reinitiation may elevate the K-from-TR estimate.

WP-1.6—This test was classified as better. Fibrous tearing began at the first arrest ($T - RT_{NDT} = 78°C$). A high degree of symmetry of the TR between the top and bottom of the specimen indicated relatively little deviation of the crack plane from the side grooves. The K_a estimates at the first arrest are acceptable. The meaning of the estimates at the second arrest ($T - RT_{NDT} = 103°C$) is uncertain because the cleavage areas do not extend to the side grooves.

WP-1.7—The results for this first 150-mm specimen in the WP-1 series were good. The fracture appearance is uniformly rough and out of the side grooves. Therefore, all K estimates are of doubtful value. These estimates deserve retention only for comparison purposes.

WP-1.8—The top-to-bottom asymmetry in the contours (Fig. 3*a*) reflect the fact that the crack plane was curved and 40 mm above the side-grooved plane. No K estimate data for this plate is acceptable due to this extreme out-of-side-grooved plane behavior.

WP-CE-1—Deviation of the crack plane from the side grooves was relatively small, but the crack front led strongly near one face producing a slanted crack front. Furthermore, the crack did not reinitiate and propagate dynamically after the arrest. Slow reloading resulted in a very large TR at the crack arrest position. Therefore this test was disqualified from the TR calculation.

WP-CE-2—Deviations of the crack plane from the side grooves was substantial. The results of this test were classified as good. The K estimates deserve retention for a "lower-bound" estimate.

WP-2.1—The arrested crack fronts were somewhat slanted and the fracture surface was slightly out of the side-grooved plane. Therefore, results of this test represent above "lower-bound" behavior.

WP-2.2—This test meets all the criteria for a good analysis and is therefore the other best test. As Fig. 8*b* shows, it represents "lower-bound" behavior.

WP-2.3—The arrested crack fronts were curved and lagged behind on one side. There was undercutting of the cleavage in the region beyond $T - RT_{NDT} = 37°C$. This places doubt on subsequent K estimates. The K-from-TR values are increasingly too high above that temperature (Fig. 8*b*) and the K_a estimates do not follow an expected trend. Retain only the K_a estimates at the first crack arrest for "lower-bound" behavior.

WP-2.4—The fracture surface of this test becomes increasingly out-of-plane with the side grooves. The arrested crack fronts were curved. More importantly, ORNL reports some K_a values higher than K_c at the same position. Until a better understanding of these data is available, this test cannot be analyzed.

WP-2.5—The fracture plane was tilted with respect to the side-grooved plane and the arrest crack fronts were slanted and lagged on one side. The results for this 100-mm-thick specimen in the WP-2 series were classified as better. Interpretation of K_c estimates is difficult since cleavage is mixed with fibrous fracture across the arrest locations. The K_a estimates seem acceptable.

WP-2.6—The fracture plane was acceptably flat, but the lag at the side grooves is considerable. The results of this test are also classified as better. The K-from-TR values are uniformly high. All K_a estimates correspond to above "lower-bound" behavior.

Summary Comparison

The summary comparison for all test series of the K-from-TR calculations with the ORNL finite-element arrest analyses is given in Fig. 8. The finite element results generally appear lower than the TR trends, because the TR results are elevated when the fracture behavior criteria for a good calculation are not met. As seen, there is good support for the elastodynamic generation-mode analyses from the K-from-TR trends, especially from those that have been assessed as best, the solid curves. Within the data scatter of the present experiments there was also no significant effect of plate thickness either on computed K_a or on K-from-TR values. In addition, the K_a values from ORNL high constraint tests agree well with the most acceptable results from the wide-plate low-constraint tests.

Comparison with Data from the Literature

Figure 9 shows some results from the literature for A533B steel. The curves in this figure come from the following sources. The present calculations supplied the "Average TR trend" and the "WP-1.5 TR trend" curves, the latter being the best result for the WP-1 series. The "ORNL curve" is a temperature-dependent fracture-toughness relation for crack arrest, based on small-specimen data, given by the expression [*8–10*]

$$K_{Ia} = 49.96 + 16.88 \exp[0.029(T - RT_{NDT})] \tag{8}$$

where the units for K and T are MPa$\sqrt{m}$ and °C, respectively. The "LIMIT-ASME SECTION XI" curve represents the "lower-bound" test data for SA-533 Grade B Class 1, SA-508 Class 2, and SA-508 steel, provided in Section XI, Article A-4000, of the ASME Code [*11*]. This curve is given by

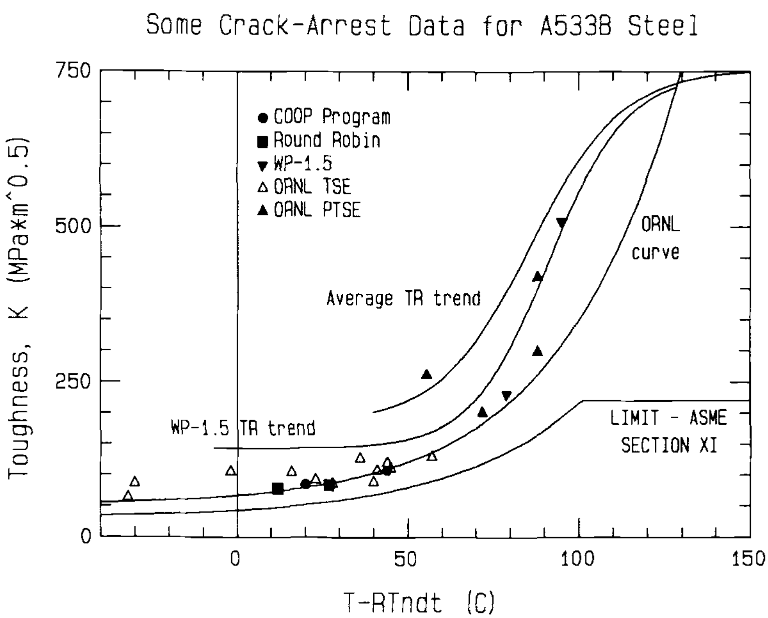

FIG. 9—*Crack-arrest toughness data versus temperature for A533B steel from various sources. Average TR trend is the high temperature average of all WP-1 series curves from Fig. 8*a. *WP-1.5 TR trend is the appropriate curve from Fig. 8*a. *ORNL curve is a curve-fit to small-specimen crack-arrest data. LIMIT-ASME SECTION XI is the lower-bound provided by section XI of the ASME code. The solid circles are from the Cooperative Test Program, the solid squares from the round robin for the proposed ASTM Method E1221, the solid triangles pointing down are the ORNL finite element arrest analyses from Fig. 8*a, *the triangles pointing up are the thermal-shock and pressurized-thermal-shock experiments from the HSST program at ORNL.*

$$K_{Ia} = 29.44 + 1.344 \exp[0.0261(T - RT_{NDT} + 88.89)] \quad \text{for } T\text{-}RT_{NDT} < 220° \tag{9}$$

where the units for K and T are MPa$\sqrt{m}$ and °C, respectively.

The sources of the data points are as follows. The "COOP Program" was a large Cooperative Test Program [*12*] using a test method employing wedge-loaded compact specimens, conducted during 1977–1979, with 29 participating laboratories, to resolve some differences of approach. The "Round Robin" [*13*] was conducted during 1983–1985 with 21 participants to evaluate the proposed ASTM Method E1221: "Standard Test Method for Determining Plane-Strain Crack-Arrest Fracture Toughness, K_{Ia}, of Ferritic Steels" [*14*]. The "WP-1.5" data are the ORNL finite-element arrest analyses shown before in Fig. 8*a*. "ORNL TSE" and "ORNL PTSE" are the crack-arrest data deduced from thermal-shock and pressurized-thermal-shock experiments conducted with large test vessels as part of the Heavy-Section Steel Technology Program [*15–17*]. It is seen that most of the data fall between the average TR trend and the ORNL curve. From previous comparisons of K_{Ia} values from large tests at ORNL and small specimen ASTM E-1221 results, constraint does not have a significant effect on K_{Ia} values. This is in agreement with the present results. The 100-mm and 150-mm thicknesses used in the wide-plate tests furnished a significant degree of plane strain constraint only at the lowest temperatures.

Conclusion

A wide-plate crack-arrest program with 16 tests was carried out over a five-year period. A quality assessment was made of the fracture surfaces to choose the acceptable tests, i.e., those in which the crack remained flat, in the plane of the side grooves, and reasonably straight across the specimen. Measurements of the thickness reduction (TR) trend near the crack plane for the acceptable tests were converted to fracture toughness and provide good support for the generation-mode finite-element analyses conducted by ORNL. Best "lower-bound" estimates can be obtained by including both the fracture appearance and the TR trend values in the complete analysis.

Acknowledgment

We wish to acknowledge the support, guidance, and advice of those at the U.S. Nuclear Regulatory Commission and the Oak Ridge National Laboratory that made this work possible under the Crack Arrest Technology Section of the Heavy Section Steel Technology Program. We would also like to thank Donald E. Harne, Samuel R. Low III, and Leonard C. Smith for performing the tests and making the measurements and contour plots of the thickness reductions.

APPENDIX

Initial *K* Value from Initiation Load

The initiation K value tie-point was estimated from the initiation load, the original crack size, and the specimen dimensions by linear-elastic fracture mechanics equations from the handbook. The basic equation for the stress-intensity factor of an edge-notched specimen under tension is [*A1*]

$$K_T = \sigma_T(2W \tan\beta)^{1/2}[0.752 + 2.02(a/W) + 0.37(1 - \sin\beta)^3]/\cos\beta \quad \text{(A1)}$$

where

$$\beta = (\pi/2)(a/W) \quad \text{(A2)}$$

and a is the crack size while W is the specimen width. The tension stress, σ_T, corrected for the effect of the side grooves, is given by

$$\sigma_T = P/[W(BB_N)^{1/2}] \quad \text{(A3)}$$

where P is the applied load, B is the specimen thickness, and B_N (0.75 B) is the net thickness at the side grooves. These expressions give a first estimate of the initiation fracture toughness. The required data and the result of the calculation for each wide-plate test are presented in Table A1.

However, it was felt that a correction was needed to the above results because the temperature gradient that was applied across the specimen caused an initial in-plane thermal bending, as shown schematically in Fig. A1. When the tension load is applied to this bent specimen, it will straighten it out and thus create a bending moment which will enhance the stress-intensity factor. This correction was determined as follows.

The "notch-edge" of the test plate was cooled to a temperature of T_{min}, and the "crack-arrest" edge was heated to a temperature of T_{max}. The extent of this temperature control along the height of the specimen was maintained over a length defined as H_1. We assumed that the temperature gradient was constant between the two edges of the specimen over this region, resulting in a uniform thermal strain. Hence, the length of the hot edge increased relative to the cool edge by

$$\Delta H = H_1(T_{max} - T_{min})\alpha \quad \text{(A4)}$$

where α is the coefficient of instantaneous thermal expansion. As a result, this region of the specimen will bend through an angle of

$$\theta = \Delta H/W \quad \text{(A5)}$$

TABLE A1—*First estimate of initiation fracture toughness.*

Test	a, mm	W, mm	B, mm	B_N, mm	P, MN	K_T, MPa $\sqrt{m}$
WP-1.1	196.9	997	101.5	76.3	20.1	245
WP-1.2	199	998	101.8	77.5	19.0	231
WP-1.3	197	998	99.5	75.4	11.3	140
WP-1.4	207.5	1000	101.4	76.9	7.95	101
WP-1.5	200	1000	101.7	76.4	11.03	136
WP-1.6	200	1000	101.8	75.5	14.5	179
WP-1.7	202	1000	152.4	114.3	26.2	217
WP-1.8	198	1000	152.4	115.1	26.5	215
WP-CE-1	200	1000	101.7	76.3	10.14	125
WP-CE-2	201	999.5	101.8	76.2	14.6	180
WP-2.1	202.6	1000	152.55	113.9	11.9	99
WP-2.2	213	1000	152.2	113.9	17.0	148
WP-2.3	200	1000	152.1	113.8	15.3	126
WP-2.4	203	1000	101.7	76.3	7.52	94
WP-2.5	199	999	101.3	76.2	7.53	93
WP-2.6	224	1000	152.4	113.9	19.33	175

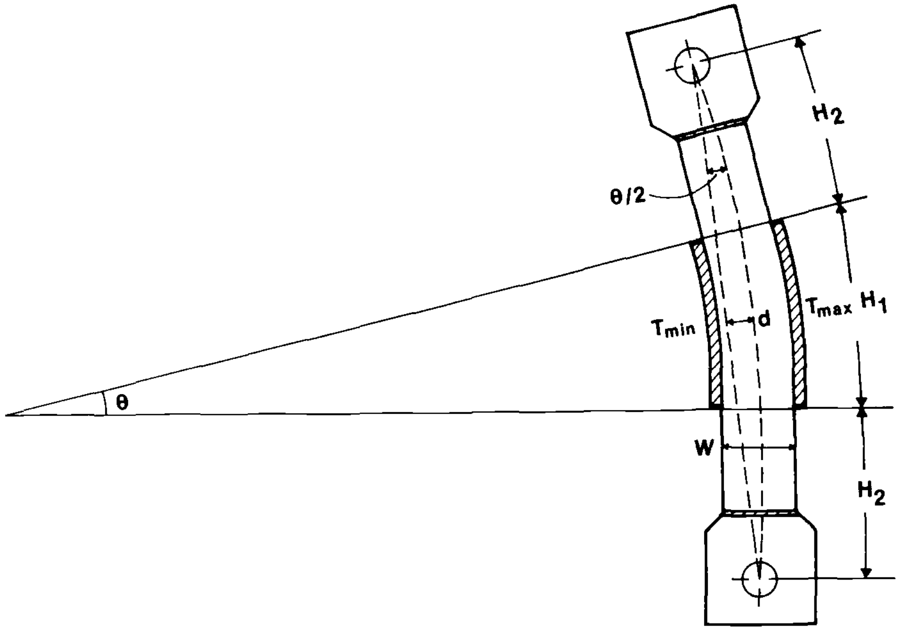

FIG. A1—*In-plane bending of wide-plate specimen due to temperature gradient.*

The length of the pull-plates from the region of temperature control to the pinhole is defined as H_2. We assumed this part of each pull-plate to be at room temperature and unstrained. However, these parts were tilted with respect to the vertical by an angle of $\theta/2$, as shown in the figure. Therefore the vertical between the two pinholes was offset from the centerline of the specimen. This offset has a maximum at the notch plane given by

$$d = H_1\theta/8 + H_2\theta/2 \tag{A6}$$

Combining Eqs A4 to A6 gives

$$d = (H_1/8W)(H_1 + 4H_2)(T_{max} - T_{min})\alpha \tag{A7}$$

When the tension load is applied to the specimen resulting in the remote stress, σ_T given by Eq A3, the offset leads to a bending moment with an outer fiber bending stress of

$$\sigma_B = (6d/W)\sigma_T \tag{A8}$$

on the cold tension edge of the specimen. The stress-intensity factor for an edge-notched specimen under pure bending is [*A1*]

$$K_B = \sigma_B(2W\tan\beta)^{1/2}[0.923 + 0.199(1 - \sin\beta)^4]/\cos\beta \tag{A9}$$

The best estimate of the initiation fracture toughness is therefore given by the sum

$$K_I = K_T + K_B \tag{A10}$$

The second term in this equation gives a correction of about 8 to 10% over the first. The following values were the same for all the tests

TABLE A2—*Initiation fracture toughness corrected for bending.*

Test	T_{min}, °C	T_{max}, °C	H_2, mm	d, mm	K_B, MPa $\sqrt{m}$	K_I, MPa $\sqrt{m}$
WP-1.1	−119.8	213.6	3582	18.8	21	266
WP-1.2	−95	205	3448	16.4	17	249
WP-1.3	−133.3	233.3	3417	19.9	13	153
WP-1.4	−133.3	233.3	3742	21.4	9	173[a]
WP-1.5	−83.3	183.3	3662	15.3	9	145
WP-1.6	−70	180	3554	14.0	12	191
WP-1.7	−70	180	3026	12.2	12	229
WP-1.8	−83.3	183.3	2971	12.8	13	228
WP-CE-1	−83.3	183.3	3262	13.9	8	133
WP-CE-2	−103.3	213.3	2923	15.0	13	193
WP-2.1	6.7	273.3	3141	15.9	7	106
WP-2.2	−2	281	2951	16.0	10	158
WP-2.3	15	265	3074	14.6	8	134
WP-2.4	−10	290	3575	19.9	8	102
WP-2.5	18.3	251.7	3473	15.1	6	99
WP-2.6	−2	281	2931	15.9	13	188

[a] For WP-1.4 a pillow-jack was used to apply additional pressure to the notch. The equivalent tensile load was 4.991 MN, which implied a notch-pressure contribution to the initiation factor of 63 MPa $\sqrt{m}$.

$$\alpha = 11 \times 10^{-6}/C$$

$$H_1 = 2440 \text{ mm}$$

The values of the other quantities in Eqs A7-A9 and the result of the calculation of K_I for each test are presented in Table A2. The value of K_I for WP-2.6 is plotted as the cross in Figs. 4 and 5.

References

[1] Letter from G. R. Irwin to W. G. Reuter, INEL, Idaho Falls, Idaho, 31 Aug. 1989.

[2] Krafft, J. M. and Irwin, G. R., "Crack-Velocity Considerations," *Fracture Toughness Testing and Its Applications, STP 381*, American Society for Testing and Materials, Philadelphia, 1965, pp. 114–129.

[3] Naus, D. J., Bass, B. R., Pugh, C. E., Nanstad, R. K., Merkle, J. G., Corwin, W. R., and Robinson, G. C., "Crack-Arrest Behavior in SEN Wide Plates of Quenched and Tempered A 533 Grade B Steel Tested Under Nonisothermal Conditions," NUREG/CR-4930 (ORNL-6388), Oak Ridge National Laboratory, prepared for the U.S. Nuclear Regulatory Commission, Office of Nuclear Regulatory Research, Washington, DC (August 1987).[4]

[4] Naus, D. J., Keeney-Walker, J., Bass, B. R., Bolt, S. E., Fields, R. J., deWit, R., and Low III, S. R., "High-Temperature Crack-Arrest Behavior in 152-mm-Thick SEN Wide Plates of Quenched and Tempered A 533 Grade B Class 1 Steel," NUREG/CR-5330 (ORNL/TM-11083), Oak Ridge National Laboratory and National Institute of Standards and Technology, prepared for the U.S. Nuclear Regulatory Commission, Office of Nuclear Regulatory Research, Washington, DC 20555 (April 1989).[4]

[5] Naus, D. J., Keeney-Walker, J., Bass, B. R., Iskander, S. K., Fields, R. J., deWit, R., and Low III, S. R., "SEN Wide-Plate Crack-Arrest Tests Using A 533 Grade B Class 1 Material: WP-CE Test Series," NUREG/CR-5408 (ORNL/TM-11269), Oak Ridge National Laboratory and National

[4] Available for purchase from the Superintendent of Documents, U.S. Government Printing Office, P.O. Box 37082, Washington, DC 20013–7982, and National Technical Information Service, Springfield, VA 22161.

Institute of Standards and Technology, prepared for the U.S. Nuclear Regulatory Commission, Office of Nuclear Regulatory Research, Washington, DC 20555 (November 1989).[4]

[6] Naus, D. J., Keeney-Walker, J., Bass, B. R., Robinson, G. C., Iskander, S. K., Fields, R. J., deWit, R., Low III, S. R., Schwartz, C. W., Alexander, D. J., and Johansson, I.-B., "Crack-Arrest Behavior in SEN Wide Plates of Low-Upper-Shelf Base Metal Tested Under Nonisothermal Conditions: WP-2 Series," NUREG/CR-5451 (ORNL/TM-6584), Oak Ridge National Laboratory, National Institute of Standards and Technology, University of Maryland Department of Mechanical Engineering, and Swedish Royal Institute of Technology, prepared for the U.S. Nuclear Regulatory Commission, Office of Nuclear Regulatory Research, Washington, DC 20555 (August 1990).[4]

[7] Naus, D. J., Keeney-Walker, J., Bass, B. R., Iskander, S. K., Fields, R. J., deWit, R., and Low III, S. R., "High-Temperature Crack-Arrest Tests Using 152-mm-Thick SEN Wide Plates of Low-Upper-Shelf Base Material: Tests WP-2.2 and WP-2.6," NUREG/CR-5450 (ORNL/TM-11352), Oak Ridge National Laboratory and National Institute of Standards and Technology, prepared for the U.S. Nuclear Regulatory Commission, Office of Nuclear Regulatory Research, Washington, DC 20555 (February 1990).[4]

[8] Pugh, C. E., Naus, D. J., Bass, B. R., Nanstad, R. K., deWit, R., Fields, R. J., and Low III, S. R., "Wide-plate Crack-Arrest Tests Utilizing a Prototypical Pressure Vessel Steel," *International Journal of Pressure Vessel and Piping*, Vol. 31, 1988, pp. 165–185.

[9] Naus, D. J., Keeney-Walker, J., Bass, B. R., Fields, R. J., deWit, R., and Low III, S. R., "High-Temperature Crack-Arrest Behavior of Prototypical and DeGraded (Simulated) Reactor Pressure Vessel Steels," *International Journal of Pressure Vessel and Piping*, Vol. 39, 1989, pp. 189–208.

[10] Naus, D. J., Bass, B. R., Keeney-Walker, J., Fields, R. J., deWit, R., and Low III, S. R., "HSST Wide-Plate Test Results and Analysis," *Nuclear Engineering and Design*, Vol. 119, 1990, pp. 283–295.

[11] ASME Boiler and Pressure Vessel Code, Section XI, "Rules for Inservice Inspection of Nuclear Power Plant Components," The American Society of Mechanical Engineers, United Engineering Center, New York, NY.

[12] Crosley, P. B., Fourney, W. L., Hahn, G. T., Hoagland, R. G., Irwin, G. R., and Ripling, E. J., "Final Report on Cooperative Test Program on Crack Arrest Toughness Measurements," NUREG/CR-3261, University of Maryland, College Park, MD, prepared for the U.S. Nuclear Regulatory Commission, Office of Nuclear Regulatory Research, Washington, DC 20555 (April 1983).[4]

[13] Barker, D. B., Chona, R., Fourney, W. L., and Irwin, G. R., "A Report on the Round Robin Program Conducted to Evaluate the Proposed ASTM Test Method for Determining the Crack Arrest Fracture Toughness, K_{Ia}, of Ferritic Materials," NUREG/CR-4996 (ORNL/Sub/79-7778/4), University of Maryland, College Park, MD, prepared for the U.S. Nuclear Regulatory Commission, Office of Nuclear Regulatory Research, Washington, DC 20555 (January 1988).[4]

[14] ASTM Designation: *E* 1221–88, "Standard Method for Determining Plane-Strain Crack-Arrest Fracture Toughness, K_{Ia}, of Ferritic Steels," *Annual Book of ASTM Standards, Section 3: Metals Test Methods and Analytical Procedures, Vol. 03.01, Metals-Mechanical Testing; Elevated and Low-Temperature Tests; Metallography*, American Society for Testing and Materials, Philadelphia.

[15] Cheverton, R. D. and Ball, D. G., "The Role of Crack Arrest in the Evaluation of PWR Pressure Vessel Integrity during PTS Transients," *Engineering Fracture Mechanics*, Vol. 23, 1986, pp. 71–80.

[16] Bryan, R. H., Bass, B. R., Bolt, S. E., Bryson, J. W., Edmonds, D. P., McCullough, R. W., Merkle, J. G., Nanstad, R. K., Robinson, G. C., Thomas, K. R., and Whitman, G. D., "Pressurized-Thermal-Shock Test of 6-in.-Thick Pressure Vessels. PTSE-1: Investigation of Warm Prestressing and Upper-Shelf Arrest," NUREG/CR-4106 (ORNL-6135), Oak Ridge National Laboratory, prepared for the U.S. Nuclear Regulatory Commission, Office of Nuclear Regulatory Research, Washington, DC, April 1985.[4]

[17] Bryan, R. H., Bass, B. R., Bolt, S. E., Bryson, J. W., Corwin, W. R., Merkle, J. G., Nanstad, R. K., and Robinson, G. C., "Pressurized-Thermal-Shock Test of 6-in.-Thick Pressure Vessels. PTSE-2: Investigation of Low Tearing Resistance and Warm Prestressing," *NUREG/CR-4888 (ORNL-6377)*, Oak Ridge National Laboratory, prepared for the U.S. Nuclear Regulatory Commission, Office of Nuclear Regulatory Research, Washington, DC, December 1987.[4]

[A1] Tada, H., Paris, P. C., and Irwin, G. R., *The Stress Analysis of Cracks Handbook*, Paris Productions, Inc., St. Louis, 1985, pp. 2.10–2.15.

[4] Available for purchase from the Superintendent of Documents, U.S. Government Printing Office, P.O. Box 37082, Washington, DC 20013-7982, and National Technical Information Service, Springfield, VA 22161.

Joseph R. Bloom,[1] *D. R. Lee,*[1] *and W. A. Van Der Sluys*[1]

An Investigation of Size and Constraint Effects on Ductile Crack Growth

REFERENCE: Bloom, J. R., Lee, D. R., and Van Der Sluys, W. A., "**An Investigation of Size and Constraint Effects on Ductile Crack Growth,**" *Constraint Effects in Fracture, ASTM STP 1171,* E. M. Hackett, K.-H. Schwalbe, and R. H. Dodds, Eds., American Society for Testing and Materials, Philadelphia, 1993, pp. 383–417.

ABSTRACT: Recent *J-R* curve testing of A302-B plate has shown significant specimen size effects. If the *J-R* curves of a material are dependent on size and the larger the size, the lower the *J-R* curve, serious questions as to the usability of *J-R* curve information from nuclear reactor pressure vessel surveillance programs could arise. It is important, then, to be able to identify the existence of this phenomenon from *J-R* curve test records and either correct the data for size effects or account for this size effect in failure assessments.

Other studies, such as the HSST irradiation work by ORNL and the EPRI-sponsored work by Westinghouse, have demonstrated mixed results. From a review of all these test results, it appears that there are two causes of the observed specimen size effects, one due to loss of constraint in the small specimen and the second due to metallurgical inhomogeneities. One of the objectives of this investigation was to develop procedures to identify if either of these conditions exists.

Several evaluation models have been applied to determine their usefulness in identifying these size effects. The models investigated were:

1. The key curve approach.
2. DPFAD (deformation plasticity failure assessment diagram) approach.
3. Load-displacement prediction based on the EPRI handbook.

The following data were analyzed:

1. HSST Irradiation Tasks II and III weld metal compacts.
2. Westinghouse/EPRI RP 1238–2 A508 $0.5T$ to $10T$ compacts.
3. A302-B plate tests by MEA.

In order for an evaluation method to be useful, the methodology must be able to identify test results in which the specimen size influences the *J-R* curve. By using a number of different evaluation schemes on test data where a range of sizes and where size effects have been observed, the effectiveness of the different methodologies can be assessed.

The results of the key curve, DPFAD, and load-displacement methodology predictions were compared to the test data. When good agreement is seen in one procedure, good agreement is seen in all procedures. Likewise, when one prediction/comparison looked bad, all the predictions were bad. However, the DPFAD approach seemed to better highlight the extent of disagreement than was shown in the other two procedures.

Any one of the procedures investigated could be used to demonstrate that a size effect is present in a data set. The DPFAD approach seems to best identify the test results from compact specimens which are not *J*-controlled and can be used when only one specimen size has been tested. The lack of *J*-control may be due to incorrect crack measurements during the test, metallurgical anomalies, or the loss of specimen constraint. The key curve can be used to identify *J-R* curve test results within a set which differs from others in the set. It, however, does not appear useful in identifying specimen size effects if only one specimen has been tested. The load-displacement

[1] Technical advisor, senior research engineer, and scientist, respectively, Babcock & Wilcox Co., Research and Development Division, Alliance, OH 44601.

procedure can be useful if a specimen exhibits plane strain behavior, but it is not as sensitive as a measure of loss of J-control growth as DPFAD.

The second objective of the investigation was the development of remedial actions to correct J-R curve data in which specimen size effects are evident. The DPFAD approach was used to demonstrate that the various size effects seen with the A302-B plate material could be corrected. The assessment points from each compact specimen which deviated from the DPFAD curve were recalculated by increasing the amount of ductile tearing and adjusting the calculated J-R point via ASTM E 1152-87 test standard such that these assessment points fall on the DPFAD curve. This has been shown to be equivalent to J-controlled crack growth up to the limit load of the specimen for displacement-controlled loading.

Conclusions are that for the A302-B plate material, the $1/2T$ and $1T$ specimens may not be large enough to produce usable J-R curves for this material.

KEY WORDS: constraint effects, J-R curve, deformation plasticity failure assessment diagram (DPFAD), load-displacement predictions, key curve, EPRI elastic-plastic handbook, size effects, ASTM E 1152-87 test standard, A302B material

Recent J-R curve testing of A302-B plate material [1] has shown significant size effects. The larger the specimen thickness, the lower and flatter is its J-R curve. If the J-R curve properties of a material are dependent of the size of the specimen, and the larger the size the lower the J-R curve, there would be a serious question as to the usability of the J-R curve information from the nuclear reactor pressure vessel surveillance programs. It is important to be able to identify the existence of this phenomenon from J-R curve test records and either correct the data for size effect or account for the size effect in the structural assessments.

Other studies on the effect of specimen size on the measured J-R curve properties of a material have demonstrated mixed results. Some German data produced at MPA Stuttgart [2] have shown a size effect similar to that observed in the A302-B study. Other studies have been performed which have not shown a size effect or have shown that small specimens produce conservative results. These include the ORNL irradiation Task II and Task III studies [3] and the EPRI studies performed by Westinghouse [4] in which specimens from 0.5 to 10 in. thick were tested.

From a review of these results, it appeared that there may be two causes of the observed specimen size effects. One of these is due to the loss of constraint in the small specimen and the second, a metallurgical effect caused by the delamination of the material due to inclusions which could lead to a loss of constraint in small specimens as well.

The first objective is to determine if one of these two hypothesized causes of the observed size effects is present. The second objective is to develop analytical procedures to correct the data if one of the effects has influenced the R curve developed in an individual or group of tests.

Technical Approach and Data Collection

The technical approach used to accomplish these objectives is summarized as follows:

1. Collect the raw test results from programs which studied the effect of specimen size.
2. Reanalyze the J-R curves from these tests using a common method.
3. Apply several evaluation models to the data to determine if they are useful in identifying size effects. These models included:
   a. key curve
   b. DPFAD (deformation plasticity failure assessment diagram)
   c. load-displacement prediction based on EPRI handbook

4. Evaluation of the above models for usefulness.
5. Recommendations on how to correct the data to eliminate these size effects.

The objective of the first task was to collect available *J-R* curve test data obtained in the different specimen size studies. These data include the HSST Irradiation Tasks II and III, the Westinghouse/EPRI RP1238-2 test data on specimens from $1/2T$ to $10T$, and the A302-B data obtained by MEA for the NRC. These data were put into digital form as required to facilitate the different analysis tasks.

All the data were reanalyzed using the procedures of ASTM E 1152-87. The methods of analyzing *J-R* curve test results have been changing over the years since the concept was first introduced in the early 1970s. Until the adoption of the ASTM Standard Test Method in 1987, there were a number of different analysis procedures. For the data described above, each of the original investigators used a different procedure to analyze their results. It was necessary, therefore, to eliminate this variable before the results from the different programs could be compared.

The computer code used in the above *J-R* curve analysis was modified to calculate the normalized load and the normalized displacement values used in the key curve analysis procedure.

Data Evaluation Methodologies

In order for an evaluation method to be useful, the methodology must be able to identify test results in which the specimen size influences the *J-R* curve when only one specimen size has been tested in the program. The *J-R* curves determined by the analysis of the data discussed above have been used to assess the usefulness of a number of different evaluation methodologies. By using a number of different evaluation schemes on these data sets (in which a range of specimen sizes have been tested and where size effects have been observed in some of the data sets while not in others), the effectiveness of the different methodologies can be assessed.

The methodologies that have been evaluated have been the key curve, DPFAD (deformation plasticity failure assessment diagram), and a comparison of predicted versus actual load-displacement diagrams. A description of each of these methodologies is as follows:

Key Curve

The key curve method of analysis originally proposed by Ernst et al. [5] assumes the existence of a universal key curve which is invariant for a given material and specimen geometry. Ernst showed that for simple geometries such as compact fracture specimens the load and displacement relationship would have the form

$$PW/Bb^2 = F_1(\Delta/W,\ a/W,\ H/W,\ B/W,\ \text{material properties}) \tag{1}$$

where

P = applied load,
Δ = load line displacement,
a = crack length,
b = uncracked ligament,
W = specimen width, and
H = specimen height.

Herrera and Landes [6] showed that this relation could be simplified to

$$P_N = PW/[Bb^2g(b/W)] = H(V_{pl}/W) \tag{2}$$

where

P = specimen load,
P_N = normalized load,
b = specimen thickness,
W = specimen width,
b = uncracked ligament,
$g(b/W) = e^{[0.522(b/W)]}$,
$H(V_{pl}/W)$ = function representing the plastic behavior of the specimen.

A plot of P_N versus V_{pl} defines graphically the functional form for H and is referred to as the key curve.

Such a key curve can be obtained from the load and displacement information determined in a *J-R* curve experiment using the procedures developed by Herrera and Landes. Since the key curve should be invariant for a single specimen geometry and material, any changes in the key curve between specimen sizes means that in some way the material has changed properties and the *J-R* curve should therefore also change. This could be caused by changes in the mechanical properties of the material or perhaps by loss of constraint in the specimen if the loss of constraint changes the effective mechanical properties of the specimen. The key curve procedure was applied to all the test records collected. The resulting key curves are presented and discussed in later sections of this paper.

Load-Displacement Curves

Analytical curves based on plane stress and plane strain solutions for the load and load-line displacement curves were taken from the EPRI elastic-plastic fracture handbook [7] to predict the load-displacement records of each individual *J-R* curve. The degree of comparison of the experimental load-displacement records to the analytically determined load-displacement curves were used to assess the geometric dependence of the specimen size investigated. The prediction of the load-displacement behavior of a compact specimen can be obtained directly by using the *J-R* curve from the specimen test and the EPRI/GE estimation formulae given by Eqs 4 and 5. Given the *J-R* curve and the initial crack length a_0, the crack length associated with a point on the R curve during the growth process is $a = a_0 + \Delta a$. When J-controlled crack growth is applicable, the condition for continued crack growth until instability is

$$J(a,P) = J_R(a - a_0) \tag{3}$$

This equation gives the value of applied J associated with the crack length, a. The values of J and a are used in

$$J = f_1(a_e)P^2/E' + \alpha\sigma_0\epsilon_0 ch\,(a/b,n)[P/P_0]^n \tag{4}$$

which is elastic-plastic estimation formulae for a compact specimen. Equation 4 is needed to solve the corresponding value of applied load numerically using the successive bisection method [8]. The values of crack length a and load P obtained are then used in

$$\Delta_L = f_3(a_e)P/E' + \alpha\epsilon_0 ah_3(a/b,n)[P/P_0]^n \tag{5}$$

to calculate the load-line displacement, Δ_L. Repeating this process for the various Δa values along the J-R curve, a complete load-displacement curve can be determined.

DPFAD Approach

The deformation plasticity failure assessment diagram approach (DPFAD) has been used extensively to predict both piping and pressure vessel failures [9,10]. Additional benefits from the use of this approach are the assessment of J-R curve, geometric or constraint independence, and J-controlled crack growth. DPFAD can be used to compare J-R curves versus J_{applied} for the different-sized specimens.

The DPFAD procedure utilizes deformation plasticity solutions for cracked specimens and/or structures (in the format of the CEGB R-6 two-criteria failure assessment diagram) to graphically solve elastic-plastic fracture mechanics problems through the solution of the nonlinear equation $J_{\text{applied}} = J_{\text{material}}$ for the load corresponding to the current crack length and tearing resistance. The general DPFAD procedure involves the following steps:

The generation of the DPFAD curve from elastic plastic analysis of a flawed structure using deformation plasticity solutions for a simple power-law strain-hardening material based on the Ramberg-Osgood stress-strain equation:

$$\epsilon/\epsilon_0 = \sigma/\sigma_0 + \alpha(\sigma/\sigma_0)^n \tag{6}$$

where

$$\sigma_0 = \sigma_{ys} \quad \text{and} \quad \epsilon_0 = \sigma_{ys}/E \tag{7}$$

The J-integral response of the structure is given by J_{applied} where

$$\frac{J_{\text{applied}}}{G} = \frac{1}{K_r^2} \tag{8}$$

or

$$K_r = \sqrt{G/J_{\text{applied}}} = f(S_r) \tag{9}$$

where S_r is the ratio of applied stress to net section plastic collapse stress and

$$G = K_I^2/E' \tag{10}$$

where G = the elastic strain energy release rate.

Equation 9 defines a curve in the $K_r - S_r$ plane which is a function of flaw geometry, structural configuration, and stress-strain behavior of the material defined uniquely by α, n from Eq 6. Since both K_r, S_r are linear in applied stress, the DPFAD curve is independent of the magnitude of applied loading.

The determination of assessment points are based on the ratio of K_I (or the square root of G) of the structure divided by the relevant material property K_{IC} (or square root of J_{IC} at initiation of flaw growth or for stable flaw growth, square root of $J_R(\Delta a)$, the tearing resistance of the material) for the ordinate, K_r and the ratio of the applied stress (load) to reference (limit load) for the abscissa, S_r. For initiation of ductile crack growth, a single assessment point is calculated. For stable crack growth, a locus of assessment points are determined by incrementing the crack size "a" by "$a + \Delta a$" in the calculation of G. For assessing specimen test data, the following is needed: $[P, a_0 + \Delta a, J_R(\Delta a)]$. The position of the assessment point (S_r', K_r') relative to the failure assessment curve determines how close the specimen is to the initiation of ductile tearing, as shown in Fig. 1 by the point L_1'. Since both S_r', K_r' are directly proportional to applied load (L), when the load is increased, point L_1' moves radially from the origin of the diagram to point L_i, which is the initiation point of ductile tearing. After initiation of ductile tearing, the locus of (S_r', K_r') follows the failure assessment curve between the initiation load (L_i) and the maximum load point (L_m). This defines the path of stable crack growth. For displacement-controlled specimens, the path follows the failure assessment curve up to the limit load cutoff. For load-controlled specimens, the path will go outside the assessment curve after the maximum load point (L_m) has been reached, indicating that the structure has become unstable. To calculate the locus of points which follows the failure assessment curve, K_r' and S_r' are defined by

$$K_r'(a_0 + \Delta a) = \sqrt{G(a_0 + \Delta a)/J_R(\Delta a)} \tag{11}$$

and

$$S_r'(a_0 + \Delta a) = P/[P_0(a_0 + \Delta a)] \tag{12}$$

where P_0 is the reference limit load for a compact specimen. J_R is the experimentally measured J-resistance curve plotted as a function of slow stable crack growth, Δa. G is calculated as before from the elastic stress intensity factor (Eq 10) for the current crack length, $a_0 + \Delta a$. The condition that the assessment points must follow the failure assessment diagram curve is the same as given by Eq 3.

The first set of experimental data used for validation of the DPFAD approach was taken from General Electric's EPRI contract RP601-2 [11], which included tests on side-grooved compact specimens. Figure 2*a* illustrates the failure assessment curves for plane strain compact specimens of $a/W = 0.625$ and 0.750 along with the (S_r', K_r') points calculated from the test data of the General Electric/EPRI A533B 4*T* compact specimens. The test results are plotted from the $[P, a_0 + \Delta a, J_R(\Delta a)]$ data sets. The coordinate points (S_r', K_r') were determined

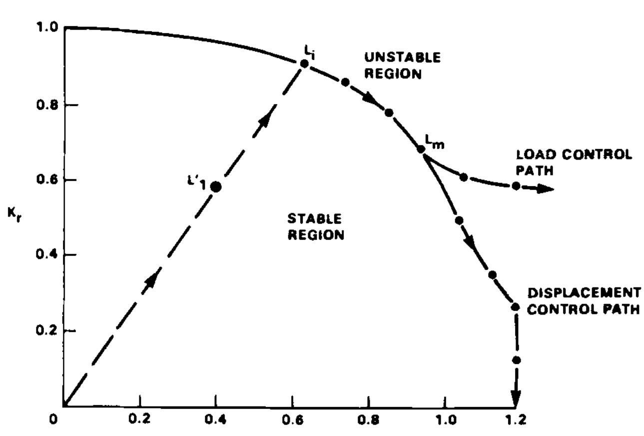

FIG. 1—*Failure assessment diagram in terms of stable crack growth.*

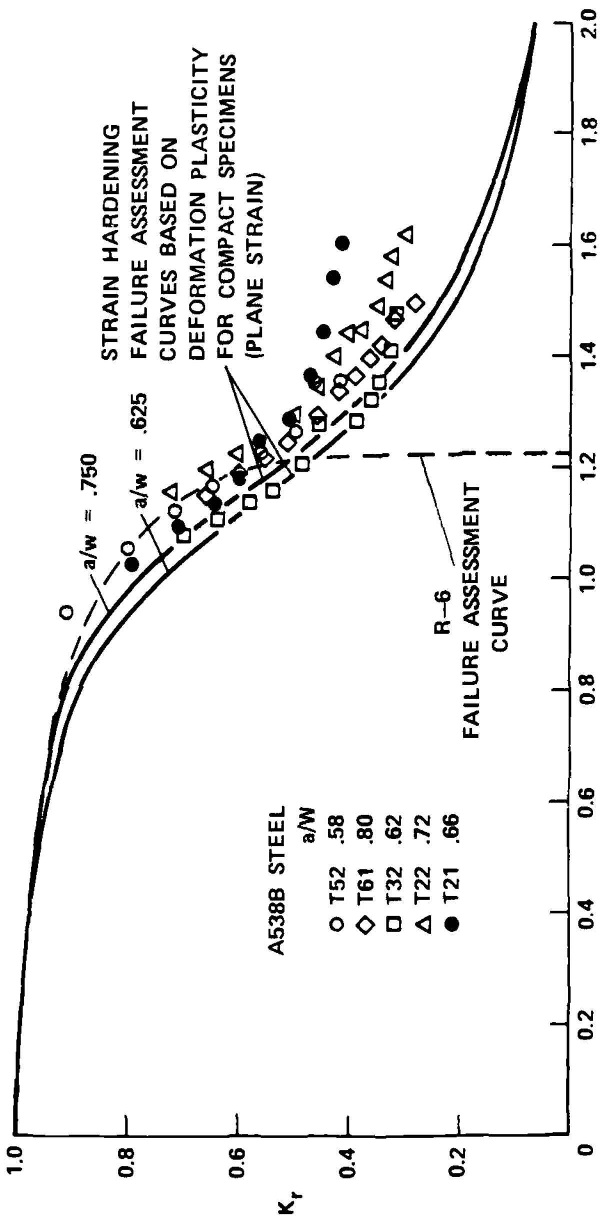

FIG. 2a—*Failure assessment of EPRI/GE A533B compact specimens.*

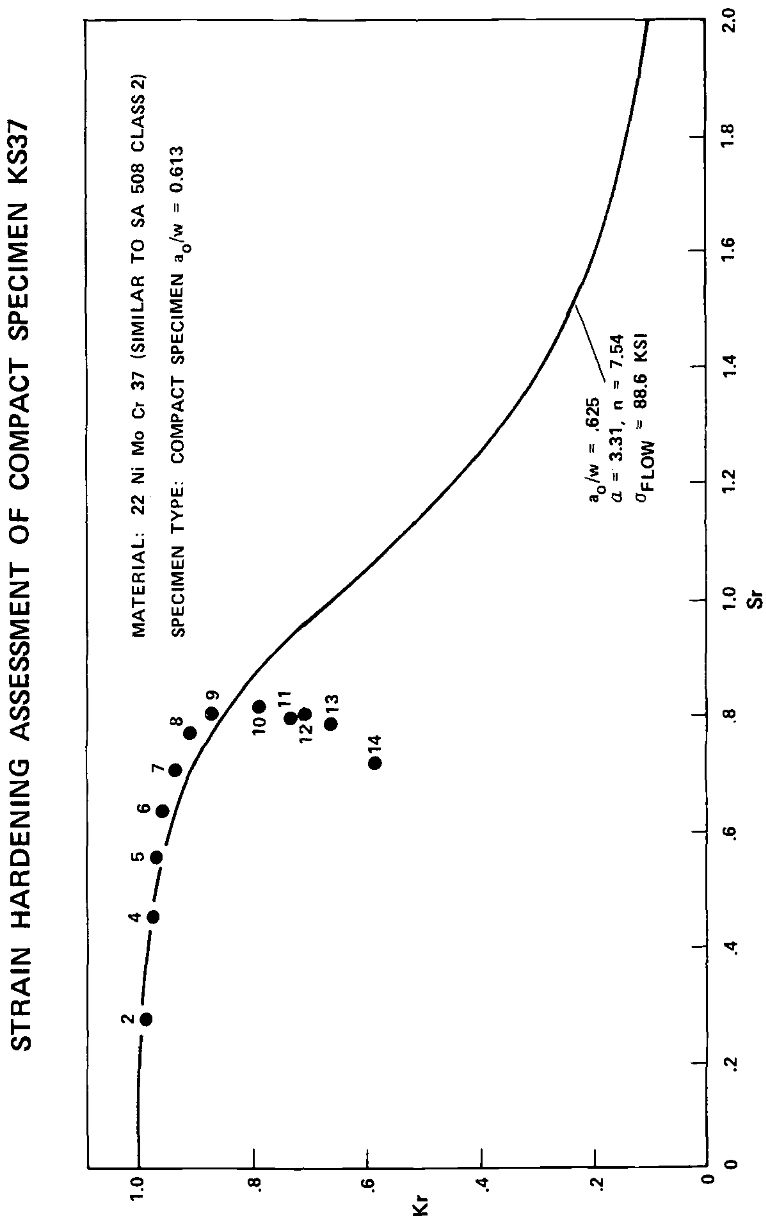

FIG. 2b—*Failure assessment of Babcock & Wilcox tested 22NiMoCr37 (modified) steel compact specimen KS37.*

using Eqs 11 and 12, where the applied load is the experimentally measured value and P_0 is the plastic collapse stress for a compact specimen for a crack of length, $a_0 + \Delta a$. The limit load expression used for S_r' plotted in Figure 2*a* is based on an expression developed by Rice [*12*].

The 4*T* General Electric specimens show consistent deformation *J*-controlled crack growth behavior. However, other validation work under EPRI RP 1237-2 [*9*] looked at the modified ferritic steel (22Ni MoCr37) obtained from MPA Stuttgart from *J-R* curves developed at B&W Alliance Research Center. Three 2*T* compact specimens of this material were tested and *J-R* curves were determined. The equivalent (S_r', K_r') points were calculated and plotted on the corresponding DPFAD. Figure 2*b*, representing one of the compact specimens, was typical of the results of the other compact specimens tested. In all three specimens after the maximum load point, the (S_r', K_r') points dropped below the failure assessment curve. Subsequent examinations after the test when the specimens were broken open showed that the crack surfaces were irregular and that there were many untorn ligaments, out-of-plane crack growth, and nonuniform crack growth. Physically the material had many laminations, and the crack seemed to be trying to propagate perpendicular to these laminations. The unloading compliance method gave crack growth measurements which were in error by as much as 100%. The (S_r', K_r') points which fell below the failure assessment curve were recalculated by changing the amount of slow stable crack growth in the calculations such that these resultant recalculated points fell on the failure assessment curve. The resulting "equilibrium Δa's" were found to be consistent with the physically measured crack growth made after the specimens were broken open. For this material the place where the assessment points deviated from the failure assessment curve was where the measured *J-R* curves became invalid. Note that it was only after the specimens were broken open that physical evidence was obtained. This strongly suggested that the failure assessment curve approach might be useful in detecting the breakdown of the *J-R* curve due either to the irregular crack growth due to laminations or other metallurgical anomalies or a breakdown of the experimentally determined crack growth measurements.

The key curve evaluation methodology is based on similarity of the load displacement curves for specimens of the same material. The other two procedures, the DPFAD and the load-displacement curve prediction methodologies, provide measures of *J*-controlled crack growth through the satisfaction of $J_{\text{applied}} = J_{\text{material}}$ or

$$J(a,P) = J_R(a - a_0)$$

for the specimen up to the instability point of load controlled or up to the limit load of the specimen for displacement controlled. In both these evaluation procedures the experimentally determined *J-R* curve (J_{material}) is used to check *J*-controlled crack growth through the utilization of the EPRI/GE estimation formulae to predict the response of the specimen in terms of load versus load-line displacement for the load displacement method and through comparison of the assessment points (S_r', K_r') to the failure assessment diagram curve (S_r, K_r).

The measurement of constraint for these two methods is limited to the required assumption of plane strain versus plane stress, the two extremes of constraint. The actual constraint of a specimen can only be determined through detailed finite element analysis of three-dimensional cracked compact specimens loaded under elastic-plastic conditions. The significance of *J*-controlled crack growth is that the *J-R* curve obtained from fully yielded specimens will be the same as the *J-R* curve from specimens with limited yielding (small-scale yielding). For *J*-controlled crack growth, the *J-R* curve will be independent of the crack configuration and be a material property.

General Results of Data Evaluations

A selected set of the data evaluations are presented in Figs. 3 through 15. The data evaluations presented were selected as being representative of those performed. The results from the A302-B evaluation are presented in Figs. 3 through 7. In Fig. 3, ten *J-R* curves obtained from the analysis of the MEA A302-B data are shown. These curves show the extreme size effect which initiated the size effect concern. The 6*T* results are substantially below the 1/2*T* and the 1*T* results. The 2*T* and the 4*T* results are spaced between the smaller specimen results and the 6*T* results. The data are well ordered with specimen size with the highest *J-R* curves from the smallest specimens and the lowest from the largest 6*T* specimen. The key curves are plotted in Fig. 4. There is not a single key curve for these data but rather a separate curve for each of the specimen sizes tested. In Figs. 5 through 7 the DPFAD and the load-displacement curve evaluations of the A302-B data are presented. For all the specimen sizes the test results do not fall on the failure assessment curve or on the predicted load-displacement curve.

The results from the analysis of the HSST data are shown in Figs. 8 through 11. Figure 8 is a presentation of the *J-R* curves for the specimens, which ranged in size from 1/2 to 4 in. These *J-R* curves are quite different from the A302-B curves in that although they are ordered by specimen size, the smallest specimens have the lowest curves and the largest specimen produced the highest curve. The key curves which are presented in Fig. 9 show the same curve for all the specimen sizes with the exception of the 1/2*T* specimen, which produced a totally different key curve, much higher than that produced by the other specimens. A possible explanation for this is that the 1/2*T* specimen is made entirely of weld metal and the weld metal is much stronger than the base metal. Figures 10 and 11 present the DPFAD and the load-displacement predictions. The test results follow very closely the predicted results in both the DPFAD and the load-displacement predictions.

The results of the analysis of the Westinghouse data are presented in Figs. 12 through 15. The *J-R* curves are displayed in Fig. 12. There is no obvious size effect in these *J-R* curves. It appears that the 4*T* experiments may have been conducted to a longer crack extension than

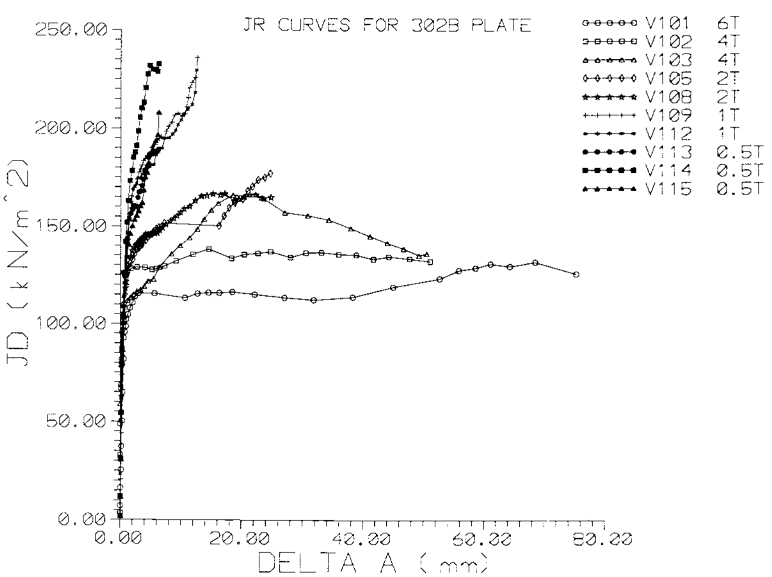

FIG. 3—J_R *curves for MEA 302B plate.*

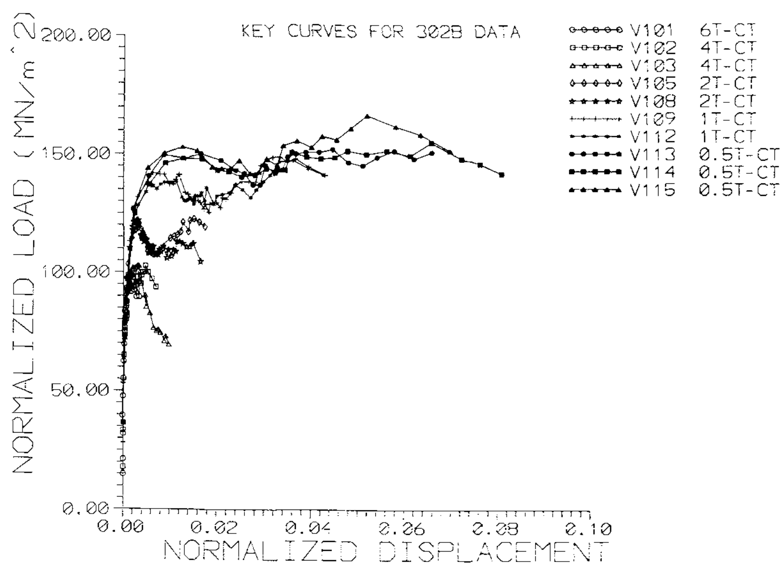

FIG. 4—*Key curves for MEA 302B plate.*

should be considered valid for a deformation J analysis because the J-R curves are starting to curve down. The key curves in Fig. 13 show a similar effect. All the specimen sizes appear to have produced the same key curve. The information presented in Figs. 14 and 15 continue the same trends seen in the other figures. From both the DPFAD and the load-displacement analysis standpoint there does not appear to be a size dependency in these data.

Discussion of Results

Comparison of the various test results for the three material categories:

1. MEA A302B plate tests.
2. Westinghouse A508 $0.5T$ to $10T$ compacts.
3. HSST weld metal compacts.

were made through comparisons of the various J_R curves, key curves, DPFADs, and load-displacement curves.

In all of the figures, only J_D results are shown. The J_M results are almost identical to the J_D results showing the same trends and effects.

For two of the comparison methodologies, the DPFAD and the predicted load-displacement curves, a knowledge of the true stress-true strain behavior as measured by the Ramberg-Osgood stress-strain relationship is required. Of the various J-R curve data sets evaluated, only for the MEA A302B and the Westinghouse A508 materials were the Ramberg-Osgood constants, α,n, obtained directly from a tension test. The α,n constants for the HSST data set were determined using the Bloom [9] approximation from estimates of the engineering yield and ultimate strength of the material. This approximation assumes that the plot of true stress versus true plastic strain on a log-log scale is linear between the true yield strength and true ultimate strength.

For the DPFAD procedure and the predicted load-displacement method, the extremes of

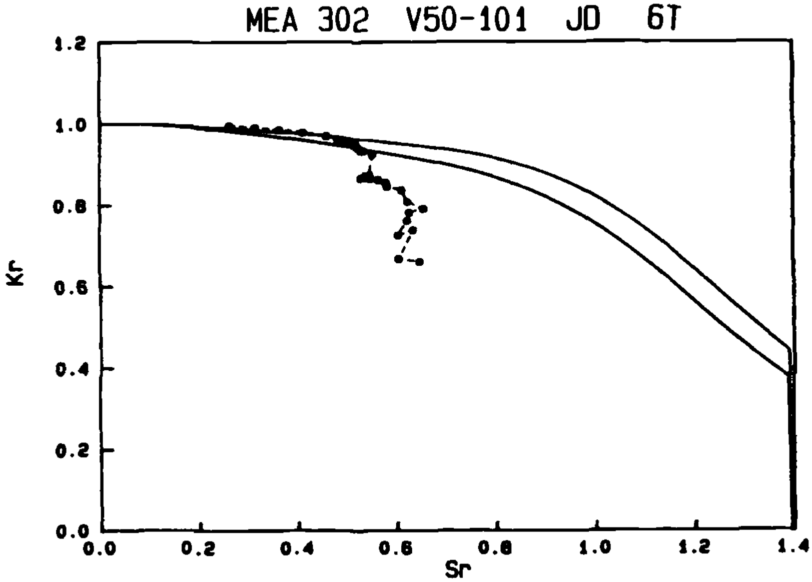

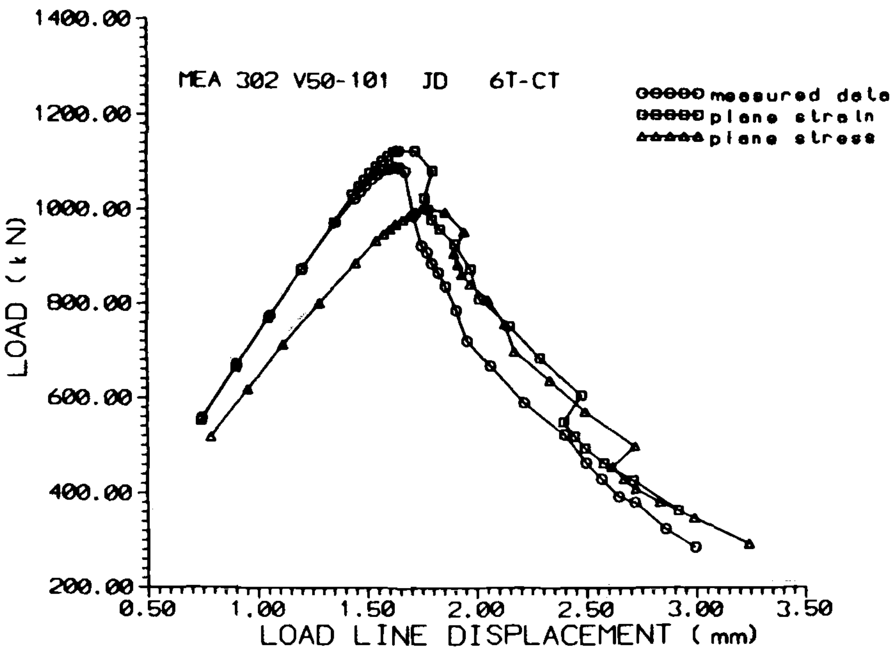

FIG. 5—*DPFAD and load versus load-line displacement plots for MEA 302B 6*T *and 4*T.

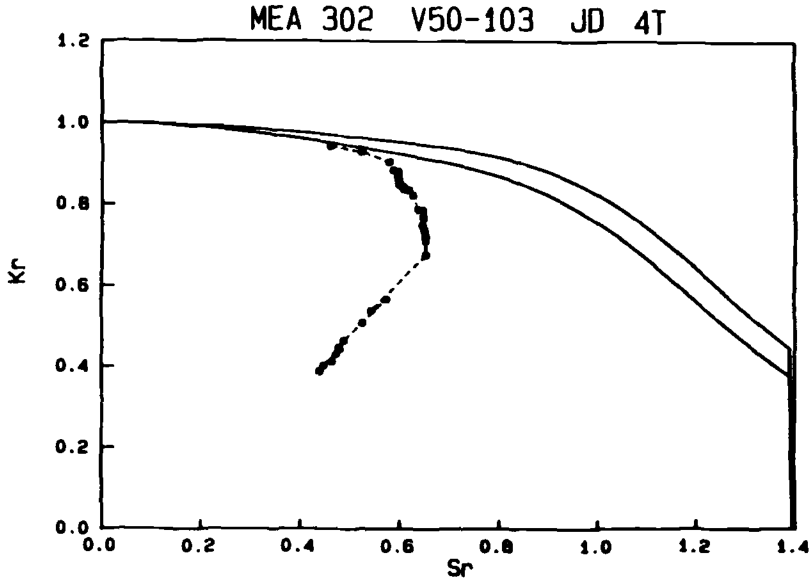

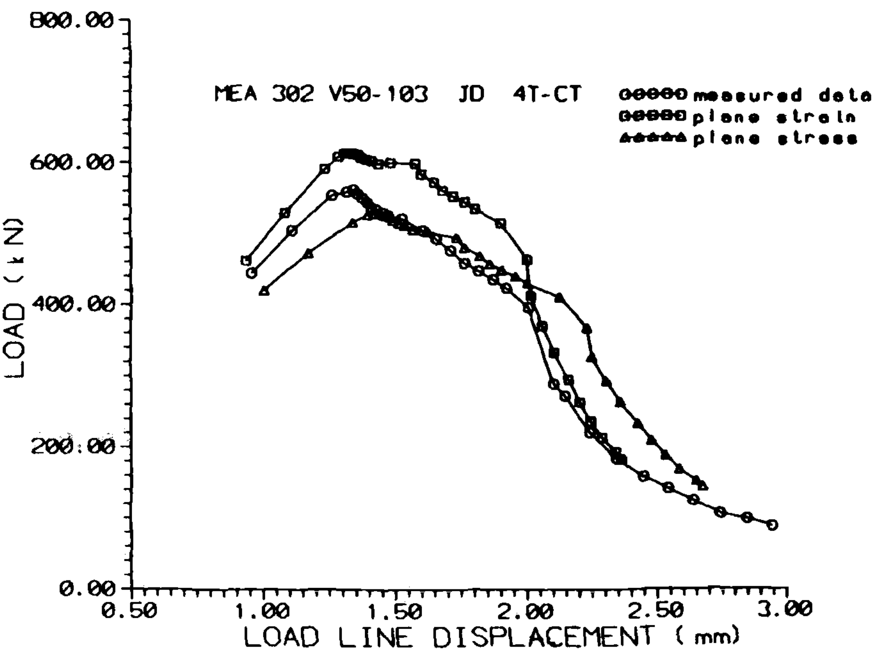

FIG. 5—*Continued*

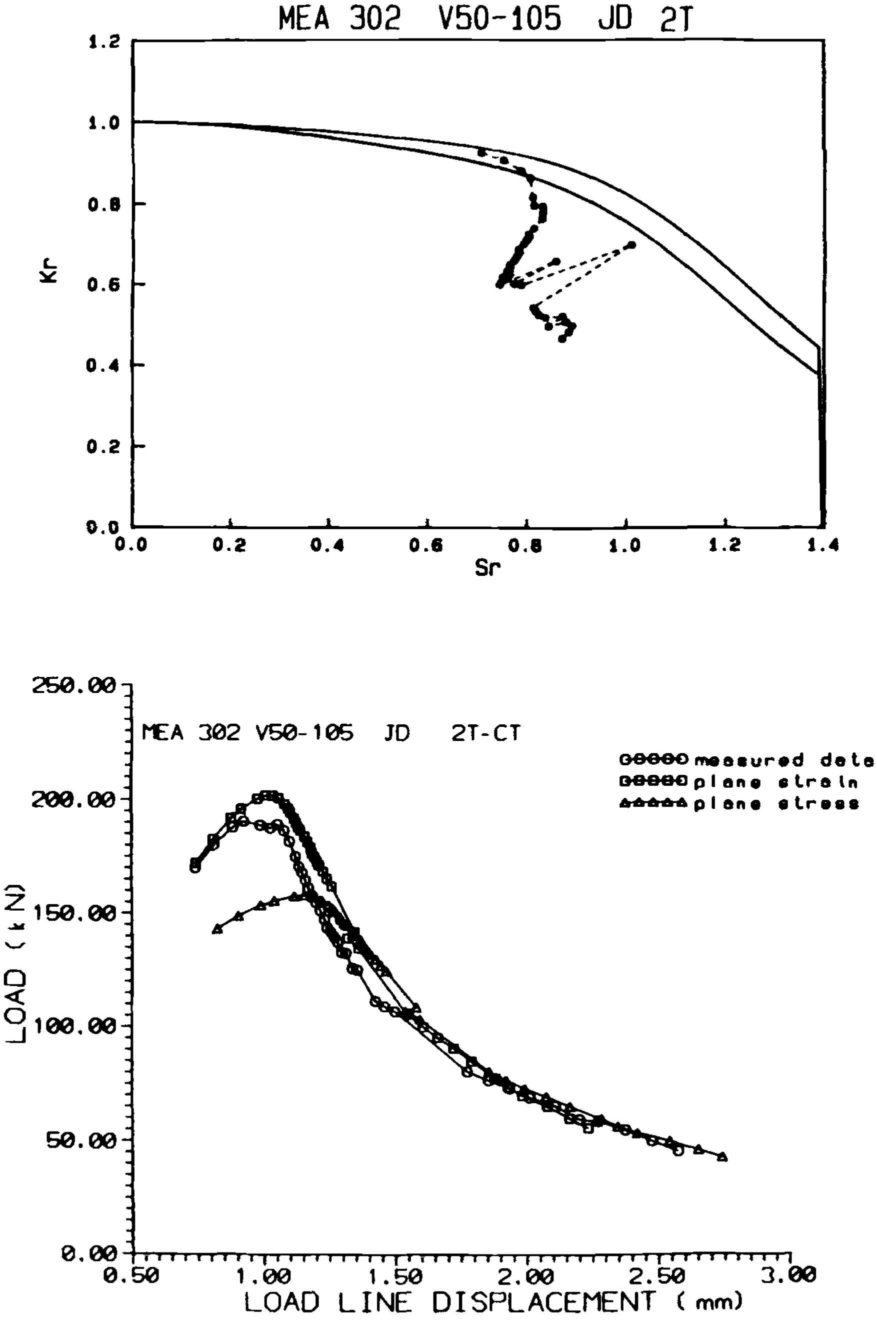

FIG. 6—*DPFAD and load versus load-line displacement plots for MEA 302B 2*T *and 1*T.

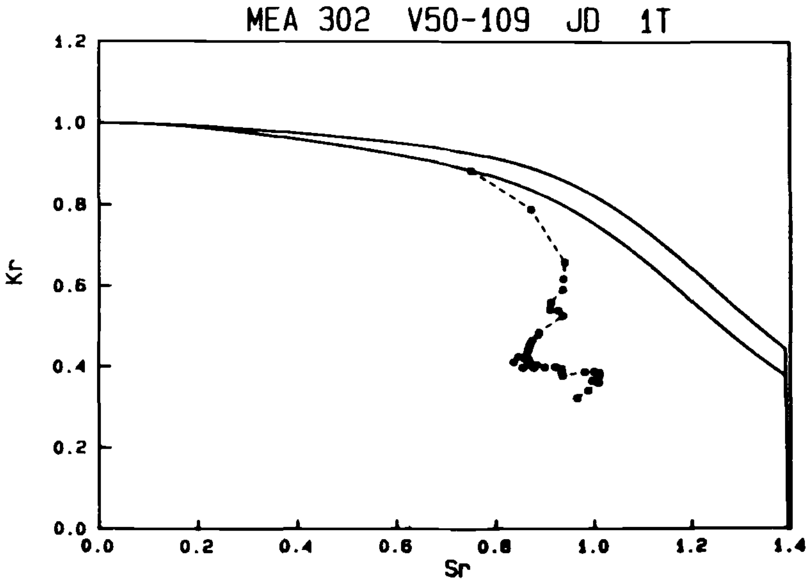

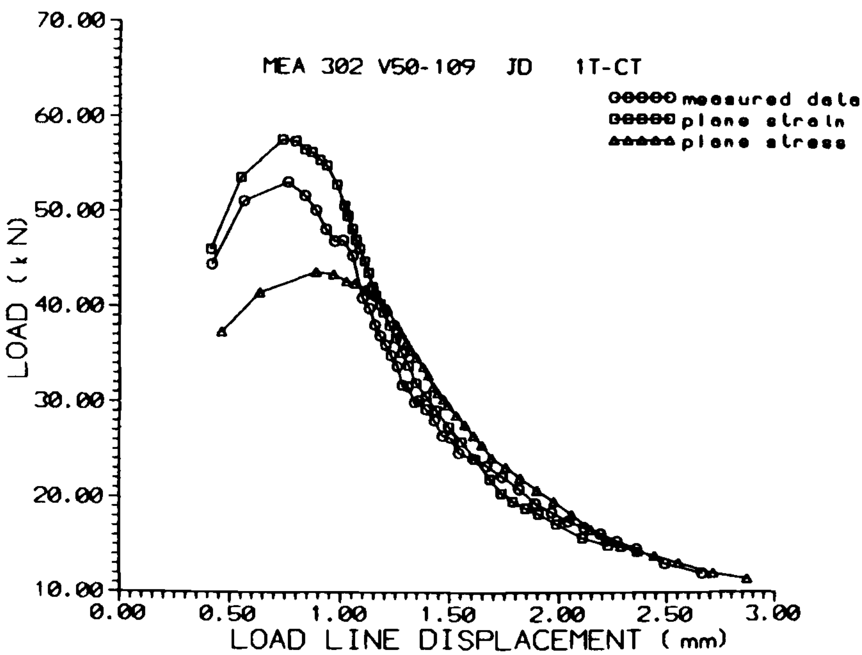

FIG. 6—*Continued*

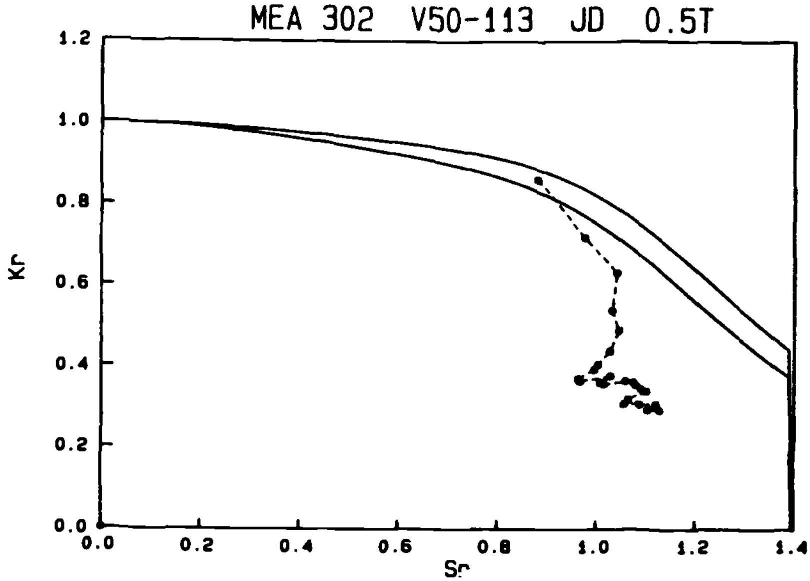

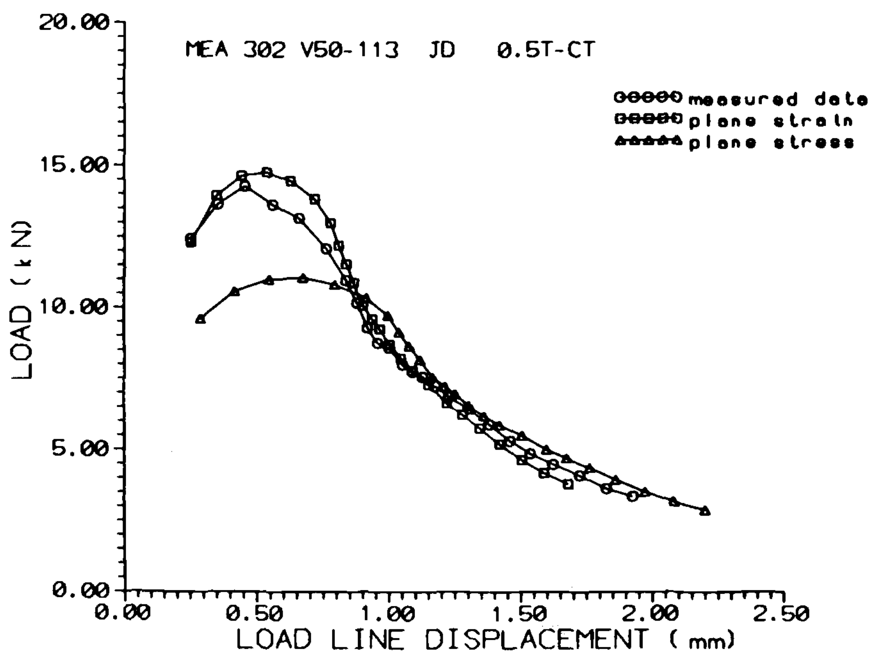

FIG. 7—*DPFAD and load versus load-line displacement plots for MEA 302B 0.5*T.

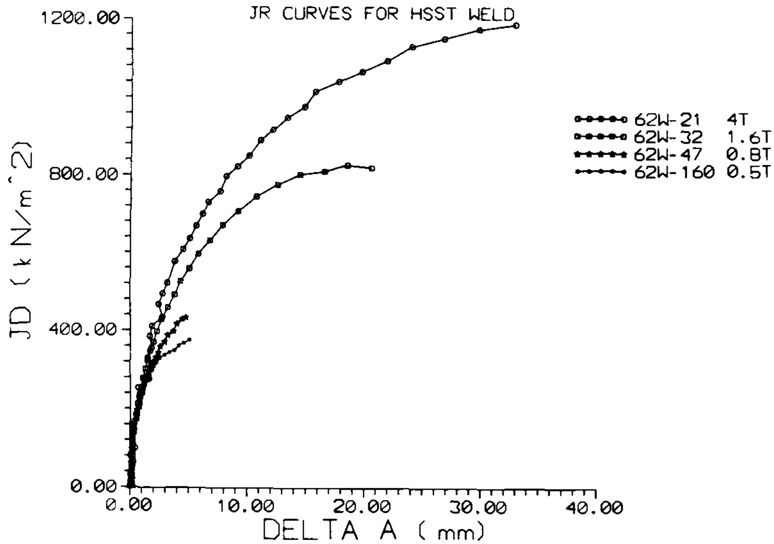

FIG. 8—J_R *curves for HSST weld metal.*

constraint—plane stress and plane strain—were determined, resulting in two lines on the plots. The DPFAD curves were relatively insensitive to constraint effects as measured by plane strain versus plane stress predictions, while the predicted load-displacement plots are extremely sensitive to the constraint assumptions. These trends occur for all material data sets. The cutoffs, vertical lines at the maximum value of S_r, for the DPFAD curves were conservatively based on the ratio of engineering ultimate and the yield strength. These cutoffs should have been based on true ultimate strength, resulting in a shift of the cutoff.

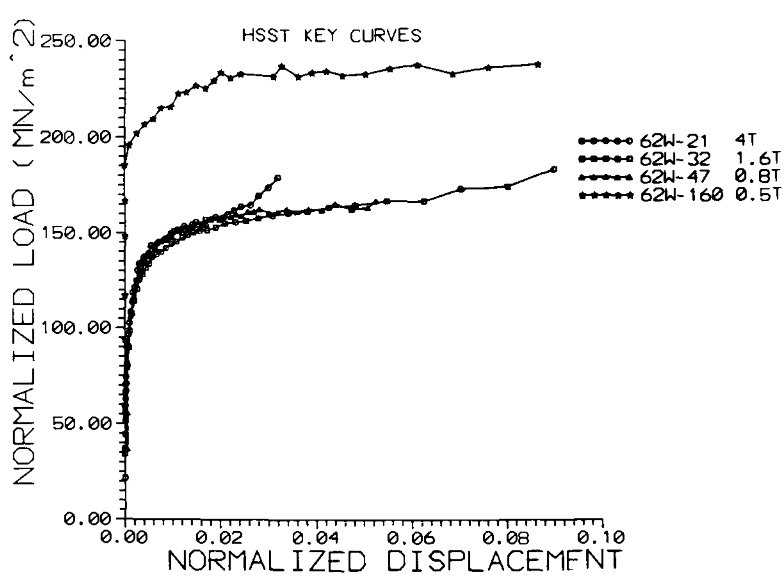

FIG. 9—*Key curves for HSST weld metal.*

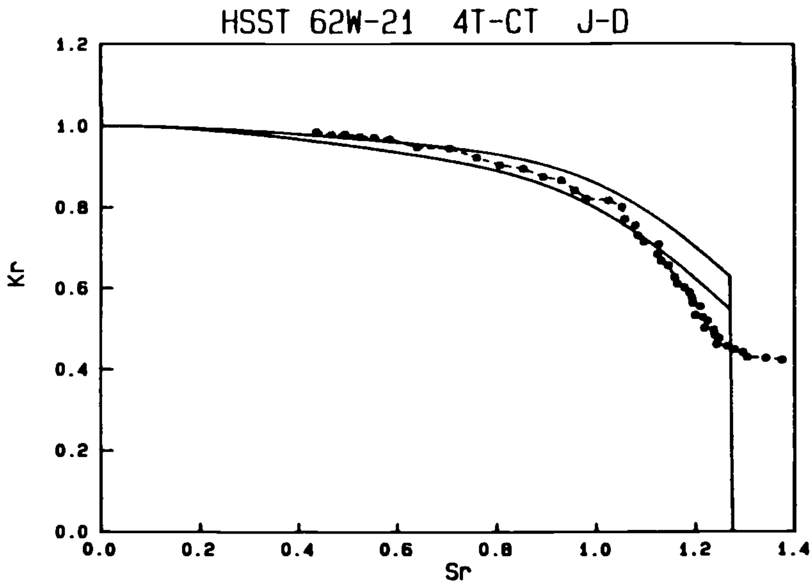

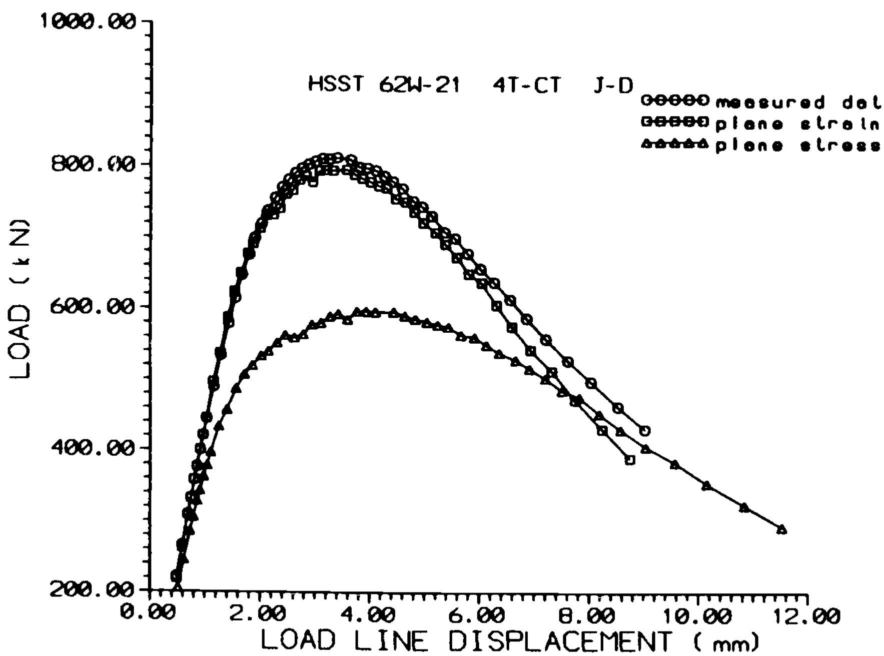

FIG. 10—*DPFAD and load versus load-line displacement plots for HSST weld 4*T *and 1.6*T.

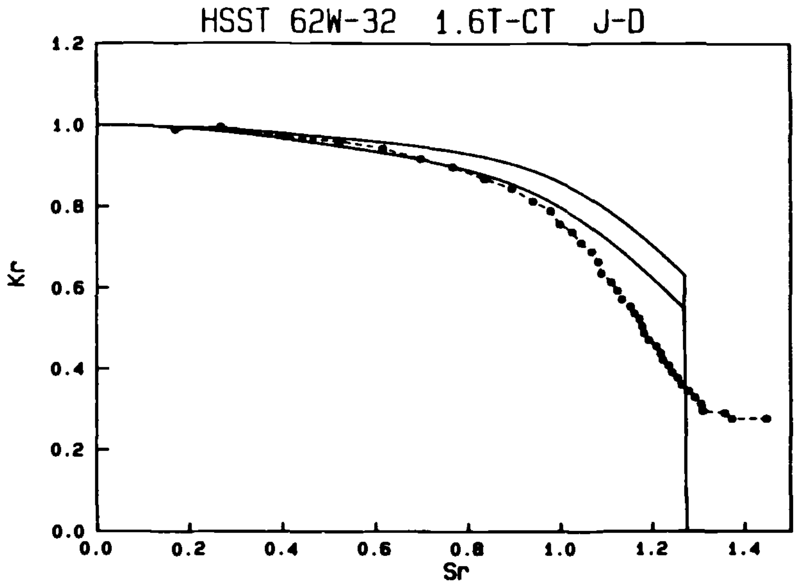

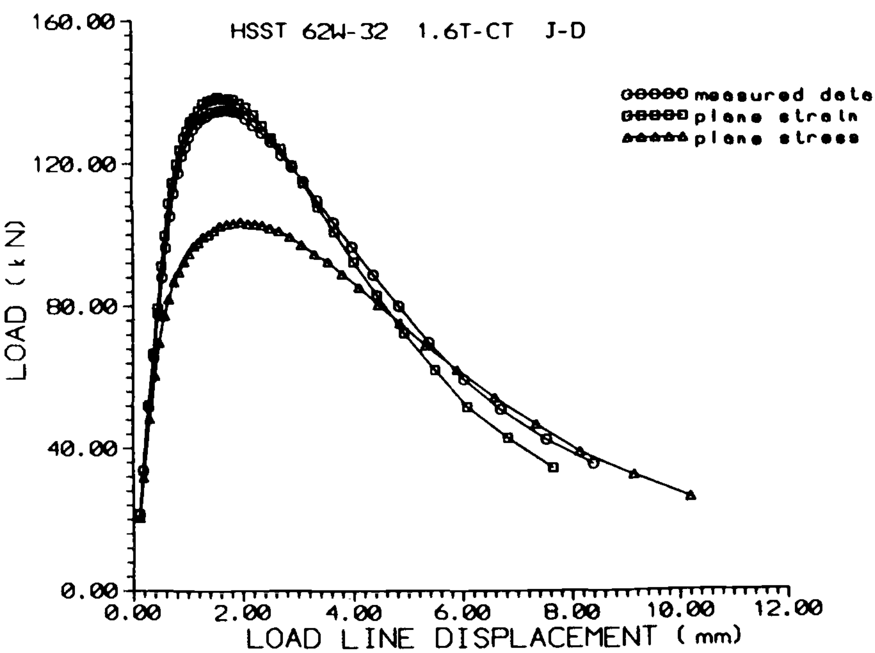

FIG. 10—*Continued*

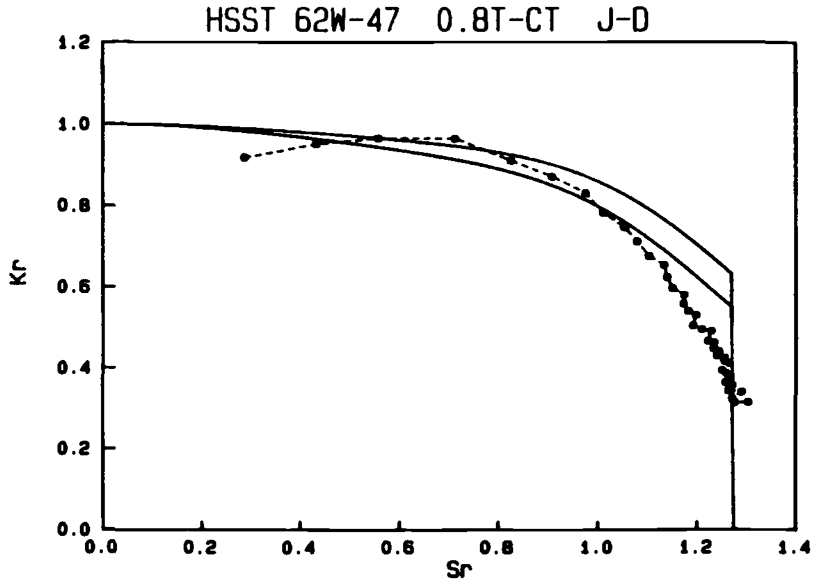

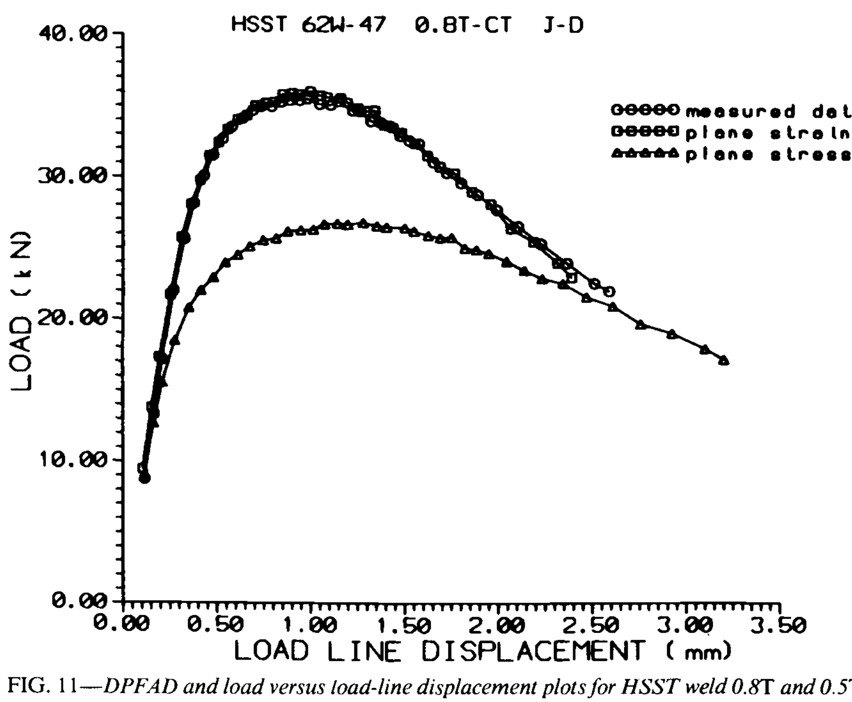

FIG. 11—*DPFAD and load versus load-line displacement plots for HSST weld 0.8*T *and 0.5*T.

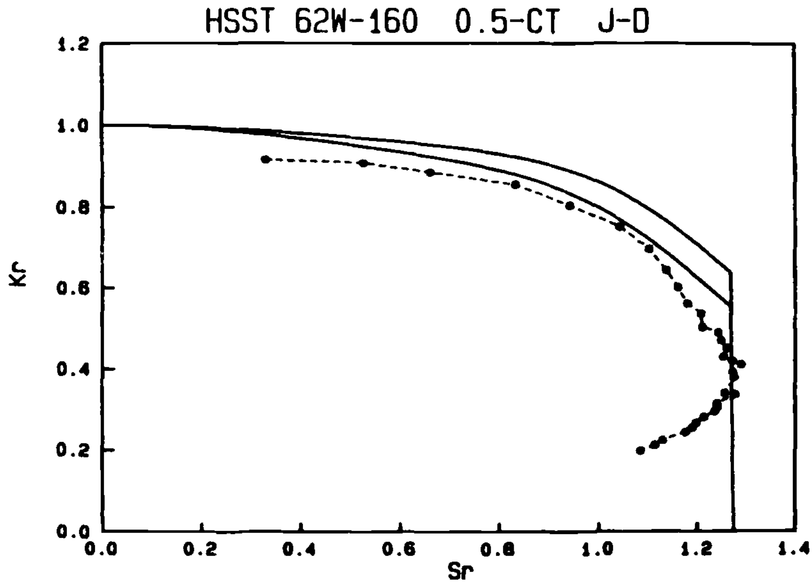

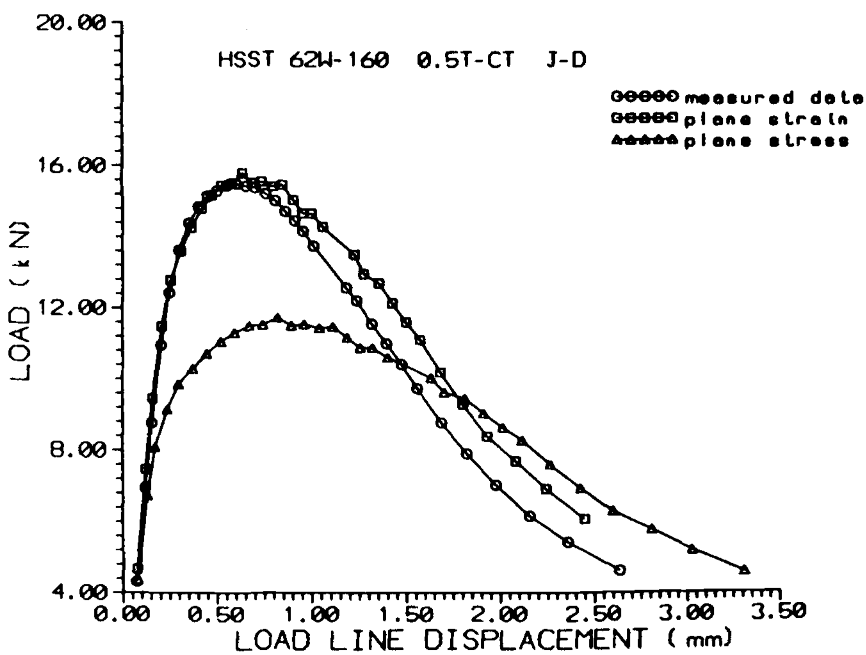

FIG. 11—*Continued*

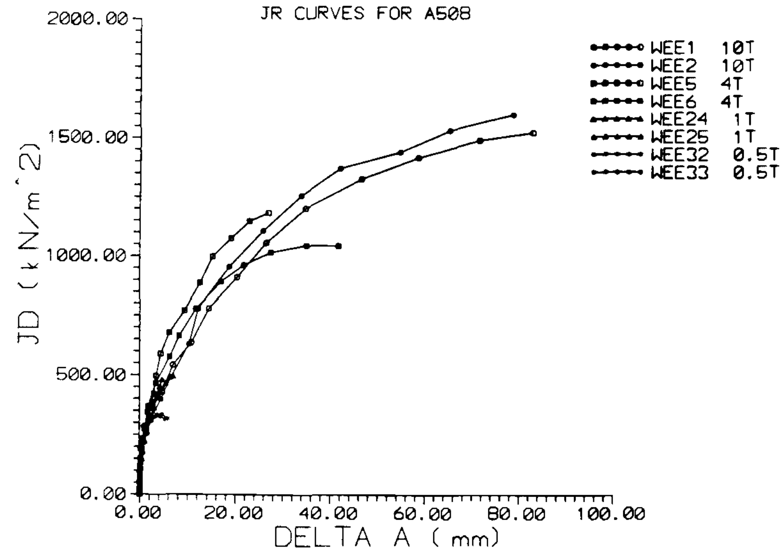

FIG. 12—J_R *curves for Westinghouse A508.*

The plane strain predictions of the load-displacement curves in general overpredict the measured load-displacement. The trends of the assessment points (S_r', K_r') are quite similar for A302B plate as the MPA material discussed earlier and shown in Fig. 2*b*. In this earlier work the condition was due to laminations and inclusions in the material, which resulted in uneven crack extension and unbroken ligaments on the fracture face. In the A302B material, the

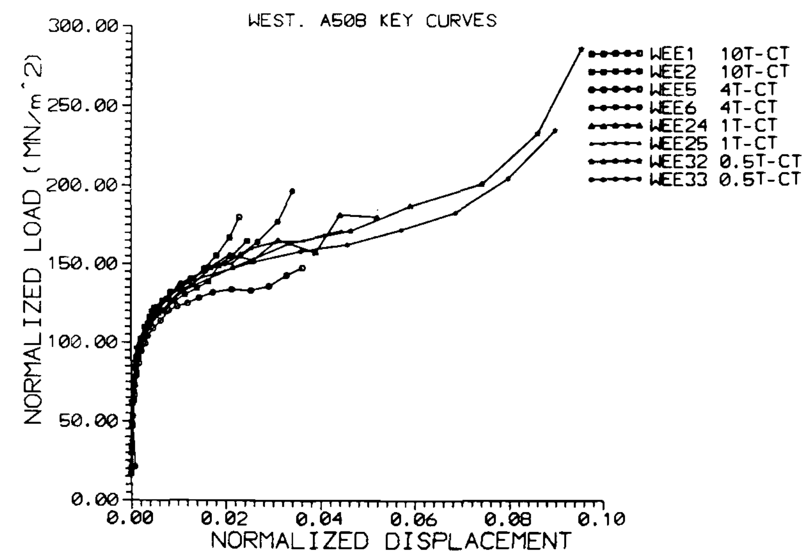

FIG. 13—*Key curves for Westinghouse JA508.*

delaminations could produce a reduction of effective thickness with a resulting loss of constraint of the specimen.

The key curves for the A302 data are size dependent. There is a separate key curve for each of the specimen sizes tested. This is not the case for the other two materials. All of the key curves for these materials fall in tight groups with the exception of the $1/2T$ data in the HSST data set. For this specimen, the key curve was significantly higher than for the other specimens. The DPFAD and the load-displacement predictions for this specimen were not as good as for the other specimens in the data set.

When the results of the key curve, DPFAD, and load-displacement predictions methodologies are compared for the material data sets and when good agreement with the predictions of one procedure is seen, good agreement is seen in all the procedures. Likewise, when the prediction looks bad, all the predictions look bad. However, the DPFAD approach seems to better highlight the extent of disagreement shown in the other two procedures. This is seen best with the Westinghouse A508 specimens where the $10T$ specimen is in excellent agreement with the DPFAD curve, while the agreement between load-displacement prediction and the measured load-displacement is not as good. The $4T$ DPFAD curve plot (Fig. 14) suggests that a plane stress constraint condition may be valid, while the load-displacement plot shows excellent agreement with a plane strain assumption. The $1T$ again better correlates with theory for the DPFAD.

Any one of the procedures could be used to demonstrate that a size effect is present in a data set and perhaps be able to identify if it is due to metallurgical or specimen constraint effects. The DPFAD is, however, the only procedure evaluated in which the size effect can be identified when a single specimen is tested. In addition, it appears that the DPFAD can also be used to identify the observed size effect, which is due to loss of specimen constraint or metallurgical effects. This can be seen by observing the DPFAD plots presented in Figs. 5 and 11. The size effect seen in Fig. 5 is due to metallurgical reasons, while that in Fig. 11 is due to loss of constraint.

The HSST data set represents the type of data to be evaluated in nuclear reactor pressure vessel surveillance programs. The material in HSST data set is identical to some of the material in surveillance programs. The surveillance program data do not show the type of size effect seen in the MEA A302B data. The only size effect observed is that when the specimen gets very small it produces conservative results. No test information to date has been observed which would question the usability of the *J-R* curves obtained in surveillance programs for evaluation of the NRC low-upper shelf toughness issue.

Results of the Application of a Corrective Procedure

The second objective of the investigation was the development of a corrective procedure for *J-R* curve data where specimen size effects are evident. The DPFAD approach was used to demonstrate that the various size effects seen with the A302B plate material could be corrected. The first step in the corrective procedure is the identification that there is a size effect problem. This has been discussed in the preceding sections.

The *J-R* curves for the uncorrected data are shown in Fig. 16. Note that the smaller the specimen as measured by thickness (T), the higher the *J-R* curves with the $6T$ compact lower bounding the *J-R* curves. Duplicate specimens for the $1/2T$, $1T$, $2T$, and $4T$ are not shown for clarity, but the trends are similar to those shown in Fig. 16.

The DPFAD approach first consists of plotting load, J_R, Δa in terms of the K_r', S_r' coordinates from the test data on a DPFAD curve generated for plane strain compact specimens with corresponding a/W ratio (at crack initiation) using the best fit α,n, material properties found from

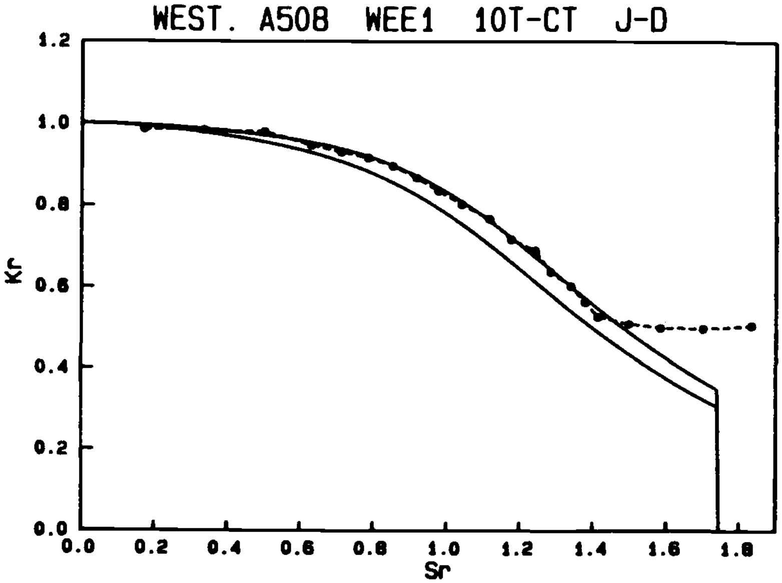

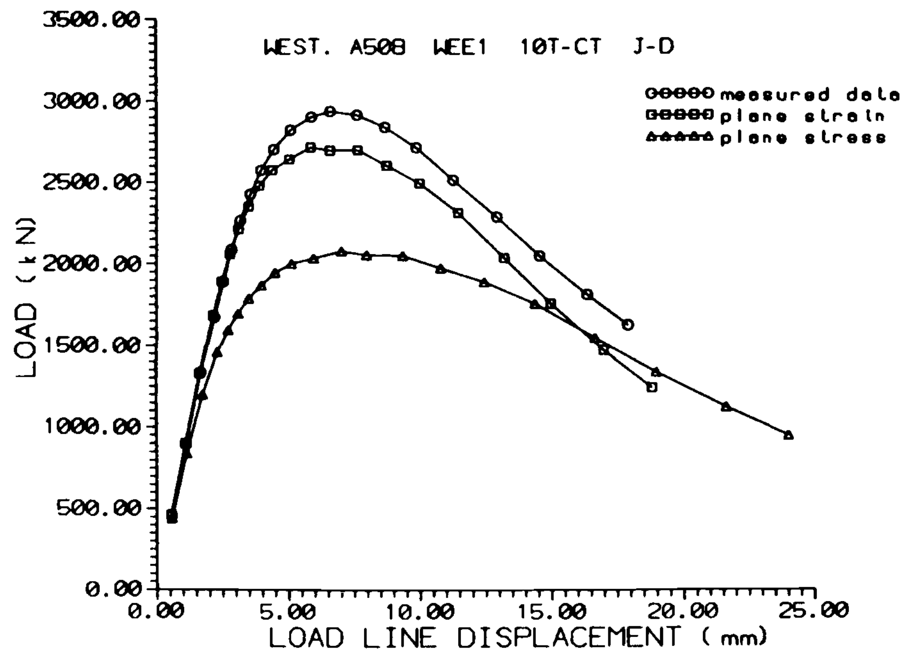

FIG. 14—*DPFAD and load versus load-line displacement plots for Westinghouse A508 10*T *and 4*T.

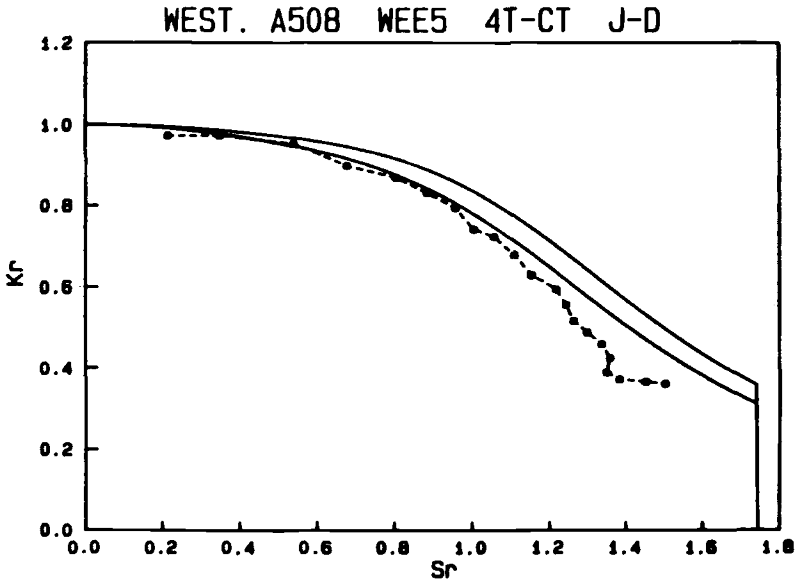

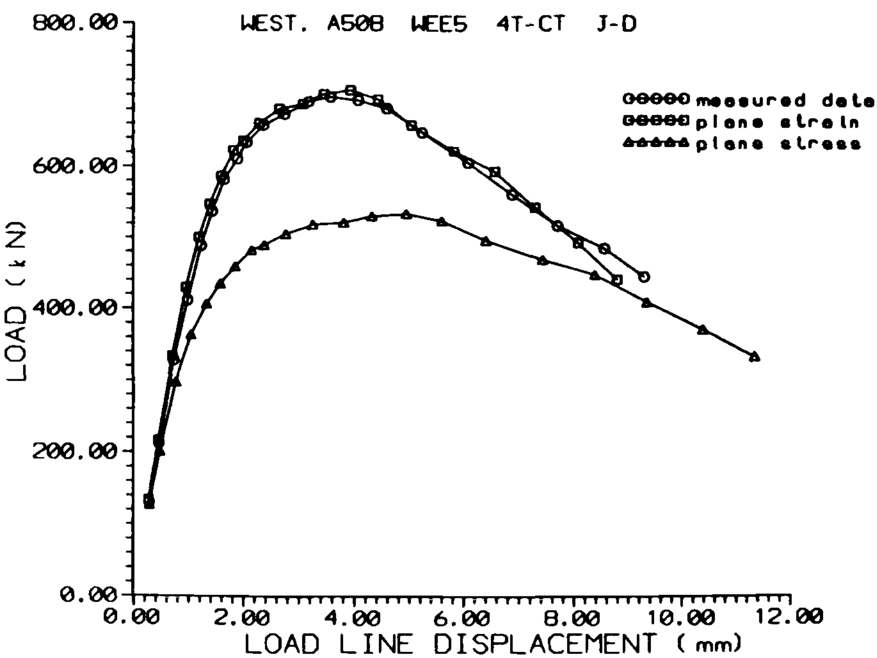

FIG 14—*Continued*

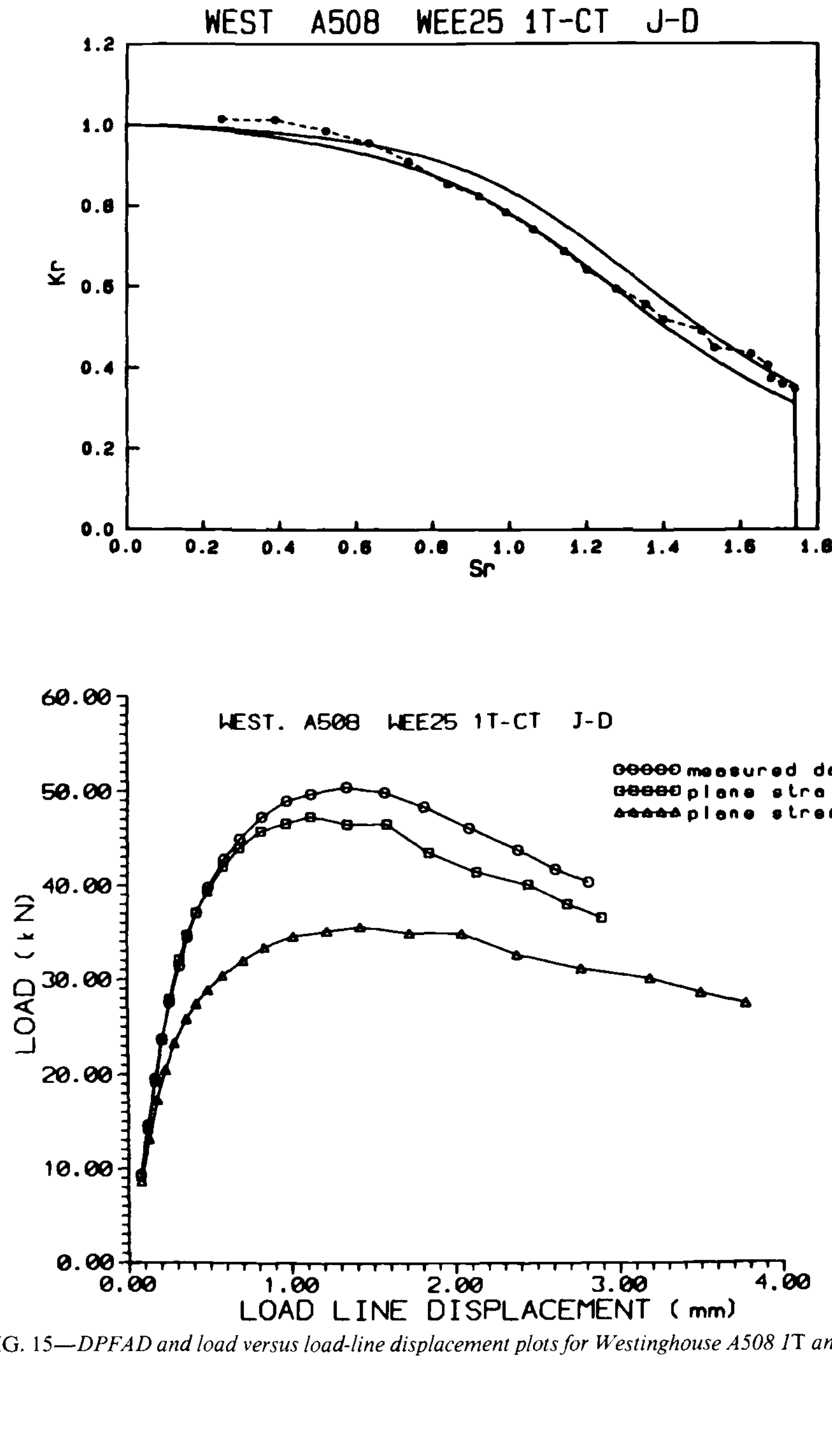

FIG. 15—*DPFAD and load versus load-line displacement plots for Westinghouse A508 1*T *and 0.5*T.

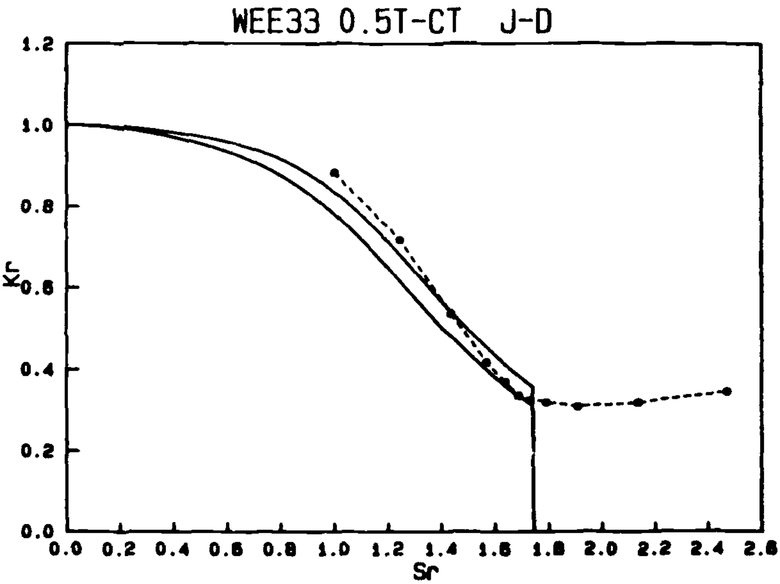

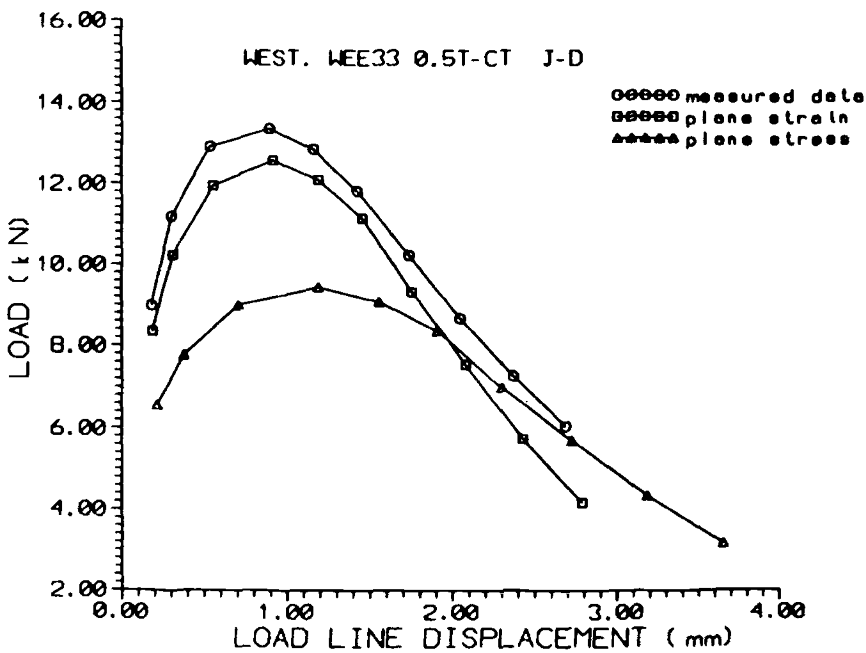

FIG 15—*Continued*

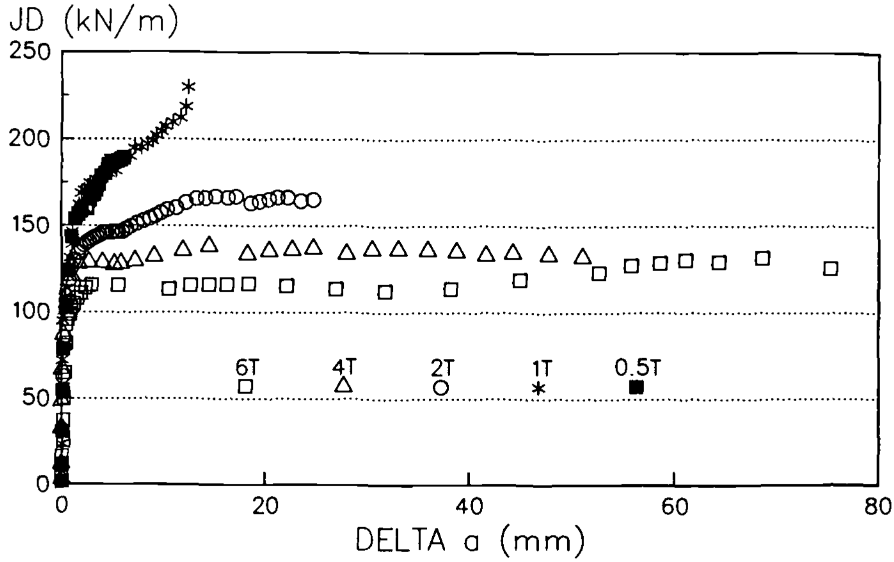

FIG. 16—J_R *curves for 302B plate—uncorrected.*

tension tests. Figure 17 through Fig. 21 present the *J-R* curve data in terms of (K_r', S_r') data points for the 6*T*(V101), 4*T*(V102), 2*T*(V108), 1*T*(V112), and 1/2*T*(V113) specimens. Note that in all cases, the (K_r', S_r') points eventually deviate from the DPFAD curve (K_r,S_r). The points which deviated from the DPFAD curve were recalculated by adjusting Δa and recalculating J_R value using the ASTM E1152–87 test standard such that the K_r', S_r' point now falls on the DPFAD curve. This is equivalent to *J*-controlled crack growth through the satisfaction of $J_{\text{applied}} = J_{\text{material}}$ or $J(a,P) = J_R(a - a_0)$ up to the instability point for load controlled spec-

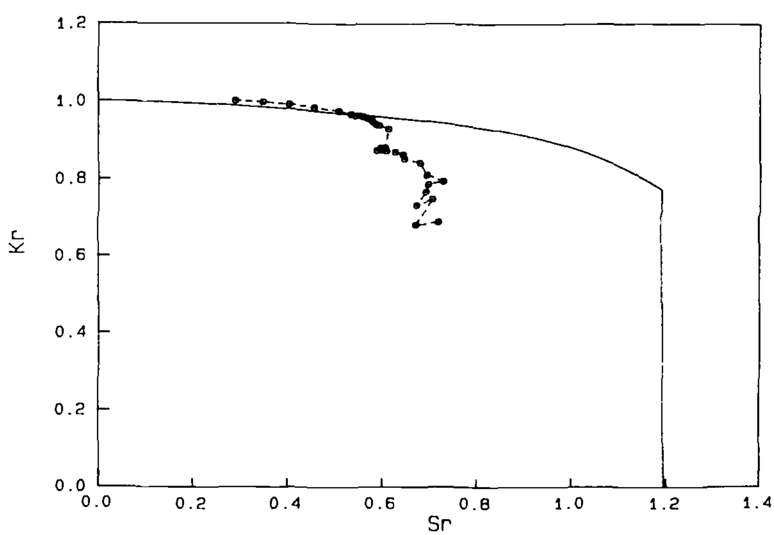

FIG. 17—*DPFAD* 6T *(V101) uncorrected.*

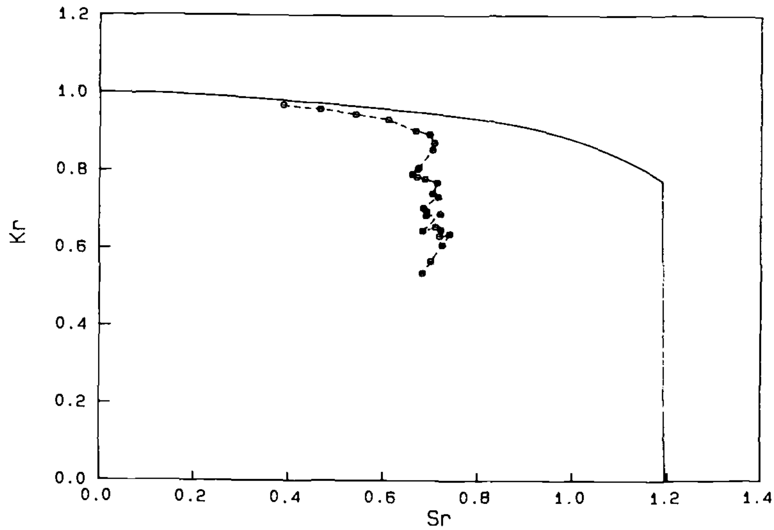

FIG. 18—*DPFAD 4*T *(V102) uncorrected.*

imens or up to the limit load of the specimen under displacement control. The limit load of the specimen is independent of size and only a function of the ratio of flow stress to yield strength when plotted on a DPFAD plot. The flow stress was taken as the average of the yield and ultimate strengths. The result is a vertical cut off or limit load line at approximately S_r = 1.20 for the A302B plate material. This approach is consistent with recent work by Hu and Albrecht [*13,14*]. The corrected DPFAD points are shown replotted in Fig. 22 through Fig. 26 for the 6*T*, 4*T*, 2*T*, 1*T* and 1/2*T* specimens. Note that the (K_r', S_r') points of specimens of 2*T*, 1*T* and 1/2*T* at some point exceed the flow stress defined limit load (S_r = 1.2).

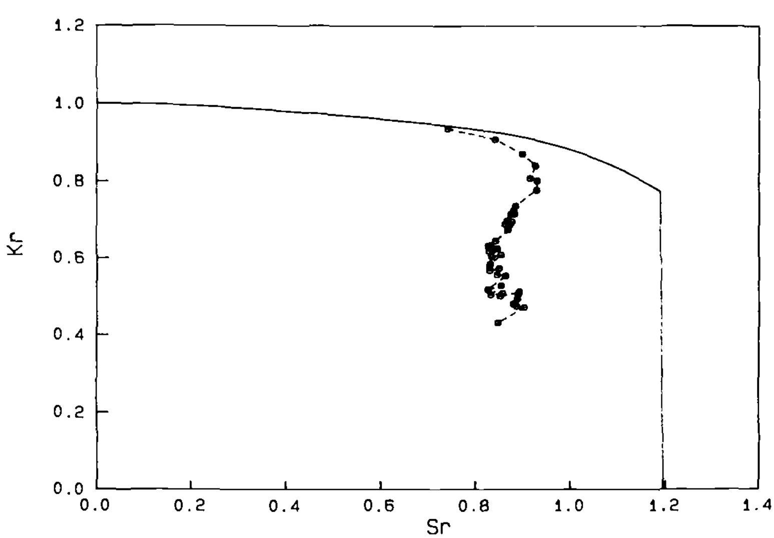

FIG. 19—*DPFAD 2*T *(V108) uncorrected.*

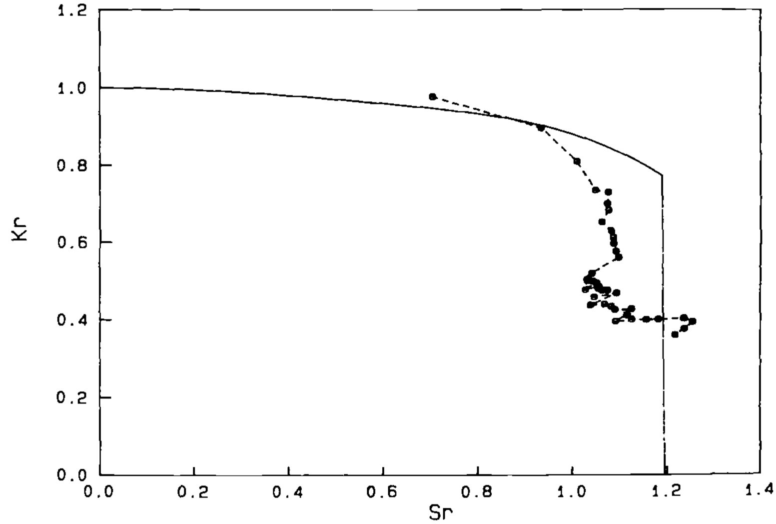

FIG. 20—*DPFAD 1*T *(V112) uncorrected.*

The points which exceed the flow stress defined limit load of the specimens are hypothesized as not being relevant to the material toughness of the A302B plate and, therefore, only those points less than $S_r = 1.2$ were plotted in the resulting corrected *J-R* curves shown in Fig. 27. Note that the corrected *J-R* curves now all fall on each other almost independent of the specimen thickness (T). In the case of the $1/2T$ and $1T$ specimens, the *J-R* curves do not extend beyond the blunting line of the $2T$, $4T$, and $6T$ specimens.

As a further check on the validity of this approach, the final measured crack length deter-

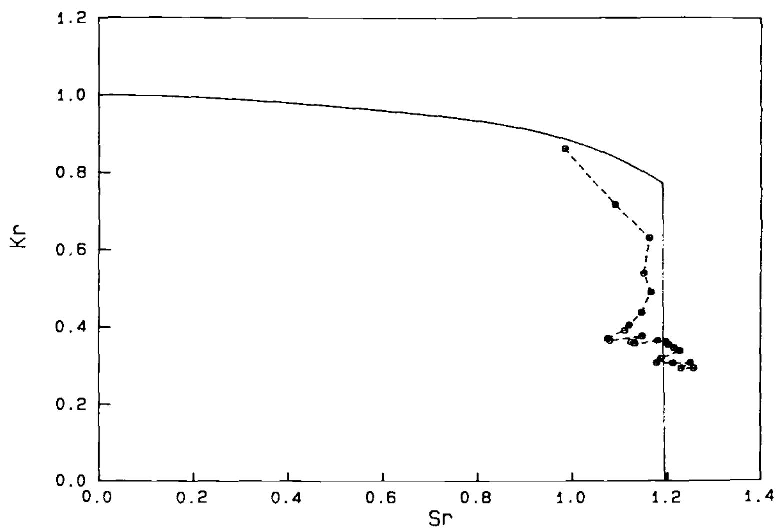

FIG. 21—*DPFAD 0.5*T *(V113) uncorrected.*

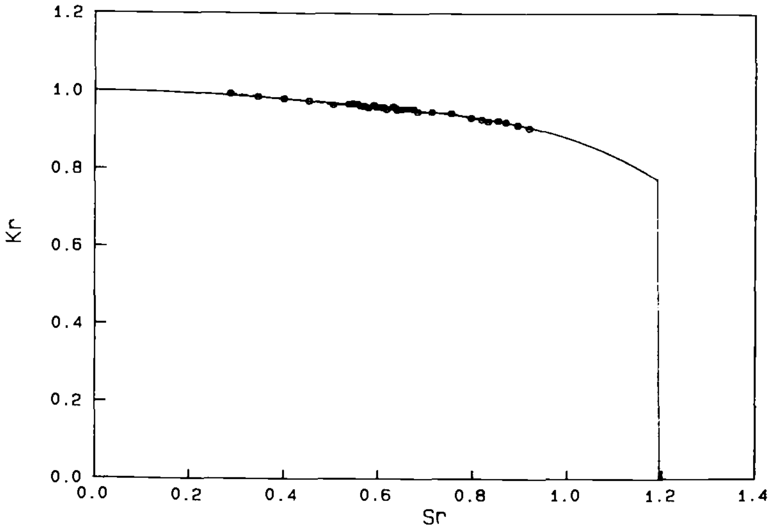

FIG. 22—*DPFAD* 6T *(V101) corrected.*

mined after each specimen was broken open (optical measurement) was compared to the calculated crack growth for "equilibrium" for each specimen (DPFAD value) and the unloading compliance value. Table 1 presents the results of these comparisons. From the results given in the table, it can be seen that the agreement between the final measured crack lengths and the calculated DPFAD values is much better than the unloading compliance values.

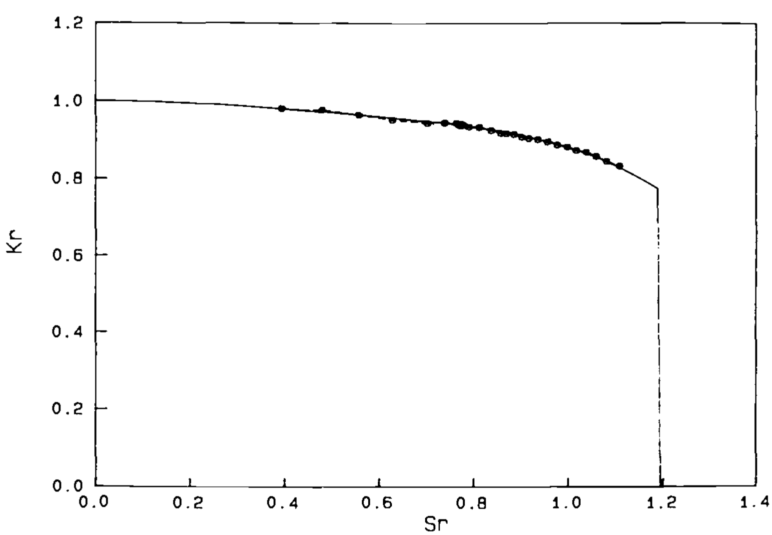

FIG. 23—*DPFAD* 4T *(V102) corrected.*

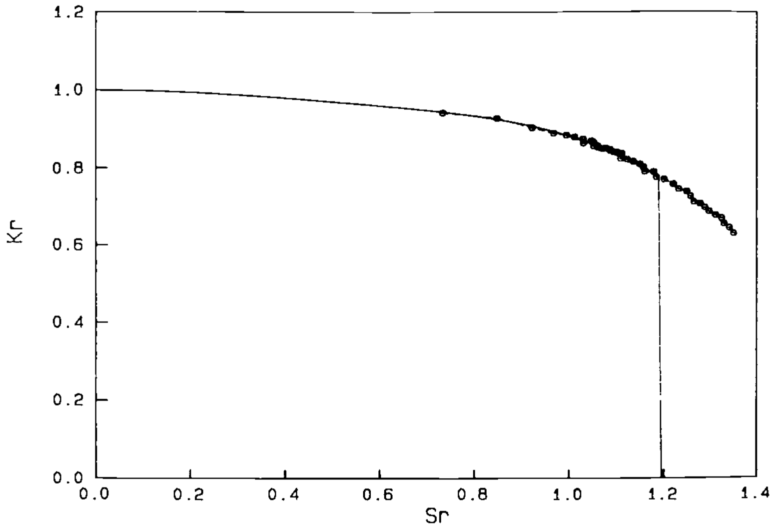

FIG. 24—*DPFAD 2T (V108) corrected.*

Conclusions

Based on the results of the analyses of the four sets of test data, the following conclusions can be made.

1. The DPFAD methodology seems to best identify the test results from the compact specimens which are not *J*-controlled. The lack of *J*-control may be due to incorrect crack length measurements during the test, metallurgical anomalies, and loss of specimen constraint.

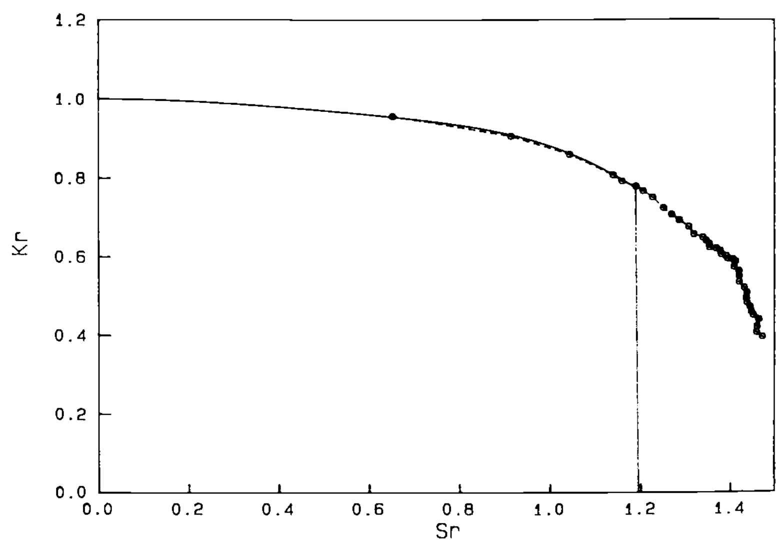

FIG. 25—*DPFAD 1T (V112) corrected.*

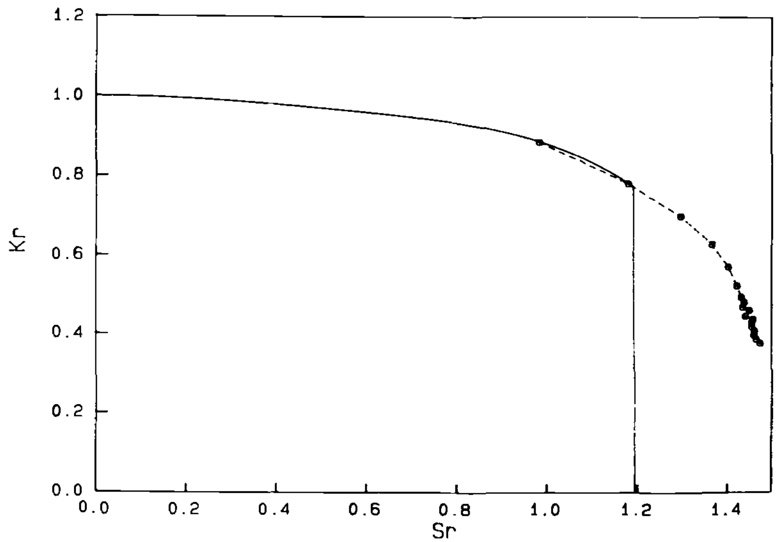

FIG. 26—*DPFAD 0.5*T *(V113) corrected.*

2. The key curve methodology can be used to identify *J-R* curve test results within a set which differ from the other results in the set. It does not appear useful in identifying specimen size effects if only one specimen size has been tested.
3. The predicted load-displacement curve methodology can be used if a specimen exhibits plane strain behavior, but it is not as sensitive a measure to loss of *J*-control as the DPFAD.

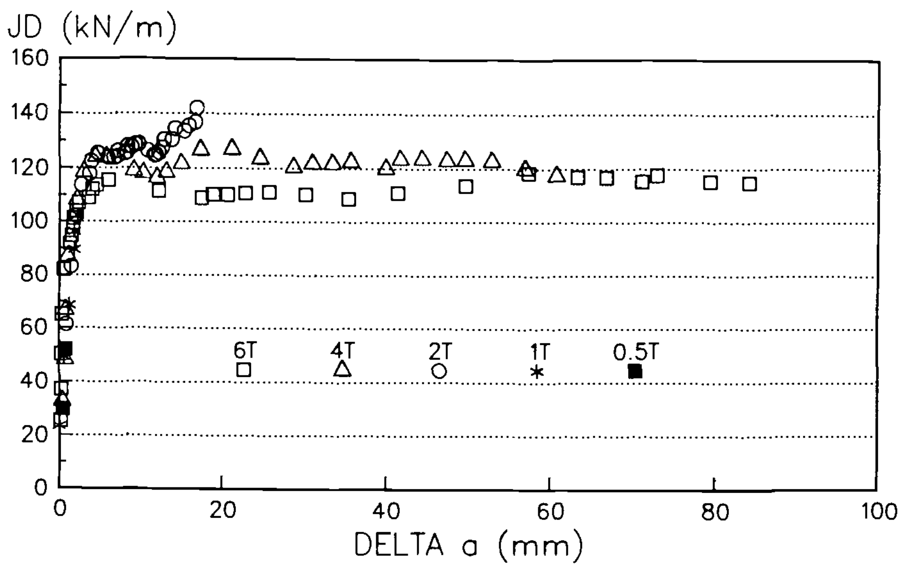

FIG. 27—J_R *curves for 302B plate—corrected.*

TABLE 1—*Verification of DPFAD methodology for A302B plate.*

Specimen Thickness	Final Crack Size, Δa				
	Optical Measurement, in.	Unloading Compliance, in.	% Difference	DPFAD, in.	% Difference
6T	3.41	2.96	−13.2	3.31	+2.9
4T	2.32	2.01	−13.4	2.39	+3.0
2T	1.12	0.97	−13.4	1.21	+8.0
1T	0.51	0.49	−3.9	...[a]	...[a]
0.5T	0.27	0.25	−7.4	...[a]	...[a]

NOTE: 1 in. = 2.54 cm.
[a] DPFAD values not given due to the truncation of the J_R curves at limit load for the $1T$ and $0.5T$ specimens.

4. *J-R* curves determined from small specimens fabricated from weld metals of the type tested in the HSST program appear to produce correct or conservative results.
5. For the specimens of the A302B data set, the $1/2T$ and $1T$ specimens may not be large enough to produce usable *J-R* curve for this material. The resulting nearly flat *J-R* curve shown in Fig. 27 can be used for the prediction of flaw instability in thick walled reactor vessels for A302B material.
6. In general, it appears that the DPFAD approach might be useful in correcting *J-R* curve data to account for specimen size effects due to metallurgical inhomogeneities.

Acknowledgments

This work was supported under the EPRI Contract RP-2975-6 "Management of Reactor Vessel Irradiation Embrittlement Phase II" under Task 2.3 "Investigation of Size and Constraint Effects on Ductile Crack Growth" under the direction of T. J. Griesbach, project manager, Structural Mechanics Group at EPRI.

The authors wish to express their gratitude to K. E. Moore and K. K. Yoon of BWNS, Lynchburg for their constructive suggestions during the development of this project.

References

[1] Hiser, A. L., and Terrell, J. B., "Size Effects on J-R Curves for A302-B Plate," NUREG/CR-5265, U.S. Nuclear Regulatory Commission, Washington, DC, January 1989.

[2] Roos, E., Eisele, U., and Silcher, H., "A Procedure for the Experimental Assessment of the J-Integral by Means of Specimens of Different Geometries," *International Journal of Pressure Vessels and Piping*, Vol. 23, 1986, pp. 81–93.

[3] Hiser, A. L., Loss, F. J., Menke, B. H., "J-R Curve Characterization of Irradiated Low Upper Shelf Welds," NUREG/CR-3506, U.S. Nuclear Regulatory Commission, Washington, DC, April 1984.

[4] McCabe, D. E. and Landes, J. D., "Elastic-Plastic Methodology to Establish R-Curves and Instability Criteria," EPRI Topical Report, Compilation of Data, Contract No. RP1238-2, Electric Power Research Institute, Palo Alto, December 1981.

[5] Ernst, H. A., Paris, P. C., Rossow, M., and Hutchinson, J. W., "Analysis of Load Displacement Relationship to Determine J-R Curve and Tearing Instability Material Properties," *Fracture Mechanics (11th Conference), ASTM STP 677*, 1979, pp. 581–599.

[6] Herrera, R. and Landes, J. D., "A Direct *J-R* Curve Analysis of Fracture Toughness Tests," *Journal of Testing and Evaluation*, JTEVA, Vol. 16, No. 5, September 1988, pp. 427–449.

[7] Kumar, V., German, M. D., and Shih, C. F., "An Engineering Approach for Elastic-Plastic Fracture Analysis," EPRI Topical Report NP 1931, Topical Report, Electric Power Research Institute, Palo Alto, CA, July 1981.

[8] McCalla, T. R., *Introduction to Numerical Methods and Fortran Programming*, John Wiley & Sons, New York, 1967, p. 76.

[9] Bloom, J. M. and Malik, S. N., "A Procedure for the Assessment of the Integrity of Nuclear Pressure Vessels and Piping Containing Defects," EPRI Topical Report NP-2431, Research Project 1237-2, Electric Power Research Institute, Palo Alto, CA, June 1982.

[10] Bloom, J. M., "Validation of the Deformation Plasticity Failure Assessment Diagram (DPFAD) Approach—The Case of an Axial Flaw in a Pressurized Cylinder," ASME Winter Annual Meeting, Chicago 1988, also in *ASME Journal of PVP*, Vol. 112, August 1990.

[11] Shih, C. F., Andrews, W. R., de Lorenzi, H. G., German, M. D., Van Stone, R. H., and Mowbray, D. F., "Methodology for Plastic Fracture," Final Report to EPRI, Contract No. RP601-2, General Electric Co., Schenectady, NY, August 1980.

[12] Rice, J. R., "The Surface Crack: Physical Problems and Computational Solutions," J. F. Swedlow, Ed., American Society of Mechanical Engineers, New York, 1972.

[13] Hu, J. M. and Albrecht, P., "Deformation Behavior During Plastic Fracture of C(T) Specimen," Second Symposium on User Experience With Elastic-Plastic Fracture Test Methods, ASTM, Orlando, Florida, 8–9 Nov. 1989.

[14] Hu, J. M. and Albrecht, P., "Load Ratio Method for Estimating Crack Length," 22nd National Symposium on Fracture Mechanics, ASTM, 26–28 June 1990, Atlanta, GA.

Edwin Smith[1] *and Timothy J. Griesbach*[2]

Assessing a Material's Susceptibility to Constraint and Thickness Using Compact Tension Specimens

REFERENCE: Smith, E. and Griesbach, T. J., **"Assessing a Material's Susceptibility to Constraint and Thickness Using Compact Tension Specimens,"** *Constraint Effects in Fracture, ASTM STP 1171*, E. M. Hackett, K.-H. Schwalbe, and R. H. Dodds, Eds., American Society for Testing and Materials, 1993, pp. 418–428.

ABSTRACT: If the plastic component J_{DP} of the deformation J integral J_D for a nongrowing crack can be related, via a single eta factor, to the plastic work integral, using a single expression that is valid for all deformation levels, both J_D and modified J integral J_M crack growth resistance curves can be obtained from load, load-point displacement, and crack extension measurements using a single specimen. A theoretical analysis of a simulation model shows that the compact tension specimen, where the deformation is predominantly bending, satisfies this condition; it is not satisfied when there is significant tensile deformation. It is thereby argued that compact tension specimen J_M (or J_D) resistance curves provide an ideal basis for assessing the susceptibility of a material to thickness-induced constraint effects.

KEY WORDS: crack growth resistance, constraint, compact tension, J-integral, thickness and geometrical effects

When assessing the integrity of a cracked engineering structure, the usual practice is to compare the structure's crack driving force curve with the material's crack growth resistance curve as obtained from small laboratory specimens. The resistance curve is usually expressed in terms of the deformation J integral J_D, though there is a growing tendency in some quarters to use the modified J integral J_M [*1,2*] to characterize the resistance curve. A key issue relevant to such an assessment is the effect of constraint on the crack growth resistance, and especially the effect of the thickness dimension in the case of a through-thickness crack. In assessing a material's susceptibility to thickness effects via laboratory test methods, it is not easy to make a clear assessment since the underlying methodology upon which the determination of the crack growth resistance is based often depends on various simplifying assumptions.

It is against this background that this paper's overall objective is to strive for a procedural approach that will allow the effect of thickness on a material's crack growth resistance to be assessed unequivocally. Thus the paper examines the behavior of a simulation model of the compact tension specimen where the deformation is primarily bending, and, by analyzing the two behavioral extremes of small-scale yielding and extensive yield, shows that the compact tension specimen characteristics are such that both J_D and J_M crack growth resistance curves can be obtained from load, load-point displacement, and crack extension measurements using a single specimen, via expressions that are applicable across the complete spectrum of defor-

[1] Professor, Manchester University, UMIST Materials Science Centre, Grosvenor St., Manchester, United Kingdom M1 7HS.
[2] Program manager, Electric Power Research Institute, 3412 Hillview Ave., Palo Alto, CA 94303.

mation levels. As demonstrated in the paper, this is not the case when the test procedure involves significant tensile deformation. This conclusion is used as a basis for arguing the merits of using compact tension J_M (or J_D) resistance curves to assess the susceptibility of a material to thickness effects. By so doing, however, we do not imply that the effect of thickness will be the same with a primarily tensile loading configuration.

Background Theoretical Considerations

There are obvious merits in being able to obtain a material's crack growth resistance curve from load, P, load-point displacement, Δ, and crack extension measurements using a single laboratory specimen. As a basis, it is necessary to have a reliable expression for the deformation J integral J_D for a nongrowing crack in terms of P, Δ, and crack size, a. Recognizing that J_D can be separated into an elastic component J_E, which is directly related to the stress intensity factor K_I, and a plastic component J_{DP}, while Δ can also be separated into elastic (Δ_E) and plastic (A_p) components, it is important to have an expression for J_{DP} for a nongrowing crack in terms of P, A_p, and a. Consequently, there has been extensive discussion, during the last decade, of the description of J_{DP} for a nongrowing crack using the energy and complementary energy integrals and a relation of the form

$$J_{DP} = \frac{\eta}{B}\int_0^{\Delta_p} Pd\,\Delta_p + \frac{\eta_c}{B}\int_0^P \Delta_p\,dP \tag{1}$$

where B is the thickness of the configuration under consideration, with Mode I plane deformation being assumed. When such a description is used, it is implicitly assumed that it is applicable for all levels of deformation, from small-scale yielding to extensive yield at limit load conditions, with η and η_c being eta factors having dimensions length^{-1}, but are independent of the thickness B and the level of deformation.

It has been demonstrated elsewhere [*3,4*] that if J_{DP} is to be given by Eq 1, so that a two eta factor J_{DP} description, that is, $\eta \neq 0$, $\eta_c \neq 0$, for a nongrowing crack is appropriate, then Δ_p must be expressible in the functional form

$$\Delta p = \varphi(a)H\{P\Psi(a)\} \tag{2}$$

where φ and ψ are functions of the crack size a, and any other geometrical parameters of the configuration, but not of the load P. The eta factors η and η_c are then given [*4*] by the expressions

$$\left.\begin{aligned} \eta &= \frac{1}{\Psi}\frac{d\Psi}{da} \\ \eta_c &= \frac{1}{\varphi}\frac{d\varphi}{da} \end{aligned}\right\} \tag{3}$$

Most importantly, however, it has been shown [*4*] that the functional form (Eq 2) is possible only when the solid's geometry involves a single length parameter, that is, the ligament width b or crack size a, apart from the thickness B. The implication is that a two eta factor J_{DP} description of the form (Eq 1), applicable for all levels of deformation, is strictly accurate only when the solid has a single length parameter; examples are bending of a small remaining ligament (width b) when $\eta = 2/b$, $\eta_c = 0$, and tension of a small remaining ligament between two deep cracks when $\eta = 1/b$, $\eta_c = -1/b$. A J_{DP} description of the form (Eq 1) is also possible for the two separate situations of small-scale yielding and extensive deformation at limit load conditions, though the eta factors are in general different for these two cases.

If a two eta factor J_{DP} description is used for more general situations, that is, for the complete spectrum of deformation levels and for a configuration with more than one length parameter other than B, the description must be viewed as giving only an approximate value for J_{DP}. Notwithstanding, if Eq 1 is used for J_{DP} for a nongrowing crack, both Zahoor [3] and Ernst [5] have show that J_{DP} for a crack that grows from a length a_0 to a length a, is given by the expression

$$J_{DP} = \frac{1}{B}\int_0^{\Delta p} \eta P d\,\Delta_p + \frac{1}{B}\int_0^{P} \eta_c\,\Delta_p\,dP + \int_{a_0}^{a} J_{DP}\{\eta_c - \eta + \eta_1\}\,da + \frac{1}{B}\int_{a_0}^{a} \eta_c(\eta_2 - \eta_1)P\,\Delta_p\,da \tag{4}$$

with $\eta_1 = (\eta' - \eta_c')/(\eta - \eta_c)$ and $\eta_2 = \eta_c'/\eta_c$, where the primed quantities are total derivatives with respect to a; J_{DP} within the integral sign in the third term on the right-hand side of Eq 4 is given by Eq 1. Thus Eq 4 allows J_{DP} (and consequently $J_D = J_E + J_{DP}$) for a growing crack to be obtained from P, Δ_p (and consequently $\Delta = \Delta_E + \Delta_p$), and crack extension measurements using a single specimen, provided that η and η_c are known.

As indicated at the beginning of the paper, there is a growing tendency in some quarters to use the modified J integral J_M [1,2]. A strong argument [1] for using J_M, rather than J_D, to characterize crack growth is that it always satisfies the Rice condition that the rate of increase of the characterizing parameter must not be a function of the rate of increase of crack length. Furthermore, it has been demonstrated that, in some cases presumably where the material is not especially sensitive to constraint effects, much of the geometry dependence of a material's crack growth resistance curve is removed when the curve is expressed in terms of J_M rather than J_D. For example, with the use of J_M, data from proportional compact tension specimens of A508 steel differing 20 times in size have been successfully correlated [6,7] with crack growth up to 40% of the initial uncracked ligament (with the smaller specimens). A reduced geometry dependence of the crack growth behavior has also been observed in more recent studies [8,9] involving other materials and primarily plane stress loading conditions. If J_M is separated into its elastic (J_E) and plastic (J_{MP}) components, J_{MP} for a growing crack is given by the relation [1]

$$J_{MP} = J_{DP} - \int_{a_0}^{a}\left[\frac{\partial J_{DP}}{\partial a}\right]_{\Delta p} da \tag{5}$$

with the first term on the right-hand side being given by Eq 4 and the J_{DP} within the integral being given by Eq 1, presuming a two eta factor J_{DP} description to be appropriate. Using Eq 5 as a definition for J_{MP}, Ernst [5] has presented the full details of an analysis that leads to the following expression for J_{MP}

$$J_{MP} = \left\{\frac{1}{B}\int_0^{\Delta_p} \eta P d\,\Delta_p + \frac{1}{B}\int_0^{P} \eta_c\,\Delta_p\,dP\right\} - \frac{1}{B}\int_{a_0}^{a} \eta_c\,\Delta_p\left(\frac{\partial P}{\partial a}\right)_{\Delta p} da \tag{6}$$

Zahoor [3] has also quoted a result for J_{MP} that is different to that given by Eq 6 in that his J_{MP} expression does not contain the last term in Eq 6. However, he does not present the details of his analysis; one of the authors (E. Smith) has checked the Ernst J_{MP} analysis very carefully, and, believing it to be correct, is therefore supportive of the Ernst J_{MP} formulation rather than the Zahoor J_{MP} formulation. With Eq 6 for J_{MP}, it is difficult to see how this can be used as a basis for obtaining J_{MP} from P, Δ_p, and crack extension measurements from a single specimen; this is due to the presence of the function $(\partial P/\partial a)\ \Delta_p$ within the third term.

In a situation where it is possible to represent J_{DP} satisfactorily via a single eta factor with $\eta_c = 0$, that is, J_{DP} for a nongrowing crack is given by the expression

$$J_{DP} = \frac{\eta}{B}\int_0^{\Delta_p} P d\,\Delta_p \tag{7}$$

then Eq 4 for J_{DP} for a growing crack simplifies to

$$J_{DP} = \frac{1}{B}\int_0^{\Delta p} \eta P d\,\Delta_p - \int_{a_0}^{a} \gamma J_{DP}\, da \tag{8}$$

where $\gamma = \eta - (\eta'/\eta)$, with J_{DP} within the integral sign being given by Eq 7. Furthermore, Eq 6 for J_{MP} for a growing crack simplifies to

$$J_{MP} = \frac{1}{B}\int_0^{\Delta p} \eta P d\,\Delta_p \tag{9}$$

or, by using Eq 8, to

$$J_{MP} = J_{DP} + \int_{a_0}^{a} \gamma J_{DP}\, da \tag{10}$$

Inspection of Eq 9 shows that, unlike the case where $\eta_c \neq 0$, J_{MP} can be obtained from P, Δ_p, and crack extension measurements using a single specimen. There is therefore obvious merit in being able to represent J_{DP} for a nongrowing crack via a single eta factor, that is, $c = 0$, for then both J_D and J_M crack growth resistance curves can be obtained from load, load-point displacement, and crack extension measurements using a single specimen, via expressions that are applicable across the complete spectrum of deformation levels. It is against this background that the next section examines a model that simulates the behavior of a compact tension specimen.

Analysis of a Simulation Model of a Compact Tension Specimen

Ernst, Paris, and Landes [*10*] showed that with the compact tension (CT) specimen geometry, the P-Δ_p records approximately collapse into a single record if the following functional relation is used for Δ_p

$$\frac{\Delta_p}{W} H \left\{ \frac{PW}{Bb^2 \exp\left\{\frac{\alpha b}{W}\right\}} \right\} \tag{11}$$

where B is the thickness, W is the distance between the loading points and the back free surface, $b = (W - a)$ is the remaining ligament width, a is the distance between the loading points and the crack tip, and α is a constant with the value 0.522. By reference to Eq 2, it immediately follows that adoption of the functional Eq 11 allows for a two eta factor representation of J_{DP} for a nongrowing crack. Comparison with Eq 2 gives

$$\left.\begin{aligned} \varphi &= W \\ \Psi &= \frac{W}{Bb^2 \exp\left\{\dfrac{\alpha b}{W}\right\}} \end{aligned}\right\} \tag{12}$$

whereupon the relations in Eq 3 show that the two eta factors η and η_c are

$$\left.\begin{aligned} \eta &= -\frac{1}{\Psi}\frac{d\Psi}{db} = \frac{1}{b}\left(2 + \frac{\alpha b}{W}\right) = \frac{1}{b}\left(2 + 0.522\frac{b}{W}\right) \\ \eta_c &= -\frac{1}{\varphi}\frac{d\varphi}{db} = 0 \end{aligned}\right\} \tag{13}$$

The resulting J_{DP} expression, in fact a single eta factor description, is the ASTM standard representation [*11*] for the compact tension specimen geometry.

The simulation model of a compact tension specimen upon which this section's considerations are based is shown in Fig. 1, where a semi-infinite solid of thickness B in the direction of the figure normal contains a very deep crack such that the remaining ligament width is b, the solid being subjected to tensile loads P that are applied at a distance W from the right-hand free surface ($W = b - a$). With this model, which has been used by Merkle and Corten [*12*] and also Ernst [*13*], the presence of all surfaces in the CT specimen, other than the back free surface, are ignored. The model has also been used by the author [*14*] in some preliminary considerations of the CT specimen characteristics; these considerations provide the spring-

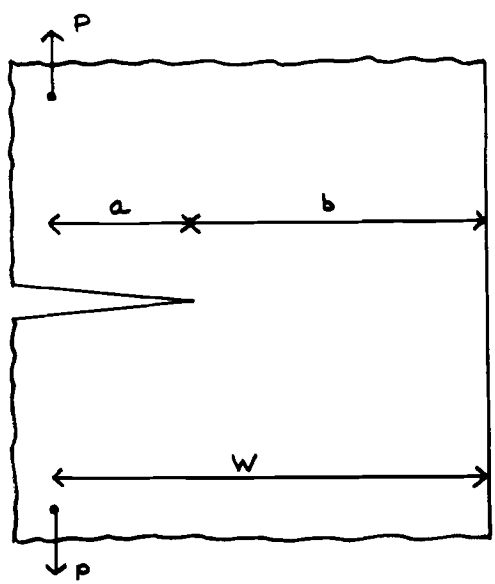

FIG. 1—*The simulation model of the compact tension specimen geometry.*

board for the present study. It is worth mentioning that it is not necessary that W should be greater than b, and consequently the model can be used, with $W < b$, to examine situations where the remaining ligament is subjected to tensile deformation.

In addressing, for a nongrowing crack, the extensive deformation situation, let P_L be the limit load corresponding to the behavior of perfectly plastic material; that is, the tensile stress ahead of the crack tip is Y up to the point of stress reversal when the stress becomes compressive with magnitude Y (Fig. 2). Now J_{DP} can always be expressed as [15]

$$J_{DP} = \frac{1}{B}\int_0^{\Delta p}\left(\frac{\partial P}{\partial b}\right)_{\Delta p} d\,\Delta_p \tag{14}$$

simplifying, in the case of very large deformations, to

$$J_{DP} = \frac{\Delta_p}{B}\frac{dP_L}{db} \tag{15}$$

But, again, for very large deformations

$$\int_0^{\Delta p} Pd\,\Delta_p = P_L\,\Delta p \tag{16}$$

whereupon it follows from Eqs 15 and 16, by elimination of Δp, that J_{DP} can be expressed in the form

$$J_{DP} = \frac{\eta_L}{B}\int_0^{\Delta p} Pd\,\Delta_p \tag{17}$$

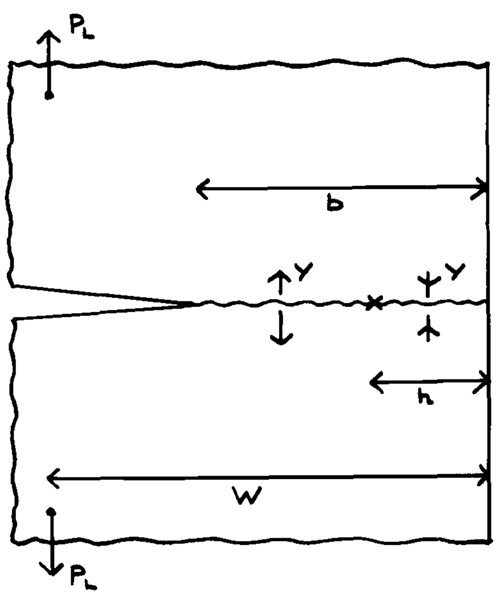

FIG. 2—*The extensive deformation situation: stress distribution across ligament.*

with η_L, the eta factor appropriate to the large deformation situation, being given by the expression

$$\eta_L = \frac{1}{P_L}\frac{dP_L}{db} \tag{18}$$

The limit load P_L is readily determined, via a very simple analysis [*12*], by reference to Fig. 2, with h being the distance of the stress reversal point from the back surface. Force and moment equilibrium conditions are satisfied if

$$\left.\begin{aligned} P_L &= BY(b - 2h) \\ P_L W &= \frac{BY}{2}(b^2 - 2h^2) \end{aligned}\right\} \tag{19}$$

whereupon elimination of h gives

$$\frac{P_L}{BY} = \sqrt{b^2 + (2W - b)^2} - (2W - b) \tag{20}$$

It then follows by reference to Eq 18 that

$$\eta_L = \frac{1}{b} + \frac{2}{b\sqrt{\left(\frac{b}{W}\right)^2 + \left(2 - \frac{b}{w}\right)^2}} \tag{21}$$

a value that was also obtained by Merkle and Corten [*12*] using limit load considerations. Ernst [*13*] also used limit load considerations but compromised them in using different ligament deformation assumptions to those used by Merkle and Corten; he consequently obtained a slightly different η_L value to that given by Eq 21.

Now consider the other extreme of small-scale yielding. In this situation, Irwin's method for modifying the crack length by accounting for localized plastic deformation shows [*16*] that Δp is proportional to P^3. J_{DP} can then be expressed in the form

$$J_{DP} = \frac{\eta_s}{B}\int_0^{\Delta p} Pd\,\Delta_p \tag{22}$$

Furthermore, the small-scale yielding analysis [*16*], which is applicable to all configurations, gives η_s in the form

$$\eta_s = +\frac{1}{3G^4}\frac{1}{da}(G^4) = -\frac{1}{3G^4}\frac{d}{db}(G^4) \tag{23}$$

if the stress intensity factor K_I is expressed in the form $K_I = PG$, G being a function of the geometrical parameters of the configuration. For the configuration in Fig. 1, the function G is given by the expression [*17*]

$$G = \frac{7.044}{B\sqrt{\pi b}}\left\{\frac{W}{b} - 0.368\right\} \tag{24}$$

whereupon it follows from Eq 23 that

$$\eta_s = \frac{2}{b}\frac{\left[1 - 0.123\,\frac{b}{W}\right]}{\left[1 - 0.368\,\frac{b}{W}\right]} \tag{25}$$

The results for η_L (Eq 21) and η_s (Eq 25) are shown in Table 1 for the range of values $b/W = 0$ to $b/W = 2$, and they are compared with the values obtained from the ASTM Test Method for Determining *J-R* Curves (E 1152-87) for the CT specimen, that is, Eq 13, remembering that this relation is supposed to be valid for all levels of deformation. The difference between the η_L and η_s values is less than ~5% up to $b/W = 0.8$, and both sets of values are in close accord with the ASTM η value over the same range. These results therefore suggest that for $b/W < 0.8$, a single eta factor representation for J_{DP} is appropriate for all levels of deformation, and that the ASTM E 1152 eta value is a very accurate description. Furthermore, inspection of the results in Table 1 shows that with larger values of b/W, that is, 1.5 and 2.0, when the remaining ligament is subjected to a predominantly tensile loading, a single eta factor J_{DP} representation that is valid for all deformation levels is not possible; such a representation is possible only when the deformation is primarily bending.

The preceding considerations for the CT simulation model have been with regard to a nongrowing crack. When J_{DP} for a nongrowing crack can be expressed in terms of a single eta factor (η), general expressions for J_{DP} and J_{MP} for a growing crack are given by Eqs 8 and 9, respectively; the latter involves only the parameter η, but the former also involves the parameter $\gamma = \eta - (\eta'/\eta)$, where η' is the total derivative of η with respect to a. We therefore need to determine the values of γ for the extensive deformation (γ_L) and small-scale yielding (γ_s) situations. As regards the former, γ_L is given via Eq 21 as

TABLE 1—η_L *(extensive deformation) and* η_s *(small-scale yielding) values for a nongrowing crack, together with the ASTM standard E 1152* η *value.*

$\frac{b}{W}$	$b\eta_L$	$b\eta_s$	$b\eta$, ASTM
0	2.000	2.000	2.000
0.1	2.051	2.051	2.052
0.2	2.104	2.106	2.104
0.3	2.159	2.165	2.157
0.4	2.213	2.230	2.209
0.5	2.265	2.300	2.261
0.6	2.313	2.377	2.313
0.7	2.355	2.462	2.365
0.8	2.387	2.556	2.418
0.9	2.407	2.659	2.470
1.0	2.414	2.777	2.522
1.5	2.265	3.638	...
2.0	2.000	5.712	...

$$\gamma_L = \eta_L + \frac{1}{\eta_L}\frac{d\eta_L}{db} = \frac{\frac{1}{b}\left[1 - \phi + \sqrt{1 - \phi + \frac{\phi^2}{2}}\right]}{2\left[1 - \frac{\phi}{2}\right]\left[1 - \phi + \frac{\phi^2}{2}\right]} \tag{26}$$

with $\phi = b/W$. As regards the small-scale yielding situation, γ_s is given via Eq 25 as

$$\gamma_s = \eta_s + \frac{1}{\eta_s}\frac{d\eta_s}{db} = \frac{\frac{1}{b}\left[1 + \frac{2\lambda\phi}{3} - \frac{\lambda^2\phi^2}{9}\right]}{\left[1 - \frac{4\lambda\phi}{3} + \frac{\lambda^2\phi^2}{3}\right]} \tag{27}$$

with $\lambda = 0.368$. The results for γ_L (Eq 26) and γ_s (Eq 27) are shown in Table 2 for the range of values from $b/W = 0$ to $b/W = 2$. They are also compared with the value that has been used [6,7,9] for the CT specimen; this value is based on the ASTM E 1152 expression for η, that is, Eq 13, and is obtained by using the relation $\gamma = \eta - (\eta'/\eta)$ and taking the first two terms in the resulting expression, that is

$$\gamma = \frac{1}{b}\left(1 + 0.76\,\frac{b}{w}\right) \tag{28}$$

The difference between the γ_L and γ_s values is less than ~5% up to $b/W = 0.5$, and, over the same range, both sets of values are in accord with the γ value obtained from the ASTM E 1152 η value. Thus, for $b/W < 0.5$, these results, together with the η results (Table 1), suggest that J_{DP} and J_{MP} for a growing crack can be expressed via Eqs 8 and 9, respectively, using η and γ values that are applicable for all levels of deformation. Furthermore, inspection of the results in Table 2 shows that, as is the case with η, for larger values of b/W, that is, as the ligament loading becomes progressively more tensile, it is not possible to have a J_{DP} expression that

TABLE 2—γ_L *(extensive deformation) and* γ_s *(small-scale yielding) values for a growing crack, together with the value obtained from the ASTM standard E 1152* η *value.*

$\frac{b}{W}$	$b\gamma_L$	$b\gamma_s$	$b\gamma$ (ASTM)
0	1.000	1.000	1.000
0.1	1.076	1.078	1.076
0.2	1.156	1.161	1.152
0.3	1.234	1.250	1.228
0.4	1.310	1.350	1.304
0.5	1.378	1.461	1.380
0.6	1.431	1.583	1.456
0.7	1.465	1.717	1.532
0.8	1.476	1.863	1.608
0.9	1.460	2.030	1.684
1.0	1.414	2.218	1.760
1.5	0.931	3.650	...
2.0	0.500	7.180	...

retains the same γ value for all deformation levels; such a representation is possible only when the deformation is primarily bending.

Discussion

The paper has argued the merits of being able to relate the plastic component J_{DP} of the deformation J integral J_D for a nongrowing crack, via a single eta factor, to the plastic work integral, through a single relation which is valid for all deformation levels. For then, both J_D and J_M (modified J integral) crack growth resistance curves can be obtained from load, load-point displacement, and crack extension measurements using a single specimen, irrespective of the deformation level. In terms of strict accuracy, this behavior pattern is possible only for the situation where a very small ligament is subjected to bending deformation. However, the results from this paper's theoretical analysis of a simulation model suggest that the characteristics of the compact tension specimen geometry are such that, provided the b/W ratio is < 0.5, J_D for a growing crack can be expressed in terms of η and γ factors and J_M in terms of an η factor, with these factors retaining the same values for all deformation levels; such a representation is not possible as the ligament deformation becomes progressively more tensile, that is, as b/W increases.

The theoretical results therefore underpin the usefulness of the compact tension specimen geometry, with $b/W < 0.5$, when its use is coupled with a J crack growth methodology, whether this be based on J_D or J_M. If one does accept the view, for the reasons quoted at the beginning of this paper, that J_M provides a more satisfactory characterization of a material's crack growth resistance, then this paper's results would suggest that a J_M crack growth resistance curve can be obtained from load, load-point displacement, and crack extension measurements using a single compact tension specimen, with the confidence that the underlying methodology upon which the determination of the crack growth resistance is based is reasonably reliable; the same cannot be said for the case where the test procedure involves significant tensile deformation. Thus compact tension J_M resistance curves can be used to assess a material's susceptibility to thickness-induced constraint effects, and in particular the effect of increasing thickness B lowering its crack growth resistance. One example is that J_M-Δa crack growth resistance curves are seemingly geometry independent, with proportional compact tension specimens of A508 steel differing 20 times in size [6,7]; this would suggest that the microstructure is such that this steel is not particularly susceptible to constraint effects, at least when the thickness exceeds a certain value. At the other extreme, the J_M-Δa crack growth resistance curves, as obtained from compact tension specimens with varying dimensions, of a particular heat of A302-B steel are very geometry dependent [18] in that the J_M-Δa curve slope is progressively reduced as the specimen thickness B increases, until the curve is essentially flat. This result has been explained [19] in terms of the effect of constraint on the "early-stage" growth of manganese sulfide induced splits oriented in the crack growth direction.

Conclusions

1. The paper has argued the merits of being able to relate the plastic component J_{DP} of the deformation J integral J_D for a nongrowing crack, via a single eta factor, to the plastic work integral, through a single relation that is valid for all deformation levels.
2. J_D and modified J integral J_M crack growth resistance curves can then be obtained from load, load-point displacement, and crack extension measurements from a single specimen, using geometrical factors (η and γ) that are independent of the deformation level.
3. A theoretical analysis of a simulation model shows that the characteristics of the compact tension specimen, with $b/W < 0.5$, follow this behavioral pattern.

4. These conclusions have been used as a basis for arguing the merits of using compact tension specimen J_M (or J_D) resistance curves to assess the susceptibility of a material to constraint effects.

Acknowledgment

This work has been undertaken as part of the Electric Power Research Institute Program on Nuclear Component Reliability.

References

[1] Ernst, H. A., in *Elastic-Plastic Fracture: Second Symposium, ASTM STP 803,* American Society for Testing and Materials, Philadelphia, 1983, p. 191.
[2] Ernst, H. A., in Nonlinear Fracture Mechanics: Time Dependent Fracture, Vol. I, *ASTM STP 995,* American Society for Testing and Materials, Philadelphia, 1989, p. 306.
[3] Zahoor, A., *Journal of Engineering Materials and Technology,* Vol. 111, 1989, p. 138.
[4] Smith, E., *International Journal of Engineering Science,* Vol. 29, 1991, p. 709.
[5] Ernst, H. A., in "Evaluation of Upper Shelf Toughness Requirements for Reactor Pressure Vessels," report prepared by Novetech Corporation, Materials Engineering Associates (MEA) and Georgia Institute of Technology, Electric Power Research Institute, Palo Alto, CA, March 1989.
[6] McCabe, D. E. and Landes, J. D., in *Elastic-Plastic Fracture: Second Symposium, ASTM STP 803,* American Society for Testing and Materials, Philadelphia, 1983, p. 353.
[7] McCabe, D. E., Landes, J. D., and Ernst, H. A., in *Elastic-Plastic Fracture: Second Symposium, ASTM STP 803,* American Society for Testing and Materials, Philadelphia, 1983, p. 562.
[8] Gibson, G. P., Druce, S. G., and Turner, C. E., *International Journal of Fracture,* Vol. 32, 1986, p. 219.
[9] Ernst, H. A., Schwalbe, K. H., Hellmann, D., and McCabe, D. E., *International Journal of Fracture,* Vol. 37, 1988, p. 83.
[10] Ernst, H. A., Paris, P. C., and Landes, J. D., in *Fracture Mechanics (13th Conference), ASTM STP 743,* American Society for Testing and Materials, Philadelphia, 1981, p. 476.
[11] "Standard Test Method for Determining *J-R* Curves," ASTM E 1152, *Annual Book of ASTM Standards,* American Society for Testing and Materials, Philadelphia, 1988.
[12] Merkle, J. G. and Corten, H., *ASME Journal of Pressure Vessel Technology,* 1974, p. 286.
[13] Ernst, H. A., in *Fracture Mechanics: Fourteenth Symposium, ASTM STP 791,* American Society for Testing and Materials, Philadelphia, 1983, p. 499.
[14] Smith, E., "The Use of Eta Factors to Describe the *J* Integral: The ASTM E 1152 Standard for the Compact Tension Specimen," *Engineering Fracture Mechanics,* Vol. 41, 1992, p. 241.
[15] Rice, J. R., Paris, P. C., and Merkle, J. G., in *Progress in Flaw Growth and Fracture Toughness Testing, ASTM STP 536,* American Society for Testing and Materials, Philadelphia, 1973, p. 231.
[16] Smith, E., *International Journal of Engineering Science,* Vol. 29, 1991, p. 717.
[17] Tada, H., Paris, P. C., and Irwin, G. R., *The Stress Analysis of Cracks Handbook,* Del Research Corp., Hellertown, PA, 1973.
[18] Hiser, A. L. and Terell, J. B., "Size Effects on *J-R* Curves for A-302-B Plate," report prepared by Materials Engineering Associates (MEA) NUREG/CR-5265, U.S. Nuclear Regulatory Commission, Washington, DC, January 1989.
[19] Griesbach, T. J. and Smith, E., "A Review of the ASME Low Upper Shelf Toughness Evaluation Procedures for Nuclear Reactor Pressure Vessels," *Proceedings of the 15th MPA Seminar,* University of Stuttgart, Stuttgart, Germany, October 1989.

J. Heerens,[1] K.-H. Schwalbe,[1] and C. Nix[1]

Influence of Specimen Size on J-, J_m- and δ_5-R-Curves for Side-Grooved Compact-Tension Specimens

REFERENCE: Heerens, J., Schwalbe, K.-H., and Nix, C., "**Influence of Specimen Size on J-, J_m-, and δ_5-R-Curves for Side-Grooved Compact-Tension Specimens,**" *Constraint Effects in Fracture, ASTM STP 1171,* E. M. Hacket, K.-H. Schwalbe, and R. H. Dodds, Eds., American Society for Testing and Materials, Philadelphia, 1993, pp. 429–472.

ABSTRACT: The influence of specimen size and geometry on R-curves has been studied for a pressure vessel steel and an aluminum alloy using side-grooved compact-tension specimens. The specimen thickness reduction (necking) was used to quantify changes of constraint in laboratory specimens. The results show that the crack tip opening displacement, δ_5, and the modified J-integral J_m, can correlate significantly more stable crack growth than the conventional J-integral.

KEY WORDS: R-curves, J-integral, modified J-integral, crack tip opening displacement, size dependence, necking of specimens, constraint, validity range

Nomenclature

a	Crack length
a_0	Fatigue precrack length
Δa	Crack extension
Δa_{max}	Application limit of the J-integral
B	Specimen thickness
B_{net}	Net thickness for side-grooved specimens
ΔB	Thickness reduction
CTOD	Crack tip opening displacement
E	Young modulus
J	J-integral
J_m	Modified J-integral
J_{max}	Application limit of J-integral
L_0	Initial ligament length
R_{eL}	Lower yield point
$R_{p0.2}$	0.2% offset yield strength
α	Quantity that defines limit of application of a correlation parameter
R_m	Tensile strength
Z	Elongation to fracture
β	Numerical constant
δ_5	Crack tip opening displacement (CTOD)
ω, ρ	Quantities that define limit of application of J-integral

[1] GKSS-Research Centre Geesthacht, Max- Planck- Strasse, D-2054 Geesthacht, Germany.

Introduction

In order to characterize stable crack extension, the crack growth resistance curve (R-curve) is usually measured using simple laboratory specimens. Due to the relatively high toughness of modern materials, R-curve tests have to be conducted under net section yielding conditions, far beyond the small-scale yielding regime where K is a proper correlation parameter for stable crack growth.

Various candidates of correlation parameters have been proposed for the elastic plastic and fully plastic regimes such as the J-integral [*1*], the crack tip opening displacement (CTOD) [*2,3*], and the modified J-integral [*4*]. However, there is a major problem which restricts the practical use of R-curves obtained from laboratory specimens: R-curves frequently depend on the size and geometry of the specimen. This means that R-curves obtained from simple standard specimens generally do not reflect the behavior of cracks located in real, geometrically complex structures.

The reasons for size and geometry effects are not fully understood. A physically sound philosophy which allows a comprehensive interpretation of experimentally observed size and geometry effects is not available. In order to contribute to a better understanding of this problem, the authors set up an experimental program which was guided by the ideas outlined below.

Fracture occurs when the driving force equals the material's resistance against crack growth; i.e.,

$$\text{Driving force} = \text{Resistance} \tag{1}$$

Any effects in fracture studied as a function of any set of parameters should distinguish between the "applied side" and the "resistance side" of the fracture equations; both sides can give rise to size effects.

Sources of Size and Geometry Effects

Parameter for Correlating Crack Growth

As a basis of the R-curve approach it is assumed that a single parameter, such as the J-integral, the modified J-integral (J_m), and the crack tip opening displacement (CTOD), characterizes the three-dimensional stress-strain field at the crack tip. The stress and strain field causes fracture (i.e., crack extension) in a material-dependent manner. Therefore discussion of the possible reasons for a size and geometry dependence on the applied side focuses on the question: *Under what testing conditions exists a size and geometry independent correlation between the parameter used for correlating crack growth and the crack field?*

It is useful to distinguish between the following two items:

- *Variation of Constraint*—Within the framework of a one-parameter characterization of the crack field, no such parameter is able to describe uniquely the stress and strain fields in specimens with different constraint conditions. Hence, if the variation of specimen size and geometry leads to different constraint conditions, a single parameter is not expected to be characteristic of the crack fields in specimens of different size and geometry.

The constraint conditions or, in other words, the triaxiality of the crack field, in a given specimen are an inherent ingredient of the driving force, and a two-parameter description of the "applied side" would be more appropriate. Thus the fracture condition:

$$\text{Driving force } (J, \text{constraint}) = \text{Resistance} \tag{2}$$

However, current practice utilizes the one-parameter characterization, so that

$$\text{Driving force } (J \text{ or CTOD or } J_m) = \text{Resistance (constraint)} \tag{3}$$

is what is usually determined, whereby the variable "constraint" on the right-hand side is mostly not well defined. Thus, if constraint varies from specimen to specimen, identical values of the crack growth correlation parameter lead to different amounts of crack extension, the difference depending on the material's susceptibility to constraint variations.

- *Range of Applicability of the Correlation Parameter*—Even in cases where the triaxiality of the stress strain field does not change from specimen to specimen, it is to be expected that the correlation between the parameter and the crack tip field will lose its size and geometry independence under the condition of crack growth. This has been investigated in detail for the J-integral [5]. A set of three criteria emerged:

(1) Maximum crack extension where the far field ceases to be a meaningful parameter:

$$\Delta a_{max} = \alpha(W - a_0) \tag{4}$$

where W is the specimen width and a_0 is the pre-crack length.

(2) Allowable gradient of the J-Δa curve:

$$\omega = (W - a_0)/J \quad (dJ/da) \tag{5}$$

(3) The condition for the maximum J characterizing the HRR field must be met:

$$J_{max} = (W - a_0)\ \sigma_f/\rho \tag{6}$$

where $\sigma_f = 0.5(R_{p0.2} + R_m)$. For bending under plane strain conditions, $\alpha = 0.06 \ldots 0.1$ and $\rho = 25$ are widely accepted figures [6–8].

As indicated by these criteria, the amount of stable crack extension which can be characterized by J is just a few percent of the initial ligament length, $(W - a_0)$. Therefore, in situations where a long R-curve is needed, very large specimens have to be tested. Thus the application range as defined by Eqs 4 to 6 is not sufficient for many practical situations and other parameters having less restrictive application ranges are needed.

The alternative crack growth correlation parameters CTOD and J_m seem to be less restrictive [9]. However, their ranges of application are not yet well established. In the case of CTOD, this may be because there are a variety of definitions of CTOD [10] and it is not fully clear yet how the CTODs are related to each other. Therefore published data can not be directly compared. A promising approach for the CTOD high potential for application has been proposed by Schwalbe and Hellmann [11]. This specific CTOD definition is called δ_5, which is the relative displacement of two points located 2.5 mm on either side of the fatigue pre-crack tip (Fig. 1). These investigations were confined to thin sections under pure plane stress conditions, which means that the constraint conditions were identical in all tests conducted. As compared to the J-integral, substantially greater amounts of crack growth could be correlated uniquely. For bending configurations, such as single edge notched (SENB) and compact tension (CT)

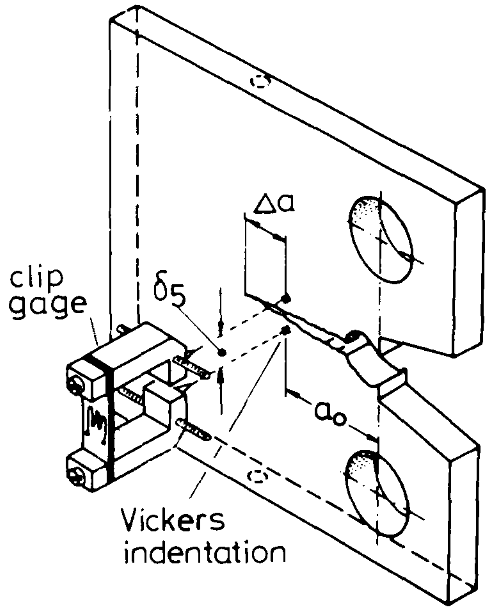

FIG. 1—*Experimental setup for measuring CTOD in terms of δ_5 (Courtesy of D. Hellmann).*

specimens, α was found to be about 0.2 . . . 0.3. Somewhat higher figures were obtained for J_m as a correlation parameter.

Following the thoughts outlined above, it is obvious that in general the "applied side" (stress and strain field at the crack tip) can not be characterized uniquely by one single parameter as is assumed in the simple R-curve approach. One has also to account for changes of the triaxiality of the stress state. Thus, in order to explore the ability of a specific parameter to correlate crack growth, experiments (or theoretical work) should be conducted under "clean" conditions, such as prevailing plane strain, plane stress, or any other constant stress and strain state in between. Otherwise, size effects would be a mixture of effects of both the applied side (due to using a correlation parameter beyond its limit of applicability) and the resistance side (due to the material's response to variation in constraint). Therefore the previous experiments on δ_5 crack growth resistance curves concentrated on the constant constraint condition plane stress.

Resistance Against Crack Growth

In order to explain variations of the R-curve one has to consider how variations of the applied side influence the fracture process. Whereas the applied side organizes the link between the correlation parameter and the stress and strain field, the material resistance side determines how the fracture process and therefore the crack extension itself responds. It can be expected that the susceptibility of the fracture process with respect to a change of the stress and strain field will depend on the fracture-controlling microstructural constituents of the material and therefore will vary from material to material. It can also be expected that in the case of materials for which the fracture mechanisms are highly susceptible to changes in the triaxiality of the stress and strain field, any size or geometry effect produced on the applied side will lead to a significant change of the R-curve. On the other hand, there may be materials for which the susceptibility of the fracture mechanisms to changes of triaxiality of the stress and strain field is low. One would expect that for this type of material the R-curves will be similar even in cases where the applied side shows a strong size and geometry variation.

Aim of the Present Work

Since we believe that we now have a clear picture of J, δ_5, and J_m as correlation parameters under plane stress conditions (for bending configurations: $\alpha = 0.06$ for J, $\alpha = 0.25$ for δ_5 and $\alpha = 0.25$ for J_m), experiments were planned for thicker sections which were assumed to have a higher constraint than plane stress, up to nominal plane strain conditions. Particular emphasis was placed on two questions:

- Can the findings obtained for thin sections be transferred to thick sections (i.e., Do the parameters δ_5 and J_m again have a wider range of application than J?)?
- As discussed above, in general a second parameter is needed to characterize the applied side. Measuring thickness reduction (necking) of the specimen was chosen as a simple experimental approach. Hence the question arises: Can the thickness reduction be used as a simple way to characterize a change of triaxiality of the stress and strain state?

Experimental Details

Material

In order to investigate how the type of the material influences the results, two different materials were used. One was a low strain hardening quenched and tempered pressure vessel steel; the second was a high strain hardening, overaged soft aluminum alloy which is almost identical to the material used in Ref *11*.

The steel was DIN 20MnMoNi55. The specimens were made from slices taken from a forged and subsequently quenched and tempered block. The heat treatment was conducted by the supplier of the steel. The size of the block was 300 by 300 by 700 mm. All specimens had the same orientation.

For the aluminum alloy, a 100 mm thick plate of Al2024 T351 was delivered by a supplier. From this plate all specimens were machined. The orientation of all specimens was L-T. The T351 version has a yield strength of 316 N/mm^2. In a pilot investigation it was found that for this material stable crack extension takes place under contained yielding condition. In order that the specimens undergo net section yielding during the R-curve tests, all specimens were heat treated as follows. The specimens were annealed at 520°C for 2 h. Then the specimens were cooled at a rate of 30°C/h.

The annealed material had a yield strength of 76 N/mm^2 and a relatively high strain hardening exponent. The tensile properties of both materials including the stress and strain curves are shown in Table 1 and Figs. 2*a* and 2*b*. In order to check whether the 100 mm thick plate of aluminum has substantial gradients and inhomogeneities of the fracture property, J-R curves were measured using 5 mm thick CT specimens taken from different positions in the plate thickness direction. For the heat treated material no gradient in fracture property was found; all R-curves fall in a narrow scatter band. Therefore it was assumed that no attention needs to be drawn to variability caused by specimen location.

Specimen Preparation and Instrumentation

The specimens were precracked in accordance with ASTM E 813 [*12*]. After precracking, the specimens were side grooved. Each side groove had a depth 10% of the specimen thickness.

TABLE 1—*Tensile properties of materials.*

	20MnMoNi55	Al2024 FC
R_{eL}, N/mm^2	450	—
$R_{p0.2}$, N/mm^2	—	76
R_m, N/mm^2	610	215
E, N/mm^2	210 000	71 000
Z, %	66	40

The angle of the side groove was 45°; the radius at the notch root was 0.25 mm. For the determination of crack extension the d-c potential-drop method was used [*13*]. The parameter δ_5 was measured using a special δ_5 clip gage mounted at the position of the fatigue precrack, on the plane side surface of the specimen (Fig. 1). For specimens thicker than 50 mm the width of the side groove is greater than 5 mm. Therefore the δ_5 clip gage could not be mounted at the specimen's plane surface. In order to solve this problem a modified side groove design was used (Fig. 3*a*). Besides δ_5, the load line displacement v_{LL}, the load, and the change of the potential drop were measured continuously during the test. The data were acquired with an on-line HP computer. The cross-head displacement rate was 0.5 W(mm)/50 mm per minute. In order to mark the final crack extension at the end of the fracture test, the specimens were subsequently refatigued. The final crack extension was determined by the nine-point method [*12*]. The accuracy of the d-c potential drop method was checked by comparing the final crack extension with the crack extension predicted by the potential drop method. Where the prediction of the potential method deviated more than 10% from the directly measured crack extension the test

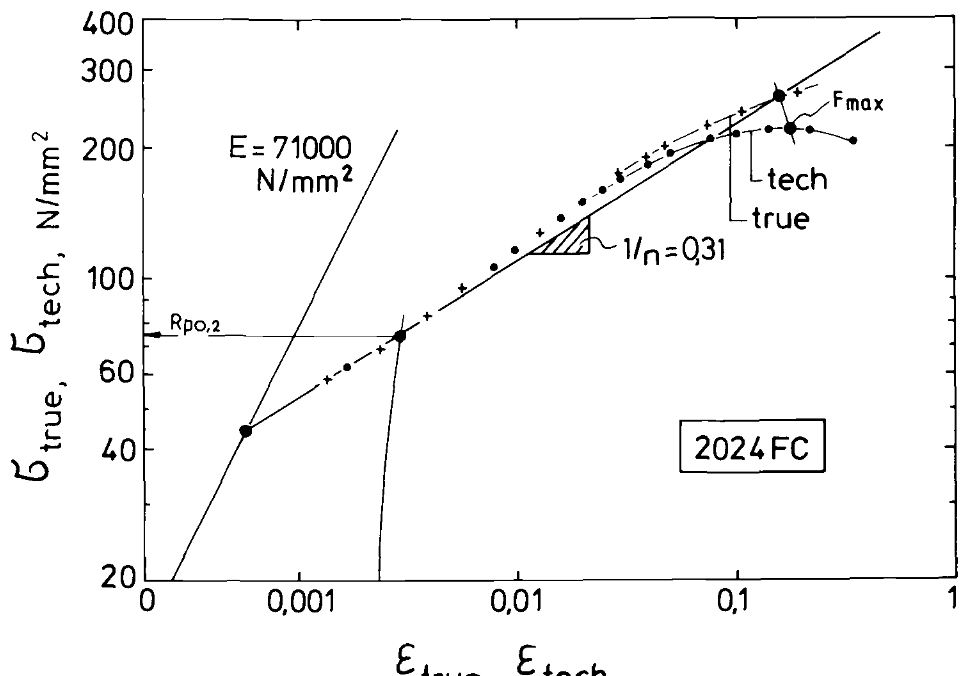

FIG. 2*a*—*Stress-strain curves obtained from tensile tests for Al 2024 FC (L-T orientation).*

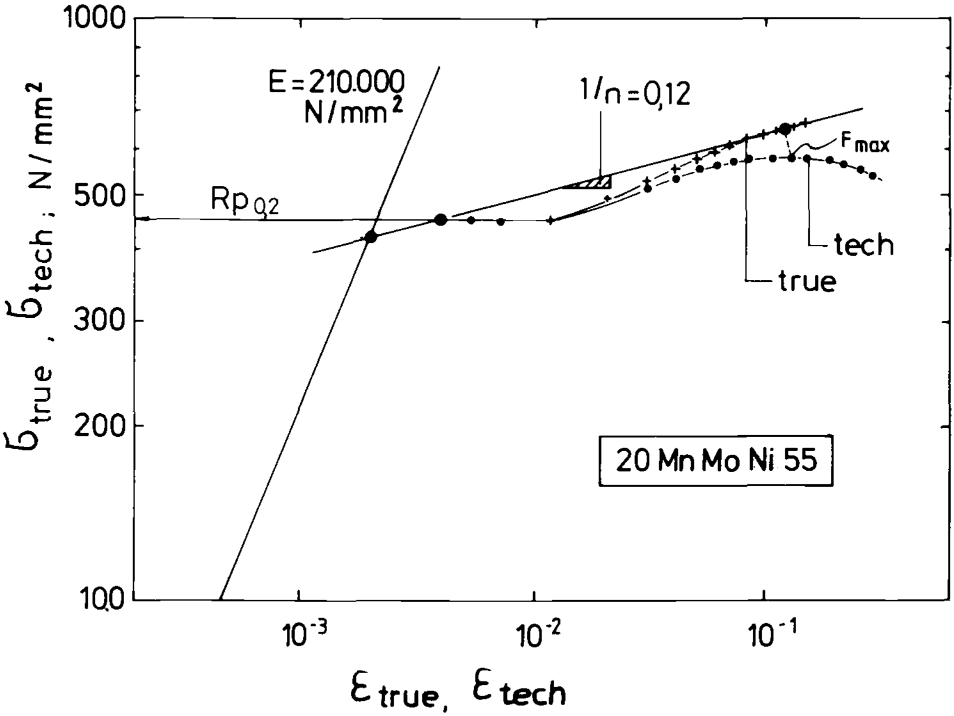

FIG. 2*b*—*Stress-strain curves obtained from tensile tests for 20MnMoNi55 pressure vessel steel.*

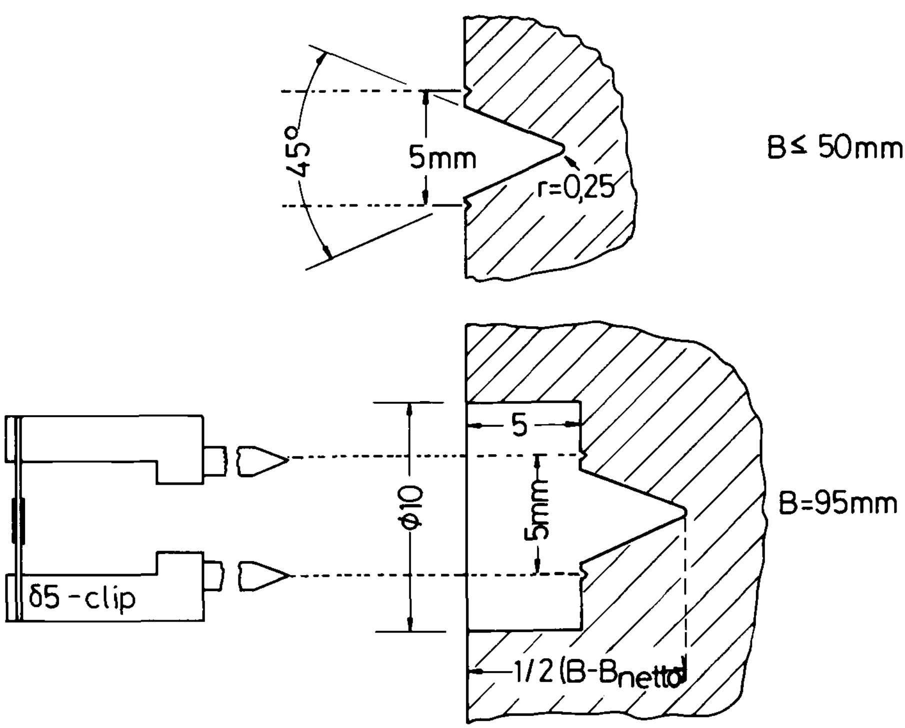

FIG. 3*a*—*Side groove design for the* R-*curve experiments.*

TABLE 2—*Matrix of tested specimens; all specimens side grooved;* B_{net}/B = *0.8.*

W, mm	a_0/W	B, mm	Specimen No.
		20MnMoNi55	
50	0.56	25	EK4
100	0.55	25	U1
100	0.60	50	C1
200	0.56	25	V200
		Al2024 FC	
50	0.55	5	A9
100	0.50	20	441
100	0.75	20	481
100	0.50	40	461, 471
100	0.75	40	451
100	0.50	50	472
100	0.75	50	462, 451
200	0.50	50	4D
200	0.50	95	15, 16

was rejected for this study. The matrix of the specimens used for this study is shown in Table 2.

Measurement of Thickness Reduction

After refatiguing the specimens, the two halves of the specimens were pulled apart. Then the thickness reduction, ΔB, was measured on the specimen's surface along the edge of the side groove using a light microscope and a digital table.

In addition to the post-test thickness reduction measurements (PTTR method) as explained above, it was also investigated how the thickness reduction developed during the test (DTTR method). A modified side groove design was used for these three tests (Fig. 3*b*). This groove design allows us to pick up the ΔB-values close to the crack plane independently of the depth of the side groove. In order to measure ΔB, the tests were interrupted at different load levels, then for each load level thickness reductions were measured at the surface of the specimen,

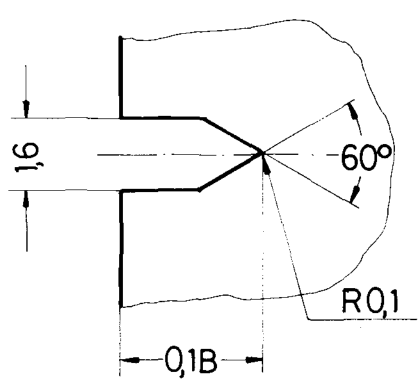

FIG. 3*b*—*Side groove design for the DTTR method.*

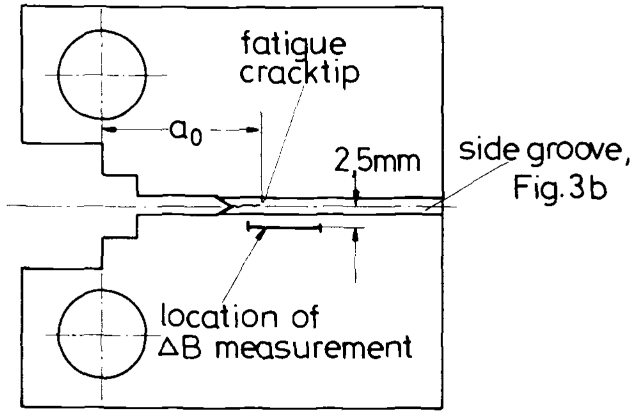

FIG. 4—*Location of* ΔB-*measurements in the case of the DTTR method.*

along a line located 2.5 mm below the crack plane (Fig. 4). The ΔB-values were picked up manually using a clip gage.

Data Evaluation

The J-integral was calculated in accordance with ASTM E 813 (including correction for crack extension) [*12*] using the load-displacement curve and the crack extension values determined from the d-c potential drop method. For the materials investigated this J-calculation gives the same results as the J-calculation per ASTM E 1152 [*14*]. The modified J-integral, J_m, was evaluated as proposed in Ref *4*.

Results and Discussion

Investigation of Necking Behavior

For all specimens, the fracture surfaces were flat and macroscopically perpendicular to the loading direction. The refatigue markings at the end of the test allow us to obtain information regarding the shape of the crack front. For the aluminum alloy the crack front was in all cases straight at the end of the tests. In the case of the steel the final crack front had a slight wave shape.

The necking was measured by the PTTR method and the DTTR method. The results of these measurements are shown in Figs. 5 and 6.

The DTTR method allows the determination of the plastic deformation at the crack tip as a function of the J-integral (or any other correlation parameter). It can be expected that changes of the triaxiality of the stress state at the crack tip which are caused by changes of the size and geometry of the specimens influence this function. This is confirmed in Fig. 6. The correlation between J and ΔB is similar for the square-sized ligaments, whereas a change of the ligament shape from square-type to slim-type changes the correlation between J and ΔB; it leads to an increase of the ΔB-values. Because ΔB-values indicate strains in the thickness direction, it is obvious that the degree of triaxiality of the stress field reduces when the ligament size changes from square-type to slim-type.

In contrast to the DTTR method, the PTTR method does not allow the measurement of the correlation between the J-parameter and ΔB directly. The ΔB-values measured by PTTR

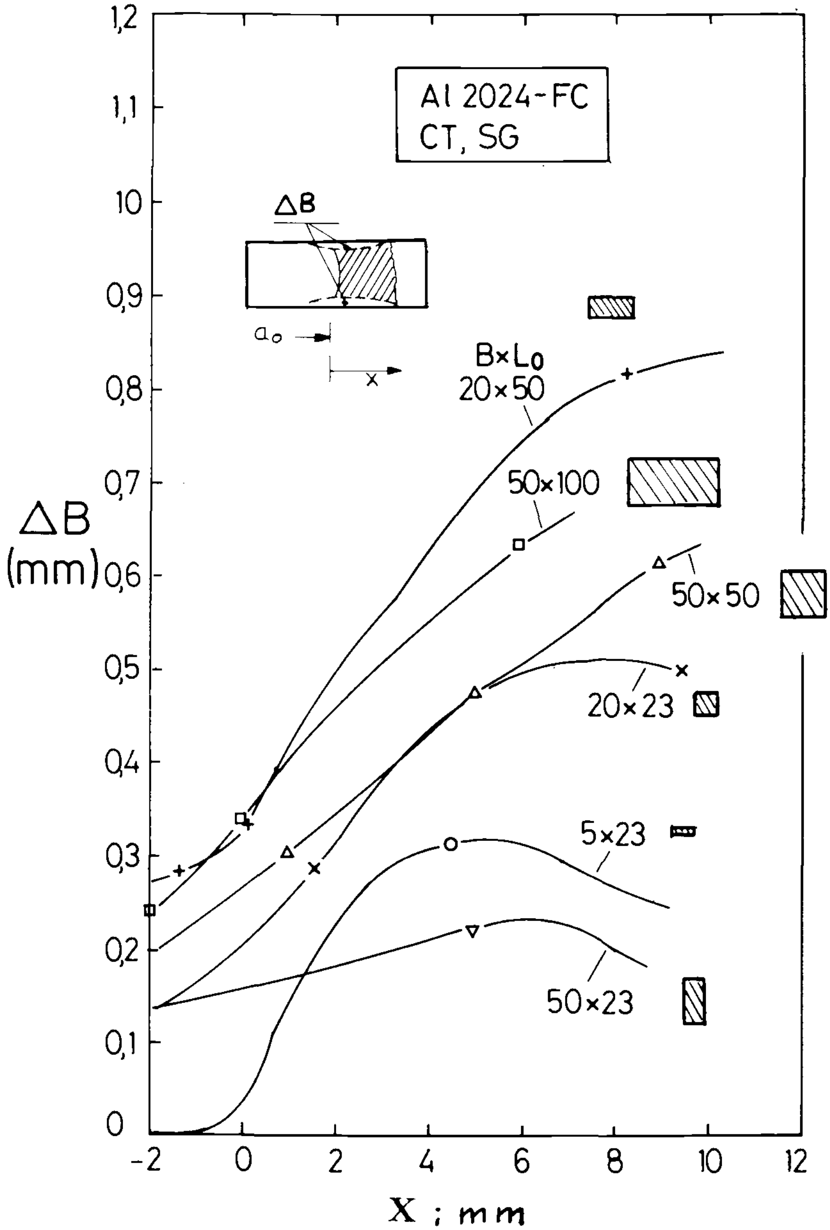

FIG. 5*a*—*Thickness reduction curves measured with the PTTR method for Al 2024 FC.*

method indicate how much the material is able to deform before it separates. In Fig. 5 it can be seen that this depends on the size of the ligament. For example, an increase of the ligament length leads to larger ΔB-values. This behavior can be interpreted as follows. The degree of triaxiality of the stress field reduces with increasing ligament length. This enables the material to undergo more necking before it fractures. This explanation is in agreement with the widely

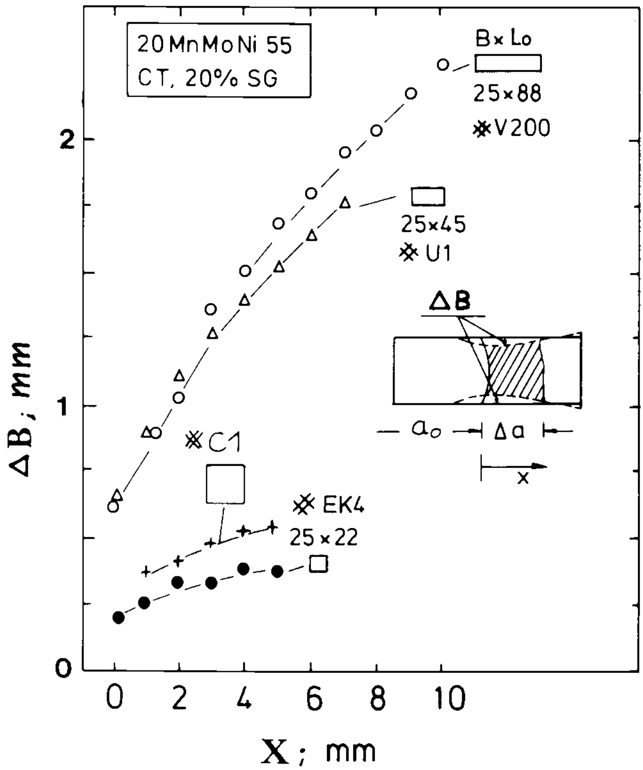

FIG. 5*b*—*Thickness reduction curves measured with the PTTR method for 20MnMoNi55 pressure vessel steel.*

accepted philosophy that the deformation capacity of a material increases with decreasing degree of triaxiality of the stress state.

Therefore it seems that the ΔB-values determined by the PTTR method or by the DTTR method can give information regarding changes of the stress and strain state at the crack tip. It can not be expected that the ΔB-values characterize all the complex details of changes in the three-dimensional stress-strain field. These can only be characterized by comprehensive three-dimensional finite element calculations. But as an approximation it will be assumed that differences between the necking curves measured by the PTTR method shown in Fig. 5 qualitatively indicate the differences of the triaxiality of the stress fields.

Interpretation of Size and Geometry Effects

As has been discussed in the Introduction, it will be assumed that two effects can give rise to size and geometry effects: (*a*) change of triaxiality of the stress field (change of constraint) and (*b*) use of the correlation parameter beyond its application regime. Using the necking curves as a measure of changes in constraint, it is now possible to distinguish experimentally between size and geometry effects due to effect (*a*) and size effects due to effect (*b*):

- R-*Curves Near Crack Initiation*—In Figs. 7 and 8 the J- and δ_5-R-curves near crack initiation are presented for the two materials. The blunting-line was calculated as proposed

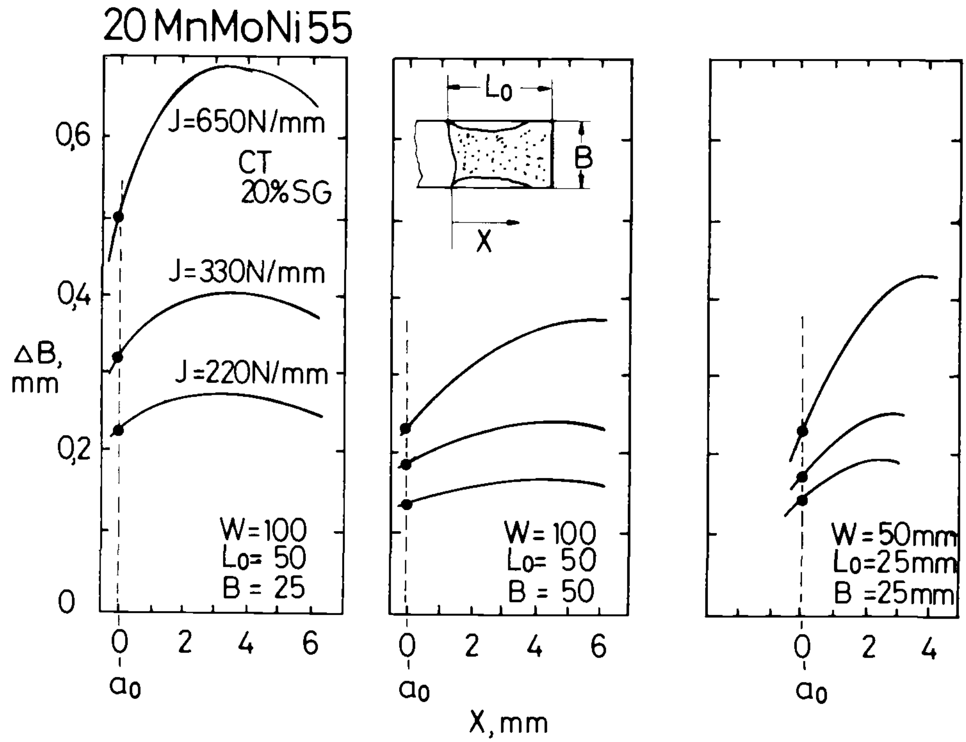

FIG. 6—*Thickness reduction curves for three different ligament sizes measured with the DTTR method (J-steps are identical for each ligament size).*

in Refs *7* and *8*. The J- and δ_5-R-curves exhibit the same trends; there is no difference with regard to correlating size independent crack growth.

In the case of the steel a split-off of the R-curves occurs when crack extension exceeds 0.5 mm (Fig. 7). Beyond the splitting point the R-curves of the specimens with square-sized ligaments fall below the R-curves obtained from specimens with slim ligaments. From Fig. 5*b* it can be seen that the flat R-curves refer to specimens with very little necking, whereas the steep R-curves arise from specimens which undergo large necking.

For the aluminum alloy the situation is different (Fig. 8). Compared to R-curves measured on the steel, the scatterband of the R-curves obtained from the aluminum alloy is wider. No clear size effect and no clear correlation between the necking-curves and the R-curves are visible. All J- and δ_5-R-curves emerge from one origin and remain in one scatterband up to more than 1.5 mm crack extension (Fig. 8).

- *Influence of Specimen Thickness*—For the pressure vessel steel a thickness effect is evident (Fig. 9). Increasing the thickness causes the J-, J_m, and δ_5-R-curves to split off. For all three parameters the split-off occurs approximately at the same amount of crack extension. Beyond the splitting point, the R-curves of the thick specimen fall below the R-curves obtained from the thin specimen. As already mentioned, the slopes of the R-curves of a specimen with small necking are lower than the slopes of R-curves obtained from specimens with large necking.

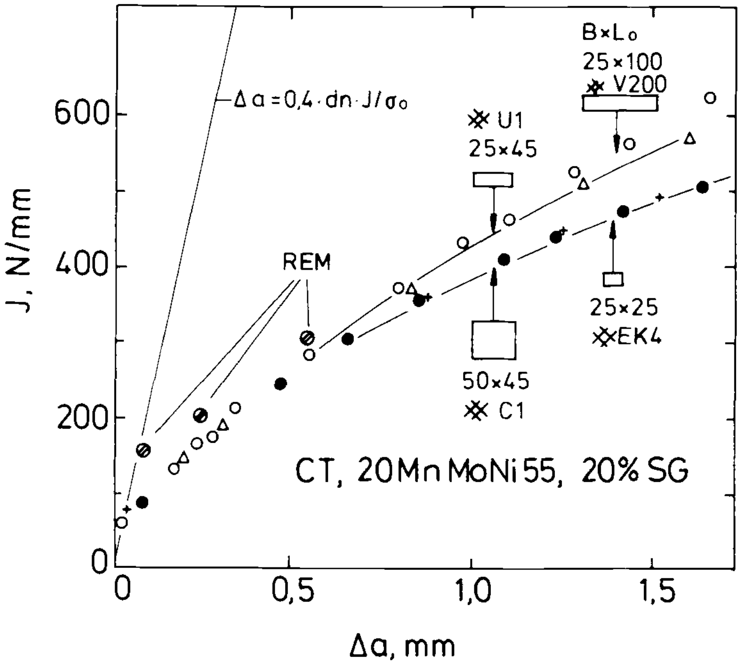

FIG. 7a—*J-R-curves for 20MnMoNi55 steel near crack initiation.*

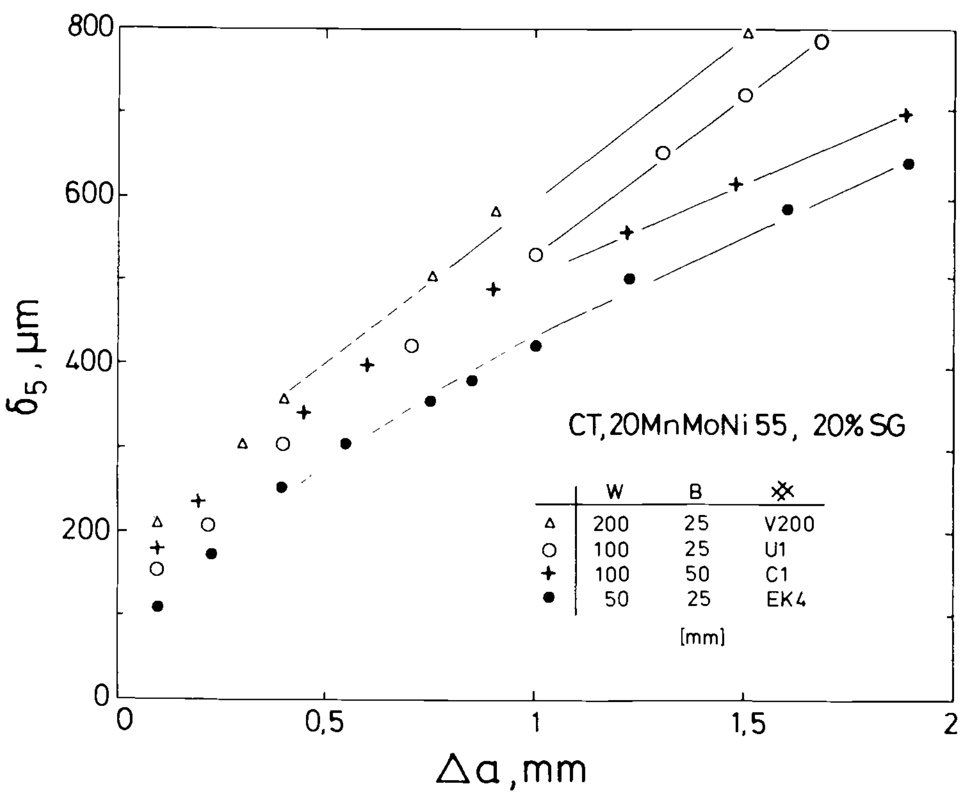

FIG. 7b—*δ_5-R-curves for 20MnMoNi55 steel near crack initiation.*

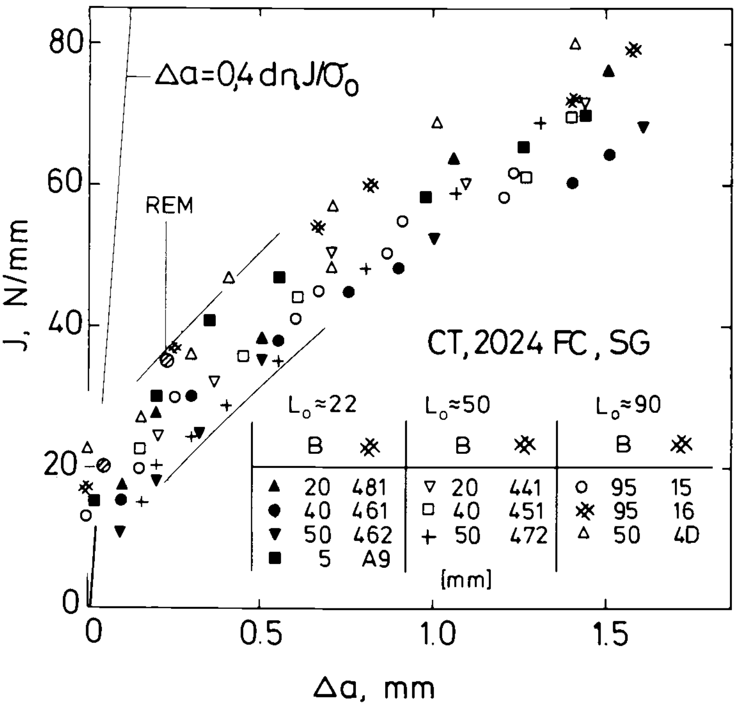

FIG. 8*a*—J-R-*curves for Al 2024 FC near crack initiation.*

Figures 10, 11, and 12 show the influence of specimen thickness on the *R*-curves of the aluminum. In contrast to the steel, for the aluminum alloy no significant influence of specimen thickness on the *R*-curves was found and no influence of the necking curves on the *R*-curves can be detected. Independent of a change of the necking-curve the fracture of the material does occur at almost identical J-, δ_5- and J_m-levels. The results indicate that the constraint effect is very small in this material. Again the general behavior of the *R*-curves is the same, regardless of the correlation parameter used: J, J_m, or δ_5.

- *Influence of Initial Ligament Length*—In Fig. 13 examples for three 25 mm thick steel specimens having initial ligament lengths of about 22, 45, and 90 mm are shown. The specimens with the slim ligaments show very similar necking-curves (Fig. 5*b*). The δ_5- and J_m-*R*-curves obtained from these two specimens do not split off till the end of the test. In contrast to this behavior the *J-R*-curves do split off when crack extension exceeds 4.5 mm, corresponding to $\alpha = 0.1$ for the specimen with the shorter ligament.

Because the constraint is assumed to be identical for this pair of specimens, a splitting of the *R*-curves indicates that in one of the specimens the correlation parameter reaches its limit of applicability. As indicated by Eqs 4 and 5 this will take place first in the specimen with the shorter ligament. In order to quantify these splitting effects, α-values were calculated using the Δa-values at which the J-, J_m- and δ_5-*R*-curves of the specimen with the short initial ligament deviate more than 5% from the J-, J_m- and δ_5-*R*-curves of the specimen with the long initial ligament. Since the J_m- and δ_5-*R*-curves do not split off prior to the termination of the tests, the split-off event, if it occurs, must occur beyond that

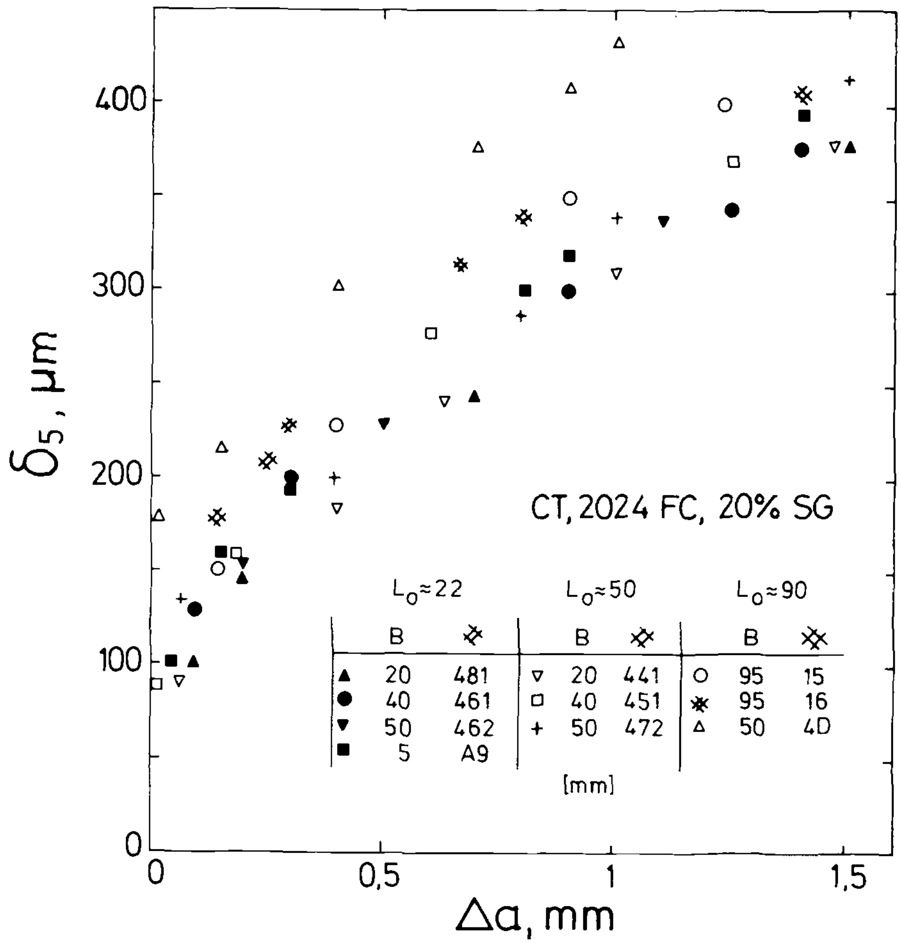

FIG. 8*b*—δ_5-R-*curves for Al 2024 FC near crack initiation.*

point. Thus the α-values evaluated at the final point of the shorter R-curve are a lower bound. The α-values of the parameters δ_5 and J_m are greater than about 0.25, whereas the α-value for J is in the neighborhood of 0.1.

The third specimen in the diagrams has a square-sized ligament. In comparison to the slim ligaments the square-sized ligament shows very little necking (Fig. 5*b*). Thus the third specimen has higher constraint. In this case, the splitting behavior of all three parameters is identical; i.e., the J-, J_m- and δ_5-R-curves start to deviate from the R-curves of the specimens with slim ligaments when crack extension reaches about 0.5 mm. Beyond this point the J-, J_m- and δ_5-R-curves of the specimen with the square-sized ligament fall below the curves obtained from specimens with slim ligaments. It does not make sense to evaluate α there, because the R-curve divergence is a consequence of constraint variation.

Figures 14, 15, and 16 show the ligament effect for the aluminum alloy for three different thicknesses. As has been discussed above, the constraint effect is very small in this material. Therefore the splitting of the R-curves in Figs. 14, 15, and 16 is obviously caused

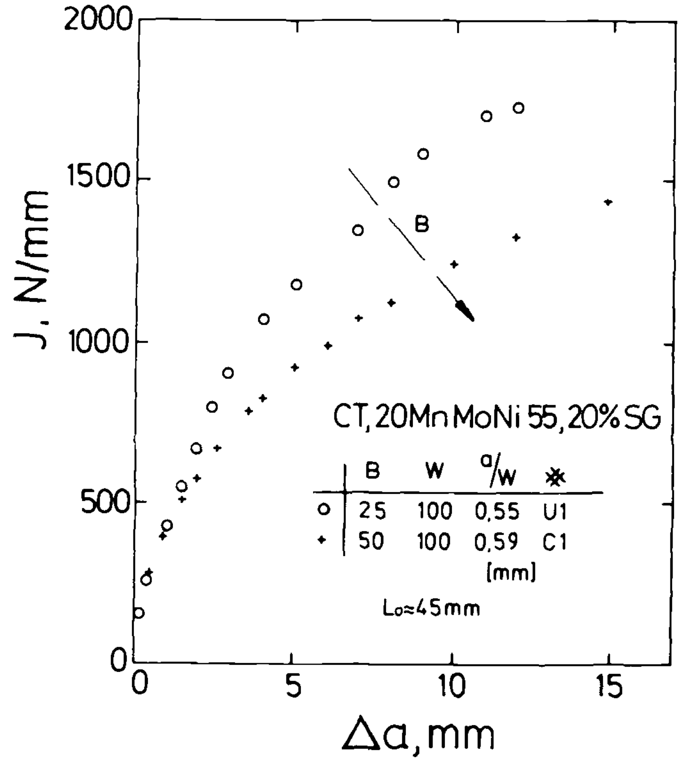

FIG. 9*a—Influence of specimen thickness for 20MnMoNi55 steel using* J-R*-curve.*

by effect (*b*); a splitting point indicates that the correlation parameter in the specimen with the short ligament reaches the limit of the application regime. The α-values of the *J*-*R*-curves in Figs. 14*a*, 15*a*, and 16*a* vary within the range of 0.7 to 0.39. This large variation may be due to the fact that the *J*-*R*-curve-split occurs gradually (as can be seen in Figs. 14*a* and 15*a*). Therefore small experimental errors in the crack length determination influence the location of a splitting point relatively strongly. If one takes the average of the three α-values for each individual correlation parameter, it appears that the parameters δ_5 and J_m have a greater application regime than the *J*-integral. This confirms the results obtained on the steel.

- *Specimens with Square-Sized Ligaments*—In Figs. 17*a* and 17*b*, the *R*-curves of two specimens having square-sized ligaments are shown. The specimens exhibit very similar necking-curves (Figs. 5 and 6). Therefore the constraint is assumed to be very similar in the two specimens. That means the split-off must be due to effect (*b*). It can be seen that for the parameters δ_5 and J_m the *R*-curve-split occurs after greater amounts of crack extension as in case of the *J*-*R*-curve. The α-values of the parameters δ_5 and J_m are about 0.24, whereas α for *J* is close to 0.1.

The α-values of the *J*-, J_m, and δ_5-parameters are summarized in Table 3. From theoretical work [5] it was concluded that the application regime of the *J*-integral is defined by the three

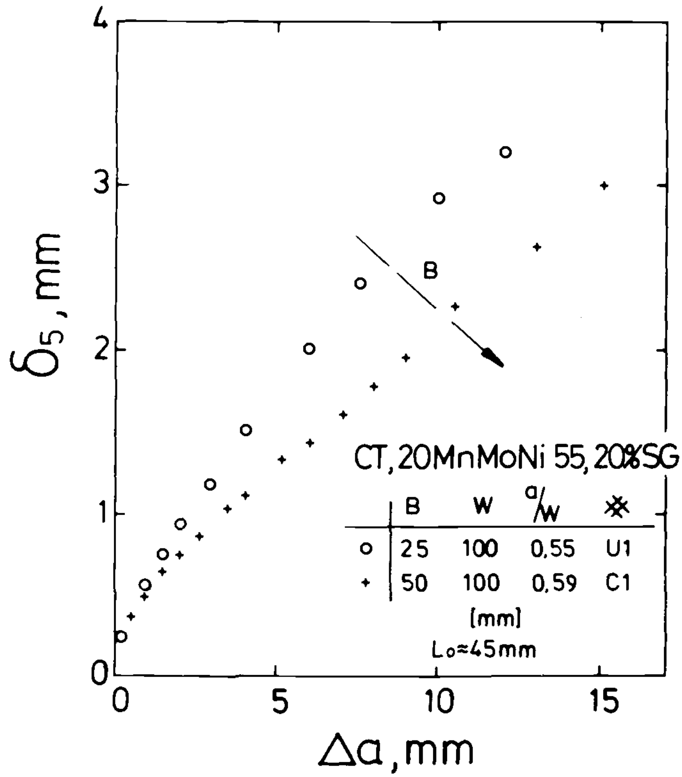

FIG. 9*b*—*Influence of specimen thickness for 20MnMoNi55 steel using* δ_5-*R-curve.*

quantities α, ω, and ρ as explained in the Introduction. In order to check whether the experimental results confirm these theoretical results, also the ω- and ρ-values at the splitting points were calculated using Eqs 4, 5, and 6. All ω- and ρ-values are shown in Table 3. They are in fairly good agreement with the figures derived from the theoretical work.

TABLE 3—α-, ω- *and* ρ-*values at splitting points.*

	J-Integral			J_m	δ_5
Specimen No.	α	ρ	ω	α	α
441/481	0.39	18	7	0.21	0.21
451, 471/461	0.08	40	6	>0.25[a]	>0.25[a]
472/462	0.07	40	8	>0.40[a]	>0.23[a]
4D/472	0.25	30	2	0.23	0.37
Average	0.20	32	6	>0.28[a]	>0.27[a]
EK4/C1	0.10	21	5	0.23	0.25
U1/V200	0.08	21	5	>0.25[a]	>0.25[a]

[a] No splitting until the end of test.

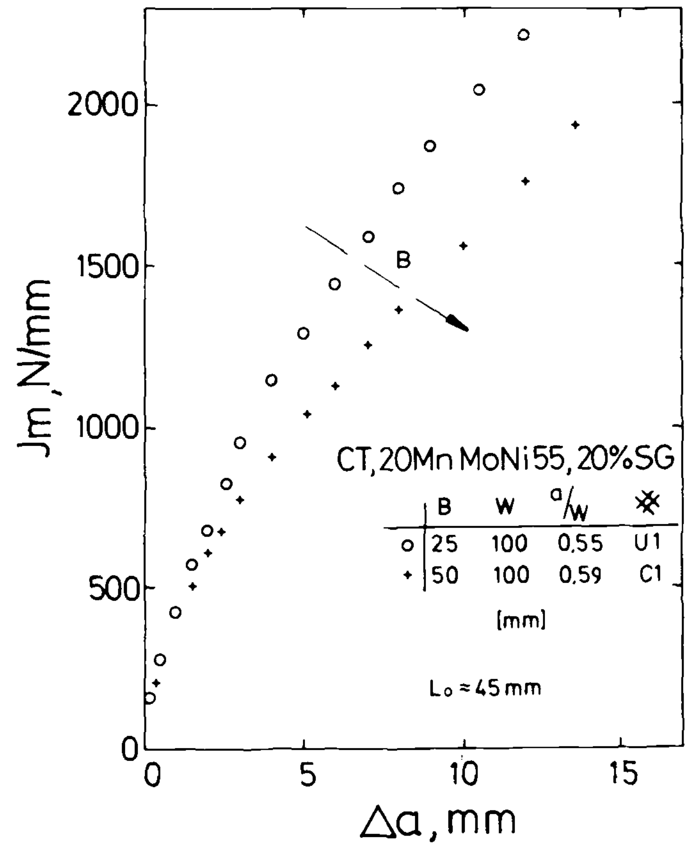

FIG. 9c—*Influence of specimen thickness for 20MnMoNi55 steel using* J_m-*R-curve.*

Relationship Between the Correlation Parameters δ_5, J_m *and J*

The experiments indicate that the δ_5- and J_m-R-curves behave very similarly because both types of R-curves exhibit similar a-values and both types of curves show a pronounced upswing beyond the splitting points. This impression is confirmed by Fig. 18. There is a specimen size independent correlation between δ_5 and J_m for each material. This means that both parameters (δ_5 and J_m) have identical quality to characterizing stable crack growth.

This close correlation between δ_5 and J_m was also found for stable crack growth in thin sections [*15*]. It was stated there that this unique correlation between δ_5 and J_m can theoretically be explained on the basis of the crack growth analysis by Rice, Drugan, and Sham [*16*]. The analysis is based on plane strain, small-scale yielding, and elastic ideally plastic deformation behavior of the material. The following equation emerged from the analysis in Ref *14*:

$$\delta_5 = \beta J_m / R_{el} \tag{7}$$

In Fig. 18 this equation is compared with the experimental results for the two materials investigated. As proposed in Ref *16*, the numerical constant β was assumed to be 0.65. It can be seen that for steel which has low strain hardening the prediction agrees very well with the

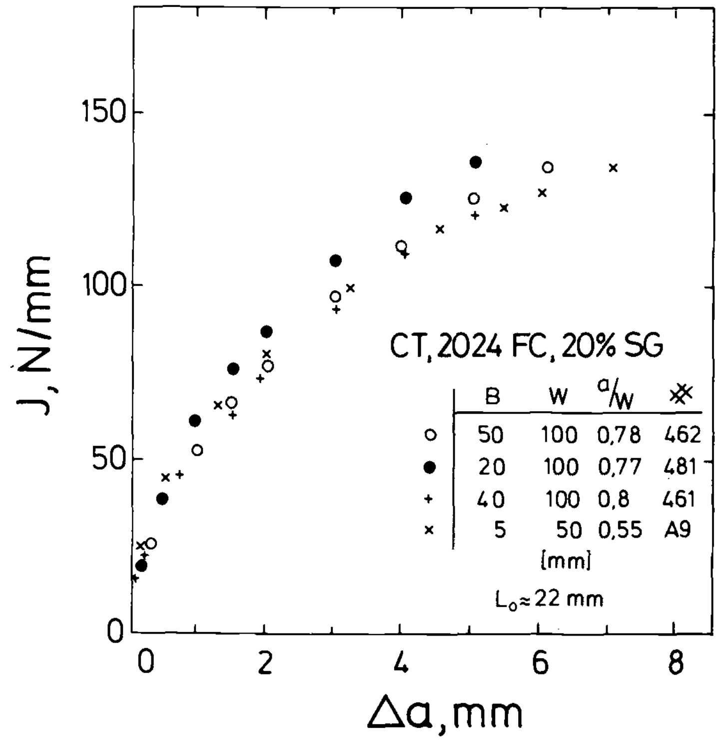

FIG. 10*a*—*Influence of specimen thickness for Al2024 FC (initial ligament length: 22 mm) using* J-R-*curve.*

experimental results. For aluminum alloy which has a relatively high strain hardening, the equation overestimates δ_5 slightly. This may be due to the fact that Eq 7 does not account for strain hardening, because hardening leads to lower CTODs as compared to the non-hardening case.

In Fig. 19 the correlation between J and δ_5 is shown for both materials investigated. For each material there exists a regime of size and geometry independent correlation between the two parameters. This regime of J-controlled crack growth increases with increasing ligament length as predicted by Eqs 4 and 6. Figures 18 and 19 show clearly that δ_5 and J are much less correlated in a unique manner than it is the case for δ_5 and J_m.

The discussion on the size and geometry effects can be summarized as follows. In cases where the constraint does not change from specimen to specimen as well as in cases where the material's fracture mechanisms are not susceptible to changes of the triaxiality of the stress state (see 2024FC), the α-values of the correlation parameters δ_5 and J_m are by a factor of roughly 2.5 greater than the α-values for the J-integral. This means that δ_5 and J_m can correlate 2.5 times more stable crack growth than the J-integral (Fig. 20).

The situation of constant constraint in different specimens is also realized in thin sections which exhibit pure shear fracture. In that case fracture occurs under plane stress conditions. This was the case for the investigations conducted by Schwalbe and Hellmann [*11*]. Therefore the findings obtained on thick sections are in very good agreement with the results obtained on thin sections.

The present investigation has demonstrated that size and geometry effects on crack growth

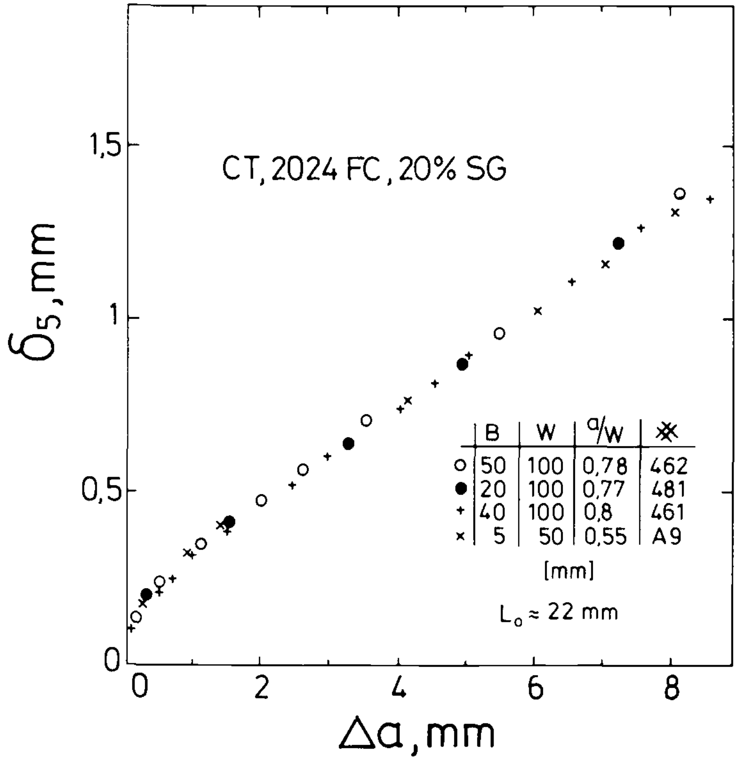

FIG. 10*b*—*Influence of specimen thickness for Al2024 FC (initial ligament length: 22 mm) using* δ_5-R-*curve.*

resistance have to be carefully looked at, even within one specific class of specimens, here, compact specimens. It has been shown that these effects are twofold:

1. Size and geometry variations may lead to constraint variations, and since constraint controls fracture, size and geometry effects occur, provided the material is susceptible to constraint variations. This is a *true* size and geometry effect.
2. The second effect emerges from exhaustion (approaching the "validity limit") of a crack growth correlation parameter; we therefore call it a *quasi* effect. It is only related to the ligament length which is the controlling variable for the ability of J, J_m, or δ_5 to uniquely correlate crack growth and thus to be a measure of the driving force for crack growth. The validity limits for these parameters can only be studied if the constraint conditions of different specimens are constant. Hence, if the correlation parameters are only used within their validity limits, any size and geometry effects should be due to constraint effects.

The present situation in this area is not satisfactory; any change of size and geometry parameters may give rise to a different R-curve for a given material. Furthermore, as was pointed out in the introduction of this article, at the present time there is no widely accepted quantitative measure of constraint. A promising approach is represented by the Q-parameter [*17*]. How-

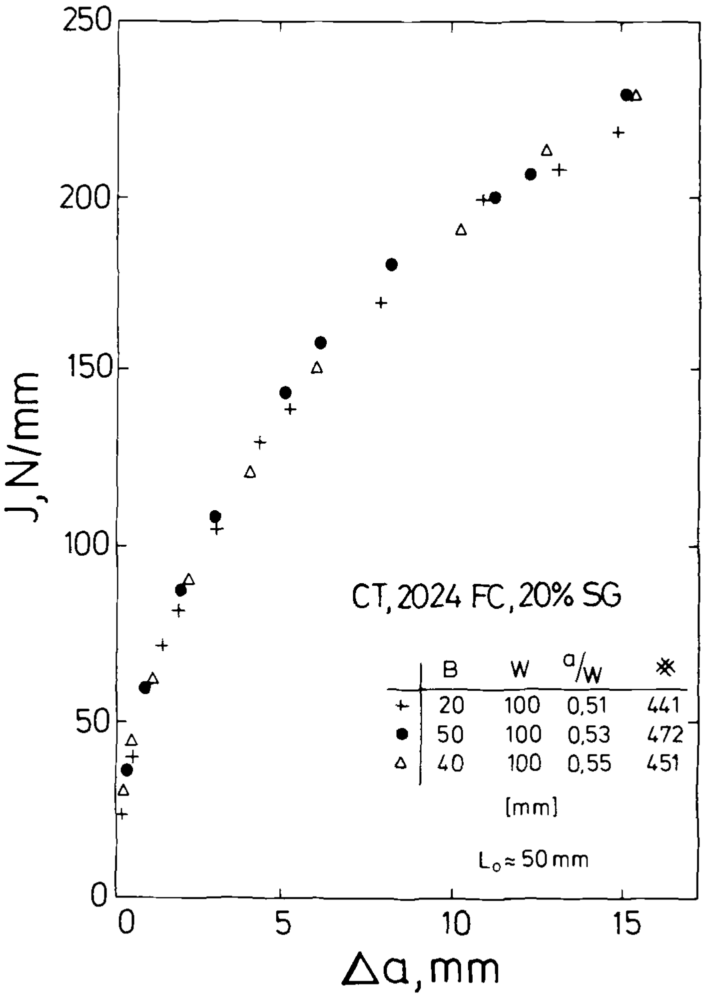

FIG. 11*a—Influence of specimen thickness for Al 2024 FC (initial ligament length: 50 mm) using* J-R-*curve.*

ever, even if we were able to quantify constraint easily and correctly, we will end up with a family of R-curves for each material, with constraint—maybe measured by Q—as a parameter. A single crack growth resistance curve characterizing the material should be the final goal. To achieve this, the driving force in Eq 2 must be given by a single parameter $P(J,Q)$ (or $P(J_m,Q)$ or $P(\delta_5,Q)$) describing uniquely the stress and strain field at a crack. We are therefore asking the theoretical mechanists to find a solution to this problem; it would be a major step forward.

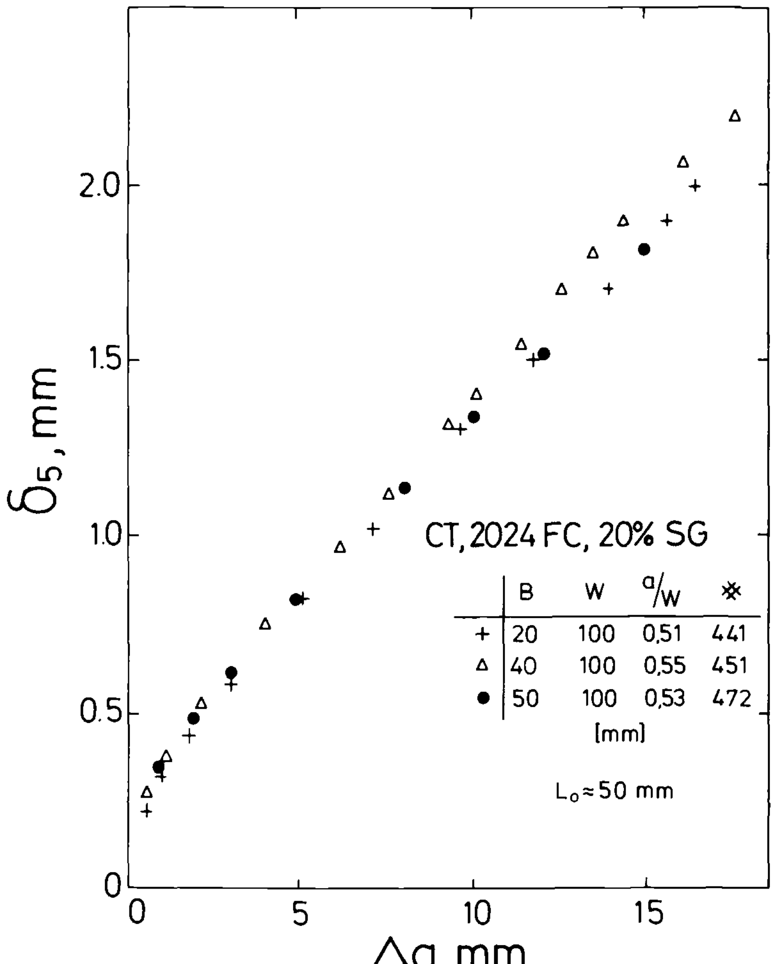

FIG. 11*b*—*Influence of specimen thickness for Al 2024 FC (initial ligament length: 50 mm) using* δ_5-R-*curve.*

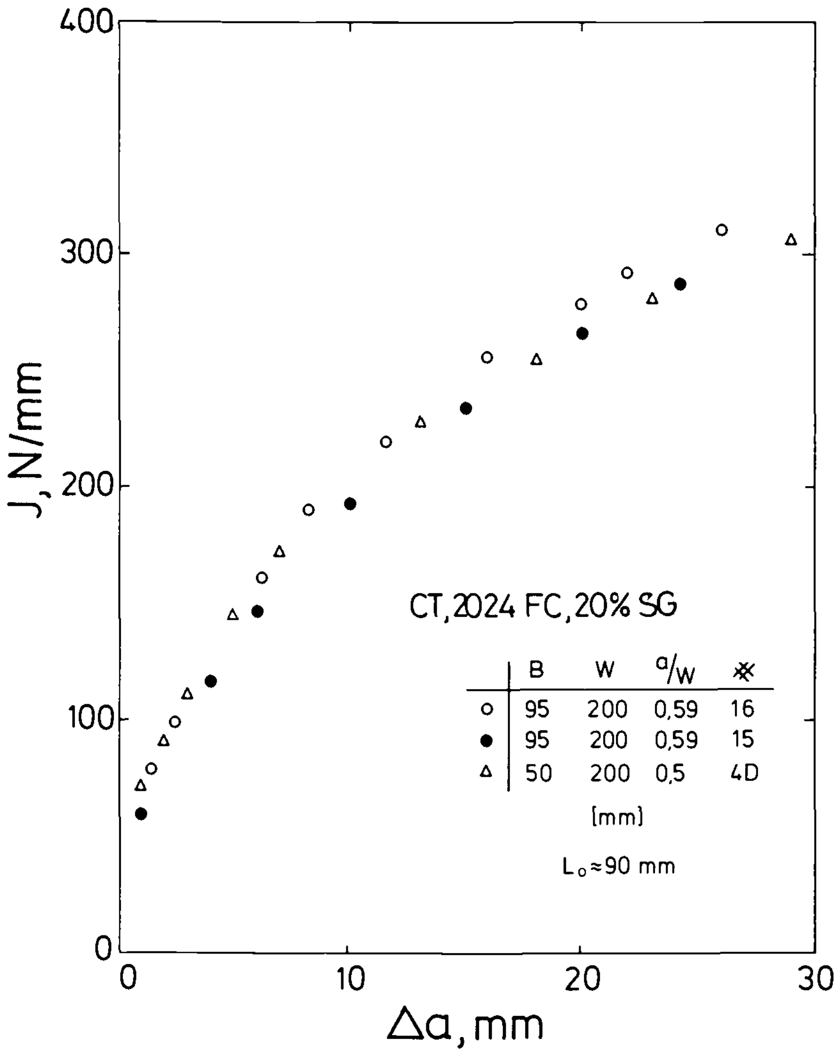

FIG. 12*a*—*Influence of specimen thickness for Al 2024 FC (initial ligament length: 90 mm) using* J-R-*curve.*

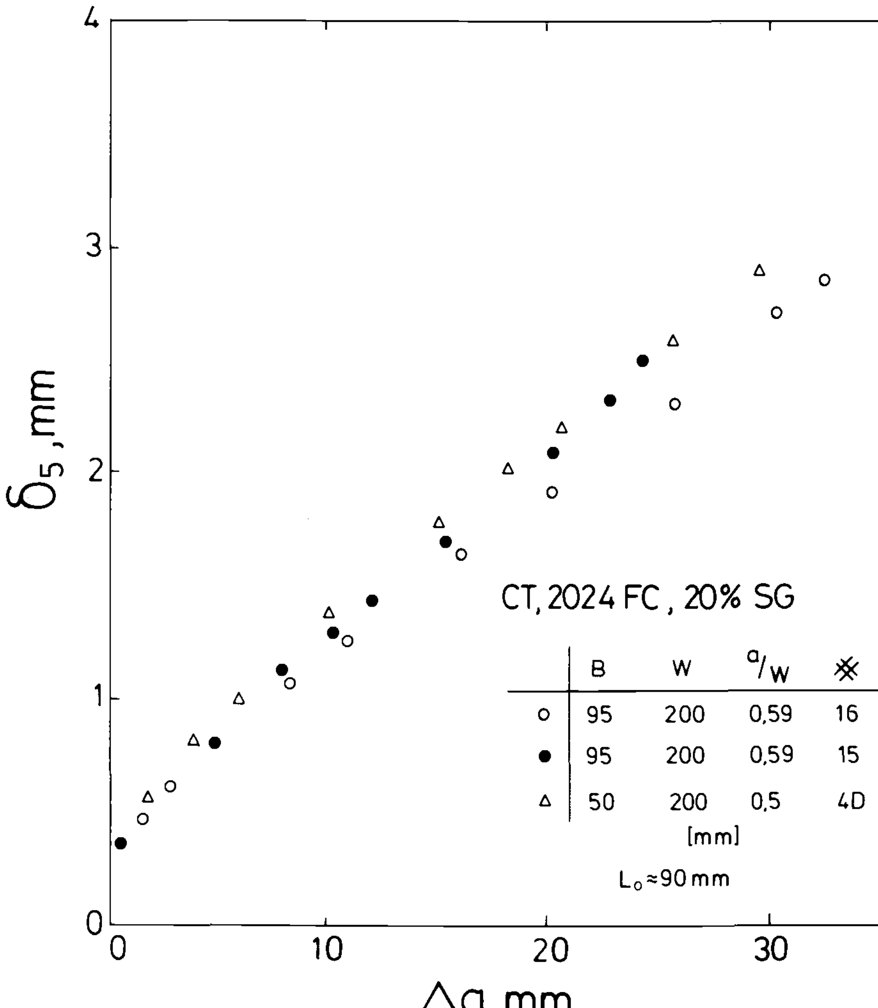

FIG. 12*b*—*Influence of specimen thickness for Al 2024 FC (initial ligament length: 90 mm) using* δ_5-R-*curve.*

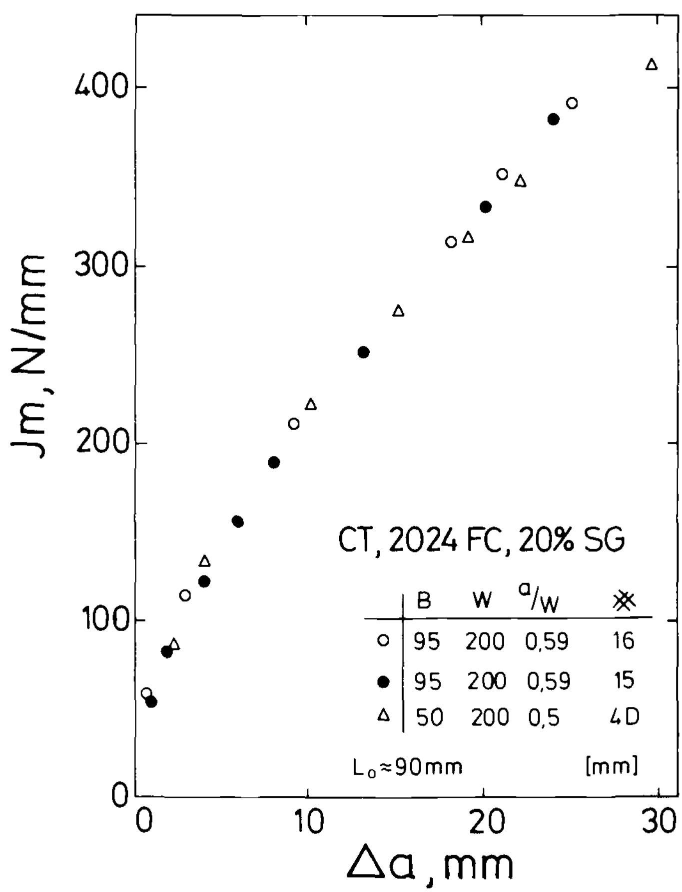

FIG. 12c—*Influence of specimen thickness for Al 2024 FC (initial ligament length: 90 mm) using* J_m-R-*curve.*

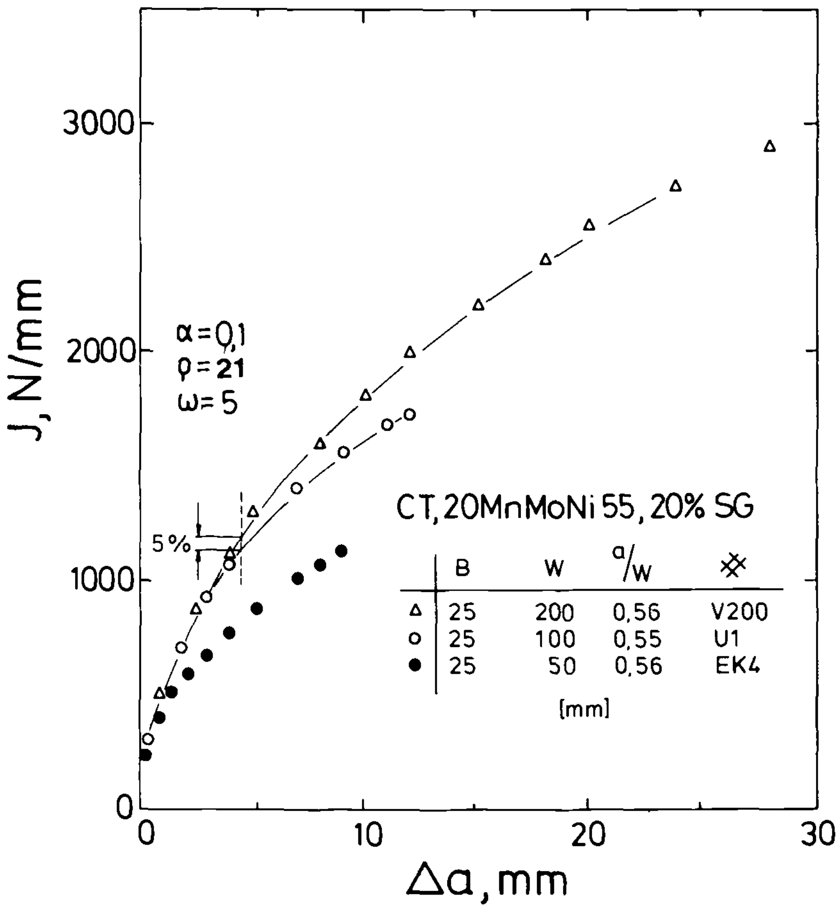

FIG. 13*a*—*Influence of ligament size for 20MnMoNi55 steel using* J-R-*curve.*

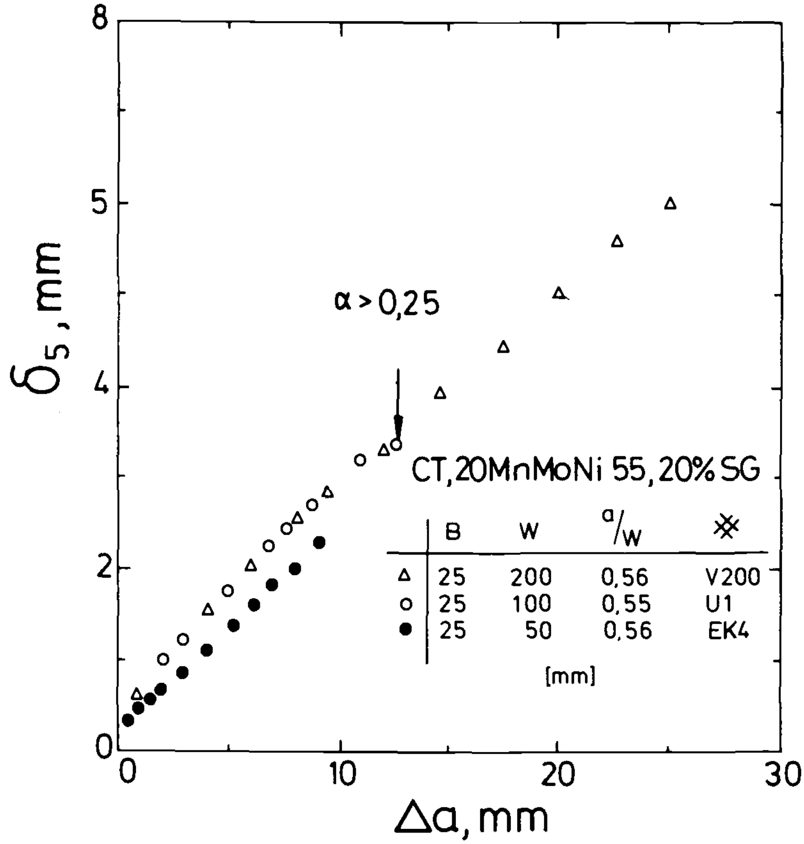

FIG. 13*b*—*Influence of ligament size for 20MnMoNi55 steel using* δ_5-R-*curve.*

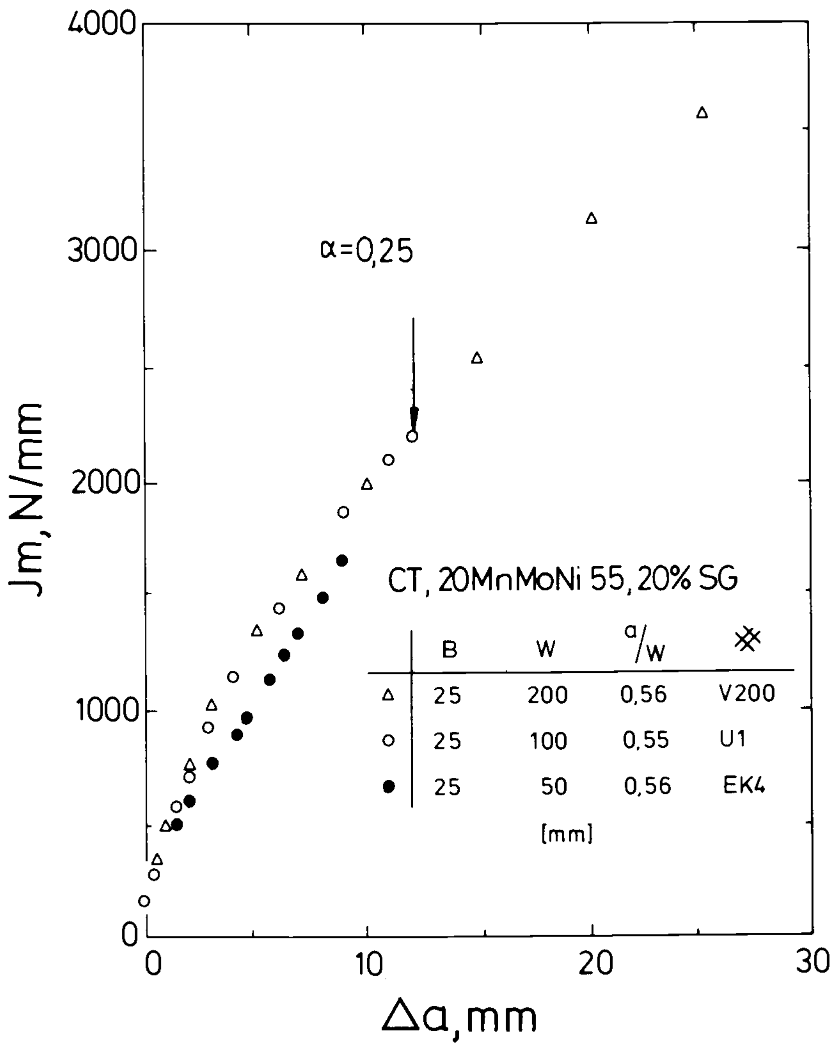

FIG. 13c—*Influence of ligament size for 20MnMoNi55 steel using* J_m-R-*curve.*

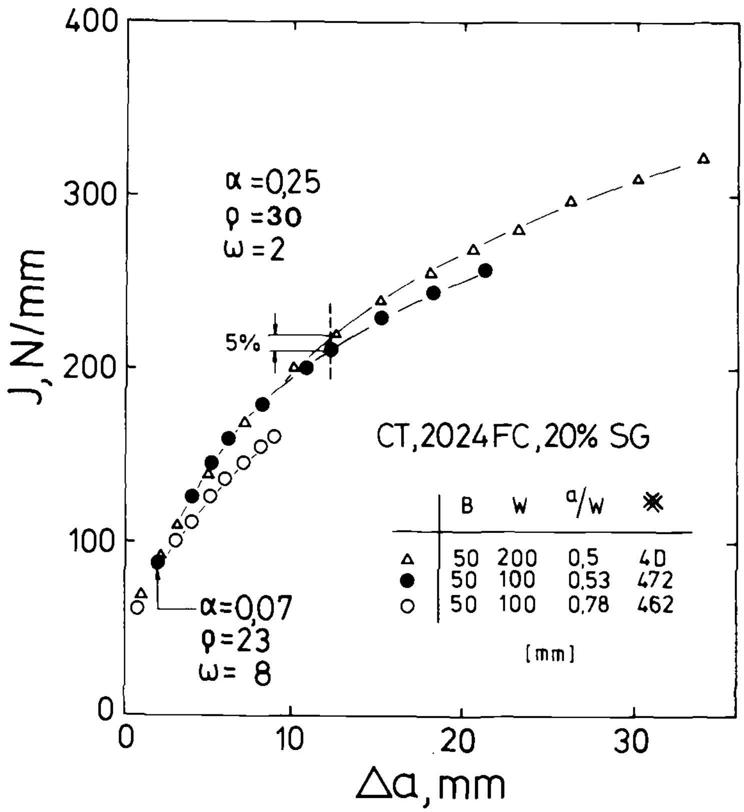

FIG. 14*a*—*Influence of ligament size for Al 2024 FC (thickness of specimen: 50 mm) using* J-R-*curve.*

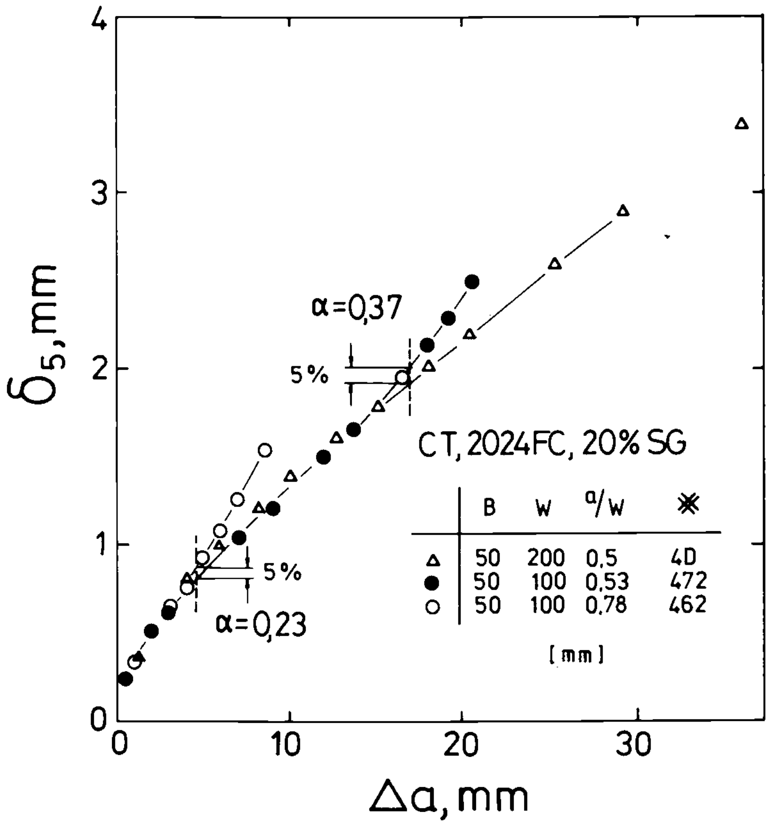

FIG. 14*b*—*Influence of ligament size for Al 2024 FC (thickness of specimen: 50 mm) using* δ_5-R-*curve.*

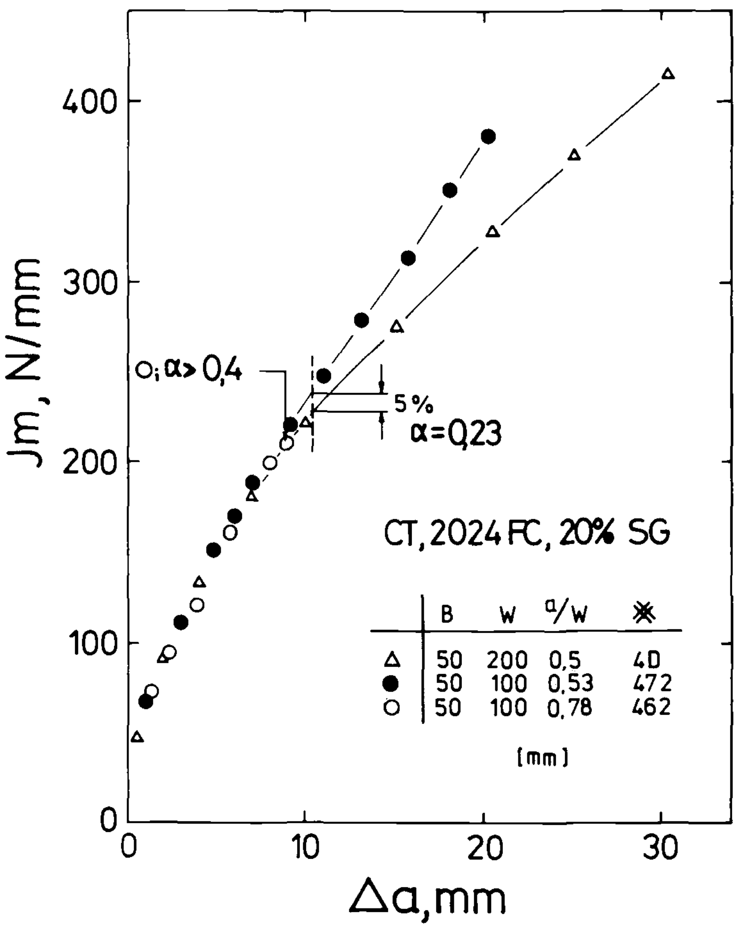

FIG. 14c—*Influence of ligament size for Al 2024 FC (thickness of specimen: 50 mm) using* J_m-R-*curve.*

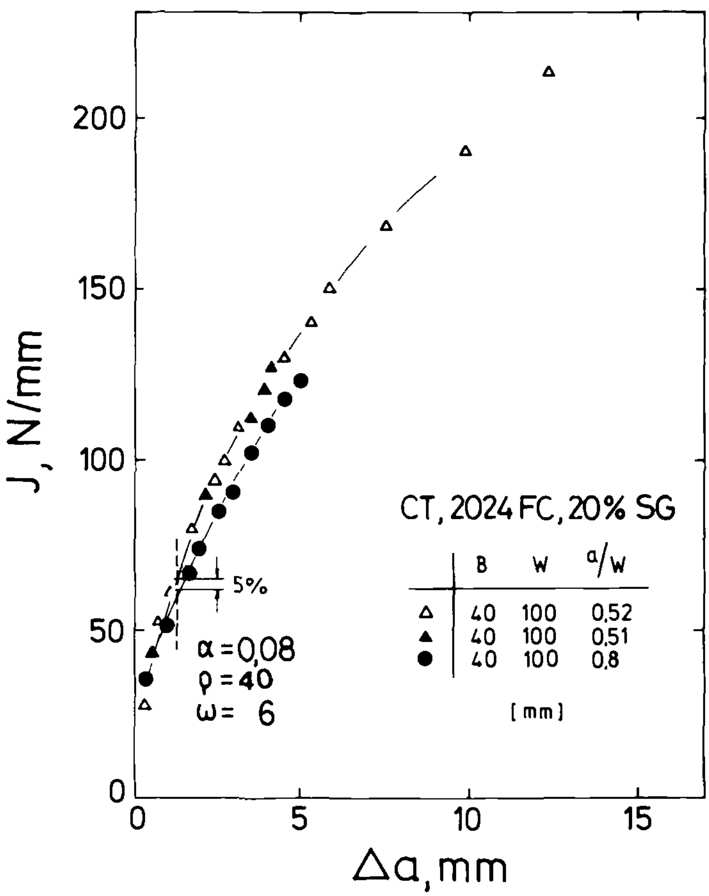

FIG. 15*a*—*Influence of ligament size for Al 2024 FC (thickness of specimen: 40 mm) using* J-R-*curve.*

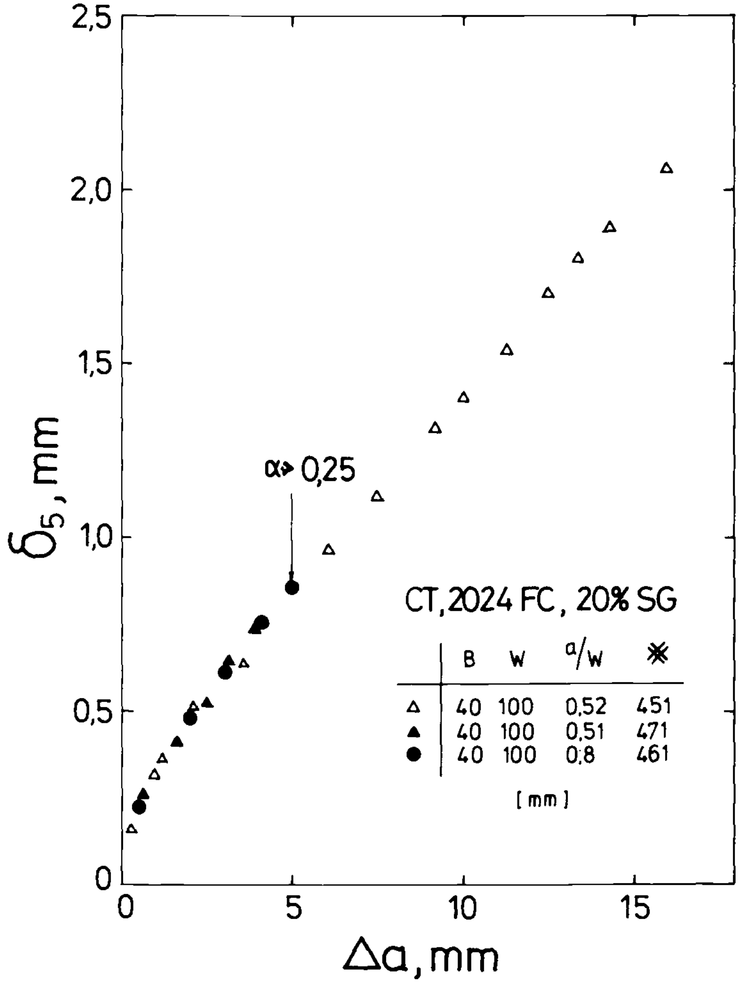

FIG. 15*b*—*Influence of ligament size for Al 2024 FC (thickness of specimen: 40 mm) using* δ_5-R-*curve.*

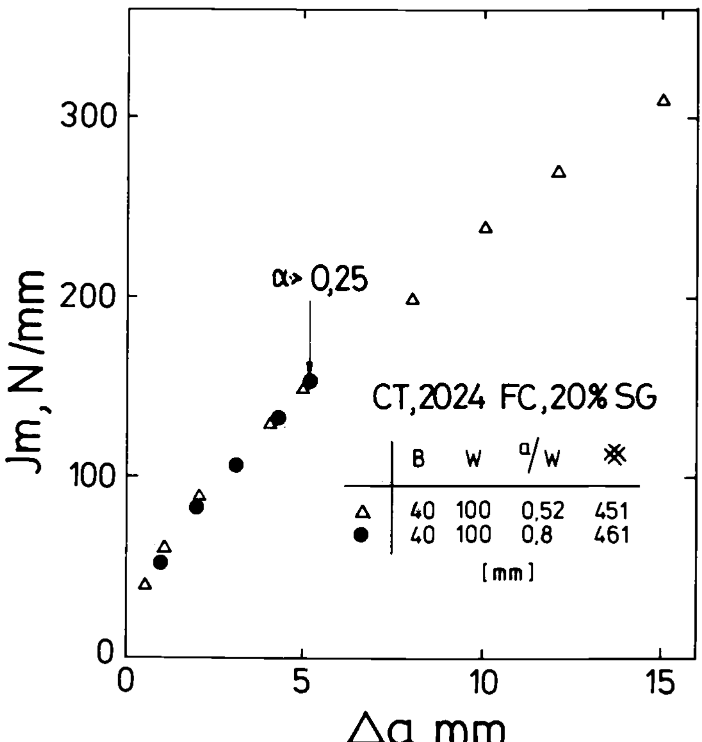

FIG. 15c—*Influence of ligament size for Al 2024 FC (thickness of specimen: 40 mm) using* J_m-R-*curve.*

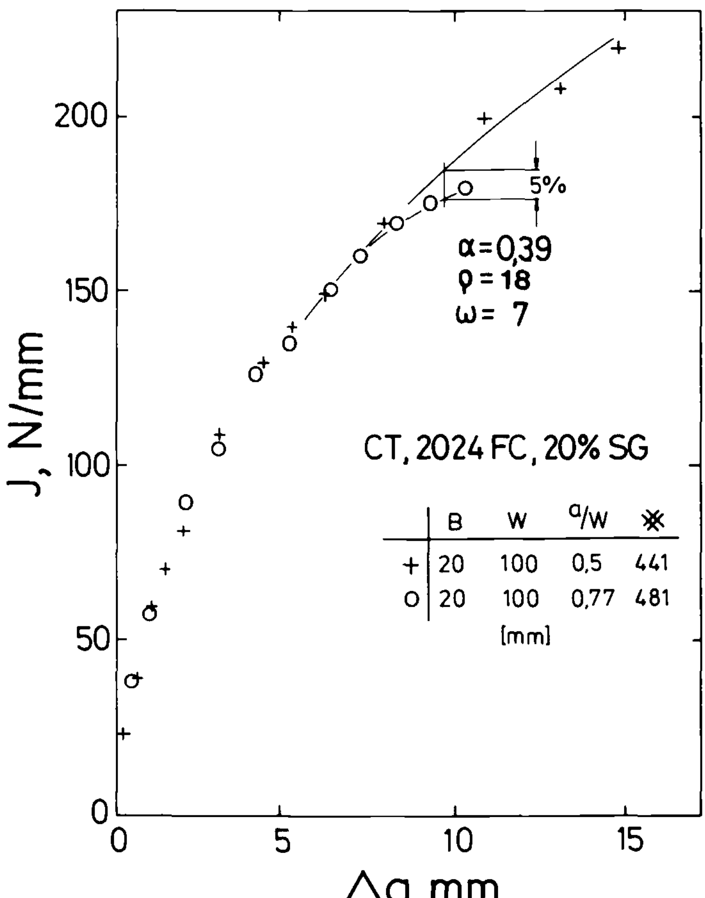

FIG. 16*a*—*Influence of ligament size for Al 2024 FC (thickness of specimen: 20 mm) using* J-R-*curve.*

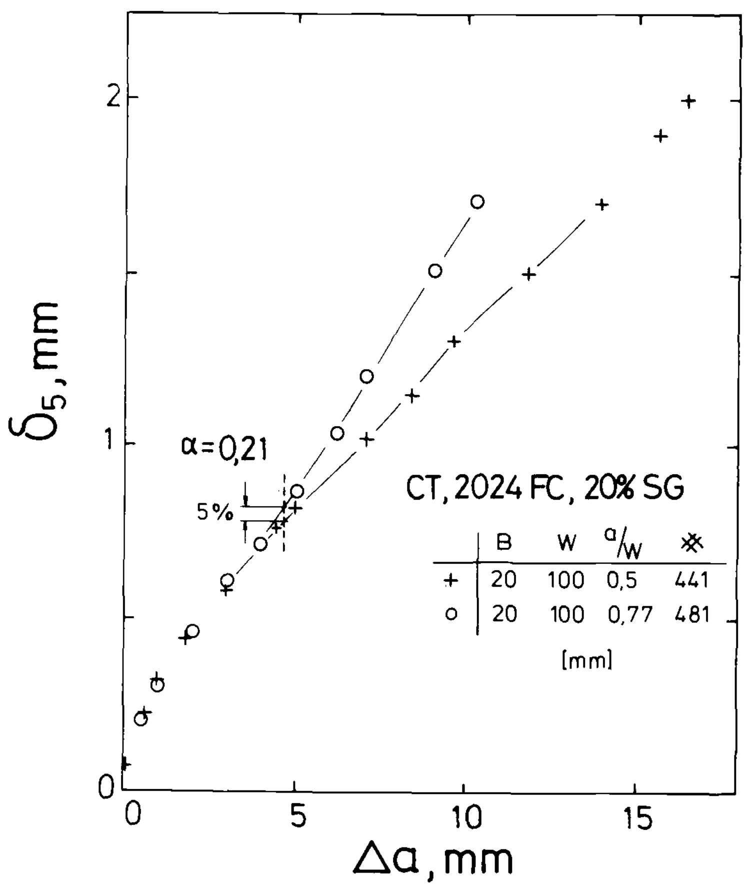

FIG. 16b—*Influence of ligament size for Al 2024 FC (thickness of specimen: 20 mm) using δ_5-R-curve.*

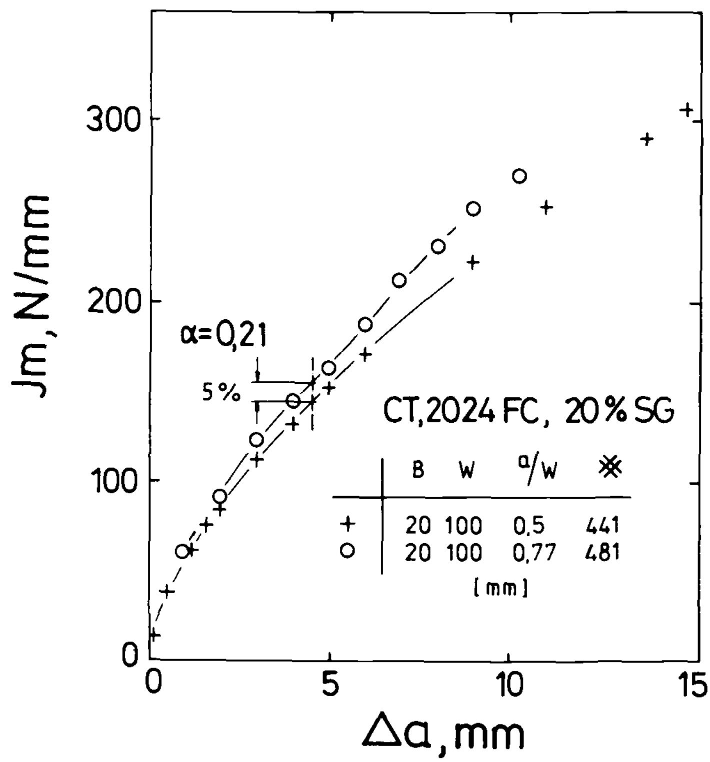

FIG. 16c—*Influence of ligament size for Al 2024 FC (thickness of specimen: 20 mm) using* J_m-R-*curve.*

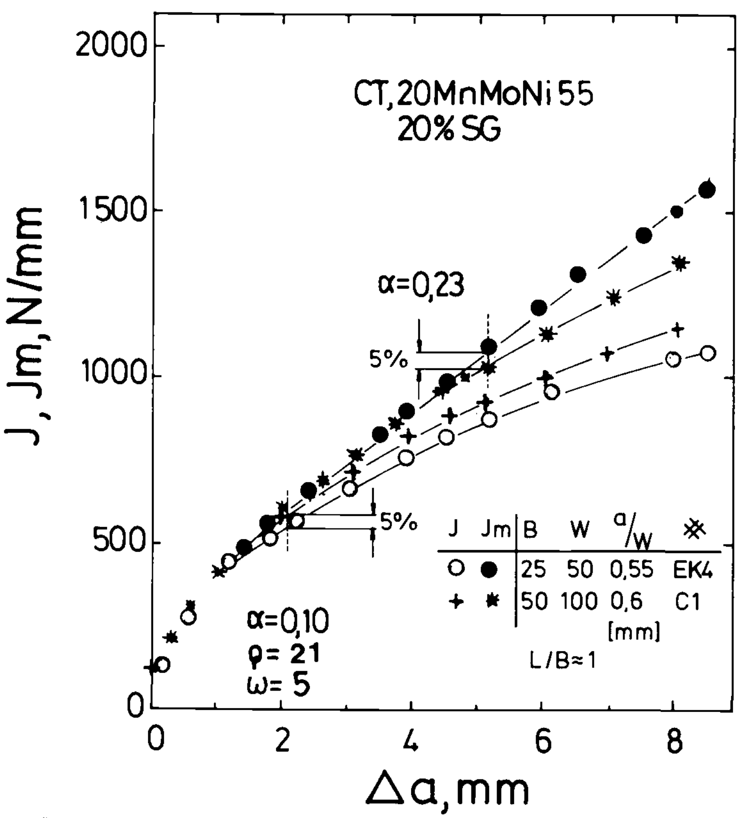

FIG. 17*a—Influence of ligament size for 20MnMoNi55 (two square square-sized ligaments) using* J-R-*curve and* J_m-R-*curve.*

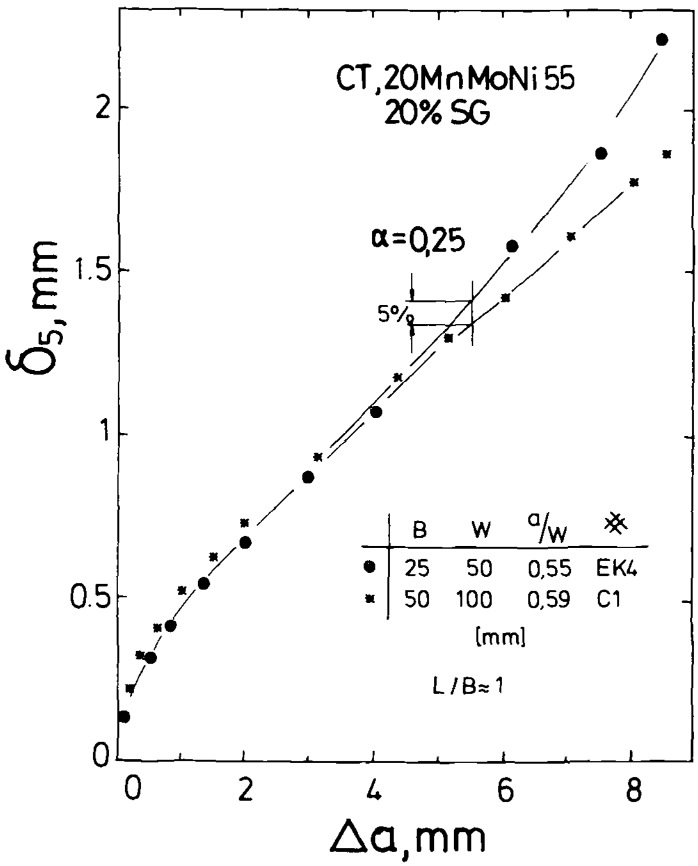

FIG. 17b—*Influence of ligament size for 20MnMoNi55 (two square square-sized ligaments) using* δ_5-*R-curve.*

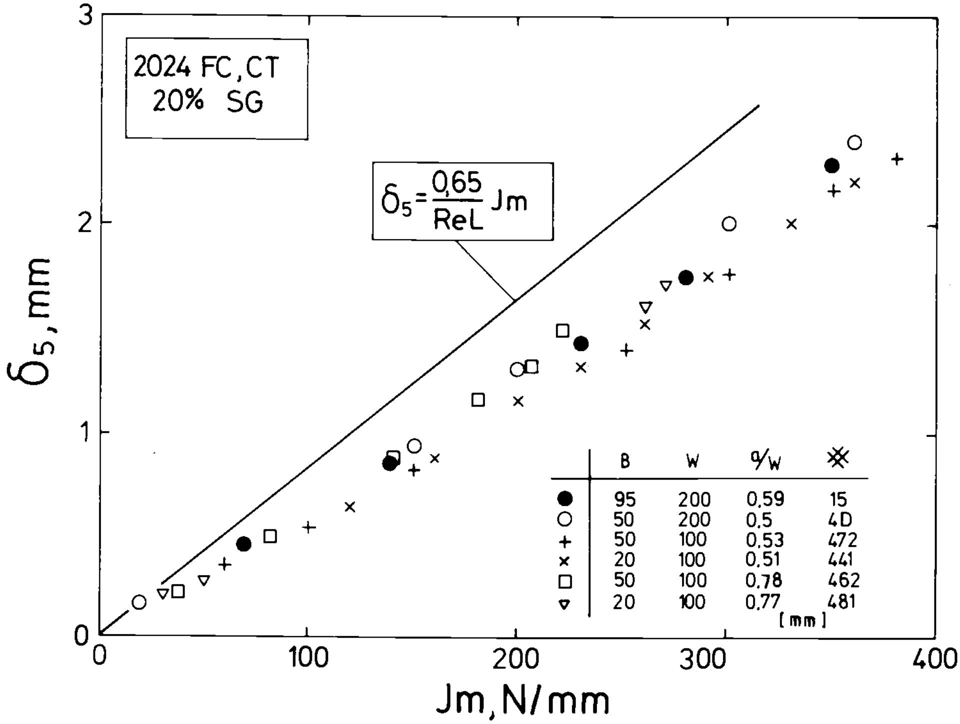

FIG. 18*a—Correlation between the modified* J*-integral,* J_m *and* δ_5 *for Al2024 FC.*

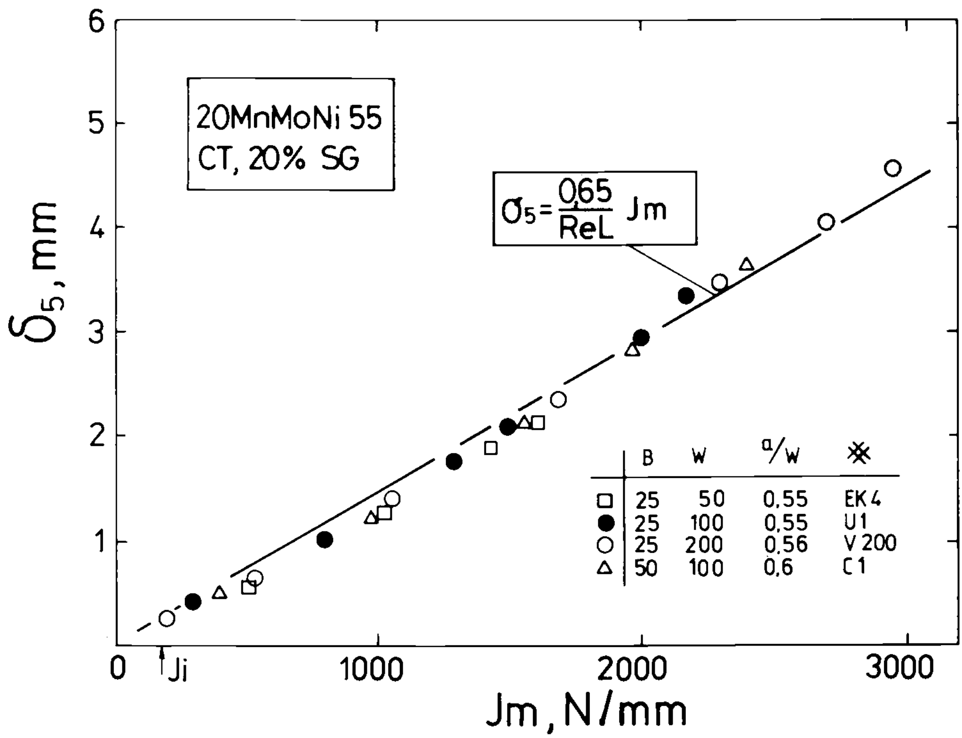

FIG. 18*b—Correlation between the modified* J*-integral,* J_m *and* δ_5 *for 20MnMoNi55 steel.*

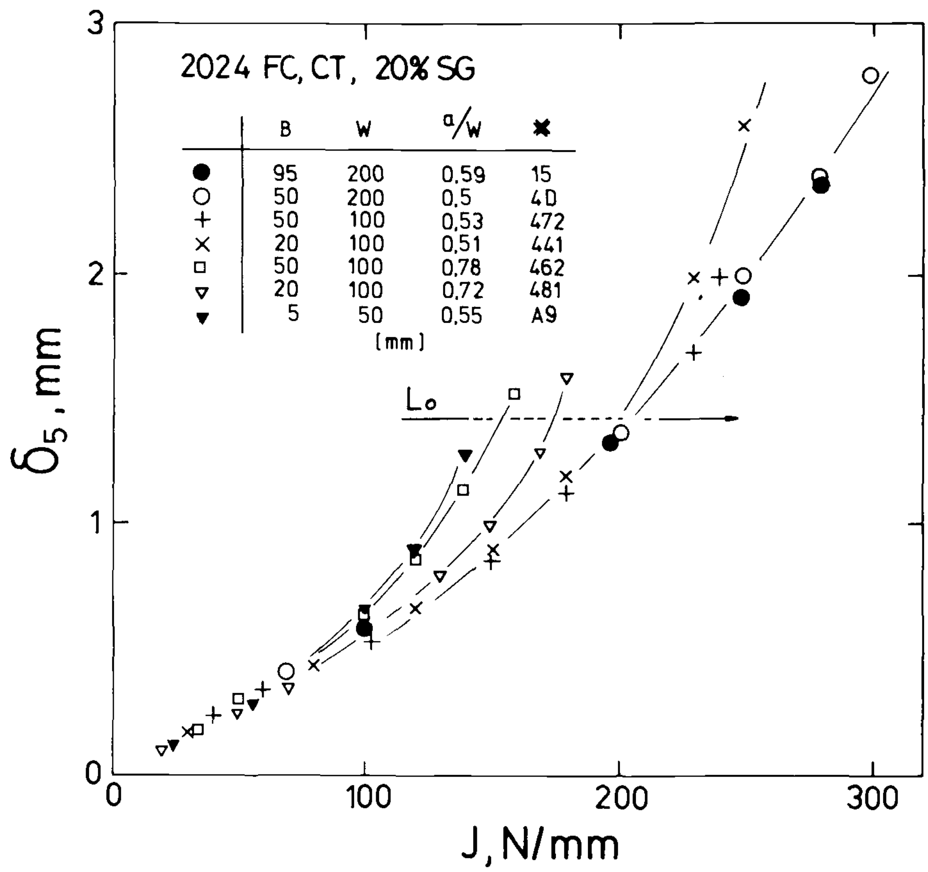

FIG. 19*a*—*Correlation between the* J*-integral and* δ_5 *for Al2024 FC.*

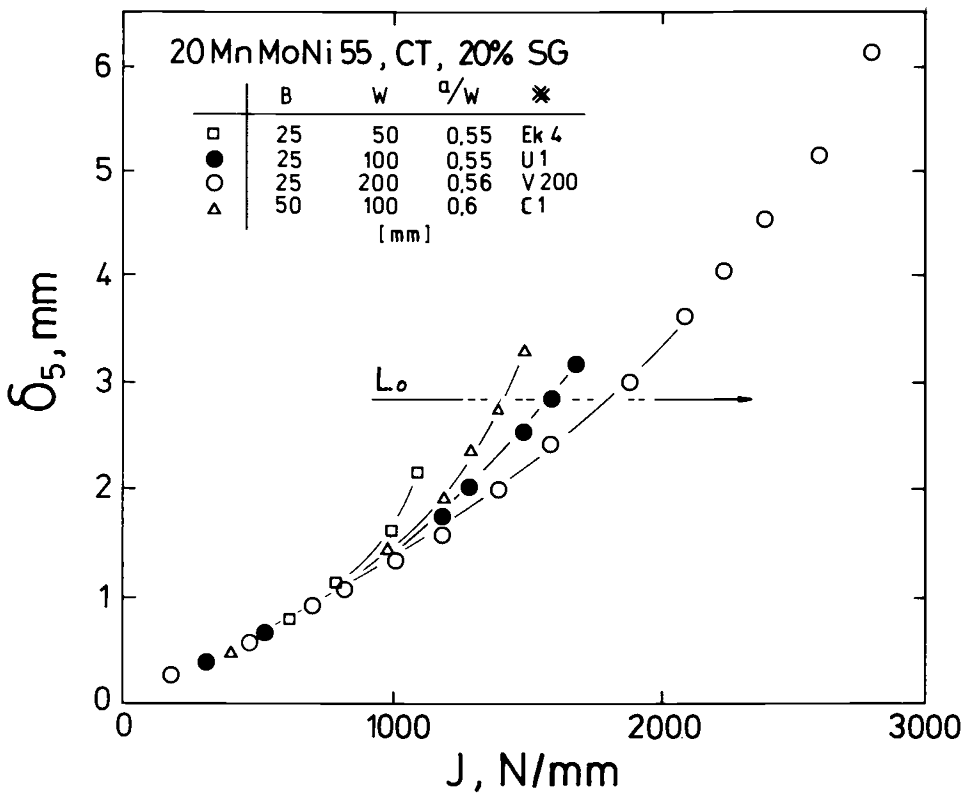

FIG. 19*b*—*Correlation between the* J*-integral and* δ_5 *for 20MnMoNi55 steel.*

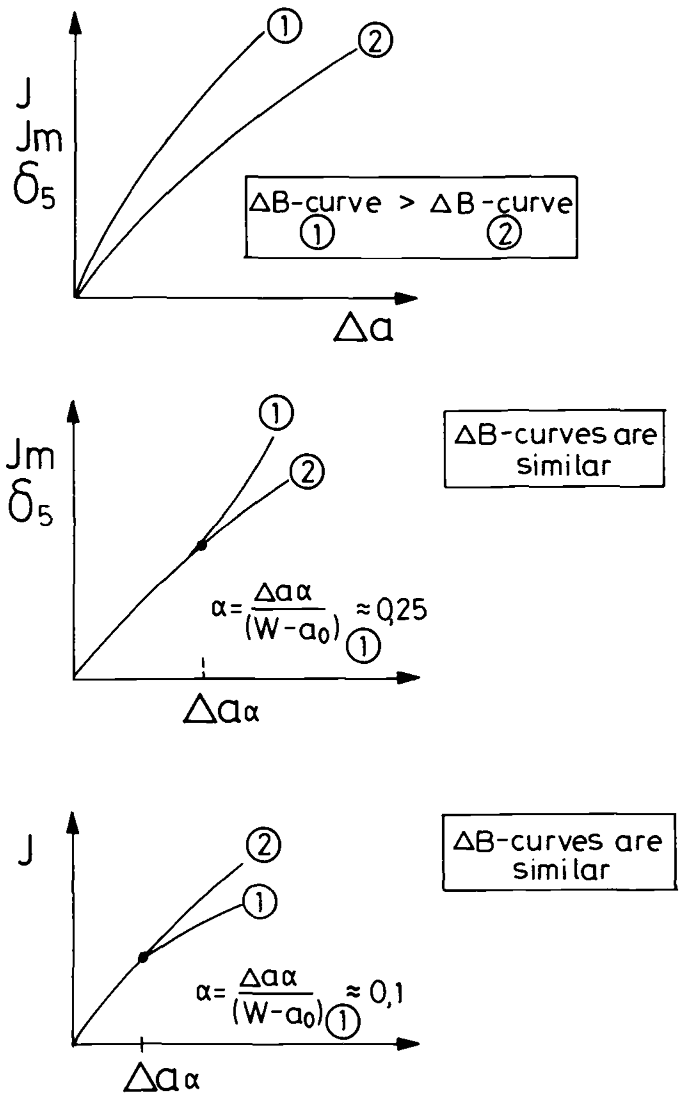

FIG. 20—*Influence of specimen size on* J-, J_m *and* δ_5-R-*curves for side-grooved compact-tension specimens.*

Conclusions

The influence of specimen size and geometry on J-, J_m- and δ_5-R-curves has been investigated for two materials using side-grooved CT specimens. Depending on the size of the ligament all specimens undergo more or less necking during the fracture tests. This thickness reduction was used as a qualitative measure of constraint and to qualify the influence of constraint on the R-curve.

As has been found previously on thin sections, so in thick sections the ability of δ_5 and J_m to correlate stable crack growth is significantly better than that of the J-integral.

The experiments exhibited a size and geometry independent correlation between δ_5 and J_m. This means that both parameters have identical potential to characterize stable crack extension in laboratory specimens.

Acknowledgments

The authors thank Dr. A. Cornec for his comments. We thank K. H. Balzereit, O. Kreienbring, and J. Knaack for their technical assistance.

References

[*1*] Rice, J. R., "A Path Independent Integral and the Approximate Analysis of Strain Concentration by Notches and Cracks," *Journal of Applied Mechanics,* 1968, pp. 379–386.
[*2*] Wells, A. A., "Application of Fracture Mechanics at and Beyond General Yield," *British Welding Journal,* 1963, pp. 563–570.
[*3*] Wells, R. R., "Crack Tip Opening Displacement for Elastic Plastic Analysis of Externally Notched Tension Bars," *Engineering Fracture Mechanics,* Vol. 1, 1969, pp. 399–410.
[*4*] Ernst, H. A., "Material Resistance and Instability Beyond *J*-Controlled Crack Growth," in *Elastic-Plastic Fracture: Second Symposium, Volume I—Inelastic Crack Analysis, ASTM STP 803,* American Society for Testing and Materials, Philadelphia, 1983, pp. 191–213.
[*5*] Hutchinson, L. M. and Paris, P. C., "The Theory of Stability Analysis of *J*-Controlled Crack Growth," in *Elastic-Plastic Fracture, ASTM STP 668,* American Society for Testing and Materials, Philadelphia, 1979, pp. 37–64.
[*6*] ASTM E 813-87, "Standard Test Method for J_{Ic}, A Measure of Fracture Toughness," *Annual Book of ASTM Standards,* Part 10, 1989.
[*7*] EGF P1-90, "EGF Recommendation for Determining the Fracture Resistance of Ductile Material," 1989.
[*8*] DVM Merkblatt 002, "Ermittlung von Rißinitiierungswerten und Rißwiderstandskurven bei Anwendung des *J*-Integrals," 1987.
[*9*] Steenkamp P. A. J. M., "Investigation into the Validation of *J*-Based Methods for the Prediction of Ductile Tearing and Fracture," Ph.D. thesis, University of Delft, 1987.
[*10*] Schwalbe, K.-H., Heerens, J., Hellman, D., and Cornec, A., "Relationships Between Various Definitions of the Crack Tip Opening Displacement," in *The Crack Tip Opening Displacement in Elastic-Plastic Fracture Mechanics,* K.-H. Schwalbe, Ed., Springer Verlag, 1986, p. 133.
[*11*] Schwalbe, K.-H. and Hellmann, D., "Correlation of Stable Crack Growth with the *J*-Integral and Crack Tip Opening Displacement: Effects of Geometry, Size and Material," GKSS/E/37, 1984.
[*12*] ASTM E 813-81, "Standard Test Method for J_{Ic}, A Measure of Fracture Toughness," *Annual Book of ASTM Standards, Part 10,* 1983.
[*13*] Schwalbe, K.-H. and Hellmann, D., "Application of the Electrical Potential Method to Crack Length Measurements Using Johnson's Formulae," GKSS 81/E/40, 1981.
[*14*] ASTM E 1152-87, "Standard Test Method for Determining *J-R* Curves," *Annual Book of ASTM Standards, Vol. 03.01,* 1990.
[*15*] Ernst, H. A., "Relationship Between Crack Tip Opening Displacement and J_m," in *The Crack Tip Opening Displacement in Elastic-Plastic Fracture Mechanics,* K.-H. Schwalbe, Springer Verlag, 1986, p. 197.
[*16*] Rice, J. R., Drugan, W. J., and Sham, T. L., "Elastic-Plastic Analysis of Growing Cracks," in *Fracture Mechanics (12th Conference), ASTM STP 700,* American Society for Testing and Materials, Philadelphia, 1980, pp. 189–221.
[*17*] Shih, F. C., O'Dowd, N. P. and Kirk, M. T., "A Framework for Quantifying Crack Tip Constraint," this publication, pp. 2–20.

T. L. Anderson,[1] *N. M. R. Vanaparthy,*[1] *and R. H. Dodds, Jr.*[2]

Predictions of Specimen Size Dependence on Fracture Toughness for Cleavage and Ductile Tearing

REFERENCE: Anderson, T. L., Vanaparthy, N. M. R., and Dodds, R. H., Jr., **"Predictions of Specimen Size Dependence on Fracture Toughness for Cleavage and Ductile Tearing,"** *Constraint Effects in Fracture, ASTM STP 1171,* E. M. Hackett, K.-H. Schwalbe, and R. H. Dodds, Eds., American Society for Testing and Materials, Philadelphia, 1993, pp. 473–491.

ABSTRACT: A framework for predicting the effect of crack-tip triaxiality on fracture toughness is outlined. This methodology is a two-parameter approach that considers the micromechanism of failure. A local damage parameter is used in conjunction with a crack-tip stress analysis to predict the effect of specimen dimensions on toughness. In the case of cleavage fracture, the local criterion involves the maximum principal normal stress, σ_1, as well as the volume over which σ_1 acts. The agreement between predictions and experimental data is very good in this case. For initiation of ductile tearing, we defined a damage parameter based on a modified version of the Rice and Tracey hole growth model. The analysis indicates that ductile fracture is less sensitive than cleavage to triaxiality. While this result is broadly consistent with experimental observations, further work is necessary to develop improved local criteria for ductile fracture.

The micromechanics approach proposed by the authors was compared with two-parameter fracture mechanics methodologies based on continuum theory, such as the *K-T* and *J-Q* approaches. These continuum methodologies, which involve two-term expansions of the crack tip fields, are descriptive rather than predictive. That is, these approaches describe the crack tip triaxiality, but they do not predict the effect of triaxiality on fracture behavior. The micromechanics approach, however, was developed for the purpose of making such predictions. Thus, the continuum and micromechanics approaches to two-parameter fracture mechanics are complementary.

KEY WORDS: fracture toughness, cleavage, ductile tearing, micromechanisms, constraint, size effects, *J*-integral, finite element analysis

Classical fracture mechanics theory assumes that a single parameter, such as the stress intensity factor or J contour integral, uniquely defines the conditions at the tip of a crack; a critical value of K or J at fracture is assumed to be a material constant. The single-parameter assumption, however, is rigorously correct only in an infinite body. In a finite body, the single-parameter assumption is suspect when the plastic zone size is significant compared to the dimensions of the body or the crack. The breakdown of single-parameter fracture mechanics is gradual in highly constrained geometries, such as deeply notched bend specimens, but occurs at relatively low load levels in notched panels in uniaxial tension.

Several existing ASTM standards for fracture toughness testing include minimum specimen size requirements that are designed to ensure that the single parameter assumption is approximately valid. For example, the ASTM Test Method for J_{Ic}, a Measure of Fracture Toughness

[1] Associate professor and research assistant, respectively, Department of Mechanical Engineering, Texas A&M University, College Station, TX 77843-3123.

[2] Professor, Department of Civil Engineering, University of Illinois, Urbana, IL 61801.

(E 813-87), contains the following size requirement for specimens loaded predominantly in bending

$$B,\ b_0 \geq \frac{25 J_{Ic}}{\sigma_Y} \tag{1}$$

where

B = the specimen thickness,
b_0 = the initial ligament length, and
σ_Y = the flow stress, defined as the average of the yield and tensile strengths (σ_{YS} and σ_{TS}, respectively).

Equation 1 applies only to the initiation of ductile tearing in metals. Cleavage fracture toughness is more sensitive to losses in crack tip triaxiality, and thus larger specimens are required to achieve a single-parameter description of failure conditions. The authors [*1,2*] have proposed size requirements for cleavage fracture toughness that are eight times as stringent as Eq 1.

Two-Parameter Fracture Mechanics

In many situations, it is not possible to satisfy the single-parameter assumption of classical fracture mechanics. Recently, a number of researchers have attempted to extend the limits of fracture mechanics by introducing a second parameter to characterize crack tip conditions. Most of these two-parameter approaches are based solely on a continuum analysis, but the present authors have developed a methodology that considers the micromechanism of fracture.

Continuum Approaches

The approach that has received the most attention recently involves a two-term asymptotic expansion of the elastic crack tip fields. For Mode I loading, the stress field ahead of a crack in an elastic solid is given by

$$\sigma_{ij} = \frac{K_I}{\sqrt{2\pi r}} f_{ij}(\theta) + T\delta_{1i}\delta_{1j} + \text{higher order terms} \tag{2}$$

where the first term is the familiar singular solution, T is the amplitude of the second-order stress field, and δ_{ij} is the Kroneker delta. Equation 2 was first derived by Williams [*3*]. Subsequent researchers [*4,5*] noted that the second term has a significant effect on the shape of the plastic zone. More recently, it has been shown that the T stress can influence the stress and strain fields well inside of the plastic zone [*6–8*]. Geometries that exhibit a negative T stress experience a loss in crack tip triaxiality at relatively low load levels. The T stress characterizes triaxiality under contained yielding conditions, but T is undefined when the body is fully yielded.

To address crack tip triaxiality in bodies subject to large-scale plasticity, several researchers [*9–11*] have considered an asymptotic expansion of the near-tip fields in a power law material. These analyses begin by assuming a Ramberg-Osgood stress-strain relationship, which for uniaxial deformation is given by

$$\frac{\varepsilon}{\varepsilon_0} = \frac{\sigma}{\sigma_0} + \alpha\left(\frac{\sigma}{\sigma_0}\right)^n \tag{3}$$

where

ε = strain,
σ = stress,
σ_0 = a reference stress,
$\varepsilon_0 = \sigma_0/E$,
and α and n = dimensionless constants.

Near the tip of a crack, well within the plastic zone, the elastic strains are negligible, and the stress-strain relationship is a simple power law. Following the notation of O'Dowd and Shih [*10,11*], the stress fields can be written in the following form

$$\frac{\sigma_{ij}}{\sigma_0} = \left(\frac{J}{\alpha\varepsilon_0\sigma_0 I_n r}\right)^{1/n+1} \tilde{\sigma}_{ij}(n,\theta) + Q\left(\frac{r\sigma_0}{J}\right)^q \hat{\sigma}_{ij}(n,\theta) + \text{higher order terms} \tag{4}$$

where the first term is the Hutchinson-Rice-Rosengren (HRR) singularity [*12,13*], Q is the amplitude of the second-order term, and $\hat{\sigma}_{ij}$ is a dimensionless function that quantifies the angular variation of the second-order correction to the stress tensor. The numerical values of Q, q, and $\hat{\sigma}_{ij}$ are undetermined by the asymptotic analysis. Finite element results of O'Dowd and Shih showed that when the near tip fields are represented by the first two terms in Eq 3, the exponent q is small, indicating that the second order term does not vary significantly with r. Moreover, in the forward sector ($\theta < \pm\pi/2$), $\hat{\sigma}_{r\theta} \approx 0$ and $\hat{\sigma}_{rr} \approx \hat{\sigma}_{\theta\theta}$, both $\hat{\sigma}_{rr}$ and $\hat{\sigma}_{\theta\theta}$ are nearly independent of θ in the forward sector. Thus the stress fields in the forward sector can be approximated by

$$\frac{\sigma_{ij}}{\sigma_0} = \left(\frac{\sigma_{ij}}{\sigma_0}\right)_{\text{HRR}} + Q\delta_{ij} \tag{5}$$

O'Dowd and Shih also showed that the strain field can be represented by a two-term expansion where the first term corresponds to the small-scale yielding limit.

Note that Q only affects the hydrostatic component of the stress tensor. Thus Q is a measure of the crack tip triaxiality relative to the small scale yielding limit. In finite geometries, Q is usually negative. In contained yielding, there is a unique relationship between Q and the T stress [*11*]. Unlike the T stress, however, Q can be evaluated in fully yielded bodies.

Figure 1 shows the variation in Q with loading in an edge-cracked bend specimen and a center-cracked panel in tension [*11*]. In the deeply notched bend specimen, Q is nearly zero at low and moderate J values, indicating a high level of triaxiality. The triaxiality in the center-cracked panel decreases rapidly from the small scale yielding limit ($Q = 0$).

In classical fracture mechanics, a critical J value (J_{crit}) is assumed to be a material constant. The two-parameter approach, however, introduces an additional degree of freedom. Consequently, fracture in a given material is defined by a J-Q failure locus

$$J_{crit} = J_{crit}(Q) \tag{6}$$

For contained yielding, Eq 4 can also be expressed in terms of a J-T or K-T failure locus.

A continuum analysis can characterize the relationship between Q and loading parameters

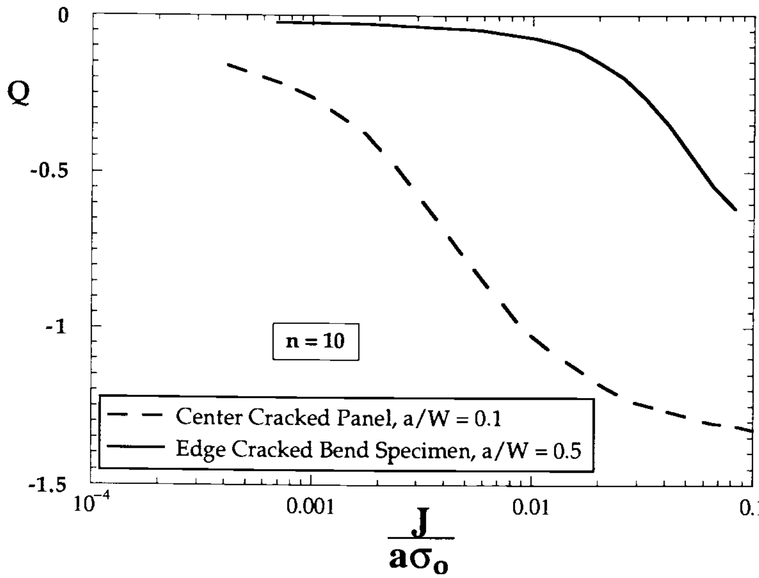

FIG. 1—*Effect of loading on the crack tip triaxiality in two configurations* [11].

(Fig. 1), but cannot predict the functional relationship between J_{crit} and Q. The precise form of this function depends on the micromechanism of fracture, as discussed below.

Micromechanics Approach

The present authors [*1,2*] have developed a framework for quantifying the effect of triaxiality on fracture behavior. This approach involves a local failure criterion that corresponds to the micromechanism of interest. The failure criterion is used in conjunction with a crack tip stress analysis to predict effect of specimen size and geometry on fracture toughness.

This micromechanics approach has been very successful in predicting the effect of crack tip triaxiality on cleavage fracture toughness. These results are described briefly in the present article, and in more detail in Refs *1* and *2*. This article also describes recent attempts to characterize the effect of triaxiality on ductile initiation toughness in metals.

Analytical Procedures

Finite Element Analysis

Plane strain elastic-plastic finite element analysis was performed on four configurations with three strain hardening rates, resulting in a total of twelve cases. The crack tip stress fields for small-scale yielding were evaluated, as well as for single-edge notched bend [SE(B)] specimens with a/W ratios of 0.05, 0.15, and 0.50. The material stress-strain behavior was modeled with a Ramberg-Osgood power law expression (Eq 3). For the present study, $\alpha = 1.0$, $\varepsilon_0 = 0.002$, and $\sigma_0 = 414$ MPa (60 ksi); in this case σ_0 corresponds to the 0.2% offset yield strength, σ_{YS}. The strain hardening exponent, n, was assigned values of 5, 10, and 50, which correspond to high, medium, and low work hardening, respectively.

The small-scale yielding solution was obtained by means of a modified boundary layer technique [*14*]. Displacements of the elastic Mode I singular field were imposed at the boundary of a circular domain that contained a crack. The applied K was sufficiently low to confine the plastic zone to well within the domain. This model is designed to simulate a crack in an infinite body.

The finite element analyses utilized deformation plasticity and small strain theory. In all cases, the meshes were sufficiently refined to resolve the near-tip stress and strain fields. For each analysis, the J integral was evaluated by means of the energy domain integral approach [*15*]. The crack tip opening displacement (CTOD) was defined as the intersection of the crack flanks with a 90° vertex emanating from the crack tip.

Additional details of the finite element analysis are given in Refs *1* and *2*.

Cleavage Fracture Criterion

To quantify size effects on fracture toughness, one must assume a local failure criterion. Cleavage fracture involves a local Griffith instability of a microcrack that forms from a microstructural feature such as a carbide or inclusion in the case of ferritic steels; the Griffith energy balance is satisfied when a critical stress is reached in the vicinity of the microcrack. The size and location of the critical microstructural feature dictate the fracture toughness; thus, cleavage toughness is subject to considerable scatter [*16,17*].

The Griffith instability criterion implies fracture at a critical normal stress near the tip of the crack; the statistical sampling nature of cleavage initiation (that is, the probability of finding a critical microstructural feature near the crack tip) suggests that the volume of the process zone is also important. Thus, the probability of cleavage fracture in a cracked specimen of ferritic steel can be expressed in the following general form

$$F = F\{V(\sigma_1)\} \tag{7}$$

where F is the failure probability, σ_1 is the maximum principle stress at a point, and $V(\sigma_1)$ is the cumulative volume sampled where the principal stress is $\geq \sigma_1$. For a specimen subjected to plane strain conditions, $V = BA$, where A is cumulative area on the x-y plane. (This article uses the conventional fracture mechanics coordinate axes, where x is the direction of crack propagation, y is normal to the crack plane, and z is parallel to the crack front.) For small scale yielding, dimensional analysis shows that the principal stress ahead of the crack tip can be written as

$$\frac{\sigma_1}{\sigma_0} = f\left(\frac{J}{\sigma_0 r, \theta}\right) \tag{8}$$

It can be shown that the HRR singularity is a special case of Eq 8. When J dominance is lost, there is a relaxation in triaxiality; the principal stress at a fixed r and θ is less than the small-scale yielding value.

Equation 5 can be inverted to solve for the radius corresponding to a given stress and angle

$$r(\sigma_1/\sigma_0, \theta) = \frac{J}{\sigma_0} g(\sigma_1/\sigma_0, \theta) \tag{9}$$

Solving for the area inside a specific principal stress contour gives

$$A(\sigma_1/\sigma_0) = \frac{J^2}{\sigma_0^2} h(\sigma_1/\sigma_0) \tag{10}$$

where

$$h(\sigma_1/\sigma_0) = \frac{1}{2}\int_{-\pi}^{\pi} g^2(\sigma_1/\sigma_0, \theta)\, d\theta \tag{11}$$

Thus for a given stress, the area scales with J^2 in the case of small-scale yielding. Under large-scale yielding conditions, the specimen or structure experiences a loss in constraint, and the area inside a given principal stress contour (at a given J value) is less than predicted from small scale yielding

$$A(\sigma_1/\sigma_0) = \phi \frac{J^2}{\sigma_0^2} h(\sigma_1/\sigma_0) \tag{12}$$

where ϕ is a constraint factor that is ≤ 1. Let us define an *effective J* in large-scale yielding that relates the area inside the principal stress contour to the small-scale yielding case

$$A(\sigma_1/\sigma_0) = \frac{(J_{ssy})^2}{\sigma_0^2} h(\sigma_1/\sigma_0) \tag{13}$$

where J_{ssy} is the effective small-scale yielding J, that is, the value of J that would result in the area $A(\sigma_1/\sigma_o)$ if the structure were large relative to the plastic zone. Therefore, the ratio of the applied J to the effective J is given by

$$\frac{J}{J_{ssy}} = \sqrt{\frac{1}{\phi}} \tag{14}$$

The small scale yielding J value (J_{ssy}) can be viewed as *the effective driving force for cleavage*, while J is the *apparent* driving force. Alternatively, *J_{ssy} can be viewed as the amplitude of the σ_1 field ahead of the crack.*

The procedure for determining J_{ssy} for cleavage fracture is illustrated schematically in Fig. 2. The dimensionless quantity $A\sigma_0^2/J^2$ is plotted against σ_1/σ_0 for both the small-scale yielding solution (that is, infinite body) and a finite size specimen. In the latter case, each value of J gives a different curve, because ϕ varies during deformation; the small-scale yielding curve is invariant, since $\phi = 1$. The ratio J/J_{ssy} is determined for a given J and σ_1 value through the ratio of $A\sigma_0^2/J^2$ values for small- and large-scale yielding, as illustrated in Fig. 2*B*. The J/J_{ssy} ratio is insensitive to the σ_1 at which contour areas are evaluated [*1*]. Thus it is possible to define a single J/J_{ssy} ratio for the specimen and loading of interest.

The J/J_{ssy} ratio quantifies the size dependence of cleavage fracture toughness. Consider, for example, a finite size specimen that fails at $J_c = 200$ kJ/m^2. If the J/J_{ssy} ratio were 2.0 in this case, a very large specimen made from the same material would fail at $J_c = 100$ kJ/m^2.

Ductile Fracture Criterion

The microscopic events that lead to ductile fracture differ considerably from the micromechanism of cleavage. Consequently, different failure criteria are needed for the two fracture mechanisms. While few would argue with the assumption that cleavage is stress-controlled, a universally accepted mathematical model for ductile fracture in metals is not yet available.

Ductile fracture involves three stages: void nucleation, void growth, and void coalescence. Failure occurs after very large local plastic strains. The stress also plays a role in the failure

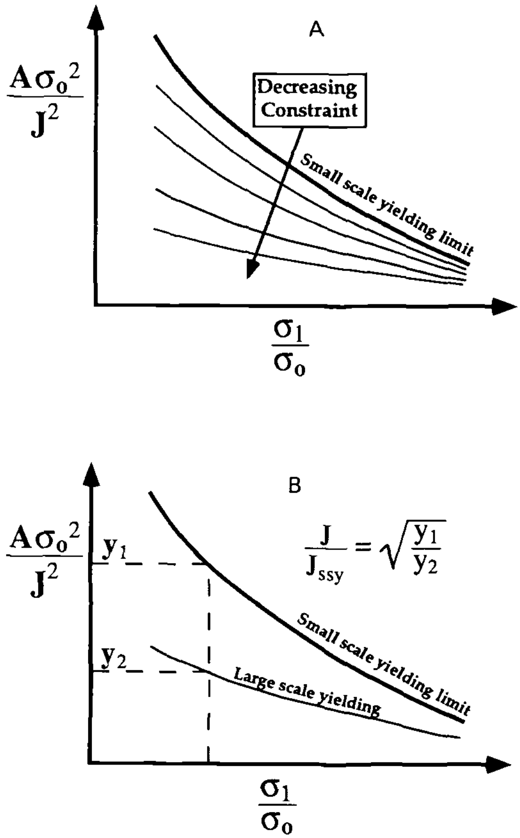

FIG. 2—*Procedure for determining the effective small-scale yielding* J *integral,* J_{ssy} *for cleavage.*

process: void nucleation and growth are aided by the hydrostatic component of the stress tensor. Thus an appropriate failure criterion for ductile fracture in metals must, at a minimum, incorporate both plastic strain and hydrostatic stress.

Rice and Tracey [*18*] developed a model for the growth of an initially spherical void in an infinite medium. Based on numerical calculations with their model, they developed the following semiempirical equation for void growth

$$\ln\left(\frac{\overline{R}}{R_0}\right) = 0.283 \int_0^{\bar{\varepsilon}_{pl}} \exp\left(\frac{1.5\sigma_m}{\sigma_{YS}}\right) d\bar{\varepsilon}_{pl} \tag{15}$$

where $\overline{R}$ is the nominal void radius, R_0 is the initial radius, and $\bar{\varepsilon}_{pl}$ is the equivalent plastic strain. Although the void is initially spherical, it becomes ellipsoidal with plastic deformation. The nominal radius corresponds to the average of the radii in the three principal directions. A number of researchers, including d'Escata and Devaux [*19*], have modified Eq 15 for strain hardening by replacing σ_{YS} with σ_e, the von Mises stress.

The modified Rice and Tracey equation can be used as a ductile fracture criterion by assuming that failure occurs when the nominal void radius reaches a critical value. Let us define a local damage integral as follows

$$\Phi = \int_0^{\bar{\varepsilon}_{pl}} \exp\left(\frac{1.5\sigma_m}{\sigma_e}\right) d\bar{\varepsilon}_{pl} \tag{16}$$

Furthermore, let us assume that ductile crack growth occurs when $\Phi = \Phi_c$ at a critical distance ahead of the crack tip. For the present study, it was necessary to evaluate Φ at r greater than twice the CTOD because the finite element analyses utilized small strain theory.

For purposes of evaluating the effect of crack tip triaxiality on ductile initiation toughness, it is not necessary to know the absolute value of Φ_c for a given material. It is sufficient merely to evaluate the distribution of Φ ahead of the crack tip and compare this distribution to the small-scale yielding limit. This procedure is analogous to the approach that was applied to cleavage fracture, where toughness was scaled by comparing σ_1 distributions for finite bodies with the small-scale yielding limit.

It is possible to define an effective J for ductile initiation, as Fig. 3 illustrates. The damage integral, Φ, is plotted against $r\sigma_0/J$ (at a fixed θ) for both a finite body and the small-scale yielding limit. The J/J_{ssy} ratio for ductile initiation is inferred by scaling the two curves on the horizontal axis. This scaling is performed at a fixed Φ value; ideally, the J/J_{ssy} ratio should not depend on the choice of Φ.

In this study Φ was plotted at $\theta = \pi/4$ (45°), which corresponds to the plane on which Φ is at a maximum. The J/J_{ssy} ratio was evaluated at a fixed Φ, which was chosen to correspond to $r\sigma_0/J$ ratios ranging from 1 to 2. The J/J_{ssy} ratio was relatively insensitive to the Φ at which the curves were scaled.

Results

Cleavage Fracture Toughness

Figure 4*A* illustrates the effect of large-scale yielding on nondimensional principal stress contours for an SE(B) specimen with $n = 10$ and $a/W = 0.5$. Although the contours maintain a constant shape, their size (when normalized by J) decreases with plasticity. (The absolute size of the contour actually increases with J but at a slower rate than predicted from Eq 9.) Figure 4*B* shows that the contours coincide for a constant σ_1 when the data are normalized by the equivalent small-scale yielding J values, J_{ssy}, for cleavage.

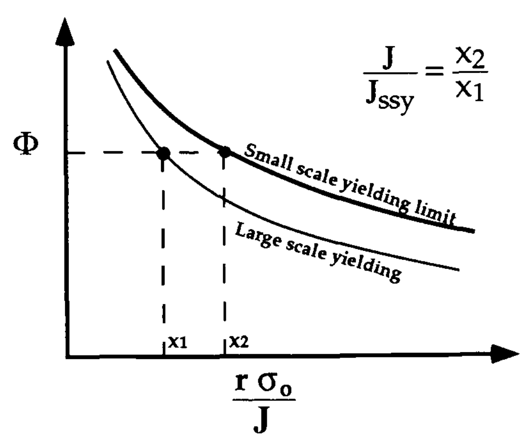

FIG. 3—*Procedure for determining the effective small-scale yielding* J *integral,* J_{ssy} *for ductile tearing.*

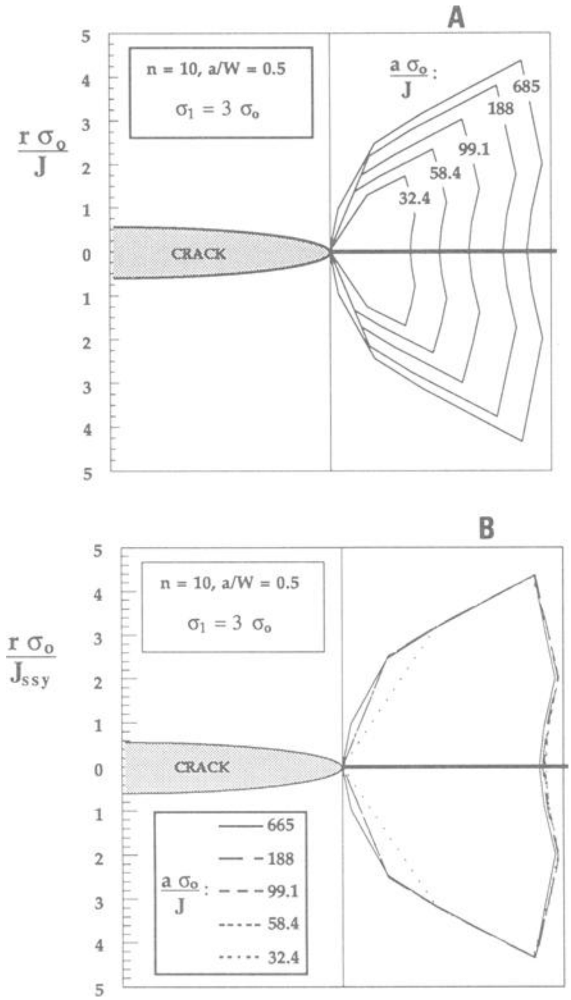

FIG. 4—*Principal stress contours for* n = *10 and* a/W = *0.5 in an SE(B) specimen.* (a) *Normalized by* J, *and* (b) *Normalized by* J_{ssy} *for cleavage.*

Figure 5 illustrates the effect of a/W and specimen size on the J/J_{ssy} ratio for an SE(B) specimen with $n = 10$. Since a critical value of J_{ssy} represents a size-independent cleavage toughness, the J/J_{ssy} ratio quantifies the geometry dependence of J_c, the measured fracture toughness. For the deeply notched specimens ($a/W = 0.5$), J_c approaches the small-scale yielding value when the ratio $a\sigma_0/J$ is greater than ~200, but the shallow-notched specimens do not produce small-scale yielding behavior unless the specimen is very large relative to J/σ_0.

The effective driving force for cleavage, J_{ssy}, is plotted against the apparent driving force, J, in Fig. 6. The dashed line represents the small-scale yielding limit, where $J = J_{ssy}$ by definition. Note that the horizontal axis is expanded relative to the vertical axis for clarity. Each of the curves in Fig. 6 agrees with the small-scale yielding limit at low J values, but deviates as J increases. The deviation from small-scale yielding occurs more rapidly and at lower J values in shallow-notched specimens and in low-hardening materials. Under large-scale yielding con-

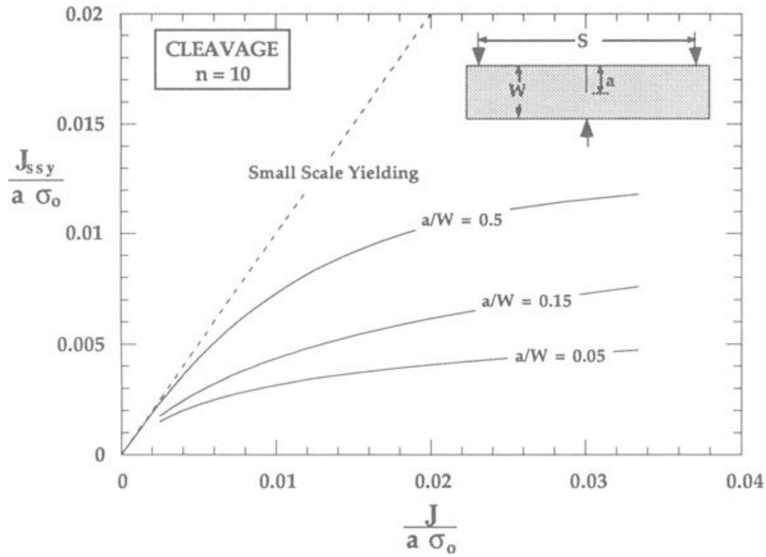

FIG. 5—*Effect of crack length and* a/W *on the* J/J_{ssy} *ratio for cleavage fracture in an SE(B) specimen.*

ditions, the effective driving force saturates at a relatively constant value; further increases in J do not significantly affect J_{ssy}. Once a specimen reaches the saturation value of J_{ssy}, the likelihood of cleavage fracture with further loading decreases considerably. Such a specimen could cleave only if the crack grew by ductile tearing and sampled a critical microstructural feature.

Figure 7 is a plot of J/J_{ssy} as a function of n and specimen size, which is normalized by flow

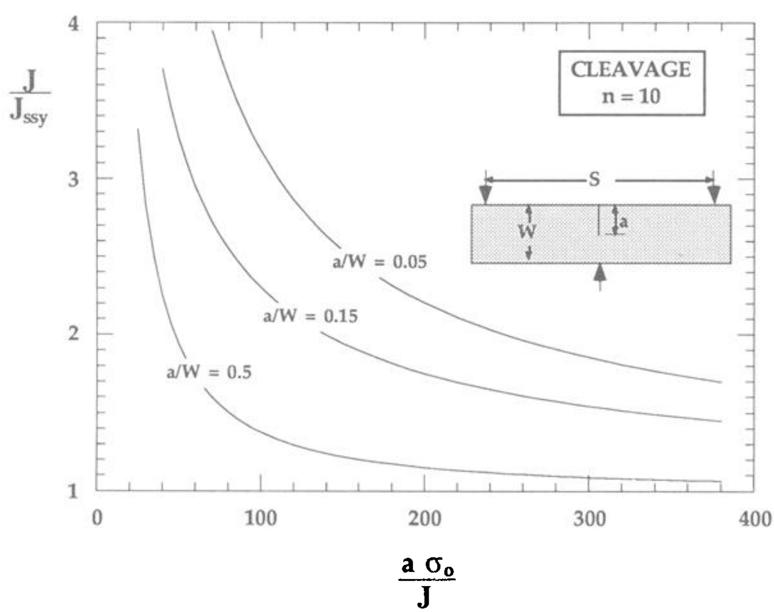

FIG. 6—*Comparison of effective and apparent driving force for cleavage fracture in an SE(B) specimen.*

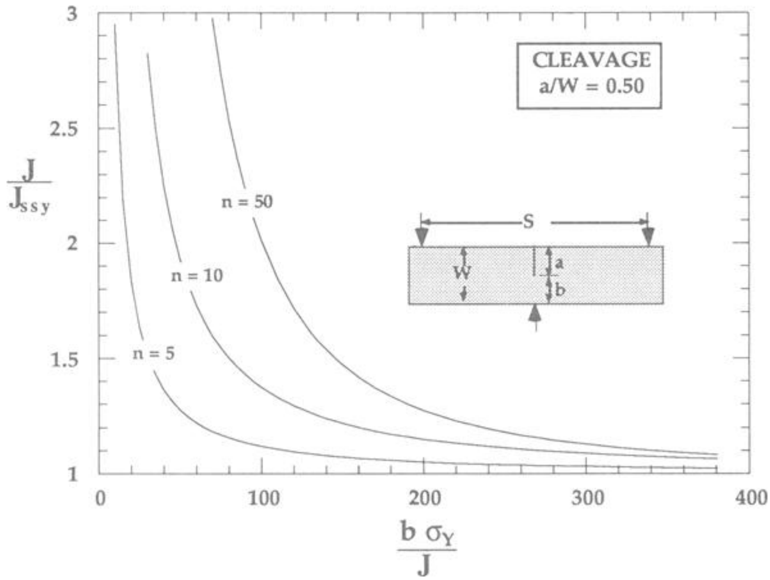

FIG. 7—J/J_{ssy} *for cleavage as a function of strain hardening,* J, *and flow stress.*

stress in order to be consistent with the ASTM E 813 size criteria (Eq 1) and to reduce the effect of strain hardening on the size dependence. The flow stress for the Ramberg-Osgood materials was estimated from the following relationship

$$\sigma_Y = \frac{\sigma_0}{2}\left[1 + \frac{\left(\frac{N}{0.002}\right)^N}{\exp(N)}\right] \tag{17}$$

where $N = 1/n$. Equation 17 was derived by solving for the tensile instability point in Eq 3, converting true stress to engineering stress, and averaging σ_0 and the estimated tensile strength. The J/J_{ssy} ratio becomes relatively flat and approaches 1.0 when the $b\sigma_Y/J$ ratio exceeds ~200, although the rate at which each curve approaches the small-scale yielding limit depends on the hardening exponent.

Figures 5 to 7 provide the capability to correct cleavage fracture toughness for constraint loss. Given the measured toughness, specimen size, and material hardening characteristics, it is possible to estimate the toughness of an infinite specimen.

Fracture toughness data recently published by Sorem *[20]* were used to assess the ability of these analyses to characterize constraint loss. Sorem performed fracture toughness tests on SE(B) specimens of A36 (UNS K02600) steel over a range of temperatures. The specimens were square section (B by B) with the thickness equal to 31.8 mm (1.25 in.). Two aspect ratios were tested: $a/W = 0.50$ and $a/W = 0.15$. Because the material is a mild steel that exhibits a yield point, the flow behavior does not match the Ramberg-Osgood expression perfectly, but a slight deviation from the Ramberg-Osgood idealization should not affect the results significantly. Based on the σ_{TS}/σ_{YS} ratio and Eq 17, we estimated $n = 6$ for this material in the temperature range of interest.

Figure 8 shows J_c data for the A36 steel at two temperatures in the transition region. The

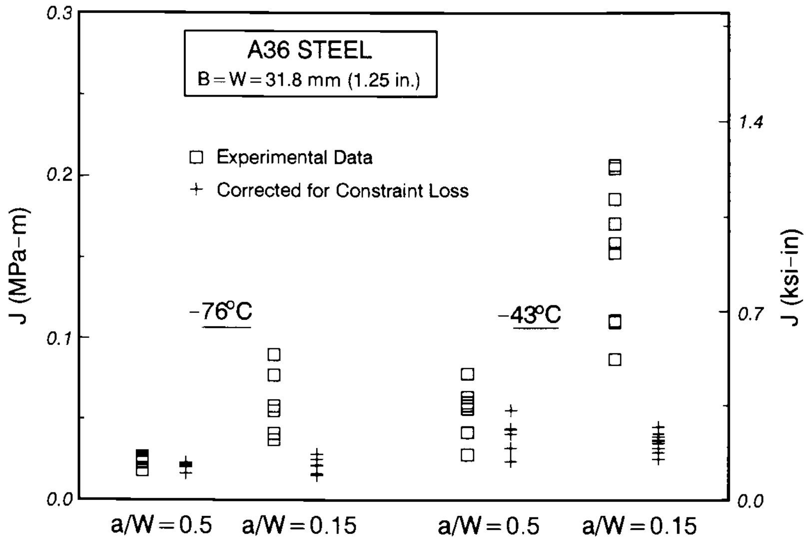

FIG. 8—*Comparison of* J_c *values for cleavage in A 36 steel, with* J_c *corrected for constraint loss. Data were obtained from Sorem* [19].

solid diamonds represent the experimental data, while the crosses indicate predicted small-scale yielding values. Every specimen but one (the highest J_c value for $a/W = 0.15$ at $-43°C$) failed by cleavage without significant prior stable crack growth. At both temperatures, the shallow-notched specimens have a higher apparent toughness than the deep-notched specimens, but the corrected values agree reasonably well. Relatively small corrections are needed for specimens with $a/W = 0.50$, but the constraint correction has a major effect when $a/W = 0.15$. The small scale yielding J_c are less scattered than the uncorrected data; for a given data set, the coefficient of variation decreases and the Weibull slope increases when the J_c data are corrected down to their J_{ssy} values [*1,2*].

Initiation of Ductile Tearing

Figures 9 and 10 show the computed J/J_{ssy} values for ductile initiation in materials with $n = 5$ and $n = 10$. For the high-hardening material ($n = 5$), higher J/J_{ssy} values are predicted for the shallow-notched specimens, which have experienced a significant loss in crack tip triaxiality. The effect is reversed for $n = 10$ (Fig. 10), however. The curves in Fig. 10 are inconsistent with experimental observation; shallow-notched specimens tend to exhibit higher resistance to ductile crack growth than do deep-notched specimens [*21*].

Figure 11 illustrates the predicted effect of strain-hardening exponent on the J/J_{ssy} ratio for $a/W = 0.5$. The analysis predicts that ductile fracture toughness in low-hardening materials is more sensitive to triaxiality, which is the same trend that was observed for cleavage fracture (Fig. 7). According to this analysis, a specimen that barely meets the size requirements of ASTM E 813-87 will exhibit a J_{IC} value that is approximately 30% greater than the J_{IC} that would be measured in an infinite body, provided the specimen is made from a low- or medium-hardening material.

Cleavage fracture is much more sensitive to specimen dimensions than ductile fracture, as Fig. 12 illustrates. A slight relaxation in triaxiality has a significant effect on cleavage fracture

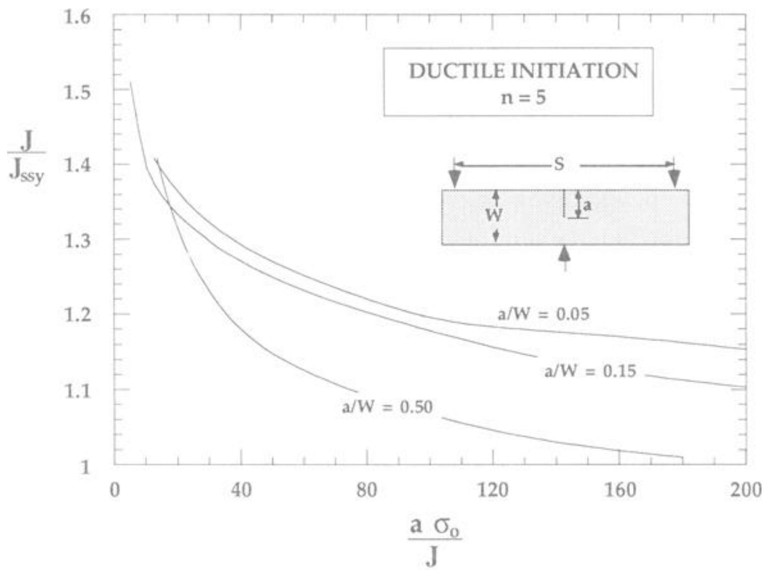

FIG. 9—J/J_{ssy} *ratio for ductile initiation in a high-hardening material.*

toughness, but the effect on ductile initiation toughness is minimal. This phenomenon, which is consistent with experimental observations [*20,21*], can be explained by considering the assumed failure criterion for ductile fracture (Eq 16). Note that Φ depends on both the hydrostatic stress and the equivalent plastic strain. When there is a relaxation in triaxiality, σ_m decreases (by definition), but the plastic strain at a given J value is greater than it is under fully

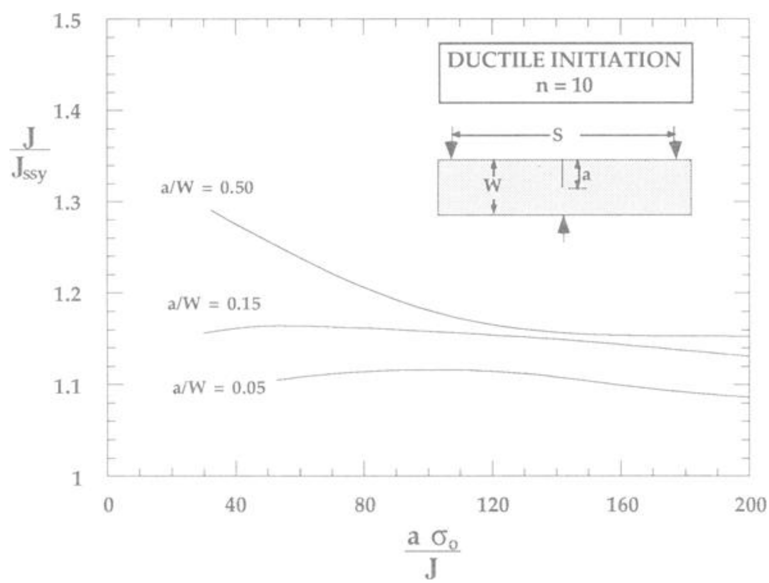

FIG. 10—J/J_{ssy} *ratio for ductile initiation in a medium-hardening material.*

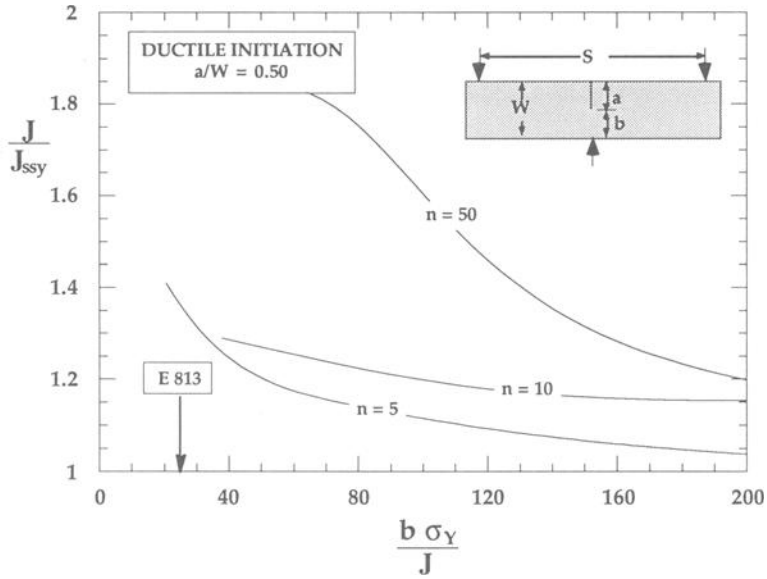

FIG. 11—*Effect of specimen size and strain hardening exponent on the* J/J_{ssy} *ratio for ductile initiation.*

constrained conditions. Thus there are two competing effects that tend to cancel one another, with the result that ductile fracture toughness increases only slightly when constraint relaxes.

Discussion

The micromechanics approach to two-parameter fracture mechanics provides a framework for predicting the effect of specimen dimensions on fracture toughness. This methodology appears to work very well for cleavage fracture toughness, but further work is needed to obtain reliable predictions of the effect of triaxiality on microvoid nucleation, growth, and coalescence.

Cleavage Toughness

Cleavage fracture is stress controlled, and therefore cleavage toughness is highly sensitive to crack tip triaxiality. Specimens must be approximately eight times as large as required by ASTM E 813-87 in order for critical J values for cleavage to satisfy the single-parameter assumption. When the single-parameter assumption is violated, it is possible to correct J_c values down to their equivalent small-scale yielding values. Figure 8 shows that this correction removes the geometry dependence from cleavage fracture toughness data.

The small scale yielding $J(J_{ssy})$ represents the effective driving force for cleavage. A critical value of J_{ssy} corresponds to the fracture toughness in a very large structure. In this limiting case, the structure would be linear elastic and the fracture toughness could also be described by $K_{IC} = \sqrt{EJ_{ssy}/(1 - \nu^2)}$. Thus J_{ssy} values can be converted to equivalent K_{IC} values that can be applied to large structures subject to linear elastic loading.

So far, our research has focused primarily on the effect of in-plane dimensions on fracture toughness; the effect of thickness requires further study. Recent three-dimensional finite element results [*22*] show that specimens can maintain nearly plane strain conditions at mid-

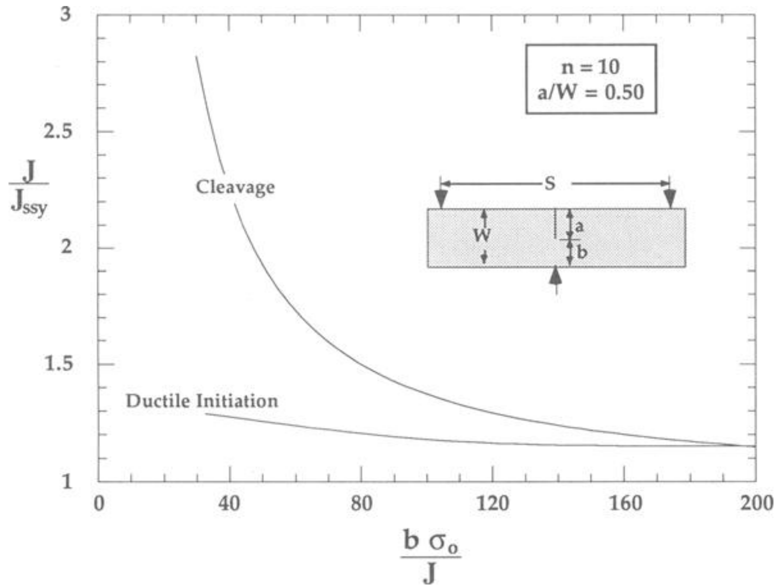

FIG. 12—*Comparison of* J/J_{ssy} *ratios for cleavage and ductile initiation.*

thickness to relatively high J values, but the size of the plane strain region decreases with plasticity. It should be possible to define an effective thickness, which equals the actual thickness for small-scale yielding but decreases with J. The effective thickness can then be taken into account through statistical models for cleavage fracture [*16,17*].

The effect of prior ductile crack growth also requires further study. The results presented in this article apply only to stationary cracks. Ductile crack growth affects the cleavage toughness in at least two ways: (1) the crack tip stress field ahead of a growing crack is undoubtedly different from that of a stationary crack, and (2) the growing crack samples more material than a stationary crack, increasing the likelihood of finding a critical cleavage trigger.

Ductile Fracture

The predictions of the size dependence of ductile fracture must be regarded as preliminary, since these results have not been validated experimentally. Some of the predictions contradict what one might expect to observe through experiment. Figure 10, for example, predicts that the ductile fracture toughness *decreases* as triaxiality is relaxed. While such behavior is possible in principle, the authors are not aware of any experimental data that exhibit this trend.

The ductile fracture analysis could be improved by performing finite element analyses that incorporate large strain theory. The present analysis, based on small strain theory, precluded examining stresses and strains where $r\sigma_0/J < 1$. While this restriction did not handicap the cleavage analysis (since cleavage initiates at a finite distance from the crack tip), the important microscopic events that lead to ductile crack growth occur very close to the tip [*23*].

Another shortcoming of the present analysis is the assumed failure criterion. The modified Rice and Tracey equation considers only the growth of a single void in an infinite medium; this model does not consider void nucleation, nor does it take account of void interactions that lead to local instabilities between voids. Moreover, we assumed failure occurs when the nominal radius of an ellipsoidal void reaches a critical value. Since the shape of the void is a function of the level of stress triaxiality, it is unlikely that an average or nominal void radius at failure is a material constant. A better failure criterion for ductile initiation is definitely needed.

Comparison with Continuum Approaches

The micromechanics approach is a two-parameter methodology, where J and J_{ssy} are necessary to define the fracture behavior. It is possible to relate this methodology to the J-Q approach described earlier. By assuming that Eq 5 defines the neartip stress field, we can define J_{ssy} for cleavage fracture as follows

$$\frac{\sigma_1}{\sigma_0} = \left(\frac{J}{\alpha\varepsilon_0\sigma_0 I_n r}\right)^{1/n+1} \tilde{\sigma}_1(n,\theta) + Q = \left(\frac{J_{ssy}}{\alpha\varepsilon_0\sigma_0 I_n r}\right)^{1/n+1} \tilde{\sigma}_1(n,\theta) \tag{18}$$

Rearranging gives

$$\frac{J}{J_{ssy}} = \left[1 - Q\left(\frac{\sigma_0}{\sigma_1}\right)_{\text{HRR}}\right]^{n+1} \tag{19}$$

Equation 19 defines a J-Q failure locus, that is, an explicit expression for Eq 6. This relationship, however, only applies to fracture mechanisms that are controlled by σ_1. A material whose fracture behavior is strain-controlled or controlled by a combination of stress and strain would exhibit a different J-Q failure locus. According to Fig. 10, for example, cleavage is more sensitive to specimen size than is ductile initiation.

The effect of micromechanism on the J-Q failure locus can be understood by performing a simple parametric study. Consider a local damage parameter of the form

$$\Phi = \left(\frac{\sigma_m}{\sigma_0}\right)^{\beta} \bar{\varepsilon}_{pl}^{1-\beta} \qquad (0 \leq \beta \leq 1) \tag{20}$$

As with the Rice and Tracey criterion for ductile fracture (Eq 16), failure is assumed when $\Phi = \Phi_c$ at a specified distance ahead of the crack tip, where Φ_c is a material constant. The exponent β characterizes the relative influence of stress and plastic strain on local fracture; $\beta = 1$ corresponds to stress controlled fracture, while $\beta = 0$ describes a material that fractures at a critical strain, independent of the hydrostatic stress.

Equation 20 was used in conjunction with finite element results of O'Dowd and Shih [*10,11*] to predict the effect of triaxiality on various failure mechanisms. Stresses and strains were evaluated at $\theta = \pi/4$. The critical distance at which Φ was evaluated at $r\sigma_0/J = 2$, although the predictions were insensitive to the choice of distance.

Figure 13 is a plot of J-Q failure loci for $\beta = 0$, 0.25, 0.5, 0.75, and 1.0. The critical J is normalized by J_0, the critical J at $Q = 0$. Note that stress-controlled failure is highly sensitive to triaxiality while strain-controlled failure is relatively insensitive to Q. When $\beta < 0.5$, the critical J value actually increases with increasing triaxiality, a behavior that is not normally observed in real materials.

Equation 20 assumes that fracture is controlled only by the current values of stress and strain. In some cases, however, prior strain history may influence fracture behavior. Equation 16 is an example of such a failure criterion. Figure 14 shows the predicted failure loci for two configurations. In this case, Φ was evaluated at $r\sigma_0/J = 1$. Because the variation in Q with loading history differs for the two configurations (Fig. 1), the J-Q failure locus is geometry

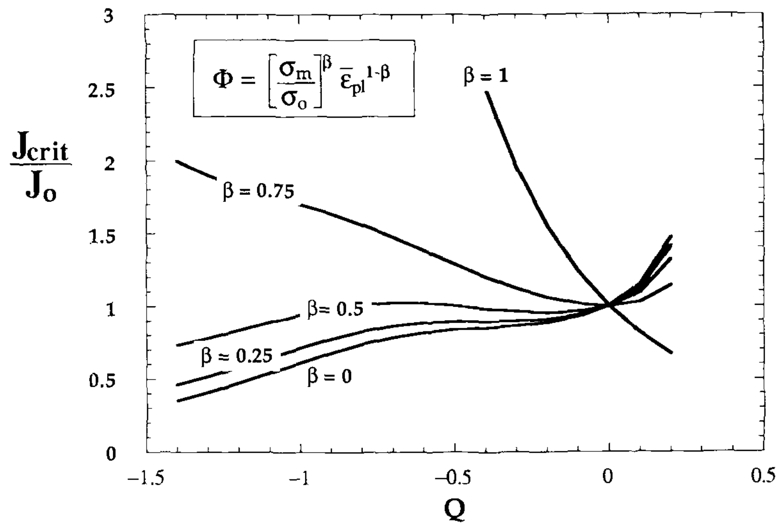

FIG. 13—J-Q *failure loci for various failure mechanisms, ranging from stress-controlled to strain-controlled fracture (β = 1 and β = 0, respectively.)*

dependent. Thus J and Q may not uniquely characterize fracture in materials whose failure mechanism depends on deformation history.

The foregoing exercise was intended to demonstrate that two-parameter approaches based on continuum theory and micromechanics are complementary. The continuum approaches are descriptive rather than predictive. That is, these methodologies describe the near-tip fields but they cannot predict fracture. A fracture toughness result from a laboratory specimen cannot be applied to a structure unless both configurations experience the same level of crack tip

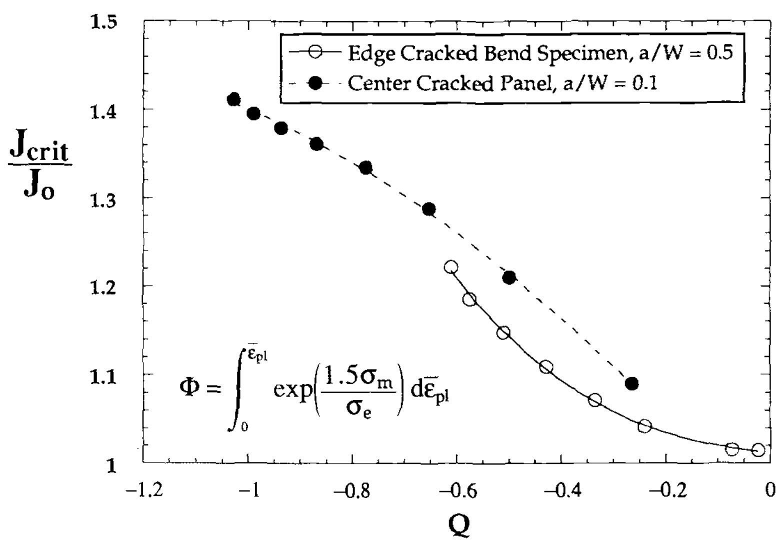

FIG. 14—J-Q *failure loci for fracture controlled by a hole growth mechanism.*

triaxiality. In principle, it is possible to determine a *J-Q* (or *K-T*) failure locus by performing a series of experiments on specimens with varying levels of crack tip constraint. Such an approach may not be practical, however, because of the enormous testing requirements. The *J-Q* failure locus would vary with temperature, material, and micromechanism. The inherent scatter in fracture toughness data would preclude determining a unique *J-Q* curve for a given material and temperature. In addition, the *J-Q* failure locus may depend on deformation history in some cases, as Fig. 14 illustrates; it would not be sufficient merely to match the *Q* or *T* values at failure in the laboratory specimen and the structure.

The micromechanics approach provides an alternative to unruly fracture toughness test matrices. This methodology *predicts* the effect of triaxiality on fracture behavior. The predictions can be expressed in terms of *J-Q* failure locii, as in Figs. 13 and 14, or the effect of specimen dimensions on fracture toughness can be inferred directly from plots such as Figs. 5 to 7 and Figs. 9 to 12.

Conclusions

1. A two-parameter approach that considers the micromechanism of failure provides framework for predicting the effect of triaxiality on fracture toughness.
2. While the micromechanics approach appears to work very well for cleavage fracture, improved failure criteria for microvoid coalescence are needed before this methodology can provide accurate predictions for ductile fracture.
3. Two-parameter approaches based on continuum theory can describe crack tip triaxiality, but these methods cannot predict the effect of triaxiality on fracture toughness.

References

[1] Anderson, T. L. and Dodds, R. H., Jr., "Specimen Size Requirements for Fracture Toughness Testing in the Ductile-Brittle Transition Region," *Journal of Testing and Evaluation*, Vol. 19, 1991, pp. 123–134.

[2] Dodds, R. H. Jr., Anderson, T. L., and Kirk, M. T., "A Framework to Correlate a/W Effects on Elastic-Plastic Fracture Toughness (J_c)," *International Journal of Fracture*, Vol. 88, 1991, pp. 1–22.

[3] Williams, M. L., "On the Stress Distribution at the Base of a Stationary Crack," *Journal of Applied Mechanics*, Vol. 24, 1957, pp. 109–114.

[4] Larsson, S. G. and Carlsson, A. J., "Influence of Non-Singular Stress Terms and Specimen Geometry on Small-Scale Yielding at Crack Tips in Elastic-Plastic Materials," *Journal of the Mechanics and Physics of Solids*, Vol. 21, 1973, pp. 263–278.

[5] Rice, J. R., "Limitations to the Small-Scale Yielding Approximation for Crack Tip Plasticity," *Journal of the Mechanics and Physics of Solids*, Vol. 22, 1974, pp. 17–26.

[6] Bilby, B. A., Cardew, G. E., Goldthorpe, M. R., and Howard, I. C., *Size Effects in Fracture*, Institute of Mechanical Engineers, London, 1986, pp. 37–46.

[7] Betegon, C. and Hancock, J. W., "Two Parameter Characterisation of Elastic-Plastic Crack Tip Fields," *Journal of Applied Mechanics*, Vol. 58, 1991, pp. 263–277.

[8] Wang, Y.-Y., "On the Two-Parameter Characterization of Elastic-Plastic Crack Front Fields in Surface-Cracked Plates," this publication.

[9] Li, Y. C. and Wang, T. C., *Scientia Sinica (Series A)*, Vol. 29, 1986, pp. 941–955.

[10] O'Dowd, N. P. and Shih, C. F., "Family of Crack-Tip Fields Characterized by a Triaxiality Parameter: Part I-Structure of Fields," *Journal of the Mechanics and Physics of Solids*, Vol. 39, 1991, pp. 989–1015.

[11] O'Dowd, N. P. and Shih, C. F., "Family of Crack-Tip Fields Characterized by a Triaxiality Parameter: Part II-Fracture Applications," to appear in *Journal of the Mechanics and Physics of Solids*, 1992.

[12] Hutchinson, J. W., "Singular Behavior at the End of a Tensile Crack Tip in a Hardening Material," *Journal of the Mechanics and Physics of Solids*, Vol. 16, 1968, pp. 13–31.

[13] Rice, J. R. and Rosengren, G. F., "Plane Strain Deformation Near a Crack Tip in a Power-Law Hardening Material," *Journal of the Mechanics and Physics of Solids*, Vol. 16, 1968, pp. 1–12.

[14] McMeeking, R. M. and Parks, D. M., "On Criteria for *J*-Dominance of Crack Tip Fields in Large-Scale Yielding," *Elastic-Plastic Fracture, ASTM STP 668*, American Society for Testing and Materials, Philadelphia, 1979, pp. 175–194.
[15] Shih, C. F., Moran, B., and Nakamura, T., "Energy Release Rate Along a Three-Dimensional Crack Front in a Thermally Stressed Body," *International Journal of Fracture*, Vol. 30, 1986, pp. 79–102.
[16] Anderson, T. L. and Stienstra, D., "A Model to Predict the Sources and Magnitude of Scatter in Toughness Data in the Transition Region," *Journal of Testing and Evaluation*, Vol. 17, 1989, pp. 46–53.
[17] Wallin, K., "Statistical Aspects of Constraint with Emphasis to Testing and Analysis of Laboratory Specimens in the Transition Region," this publication.
[18] Rice, J. R. and Tracey, D. M., "On the Ductile Enlargement of Voids in Triaxial Stress Fields," *Journal of the Mechanics and Physics of Solids*, Vol. 17, 1969, pp. 201–217.
[19] d'Escata, Y. and Devaux, J. C., "Numerical Study of Initiation, Stable Crack Growth, and Maximum Load with a Ductile Fracture Criterion Based on the Growth of Holes," *Elastic-Plastic Fracture, ASTM STP 668*, American Society of Testing and Materials, Philadelphia, 1979, pp. 229–248.
[20] Sorem, W. A., "The Effect of Specimen Size and Crack Depth on the Elastic-Plastic Fracture Toughness of a Low-Strength High-Strain Hardening Steel," Ph.D. dissertation, The University of Kansas, Lawrence, KS, May 1989.
[21] Towers, O. L. and Garwood, S. J., "Influence of Crack Depth on Resistance Curves for Three-Point Bend Specimens in HY130," *Fracture Mechanics: Seventeenth Volume, ASTM STP 905*, American Society for Testing and Materials, Philadelphia, 1986, pp. 454–484.
[22] Narasimhan, R. and Rosakis, A. J., "Three Dimensional Effects Near a Crack Tip in a Ductile Three Point Bend Specimen, Part I: A Numerical Investigation," Report SM 88-6, California Institute of Technology, Division of Engineering and Applied Science, Pasadena, CA, Jan. 1988.
[23] Knott, J. F., "Micromechanisms of Fracture and the Fracture Toughness of Engineering Alloys," *Fracture 1977*, Vol. 1, ICF4, Waterloo, Canada, June 1977, pp. 61–91.

John D. G. Sumpter[1]

An Experimental Investigation of the *T* Stress Approach

REFERENCE: Sumpter, J. D. G., **"An Experimental Investigation of the *T* Stress Approach,"** *Constraint Effects in Fracture, ASTM STP 1171,* E. M. Hackett, K.-H. Schwalbe, and R. H. Dodds, Eds., American Society for Testing and Materials, 1993, pp. 492–502.

ABSTRACT: Many investigations have identified geometry dependence of J_c at initiation of cleavage fracture and J_i at initiation of fibrous tearing. This geometry dependence is predictable from elastic-plastic finite element analyses, which show that the crack tip stress-strain distribution is not always uniquely defined by J. This paper investigates the ability of the elastic T stress to explain experimentally observed trends in J_c with changes in specimen geometry. Data on mild steel three-point bend and center-cracked tension specimens are presented.

KEY WORDS: fracture, J, T stress, mild steel, three-point bend specimens, center-cracked tension specimen

The limited ability of a single parameter such as J to fully characterize crack tip conditions irrespective of geometry and load level has been recognized for many years [*1,2*]. In practical terms this is evidenced by a tendency for a given material to show variations in the value of J at the onset of fracture (J_c for cleavage, J_i for fibrous tearing) as the loading configuration is changed. To avoid this geometry dependence, testing standards usually specify size requirements the specimen must meet for the measurement of toughness to be considered valid. Thus, for valid J_{IC} measurement [ASTM Test for J_{IC}, a Measure of Fracture Toughness (E 813-89)], it is required that

$$b, B > \frac{25 J_{IC}}{\sigma_y} \tag{1}$$

where b is the initial uncracked ligament, B is the thickness of the specimen, and σ_y is the yield stress. No testing standards yet exist for measurement of J_c, but in a recent paper [*3*] Anderson and Dodds have suggested

$$a, b, B > \frac{200 J_c}{\sigma_y} \tag{2}$$

where a is the initial crack length. It should be noted that Eqs 1 and 2 are specific to deeply notched specimens loaded predominately in bending. Meeting the same conditions in a tension specimen, or with a shallow crack, will not necessarily ensure that failure occurs at the same value of J_c or J_i. It is known from finite element analysis that both shallow crack and

[1] Senior principal scientific officer, Admiralty Research Establishment, St. Leonard's Hill, Dunfermline, Scotland, United Kingdom KY11 5PW.

tension configurations give less severe crack tip stress triaxiality than deeply notched bending at a given value of J [2,4]. Because the main purpose of fracture mechanics is to allow extrapolation of results from one geometry to another (particularly from the specimen to the structure), the geometry dependence of J_c and J_i is a severe drawback. The current approach is to argue that the deeply notched bend specimen provides a safe lower bound toughness. While this is adequate in some circumstances, it may also result in the unnecessary rejection of a material or the imposition of costly nondestructive evaluation and repair policies.

In the past few years, a technology has begun to emerge that offers the hope of removing these conservatisms and allowing a more precise prediction of structural failure conditions irrespective of geometry and load level. This new approach is centered on the use of a two-parameter description of the crack tip stress-strain state [5–7]. J is retained as a measure of the crack tip deformation state, but a second parameter, known as the T stress, is added to characterize fully the crack tip stress state. The T stress is the first nonsingular term, representing the constant stress parallel to the crack flanks, in the Williams [8] expansion of the crack tip stress distribution. The magnitude of the T stress varies with remotely applied stress, and its geometry dependence is best indexed by a nondimensional geometry factor, β, which has the form

$$\beta = T\frac{\sqrt{\pi a}}{K} \tag{3}$$

or

$$\frac{T}{\sigma_y} = \frac{\beta Y \sigma}{\sigma_y} \tag{4}$$

where K is the elastic stress intensity factor, Y is the geometric function of a/W associated with K, and σ is the nominal applied stress. The T stress parallel to the crack flank may be tensile (β positive) or compressive (β negative). Positive β values occur in deeply notched bending and promote high crack tip triaxiality. Negative β values are associated with shallow cracks and with tension loading and depress the maximum tensile stress achievable at the crack tip. These trends are in qualitative agreement with the observed tendency of shallow cracks and tension loading to give elevated toughness compared to deeply cracked bending.

The necessary steps to perform a structural analysis by the J plus T stress approach are as follows:

1. Perform an elastic finite element (FE) analysis of the structure to determine the nondimensional biaxiality factor, β, and hence T, as a function of crack size.
2. Identify a range of specimen geometries that encompass the same T stress range as the structure.
3. Determine the J_c (or J_i) versus T stress failure scatterband for the material of interest.
4. Superimpose the structurally applied J (elastic-plastic calculation) for given crack sizes as a function of T stress.
5. Determine structural failure stress or strain for each crack size by the intersection of the applied J lines with the envelope around the experimental J_c (or J_i) versus T stress scatterband from the laboratory tests.

The major advantage of this approach is that the constraint index for the structure, β, can be determined elastically by a universally available method (elastic FE analysis). Elastic-plastic J estimates can be made readily for most structural configurations.

The T stress is a purely elastic parameter. The idea that it will successfully index constraint after extensive plasticity rests on empirical observation of crack tip stresses in elastic-plastic finite element studies [4–7]. The next obvious requirement is an experimental demonstration that the J_c plus T stress approach does provide an adequate prediction of geometry-dependent toughness trends. This paper describes an investigation carried out on mild steel plate with this aim in mind.

Ultimately, for structural application, it will be necessary to consider the additional effect of the out-of-plane stress (S stress) on fracture behavior. Theoretical modelling on this topic has already begun. The first priority is, however, a demonstration that the T stress is useful in rationalizing the effect of in-plane geometry on J_c for through-thickness cracks under similar conditions of out-of-plane constraint.

Experimental Philosophy

Finite element studies [5] have shown that a positive T stress has little effect on the crack tip stress state. No matter how positive the T stress, the crack tip stress distribution remains close to that predicted in small-scale yielding at the same J value, except after very extensive plasticity ($J > 0.04\sigma_y b$). As the T stress becomes negative, however, a gradual deviation of crack tip stresses below the small-scale yielding field is observed. The more negative the T stress, the more rapidly crack tip stress elevation falls as loading is increased beyond small-scale yielding and the lower the eventual stress elevation at high load levels. The effect of this on observed values of J at fracture will depend on the material and on the failure mode.

This paper is concerned only with cleavage fracture characterized by J_c. Cleavage fracture is triggered by achievement of a critical tensile stress normal to the crack plane a short distance ahead of the crack tip. Some sensitivity of J_c to the imposition of negative T stresses is consequently inevitable. Nevertheless, the degree of sensitivity will be dependent on a number of factors including work hardening, the ratio of cleavage stress to yield stress, and the distribution of cleavage initiation sites. It thus seems unlikely that there will be any universal, predictable interdependence between J_c and T. The shape of the J_c versus T failure envelope should be developed experimentally for each different material for which structural fracture analysis is required.

The most convenient way of altering the T stress in a series of laboratory tests is to alter the crack depth to specimen width ratio in three-point bending (3PB). As a/W is increased in a bend specimen, β moves from negative (around -0.4 when a/W is small) to positive (around $+1.0$ when a/W is large) [9]. It is thus possible to encompass a wide range of in-plane constraint conditions with a relatively simple change in specimen geometry. However, to achieve very negative T stresses it is necessary to test very shallow cracks ($a/W \leq 0.15$). This does pose practical problems, both in test technique and in interpretation of the data, which will be discussed later.

To prove that a new fracture mechanics theory works, it is desirable to test radically different specimen geometries. To highlight possible effects of geometry on J_c, it is necessary to test a configuration with negative T stress. Both these requirements are met by the center-cracked tension (CCT) specimen under uniaxial stress. The biaxiality factor, β, for this geometry lies between -1.0 and -1.1 for all a/W [10]. As will be shown, this makes it possible to have a shallow-cracked 3PB specimen and a deeply cracked CCT specimen with the same negative T stress at fracture. If it can be shown that these two totally different specimen geometries fail at the same value of J_c, the value of T as a constraint indexing parameter will have been demonstrated.

Determination of T Stress for 3PB and CCT Specimens

Since T stress is dependent on load level, the maximum value that can be developed in a given specimen depends on the plastic limit stress, σ_L [*11*].

1. For the CCT specimen (σ_L is the uniform remote stress at the end of the specimen)

$$\sigma_L = 1.155\sigma_y(1 - a/W) \tag{5}$$

2. For the 3PB specimen (σ_L is the nominal outer fiber bending stress in the absence of the crack)

$$\sigma_L = m\sigma_y(1 - a/W)^2 \tag{6}$$

where

$m = 2.184$ for $a/W > 0.295$
$m = 1.73(1 + 1.686a/W - 2.72a/W^2)$ for $a/W < 0.295$

Substituting σ_L and appropriate β and Y values in Eq 4 results in the T/σ_y values at limit load shown in Table 1. These values are for test planning purposes only. When analyzing actual test data, individual T/σ_y values are calculated for each specimen based on the observed failure load for that particular specimen. Hence, if a specimen fails well short of limit load, its absolute T/σ_y value will be less than that listed in Table 1. Conversely, if the specimen fails after its predicted limit load (based on yield stress), work hardening may cause the magnitude of T/σ_y to exceed the values in Table 1.

With this proviso it can be seen that testing 3PB specimens with a/W near 0.1, and CCT specimens with a/W near 0.7, offers a good chance that failure will occur at identical negative T stress.

Experimental Material

In choosing material for a preliminary study of the concepts described above the following requirements were felt to be important.

TABLE 1—*Values of* T/σ_y *at limit load for 3PB and CCT specimens.*

a/W	3PB	CCT
0.0	−0.87	−1.16
0.1	−0.59	−1.04
0.2	−0.31	−0.97
0.3	−0.10	−0.90
0.4	+0.06	−0.80
0.5	+0.17	−0.72
0.6	+0.25	−0.63
0.7	+0.29	−0.54
0.8	+0.30	−0.45

1. The material should cleave in all specimen configurations (J_c is easier to define than J_i).
2. The material should cleave before fibrous tearing so that J_c is unambiguously defined at the position of the initial crack tip.
3. Cleavage should occur after significant plasticity in specimens with negative T stresses.
4. It should not be necessary to cool the specimens to excessively low temperatures to induce cleavage (low temperatures pose significant testing problems with vertically mounted tension specimens).
5. There should be minimum scatter in J_c at a given test condition.
6. Failure in the tension specimens should occur within the available load capacity (2000 KN).

Having reviewed the available materials, it was considered that these requirements were most likely to be met by the use of a sample of old (circa 1960) 25-mm-thick mild steel plate. From previous studies it was known that this steel cleaved readily near ambient temperatures and that plasticity, but no fibrous tearing, occurred prior to cleavage. Chemical composition of the steel was 0.19 carbon, 0.59 manganese, 0.045 silicon, 0.01 phosphorus, and 0.032 sulfur. Room temperature yield stress was 235 MPa. Charpy energy at 0°C was only 20 J. The steel had probably been supplied in the as-rolled condition. Its properties conform to specification BS4360 43A.

Specimen Design

Figure 1 shows the specimen designs used in this study. A full list of specimen dimensions is given in Table 2. In designing the specimens, care was taken to ensure that similar out-of-plane constraint conditions were maintained by making the uncracked ligaments close to, or less than, the specimen thickness (23 mm) in all cases.

Both CCT and 3PB specimens had nonstandard features. The CCT specimens had a 40-mm-diameter hole that was introduced to allow the notches to be cut. This is remote enough from the crack tip to have only a small influence on stress intensity. The 3PB specimens had integral knife edges for mounting a mouth-opening clip gage. This is certainly no problem as far as the deeply cracked specimens are concerned but could possibly influence crack tip stresses at $a/W = 0.15$. An elastic-plastic finite element analysis would be needed to check this. Ideally, specimens with smaller a/W should have been tested. However, the measurement of crack displacement for J calculation then becomes very problematical. Load point displacement cannot be used as this will include some plastic displacement remote from the crack which does not contribute to J, and mouth-opening displacement is difficult to measure unam-

TABLE 2—*Specimen dimensions.*

Dimension	W	S	a	b	a/W
3PB	50	200	35	15	0.70
	50	200	25	25	0.50
	40	160	14	26	0.35
	35	140	9	26	0.25
	30	120	5	25	0.15
Dimension	$2W$	$2H$	$2a$	b	a/W
CCT	140	370	90	25	0.65
	140	370	110	15	0.80

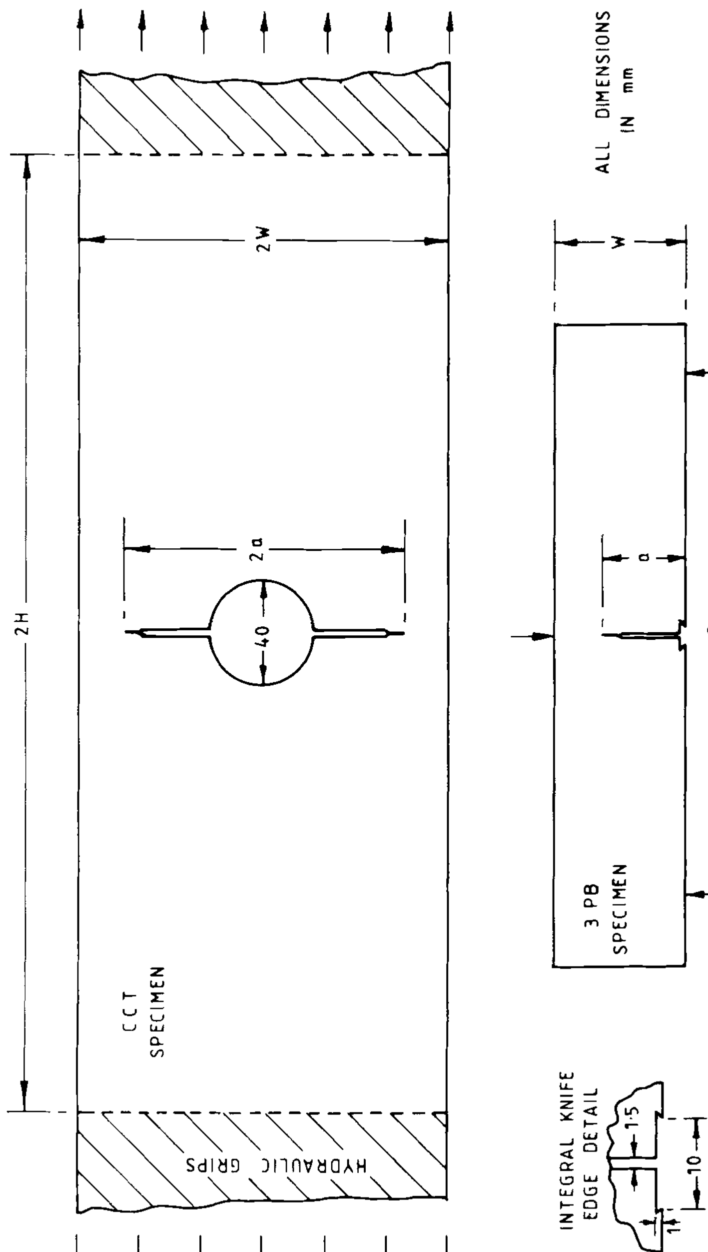

FIG. 1—*Specimen geometries used in this study. (Actual dimensions are given in Table 2.)*

biguously because of clip gage mounting problems. More elaborate techniques can be envisaged but were not possible for this study because of time constraints.

Experimental Details

Fatigue precracking of all specimens was performed at a stress intensity of around 20 to 25 MPa $\sqrt{m}$, taking care to keep the loads at below half the specimen plastic limit loads. No major difficulties were experienced either with the 3PB or the CCT specimens.

All tests were performed at $-50°C$. This temperature was easily maintainable in the 3PB tests by testing in a cold bath environment. For the CCT specimen, trays containing packed solid carbon dioxide were attached to both faces of the specimen. All specimens were individually thermocoupled to ensure temperature continuity throughout the test.

Instrumentation in the 3PB comprised a displacement transducer mounted across the specimen to obtain the plastic component of load point displacement and a mouth-opening clip gage mounted on integral knife edges as discussed previously. Displacement measurement in the CCT specimens was by two linear displacement transducers mounted at each edge of the specimen over a gage length of ± 70 mm either side of the crack plane. This gage length is sufficient to ensure that all crack tip plasticity is included in the displacement measurement. The elastic part of the displacement is not needed for the J calculation. Figure 2 shows a CCT specimen mounted in the test machine.

Forty 3PB specimens were tested in the a/W range 0.15 go 0.75. Sixteen CCT tests were carried out with a/W 0.65 to 0.8.

Calculation of J

J calculations for the 3PB specimens were made from

$$J = \frac{K^2}{E}(1 - \nu^2) + \frac{\eta_p U_p}{Bb} \tag{7}$$

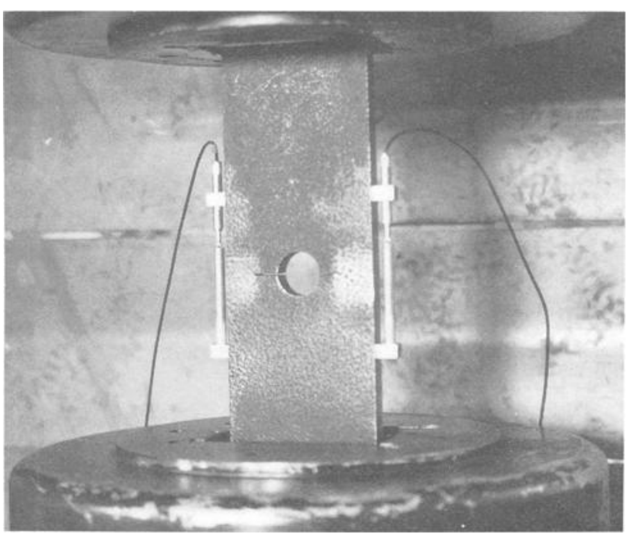

FIG. 2—*View of CCT specimen in test machine.*

where

$$\eta_p = 2.0 \text{ for } a/W \geq 0.282$$
$$= 0.32 + 12.0\, a/W - 49.5a/W^2 + 99.8a/W^3 \text{ for } a/W < 0.282$$

K is the elastic stress intensity factor, E is Young's modulus, ν is Poisson's ratio, and U_p is the area under the load versus plastic load point displacement curve.

An alternative calculation of J was made for the 3PB specimens using the area under the load versus plastic mouth opening clip gage trace, U_{vp}

$$J = \frac{K^2}{E}(1 - \nu^2) + \frac{\eta_p U_{vp}}{Bb}\frac{W}{a + rb} \tag{8}$$

where

$$r = 0.45 \qquad a/W \geq 0.3$$
$$= 0.3 + 0.5a/W \qquad a/W < 0.3$$

The derivation of Eqs 7 and 8 is given in Ref *12*.

J for the CCT specimens was calculated from

$$J = \frac{K^2}{E}(1 - \nu^2) + \frac{U_p}{2Bb} \tag{9}$$

U_p was calculated from the average of the edge-mounted displacement transducers (Fig. 2). An interesting feature of the results was the appearance of an upper yield on the load versus displacement traces. No special account was taken of this. It was simply included in U_p. J_c was calculated at cleavage fracture, which was well defined in all tests.

Results

Figure 3 compares J_c for the 3PB specimens calculated from load point displacement, Eq 7, and from mouth-opening displacement, Eq 8. Over the main a/W range tested (0.15 to 0.75), the two methods give nearly identical J_c.

Figure 4 shows J_c from load point displacement as a function of a/W for the 3PB specimens. There is a gradual trend for average J_c to increase with decreasing a/W, but the effect is very much less marked than previously found by the author in weld metals [*13*]. There is also considerable scatter, with one very low individual J_c result being recorded for a specimen with a/W of 0.19.

This specimen together with a total of three others, marked with an asterisk in Fig. 4, was found to have virtually no fatigue crack (approximately 0.5 mm). These results could have been discarded as invalid, but as one data point (at $a/W = 0.19$) lies well below the scatter band while two others (at $a/W = 0.11$) lie well above the scatter band, it is impossible to ignore them without comment. The absence of a fatigue crack would normally be expected to elevate toughness. However, if this particular material is not very sensitive to notch acuity, as would be suggested by the low result at $a/W = 0.19$, the two results at $a/W = 0.11$ could be the result of a sharp upswing in toughness at small a/W.

Figure 5 show J_c as a function of T/σ_y for both the 3PB and CCT specimens. As noted earlier, the T/σ_y values have been individually calculated from the failure load in each specimen. All data points, including those invalid through absence of fatigue cracks, have been included. The

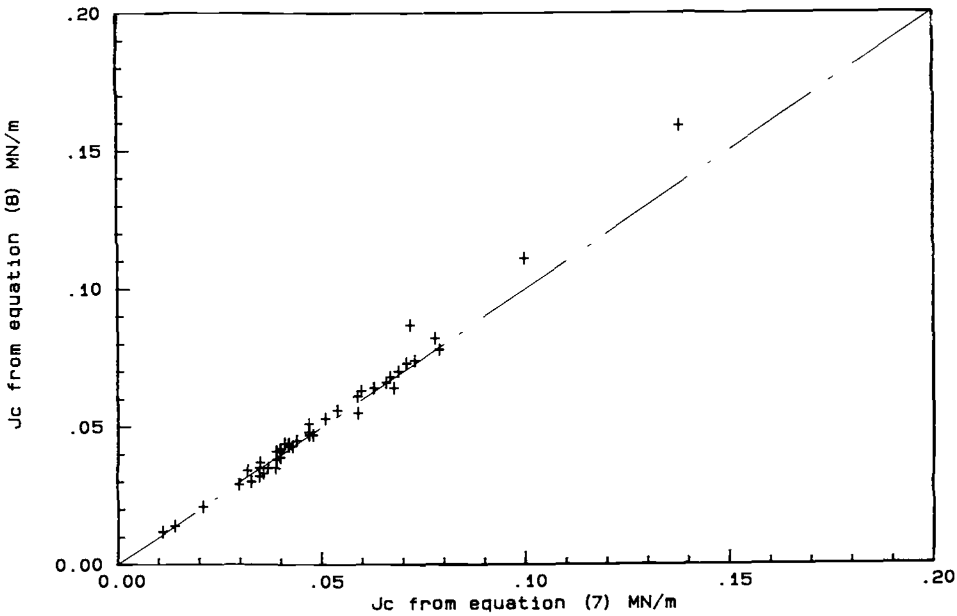

FIG. 3—*Comparison of different* J_c *calculation methods for 3PB specimens.*

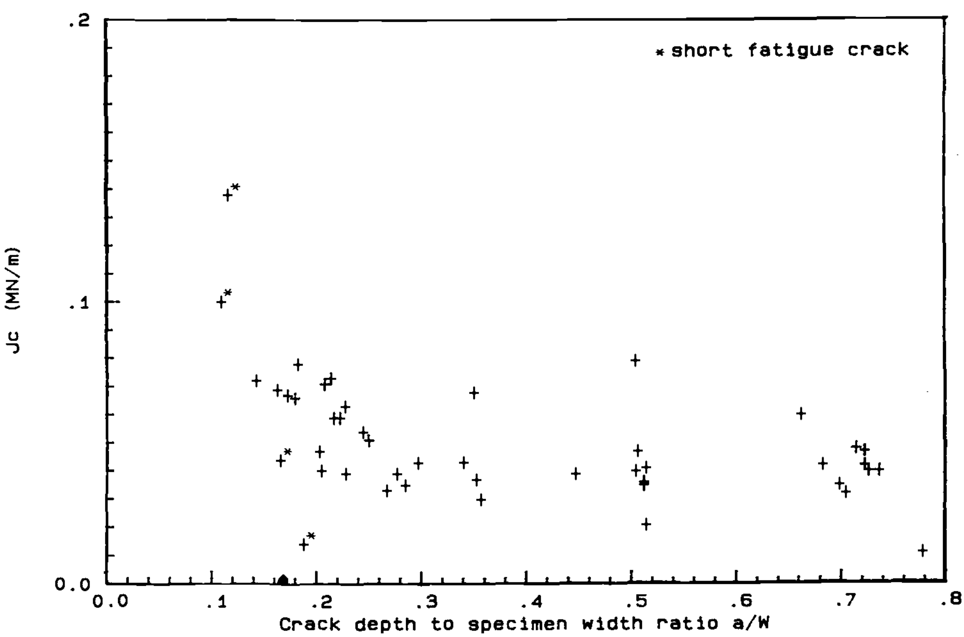

FIG. 4—J_c *as a function of* a/W *for 3PB specimens.*

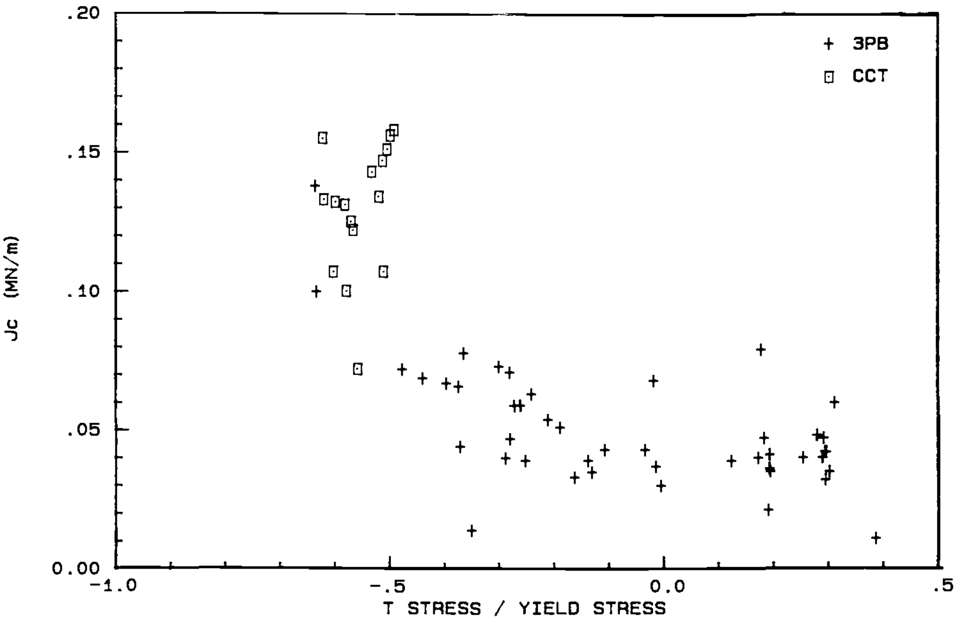

FIG. 5—J_c *as a function of nondimensional* T *stress for 3PB and CCT specimens.*

yield stress used to normalize the T stress was 270 MPa. This value was derived from an average of limit loads in the CCT specimens.

The elastic component of J in all tests (3PB and CCT) lay in the range 0.010 to 0.018 MN/m. It can thus be seen from the J_c values in Fig. 5 that cleavage fracture is only occurring in most specimens after significant plastic flow. In some of the CCT tests, the plastic component of J accounts for more than 90% of J_c.

The CCT J_c values are consistently higher than those from the 3PB tests with $a/W \geq 0.15$. The only two 3PB specimens which show comparable J_c values to the CCT specimens are those with invalid fatigue cracks at $a/W = 0.11$. The fact that T/σ_y values for some 3PB specimens in Fig. 5 are larger than those in Table 1 is due to the experimental loads exceeding the theoretically predicted plastic limit loads.

Conclusions

A number of theoretical studies have identified the T stress as a useful parameter to index the severity of crack tip stress elevation in different plane strain geometries at a given applied J. It is implied that if two different specimens have the same T stress they will fail at the same value of applied J (J_c for cleavage).

It is shown that this hypothesis can be tested by using shallow-cracked three-point-bend (3PB) and deeply cracked center-cracked-tension (CCT) specimens. These two geometries have the same negative T stress at plastic limit load, which implies they will show elevated J_c compared with conventional deeply cracked bend specimens where T stress is positive.

Experimental data have been presented for a low-grade mild steel at −50°C. The 3PB specimens showed only a small elevation of J_c with considerable scatter, as a/W was decreased from 0.75 to 0.15. Limited evidence of an upswing in J_c was obtained from two 3PB specimens with invalid fatigue cracks at a/W of 0.11. The CCT data ($0.65 < a/W < 0.8$) showed consistently higher J_c values than those obtained in the 3PB specimens with $a/W \geq 0.15$. There was, however, an overlap with the two invalid 3PB tests at $a/W = 0.11$.

It is concluded that rationalization of J_c data from 3PB and CCT specimens in terms of T stress looks promising, but it requires further experimental confirmation. To increase the data base presented here for mild steel, it is planned to perform further 3PB tests at a/W near 0.1. This will be done using material from the broken halves of the CCT specimens.

Acknowledgments

Thanks are due to Andrew Forbes, who performed all the tests described in this paper.

References

[*1*] Larsson, S. G. and Carlsson, A. J., "Influence of Non-Singular Stress Terms on Small Scale Yielding at Crack Tips in Elastic-Plastic Materials, "*Journal of Mechanics and Physics of Solids,* Vol. 21, 1973, pp. 263–277.

[*2*] Shih, C. F. and German, M. D., "Requirements for a One Parameter Characterization of Crack Tip Fields by the HRR Singularity," *International Journal of Fracture,* Vol. 17, No. 1, 1981, pp. 27–43.

[*3*] Anderson, T. R. and Dodds, R. H., "Specimen Size Requirements for Fracture Toughness Testing in the Transition Region," submitted to *Journal of Testing and Evaluation.*

[*4*] Al-Ani, A. A. and Hancock, J. W., "*J* Dominance of Short Cracks in Tension and Bending," *Journal of Mechanics and Physics of Solids,* Vol. 39, No. 1, 1991, pp. 23–43.

[*5*] Betegón, C. and Hancock, J. W., "Two Parameter Characterization of Elastic-Plastic Crack Tip Fields," to be published in *ASME Journal of Applied Mechanics.*

[*6*] Bilby, B. A., Cardew, G. E., Goldthorpe, M. R., and Howard, I. C., "A Finite Element Investigation of the Effect of Specimen Geometry on the Fields of Stress and Strain at the Tips of Stationary Cracks," *Size Effects in Fracture,* Institution of Mechanical Engineers, 1986.

[*7*] Harlin, G. and Willis, J. R., "The Influence of Crack Size on the Ductile to Brittle Transition," *Proceedings of the Royal Society of London,* Vol. A415, 1988, pp. 197–226.

[*8*] Williams, M. L., "On the Stress Distribution at the Base of a Stationary Crack," *ASME Journal of Applied Mechanics,* Vol. 24, 1957, pp. 109–114.

[*9*] Sham, T. L., "The Determination of the Elastic T-term Using Higher Order Weight Functions," Department of Mechanical Engineering Report, Rensselaer Polytechnic Institute, Troy, NY, 1989.

[*10*] Leevers, P. S. and Radon, J. C., "Inherent Stress Biaxiality in Various Fracture Specimen Geometries," *International Journal of Fracture,* Vol. 19, 1982, pp. 311–325.

[*11*] Millar, A. G., "Review of Limit Loads of Structures Containing Defects," *International Journal of Pressure Vessels and Piping,* Vol. 32, Nos. 1–4, 1988, pp. 197–327.

[*12*] Sumpter, J. D. G., "J_c Determination for Shallow Notch Welded Bend Specimens," *Fatigue and Fracture of Engineering Materials and Structures,* Vol. 10, No. 6, 1987, pp. 479–493.

[*13*] Sumpter, J. D. G., "Prediction of Critical Crack Size in Plastically Strained Welded Panels," *Nonlinear Fracture Mechanics, Vol. II: Elastic-Plastic Fracture, ASTM STP 995,* American Society for Testing and Materials, Philadelphia, 1989, pp. 415–432.

Author Index

Subject Index

ISBN 0-8031-1481-8